Research on Engineering Structures Materials

P-ISSN: 2148-9807 E-ISSN: 2149-4088 www.jresm.org

Volume 9

Issue 1

February 2023

MIM Research Group

The International Journal of **Research on Engineering Structures and Materials (RESM**) is a peer-reviewed open access journal (p-ISSN: 2148-9807; o-ISSN: 2149-4088) published by MIM Research Group. It is published in February, June, September, and December.

The main objective of RESM is to provide an International academic platform for researchers to share scientific results related to all aspects of mechanical, civil, and material engineering areas.

RESM aims the publication of original research articles, reviews, short communications technical reports, and letters to the editor on the latest developments in the related fields.

All expenditures for the publication of the manuscripts are most kindly reimbursed by *MIM Research Group*. Thus, authors do not need to pay for publishing their studies in the journal.

The scope of the journal covers (but not limited to) behavior of structures, machines and mechanical systems, vibration, impact loadings and structural dynamics, mechanics of materials (elasticity, plasticity, fracture mechanics), material science (structure and properties of concrete, metals, ceramics, composites, plastics, wood, etc.,), nano-materials performances of new and existing buildings and other structural systems, design of buildings and other structural systems, seismic behavior of buildings and other structural systems, repair and strengthening of structural systems, case studies and failure of structural systems, safety and reliability in structural and material engineering, use of new and innovative materials and techniques in energy systems and mechanical aspects of biological systems (biomechanics and biomimetics).

The topics covered in JRESM include:

- Structural Engineering
- Mechanical Engineering
- Material Engineering
- Earthquake Engineering
- Nano-technology
- Energy Systems (Focus on Renewable)
- Biomechanics and Biomimetics
- Environment (Material and Engineering System Related Issues)
- Computer Engineering and Data Science (Material and Engineering System-Related Issues)

Abstracting and Indexing
Please visit http://www.jresm.org for more information.

Graphics and Design

Yunus Demirtaş ydemirtas@jresm.net

RESEARCH on ENGINEERING STRUCTURES & MATERIALS

Research Group

RESEARCH on ENGINEERING STRUCTURES & MATERIALS

Editorial Board

Editorial Office

In This Issue

Research on Engineering Structures & Materials
MIM Research Group Publications
P-ISSN: 2148-9807
E-ISSN: 2149-4088
http://www.jresm.org

ABSTRACTING / INDEXING

The international journal of Research on Engineering Structures and Materials (RESM) is currently Abstracted/Indexed by Asos Indeks, CiteFactor, Cosmos, CrossRef, Directory of Research Journal Indexing, Engineering Journals (ProQuest), EZB Electronic Journal Library, Global Impact Factor, Google Scholar, International Institute of Organized Research (I2OR), International Scientific Indexing (ISI), Materials Science & Engineering Database (ProQuest), Open Academic Journals Index, Publication Forum, Research BibleScientific Indexing Service, Root Indexing, Scopus, Ulakbim TR Index (Tubitak), Universal Impact Factor and under evaluation by many other respected indexes.

Check web site for current indexing info, www.jresm.org

Research on Engineering Structures & Materials
journal homepage: http://www.jresm.org
Research Group

Research Article

Wear studies on Al-Si automotive alloy under dry, fresh and used engine oil sliding environments

Akib Abdullah Khan[1,a], Mohammad Salim Kaiser[*2,b]

[1]*Department of Mechanical Engineering, Bangladesh University of Engineering and Technology, Dhaka-1000, Bangladesh*
[2]*Directorate of Advisory, Extension and Research Services, Bangladesh University of Engineering and Technology, Dhaka-1000, Bangladesh*

Article Info

Article history:

Received 16 Aug 2022
Revised 17 Sep 2022
Accepted 20 Sep 2022

Keywords:

Al-Si alloy;
Tribological properties;
Engine oil;
Worn surfaces;
Micrographs

Abstract

A comparative study has been made on the wear behavior of eutectic Al-Si automotive alloy under a dry, fresh and used engine oil sliding environment. The wear tests have been conducted using a standard pin-on-disc apparatus. The results show that with silicon content, the wear loss decreases up to the eutectic composition, mainly for an increase in strength through Si-rich intermetallics. Therefore the lower wear rate along with the coefficient of friction is observed under dry sliding environment. Under the engine oil environment, the lubricating film controls the wear, so the results are the lowest wear rate and coefficient of friction. Used oil shows both wear rate and friction coefficient to some extent higher due to the presence of heavy and harmful chemical compounds. Wear test surfaces are examined by optical and SEM analysis and found that higher abrasive wear and plastic deformation on the worn surfaces are created in dry sliding condition as well as lower Si added alloy. On the worn surface under engine oil lubricating condition, smooth surface morphology is observed as form a lubrication film and thumbs down any direct contact on the moveable surfaces. Higher Si-added alloys contain superior fine intermetallics due to ageing, which is responsible for such smooth worn surfaces.

1. Introduction

Aluminum alloys are widely used in transportation and other industries because they offer different useful properties like improved wear and corrosion resistance, good castability and a better combination of mechanical properties [1-3]. Among the various cast aluminum alloys known, Al-Si alloys have been well considered for these applications, mainly in automobile industries, e.g. cylinder heads, engine blocks, pistons, bearings etc. When Si is alloyed as the major elemental, it belongs to the 4xxx series of aluminum alloys. This series of alloys can be hypo-eutectic, eutectic, or hyper-eutectic, depending on the concentration of Si in it. The Al-Si alloy with 12.6 wt% Si is eutectic. The alloy is hypo-eutectic and hyper-eutectic if the concentration of Si is lower and higher than the eutectic composition, respectively [4, 5]. It has been previously studied and found that a certain amount of Si in automotive alloys enhances the strength to meet the required demand. Therefore, hypoeutectic Al-Si alloys can be used in light applications, and eutectic alloys have moderate automotive applications. On the other hand, hyper-eutectic alloys are used for heavy structures [6]. Al-Si alloys are also used in the aviation industry. Saracyakupoglu et al [7, 8] conducted wear-based fractographic investigations on aviation-grade parts. In these studies, it was shown that Al-Si alloy-based aviation-grade parts are commonly used while there are fatigue possibilities depending on the

[*]Corresponding author: mskaiser@iat.buet.ac.bd
[a] orcid.org/0000-0001-9237-6408; [b] orcid.org/0000-0002-3796-2209
DOI: http://dx.doi.org/10.17515/resm2022.505ma0816

working conditions of the aircraft. It is well established that Al-Si alloys are the most important alloys in terms of wear properties and improve with the concentration of Si in the alloys [9]. Wear is one of the most commonly encountered problems in industries, necessitating the replacement of mechanical components that are required but unserviceable. Although the consequences of wear are rarely catastrophic, it significantly reduces operating efficiency and brings about increased power losses [10]. For enhancement of the strength, other alloying elements such as Fe, Ni, Cu, Mg etc. are added to Al-Si alloys [11]. However, in most cases, Cu and Mg have been considered alloying elements for the reason that the strength of the alloys accelerates through heat treatment. Eutectic or near eutectic Al-Si alloys form needle or plate-like silicon particles [12-14]. On the other hand, hyper-eutectic alloys form silicon particles as large cuboids, which control the strength and fracture behavior of the alloys [15-17]. Alloying elements play a vital role in the structure of these alloys. It includes type of bonding, atomic or molecular arrangements, microstructure etc. [18-20].

The lubrication method is normally employed to reduce the wear and friction for two or more moving surfaces. Engine oil as a lubricant helps to reduce wear by creating a lubricating film between two moving mating parts, therefore, decreasing the contact between them. Due to the prolonged use of engine oil, it loses lots of its quality, as dust, combustion byproducts, blow-by gases or worn or corroded particles get mixed with it. Among the foreign materials, there are carbon, metal particles, road dust and burnt oil, and these do not separate from the oil easily [21]. So the quality of used oil has a significant role in the performance and long life of an engine. That is why the engine oil must be changed on regular basis [22, 23].

Nevertheless, there is no sufficient report regarding the influence of Si on friction and wear behavior of Al-Si alloy automotive alloys under fresh and used engine oil conditions. The primary purpose of this study is to analyze the wear performance of the automotive Al-Si alloys for different concentrations of Si under a dry sliding environment while keeping the percentages of other prime elements fixed. As there is lubricating motor oil flowing between the machine parts in engines, wear study under engine oil environment is of great interest. Again, as many particles are intruded into the engine oil after prolonged use, properties of oil like viscosity, thermal stability, oxygen stability etc. are changed, which may have a substantial effect on the wear behavior of automotive alloys. Hence, an additional investigation has been made for the best performed Al-Si alloy on the wear behavior in fresh engine oil and in the same graded oil collected from a vehicle after running for around 5000 km.

2. Materials and Methods

The intention was to add different levels of Si into the automotive alloys while keeping the other alloying elements such as Cu, Mg and Fe constant. The chemical composition analyzed by spectrochemical methods after melting is shown in the following Table 1.

Table 1. Chemical composition by wt% of the experimental alloys

	Si	Cu	Mg	Fe	Ni	Al
Alloy 1	0.244	2.158	0.767	0.211	0.199	Balance
Alloy 2	3.539	2.309	0.784	0.273	0.217	Balance
Alloy 3	6.149	2.113	0.754	0.301	0.264	Balance
Alloy 4	12.656	2.130	0.770	0.311	0.277	Balance
Alloy 5	17.851	2.190	0.755	0.321	0.281	Balance

For developing these alloys, aluminum (Al99.750), copper (Cu99.997), magnesium (Mg99.80) and the master alloy of Al–50%Si alloys were melted in a graphite crucible using a natural gas-fired pit furnace. A suitable flux cover was used to avoid oxidation during melting. Casting was done at 700 °C in a mild steel mould of 20 mm x 200 mm x 300 mm size, which was preheated at 250 °C. The cast alloys were homogenized at 450 °C for 12 hours, and the samples were solutionized at 535 °C for 2 hours, followed by salt water quenching using an electric muffle furnace. The sample of 14 mm in length and 5 mm in diameter were machined from the experimental alloys for wear study. The samples were aged at 200 °C for 240 minutes to attend the peak aged condition [24, 25]. Alloy densities were considered from the chemical composition. The hardness of the aged samples was measured using a Rockwell Hardness testing machine where a 1/8th inch ball in the B scale was used. Tensile testing was carried out according to ASTM specification at room temperature in an Instron testing machine at the strain rate of 10^{-3} s^{-1}.

The frictional and wear behavior of the aluminum alloys were investigated in a pin-on-disc type wear apparatus by the following ASTM standard G99-05 [26]. The 309s stainless steel disc was used as the counter surface material having hardness and roughness around HRB 95 and 40 μm, respectively. A load of 20 N was used for all the samples in the dry sliding condition, where the calculated contact pressure was active at 1.02 MPa. Moreover, the load was incremented from 5 to 50 N in other experiments. During the test, the disc was rotated at 200 rpm on a track of 49 mm diameter at the sliding speed of 0.51 ms^{-1} with variable sliding distances ranging from 154 m to 2770 m. All the tests were carried out in ambient conditions at 22 °C and 70% humidity. At least five tests were completed for every material. The specimens were first subjected to dry sliding conditions and then chronologically to the fresh engine oil and used engine oil. For both the oil environments, drip-type single-point lubrication at the contact interface of the sample and the stainless steel counter plate was maintained with a constant rate of discharge throughout the experiment. The multigrade motor oil 20W-50 was considered for wear test under a lubricant environment. This type of engine oil contains 78 wt% base oil, 10% viscosity improvement additive and 3% detergent [27].

The engine oil of the same grade was collected from an automobile after 6 months of running 4950 km and was considered as used oil. The wear rate was calculated from the measured weight loss (ΔW), the distance run during the test (*S.D.*), and the normal load (L) applied to the samples [10]. The sliding distances were calculated from the track diameter and speed of rotation of the disc. The reading from the load cell (F) was normalized by the applied normal load, L, to determine the coefficient of friction (μ). The mathematical relations to obtain the weight loss, specific wear rate (*S.W.R.*) and the coefficient of friction are expressed by the following equations:

$$\Delta W = W_{initial} - W_{final} \tag{1}$$

$$S.W.R. = \frac{\Delta W}{S.D. \times L} \tag{2}$$

$$\mu = \frac{F}{L} \tag{3}$$

Microstructural observation of the worn specimen surfaces and wear debris from the test were done by using USB digital microscope. The SEM analyses were conducted by using a JEOL scanning electron microscope type of JSM-5200. Some photographs of the prepared sample, counter disc and the experimental setup are shown in Fig. 1.

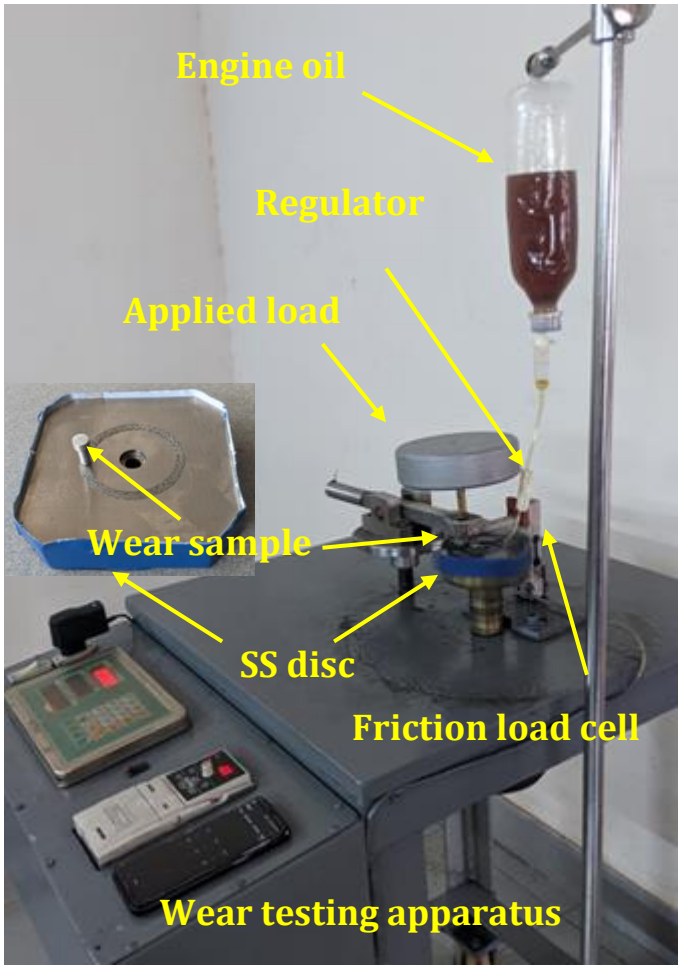

Fig. 1 Photographs of wear testing machine setup with wear sample and friction disc

3. Results and Discussion

3.1. Physical and Mechanical Properties

Figs. 2 to 5 show the different physical and mechanical properties such as density, hardness, tensile strength and elongation of different Si-added automotive alloys, respectively. From the chart, it is observed that density decreases with the addition of Si (Fig. 2). It is known that the density of Si is 2.329 gm/cm^3, which is lower than that of Al, 2.7 gm/cm^3. The percentages of the other elements in the alloys are more or less constant except Si and Al [28]. So, the higher levels of Si make the alloy lighter.

Similarly, the figure associated with the Rockwell hardness displays the opposite nature of density (Fig. 3), where the hardness of the aged alloys increases with the concentration of Si percentages into the alloys. The aged samples contain different types of intermetallics but Al_2Cu, Al_2CuMg, Mg_2Si and Al_5FeSi phases are common which are responsible for the higher hardness. Higher amount of Si into the alloys produces higher amount of Si-rich intermetallics, resulting in higher hardness [24, 29].

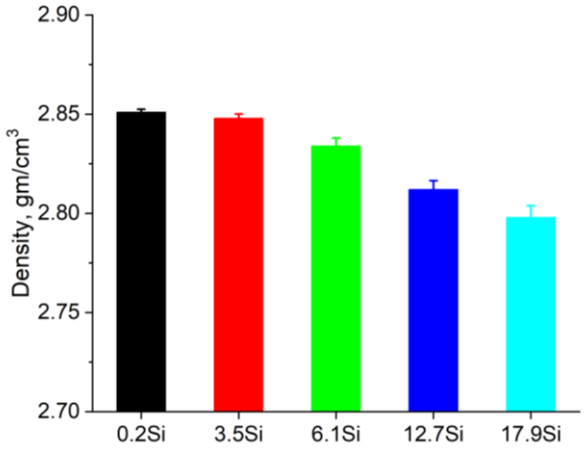

Fig. 2 Variation of density of the experimental alloys

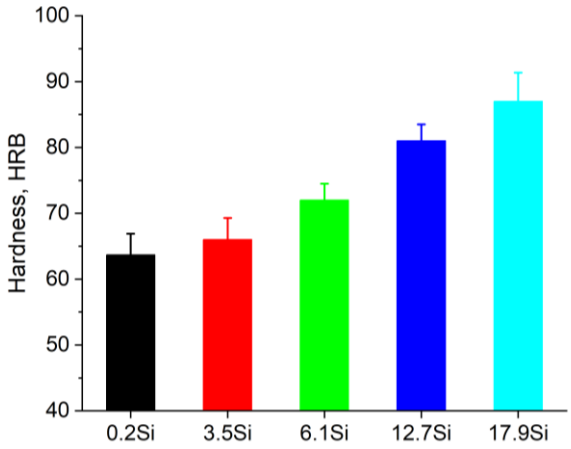

Fig. 3 Variation of hardness of the experimental alloys

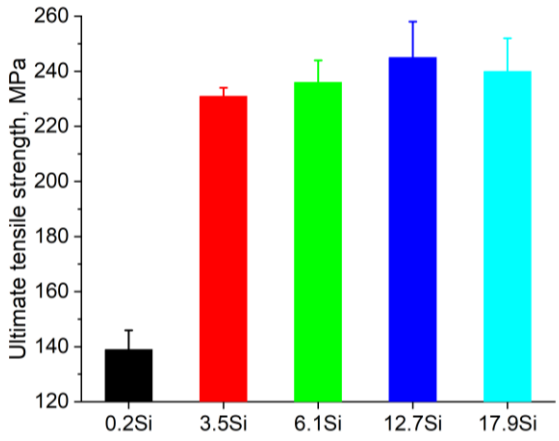

Fig. 4 Variation of ultimate tensile strength of the experimental alloys

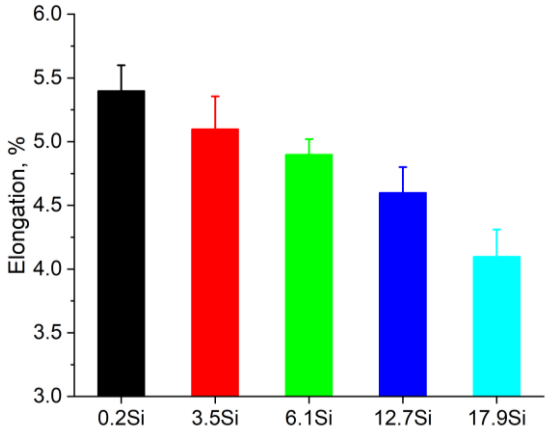

Fig. 5 Variation of % elongation of the experimental alloys

It is seen from Fig. 4 that Si addition into the aged alloys increases the tensile strength up to the eutectic composition of the alloys. During ageing, it forms the intermetallic hardening phase Mg_2Si, in addition to Al_2Cu, which precipitates in the α-aluminum matrix and increases the tensile strength. Higher levels of Mg_2Si precipitates in higher Si added alloys make strength of the alloy superior [30]. However, when the primary silicon appears as coarse polyhedral particles, the strength properties decrease with increasing silicon content [31].

The figure of percentages elongation confirmed that Si has an impact showing the reduction of this property (Fig. 5). The rate of ductility minimizing with the Si content is easily understandable. Higher Si means the density of fine precipitates are maximum into the alloy, which makes the alloys brittle resulting in lower elongation [32]. Another cause of lower elongation is, higher amount of Si stays slackly into the alloy's matrix [20, 33].

3.2. Wear Behavior

The weight losses, as a function of sliding distance for all the alloys at a constant pressure of 20 N or 1.02 MPa and velocity of 0.51 m/s under dry sliding conditions is shown in Fig. 6. The weight loss of the alloys increases with sliding distance, but higher Si added alloys show lower weight loss compared to the other lower Si added alloys. But the hyper-eutectic 17.9Si added alloy shows some deviation. During wear test, with increasing the sliding distance, the duration of contact between the rotating disc and sample surface also increased, resulting in further weight loss. Present results on the general wear loss behavior of aluminum alloys agree to some extent with the previous study [10]. These types of alloys consist of different particles like Al, Si, Cu, Mg, and Fe elements. Due to solution treatment and ageing, it forms different intermetallics into the Al matrix. It should be stated that especially formation of the Mg_2Si phase improved the friction and wear properties of the alloys. Higher Si addition means a higher level of Mg_2Si phase is formed, which inhibits weight loss. The obtained results are supported by the hardness values in Fig. 3. It is revealed that the Al-Si alloy with Si content beyond the eutectic composition 12.7Si has the primary Si particles. During the test, increased amount of Si may have a tendency to pull out, which could eventually result in a three-body abrasive wear process [34-36]. It means that, the fractured primary Si particles promote worn surface damage and act as third-body abrasives [37]. So the conventional casting and heat treatment of this type of the eutectic Al-Si automotive alloy offers the best wear properties, and beyond eutectic composition there is deterioration of wear property.

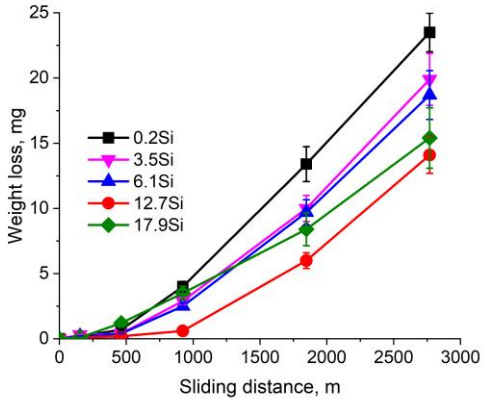

Fig. 6 Variation of the weight loss with sliding distance in dry sliding environment

The influence of sliding distance on the wear rate of 0.2Si and 12.7Si added automotive alloys under dry, fresh and used engine oil sliding environment is shown in Figs. 7 to 9 respectively. Figure 7 clearly reveals that under the dry sliding condition, as distance increases, wear rate increases in both alloys. The increase in wear rate can be attributed to frictional heat and softening of materials as prolonged intimate contact between the two mating surfaces [38]. The thermal softening of alloys is initiated due to excessive pressure and temperature and is time-dependent. So it occurs more effectively if dry sliding is continued for a prolonged period [39-41]. However, the automotive alloy with higher Si addition has shown relatively better wear resistance when compared to 0.2Si alloy. Probably, the addition of Si has resulted in microstructural modifications which contribute to an increase in hardness and strength of the base alloy, thereby reducing the surface damage and thereby increasing wear resistance. Furthermore, during wear tests, the generation of an intermediate oxide layer between mating surfaces is also one of the probable reasons for increased wear resistance. The additional amount of Si forms Mg_2Si phases with the Mg particles present in the alloys. When the alloy surface gets into contact with air, Mg_2Si further forms MgO and SiO_2 layers [42, 43]. In addition, the fine and uniformly distributed Si phase usually enhances passivation on edges during friction and can reduce the stress concentration, thereby increasing the strength between the Si and the matrix and improving the wear resistance [36].

The wear rate of the alloys drastically decreases under engine oil sliding environment. Under dry sliding condition, there are direct contacts between two mating surfaces which dominate the properties, as a result, higher loss of materials. When the materials go under engine oil environment, the material removed through the wear to a certain extent take over on the lubricating film [44]. In case of wear under fresh and used engine oil sliding environment, the graphs show the opposite phenomenon where wear rate decreases with the sliding distance (Figs. 8 and 9). It is because engine oil slows down the heat generation moreover preventing the softening of contact materials. In both environments, the higher 12.7Si alloy shows better wear performance since its higher strength. In the case of wear in used oil, both alloys show an inferior property in terms of wear rate. The used engine oil contains several metal particles, combustion by-products and gases, worn particles, so loses its quality. Foreign particles are highly toxic along with the corrosive products, which affects the wear rate of the alloys resulting in higher wear rate [21]. Early obsession noted that 12.7Si added alloy shows relatively lower wear rate as Si-rich intermetallics inhibit the wear in such environment [10].

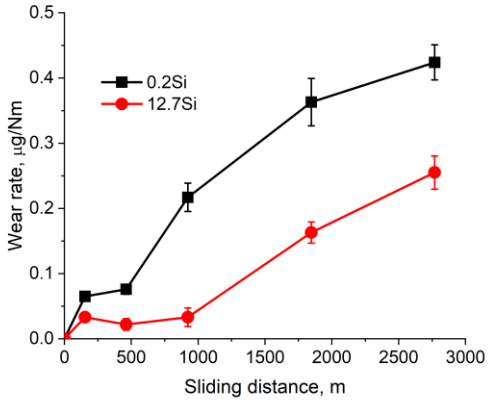

Fig. 7 Variation of wear rate with sliding distance in dry sliding environment

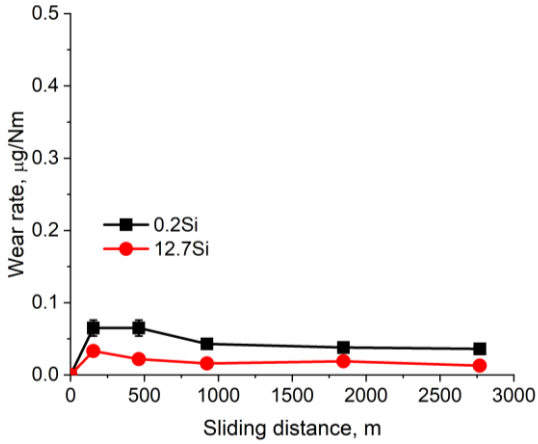

Fig. 8 Variation of wear rate with sliding distance in fresh oil sliding environment

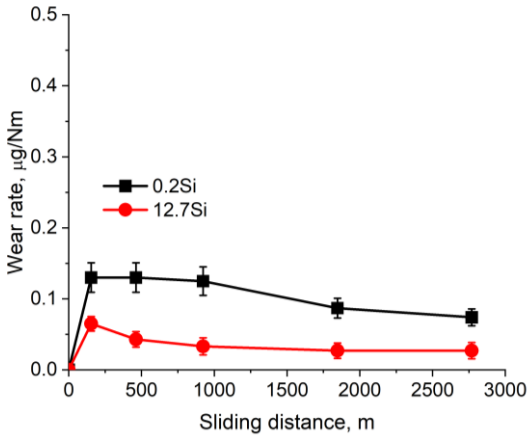

Fig. 9 Variation of wear rate with sliding distance in used oil sliding environment

Influences on the frictional force at different sliding distances for the 0.2Si and 12.7Si automotive alloys under the above-said sliding environments are represented in Figs. 10

to 12. It clearly reflects that the frictional coefficient of both alloys fluctuates at the lower sliding distances at a constant pressure of 1.02 MPa and at a constant sliding speed of 0.51 m/s. As initially, the surfaces in contact are comparatively rougher, the coefficient of friction is not steady in the beginning. However, the frictional coefficient is relatively lower for 12.7Si added alloy than that of 0.2Si alloy. A decrease in frictional force can be attributed to better hardness and strength, as the low plastic deformation of the alloy at real contact areas may lead to a lack of friction coefficient [45]. It is also due to the creation of an intermediate oxide-rich layer between mating surfaces which acts as a solid lubricant [46]. At the initial stage, the friction coefficient of the sample increases to a peak value, followed by a gradual steady-state value. The increased coefficient of friction is attributed to a localized adhering of the worn debris to the Al surface, as reported in previous investigations [37].

The coefficient of friction for both alloys in the engine oil environment is much lower than under dry conditions. It is because an oil film is developed between the tribo-pair, which reduces the roughness of the contact surfaces. In the used engine oil environment, there is some additional friction coefficient as some foreign particles are there. Foreign particles like worn-out metal, carbon, road dust etc. hinder relative motion. It also rapidly attains a steady state while establishing the lubricating mechanism. In the case of wear under engine oil environment, the scenario of the coefficient of friction is changed, where 12.7Si added alloy attains the higher coefficient of friction. In this condition, the friction is controlled by the lubricating film leading to the lower value of 0.2Si alloy. Under these circumstances, the Si particles lose their role of frictional properties. The film produced by the used oil makes the higher coefficient of friction [44, 47].

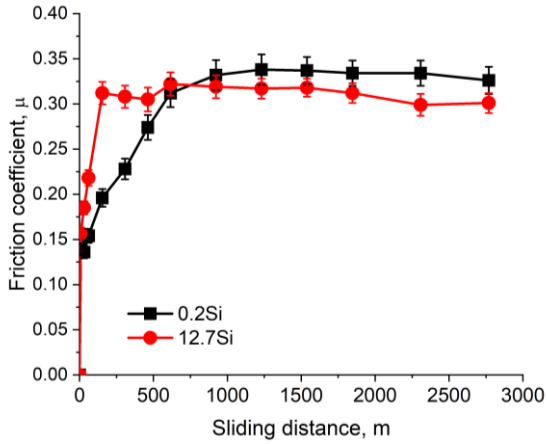

Fig. 10 Variation of coefficient of friction with sliding distance in dry sliding environment

Fig. 13 shows the deviation in the coefficient of friction for both alloys during dry sliding under different loads. Such a reduction in friction coefficient may be associated with the development of oxide layers. The increase in temperature between the disc and pin surfaces due to increasing load acts as the driving force for oxidation increase. Apart from Si particles are deformed into tiny fragments and act as a solid lubricant at the interface. These deformed particles carry the majority of the applied load under incessant sliding, so there is an inferior coefficient of friction [48].

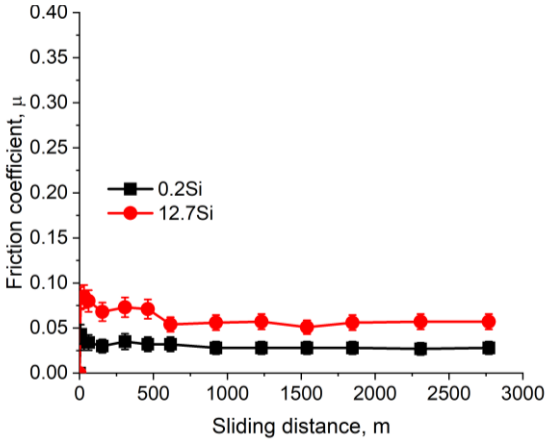

Fig. 11 Variation of coefficient of friction with sliding distance in fresh engine oil sliding environment

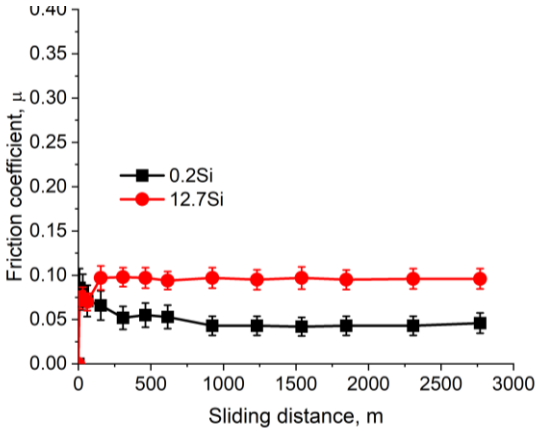

Fig. 12 Variation of coefficient of friction with sliding distance in used engine oil sliding environment

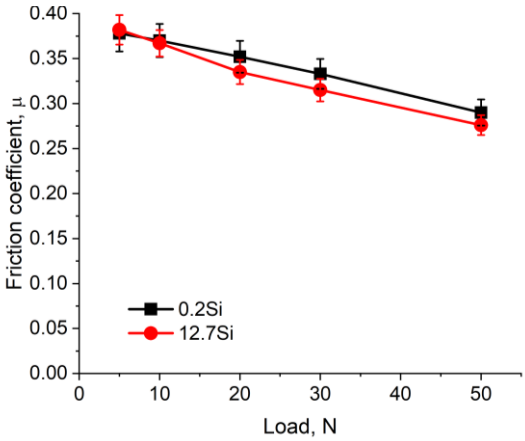

Fig. 13 Variation of friction coefficient with applied load in the dry sliding environment

Again, under the engine oil environment, opposite scenario is observed as the increasing trend of coefficient of friction with a normal load. These related graphs are shown in Figs. 14 and 15. This phenomenon occurred because the increased amount of worn-out particles from the counter body are mixed with the engine oil continuously, changing the oil film between the tribo-pair, in case of alloys with higher Si content. The harder surface of the alloys with higher Si wears away material from the counter surface. As a result, there is a continuous increase in the coefficient of friction with the load. This tendency goes up as the used oil already contains a number of heavy particles and additional components from engine wear. It is already discussed earlier regarding the quality of used engine oil.

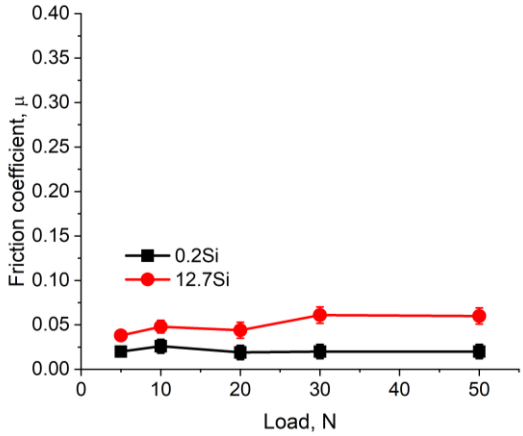

Fig. 14 Variation of friction coefficient with applied load in fresh engine oil sliding environment

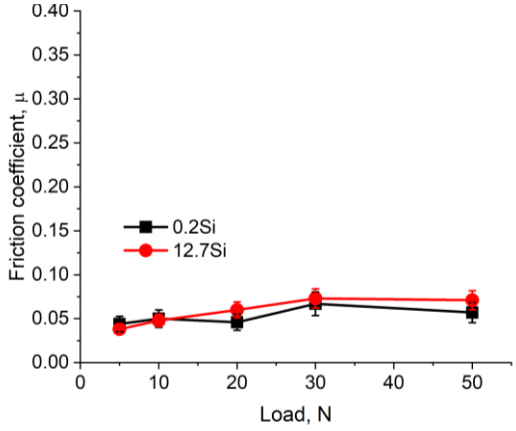

Fig. 15 Variation of friction coefficient with applied load in used engine oil sliding environment

3.3. Optical microscopy

The optical images presented in Fig. 16 are of the worn surfaces of 0.2Si, and 12.7Si added automotive alloys before and after wear for 2770 m at applied pressure of 1.02 MPa and sliding velocity of 0.51 m/s under dry, fresh and used engine oil sliding condition.

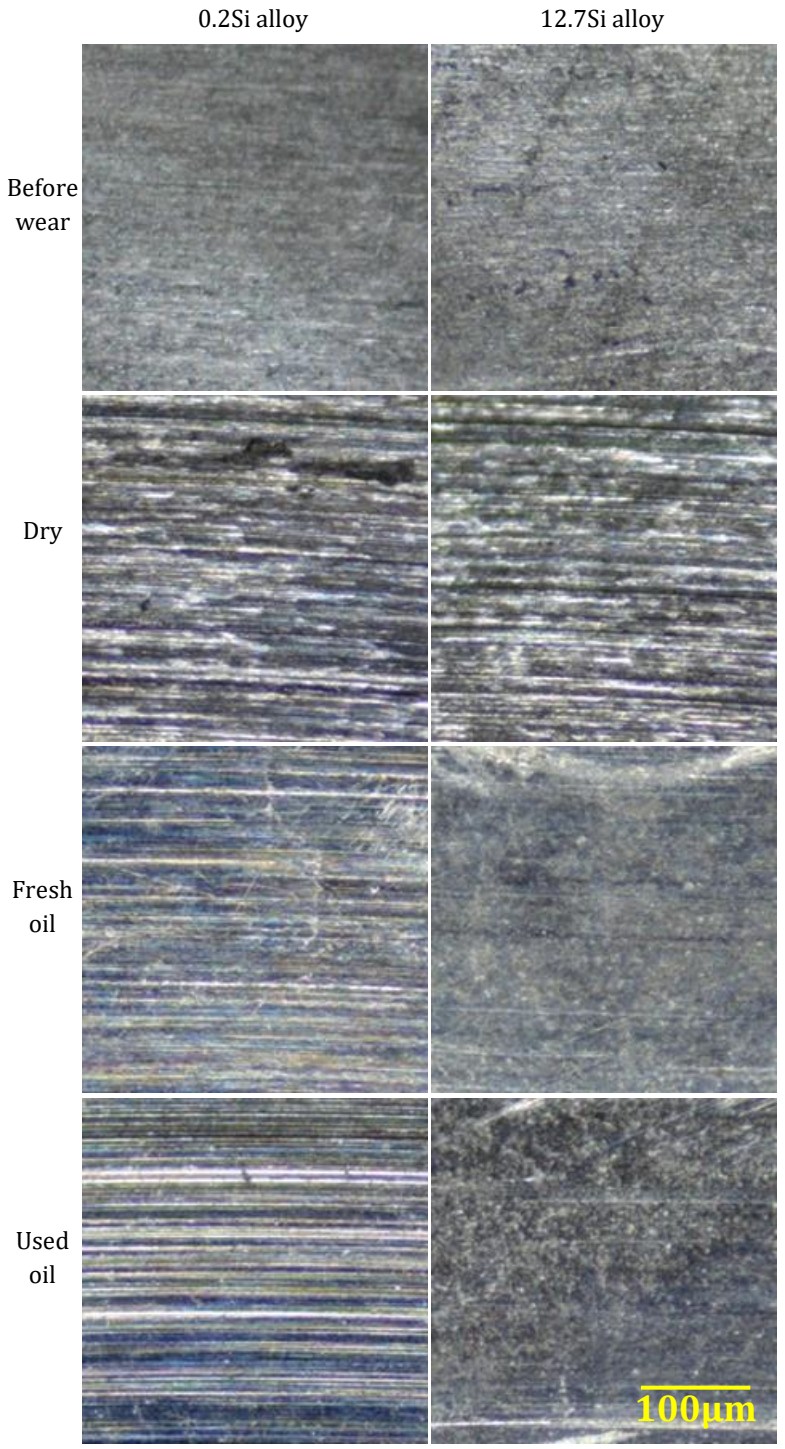

Fig. 16 Optical micrograph of polished surfaces of experimental alloys before and after wear in dry, fresh and used engine oil sliding environment for 2770 m at applied pressure of 1.02 MPa

Before wear, both the alloys display smooth and no evidence of plastically deformation surfaces. Without etching, the polished microstructure does not offer available information. However, this type of alloy consists of Al-rich dendritic matrix, α-Al phase, and a eutectic mixture in the interdendritic region. Therefore polished surfaces display some different tones since various levels of alloying elements are present in the alloys. The tone turns lighter and darker depending on the number of elements present in the alloys. However, the dark spots became more prominent on the surface of the 12.7Si added alloy because of the increasing percentage of Si in the Al matrix [49].

In dry sliding condition, the worn surfaces clearly show grooves running parallel to the sliding direction, the localized flow of surface material followed by delaminating of material and surface cracks. From the figure, it can also be observed that the wear marks in the worn surfaces of higher Si-added alloy were lower as the higher Si-rich phase increased the strength of this alloy. In the fresh oil sliding environment, the worn surfaces of both the alloys display a smooth surface, but the smoothness of 12.7Si alloys is higher than that of 0.2Si alloy. It is because the oil inhibits the thermal softening as well as the direct contact between two moving surfaces of the material, causing minimum removal of metal. The higher Si added alloy contains different fine precipitates and so higher smooth surfaces. As discussed earlier, the used engine oil contains different harmful particles and so produces higher wear marks on the surfaces. The alloy of 12.7Si displays a smoother surface than that of 0.2Si alloy because of Si-rich intermetallics prevent wear [50].

Figure 17 shows the optical micrographs of the dust particles created from the friction of 0.2Si and 12.7Si automotive alloys under dry conditions. The dust particles of the 0.2Si alloy, which are granular and not adherent to other particles, are mixed with some chips originating from the stainless-steel disc (Fig. 17a). Whereas Fig. 17b shows different nature, the wear particles of the 12.7Si added alloy are fused together in an almost flat continuous amount of material. Higher Si means a higher number of fine precipitates into the alloys along with the refined grain structures. This affects the size of the counter body particle as the fine grinding wheel produces the fine particles during grinding. One observation is the counter body particles are seen higher with respect to increasing Si contents alloys as higher hardness [51].

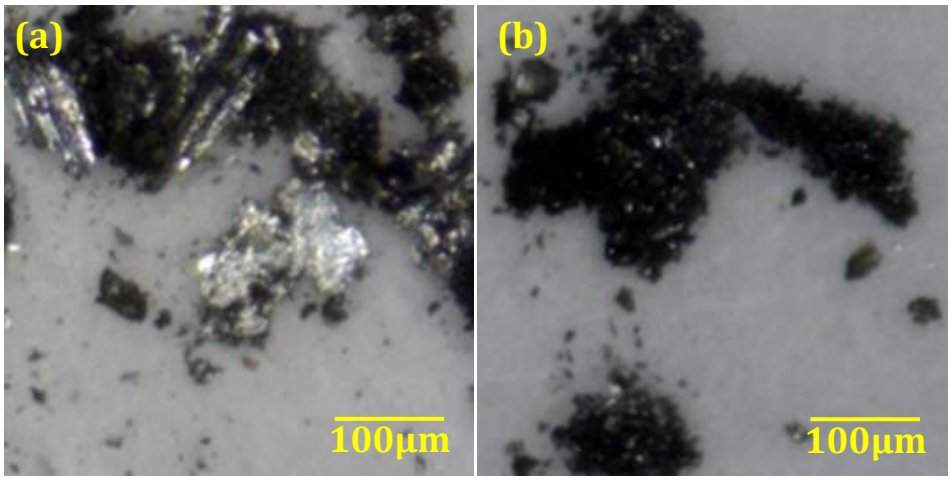

Fig. 17 Optical micrograph of dust of dry sliding condition (a) 0.2Si and (b) 12.7Si

3.4. Scanning electron microscopy

SEM microphotographs of 0.2Si and 12.7Si automotive alloys after wear test under different conditions at a distance of 2770 m are presented in Fig. 18. It is clearly suggesting abrasive wear in 0.2Si alloy revealing grooves due to abrading action by the hard particles, which got entrapped (Fig. 18a). For the 12.7Si added alloy under same wear environment the microphotograph revealed small cracks with grooves and dislodging of material clearly indicating combination of abrasive and delaminative wear (Fig. 18b). Further, SEM microphotographs of 12.7Si addition have revealed a reduced wear rate than that of 0.2Si alloy. The addition of Si has reduced the depth of abrasive

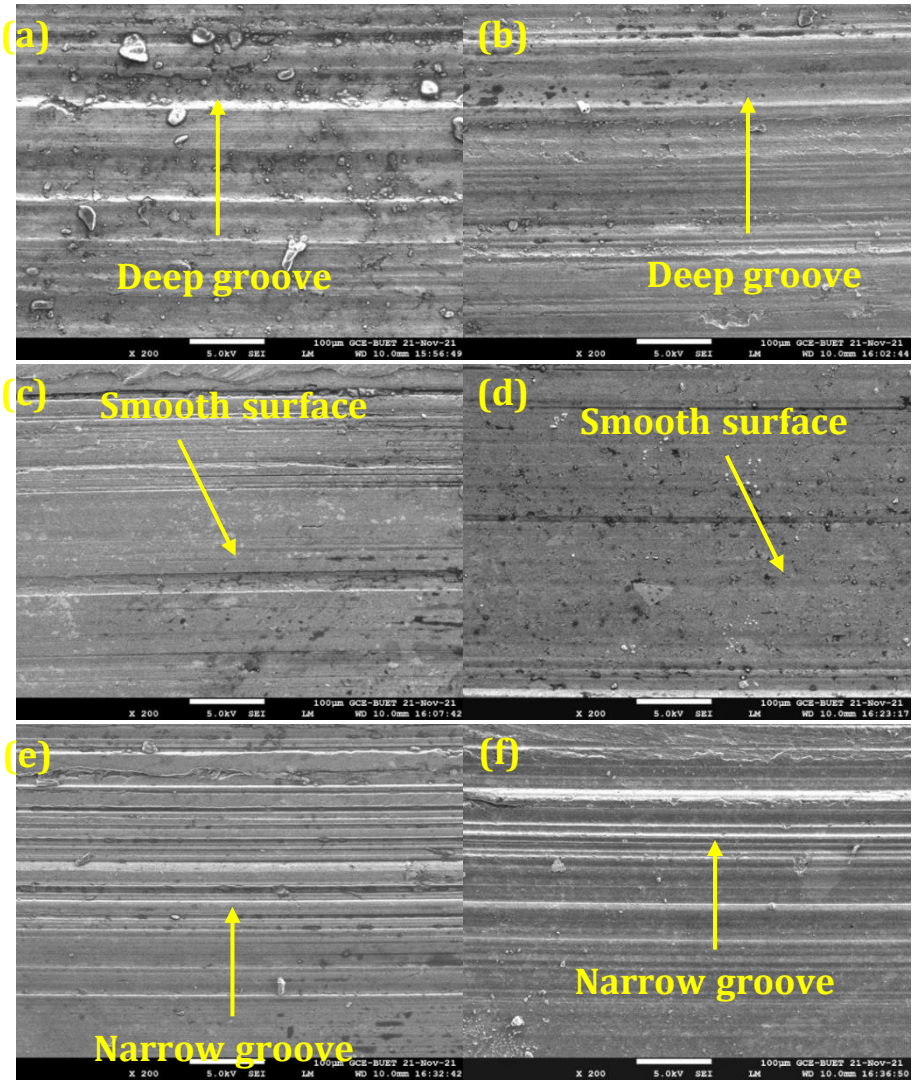

Fig. 18 SEM images of the worn surfaces of the experimental alloys in the dry condition a) 0.2Si, b) 12.7Si, in fresh oil c) 0.2Si, d) 12.7Si and used oil e) 0.2Si, d) 12.7Si after wear for 2770 m at applied pressure of 1.02 MPa

grooves due to higher hardness and an increased intermediate layer of oxide. The alloys under engine oil sliding conditions have smooth surfaces as the oil produces a thin layer

which reduces the direct contact between two movable surfaces (Fig. 18c and d). Wear is created through the engine oil under lower temperatures. While going through the used engine oil environment, both the alloys have resulted in severe wear in terms of deep grooves, as evident in Fig. 18e and 18f. SEM microphotographs of 12.7Si added alloy have revealed decreased wear rate at both conditions when compared to the lower 0.2Si added alloy. The addition of Si has reduced the depth of abrasive grooves due to higher hardness and an increased intermediate layer of oxide [22, 24].

4. Conclusions

This study investigated the influence of Si on tribological properties of the Al-based automotive alloy and made a comparison of the influence of fresh and used engine oil along with the dry sliding condition. From the study following conclusions can be drawn.

- Higher Si-added alloys achieved higher hardness due to the formation of different rigid Si-rich intermetallics through the ageing treatment. As a result, it improves the wear properties of the Al-based automotive alloys but beyond the eutectic composition forms the higher rate of primacy Si into the alloy, which weakens the matrix strength.
- The wear rate increases with sliding distance at dry sliding conditions due to thermal softening of the material but under an engine oil environment wear rate decreases as it holds back the heat generation to prevent the softening of contact materials. Heavy and harmful chemical particles in used oil increase the wear rate to some extent.
- Friction coefficient is too higher under dry sliding condition for their direct contact but lowers under engine oil environment due to the formation of thin film between the contact surfaces, which reduce the roughness. Used oil exhibits some degree of higher friction coefficient for its damaged quality.
- At dry sliding conditions, the lower coefficient of friction is observed for higher Si added alloy for its higher hardness and worked as a solid lubricant. On the other hand, under the engine oil environment, the opposite phenomenon is shown where there is a higher coefficient of friction for higher Si added alloy because the oil forms a thin lubricating film between the contact surfaces, which controls the wear properties.
- Worn surfaces in dry sliding conditions are found with higher abrasive wear and plastic deformation due to thermal softening of the material during wear. Under oil sliding condition, a smooth surface is observed as the oil forms the lubrication film and thumbs down direct contact on the moveable surfaces. Different types of harmful foreign particles in the used oil play an unenthusiastic role on the surface. Higher Si added alloy contains superior intermetallics due to ageing since responsible for such smooth worn surfaces.

Acknowledgement

The authors thank the Department of Mechanical Engineering, Bangladesh University of Engineering and Technology, Dhaka for providing the necessary facilities to carry out this work.

References

[1] Ye H. An Overview of the Development of Al-Si-Alloy Based Material for Engine Applications. Journal of Materials Engineering and Performance. 2003 Jun 1;12(3):288-97. https://doi.org/10.1361/105994903770343132

[2] Guo M, Sun M, Huang J, Pang S. A Comparative Study on the Microstructures and Mechanical Properties of Al-10Si-0.5Mg Alloys Prepared under Different Conditions. Metals. 2022 Jan 12;12(1):142. https://doi.org/10.3390/met12010142
[3] Smokvina Hanza S, Vrsalović L, Štic L, Liverić L. Corrosion investigations of Al-Si casting alloys in 0.6 M NaCl solution. Eng rev (Online). 2021;41(3):115-23. https://doi.org/10.30765/er.1577
[4] Haghshenas M, Jamali J. Assessment of circumferential cracks in hypereutectic Al-Si clutch housings. Case Studies in Engineering Failure Analysis. 2017 Apr;8:11-20. https://doi.org/10.1016/j.csefa.2016.11.003
[5] Alshmri F. Lightweight Material: Aluminium High Silicon Alloys in the Automotive Industry. AMR. 2013 Sep;774-776:1271-6. https://doi.org/10.4028/www.scientific.net/AMR.774-776.1271
[6] Javidani M, Larouche D. Application of cast Al-Si alloys in internal combustion engine components. International Materials Reviews. 2014 Apr;59(3):132-58. https://doi.org/10.1179/1743280413Y.0000000027
[7] Saraçyakupoğlu T. Failure analysis of J85-CAN-15 turbojet engine compressor disc. Engineering Failure Analysis. 2021 Jan;119:104975. https://doi.org/10.1016/j.engfailanal.2020.104975
[8] Saraçyakupoğlu T. Fracture and failure analysis of the trainer aircraft rudder pedal hanger. Engineering Failure Analysis. 2021 Apr;122:105254. https://doi.org/10.1016/j.engfailanal.2021.105254
[9] Mwema F, Obiko J, Leso T, Mbuya T, Mose B, Akinlabi E. Wear Characteristics of Recycled Cast Al-6Si-3Cu Alloys. Tribol Ind. 2019 Dec 15;41(4):613-21. https://doi.org/10.24874/ti.2019.41.04.13
[10] Kaiser MS, Sabbir SH, Kabir MS, Soummo MR, Nur MA. Study of Mechanical and Wear Behaviour of Hyper-Eutectic Al-Si Automotive Alloy Through Fe, Ni and Cr Addition. Mat Res. 2018 Jun 11;21(4):1-9. https://doi.org/10.1590/1980-5373-mr-2017-1096
[11] Khan AA, Shoummo MR, Kaiser MS. Surface Quality of Fe, Ni and Cr added Hyper-eutectic Al-Si Automotive Alloys under Up-milling and Down-milling Operation. JMEST. 2022 Jul 19;6(1):9. https://doi.org/10.17977/um016v6i12022p009
[12] Kral M. Identification of intermetallic phases in a eutectic Al?Si casting alloy using electron backscatter diffraction pattern analysis. Scripta Materialia. 2004 Aug;51(3):215-9. https://doi.org/10.1016/j.scriptamat.2004.04.015
[13] Kral M. A crystallographic identification of intermetallic phases in Al-Si alloys. Materials Letters. 2005 Aug;59(18):2271-6. https://doi.org/10.1016/j.matlet.2004.05.091
[14] Samuel E, Samuel AM, Doty HW, Valtierra S, Samuel FH. Intermetallic phases in Al-Si based cast alloys: new perspective. International Journal of Cast Metals Research. 2014 Jan;27(2):107-14. https://doi.org/10.1179/1743133613Y.0000000083
[15] Lu L, Dahle AK. Iron-rich intermetallic phases and their role in casting defect formation in hypoeutectic Al-Si alloys. Metall and Mat Trans A. 2005 Mar;36(3):819-35. https://doi.org/10.1007/s11661-005-0196-y
[16] Tupaj M, Orłowicz AW, Mróz M, Trytek A, Dolata AJ, Dziedzic A. A Study on Material Properties of Intermetallic Phases in a Multicomponent Hypereutectic Al-Si Alloy with the Use of Nanoindentation Testing. Materials. 2020 Dec 9;13(24):5612. https://doi.org/10.3390/ma13245612
[17] Ferrarini C, Bolfarini C, Kiminami C, Botta F W. Microstructure and mechanical properties of spray deposited hypoeutectic Al-Si alloy. Materials Science and Engineering: A. 2004 Jul;375-377:577-80. https://doi.org/10.1016/j.msea.2003.10.062
[18] Yang Z, He X, Li B, Atrens A, Yang X, Cheng H. Influence of Si, Cu, B, and Trace Alloying Elements on the Conductivity of the Al-Si-Cu Alloy. Materials. 2022 Jan 6;15(2):426. https://doi.org/10.3390/ma15020426

[19] Gomes LF, Kugelmeier CL, Garcia A, Della Rovere CA, Spinelli JE. Influences of alloying elements and dendritic spacing on the corrosion behavior of Al-Si-Ag alloys. Journal of Materials Research and Technology. 2021 Nov;15:5880-93. https://doi.org/10.1016/j.jmrt.2021.11.043
[20] Ervina Efzan MN, Kong H, Kok C. Review: Effe ct of Alloying Element on Al-Si Alloys. AMR. 2013 Dec;845:355-9. https://doi.org/10.4028/www.scientific.net/AMR.845.355
[21] G.A. Round, Foreign Material in Used Oil: Its Effect on Engine Design, SAE Transactions, vol. 20, pp. 65-79, 1925 https://doi.org/10.4271/250004
[22] Akintunde WO, Olugbenga OA, Olufemi OO. Some Adverse Effects of Used Engine Oil (Common Waste Pollutant) On Reproduction of Male Sprague Dawley Rats. Open Access Maced J Med Sci. 2015 Mar 8;3(1):46-51 https://doi.org/10.3889/oamjms.2015.035
[23] Ratiu SA, Tirian GO, Mihon NL, Armioni MD. Overview on globally applied used engine oil recycling technologies. IOP Conf Ser: Mater Sci Eng. 2022 Jan 1;1220(1):012034. https://doi.org/10.1088/1757-899X/1220/1/012034
[24] Toschi S. Optimization of A354 Al-Si-Cu-Mg Alloy Heat Treatment: Effect on Microstructure, Hardness, and Tensile Properties of Peak Aged and Overaged Alloy. Metals. 2018 Nov 17;8(11):961. https://doi.org/10.3390/met8110961
[25] Kaiser MS, Basher MR, Kurny ASW. Effect of Scandium on Microstructure and Mechanical Properties of Cast Al-Si-Mg Alloy. J of Materi Eng and Perform. 2012 Jul;21(7):1504-8. https://doi.org/10.1007/s11665-011-0057-3
[26] Kaiser S, Kaiser MS. Comparison of wood and knot on wear behaviour of pine timber. Res Eng Struct Mat. 2019;6(1):35-44 https://doi.org/10.17515/resm2019.115ma0207
[27] Engine Oil Composition. https://www.my-cardictionary.com/lubrication/engine-oil.html
[28] I.J. Polmear, Light Alloys-Metallurgy of the Light Metals, 3rd ed., London: Arnold, 1995
[29] Nikzad Khangholi S, Javidani M, Maltais A, Chen X. Investigation on electrical conductivity and hardness of 6xxx aluminum conductor alloys with different Si levels. MATEC Web Conf. 2020;326:08002. https://doi.org/10.1051/matecconf/202032608002
[30] Gupta A, Lloyd D, Court S. Precipitation hardening in Al-Mg-Si alloys with and without excess Si. Materials Science and Engineering: A. 2001 Nov;316(1-2):11-7. https://doi.org/10.1016/S0921-5093(01)01247-3
[31] Han Y, Samuel A, Doty H, Valtierra S, Samuel F. Optimizing the tensile properties of Al-Si-Cu-Mg 319-type alloys: Role of solution heat treatment. Materials & Design. 2014 Jun;58:426-38. https://doi.org/10.1016/j.matdes.2014.01.060
[32] Razin AA, Ahammed DS, Nur MA, Kaiser MS. Role of Si on machined surfaces of Al-based automotive alloys under varying machining parameters. Journal of Mechanical and Energy Engineering. 2022 Jul 1;6(1):43-52. https://doi.org/10.30464/jmee.2022.6.1.43
[33] Kaiser MS. Solution Treatment Effect on Tensile, Impact and Fracture Behaviour of Trace Zr Added Al-12Si-1Mg-1Cu Piston Alloy. J Inst Eng India Ser D. 2018 Apr;99(1):109-14. https://doi.org/10.1007/s40033-017-0140-5
[34] Zeng J, Zhu C, Wang W, Li X, Li H. Evolution of primary Si phase, surface roughness and mechanical properties of hypereutectic Al-Si alloys with different Si contents and cooling rates. Philosophical Magazine Letters. 2020 Dec 1;100(12):581-7. https://doi.org/10.1080/09500839.2020.1824081
[35] Alshmri F, Atkinson H, Hainsworth S, Haidon C, Lawes S. Dry sliding wear of aluminium-high silicon hypereutectic alloys. Wear. 2014 May;313(1-2):106-16. https://doi.org/10.1016/j.wear.2014.02.010

[36] Mu W, Dogan N, Coley KS. Agglomeration of Non-metallic Inclusions at Steel/Ar Interface: In-Situ Observation Experiments and Model Validation. Metall and Materi Trans B. 2017 Oct;48(5):2379-88. https://doi.org/10.1007/s11663-017-1027-4
[37] G.E. Totten, Friction, Lubrication and Wear Technology, vol. 18, Materials Park, Ohio, USA, 1992
[38] Prabhudev M, Auradi V, Venkateswarlu K, Siddalingswamy N, Kori S. Influence of Cu Addition on Dry Sliding Wear Behaviour of A356 Alloy. Procedia Engineering. 2014;97:1361-7. https://doi.org/10.1016/j.proeng.2014.12.417
[39] Wilson S, Alpas A. Effect of temperature on the sliding wear performance of Al alloys and Al matrix composites. Wear. 1996 Aug;196(1-2):270-8. https://doi.org/10.1016/0043-1648(96)06923-2
[40] B. Azarhoushang, M. Kadivar, Thermal aspects of abrasive machining processes, in Tribology and Fundamentals of Abrasive Machining Processes, Elsevier, 2022: 555-573 https://doi.org/10.1016/B978-0-12-823777-9.00008-2
[41] Sonne M, Tutum C, Hattel J, Simar A, de Meester B. The effect of hardening laws and thermal softening on modeling residual stresses in FSW of aluminum alloy 2024-T3. Journal of Materials Processing Technology. 2013 Mar;213(3):477-86. https://doi.org/10.1016/j.jmatprotec.2012.11.001
[42] Al Nur M, Khan AA, Dev Sharma S, Kaiser MS. Electrochemical corrosion performance of Si-doped Al-based automotive alloy in 0.1 M NaCl solution. J Electrochem Sci Eng. 2022 Jun 13;12(3):565-76. https://doi.org/10.5599/jese.1373
[43] Escalera-Lozano R, Pech-Canul MI, Pech-Canul MA, Montoya-Davila M, Uribe-Salas A. The Role of Mg2Si in the Corrosion Behavior of Al-Si-Mg Alloys for Pressureless Infiltration. TOCORRJ. 2010 Sep 3;3(1):73-9. https://doi.org/10.2174/1876503301003010073
[44] Hsu SM, Munro R, Shen MC. Wear in boundary lubrication. Proceedings of the Institution of Mechanical Engineers, Part J: Journal of Engineering Tribology. 2002 Jun 1;216(6):427-41. https://doi.org/10.1243/135065002762355343
[45] Moore AJW, Tegart WJM. Relation between friction and hardness, Proceedings of the Royal Society of London. Series A. Mathematical and Physical Sciences. 1952; 212(1111):452-458. https://doi.org/10.1098/rspa.1952.023
[46] Malleswararao.K N, Niranjan Kumar I, Nagesh BN. Friction and Wear Properties of Rapid Solidified H-Al-17Si Alloys Processed by UV Assisted Stir - Squeeze Casting with DLC-Star (CrN + a-c:H) Coating Under HFRR. Tribol Ind. 2020 Dec 15;42(4):529-46. https://doi.org/10.24874/ti.870.04.20.09
[47] Kaiser MS, Matin MA, Shorowordi KM. Role of magnesium and minor zirconium on the wear behavior of 5xxx series aluminum alloys under different environments. Journal of Mechanical and Energy Engineering. 2020 Dec 10;4(3):209-20. https://doi.org/10.30464/jmee.2020.4.3.209
[48] Kori S, Chandrashekharaiah T. Studies on the dry sliding wear behaviour of hypoeutectic and eutectic Al-Si alloys. Wear. 2007 Sep;263(1-6):745-55. https://doi.org/10.1016/j.wear.2006.11.026
[49] Kaiser MS, Qadir MR, Dutta S. Electrochemical corrosion performance of commercially used aluminum engine block and piston in 0.1M NaCl. J mech eng. 2015 Jul 30;45(1):48-52. https://doi.org/10.3329/jme.v45i1.24384
[50] Abdo HS, Seikh AH, Mohammed JA, Soliman MS. Alloying Elements Effects on Electrical Conductivity and Mechanical Properties of Newly Fabricated Al Based Alloys Produced by Conventional Casting Process. Materials. 2021 Jul 16;14(14):3971. https://doi.org/10.3390/ma14143971
[51] Zedan Y, Samuel AM, Doty HW, Songmene V, Samuel FH. Effects of Trace Elements on the Microstructural and Machinability Characteristics of Al-Si-Cu-Mg Castings. Materials. 2022 Jan 5;15(1):377. https://doi.org/10.3390/ma15010377

Research on Engineering Structures & Materials
journal homepage: http://www.jresm.org
MIM Research Group

Research Article

Effect of addition of TiC nanoparticles on the tensile strength of Al7075-graphene hybrid composites

Lingaraju Sannananjapla Vageshappa[*1,a], Mallikarjuna Channabasappa[2,b], Saleemsab Doddamani[3,c]

[1]*Department of Mechanical Engineering, TKIET Warananagar, India*
[2]*Department of Mechanical Engineering, VTU Center for Post-Graduate Studies, Mysore, India*
[3]*Department of Mechanical Engineering, National Institute of Technology Karnataka, Surathkal, India*

Article Info

Article history:

Received 25 Jul 2022
Revised 23 Nov 2022
Accepted 29 Nov 2022

Keywords:

Al7075-TiC/Graphene; Tensile Strength; Ultrasonic stir casting; Nano-particle composites

Abstract

In the current work, the effect of the addition of titanium carbide and graphene nanoparticles on the tensile strength of the aluminum 7075 matrix composites is investigated. The preparation of the mentioned composites is made using a novel ultrasonic stir casting process. The reinforcements used are 0.25wt% graphene nanoparticles and 0.5wt% to 2.5wt% of titanium carbide nanoparticles. Ultrasonic stir casting techniques are used to enhance the wettability of TiC and graphene nanoparticles. To quantify the microstructure of the prepared composites, SEM and EDS are used. An experimental investigation has been carried out to determine the influence of the addition of TiC and graphene nanoparticles on the tensile strength of the mentioned composite. From the SEM analysis, it is observed that the prepared composites have a uniform distribution of the reinforcements and the EDS analysis confirms the existence of reinforcing elements in the Al7075-TiC/Graphene composites. Experimental results show that the addition of TiC and graphene enhances the hardness and tensile strength. This enhancement is lost with the ductility of the Al7075-TiC/Graphene composites. The fractographic samples of the Al7075- TiC/graphene composites shows cracks in the vicinity of the matrix and reinforcements and also show a brittle fracture.

1. Introduction

The limitations of traditional monolithic materials in terms of achieving good strength, toughness, hardness, density, and strength to weight ratio, etc., recent years have seen an exponential increase in the need for low-cost, high performance materials. This has led to the development of new advanced materials. A composite material is one that is made up of two or more separate materials, each of which has its own unique set of physical and chemical properties. Metal matrix composite is a material constituting of metallic matrix combined with reinforcements. The most used matrix material is aluminium, magnesium, copper, zinc, titanium. The most commonly used reinforcements are SiC, alumina, boron, graphite and fly ash [1,2] .

One of the matrix materials which is commonly used in aerospace and aircraft applications is the reinforced aluminum matrix. Aluminum has a high strength [3] when it is chosen as low-density matrix and the main reinforcements used for improving mechanical properties are the ceramics like SiC, Al2O3, TiC, and Boron carbide. Limitations in terms of mechanical properties, working difficulties of B4C particles reinforced composites which is currently ruled in industrial applications can be significantly addressed by using aluminum as a matrix [4].

*Corresponding author: svlingaraju@tkietwarana.ac.in
[a] orcid.org/0000-0003-3882-8228; [b] orcid.org/0000-0003-3823-0015; [c] orcid.org/0000-0002-8498-1488;
DOI: http://dx.doi.org/10.17515/resm2022.486ma0725

The various processing methods of composites are stir casting, powder metallurgy, spray forming, liquid infiltration, ball milling, diffusion bonding, and soon. But the most commonly used process is stir casting & powder metallurgy due to their cost effectiveness as compared to other techniques [5] . In the present work, the ultrasonic liquid stir casting technique has been used owing to its simplicity, cost-effectiveness & complex structures can be easily developed [6–8] . Addition of B4C was done in stages preferably two (or more) to get uniform distribution of the alloy [9,10] . In the said process aluminium was heated to above melting point temperature to soften it, and the melt was stirred continuously for an appropriate time period with simultaneous addition of reinforcement in stages. The prepared specimens were examined for their microstructure using a SEM, an X-ray diffractometer (XRD), tensile tests using a UTM to determine the material behaviour, as well as hardness and wear tests. The Density of the amalgamate is also investigated & compared with the base matrix alloy [11,12] . Many researchers used nanoparticles as reinforcements in the aluminum matrix and found enhanced mechanical properties in comparison with the unreinforced and single-reinforced aluminum alloy composites [13,14].

Al7075 alloys are widely used for applications where it requires withstanding high temperatures, high hardness, and strength. The main reinforcing elements in the Al7075 are Si, Mg, Zn, and Fe. The nanoparticles of alumina [15,16] , graphene [17] , TiC [18–20] , SiC [21] , and also in combinations of many reinforcements are introduced in the Al7075 matrix to produce the hybrid composites. Various other composites were prepared using the nano-particle reinforcements are nano-MWCNT [22] , B4C-Al2O3 [23] , B4C-SiC [24], TiC-SiC [25,26], and graphene-Beryl [27] . Researchers also used the nano B4C particles in Al7075 matrix and concluded that addition of reinforcement increase the strength of composites with little increases in weight, in contrast with the monolithic aluminum, and with loss of ductility [28–30].

The mechanical behavior of aluminium matrix augmented with different nano-particulate composites has received a lot of attention in the scientific literature. This context opens up opportunities for research into the mechanical properties of hybrid aluminium composites reinforced with TiC and graphene nanoparticles. This study aims to determine how incorporating TiC and graphene nanoparticles into Al7075-TiC/graphene hybrid composites changes their microstructure and tensile behaviour.

2. Materials and Preparations

2.1. Materials

The Al7075 (aluminium alloy) is used as a matrix in this study, and TiC and graphene nano-particles (Fig.1(a-b)) are used as reinforcements to reinforce the structure. The fundamental reason for using these materials is that their densities are practically the same, for example, Al7075 having density of 2.81g/cc and graphene having density of 2.267g/cc. As a result, if the composite is manufactured using the liquid metallurgical method, the dispersion of reinforcements in the matrix will become nearly homogeneous. Aside from that, pure Al7075 has unusually low tensile and yield strengths, with a tensile strength of 80-130MPa and the yield strength measuring 60 MPa, respectively. Ceramics such as TiC and graphene, in particular, are used in high-temperature applications because their melting temperatures are higher than those of other ceramics. Graphene has a melting point of 4250 °C, while SiC has a melting point of 3100 °C. As a result, developing hybrid composites with titanium carbide (TiC) and graphene increases their hardness and tensile strength while reducing their elongation. They are also employed in situations where high temperature resistance is required.

It is the reinforcement's particle size that is most important in determining the material characteristics of the composites. The reinforcement's particle size will have a considerable impact on the microstructure of the composites, among a variety of other aspects. The particle sizes of the reinforcements that were used in this experiment are as follows: TiC has a diameter of 50 nm and graphene has a thickness of 5-10 nm. It is preferred to manufacture the mentioned composite utilizing the liquid metallurgical approach, like the ultrasonic stir casting method (Fig.1(c)) , because it has numerous advantages, like being more cost- effective and simpler to use, as well as ensuring equal dispersion of the reinforcements throughout the matrix.

(a)

(b)

(c)

(d)

(e)

(f)

Fig. 1 (a) Al7075 blocks; (b) TiC and Graphene particles; (c) Ultrasonic stir casting setup used in the fabrication of MMC; (d) Casted composites; (e) Hardness and (f) Tensile specimens

2.2. Processing

The graphite crucible was charged with Al7075 and heated to 800°C. The temperature was kept near around 800°C for an hour and to decrease the amount of gas in the aluminium melt, a C_2Cl_6 degassing tablet was employed. Mg particles with a larger grain size were used as a flux to improve the wettability of reinforcements when stirring molten liquid. The nanoparticles were dispersed into the liquid using an adaptation of the double stir casting technique.

The liquid metal pool was introduced to and agitated with, preheated titanium carbide (TiC) and graphene nano-particles at vertex formation speed at 370 to 420 rpm for 30 minutes at 450°C to ensure compatibility with the liquid metal and to avoid organic contaminants and moisture.

In terms of two equal steps, this process will be continued for 20 minutes. A 10-minute stirring period preceded the creation of a semisolid state in between each stage. Adding nanoparticles automatically increased the viscosity of the melt of the aluminum alloy. The

flow ability of nanoparticles in a liquid substance was improved to reduce viscosity, and a higher melting temperature of 800°C was maintained inside the crucible to assure the effectiveness of the sonication process. After that, an ultrasonic cavitation process was used for 10 minutes using the probe made of titanium alloy, which is high-temperature resistant. The liquid metal was stirred by a mechanical stirrer for five minutes after the sonication procedure to disperse the blasted clusters and agglomerations. An ultrasonicator with a frequency of 18 to 25 kHz has been used to avoid amalgamation of nanoparticles in casting, and vibrating waves generated by the ultrasonicator will help in uniform distribution of hybrid nanoparticles. The liquid metal was stirred by a mechanical stirrer for five minutes after the sonication procedure to disperse the blasted clusters and agglomerations. The molten liquid was then immediately poured into a graphite mold that had been preheated to 500°C and let to cool naturally at room temperature for 24 hours. The cylindrical work pieces (Fig.1 (d)) were taken out of the mold after they had solidified and machined as per ASTM standards for various tests (Fig.1 (e-f)). Similarly, the processing of aluminum matrix hybrid composites with various wt.% of nano-TiC, including 0.5 to 2.5wt%, and nano-graphene, 0.25wt%, were made. The tensile and micro hardness test specimens were prepared in accordance with ASTM standards.

3. Experimentation

Universal testing equipment was used for tensile tests as per ASTM E8, and the Micro Vickers hardness machine for hardness tests as per ASTM E384. SEM was used to examine the dissemination of ceramic particle reinforcement in the composites. The various elements present in the various parts of the sample were identified using an energy-dispersive spectroscopy (EDS) record. The test specimen is indented using a diamond indenter as part of Vickers' indentation hardness testing process. The diamond indenters in use have a square base, a pyramidal shape, and a point at a 136^0 degree angle in the middle. The indenter applies the load of 0.5kgf on the specimen material for 10sec. After the applied force has been removed, the specimen's indentation has been measured using a microscope for both surface diagonals, and the average value has been considered. The area of diagonal slant surfaces' is calculated. The ratio obtained by dividing the kgf load by the square mm indentation area is known as the Vickers hardness. The circular rod of mentioned hybrid composites is tested to evaluate the ultimate tensile strength as per ASTM E8 standard. To brighten and reduction of the effects of surface area faults on the specimen, fine grit grinding mesh paper was utilized. The tensile test was carried out using a computerized universal testing machine (UTM) loaded with a 50 kN load. The values of the load and displacement were recorded.

4. Results and Discussions

4.1 Microstructure

The existence of the three principal alloying elements (Zn, Mg, and Cu) confirmed by the energy dispersive spectroscopy (EDS) study of the matrix Al7075 (Fig. 2a).

Due to their low content, alloying elements of less than 0.1wt% cannot be seen in the graph. Additionally, a small oxygen peak can be seen in the Al7075 EDS spectra. To confirm that the created hybrid composites contained an Al7075 matrix, 0.5 to 2.5wt% TiC reinforcements, and 0.25wt% of graphene, the EDS analysis of the hybrid composites was conducted (Fig 2(b-f)). It should be highlighted that the spectrum of the Al, Ti, and C peaks confirms the presence of Al7075, TiC, and graphene in the casted hybrid composite samples. The peaks of the alloying elements Cu, Zn, and Mg could be seen in the hybrid composite sample. Oxygen peaks, on the other hand, were furthermore noticed and are

related to the creation of oxides during the ultrasonic stir casting process. Table inside the Fig 2 shows the various alloying elements of the mentioned hybrid composites. Thus, it confirms the presence of Zn, Mg, and Cu which are the reinforcing elements in Al7075. The presence of Ti and C indicates the reinforcing elements such as TiC and graphene in the prepared hybrid composites.

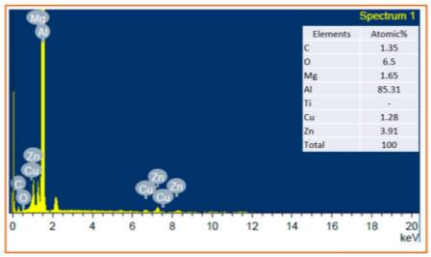

(a) Al7075+0wt%TiC+0.25wt% Graphene

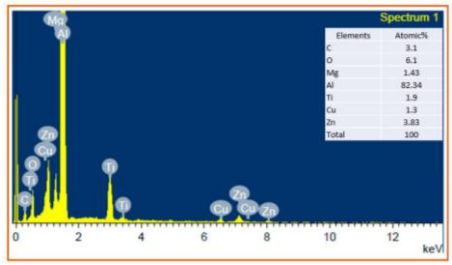

(b) Al7075+0.5wt%TiC+0.25wt% Graphene

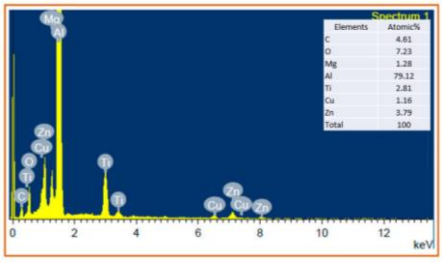

(c) Al7075+1.0wt%TiC+0.25wt% Graphene

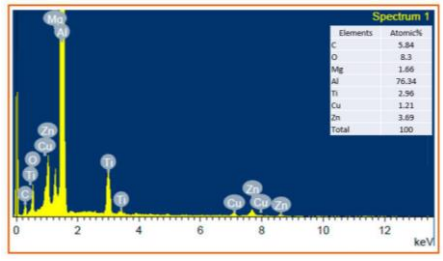

(d) Al7075+1.5wt%TiC+0.25wt% Graphene

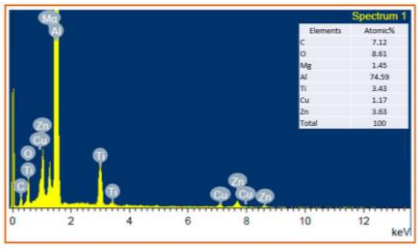

(e) Al7075+2.0wt%TiC+0.25wt% Graphene

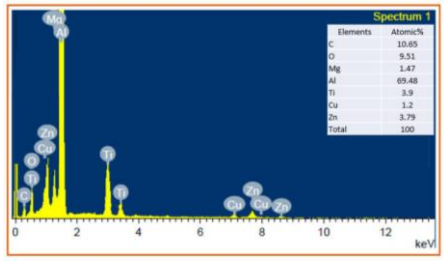

(f) Al7075+2.5wt%TiC+0.25wt% Graphene

Fig. 2 EDS Spectrum of Al7075-graphene and Al7075-graphene-TiCp composites

The elemental mapping analysis reveals that TiC and graphite (carbon) are distributed equally throughout the matrix Al7075. The EDS mapping of the mentioned hybrid composites and their reinforcements may be seen in Fig. 3. The composite was effectively cast with a random and uniform distribution of TiC and graphene in the Al7075 matrix. The presence of an 'O' indicates the development of different oxides during casting and machining.

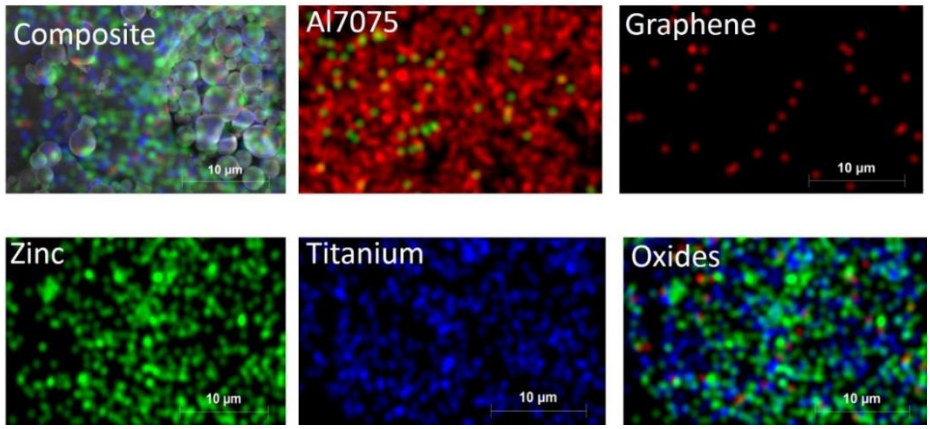

Fig. 3 EDS Images showing the mapping of composites and reinforcements

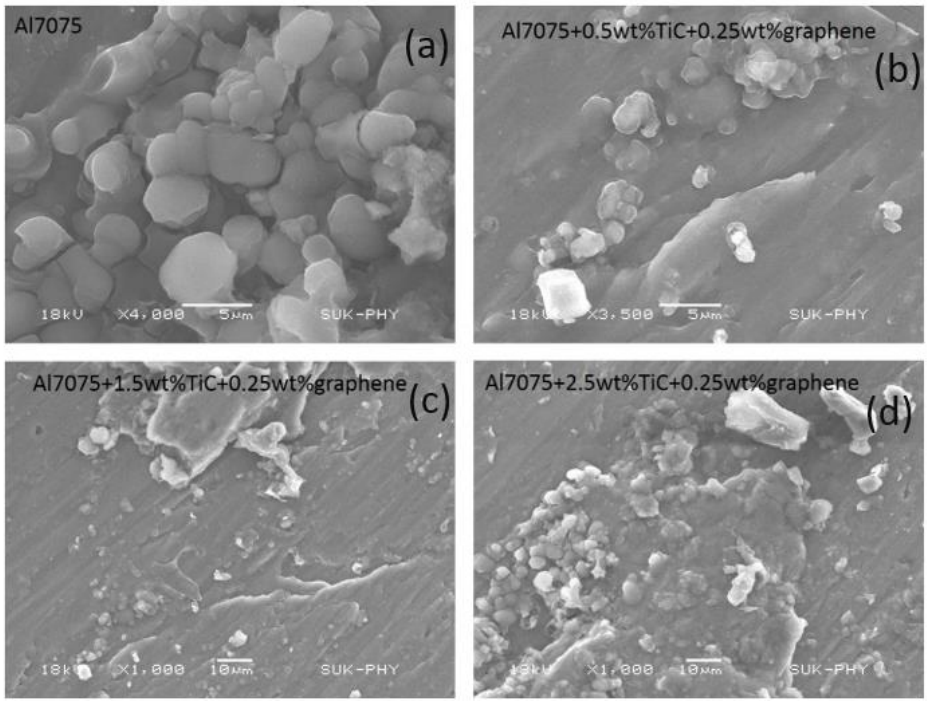

Fig. 4 SEM micrographs: (a) Al7075 alloy, (b-d) Al7075-TiC/graphene hybrid composites

4.2 Micro-Hardness

Al7075 alloy micro hardness values and different TiC concentrations in Al7075-TiC/graphene hybrid composites were measured. Fig. 5 presents a summary of the findings. The micro hardness of the composites increases as the content of nanoparticles of TiC rises. Al7075 alloy sample has a micro hardness of 88 HV. For identical experimental settings, the micro hardness of Al7075-TiC/graphene hybrid composites is increased from 88 to 127.3 HV, 44.5 percent increase over the unreinforced Al7075. This result is due to the addition of nanoparticles of TiC and graphene which can prevent grain

growth in an aluminum matrix by the pinning of grain boundaries, resulting in an aluminum alloy with finer grains. Higher micro hardness levels may be the result of finer grain formations.

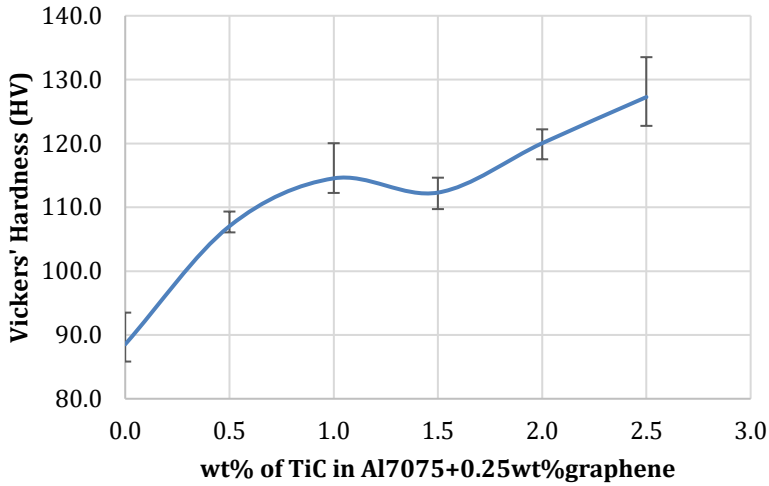

Fig. 5 Micro hardness of Al7075 alloy and the composites

4.3 Tensile Strength

The tensile strength figures for the TiC and graphene reinforced Al7075 hybrid metal matrix composites are shown in Fig 6. Al7075 hybrid composites outperform the base alloy in terms of tensile strength. The presence of hard reinforcing particles underlies the composites' strengthening effect. The aluminium alloy composite's uniform ceramic particle distribution (TiC and graphene) serves as a barrier to the matrix alloy's dislocation motion, reducing fracture. By transferring stress from the aluminum matrix's (ductile) to the reinforced particles' (brittle) surfaces, the addition of ceramic particles primarily increases the composite material's impacting fracture and tensile strength. This is due to the Orowan mechanism, which allows a dislocation to avoid significant impediments when one is constrained around a particle. This results in an increase in tensile strength. When compared to the base alloy, Al7075+2.0wt% TiC+0.25wt% graphene shows the maximum strength of 192.5 MPa, which is rose by roughly 122 MPa (or 58 percent). Fracture will result from the buildup of stress at the nucleation point.

The fracture surfaces of Al7075 hybrid MMC are shown in Fig 7. A small degree of material displacement and matrix cracks near the TiC and graphene particles are shown in the fractography of aluminum alloy composites with a higher reinforcing content. In the current study, Al7075-TiC/graphene hybrid composite fractured tensile specimens were subjected to scanning electron fractography. Investigation of the materials' failure mechanisms was done using a fractography study.

In Al7075-1.0wt%TiC/0.25wt%graphene, shallow dimples, ductile initiated brittle fractures were seen in SEM fractography. The transgranular fracture surface is provided by the presence of hard, very brittle TiC and graphene particles. Perpendicular to the applied tensile load, the TiC and graphene particles exhibit plastic deformation. Additionally, it has been noted that when TiC content increases, the production of

dimples decreases, and ductility decreases as a result. The greater TiC content causes brittle fracture, and when tensile stress was applied, TiC particles were drawn out and dragged off. Therefore, a notable transfer of external stress from Al7075 to hard particles of TiC and graphene occurred, increasing the strength as depicted in Fig.7.

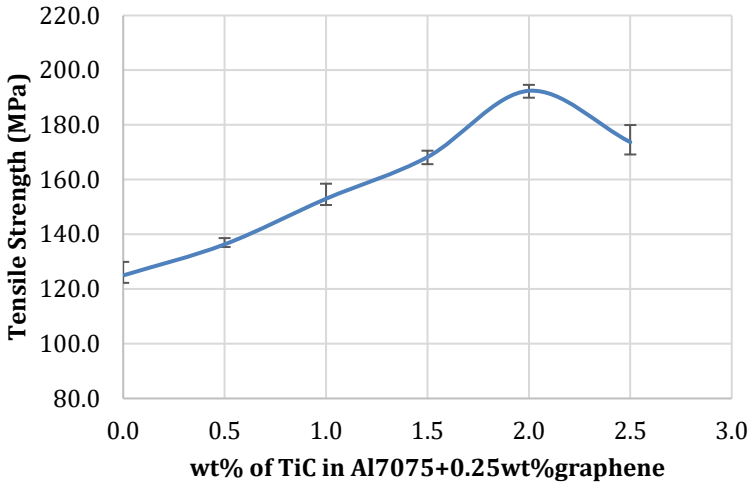

Fig. 6 Tensile strength of TiC and graphene reinforced Al7075 composites

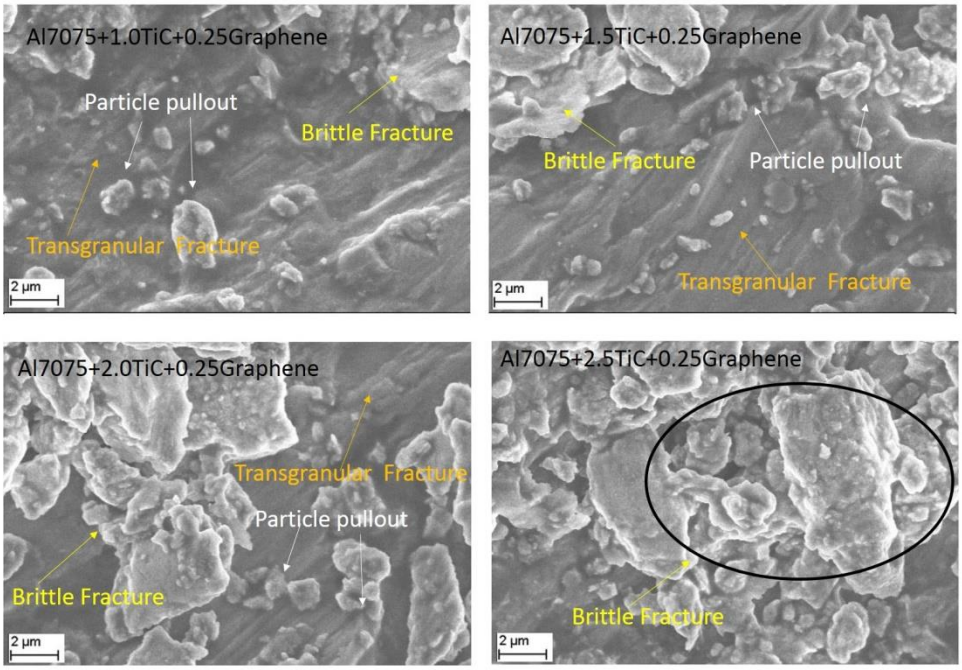

Fig. 7 SEM micrographs of the tensile fracture surface

4.4 Yield Strength and Elongation

The tensile yield strength and elongation for the TiC and graphene reinforced Al7075 hybrid metal matrix composites are listed in the Table 1.

Table 1 Mechanical properties of the Al7075-TiC/graphene composite

Sl. No	Composite	Yield Strength (MPa)	Percentage Elongation
1	Pure Al7075	94.5	14.47
2	AL7075+0.5%TiC+0.25 % Graphene	98.3	14.15
3	AL7075+1.0%TiC+0.25 % Graphene	105.0	13.76
4	AL7075+1.5%TiC+0.25 % Graphene	118.5	13.12
5	AL7075+2.0%TiC+0.25 % Graphene	133.0	12.87
6	AL7075+2.5%TiC+0.25 % Graphene	122.2	12.01

From the Table 1 it can be observed that the increment in the reinforcement such as TiC increases the yield strength of the mentioned hybrid composite material whereas addition of TiC and graphene decreases elongation. The addition of hard particles in the aluminum matrix increases the strength whereas decreases the ductility. The decrement in the ductility observed is 17% whereas the increment in the yield strength is 29%.

Table 2 shows the comparison of the properties of Al7075-TiC/graphene composite with Al7075 matrix composites.

Table 2 Comparison of mechanical properties of different composites

Sl. No	Properties	Al7075-TiC/ graphene [PW]	Al7075+TiC+Si [25]	Al7075-TiC [18]
1	Tensile Strength, MPa	192.5	155	184
2	Yield Strength, MPa	133.0	120	-
3	Percentage elongation, %	12.01	13	10
4	Density, g/cc	2.75	2.82	2.73
5	Hardness, HV	127.3	150	102

From the table it can be observed that Al7075-2.0wt%TiC/ 0.25wt%graphene composite is better than the Al7075-TiC composites and Al7075+TiC+Si hybrid composites.

5. Conclusion

- In this experimental work, the influence of the addition of the TiC and graphene nanoparticles on the tensile strength and hardness of Al7075-TiC/graphene hybrid composite has been studied. The Al7075-TiC/graphene nano-particulate hybrid composite is prepared using an ultrasonic two-step stir casting method as shown in fig.1 (a-f).
- It is confirmed by the EDX analysis, as shown in Figs. 2 and 3, that Al7075 contains reinforcing elements including Zn, Mg, and Cu. The presence of Ti and C suggests that the cast hybrid composites have reinforcements made of TiC and graphene. The random and uniform distribution of reinforcements in the aluminum matrix is confirmed by EDS elemental mapping analysis. When an "O" is present, it means that distinct oxides have formed during casting and machining. The Al7075 matrix contains reinforcement nanoparticles that are uniformly distributed without clumping, according to SEM examination.
- The micro-hardness of the Al7075-TiC/graphene hybrid composites increases with an increase in wt.% of TiC as shown in fig.5. This increment is due to the

pinning of matrix grain boundaries by the reinforcements which results in the finer grains of aluminum. The maximum micro-hardness that is obtained is 127.3HV for 2.5wt% of TiC, which is 44% higher than the unreinforced Al7075.

- The presence of uniformly distributed reinforcing particles in the Al7075 matrix as shown in fig.4, which acts as a block-off for the matrix alloy's dislocation motion, leads to increase in the strength of the composites. Also, the addition of the ceramic reinforcements takes the load of the matrix material, thus increases the tensile strength. Al7075+2.0wt% TiC+0.25wt% graphene composites as shown in fig.6 exhibits the higher tensile strength of 192.5MPa which is 54% higher than the unreinforced Al7075.
- Above results from fig.5, fig.6, and fig.7 shows that addition of TiC and graphene nanoparticles in Al7075- TiC/graphene hybrid composite, the tensile strength and hardness of the composite increases. However, this growth is gained with the loss of ductility, which is evident from the SEM images showing the brittle fracture.

References

[1] V AB, Saravanan R, Bharath V, Auradi V, Nagaral M. Mechanical and Wear Characterisation of Boron Carbide Particles Reinforced Al2030 Alloy Composites Developed by Two Stage Stir cast Method. Adv Mater Process Technol. 2022;1-15. https://doi.org/10.1080/2374068X.2022.2072084

[2] Rajesh AM, Mohamed Kaleemulla K, Saleemsab Doddamani BK. Effect of addition of SiC and Al2O3 on wear behavior of hybrid aluminum metal matrix composites. ACTA Tech Corviniensis - Bull Eng. 2019;12(1):43-52.

[3] Doddamani S, Kaleemulla MK. Effect of Aging on Fracture Toughness of Al6061-Graphite Particulate Composites. Mech Adv Compos Struct. 2019;6:139-46. https://doi.org/10.3233/SFC-180230

[4] Doddamani S, Kaleemulla M. Experimental investigation on fracture toughness of Al6061-graphite by using Circumferential Notched Tensile Specimens. Frat ed Integrità Strutt. 2017;39:274-81. https://doi.org/10.3221/IGF-ESIS.39.25

[5] Doddamani S. Fracture toughness investigations of Al6061-Graphite particulate composite using compact specimens. Frat ed Integrità Strutt. 2017;41:484-90. https://doi.org/10.3221/IGF-ESIS.41.60

[6] Madhukar P, Selvaraj N, Rao CSP, Kumar GBV. Fabrication and characterization two step stir casting with ultrasonic assisted novel AA7150-hBN nanocomposites. J Alloys Compd. 2020;815:152464. https://doi.org/10.1016/j.jallcom.2019.152464

[7] Pushpendra Kumar Jain, Prashant Baredar SCS. Development Of Silicon Carbide Particle Reinforced Aluminium 6101 Metal Matrix Composite Using Two-Step Stir Casting. Mater Today Proc. 2019;18(7):3521-5. https://doi.org/10.1016/j.matpr.2019.07.281

[8] Q. Hu, H. Zhao and JG. Microstructure and mechanical properties of (B 4 C þ Al 3 Ti)/ Al hybrid composites fabricated by a two-step stir casting process. Mater Sci Eng A. 2016;650:478-482. https://doi.org/10.1016/j.msea.2015.10.041

[9] Lakshmanan P, Vijayananth S, Sivaganesan S. Optimizing Ultrasonic Power on Fabricating Aluminum Nanocomposites Reinforced with Boron Carbide Nanoparticles. 2020;979:28-33. https://doi.org/10.4028/www.scientific.net/MSF.979.28

[10] Mohamed Kaleemulla K, Rajesh AM, Saleemsab Doddamani BKN. Generation of mechanically mixed layer during wear in hybrid aluminum MMC under as - cast and age hardened conditions. SN Appl Sci. 2019;1(860). https://doi.org/10.1007/s42452-019-0906-5

[11] Rajesh AM, Mohammed Kaleemulla K, Saleemsab Doddamani BKN. Material characterization of SiC and Al2O3 reinforced hybrid aluminum metal matrix composites on wear behavior. Adv Compos Lett. 2019;28(1-10). https://doi.org/10.1177/0963693519856356
[12] Rajesh AM, Mohammed Kaleemulla K SD. Development And Characterization Of Hybrid Aluminum Metal Matrix Composites. ACTA Tech Corviniensis - Bull Eng. 2019;12(3):63-6. https://doi.org/10.24874/ti.2019.41.03.04
[13] Jufu Jiang YW. Microstructure and mechanical properties of the semisolid slurries and rheoformed component of nano-sized SiC/7075 aluminum matrix composite prepared by ultrasonic-assisted semisolid stirring. Mater Sci Eng A. 2015;639:350-8. https://doi.org/10.1016/j.msea.2015.04.064
[14] Aravindan S, Rao PV, Ponappa K. Evaluation of physical and mechanical properties of AZ91D / SiC composites by two step stir casting process. J Magnes Alloy. 2015;3(1):52-62. https://doi.org/10.1016/j.jma.2014.12.008
[15] Suresh S, Gowd GH, Devakumar MLS. Mechanical and wear Characteristics of Aluminium Alloy 7075 Reinforced with Nano-Aluminium Oxide / Magnesium Particles by Stir casting Method. Mater Today Proc. 2020;24:273-83. https://doi.org/10.1016/j.matpr.2020.04.276
[16] K. Varna, Vijay Kumar S, M. M. Lakshmidevamma, M. M. Benal, Chithirai. Pon Selvan M, Ali Ercetin PLSM. Comparison Study of Tensile Strength Characteristics of Al2O3 reinforced Al7075 and Al6061. Adv Sci Eng Technol Int Conf. 2022;1-8. https://doi.org/10.1109/ASET53988.2022.9734894
[17] Ghazanlou SI, Eghbali B, Petrov R. EBSD characterization of Al7075 / graphene nanoplates / carbon nanotubes composites processed through post-deformation annealing. Trans Nonferrous Met Soc China. 2021;31(8):2250-63. https://doi.org/10.1016/S1003-6326(21)65652-2
[18] Scaria CT, Pugazhenthi R. Effect of process parameter on synthesizing of TiC reinforced Al7075 aluminium alloy nano composites. Mater Today Proc. 2021;37:1978-81. https://doi.org/10.1016/j.matpr.2020.07.490
[19] Ramakoteswara V, Ramanaiah N, Moulana M, Sarcar M. Mechanical and tribological properties of AA7075 - TiC metal matrix composites under heat treated (T6) and cast conditions. Integr Med Res. 2016;1-7.
[20] Du XM, Zheng KF, Zhao T, Liu FG. Fabrication and characterization of al 7075 hybrid composite reinforced with graphene and sic nanoparticles by powder metallurgy. Dig J Nanomater Biostructures. 2018;13(4):1133-40.
[21] Suresh, S., Gowd, G.H. Kumar MLSD. Mechanical and wear behavior of Al 7075 / Al 2 O 3 / SiC / mg metal matrix nanocomposite by liquid state process. Adv Compos Hybrid Mater. 2019;2:530-539. https://doi.org/10.1007/s42114-019-00101-y
[22] Bamane O, Patil S, Agarwal L, Kuppan P. Fabrication and Characterization of AA7075 Metal Matrix Composite Reinforced With MWCNT. Mater Today Proc. 2018;5(2):8001-7. https://doi.org/10.1016/j.matpr.2017.11.484
[23] Torabi O, Ebrahimi-kahrizsangi R. Synthesis of B4C, Al2O3, and AlB12 reinforced Al matrix nano composites via mechanochemical method. J Compos Mater. 2012;46(18):2227-37. https://doi.org/10.1177/0021998311430867
[24] Senthilvelan SG and T. Synthesis and Characterisation of Al 7075 reinforced with SiC and B 4 C nano particles fabricated by ultrasonic cavitation method. J Sci Ind Res. 2015;74(May):281-5.
[25] Srinivas KS, Mohan MM. Experimental Investigation of Mechanical Properties of Ceramic Reinforced Al-7075 Metal Matrix Hybrid Composites. 2020;979:34-9. https://doi.org/10.4028/www.scientific.net/MSF.979.34
[26] M. Sambathkumar, P. Navaneethakrishnan, K. Ponappa KSKS. Mechanical and Corrosion Behavior of Al7075 (Hybrid) Metal Matrix Composites by Two Step Stir

Casting Process. Lat Am J Solids Struct. 2017;14:243-55. https://doi.org/10.1590/1679-78253132

[27] Patil S, Raju BS, Haneef M, Nagaral M. Reinforcement with graphene nano platelets and Beryl in Al7075 matrix composites. Mater Today Proc. 2020;45:27-33. https://doi.org/10.1016/j.matpr.2020.09.226

[28] Shantharaj P, Prashanth AS, Nagaral M, Bharath V, Auradi V, Dharshan K. Microstructure, tensile and compression behaviour of B4C particles reinforced Al7075 matrix composites. Mater Today Proc. 2022;52:1135-9. https://doi.org/10.1016/j.matpr.2021.11.008

[29] Manjunatha TH, Basavaraj Y, Nagaral M, Venkataramana V, Harti JI. Investigations on mechanical behavior of Al7075 - Nano B4C composites. IOP Conf Ser Mater Sci Eng. 2018;376(1). https://doi.org/10.1088/1757-899X/376/1/012091

[30] M N, Reddappa HN AS. Mechanical Behavior of Al7025-B4C Particulate Reinforced Composites. J Appl Mech Eng. 2015;04(06):4-7. https://doi.org/10.4172/2168-9873.1000186

Research on Engineering Structures & Materials
journal homepage: http://www.jresm.org
Research Group

Research Article

Short-term mechanical performance and flexural behavior of reinforced slag-fly ash-based geopolymer concrete beams in comparison to OPC-based concrete beams

P.N. Ojha[1,a], Brijesh Singh[1,b*], Amit Trivedi[1,c], Pranay Singh[1,d], Abhishek Singh[1,e], Chirag Pede[1,f]

[1]*Centre for Construction Development and Research, National Council for Cement and Building Materials, India*

Article Info

Article history:

Received 02.09.2022
Revised 15.11.2022
Accepted 16.11.2022

Keywords:

Geopolymer concrete; Reinforced concrete; Mechanical properties; Flexural behavior; High strength concrete; Four-point bending test

Abstract

The study presents experimental investigation on short term mechanical properties and flexural behaviour of conventional Ordinary Portland Cement (OPC) based concrete and slag-fly ash based geopolymer concrete. Conventional and geopolymer concrete mixes were designed to achieve compressive strength equivalent to M40 and M70 grade as per Indian standard code. Mechanical properties of concrete mixes such as compressive strength, split tensile strength, flexural strength, modulus of elasticity and Poisson's ratio were evaluated and compared. The flexural behaviour of reinforced concrete beams for both conventional and geopolymer concrete has been studied using 4-point bend test. The findings suggest that geopolymer concrete shows comparable mechanical properties in terms of split tensile strength, flexural strength and Poisson's ratio. However, modulus of elasticity of geopolymer concrete is lower than the conventional concrete of equivalent strength. Studies on flexure behaviour of reinforced concrete beams shows that both geopolymer and conventional concrete exhibit comparable flexural behavior in terms of load-deflection curves, yield load and yield moment. The amount of energy dissipated in flexure is marginally higher for high strength conventional concrete. Based on the visible cracks developed in flexure, it was concluded that the reinforced conventional concrete and reinforced geopolymer concrete show similar number and type of cracks in flexure.

1. Introduction

Usage of conventional Ordinary Portland Cement (OPC) based concrete has many adverse environmental impacts. OPC production is an energy-intensive process and is a significant source of CO_2 emissions in the environment. With the growth of construction sector, the production of OPC is expected to rise exponentially, especially in developing countries. Many researchers have tried to find alternate ways to find environment friendly alternative cementitious systems, including attempts to create eco-friendly cement-free concrete to solve the issue [1, 2, 3]. As a result, geopolymer concrete has emerged as one of the widely accepted replacement for OPC based concrete. The geopolymer concrete has shown excellent structural performance [4], durability [5], better resistance to acid attack [6], good mechanical properties under chemical attack [7] and better chemical stability than conventional concrete [8]. The mechanical performance of geopolymer concrete in terms of split tensile strength and compressive strength, is also comparable to that of OPC concrete [9]. Some further advantages of geopolymer concrete include high early strength

*Corresponding author: brijeshsehwagiitr96@gmail.com
[a] orcid.org/0000-0003-1754-4488; [b]orcid.org/0000-0002-6512-1968; [c]orcid.org/0000-0002-2594-4679; [d]orcid.org/0000-0001-6169-9482; [e]orcid.org/0000-0002-2343-5934; [f]orcid.org/0000-0003-4942-9441
DOI: http://dx.doi.org/10.17515/resm2022.515me0902

[10] and good temperature resistance [11]. Geopolymer is amorphous rather than crystalline, as compared to other natural zeolitic materials [12]. Geopolymer concrete differs from conventional concrete as it does not use conventional Portland cement as a cementitious material. It uses industrial waste like fly-ash and Ground Granulated Blast Furnace Slag (GGBS). These materials act as precursors and are activated using alkaline solutions like Sodium hydroxide (NaOH) and Sodium Silicate (Na_2SiO_3). The hydration product of geopolymer concrete does not involve water; instead, as geopolymerisation reaction occur, water added to the mix gets expelled out during the subsequent drying and curing process. Activation of precursors in geopolymers is different from the hydration reactions when Portland cement is mixed with water, which produces the primary hydration products. i.e., calcium silicate hydrate (C-S-H) gel and calcium hydroxide in conventional concrete. The difference causes variations in these two concrete systems' mechanical, durability, and chemical properties [13].

Studies on conventional concrete are extensively available in literature [14]–[17] for both normal and high strength concrete. Some past studies have highlighted the mechanical properties of geopolymer concrete to establish it as a suitable replacement for conventional concrete as construction material. Numerous experiments on the fresh and hardened properties of geopolymer concrete utilizing various precursors and activators have been done by researchers across the world. It is known that the major ingredients in the geopolymerization reaction—alumina (Al_2O_3) and silica (SiO_2)—present in the precursors dissolve in water and react with alkali from the activators to form an aluminosilicate gel, which gives the geopolymer concrete mix its mechanical strength [18]. According to Ojha et al [1]. , the workability of geopolymer concrete depends on the proportion of precursors to alkaline solution as well as the ratio of Na_2SiO_3/NaOH. Due to the viscous nature of sodium silicate, an increase in the aforementioned ratios results in a larger water requirement for the creation of a workable geopolymer concrete mix.

Hutagi and Khadiranaikar [19]studied the flexural behavior of reinforced geopolymer concrete beams cured under ambient temperature. The study involved twelve reinforced concrete beams tested using four-point bend test. The authors reported geopolymer beams' behavior to be similar to the conventional concrete beams in flexure. In a similar study, El-Sayed and Algash [20] evaluated the flexural behavior of ultra-high performance geopolymer concrete reinforced with Glass Fiber Reinforced Polymer (GFRP) bars. The study reported a higher crack width in Geopolymer concrete beams reinforced with GFRP bars than the steel reinforcement control beam. GFRP bars as reinforcement improve mechanical behavior like deflection, crack pattern, number of cracks, and mode of failure. Mo et al., [21] have reviewed past investigations on the structural performance of geopolymer concrete. The structural elements considered in the study included the reinforced concrete beams, columns, slabs, and panels. Based on the review, the authors found no negative effect of geopolymer beams on the structural performance of the elements considered. Study conducted earlier [14] using four-point bend test on reinforced geopolymer concrete beams the behavior of the beam was studied based on the ultimate load values. The results have shown similar performance for both geopolymers as well as conventional concrete beams. Saranya et al. [13] studied application of binary geopolymer beam with GGBS and dolomite as source material. Ten beams were cast and tested. Experimental and numerical simulations of beams were conducted under monotonic loading and has been found to have superior properties. Mohammed et al., [22] performed a similar review and data analysis on the mechanical properties of the Geopolymer concrete. The study attempted to establish a correlation between various mechanical properties and the compressive strength of the Geopolymer concrete.

Under reinforced fly ash based (low calcium) geopolymer concrete beams as seen in past [13, 19, 20, 21] have indicated similar first cracking load, crack width, load–deflection

relationship, flexural stiffness, ultimate load and failure mode compared to conventional reinforced concrete beams subjected to flexural loading. In few cases, it was seen that the reinforced geopolymer concrete beams gave higher first crack load, ultimate load, mid deflection and smaller crack width when compared to conventional concrete beams. Studies done on flexural behavior of reinforced geopolymer concrete with combination of different constituents of geopolymers with fly ash to compare with conventional concrete that has indicated capability to take more flexural load, decrease of deflection and increase of first cracking load, ultimate load carrying capacity and higher ductility but a greater number of narrow cracks.

Study conducted by past researchers on flexural behaviour of reinforced geopolymer concrete beams are with fly ash-based system mostly. Studies conducted by Saranya et al. [13] was on application of binary geopolymer beam with GGBS and dolomite as source material. Past studies done by researchers such as Mo et al. [21] evaluated structural performance of geopolymer concrete after being subjected to elevated temperature and indicated that flexural behaviour was influenced by multiple factors, and the material demonstrated some defects; which was inconsistent to the behaviour of the ambient beams. Hutagi and Khadiranaikar [19] conducted the study with low calcium geopolymer concrete with fly ash instead of GGBS.

Research Significance: The literature on combined slag and fly ash based geopolymer concrete which is high calcium system is limited when it comes to study on flexural behaviour of reinforced slag and flyash based geopolymer concrete. Before putting any new building materials into practice, its structural performance in terms of flexure, shear and compression in very essential and present study covers mechanical and flexural behaviour of reinforced geopolymer concrete having combined slag: fly ash based high calcium system wherein ratio of GGBS and fly ash is kept at 70:30 respectively by weight, the activator modulus is maintained as 1 and curing regime is kept as ambient. Majority of the previous studies conducted in the area of alkali activated (geopolymer) concrete were primarily focused on normal strength concrete mix and present study deals with the comparison of mechanical and flexural behaviour of both normal and high strength reinforced high calcium geopolymer concrete with conventional concrete.

The present study gives an experimental analysis of the flexural behavior and short-term mechanical characteristics of OPC concrete and slag and fly ash based geopolymer concrete. Two separate mixtures—one for M40 grade and the other for M70 grade, are used to make geopolymer and conventional concrete. Cube compressive strength, split tensile strength, flexural strength, elastic modulus, and Poisson's ratio are among the mechanical parameters that were examined. Further, using a 4-point bend test on beams with dimensions of 200 mm x 200 mm x 2400 mm, the flexural behavior of concrete has been investigated. Energy dissipation performance of conventional beams and geopolymer beams has been also evaluated.

2. Materials and methods

2.1 Materials

In conventional concrete mix OPC-53, fly ash and silica fume were used as cementitious materials. In the geopolymer mix fly ash, and GGBS are used. The properties of OPC complies with IS 269: 2015[23]. Fly ash and silica fume are used as per IS 3812: 2013[24] and 15388: 2003[25] respectively. GGBS confirms the requirement of IS 16714: 2018[26]. The physical characteristics of OPC, silica fume, fly ash and GGBS have been evaluated as per test procedure laid down in relevant parts of IS 4031. The chemical characteristics of OPC, silica fume, fly ash and GGBS have been evaluated as per IS 4032: 1985 [27]. Coarse aggregate had the maximum nominal size of 20mm and the fine aggregate confirms to the

Table 1. Physical characteristics of GGBS, fly ash, OPC and silica fume

Properties	Indian Standard for Testing	OPC -53 Grade	Silica Fume	Fly Ash	GGBS
Fineness Blaine's (m^2/kg)	IS 4031 (Pt-2): 1999	320	22000	403	335
Soundness Autoclave (%)	IS 4031 (Pt-3): 1988	0.05	-	-	-
Soundness Le Chatelier (mm)	IS 4031 (Pt-3): 1988	1	-	-	-
Setting Time Initial (min.) & (max.)	IS 4031 (Pt-5): 1988	170.00 & 220.00	-	-	-
Specific gravity	IS 4031 (Pt-11): 1988	3.16	2.24	2.2	2.9

Table 2. Chemical characteristics of GGBS, fly ash, OPC and silica fume

Chemical Name	GGBS	Fly ash	OPC	Silica Fume
Calcium Oxide (CaO), %	37.66	5.80	60.73	-
Silica (SiO_2), %	34.60	48.66	20.38	95.02
Reactive Silica, %	33.96	23.52	-	-
Alumina (Al_2O_3), %	18.38	26.72	4.95	-
Iron Oxide (Fe_2O_3), %	0.98	8.87	3.96	0.80
Magnesium Oxide (MgO), %	5.15	1.43	4.78	-
Na_2O_{eq} (%)	0.60	0.74	0.52	-
Loss on Ingnition, %	0.40	4.76	1.50	1.16
Total Sulphur as SO_3 ,%	0.05	0.75	2.07	-
Sulphide sulphur (%)	0.39	0.56	-	-
Chloride (Cl), %	0.024	0.026	0.04	-
Manganese Oxide (MnO), %	1.32	0.13	-	-

Table 3. Properties of coarse and fine aggregates

Parameter		Indian Standard for Testing	Coarse Aggregate 20 mm	Coarse Aggregate 10 mm	Fine Aggregate
Specific gravity		IS 2386 (Pt-3): 1963	2.83	2.83	2.65
Water absorption (%)		IS 2386 (Pt-3): 1963	0.3	0.3	0.59
Sieve Analysis Cumulative Percentage Passing (%)	20mm	IS 2386 (Pt-1): 1963	98	100	100
	10 mm	IS 2386 (Pt-1): 1963	1	68	100
	4.75 mm	IS 2386 (Pt-1): 1963	0	2	99
	2.36 mm	IS 2386 (Pt-1): 1963	0	0	89
	1.18 mm	IS 2386 (Pt-1): 1963	0	0	64
	600 µ	IS 2386 (Pt-1): 1963	0	0	43
	300 µ	IS 2386 (Pt-1): 1963	0	0	26
	150 µ	IS 2386 (Pt-1): 1963	0	0	14
	Pan	IS 2386 (Pt-1): 1963	0	0	0
Abrasion, Crushing & Impact Value (%)			19,19,13	-	-
Flakiness % & Elongation %			29, 25	-	-

Zone II as per IS 383:2016[28]. The physical characteristics of coarse and fine aggregates have been evaluated as per test procedure laid down in relevant parts of IS 2386. Table 1

to Table 3 gives the physical and chemical properties of the materials used in the preparation of the mixes.

2.2 Concrete mix design

The mix design details for Reinforced Conventional Concrete (RCC) and Reinforced Geopolymer Concrete (RGC) for normal and high strength concrete are as shown in table 4A. The cost comparison of both normal & high strength geopolymer concrete and conventional concrete has been given in Table 4b and 4c. The conventional concrete has designed as per IS 10262: 2009 [29] . The ratio of coarse to fine aggregates has been kept as 60:40 for normal strength conventional concrete mix and 35:65 for high strength RCC mix. Slump for all the concrete mixes was kept in the range of 75-100 mm. Superplasticizer have been used in conventional concrete mixes to achieve the required slump between 75-100 mm.

Table 4A. Mix design Details

Parameter		**Mix RGC M40**	**Mix RGC M70**	**Mix RCC M40**	**Mix RCC M70**
Total cementitious/ precursor content (kg/m^3)		350	380	362	525
Individual cementitious materials / precursors (kg/m^3)	OPC	-	-	290	400
	Silica Fume	-	-	-	50
	GGBS	245	266	-	-
	Fly ash	105	114	72	75
Ratio of water to total cementitious material / precursor		0.50	0.40	0.47	0.27
Na_2O (% by weight of total precursor)		7	8	-	-
Activator Modulus (SiO_2/Na_2O)		1	1	-	-
NaOH (kg/m^3)		17.24	21.39	-	-
Na_2SiO_3 gel (kg/m^3)		74.20	92.12	-	-
Fine Aggregate (kg/m^3)		690	660.80	650	692
Coarse Aggregate – 10 mm (kg/m^3)		514.50	540	777	754
Coarse Aggregate – 20 mm (kg/m^3)		631	662	518	406
Water (kg/m^3)		132.48	107.58	170	140
Superplasticizer (%)		Nil	Nil	0.70	1.00

The effects of varying constituents of concrete in conventional concrete mix on mechanical and durability properties is a well-established fact, but this is not the case with geopolymer concrete, the hydration, chemical reaction and microstructural properties are more complex for geopolymer concrete. Various factors that can affect its strength can be said to be temperature, activator modulus, type, quality and proportions of slag and fly ash, water content etc. Hence, to obtain optimized mix trial and error method is being used and based on strength results of various mixes the mix is finalized as shown in table 4. The ratio of GGBS and fly ash is kept at 70:30 respectively by weight, the activator modulus is maintained as 1. The ratio of coarser to fine aggregates is kept at 55:45 percent for all geopolymer mixes and percentage by weight of total precursor content for Na_2O is fixed at 7 and 8 percent for M40 and M70 mix respectively. The alkaline activator solution used in

geopolymer concrete is the combination of Sodium Silicate solution (SiO_2/Na_2O), potable water and Sodium Hydroxide (NaOH), for this study the value Activator Modulus (SiO_2/Na_2O) is kept constant as 1. The activator needs to dissolve the reactive part Si and Al present in the GGBS and Fly-Ash and provide a highly alkaline medium for condensation-polymerization reaction. The sodium silicate and sodium hydroxide solutions were prepared separately and mixed at the time of casting. NaOH solution is prepared one day before casting as it generates a lot of heat, and then it is used to obtain a required amount of workability here water doesn't participate in hydration reaction but is required for maintaining the workability of geopolymer mix. Mixes were prepared in a big pan type mixer (capable of preparing 120 litres of concrete mix in a single batch. For a particular concrete mix, concrete was prepared in three batches. From each of the first and second batch, one reinforced concrete beam and one set (i.e. total 6 cubes) of concrete cubes were cast. From third batch, specimen for evaluation of split tensile strength, flexural strength, MOE, Poisson's ratio were cast along one set (i.e. total 6 cubes) of concrete cubes were cast to ascertain the compressive strength of concrete from each batch. Total 6 specimens were cast for evaluation of each parameter i.e. compressive strength, split tensile strength, flexural strength, MOE and Poisson's ratio. Average result of 6 specimen has been reported in the manuscript. As mentioned above one set (i.e. total 6 cubes) of concrete cubes were cast from each batch to ascertain the compressive strength of concrete from each batch.

Table 4B. Cost comparison for M40 grade of geopolymer & conventional concrete (per m^3)

	Geopolymer concrete				**Conventional Concrete**			
	Material	**Rate**	**Quantity (per m^3)**	**Cost (Rs.), Approx.**	**Material**	**Rate**	**Quantity per m^3**	**Cost (Rs.) Approx.**
Dry Binder	GGBFS	2.00 Rs per kg (Indian Rate)	245 kg	490	Cement	6.5 Rs per Kg (Indian Rate)	290 kg	1885
	Fly Ash	1.00 Rs per kg (Indian Rate)	105 Kg	105	Fly Ash	1.00 Rs per kg (Indian Rate)	72	72
Activator	Caustic soda	30 Rs per kg (Indian Rate)	17 kg	510	Not applicable			
	Sodium Silicate solution	12 Rs per kg (Indian Rate)	74 kg	890	Not applicable			
	Total cost of precursor and activator in Geopolymer concrete			**Rs 1995 per m^3**	**Total cost of cementitious material in conventional concrete**			**Rs 1957 per m^3**
Aggregates almost same in similar in both cases								

Table 4C. Cost comparison for M70 grade of geopolymer & conventional concrete (per m^3)

	Geopolymer concrete				Conventional Concrete			
	Material	**Rate**	**Quantity (per m^3)**	**Cost (Rs.), Approx.**	**Material**	**Rate**	**Quantity per m^3**	**Cost (Rs.) Approx.**
Dry Binder	GGBFS	2.00 Rs per kg (Indian Rate)	266 kg	532	Cement	6.5 Rs per Kg (Indian Rate)	400 kg	2600
	Fly Ash	1.00 Rs per kg (Indian Rate)	114 Kg	114	Fly Ash	1.00 Rs per kg (Indian Rate)	75 kg	75
	-	-	-	-	Silica Fume	20.00 Rs per kg (Indian Rate)	50 kg	1000
Activator	Caustic soda	30 Rs per kg (Indian Rate)	21 kg	630	Not applicable			
	Sodium Silicate solution	12 Rs per kg (Indian Rate)	92 kg	1104	Not applicable			
	Total cost of precursor and activator in Geopolymer concrete			**Rs 2380 per m^3**	**Total cost of cementitious material in conventional concrete**			**Rs 3675 per m^3**
Aggregates almost same in similar in both cases								

2.3 Methods for evaluation of mechanical properties of conventional and geopolymer mixes

Compressive strength test of concrete mixes was evaluated on concrete cubes of size 150 mm as per IS: 516 (Part 1/Sec 1): 2021 [36]. Flexural strength test of concrete mixes was determined as per IS 516 on concrete beam (size 100 × 100 × 500 mm) at the age of 28 days as per IS: 516 (Part 1/Sec 1): 2021. Split tensile strength and modulus of elasticity of concrete mixes were determined as per as per IS: 516 (Part 1/Sec 1): 2021 and IS: 516 (Part 8/Sec1): 2020 [37] respectively on concrete cylinder (150 mm diameter and 300 mm height).

2.4 Reinforced concrete beam detailing

The beam specimens were designed with an aim to obtain pure flexure failure. The cross-sectional dimensions of beams were fixed as 200 mm wide and 200 mm depth, and the beam length is kept as 2400 mm. The clear cover provided is 25 mm. The cross-sectional area and side view are as shown in figure 1(a), 1(b) and 1(c). The steel bars used in beams are 16mm, 20mm and 8mm. The reinforcement design of beam in flexure and shear is being done as per IS-456, for M40 grade beams 2 bars of 16 mm diameter and one bar of 20 mm diameter is used. Whereas, for M70 grade beams, 20 mm diameter high yield steel bars are used.

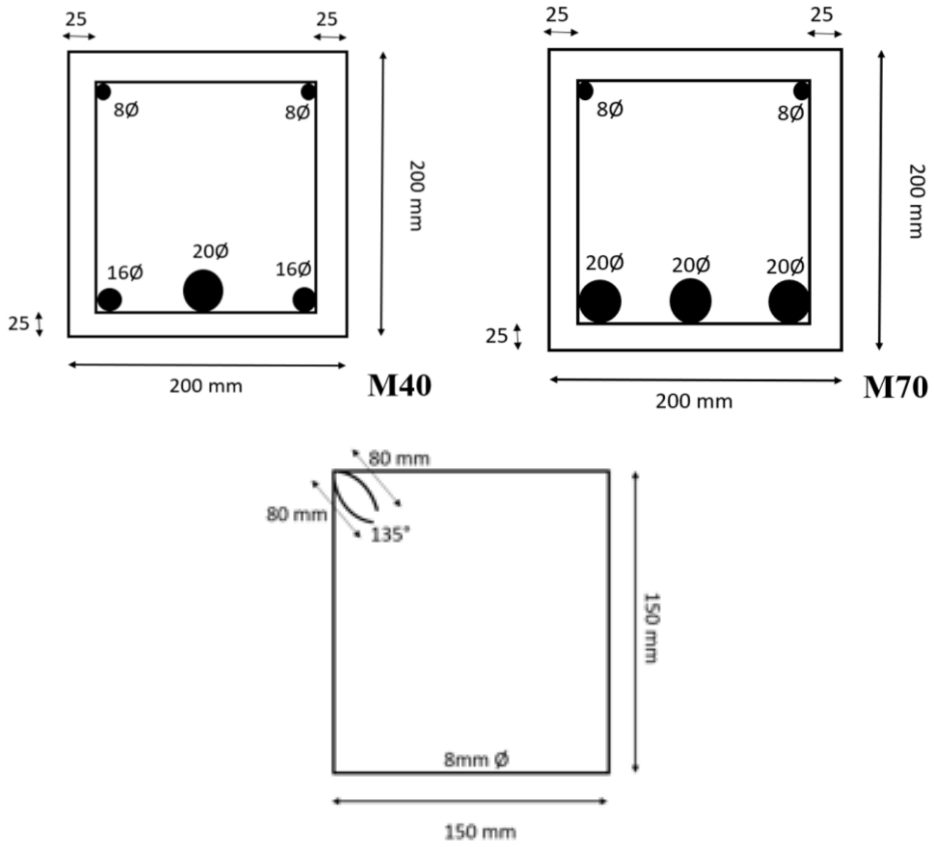

Fig. 1(a) Design details for M40 and M70 reinforced beam (Sectional View) and (b) Details of shear reinforcement

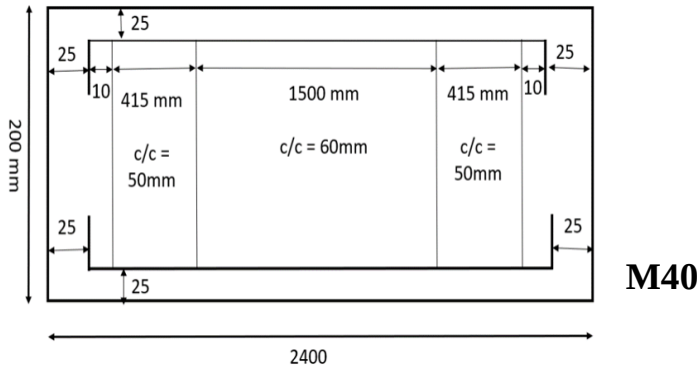

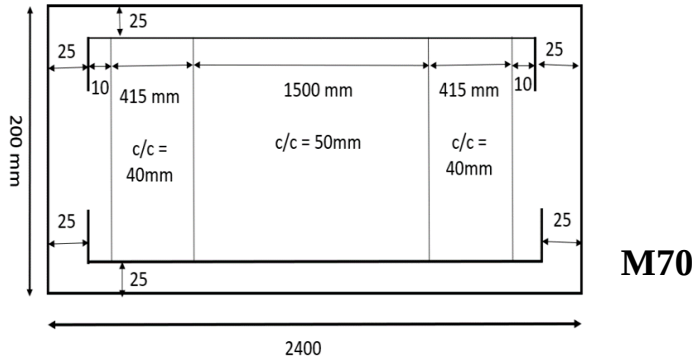

Fig. 1(c) Design details for M40 and M70 reinforced beam (Lateral View)

To make the beam extra safe in shear the shear reinforcement are provided on slightly higher side the stirrups are provided at a spacing of 60 mm c\c and 50 mm c\c for M40 and M70 grade for both RCC and RGC beams. The spacing of stirrups is reduced further to 40 mm c\c at ends where the possibility of occurrence of shear failure is slightly higher. Nominal amount of compressive reinforcement is provided in both the M40 and M70 grade beams. The reinforcement details of all beams are provided in Table 5.

Table 5. Reinforcement details of beam specimen

Specimen Id	Area of steel (mm^2)	
	A_{SC}	A_{ST}
M40 RCC	100.54	711.41
M40 RGC	100.54	711.41
M70 RCC	100.54	937.26
M70 RGC	100.54	937.26

2.5 Preparation of specimen

The steel molds of size 200*200 mm are used for both RGC and RCC beam, before filling of the molds the molds are coated with lubricating oils in order to prevent the adhesion of hardening concrete. The reinforcement cage is fixed in the mold after putting the cover blocks of 25 mm to obtain required arrangement. The concrete is being filled in the moulds in three layers of equal depths. After each layer the needle vibrator and tamping rods are used to ensure proper compaction. Figure 2 shows the moulds, reinforcement and freshly cast beams for testing.

Although, the polymerization reaction is generally accelerated in higher temperatures than in ambient behavior and gives higher early strength, yet the beams cured at ambient temperature gives better compressive strength in 28 days as compared to 7 days, thus the curing of beams is conducted at ambient room temperature. Three cubes of 150 mm are casted along with the beams to determine the compressive strength of concrete at the day of testing i.e., 28 days strength.

(a) (b)

Fig. 2 (a) Reinforcement and mould for preparing the specimen and (b) Casting of specimen

2.6 Loading and test setup

The four-point bend test is conducted on beams using Flexural Testing Machine of capacity 500 kN. The loading applied is the displacement controlled loading. The beam is being placed on the steel girder and out of the 2400 mm length of beam clear span of beam is maintained as 2000 mm. The distance between the point loads is kept as 666 mm, thus dividing the clear span of 2000 mm in three equal parts. The concrete cubes specimens were tested in a displacement-controlled compression testing machine of 3000 kN capacity at room temperature of 27 ± 2°C and relative humidity 65% or more. LVDT was used to get the deflection at the centre of beam. The first crack load was obtained by visual examination. The test setup for four-point bend test is been shown in figure 3(a) and 3(b).

Fig. 3 (a) Beam in 4 point bend test and (b) Test Setup

3. Results and discussions

3.1 Fresh concrete properties

Fresh concrete properties such as initial workability (in terms of initial slump) and air content after preparation of mix were evaluated for all the 4 concrete mixes and test results are given below in table 6.

Table 6. Fresh properties of geopolymeric and conventional concrete mixes

S. No.	Specimen Id	Initial workability in terms of slump	Air Content (%)	Superplasticizer (% by weight of cementitious content)
1.	M40 RCC	100 mm	1.30	0.80
2.	M40 RGC	Collapse	1.20	Nil (i.e. 0 %)
3.	M70 RCC	85 mm	1.60	1.20
4.	M70 RGC	80 mm	1.40	Nil (i.e. 0 %)

Superplasticizer was used in case of conventional concrete mixes to achieve sufficient initial workability (i.e. slump of at least 75 to 100 mm) as mentioned in Table 6. In case of geopolymer concrete mixes, superplasticizer was not required at all, as M40 RGC mix showed collapse behaviour immediately after preparation of mix. Whereas, M70 RGC mix showed initial slump of 80 mm without any superplasticizer. In case of, conventional concrete mixes, M40 RCC and M70 RCC required 0.80% and 1.2% superplasticizer to achieve an initial slump of 100 mm and 85 mm respectively. All the four concrete mixes were homogenous and did not show any signs of bleeding and segregation. Air content for conventional and geopolymer concrete mixes are observed to be in range of 1.2 to 1.6%.

3.2 Mechanical properties of mixes

Test results of different mechanical properties i.e. compressive strength, split tensile strength, flexural strength, modulus of elasticity and Poisson's ratio for all the concrete mixes have been tabulated below in table 7. The mechanical properties of conventional mix are compared with geopolymer concrete mix of equivalent strength. The conventional and geopolymer concrete mixes were designed and optimized to have almost similar and comparable compressive strength, so that other mechanical characteristics of conventional and geopolymer concrete can be compared. One of the significant difference in both the concrete system is the difference in their modulus of elasticity. Six specimens for each mix were tested for evaluation of every parameter and average value of test results have been tabulated in table 7.

Table 7. Mechanical properties of different mixes

Specimen Id	Cube Compressive strength (MPa)	Split Tensile Strength (MPa)	Flexural Strength (MPa)	Modulus of elasticity (GPa)	Poisson's Ratio
M40 RCC BEAM 1	46.11	4.04	4.42	32.64	0.16
M40 RCC BEAM 2	44.61				
M40 RGC BEAM 1	50.71	4.10	5.07	22.92	0.17
M40 RGC BEAM 2	51.46				
M70 RCC BEAM 1	82.15	5.05	8.52	43.13	0.14
M70 RCC BEAM 2	83.90				
M70 RGC BEAM 1	77.80	4.50	5.85	33.37	0.14
M70 RGC BEAM 2	79.80				

As per experimental plan, in order to compare the behaviour of hardened concrete properties of geopolymer and conventional concrete mixes, mixes were cast to obtain almost comparable compressive strength for geopolymer and conventional concrete mixes of equivalent grade. Flexural and split tensile strength of concrete mix has a direct

relationship with its compressive strength. Split tensile strength of M40RGC is about 101.5 % of split tensile strength of M40RCC and split tensile strength of M70RGC is about 89.00 % of split tensile strength of M70RCC. Flexural strength of M40RGC is about 115 % of flexural strength of M40RCC and Flexural strength of M70RGC is about 69 % of flexural strength of M70RCC. For concrete mixes equivalent to M40 grade, the flexural and split tensile strength values of M40 RGC are slightly higher in comparison to M40 RCC. This observation is supported by the previous findings [30] also reported that flexural strength of alkali activated concrete is higher in comparison to flexural strengths of conventional Portland cement concrete of similar grade. However, in case of high strength concrete mixes equivalent to M70 grade, trends are opposite to the observations made for flexural and split tensile strength of mixes equivalent to M40 grade. Flexural and split tensile strength of M70 RGC mix are lower in comparison to M70 RCC of equivalent grade at 28 days. This increase in flexural and split tensile strength of high strength conventional Portland cement concrete is similar to findings of Arora et.al [16, 40, 41] wherein it was reported that flexural strength of silica fume concrete was higher by 10- 15% as compared that of Portland cement concrete for about 12-15 % silica fume addition. The addition of silica fume in concrete mix leads to reduction in the development of cracks at micro level near the interface of cement paste and unreacted cement or pozzolans [30, 42, 43, 44, 45]. Modulus of elasticity of M40RGC is about 70.00 % of modulus of elasticity of M40RCC and Modulus of elasticity of M70RGC is about 77 % of Modulus of elasticity of M70RCC. Modulus of elasticity of both M40 RGC and M70 RGC are observed to be lower than their corresponding conventional concrete mixes of similar grade. This observation is supported by observations of research studies carried out by past researchers [30, 31, 32]. The intrinsic modulus of C-A-S-H gel formed in slag-based geopolymer concrete is comparable with the C-S-H gel formed in cement. But the intrinsic modulus of N-A-S-H gel formed in low-calcium fly ash gel based geopolymer concrete is much smaller than that of the C-S-H gel formed in cement. The lower value of modulus of elasticity for geopolymer concrete than conventional concrete can be attributed to the low intrinsic modulus of N-A-S-H gel and higher initial micro-cracks formulation in geopolymer concrete [30, 31, 32].

3.3 Load- deflection behaviour

Figure 4 and 5 show the load-deflection curves for the RCC beams and reinforced geopolymer beams for the M40 and M70 grade concretes respectively. The load vs displacement curves at the mid span of the beam are as mentioned in figure 5 for M40 mixes of conventional and geopolymer concrete and in figure 6 for M70 mixes.

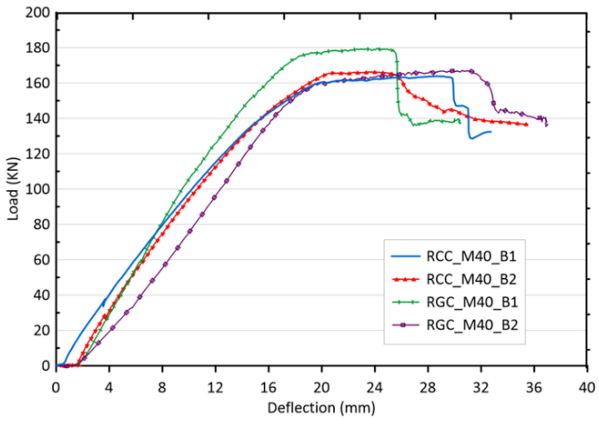

Fig 4 Load deflection curves for M40 RCC and RGC beams

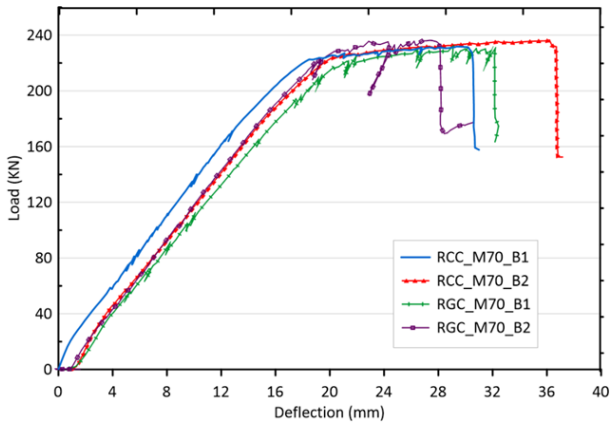

Fig 5 Load deflection curves for M70 grade RCC and RGC beams

Yield point was determined visually from load deflection curve and the yield point is stage where no significant increase in load was observed and deflection was increasing continuously. The yield points for all M40 mixes are in the displacement range of 18 to 22 mm. The drop in the curves for all mixes represents the occurrence of failure. The displacement range for ultimate or failure points of various curves of grade M40 is much higher as compared to range of yield points, it is between 26 to 33 mm. After the yield point the curves are depicting an elastic plastic behavior for all curves except for RGC M40 beam 2 where the curve slightly shows strain hardening behavior. From load displacement results it is evident that the yield points are reached at the same time for both conventional concrete and geopolymer concrete of same grade at almost similar deflection. The curves suggests that the flexural behaviour of both the conventional and geopolymer concrete are comparable. The values of experimental moment calculated from the load-deflection curve and predicted moment as per IS456 is given in Table 8.

The predicted maximum strength of beams is calculated as per the dimensions of beam and the reinforcements provided and these are calculated as per IS 456: 2000 [33]. The moment of resistance (Mp) is calculated as per IS-456. Experimental maximum value which is obtain from beam testing is obtained then from mid span moment formula for four point test the predicted maximum moment (Me) that the beam can resist is calculated. The normalized strength is calculated as given in Equation 1, whereas, the expression for normalized moments is as given in Equation 2;

$$Normalised\ Load = \frac{P}{\sigma bd} \tag{1}$$

$$Normalised\ moment = \frac{M}{\sigma bd^2} \tag{2}$$

Where, σ is the Compressive strength of the mix at 28 days, P is Load obtained from the load deflection curve, M is Moment obtained from the load deflection curve, b is Width of the beam and d is the Depth of the beam. The normalized yield strength as a percent of ultimate strength varies from 95 to 100 percent, this shows that beams are not undergoing strain hardening. Whereas, the ratio of normalized yield moment to ultimate moment varies in between. Figure 6 gives us the relationship between the normalized yield strength and normalized ultimate strength.

Table 8. Characteristics of load deflection curves of the beams

Id	Moment		Compressive Strength MPa	Normalised Moment		Predicted Moment Mp (KN-m) (as per IS 456)	Me/Mp
	Yield kN-M	Ultimate (Experimental) kN-M		Yield kN-M	Ultimate kN-M		
M40 RCC BEAM 1	53.30	54.17	46.11	0.15	0.15	44.01	1.23
M40 RCC BEAM 2	53.97	55.20	44.61	0.15	0.15	44.01	1.25
M40 RGC BEAM 1	57.03	59.57	50.72	0.15	0.15	44.01	1.35
M40 RGC BEAM 2	53.30	55.27	51.47	0.14	0.14	44.01	1.26
M75 RCC BEAM 1	74.23	75.70	82.15	0.10	0.10	67.37	1.12
M70 RCC BEAM 2	74.87	77.53	83.90	0.10	0.11	67.37	1.15
M70 RGC BEAM 1	75.70	76.47	77.80	0.11	0.11	67.37	1.14
M70 RGC BEAM 2	74.67	77.50	79.80	0.11	0.11	67.37	1.15

The findings in the study is comparable to past literatures. Hutagi and Khadiranaikar [19] studied the behavior with reference to various first crack load, service load and ultimate load. The results were found to be similar to that of conventional cement concrete reinforced beams. Kumaravel and Thirugnanasambandam [34] in their paper studied the flexural behaviour of geopolymer concrete beams and compared with control cement concrete beams. The results show that the geopolymer concrete beams exhibit increased flexural strength. The deflections at different stages including service load and peak load stage are higher for geopolymer concrete beams. Moreover the review paper by Under reinforced fly ash based (low calcium) geopolymer concrete beams as seen in past [13, 19, 20, 21] have indicated similar first cracking load, crack width, load–deflection relationship, flexural stiffness, ultimate load and failure mode compared to conventional reinforced concrete beams subjected to flexural loading. Mo et al. [21] shows that there is no detrimental effect on structural performance when geopolymer concrete is compared with the conventional concrete. For four-point bend test the theoretical maximum deflection occurs at the mid-point and is given by Equation (3);

$$\Delta max = \frac{23pl^3}{648\,EI} \tag{3}$$

Where, Δmax is the Maximum deflection at mid span, p is the Load applied on the beam, l is total length, E represents modulus of elasticity and I is the Moment of inertia of the beam cross section.

The values of normalized yield deflection to ultimate displacement is in the range between 55 to 75 percent, from this it can be said that beams follow inelastic behavior for very long time after the yield points.

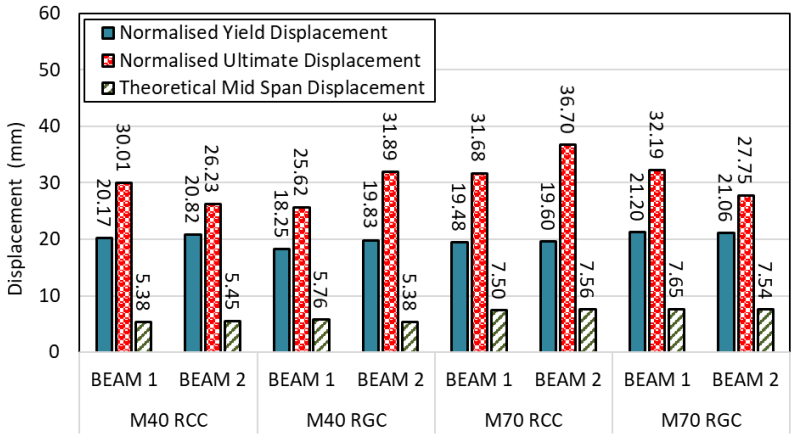

Fig. 6 Theoretical mid span displacement, normalized yield displacement and ultimate displacement for all mixes

3.4 Strength Characteristics

Table 9 and Table 10 shows the normalized yield strength and normalized ultimate moment respectively. As shown in table, the yield strength and yield moment for the comparable strength conventional and geopolymer concrete are comparable. One of the reasoning for the similarity can be attributed to the cross-linked structure in geopolymer mix which makes it capable to take similar load as conventional concrete with lower binding content. Table 9 and table 10 also confirms the action of reinforcement in OPC and the geopolymer concrete is also comparable. Figure 7 represents normalized yield strength as percentage of normalised ultimate strength. Sumajouw et al. [38] evaluated the flexural load capacity of the sixteen reinforced geopolymer concrete beams and the average experimental to prediction ratio was found to be 1.11. Considering that the beams were under-reinforced, the effect of the geopolymer concrete compressive strength was marginal. Similar trend has been observed in the study discussed in this manuscript.

Table 9. Normalized yield strength and normalized ultimate strength of the beams

Id	First Crack kN	Yield Load kN	Ultimate Load kN	Compressive Strength MPa	Normalized Yield Strength kN	Normalized Ultimate Strength kN	Py/Pu
M40 RCC BEAM 1	60.25	159.90	162.50	46.11	0.087	0.088	98.40
M40 RCC BEAM 2	64.75	161.90	165.60	44.61	0.091	0.093	97.77
M40 RGC BEAM 1	66.85	171.10	178.70	50.72	0.084	0.088	95.75
M40 RGC BEAM 2	57.90	159.90	165.80	51.47	0.078	0.081	96.44
M70 RCC BEAM 1	79.92	222.70	227.10	82.15	0.068	0.069	98.06
M70 RCC BEAM 2	82.25	224.60	232.60	83.90	0.067	0.069	96.56
M70 RGC BEAM 1	87.65	227.10	229.40	77.80	0.073	0.074	99.00
M70 RGC BEAM 2	80.75	224.00	232.50	79.80	0.070	0.073	96.34

Table 10. Normalized yield moment and normalized ultimate moment of the beams

Id	M_Y kN-M	M_U kN-M	Compressive Strength MPa	Normalized Yield Moment kN-M	Normalized Ultimate Moment kN-M	My/Mu
M40 RCC B-1	53.30	54.17	46.11	0.029	0.029	98.40
M40 RCCB-2	53.97	55.20	44.61	0.030	0.031	97.77
M40 RGC B-1	57.03	59.57	50.71	0.028	0.029	95.75
M40 RGC B-2	53.30	55.27	51.46	0.026	0.027	96.44
M70 RCC B-1	74.23	75.70	82.15	0.023	0.023	98.06
M70 RCC B-2	74.87	77.53	83.90	0.022	0.023	96.56
M70 RGC B-1	75.70	76.47	77.80	0.024	0.025	99.00
M70 RGC B-2	74.67	77.50	79.80	0.023	0.024	96.34

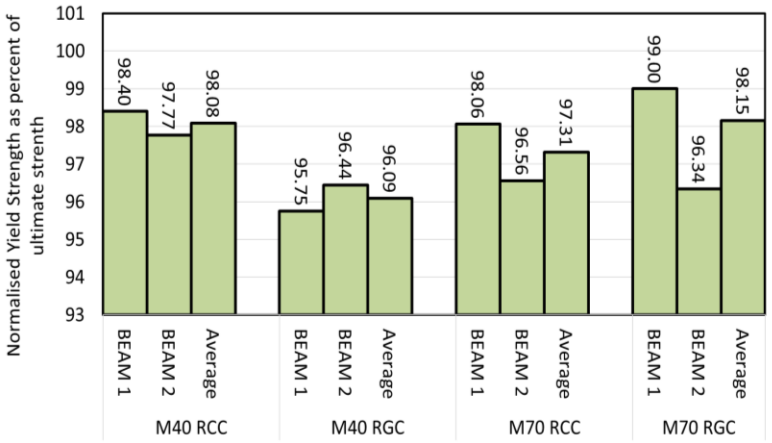

Fig. 7 Normalized yield strength as percentage of normalised ultimate strength

3.5 Energy dissipation

Figure 8 shows the values of energy dissipated by the beam during the four point bend test. It can be seen that the beams of higher grade dissipates more energy. In terms of energy dissipation, the performance of geopolymer concrete beams as compared to conventional concrete beams is almost identical. However, in high strength concrete, the energy dissipation values are found to be slightly lower in geopolymer concrete compared to conventional concrete. The observed variation in energy dissipation in higher grade concrete can be attributed to the presence of silica fume in the high strength conventional OPC concrete. The difference in the gel systems formed in these two variation of the mixes can be attributed as a possible explanation of the observed trend which is not much significant in the normal strength concrete. Findings in the literature [30] suggests that the C-S-H gel formed in OPC concrete and the N-A-S-H gel primarily found in fly ash based geopolymer have variations in their intrinsic modulus which is well reflected in high strength concrete.

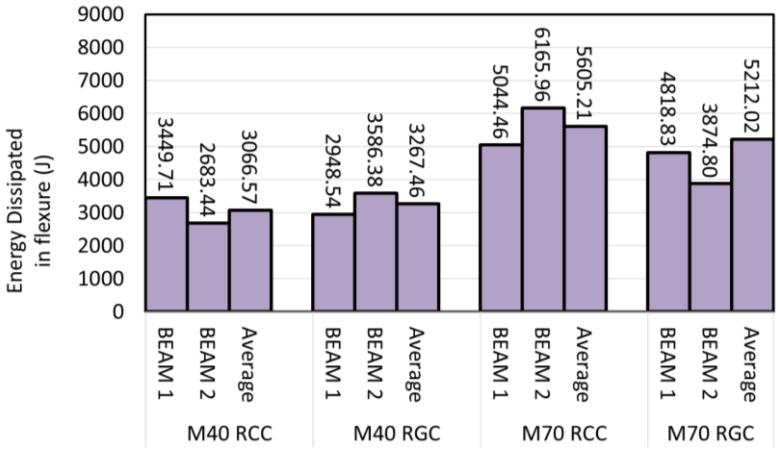

Fig. 8 Energy dissipated in flexure by beams

3.6 Crack width and pattern

Figure 9 (a) and (b) show the crack patterns observed in the beam after the completion of the test. In the test the flexural cracks were first observed at the tension zone in beam between the loading arrangements. With increase in load the cracks developed both in size and number. The patterns of cracks clearly shows that all beams have undergone pure flexure failure. It can be further depicted that the cracks patterns, crack width and number of cracks are almost identical for both reinforced as well as geopolymer concrete for both normal and high strength beams. As shown in figure 9 (a) and (b), the number of visible cracks in normal strength conventional concrete is 8 and in normal strength geopolymer beam is 10 where two cracks are smaller in size. The high strength conventional concrete bears 10 major cracks and the corresponding strength geopolymer concrete has 9 cracks of identical patterns and size. Researchers also investigated the structural behaviour of under reinforced geopolymer concrete beams containing different concrete materials. Andalib et al. [39] incorporated 30% Palm Oil Fuel Ash (POFA) into the geopolymer concrete to produce reinforced geopolymer concrete beams and they observed comparable cracking and ultimate moments as well as crack pattern as conventional reinforced concrete beams. Literature supports the findings of present study. Hutagi and Khadiranaikar [25] has also found that there is no significance difference in crack patterns of reinforced concrete beams as well as geopolymer beams

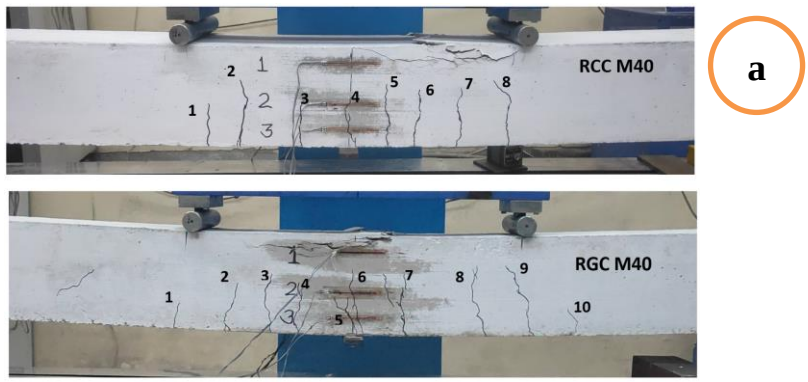

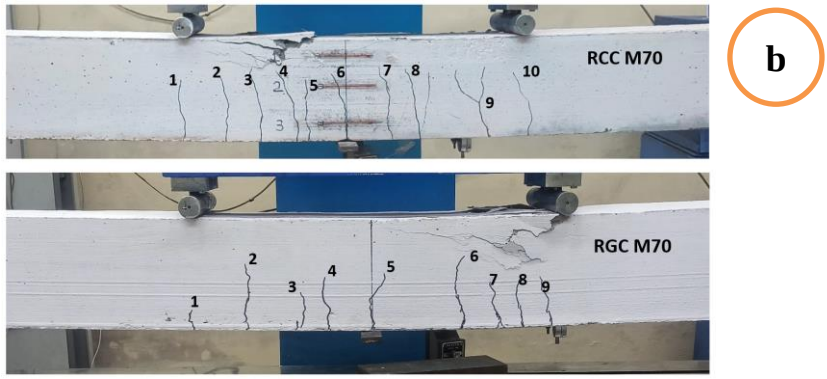

Fig. 9 (a) M40 RCC and RGC beams 9 and (b) M70 RCC and RGC

The past literature has also shown the similar trends which validates the findings of this paper. In the experimental study conducted by Ren et al. [35] geopolymer concrete beams under a flexural load resembled the mechanical performance of the OPC concrete beams.

4. Conclusions

In present study, short-term mechanical properties and flexural performance of normal and high strength reinforced conventional and geopolymer concrete were experimentally analyzed. Geopolymer and conventional concrete mixes were designed for M40 and M70 grade. The mechanical characteristics such as cube compressive Strength, split tensile strength, flexural strength, modulus of elasticity and Poisson's ratio were evaluated for all the four mixes. Further, the flexural behaviour of reinforced concrete beam was studied using 4-point bend test on reinforced concrete beams. Following conclusions can be drawn from the above study:

- Geopolymer concrete achieves similar and comparable compressive strength as in case of conventional concrete at lower precursor content in comparison to total cementitious content required in case of conventional concrete mixes.
- The modulus of elasticity of geopolymer concrete is lower than the conventional concrete of equivalent strength. The split and flexural strength of geopolymer and OPC based concrete of comparable compressive strength were observed to be similar for normal strength grade i.e. M40 grade. However, in case of high strength mixes, conventional mix showed higher flexural strength in comparison to geopolymer concrete mix. Increase in flexural and split tensile strength of high strength conventional concrete is higher by 10- 15% as compared to that of geopolymer concrete. This can be attributed to presence of 10-12% silica fume in high strength conventional concrete mix.
- The flexural performance of conventional and geopolymer concrete was observed to be comparable in 4-point bend test. The strength characteristics in terms of yield load and yield moment capacities were also comparable. This suggests that reinforced conventional and geopolymer concrete of equivalent strength behave similarly in flexure. The normalized yield strength as a percent of ultimate strength varies from 95 to 100 percent, this shows that beams are not undergoing strain hardening. The values of normalized yield deflection to ultimate displacement is in the range between

55 to 75 percent, from this it can be said that beams follow inelastic behavior for very long time after the yield points.

- Energy dissipation performance of conventional beams and geopolymer beams was observed to be identical. However, in high strength concrete the energy dissipation values are found out to be slightly lower in geopolymer concrete as compared to the conventional concrete. The added silica fume in higher compressive strength conventional concrete may be responsible for the improvement in energy dissipation capabilities of the beams.
- Based on the visual examination of flexural cracks, it can be concluded that the reinforced conventional concrete and reinforced geopolymer concrete depict similar number and type of cracks in flexure. The number of visible cracks in normal strength conventional concrete is 8 and in normal strength geopolymer beam is 10 where two cracks are smaller in size. The high strength conventional concrete bears 10 major cracks and the corresponding strength geopolymer concrete has 9 cracks of identical patterns and size.

Acknowledgements

Authors acknowledge the funding received from Ministry of Commerce & Industry, Govt. of India

References

[1] Singh B, Ishwarya G, Gupta M, Bhattacharyya S. Geopolymer concrete: A review of some recent developments. Construction and Building Materials. 2015 Jun;85:78-90. https://doi.org/10.1016/j.conbuildmat.2015.03.036

[2] Ojha PN, Singh B, Kaura P, Singh A. Lightweight geopolymer fly ash sand: an alternative to fine aggregate for concrete production. Res Eng Struct Mater. 2021; 7(3), 375-392 https://doi.org/10.17515/resm2021.257ma0205

[3] Nodehi M, Ozbakkaloglu T, Gholampour A, Mohammed T, Shi X. The effect of curing regimes on physico-mechanical, microstructural and durability properties of alkali-activated materials: A review. Construction and Building Materials. 2022 Feb;321:126335. https://doi.org/10.1016/j.conbuildmat.2022.126335

[4] Ma C, Awang AZ, Omar W. Structural and material performance of geopolymer concrete: A review. Construction and Building Materials. 2018 Oct;186:90-102. https://doi.org/10.1016/j.conbuildmat.2018.07.111

[5] Fernandez-Jimenez A, García-Lodeiro I, Palomo A. Durability of alkali-activated fly ash cementitious materials. J Mater Sci. 2007 May;42(9):3055-65. https://doi.org/10.1007/s10853-006-0584-8

[6] Mehta A, Siddique R. Sulfuric acid resistance of fly ash based geopolymer concrete. Construction and Building Materials. 2017 Aug;146:136-43. https://doi.org/10.1016/j.conbuildmat.2017.04.077

[7] Yang W, Zhu P, Liu H, Wang X, Ge W, Hua M. Resistance to Sulfuric Acid Corrosion of Geopolymer Concrete Based on Different Binding Materials and Alkali Concentrations. Materials. 2021 Nov 23;14(23):7109. https://doi.org/10.3390/ma14237109

[8] Albitar M, Mohamed Ali M, Visintin P, Drechsler M. Durability evaluation of geopolymer and conventional concretes. Construction and Building Materials. 2017 Apr;136:374-85. https://doi.org/10.1016/j.conbuildmat.2017.01.056

[9] Ramujee K, PothaRaju M. Mechanical Properties of Geopolymer Concrete Composites. Materials Today: Proceedings. 2017;4(2):2937-45. https://doi.org/10.1016/j.matpr.2017.02.175

[10] Nguyen TT, Goodier CI, Austin SA. Factors affecting the slump and strength development of geopolymer concrete. Construction and Building Materials. 2020 Nov;261:119945. https://doi.org/10.1016/j.conbuildmat.2020.119945
[11] Lyon RE, Balaguru PN, Foden A, Sorathia U, Davidovits J, Davidovics M.. Fire-resistant aluminosilicate composites. Fire and materials, 1997: 21(2), 67-73. https://doi.org/10.1002/(SICI)1099-1018(199703)21:2<67::AID-FAM596>3.0.CO;2-N
[12] Palomo A, Grutzeck M, Blanco M. Alkali-activated fly ashes. Cement and Concrete Research. 1999 Aug;29(8):1323-9. https://doi.org/10.1016/S0008-8846(98)00243-9
[13] Saranya P, Nagarajan P, Shashikala A. Performance evaluation of geopolymer concrete beams under monotonic loading. Structures. 2019 Aug;20:560-569. https://doi.org/10.1016/j.istruc.2019.06.010
[14] Patel V , Singh B, Arora V V, Study on fracture behaviour of high strength concrete including effect of steel fiber. Indian Concrete Journal. 2020; 94(4): 1-9.
[15] Arora VV, Singh B, Patel V, Daniel Y, Mohapatra BN. Stress-Strain Behaviour and Performance Evaluation of High Strength Steel Fibre Reinforced Concrete. Indian Concrete Journal.2019; 93(12): 54-61.
[16] Arora VV, Singh B, Patel V, Trivedi A. Evaluation of modulus of elasticity for normal and high strength concrete with granite and calc-granulite aggregate. Structural Concrete. 2021 Jan;22(S1): E-143-E-151. https://doi.org/10.1002/suco.202000023
[17] Ojha P, Singh P, Singh B, Singh A, Mittal P. Fracture behavior of plain and fiber-reinforced high strength concrete containing high strength steel fiber. Res Eng Struct Mater. 2022; 8(3): 583-602, https://doi.org/10.17515/resm2022.377ma1228
[18] Wattimen OK, Antoni A, Hardjito D. A review on the effect of fly ash characteristics and their variations on the synthesis of fly ash based geopolymer. AIP Conference Proceedings 1887, 020041. 2017; 020041. https://doi.org/10.1063/1.5003524
[19] Hutagi A, Khadiranaikar RB. Flexural behavior of reinforced geopolymer concrete beams. 2016 International Conference on Electrical, Electronics, and Optimization Techniques (ICEEOT), Mar. 2016; 3463-3467. https://doi.org/10.1109/ICEEOT.2016.7755347
[20] El-Sayed TA, Algash YA. Flexural behavior of ultra-high performance geopolymer RC beams reinforced with GFRP bars. Case Studies in Construction Materials. 2021 Dec;15:e00604. https://doi.org/10.1016/j.cscm.2021.e00604
[21] Mo KH, Alengaram UJ, Jumaat MZ. Structural performance of reinforced geopolymer concrete members: A review. Construction and Building Materials. 2016 Sep;120:251-64. https://doi.org/10.1016/j.conbuildmat.2016.05.088
[22] Mohammed AA, Ahmed HU, Mosavi A. Survey of Mechanical Properties of Geopolymer Concrete: A Comprehensive Review and Data Analysis. Materials. 2021 Aug 20;14(16):4690. https://doi.org/10.3390/ma14164690
[23] IS 269: 2015. Ordinary Portland Cement - Specification (Sixth Revision), (Reaffirmed Year : 2020). Bureau of Indian Standards, Delhi.
[24] IS 3812 (2013). Pulverised Fuel Ash - Specification, Part 1: For use in cement, cement mortar and concrete. Bureau of Indian Standards, Delhi.
[25] IS 15388: 2003, "Silica Fume - Specification", Bureau of Indian Standards, Delhi.
[26] IS 16714: 2018 "Ground granulated blast furnace slag for use in cement, cement mortar and concrete - specifications,'" Bureau of Indian Standards, Delhi.
[27] IS 4032: 1985 (Reaffirmed Year: 2019), "Method of chemical analysis of hydraulic cement", Bureau of Indian Standards, Delhi.
[28] IS 383-2016, 2016, "Coarse and Fine Aggregate for Concrete - Specification (Third Revision)", Bureau of Indian Standards, Delhi.
[29] IS 10262 : 2009, "Concrete mix proportioning - guidelines", Bureau of Indian Standards, Delhi".

[30] Trivedi A, Ojha PN, Singh A, Singh B, Bansal S, Sengupta L. Experimental investigations on mechanical properties of normal and high strength high calcium geopolymer concrete. JACF. 2022 Jun 30;8(1):16-25. https://doi.org/10.18702/acf.2022.6.8.1.16
[31] Kaya M. The effect of micro-SiO2 and micro-Al2O3 additive on the strength properties of ceramic powder-based geopolymer pastes. J Mater Cycles Waste Manag. 2022 Jan;24(1):333-50. https://doi.org/10.1007/s10163-021-01323-3
[32] Kaya M, Karahan O, Atiş CD. Influence of Silica Fume Additive and Activator Ratio on Mechanical Properties in Slaked Lime-Based Alkali-Activated Mortars. Iran J Sci Technol Trans Civ Eng. 2022 Sep 1:4:1-22 https://doi.org/10.1007/s40996-022-00960-4
[33] IS 456: 2000, "Reinforced Concrete - Code of Practice," Bureau of Indian Standards, Delhi.
[34] S. Kumaravel and S. Thirugnanasambandam. Flexural behaviour of geopolymer concrete beams. Int. J. Adv. Engg. Res. Studies, 2013; 04:1-4.
[35] Ren J, Chen H, Sun T, Song H, Wang M. Flexural Behaviour of Combined FA/GGBFS Geopolymer Concrete Beams after Exposure to Elevated Temperatures. Advances in Materials Science and Engineering. 2017;2017:1-9. https://doi.org/10.1155/2017/6854043
[36] IS: 516 (Part 1/Sec 1): 2021 "Hardened concrete methods of test part 1 testing of strength of hardened concrete section 1 compressive, flexural and split tensile strength (First Revision)", Bureau of Indian Standards, Delhi".
[37] IS: 516 (Part 8/Sec 1): 2020 "Hardened concrete methods of test part: 1-8 Determination of Modulus of Elasticity Section 1: Static Modulus of Elasticity and Poisson's ratio in Compression (First Revision)", Bureau of Indian Standards, Delhi".
[38] D.M.J. Sumajouw, B.V. Rangan, "Low Calcium Fly Ash-Based Geopolymer Concrete: Reinforced Beams and Columns, Research Report GC 3", Curtin University of Technology, Perth, Australia, 2006
[39] R. Andalib, M.W. Hussin, M.Z.A. Majid, M. Azrin, H.H. Ismail. Structural performance of sustainable waste palm oil fuel ash-fly ash geo-polymer concrete beams. Environ. Treat. Technol. 2014; 2 (3): 115-119.
[40] B. Singh., V. V Arora, and V. Patel. Experimental study on stress strain behaviour of normal and high strength unconfined concrete. Indian Concrete Journal. 2020; 94(4): 10-19.
[41] Ojha PN, Trivedi A, Singh B, N S AK, Patel V, Gupta RK. High performance fiber reinforced concrete – for repair in spillways of concrete dams. Res Eng Struct Mater. 2021; 7(4):505-522. https://doi.org/10.17515/resm2021.252ma0128
[42] B Singh, P N Ojha, A Trivedi, V Patel, & V V Arora (2021). Development Of Empirical Equations For Prediction Of Flexural And Split Tensile Strength For Normal And High Strength Concrete With Granite And Calc-Granulite Aggregate, Indian Concrete Journal, November 2021; 95(11): 36-46
[43] PN Ojha, B Singh, A Singh, V Patel, VV Arora. Experimental study on creep and shrinkage behaviour of high strength concrete for application in high rise buildings. Indian Concrete Journal. 2021; 95(2) 30-42.
[44] Ojha PN, Mittal P, Singh A, Singh B, Arora VV. Optimization and evaluation of ultra high-performance concrete. acf. 2020 Jun 30;6(1):26-36. https://doi.org/10.18702/acf.2020.6.6.26
[45] V V Arora & B Singh, (2016), Durability Studies on Prestressed Concrete made with Portland Pozzolana Cement, Indian Concrete Journal. 2016; 90(8):41-48

Research on Engineering Structures & Materials
journal homepage: http://www.jresm.org
Research Group

Research Article

Tensile and charpy impact properties of CNTs integrated PET/ Glass Fiber thermoplastic composites with commingled yarn

Özgür Demircan*[1,2,a], Sarah Sufyan[2,b], Ahmed Mohamed Basem[2,c]

[1]*Department of Metallurgical and Material Engineering, Ondokuz Mayıs University, Samsun, Turkey*
[2]*Department of Nanoscience and Nanotechnology, Ondokuz Mayıs University, Samsun, Turkey*

Article Info

Article history:

Received 06 Jun 2022
Revised 27 Aug 2022
Accepted 29 Aug 2022

Keywords:

Carbon nanotubes (CNTs);
Non-crimp fabric (NCF);
Glass fibre (GF);
Polyethylene terephthalate (PET);
Composite materials;
Tensile;
Charpy impact properties

Abstract

Within this study, the non-crimp fabrics (NCF) with commingled yarns that they contained hybrid structures in which two different materials in the form of fibers were mixed, which consisted of polyethylene terephthalate (PET)/glass fiber (GF), were coated with multi-walled carbon nanotubes (MWCNTs) (weight percentages were 0 and 0.9%) and modified multi-walled carbon nanotubes (MWCNTs-Carboxylic acid (COOH)) (weight percentages were 0 and 0.9%) to fabricate hybrid composites. Three types of composite materials were prepared (pure polyethylene terephthalate/glass fiber (PET/GF), PET/GF with MWCNTs and PET/GF with MWCNTs-COOH) and they were tested against tensile and Charpy impact loadings. The effects of MWCNTs contents on the micro-structure and morphology of the composites were reported by using a scanning electron microscope (SEM), fourier transform infrared spectroscopy analysis (FTIR) and optical microscopy (OM). The specimens with MWCNTs-COOH exhibited an enhancement of 33% tensile strength, 23% tensile modulus and 8% Charpy impact energy compared to the samples without MWCNTs-COOH. It can be concluded that even a small mass fraction of MWCNTs was capable of improving the mechanical performance of the glass fiber reinforced PET matrix composites. In other words, due to the presence of the carbon nanotubes on the fiber surface helped to improve interfacial adhesion in the fabricated composites.

1. Introduction

Scientists and researchers used the nanomaterials in the producing of composite materials [1]. Carbon nanotubes (CNTs) are today considered to be the most important nanomaterials. CNTs are used in numerous applications like nanotechnology, optics, water treatment, electronics and other levels of the materials science. In addition, the tensile strength of CNTs is close to 100 times higher than those in steel. CNTs are made from thin, long cylinders of the atomic layer of graphite, with diameters usually measured in nanometers [2-5]. The incorporation of nanotubes can improve the properties of composites very well [6, 7]. MWCNTs consist of several concentric graphene tubes installed inside the other with a diameter in the nanometer scale [8, 9]. In addition, MWCNTs have a higher grade of stability and stiffness compared to single-WCNTs [10].

Thermoplastic consumption is approximately 80% from the total plastic consumption. These materials permit manufacturing of composite materials in short times that makes them possible to produce large quantities [11]. Polyethylene terephthalate (PET) is used as a container for food and liquids. PET material is hard, strong material that absorbs a little water and it has resistance to impact, moisture, alcohols and solvents [12, 13, 14].

*Corresponding author: ozgur.demircan@omu.edu.tr
[a] orcid.org/0000-0001-8235-3966; [b] orcid.org/0000-0001-7469-1949; [c] orcid.org/0000-0002-1491-3308
DOI: http://dx.doi.org/10.17515/resm2022.442ma0606

Glass fibers (GF) are made from extremely fine fiber of glass. The principal advantages of the glass fibers are high tensile, low cost, high chemical resistance properties [15, 16].

Some studies were done on the commingled fiber reinforced textile composites. Effect of comingling techniques on mechanical properties of natural fibre reinforced cross-ply thermoplastic composites were studied by Abidin et al. [17].

Many researchers studied the improvement of the mechanical properties of thermoplastic and thermoset composites through adding CNTs. Gojny et al. reported the investigation of the effect of various types of CNTs on the mechanical properties of epoxy matrix materials [18]. Shazed et al. reported that the Young's modulus increased by 104% and the tensile strength improved by approx 64%, due to the presence of CNTs in the polypropylene composites [19]. The mechanical properties of CNTs integrated carbon fiber reinforced thermoplastic composites was investigated by Liu et al. [20]. They obtained an improvement of 27.0% of the impact toughness after using CNT/CF hybrid fiber in the fabrication process. Hao et al. studied the enhancing of the mechanical properties of the poly ether ketone/zinc oxide nanocomposites [21]. Glass fiber–epoxy composites with boron nitride nanotubes for enhancing interlaminar properties in structures were studied by Rahmat et al. [22].

There are many studies on improving interface properties of the CNTs integrated thermoplastic composites. Demircan et al. reported the effects of carbon nanotubes (0.0, 0.7, 0.9, and 1.1-wt %) on the mechanical properties of glass fiber thermoplastic composites [23]. The difference from the previous article [23] was that they used a low melting point temperature PET (LPET) polymer with one type of MWCNTs, they didn't conduct a Charpy impact test on specimens and they didn't modelled the tensile properties of the composites. The obtained results of our study can be inspiring for many upcoming studies in this field.

2. Experimental

2.1. Composite Constituents

The specifications of the NCFs (Metyx Composites Corporation, Istanbul/Turkey), MWCNTs and the modified MWCNTs-COOH (Ege Nanotek Kimya Sanayi, Izmir/Turkey) are given in Table 1, Table 2 and Table 3 respectively.

There are glass fiber types such as A, C, E, S etc. E-glass commonly used in most of the composite applications. We used E glass type in our research.

2.2. Fabrication Method

The NCFs with the dimensions of 200 mm x 200 mm were prepared in ten layers. Two kinds of solutions with the MWCNTs and modified MWCNTs (MWCNTs-COOH) were prepared using ethanol. At first, the MWCNTs distributed throughout the ethanol by using a magnet bar, stirred by a magnetic field. After that, an ultrasonic bath was used to disperse the MWCNTs in the ethanol.

Both faces of NCFs were coated by using the solution of MWCNTs and ethanol as shown in Figure 1 (a). The MWCNTs coated fabrics were symmetrically left in the mold cavity of the hot press machine $[90^o/0^o]_{10s}$ (Figure 1 (b)). The top views of schematic representation of the NCF layers were shown in Figure 1 (c).

The hot press machine was used to produce the NCF composites. The molding temperature and pressure were 205 ^{o}C and 22 bar, which were the same used values for all fabricated specimens. ASTM D3171-99 standard was used to calculate weight and volume fractions of the samples (Table 4).

Table 1. The specifications of non-crimp fabric (NCF)

	Biaxial yarn 0° (warp) fibers	Biaxial yarn 90° (weft) fibers	Binding fibers
Weight composition	60% E glass fibers 40% PET fibers	60% E glass fibers 40% PET fibers	100% polyester
Color	Natural white	Natural white	Natural white
Weight (g/m2)	380	380	5.0
Yarn count (Tex)	525	525	7.6

Table 2. The specifications of multi-walled carbon nanotubes (MWCNTs)

Parameter	Value
Outer diameter (nm)	10–20
Interior diameter (nm)	5–10
Length (μm)	10–30
Surface area (m^2/g)	>200
Color	Black
Ash	Mass<%1.5
Electrical conductivity (S/cm)	>100
Density (tap) (g/cm^3)	0.22
Density (true) (g/cm^3)	2.1

Table 3. The specifications of modified multi-walled carbon nanotubes (MWCNTs-COOH)

Parameter	Value
Content of-COOH (wt %)	2
Outer diameter (nm)	10–20
Interior diameter (nm)	5–10
Length (μm)	10–30
Surface area (m^2/g)	>200
Color	Black
Ash	Mass<%1.5
Electrical conductivity (S/cm)	>100
Density (tap) (g/cm^3)	0.22
Density (true) (g/cm^3)	2.1

Table 4. Weight and volume fractions of composites for the tested specimens

Weight percentages of MWCNTs (MWCNTs wt-%)	Weight percentages of glass fibers (GF wt-%)	Volume percentages of glass fibers (GF vol-%)	Density (g/cm^3)	Thickness (mm)
0.0 (Pure GF/PET)	63.38	44.47	1.824	3.42
0.9 (GF/PET with MWCNTs)	59.86	42.00	1.824	3.64
0.9 (GF/PET with MWCNTs-COOH)	63.85	45.64	1.858	3.42

2.3. Characterization

Tensile and Charpy impact tests were performed on the fabricated specimens in the 0 degree directions. Figure 2 (a) and (b) show the specimen geometries for tensile and

Charpy impact characterization tests. The tensile tests (INSTRON 5982 100KN (USA)) were conducted on the samples with the dimensions of the 160 mm x 20 mm x thickness and the thickness of the aluminum tab was 0.2 mm according to ASTM-D3039 standard (Figure 2 (a)). The linear displacement speed in the tensile test was 1 mm/min.

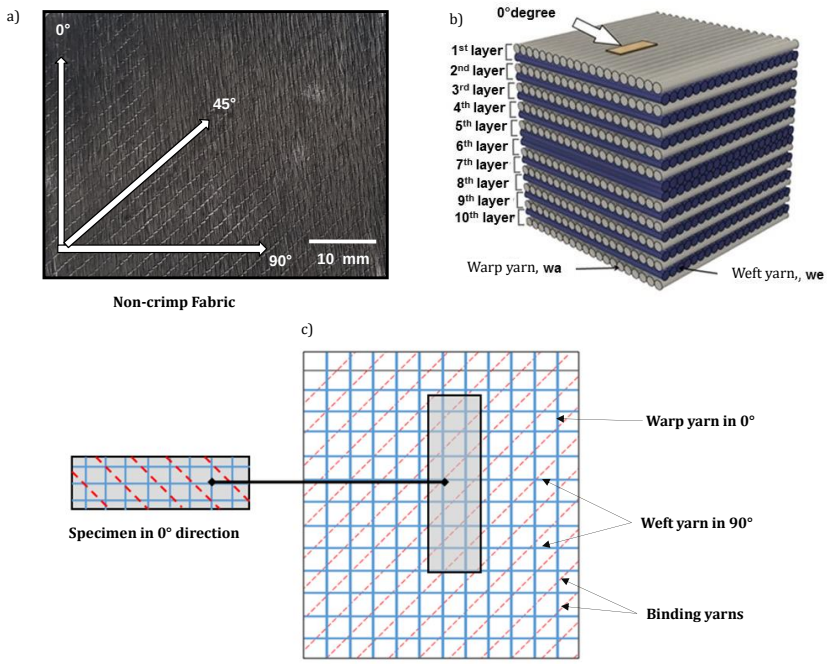

Fig. 1 (a) Real image of MWCNTs coated biaxial ($0^o/90^o$) NCF, (b) side view of schematic representation of symmetrical stacking of biaxial ($0^o/90^o$) NCF layers and (c) top view of schematic representation of symmetrical stacking of biaxial ($0^o/90^o$) NCF layers

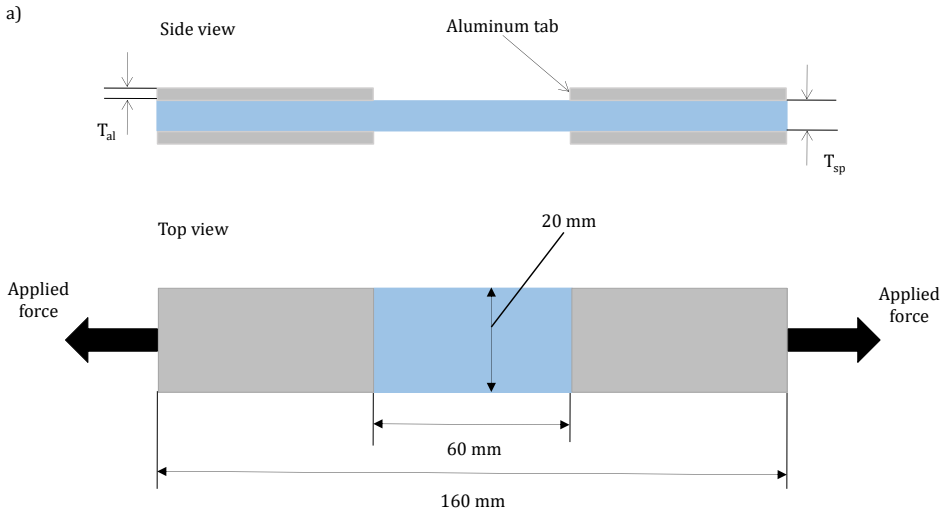

(a)

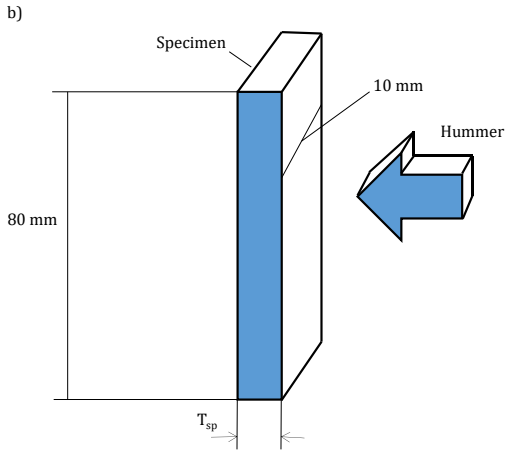

(b)

Fig. 2 (a) The sample dimensions of the tensile test, Tsp: the thickness of the specimen, Tal: the thickness of the aluminum tab, (b) The sample dimensions of the Charpy impact test

ALSA ZBC 2000, Turkey type of machine was used in the Charpy impact tests. The all types of fabricated unnotched samples were tested in size of 80 mm x 10 mm x thickness (Figure 2 (b)). The tensile and Charpy impact test set ups were shown in Figure 3.

(a) (b)

Fig. 3 (a) Tensile, (b) Charpy impact test set ups

3. Results and Discussion

3.1. Surface Characteristics of CNT-coated Fibers

Figure 4 (a) to (c) show the scanning electron microscope photographs of the commingled yarn (PET fiber/glass fiber). The homogeneous carbon nanotubes distributions on the

surfaces of the glass fibers were seen in Figure 4 (a) and (b). The CNT bridging and pullout were influenced by the homogeneous carbon nanotube distribution on fiber surface. Figure 4 (c) shows the presence of a few CNTs agglomerations on the coated the fiber.

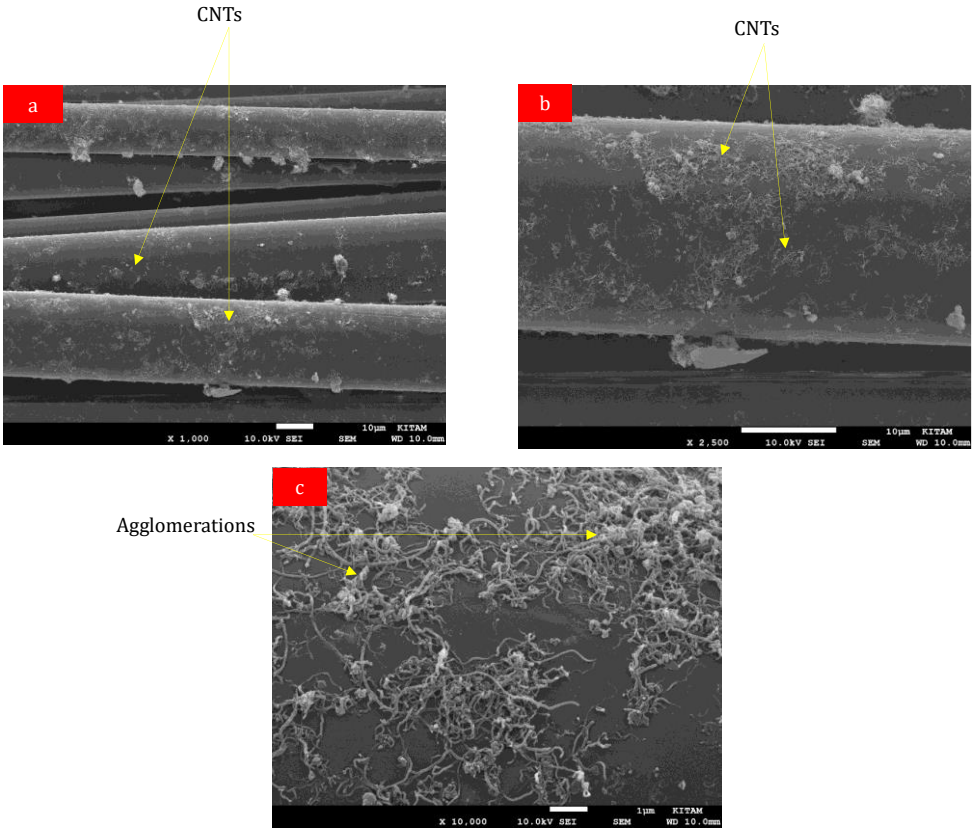

Fig. 4 (a), (b) and (c) SEM images of surface morphologies of PET-glass commingled fibers after grafting CNTs. SEM: scanning electron microscopic; PET: polyethylene terephthalate; CNTs: carbon nanotubes

The obtained data from FTIR analysis of pure MWCNTs, PET/GF and PET/GF+MWCNTs are shown in Figure 5. Figure 5 (a) (FTIR spectrum of the MWCNTs) shows the presence of the hydroxyl groups at 3731 cm^{-1}. The bands in the spectrum at 2989 and 2904 cm^{-1} are induced by C–H stretching vibrations on the nanotube surface, which reveal the –CH3 absorption [24, 25]. The appearing of the peaks and its positions depending on the bonds types of the structure. The production process of nanotubes is responsible for the generation of the functional groups on the nanotube surface [26]. The PET monomer consists of: 2 esters, 1 aromatic ring and 1 ethyl functional groups.

Group of terephthalate are bound with the ethyl group to form a PET monomer. The functional groups at the PET monomer consist of several bonds such as: C – O, C – H, C – C and aromatic ring. The main peak from the PET structure at 1715 cm^{-1} was the C=O group of terephthalic acid ester [27, 28] (Figure 5 (b)). The bands at 872 cm^{-1} and 1408 cm^{-1} refer to the groups of silanol on the surface of the fiber and the C-O groups. After grafting of the MWCNTs on the non-crimp PET/GF (Figure 5 (c)), any changes on the intensities and the characteristics of the spectrum were not seen, just a physical interaction between the MWCNTs and NCFs. Our results agreed well with the results of FTIR characterization of

Demircan et al. [23]. It can be noted that the most of the peaks that appeared in the article of Demircan et al. [23] were seemed in our experiment of FTIR test.

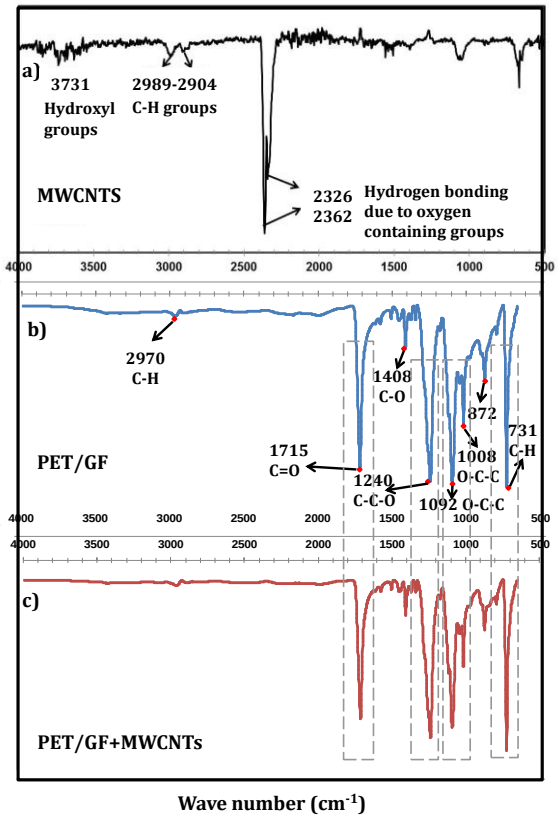

Fig. 5 (a), (b) and (c) Results of FTIR characterization

3.2. Tensile Properties

The tensile properties were calculated from the excel table of the test results. The tensile strength was the value of the maximum stress on the stress-strain graphs. Tensile modulus were calculated from the slopes of the curves of the stress-strain diagrams. The presented stress-strain diagram (Figure 6 a) was corresponding to the longitudinal direction of the loading.

The tensile properties of the fabricated composites with 0.9-wt % MWCNTs and 0.9-wt% MWCNTs-COOH showed higher value compared to the 0.0-wt% MWCNTs and 0.0-wt% MWCNTs-COOH composites. An improvement of approximately 17% and 23% tensile modulus and 20% and 33% tensile strengths were obtained from 0.9-wt% MWCNTs and MWCNTs-COOH compared to the samples without MWCNTs (Figure 6 (b)). It was expected that the possible cause for having the enhanced tensile properties for the samples with MWCNTs was the presence of the carbon nanotubes on the fiber surface.

3.3. Laminate Theory

The laminate theory was used for the calculation of the tensile modulus of the composite. The modulus of the composites were increased by adding CNTs (Table 5). The tensile modulus of the composites with MWCNTs-COOH (25.4 GPa) was highest compared to the

composites with MWCNTs (22.7 GPa) and pure GF/PET (21.4 GPa). Since the modulus of the composites were increased by adding CNTs from the experiments, the results from the laminate theory agreed well with the results from the experiments.

Effect of the binding yarns on the calculated tensile modulus could not be reflected in the laminate theory, due to this reason the modulus results of the laminate theory of the composite structures were much higher than the experimental results [29].

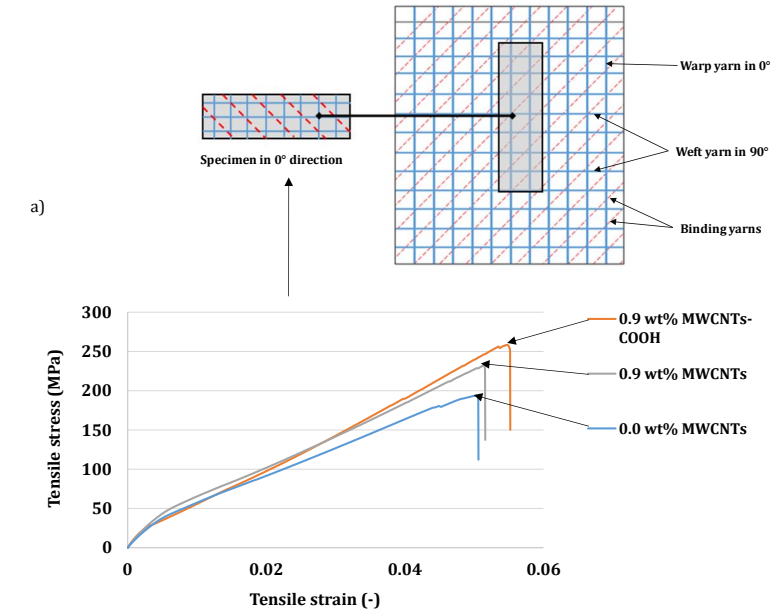

(a)

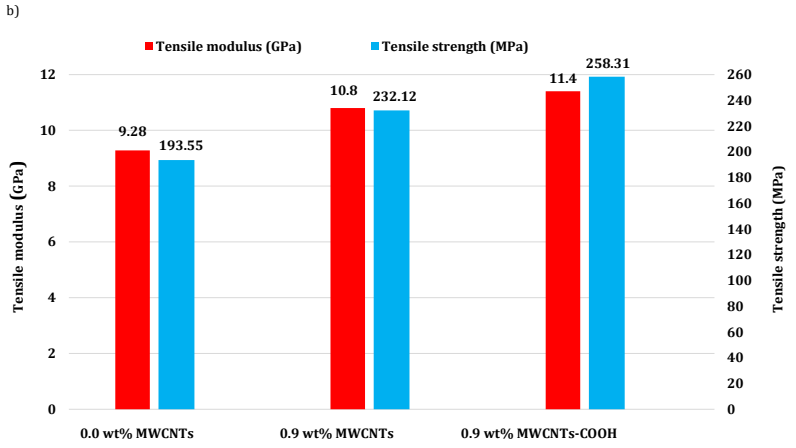

(b)

Fig. 6 (a) Stress–strain curves from tensile test, (b) Results of the tensile modulus and strength of the specimens

Table 5. The modulus results from tensile test and laminate theory

Sample	Modules from experiment E_{exp} [GPa]	Modules from laminate theory E_{Lam} [GPa]	Difference between E_{Lam} and E_{exp} [%]
0.0 (Pure GF/PET)	9.28	21.4	+130.6
0.9 (GF/PET with MWCNTs)	10.8	22.7	+110.2
0.9 (GF/PET with MWCNTs-COOH)	11.4	25.4	+122.8

3.4. Charpy Impact Properties

The fabricated specimens with 0.0-wt% MWCNTs had 4.49 J Charpy impact absorbed energy, whereas that was 5.50 J with 0.9-wt% MWCNTs and 4.85 J with 0.9-wt% MWCNTs-COOH (Figure 7).

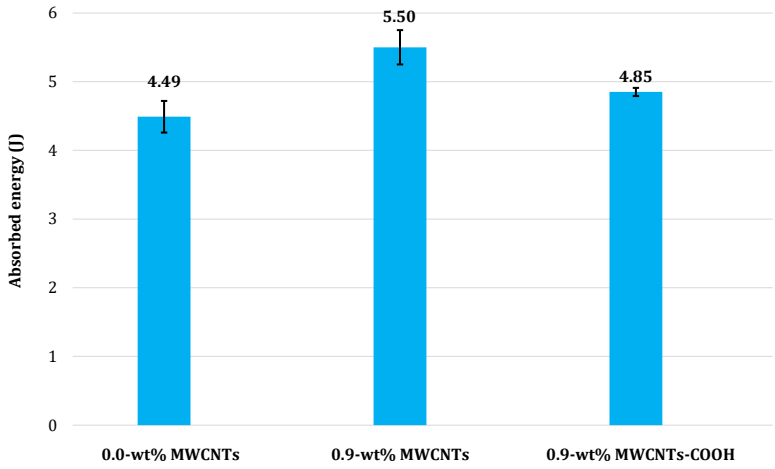

Fig. 7 Charpy impact absorbed energy of the specimens

The obtained results in our study clearly showed an enhancement of the Charpy impact absorbed energy in the fabricated composite materials combined with nanomaterial (MWCNTs and MWCNTs-COOH) compared to the fabricated composite without nanomaterial in 0°.

The Charpy impact properties of the fabricated composites with 0.9 wt-% MWCNTs and 0.9-wt% MWCNTs-COOH had higher value compared them to the 0.0-wt% MWCNTs in 0°. An enhancement of about 22% and 8% Charpy impact absorbed energies were gained from 0.9-wt% MWCNTs and MWCNTs-COOH compared to the fabricated samples without MWCNTs.

3.5. Results of Fracture Aspects of Composites

The SEM images of the through thickness parts of the samples containing 0.9-wt% of MWCNTs from the tensile test is shown in Figure 8 (a) and (b). It is believed that each of the following factors like, fiber bridging, CNT pullout and CNT bridging contributed to the fracture toughness of the specimens.

We can see in Figure 9 (a) and (b) the fracture aspects from the OM of tensile tested through thickness parts of the samples in the 0°. In Figure 9, it was shown some force application. This represents the direction of the force from the tensile test. It is a tensile force. We applied the force on the specimens on the longitudinal direction of the fabricated plates. The prominent failure mechanism was mode I in Figure 9a. The failure modes of the tensile tested composite samples with 0.0-wt% MWCNTs were matrix cracks, transverse cracks and delaminations (Figure 9 (a)). The absence of delaminations and few numbers of fiber and matrix cracks in the composite with 0.9-wt% MWCNTs (Figure 9 (b)) refers to enhanced mechanical properties of those composite structures.

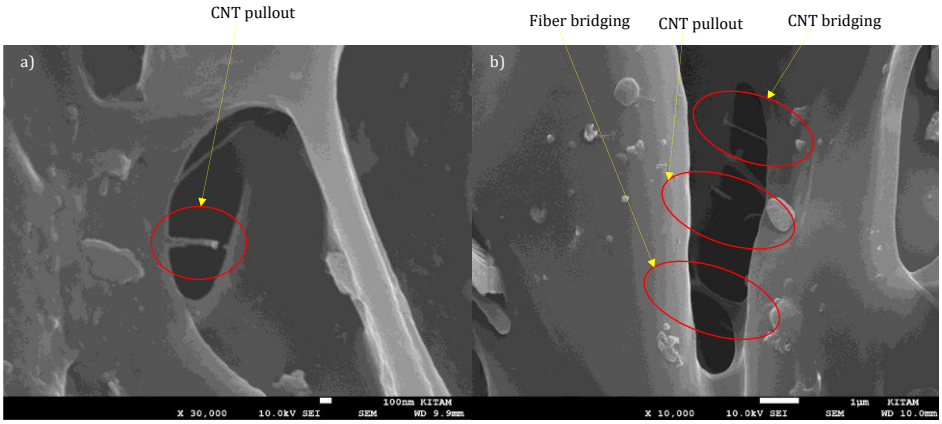

(a) (b)

Fig. 8 (a) and (b) SEM images of fractured specimens with MWCNTs from tensile test

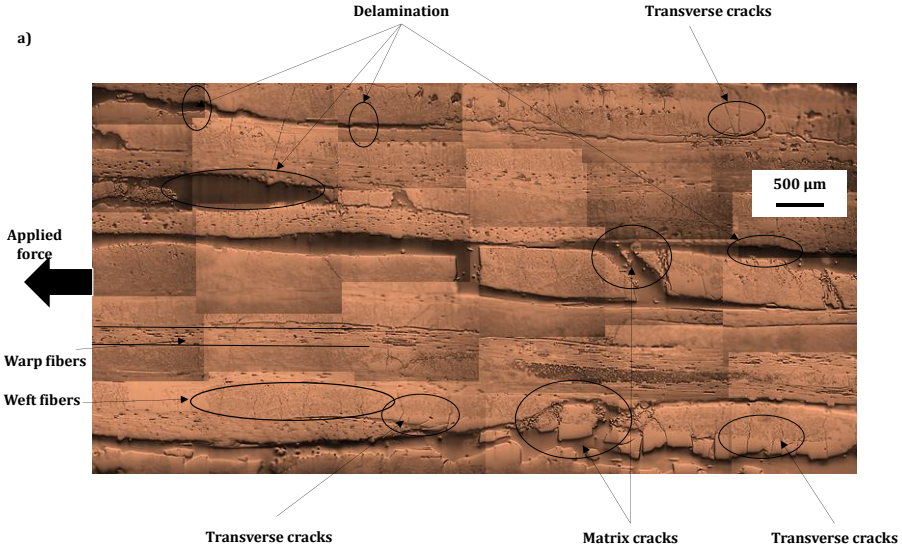

(a)

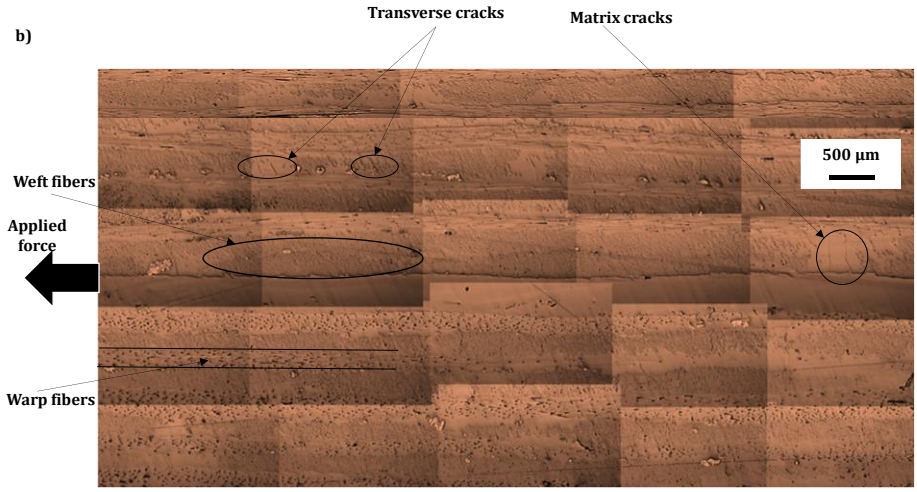

(b)

Fig. 9 (a) and (b) Fracture aspects of optical micrograph from tensile tested specimens (a) 0.0-wt% MWCNTs and (b) 0.9-wt% MWCNTs. MWCNTs: multi-walled carbon nanotubes

4. Conclusions

Within this study, the NCF with the commingled yarn of the polyethylene terephthalate (PET)/glass fiber (GF) were coated with MWCNTs and MWCNTs-COOH (the weight percentages were 0 and 0.9%) to fabricate hybrid thermoplastic composites. Three different types of thermoplastic composite materials were prepared (pure polyethylene terephthalate/glass fiber (PET/GF), PET/GF with MWCNTs and PET/GF with MWCNTs-COOH). The effects of MWCNTs contents on the micro-structure and morphology of the composites were investigated by using a SEM, FTIR analysis and OM.

The homogeneous carbon nanotubes distributions on the surfaces of the glass fibers as well as the presence of a few CNTs agglomerations on the coated the glass fibers were seen from the SEM images of the CNTs coated fibers.

Our study showed the Charpy impact and tensile properties of the fabricated PET/glass fiber reinforced thermoplastic composites with 0.9 wt% MWCNTs and 0.9 wt% MWCNTs-COOH demonstrated higher values compared to the 0.0 wt% MWCNTs fabricated composites. Furthermore, each of the following factors like, fiber bridging, CNT pullout and CNT bridging contributed to the fracture toughness of the specimens. Morover, from the tensile tested OM images of MWCNTs integrated glass fiber reinforced specimens, the absence of delaminations and few numbers of fiber and matrix cracks were appeared.

FTIR results showed that after grafting of the MWCNTs on the non-crimp PET/GF, any changes on the intensities and the characteristics of the spectrum were not seen, just a physical interaction between the MWCNTs and NCFs.

Considering the improvement in tensile modulus, tensile strength, Charpy impact strength, it can be concluded that even a small mass fraction of MWCNTs was capable of enhancing the mechanical performance of the glass fiber reinforced PET matrix composites. Our future research will be investigating the effect of nano materials on the Short Shear Beam characteristics of the thermoplastic and thermoset composite materials.

Acknowledgement

This study has been granted by Research fund of Ondokuz Mayıs University Project No: PYO.MUH.1901.16.001.

References

[1] Lue JT. Physical properties of nanomaterials. Encyclopedia of Nanoscience and Nanotechnology.2007; 10 (1): 1-46.
[2] Roco MC. National Nanotechnology Initiative - Past, Present, Future, in Handbook on Nanoscience Engineering and Technology. 2nd edn. Taylor and Francis, Oxford, 2007: 3.1- 3.26.
[3] Bonard JM, Kind H, Stockli T, Nilsson LO. Field emission from carbon nanotubes: the first five years. Solid-State Electrons. 2001; 45 (6): 893-914. https://doi.org/10.1016/S0038-1101(00)00213-6
[4] Daenen M, Fouw RD, Hamers B, Janssen PGA, Schouteden K, Veld MAJ. The wondrous world of carbon nanotubes. A Review of current carbon nanotube technologies, Endhoven University of Technology, Eindhoven. 2003;1-97.
[5] Odom TW, Huang JL, Lieber CM. Single walled carbon nanotubes: from fundamental studies to new device concepts. Annals of the New York Academy of Sciences. 2002; 960(1): 203-215. https://doi.org/10.1111/j.1749-6632.2002.tb03035.x
[6] Loos MR, Schulte K. Is it worth the effort to reinforce polymers with carbon nanotubes? Macromolecular Theory and Simulations. 2011; 20 (5): 350-362. https://doi.org/10.1002/mats.201100007
[7] Kukovecz A, Kozma G. Konya Z. Multi-walled carbon nanotubes. In: R Vajtai (ed) Springer handbook of nanomaterials. New York: Springer Dordrecht Heidelberg. 2013; 147-188. https://doi.org/10.1007/978-3-642-20595-8_5
[8] Ghavamian A, Öchsner A. Numerical investigation on the influence of defects on the buckling behavior of single-and multi-walled carbon nanotubes. Physica E: Low-dimensional Systems and Nanostructures. 2012; 46: 241-249. https://doi.org/10.1016/j.physe.2012.08.002
[9] Annu A, Bhattacharya B, Singh PK, Shukla PK, Rhee HW. Carbon nanotube using spray pyrolysis: recent scenario, Journal of Alloys and Compounds. 2017; 691: 970-982. https://doi.org/10.1016/j.jallcom.2016.08.246
[10] Lee JH, Rhee KY, Park SJ. The tensile and thermal properties of modified CNT-reinforced basalt/epoxy composites. Materials Science and Engineering: A. 2010; 527(26): 6838-6843. https://doi.org/10.1016/j.msea.2010.07.080
[11] Wiegand N, Mäder E. Commingled yarn spinning for thermoplastic/glass fiber composites. Fibers. 2017; 5(3): 26-41. https://doi.org/10.3390/fib5030026
[12] Baeurle SA, Hotta A, Gusev AA. On the glassy state of multiphase and pure polymermaterials. Polymer. 2006; 47 (17): 6243-6253. https://doi.org/10.1016/j.polymer.2006.05.076
[13] Massey LK. Permeability properties of plastics and elastomers: a guide to packaging and barrier materials. Publisher: William Andrew. 2003; 1-601. https://doi.org/10.1016/B978-188420797-6.50095-4
[14] Escala A, Stein RS. Crystallization studies of blends of polyethylene terephthalate and polybutylene terephthalate. Advances in Chemistry. 1979; 176 (24): 455-487. https://doi.org/10.1021/ba-1979-0176.ch024
[15] Rajak, D. K., Wagh, P. H., & Linul, E. A Review on Synthetic Fibers for Polymer Matrix Composites: Performance, Failure Modes and Applications. Materials, 2022 15(14), 4790. https://doi.org/10.3390/ma15144790
[16] Matthews, F. L., Davies, G. A. O., Hitchings, D., & Soutis, C. Finite element modelling of composite materials and structures. Elsevier. 2000. https://doi.org/10.1201/9781439822807

[17] Awais H, Nawab Y, Amjad A, Anjang A., Akil HM, Abidin MSZ. Effect of comingling techniques on mechanical properties of natural fibre reinforced cross-ply thermoplastic composites. Composites Part B. 2019; 177: 107279. https://doi.org/10.1016/j.compositesb.2019.107279

[18] Gojny FH, Wichmann MHG, Fiedler B, Schulte K. Influence of different carbon nanotubes on the mechanical properties of epoxy matrix composites - a comparative study. Composites Science and Technology. 2005; 65: 2300-2313. https://doi.org/10.1016/j.compscitech.2005.04.021

[19] Shazed MA, Suraya AR, Rahmanian S, Salleh MAM. Effect of fiber coating and geometry on the tensile properties of hybrid carbon nanotube coated carbon fiber reinforced composite. Materials and Design. 2014; 54: 660-669. https://doi.org/10.1016/j.matdes.2013.08.063

[20] Liu W, Li L, Zhang, S, Yang, F & Wang R. Mechanical properties of carbon nanotube/carbon fiber reinforced thermoplastic polymer composite. Polymer Composites. 2017; 38(9): 2001-2008. https://doi.org/10.1002/pc.23771

[21] Hao L, Hu Y, Zhang Y, Wei W, Hou X, Guo Y, Jiang D. Enhancing the mechanical performance of poly (ether ether ketone)/zinc oxide nanocomposites to provide promising biomaterials for trauma and orthopedic implants. RSC advances. 2018; 8(48): 27304-27317. https://doi.org/10.1039/C8RA01736K

[22] Rahmat M, Jakubinek MB., Ashrafi B, Martinez-Rubi Y, Simard B, Glass fiber–epoxy composites with boron nitride nanotubes for enhancing interlaminar properties in structures. ACS Omega. 2022; 7: 10674–10686. https://doi.org/10.1021/acsomega.2c00365

[23] Demircan O, Al-darkazali A, Inanç I, Eskizeybek V. Investigation of the effect of CNTs on the mechanical properties of LPET/glass fiber thermoplastic composites. Journal of Thermoplastic Composite Materials. 2019; 33 (12): 1652-1673. https://doi.org/10.1177/0892705719833105

[24] Eskizeybek V, Avcı A, Gulce A. The Mode I interlaminar fracture toughness of chemically carbon nanotube grafted glass fabric/epoxy multi-scale composite structures. Composites Part A: Applied Science and Manufacturing. 2014; 63: 94-102. https://doi.org/10.1016/j.compositesa.2014.04.013

[25] Qui NV, Scholz P, Krech T, Keller TF, Pollok K, Ondruschka B. Multiwalled carbon nanotubes oxidized by UV/H2O2 as catalyst for oxidative dehydrogenation of ethylbenzene.Catalysis Communications.2011; 12: 464-469. https://doi.org/10.1016/j.catcom.2010.11.007

[26] Scheibe B, Palen EB, Kalenczuk RJ. Oxidation and reduction of multiwalled carbon nanotubes-preparation and characterization. Materials Characterization. 2010; 61 (2): 185-191. https://doi.org/10.1016/j.matchar.2009.11.008

[27] Strain IN, Wu Q, Pourrahimi AM, Hedenqvist MS, Olsson RT, Andersson RL. Electrospinning of recycled PET to generate tough mesomorphic fibre membranes for smoke filtration. Journal of Materials Chemistry A. 2015; 3: 1632-1640. https://doi.org/10.1039/C4TA06191H

[28] Eskizeybek V, Avcı A, Gülce A. Preparation and mechanical properties of carbon nanotube grafted glass fabric/epoxy multi-scale composites. Advanced Composite Materials. 2017; 26 (2): 169-180.

[29] Demircan O, Kosui T, Ashibe S, Nakai A. Effect of stitch and biaxial yarn types on tensile, bending, and impact properties of biaxial weft-knitted composites. Advanced Composite Materials. 2013; 23 (3): 239-260. https://doi.org/10.1080/09243046.2013.851062

Research on Engineering Structures & Materials
journal homepage: http://www.jresm.org
Research Group

Research Article

Investigation on the effect of ultra fine rice husk ash over slag based geopolymer concrete

A. Chithambar Ganesh*[1,a], M. Vinod Kumar[2,b], K. Mukilan[3,c], A. Suresh Kumar[1,d], K. Arun Kumar[4,e]

[1]*Department of Civil Engineering, Sree Vidyanikethan Engineering College, Trupati, India.*
[2]*Department of Civil Engineering, Vel Tech Rangarajan Dr.Sagunthala R&D, Institute of Science and Technology, Chennai, India.*
[3]Department of Civil Engineering, *Kalasalingam Academy of Research and Education, Krishnankoil, India.*
[4]*Department of Civil Engineering, Mangalam College of Engineering, Kottayam, Kerala, India.*

Article Info

Article history:

Received 14 Aug 2022
Revised 26 Sep 2022
Accepted 11 Oct 2022

Keywords:

GGBS;
Ultra fine rice husk ash;
Geopolymer concrete;
Sustainability analysis

Abstract

In this study, The study investigates the production of sustainable geopolymer concrete using industrial wastes such as Ground Granulated Blast Furnace Slag and ultra fine Rice Husk Ash (URA). The effect of partial substitution of GGBS with URA in proportions such as 0, 5, 10, 15 and 20 percent is investigated for workability, drying shrinkage, compressive and tensile strength over different ages of concrete ranging from 7 to 90 days. A micro structural investigation through Scanning Electron Microscope and X-Ray Diffraction Analysis is carried out to analyze the micro structure of matrix. Further a sustainability analysis is conducted over the geopolymer specimens through the parameters such as cost efficiency, energy efficiency and CO2 efficiency. Results from the tests indicate a significant enhancement in workability, compressive and tensile strength and decrease in the drying shrinkage values with 15 percent utilization of URA in GPC. Micro structural study also exhibited a compact and dense microstructure of the specimen. Results clearly portray the coexistence of both calcium-based product and sodium-based product. Sustainability analysis indicates increased cost efficiency and Eco efficiency and reduction in the energy consumption with the utilization of 15 percent of URA. The study also reported the possibility of reduction of carbon footprint by increasing the dependency over Geopolymer concrete. The findings of the study unleash hefty potential towards utilizing grounded RHA in alkali activated concrete.

1. Introduction

The most versatile building material is concrete, and the principal constituent for producing concrete is cement. However, a substantial quantum of energy is consumed for the production of cement, that emits a hefty amount of CO_2 corresponding to the manufacturing process[1,2]. It is also to be noted that, making 1 t of cement liberates half a tonne of CO_2. Furthermore, if carbon fuel is utilised in this operation, an additional 0.45 t of CO_2 will be produced. As a result, producing 1 t of cement produces nearly 1 t of CO_2[2–4]. On the other hand, clinker is the primary raw material needed for cement manufacturing process, which is formed by processing limestone at temperatures more than 1000°C. The essential energy for this heating is obtained through the combustion of fossil fuels. As a result, the cement sector is thought to be responsible for about 8 percent of global CO_2 emissions[4,5]. A substitute for cement or a technology for concrete with no cement is the sustainable option. This demands the necessity of invention of cement less material for a sustainable progress in the construction sector.

*Corresponding author: chithambarmailid@gmail.com
[a] orcid.org/0000-0001-5004-4587; [b] orcid.org/0000-0002-7166-2330; [c] orcid.org/0000-0003-3922-5832; [d] orcid.org/0000-0001-9406-2576; [e] orchid.org/0000-0002-5745-6864
DOI: http://dx.doi.org/10.17515/resm2022.501ma0814

The concept under the creation of geopolymer concrete (GPC) is to give a long-term alternative to traditional cement concrete of lowering CO_2 emissions. Furthermore, because this method makes use of industrial by-products, economic benefits are provided owing to their inexpensive nature. Furthermore, this technology helps to solve the problem of industrial by-product disposal.

Plenty of research works focus on the utilization of flyash for the development of geopolymer concrete[6–8], bio medical waste ash[9,10], wood ash[11–15], GGBS[16–18]. Low calcium fly ash is widely preferred owing to its abundance availability and cheap cost. Geopolymer concrete synthesized from low calcium type yield fair engineering properties, elevated temperature properties, reduced drying shrinkage and creep[19–23]. The shortfall of utilization of class C type of fly ash is its requirement to be heat cured which focused its application to only precast products[24]. Another contemporary source material for the development of GC is Rice Husk Ash (RHA). The perceived benefits of RHA based geopolymer material in improving mechanical properties are mostly related to high silica concentration of RHA[25–27]. In comparison to other source materials, RHA has the highest silica concentration ranging around 95.0 percent and the lowest alumina level not higher than 2.0 percent. More RHA volume results in higher silica content enabling a higher Si/Al ratio. Komnitsas and Zaharaki claimed higher mechanical strength with the higher Si/Al ratio[28]. However on the other hand, Songpiriyakij, et al., claimed reduction in characteristic strength with a further increase in Si/Al ratio[29]. Fletcher et al., suggest 24 as the limiting value for Si/Al ratio to be efficient in achieving the engineering properties[30]. The pitfall of utilization of URA for developing a sustainable building material is its requirement for heat curing at elevated temperatures to exhibit fair engineering properties[31]. The advent of deployment of GGBS in geopolymer concrete enabled the production of geopolymer concrete without heat curing conditions with outstanding engineering properties[16,21,32,33]. Further with the utilization of GGBS, Davidoits reported minimum requirement of sodium silicate solution which forms the major part of alkaline activator solution for the polymerization reaction to happen[34]. Davidovits reported the ability of GGBS based GPC to set and harden in minimum time using less quantity of alkaline activator solution[34]. Blending of GGBS with RHA would prove beneficial in synthesizing the geopolymer concrete at ambient curing conditions[35].Hence in this work, effort has been made to develop geopolymer concrete using RHA and GGBS.

A considerable quantity of these by-products such as GGBS and RHA are produced, and disposing of them has become a big concern. Predominantly these wastes are land-filled which is against the sustainable development. Furthermore, as the iron and steel industries expand, so will the generation of slag, which poses a significant environmental risk. From the market survey, India stands first in the global RHA production with about 105 million tonnes of Rice. Kusbiantoro et al., reported 200 kilo gram of ash generation for each 1 Metric Tonne production of Rice[31,36]. Hence utilizing these wastes for the synthesise of building material would again lessen the disposal problems and strain over the environment when compared with the other alternative source material[37].

The focus of the research is to create GPC using ultra fine RHA as a fractional substitute to GGBS as a source material and examine its mechanical characteristics. While RHA has high silica oxide level, GGBS has high calcium content and lower silica oxide content. It is therefore reasonable to assume that adding RHA to the GGBS based geopolymer concrete could increase the amount of silica available for the polymerization reaction that could improve the characteristics of GPC. Further RHA is grinded in this work to ultra fine size with the objective of increasing the specific surface area and reactivity. The novelty of this research work lies in investigating the effect of ultra fine grinded RHA over GGBS based GPC over properties such as workability, drying shrinkage,

compressive and tensile strength. A micro structural investigation using Scanning Electron Microscopy (SEM) analysis and X-Ray Diffraction (XRD) was also carried out to detect the morphology, chemical composition and crystalline phases to characteristics of matrix. Further a sustainability analysis is conducted over the geopolymer specimens through the parameters such as cost efficiency, energy efficiency and CO2 efficiency.

2. Materials and Methodology

Geopolymer concrete in this investigation was made utilizing GGBS, ultra fine RHA (URA), fine and coarse aggregate and alkaline activator solution. GGBS is procured from salem steel plant in Tamil Nadu, India. URA was procured from a local Rice mill in Salem, Tamil Nadu, India. URA is then grounded using a ball mill for about 6 hours. SEM analysis and Particle Size Analysis (PSA) for URA was carried out to find out morphology and specific surface area and are depicted in Figure 1. From SEM analysis it is seen that URA are flaky in nature. Hence it can be apprehended that URA has large potential specific surface area which could enhance the dissolution of silica ions leading to the release of precursor ions necessary for the formation of monomers. PSA reports about 90 percent of the particles less than 100 micrometer thereby confirming the ultra fine nature of URA enhancing the possibility of polymerization reaction rate. Specific gravity of URA is found as 2.34. Specific gravity of GGBS was found to be 2.9. The chemical composition of URA and GGBS procured is listed in Table 1. From Table 1, it can be observed that the GGBS is having almost equal quantities of calcium oxides and silica oxides. URA contains almost 90 percent of silica oxide serving the purpose of its addition to the geopolymer matrix. Another significant factor that affects the properties of geopolymer concrete is the alkaline activator solution. A combination of NaOH and Na_2SiO_3 solution is utilized as the alkaline activator solution. Sodium hydroxide and sodium silicate solution are mixed in the ratio of 1:2.5. A 12M NaOH solution is made and combined with the sodium silicate solution 24 hours before concrete mixing. M-sand from the local quarry is used as the fine aggregate (FA) and coarse aggregate (CA) of 20 mm is used as coarse aggregate solution. Specific gravity of FA and CA was determined to be 2.54 and 2.61.

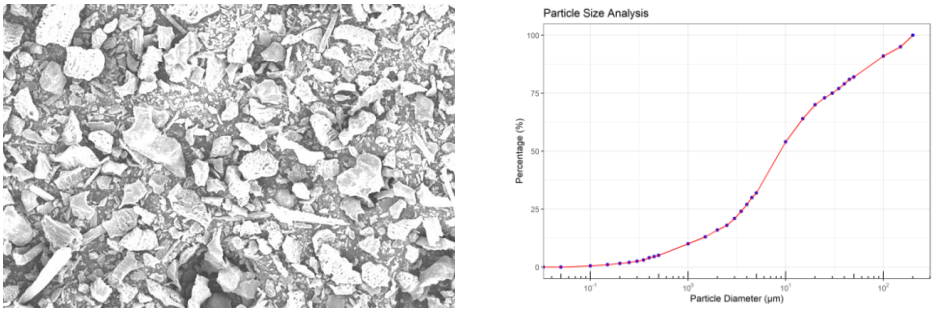

(a) (b)

Fig. 1 (a) SEM analysis of URA, (b) PSA of URA

The different materials are proportioned in accordance with modified guidelines for mix design[38]. The GGBS and URA are mixed dry first, then FA and CA are added. The alkaline solution is then added to the mixture and well stirred for about 5 minutes in the mixer. The concrete is then casted in to respective sizes and shapes depending on the test to be conducted. The total number of the specimens casted to determine the properties is listed in Table 2a. An average result value of three tested specimens is taken as the result of the particular tested mix id. The specimens are then ambient cured. Ambient curing in

this test was conducted by placing the casted specimen inside the laboratory under the shade in open condition. The ambient temperature during the entire time of casting and curing was in the range of 36 to 39 degree Celsius. URA is added as a partial substitute to GGBS in varying fractions such as 0, 5, 10, 15 and 20 percent. The mix proportions for the different mixes are listed in Table 2b. The effect of addition of URA over GGBS based geopolymer concrete is investigated in this study in three phases such as matrix performance, micro-structural characterization and sustainability analysis. Matrix characterization is carried out by determining properties such as workability, drying shrinkage, compressive and tensile strength for 3, 7, 28 and 90 days. Further micro structural characterization is carried out through SEM analysis and XRD analysis to examine morphology and flaws in the matrix. Sustainability impact is carried out by determining the cost efficiency, energy efficiency and CO_2 efficiency.

Table 1. Chemical composition of Base Materials

Chemical Composition	GGBS	URA
SiO_2	42.3	89.57
Fe_2O_3	1.14	0.51
Al_2O_3	13.6	0.81
CaO	41.1	0.69
MgO	1.1	0.39
Na_2O	0.3	0.23
K_2O	0.56	0.20
SO_3	-	0.13

Table 2 (a). Specimen details

Mix ID	Drying Shrinkage			Compressive Strength			Tensile Strength		
	7D	28D	96D	7D	28D	96D	7D	28D	96D
GR0	3	3	3	3	3	3	3	3	3
GR5	3	3	3	3	3	3	3	3	3
GR10	3	3	3	3	3	3	3	3	3
GR15	3	3	3	3	3	3	3	3	3
GR20	3	3	3	3	3	3	3	3	3
Total		45			45			45	

Table 2 (b). Mix Proportions

Mix ID	GGBS (kg/m^3)	URA (kg/m^3)	NaOH (kg/m^3)	Na_2SiO_3 (kg/m^3)	FA (kg/m^3)	CA (kg/m^3)
GR0	550	0	95.86	239.64	531.32	929.62
GR5	522.5	27.5	95.86	239.64	529.19	925.89
GR10	495	55	95.86	239.64	527.06	922.16
GR15	467.5	82.5	95.86	239.64	524.93	918.43
GR20	440	110	95.86	239.64	522.79	914.69

3. Results and Discussions

3.1 Matrix Analysis

3.1.1 Workability

The effect of addition of URA as a partial substitute of GGBS in GPC over workability is investigated through the compaction factor test and slump test as per IS 1191-2018[39].

The variation in the results with the utilization of URA is listed in Table. 3. From Table 3, it is pragmatic that with the addition of URA, there is a continuous increase in the compaction factor values. As the quantity of URA increases the workability of GPC increases due to the ultra-fine nature and very small particle size of URA compared with GGBS. This is witnessed from the particle size analysis (PSA) of URA as well. This could be witnessed during the mixing of the concrete as well. As per British Road Note 4, with addition of 20 percent URA, workability is improved to medium from low category and compaction becomes optional for better stability whereas without URA, GGBS based GPC needs hand compaction for better stability.

3.1.2 Drying Shrinkage

Concrete drying shrinkage is an important metric for assessing the durability and serviceability aspect. The blended effect of URA and GGBS over drying shrinkage in GPC specimens of size 40 x 40 x 150 mm is investigated as per IS 516-2020 (Part-6)[40].

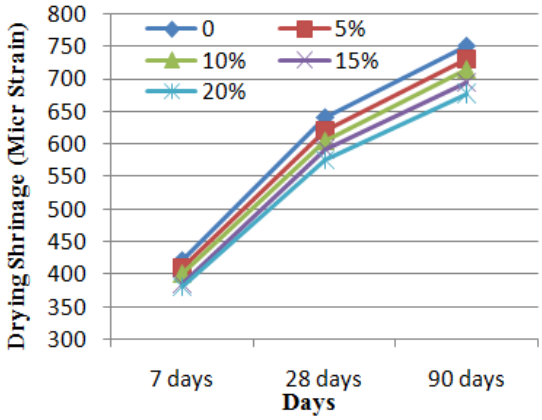

Fig. 2 Drying shrinkage results

Table 3. Mechanical characterization

Mix ID	Workability			Drying Shrinkage (Micro Strain)			Compressive Strength (MPa)			Tensile Strength (MPa)		
	CF	Slump	D.o.W	7D	28D	90D	7D	28D	90D	7D	28D	90D
GR0	0.85	30	Low	420	640	750	40.5	44.2	47.8	4.0	4.4	4.8
GR5	0.86	45	Low	410	620	730	42.3	45.8	49.4	4.3	4.7	5.1
GR10	0.88	60	Medium	400	605	715	44.6	47.5	52.7	4.4	4.9	5.3
GR15	0.89	70	Medium	385	590	695	47.4	51.8	56.5	4.8	5.3	5.8
GR20	0.9	75	Medium	380	575	675	42.4	45.2	48.5	4.3	4.6	4.8

Figure 2 depicts the variation of drying shrinkage values with addition of URA for different ages such as 7, 28 and 90 days. A gradual decrease in the drying shrinkage values throughout the addition of URA across all the ages. From Figure 2, it is observed that about 55 percent of 90 days shrinkage strain values are observed in 7 days itself and about 85 percent of the 90 days shrinkage strain values are observed in 28 days. The majority of drying shrinkage occurs in the initial few days as a result of the rapid internal loss of relative humidity from the surface of the specimens. Beyond 90 days, the increase

in drying shrinkage is insignificant. Drying shrinkage is essentially caused by the evaporation of water present in the pores due to the reduced humidity level in the environment. During drying, capillary stresses are induced in the capillary water present in the matrix are responsible for the shrinkage strain. The decrease in drying shrinkage caused by the addition of URA shows that the escape of internal moisture during drying was controlled owing to the refinement of the pore structure contributed by the ultra fine URA.

3.1.3 Compressive Strength

Compressive strength of GPC specimens for various additions of URA is investigated as per IS 516-2021 [41] for 7,28 and 90 days. GPC specimens of size 150 x 150 x 150 mm are tested. The strength values are listed in Table 3. Figure 3 depicts the variation of characteristic strength across the ages such as 7, 28 and 90 days for the utilization of URA in various proportions such as 0, 5, 10, 15 and 20 percent.

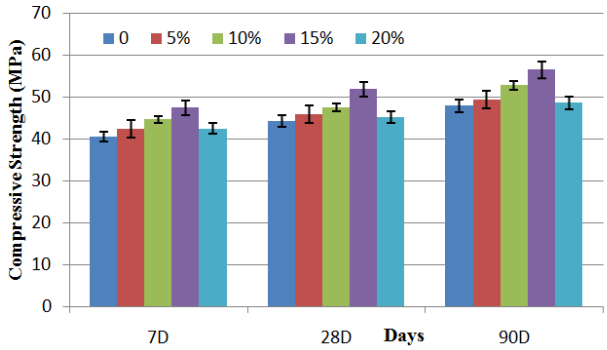

Fig. 3 Compressive strength results

About 85 percent of 90 days strength is observed in 7 days itself for the specimen with zero percent UURA and about 84 percent of the 90 days strength is observed in 7 days itself for the specimen with 15 percent URA. Hence the influence for the early attainment of strength by the URA is negligent. However, GR15, with 15 percent of URA exhibited the maximum compressive strength with 56.5 MPa at 90 days. The test reported increase in strength with the addition of URA till 15 percent and beyond that it decreases. The enhancement in compressive strength with the inclusion of URA up to 15 percent corresponds to the higher SiO_2 content of URA which increased the overall SiO_2/Al_2O_3 ratio thereby enhancing the polymerization reaction. This increase is further enhanced by the ultra-fine nature of URA than GGBS which could increase the specific surface area of the source material available for the reaction to occur [42]. The cohabitation of CSH, induced by the extra silica with the polymerization product NASH, could be related to the increase in strength with the introduction of URA. But URA when added in excess i.e.) more than 15 percent, a decrease in strength is reported. This is due to the fact that GGBS and URA has different solubility rates and at times when almost equal quantities are used, different solubility rates becomes an issue [31]. Moreover, excess URA leads to the presence of additional unreactive silica which hinders polymerization reaction. Similar research works report the reduction in compressive strength because of expansion and cracking that occurs due to the existence of excess silica in the matrix[43,44].

3.1.4 Tensile Strength

Tensile strength of GPC specimens for various additions of URA is investigated as per IS 516-2021 [41] for 7,28 and 90 days. GPC cylindrical specimens of diameter 150 mm and

height 300 mm are tested. The strength values are listed in Table 3. Figure 4 portrays the transformation of split tensile strength across the ages such as 7, 28 and 90 days for the utilization of URA in various proportions such as 0, 5, 10, 15 and 20 percent.

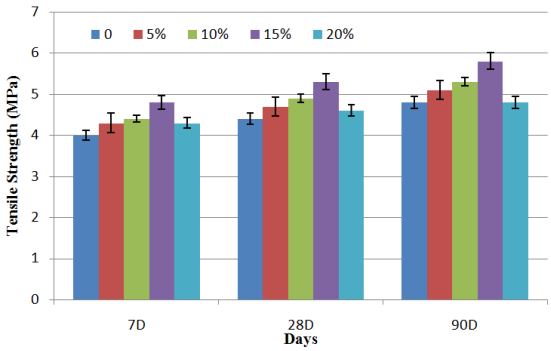

Fig. 4 Tensile strength results

About 84 percent of 90 days strength is observed in 7 days itself for the specimen with zero percent URA and about 83 % of the 90 days strength is observed in 7 days itself for the specimen with 15 percent URA. Hence the influence for the early attainment of strength by the URA is negligent. The reported values are in line with the results of compressive strength values. However, GR15, with 15 percent of URA exhibited the maximum tensile strength with 5.8 MPa at 90 days. The test reported enhancement in strength with the addition of URA till 15 percent and beyond that it decreases.

The reason for augmentation in tensile strength with the utilization of URA up to 15 percent is similar to that of observed in compressive strength and corresponds to the higher SiO2 content of URA which increased the overall SiO2/Al2O3 ratio and the ultra fine nature of URA than GGBS which could increase the specific surface area of the source material available for the reaction to occur [42]. Whereas at 20 percent of URA, about 90 percent of 90 days strength is observed in 7 days itself and about 96 percent of 90 days strength is observed in 28 days. Thereby making the presence of unreactive excess silica explicit. This excess silica hinders the polymerization reaction at higher URA dosage. Also at higher URA dosage, the Si/Al ratio increases beyond 24 which is the threshold value for the effective polymerization reaction[30].

3.2 Micro-structural Characterization

Micro-structural investigation was carried out using SEM and XRD analysis. SEM and XRD examination were performed on cracked sections of 90-day compressive strength test specimens for GPC mixes containing 15% URA. Figure 5 shows the micro structure of GPC.

From Figure 5, it is clear that there are no voids or cracks and a dense, compact microstructure is reported. This could be due to the presence of ultra fine URA which contributed to the higher surface area of the source materials favoring the formation of precursor ions. This is also due to the presence of 15 percent silica which contributed to the higher silica content thereby enhancing the polymerization reaction.

XRD analysis is carried out over the optimum specimen GR15 with 15 percent URA addition in order to identify the crystalline phases and the chemical composition. Figure 5 depicts the intensity versus position of GR15. Results clear portray the coexistence of both calcium based product and sodium based product. Calcium based products (CSH) are the result of interaction between the GGBS precursor ions and silica supplied by the

URA. Sodium based products (NaSH) are the usual polymerization products. Quartz (SiO2) with the highest peak are the silica based products. Existences of these products are responsible for the observed characteristics of GC.

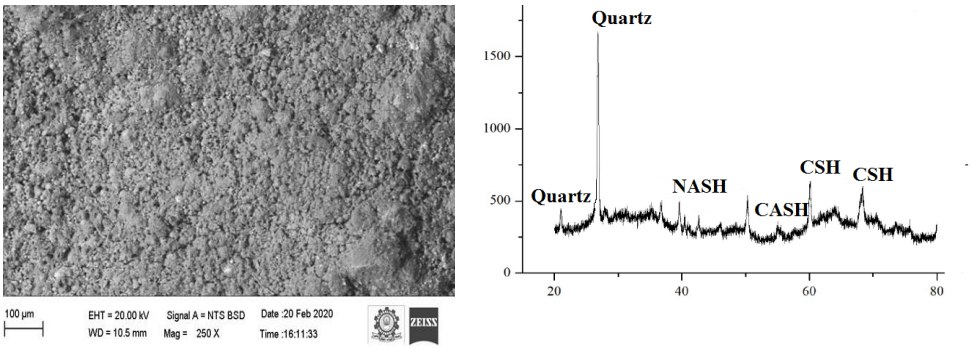

Fig. 5 SEM and XRD analysis of GR15 sample

3.3 Sustainability Analysis

3.3.1 Cost Efficiency

Cost efficiency is one of the essential parameter to be considered for sustainability. Cost efficiency of the specimens is evaluated based on the ratio of strength delivered to the incurred cost of production of different ingredients such as GGBS, URA, NaOH, Na2SiO3, FA and CA present in the matrix. Equation (1) gives the formulae to calculate the cost of efficiency. Market price of the materials is considered as the cost of materials.

$$Cost\ efficiency = \frac{Strength\ in\ MPa}{Cost\ of\ materials\ per\ cubic\ meter} \quad (1)$$

Table 4. Cost Analysis of GPC

Material	Rate / Tonne	GR0		GR5	
		Quantity (kg)	Cost (Rs)	Quantity (kg)	Cost (Rs)
GGBS	2000	550	1100	522.5	1045
URA	1500	0	0	27.5	41.25
NaOH	12250	95.86	1174.285	95.86	1174.285
Na2SiO3	10000	239.64	2396.4	239.64	2396.4
FA	900	531.32	478.188	529.19	476.271
CA	775	929.62	720.4555	925.89	717.5648
Total Cost (Rs)			5869.3285		5850.771

Material	Rate / Tonne	GR10		GR15		GR20	
		Quantity (kg)	Cost (Rs)	Quantity (kg)	Cost (Rs)	Quantity (kg)	Cost (Rs)
GGBS	2000	495	990	467.5	935	440	880
URA	1500	55	82.5	82.5	123.75	110	165
NaOH	12250	95.86	1174.285	95.86	1174.285	95.86	1174.285
Na2SiO3	10000	239.64	2396.4	239.64	2396.4	239.64	2396.4
FA	900	527.06	474.354	524.93	472.437	522.79	470.511
CA	775	922.16	714.674	918.43	711.7833	914.69	708.8848
Total Cost (Rs)			5832.213		5813.655		5795.081

The investigation is carried out in India; hence rupees was used as the currency. The various cost of the materials is listed in Table 4 and the subsequent rate of different mixes are also calculated and listed in Table 4.

Figure 6 shows the cost efficiency of different specimens for the incorporation of URA as a substitute to GGBS. In Figure 6, y axis represents the strength to cost ratio per cubic meter. From Figure 6, it is clear that there is an increase in the cost efficiency with respect to the utility of URA. An increase in cost efficiency of about 18 percent is witnessed with the utilization of URA for 15 percent. This is due to the reduced cost of URA and increased strength exhibited by the GPC specimens with addition to URA up to 15 percent. Hence the strength to cost ratio calculated for 1 cubic meter increases till 15 percent and then it decreases at 20 percent utilization of URA. The important factor that contributes for the increase in cost of the geopolymer specimens is the cost of sodium silicate solution. This could be reduced if the sodium silicate solution is prepared from rise husk solution by sol-gel method[45].

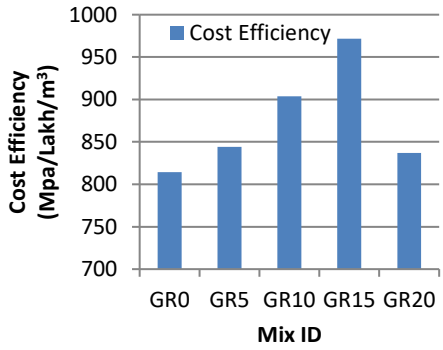

Fig. 6 Cost efficiency

3.3.2 Energy Efficiency

The primary parameter that affects sustainability is the energy efficiency. Energy efficiency is calculated as the ratio of strength exhibited to the sum of the energy consumed for the production of different ingredients such as GGBS, URA, NaOH, Na_2SiO_3, FA and CA present in the matrix. Equation (2) gives the formulae to calculate the Energy Efficiency. Energy efficiency of different specimens is indicated in Figure 7.

The quantum of energy needed for the generation of one tonne of GGBS and URA is 0.857GJ and 0.455GJ[46]. Energy consumed for the production of one tonne of FA and CA are 0.081GJ and 0.083GJ. Energy required to produce one tonne of sodium hydroxide and sodium silicate solution is 20.5GJ and 5.371GJ[47–49]. From Figure 7, it is explicit that there is a considerable decrease in the energy consumed with respect to the addition of URA.

$$Energy\ Efficiency = \frac{Strength\ in\ MPa}{Energy\ consumed\ for\ the\ Prouctiion\ of\ 1\ cubic\ meter} \quad (2)$$

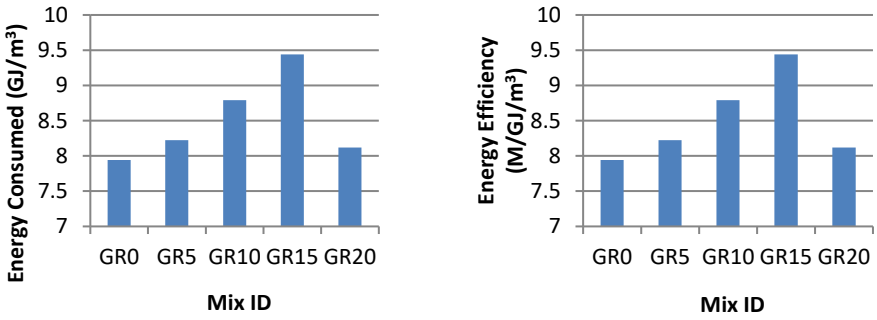

(a) (b)

Fig. 7 (a) Energy consumption, (b) Energy efficiency

3.3.3 CO_2 Efficiency

CO2 efficiency is the second most important parameter that influences the sustainability. Carbon dioxide is liberated by burning of fuels that is responsible for energy required for the production of various materials. Compared to other materials, production of fine aggregate and coarse aggregate liberate least CO2 with 0.0048 tonne of CO2 for every one tonne of production. CO2 for the GGBS and URA is 0.052 and 0.025 tonne of CO2 for every one tonne of production. CO2 emission for NaOH is 1.915 and that of Na2SiO3 is 1.915 and 1.222 tonne of CO2 for every one tonne of production[50]. CO2 emission is calculated for every one cubic meter of different mix ids and is depicted in the Figure 8.

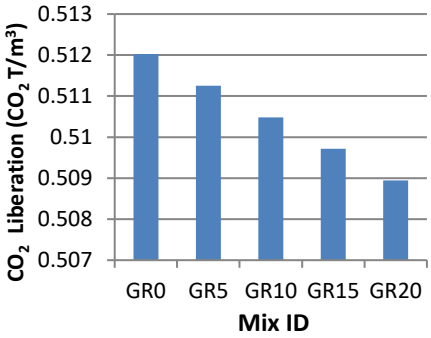

Fig. 8 CO_2 Efficiency

From Figure 8, its pragmatic that with the utilization of URA, there is a decrease in the liberation of CO_2. Eco efficiency is calculated similar to cost efficiency by the ratio of strength to the CO_2 emission and is depicted in Figure 9. Equation 3 gives the formulae to calculate the Eco Efficiency. Eco efficiency is calculated as the ratio of strength exhibited to the sum of the CO_2 liberated for the production of different ingredients such as GGBS, URA, NaOH, Na_2SiO_3, FA and CA present in the matrix.

$$Eco\ Efficiency = \frac{Strength\ in\ MPa}{CO2\ liberated\ for\ the\ Prouctiion\ of\ 1\ cubic\ meter} \quad (3)$$

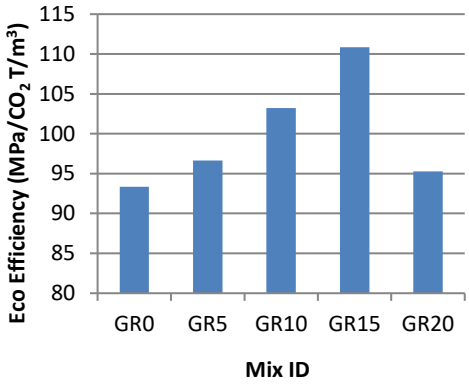

Fig. 9 Eco efficiency

From Figure 6,7 and 9, it is observed that GPC specimens with 15 percent URA addition as a substitute to GGBS exhibited better efficiency when compared to the other specimens. Also, it is observed that the strain over the environment could be reduced through the dependency on GPC.

4. Conclusion

The effect of URA addition as a partial substitution for GGBS in GPC over properties such as workability, drying shrinkage, compressive strength and tensile strength for different ages from 7 to 90 days was evaluated. With the utilization of URA, significant enhancements in engineering properties were reported. Micro-structural investigations reveal the dense microstructure and the chemical composition responsible for the enhancement in properties. Further sustainability analysis was performed to evaluate the impact of GC made to environment. Significant outcomes of this research work could be summarized as follows,

- Workability of the slag based GC increase with the increase in the utilization of URA owing to the ultra fine size and higher specific surface area of URA.
- With the incorporation of URA, there is decrease in the value of drying shrinkage strain values across all ages such as 7, 28 and 90 days. Significant reduction of about 7 percent is visible with the addition of URA at 15 % replacement level.
- There is a significant increase of about 18 percent in compressive strength and about 20 percent in tension strength with the addition of URA at 15 % replacement level.
- XRD study reveals the existence of CSH, NaSH and SiO_2 in the matrix that are responsible for the better performance of GC.
- Cost efficiency increases about 19 percent with the inclusion of URA in slag based GC.
- A gradual decrease in the energy consumption for production is reported with the utilization of URA.
- Eco efficiency increases by about 18.75 percent with the utilization of URA as a partial substitute of slag in GC.

The findings of the study open the path for the creation of URA-based sustainable construction materials. From the detailed sustainability analysis, in general it can be observed that in GC, the major decline in efficiency is due to the presence of sodium silicate solution followed by the sodium hydroxide solution. Further this efficiency can be

increased by reducing the dependency over NaOH and finding a sustainable way of producing sodium silicate solution which would prove beneficial to the scientific society. This research work could be extended by utilizing the sodium silicate solution that are synthesized using Rice Husk Ash and sodium hydroxide solution of less molarity.

Acknowledgement

The current research work didn't receive funding in any form. However, the authors like to thank the almighty and Sree Vidyanikethan Engineering Institution and Kalasalingam Academy of Research and Education for providing the necessary facilities for carrying out the project.

References

[1] Heath A, Paine K, McManus M. Minimising the global warming potential of clay based geopolymers J. Clean. Prod. 2014: 78 75-83. https://doi.org/10.1016/j.jclepro.2014.04.046
[2] Andrew RM. Global CO2 emissions from cement production, 1928-2018 Earth Syst. Sci. Data 2019: 11; 1675-710. https://doi.org/10.5194/essd-11-1675-2019
[3] Anon Cement and Concrete: The Environmental Impact - PSCI.
[4] Kajaste R, Hurme M. Cement industry greenhouse gas emissions - Management options and abatement cost J. Clean. Prod. 2016: 112; 4041-52. https://doi.org/10.1016/j.jclepro.2015.07.055
[5] Flower DJM, Sanjayan JG. Green house gas emissions due to concrete manufacture Int. J. Life Cycle Assess. 2007: 12; 282-8. https://doi.org/10.1065/lca2007.05.327
[6] Ganesh C, Sivasubramanaian J, Seshamahalingam M S, Millar J, Kumar VJ. Investigation on the Performance of Hybrid Fiber Reinforced Geopolymer Concrete Made of M-Sand under Heat Curing Mater. Sci. Forum 2021: 1019; 73-81. https://doi.org/10.4028/www.scientific.net/MSF.1019.73
[7] Mukilan K, Chithambar Ganesh A, Azik A. Investigation of utilization of Flyash in Self Compacting Concrete IOP Conf. Ser. Mater. Sci. Eng. 561 2019. https://doi.org/10.1088/1757-899X/561/1/012056
[8] Ganesh AC, Mukilan K, Srikar BPV, Teja LVS, Prasad KSV, Kumar AA, Sharath RP. Effect of Flyash-Rice Husk Ash Blend in the Energy Efficient Geopolymer Tiles Using Industrial Wastes Mater. Sci. Forum 1048 MSF 2022: 403-11. https://doi.org/10.4028/www.scientific.net/MSF.1048.403
[9] Kumar AS, Muthukannan M, Arunkumar K, Chithambar Ganesh A, Kanniga Devi R. Utilisation of waste glass powder to improve the performance of hazardous incinerated biomedical waste ash geopolymer concrete Innov. Infrastruct. Solut. 7 2022. https://doi.org/10.1007/s41062-021-00694-8
[10] Kumar AS, Muthukannan M, Kanniga Devi R, Arunkumar K, Chithambar Ganesh A. Improving the Performance of Structural Members by Incorporating Incinerated Bio-Medical Waste Ash in Reinforced Geopolymer Concrete Mater. Sci. Forum 1048 MSF 2022: 321-32. https://doi.org/10.4028/www.scientific.net/MSF.1048.321
[11] Arunkumar K, Muthukannan M, Kumar AS, Ganesh AC, Devi RK. Production of Eco-Friendly Geopolymer Concrete by using Waste Wood Ash for a Sustainable Environment Pollution 2021: 7; 993-1006.
[12] Arunkumar K, Muthukannan M, Kumar AS, Ganesh AC, Devi RK. Cleaner Environment Approach by the Utilization of Low Calcium Wood Ash in Geopolymer Concrete Appl. Sci. Eng. Prog. 2022: 15; 1-13. https://doi.org/10.14416/j.asep.2021.06.005
[13] Arunkumar K, Muthukannan M, kumar AS, Ganesh AC. Mitigation of waste rubber tire and waste wood ash by the production of rubberized low calcium waste wood ash

based geopolymer concrete and influence of waste rubber fibre in setting properties and mechanical behavior Environ. Res. 2021: 194; 110661. https://doi.org/10.1016/j.envres.2020.110661

[14] Arunkumar K, Muthukannan M, Kumar AS, Ganesh AC, Devi RK, Muthiah M, Kumar AS, Ganesh AC, Devi RK. Invention of sustainable geopolymer concrete made with low calcium waste wood ash World J. Eng. 2021. https://doi.org/10.1108/WJE-03-2021-0162

[15] Arunkumar K, Muthukannan M, Kumar AS, Ganesh AC, Devi RK. Hybrid fibre reinforced eco-friendly geopolymer concrete made with waste wood ash: A mechanical characterization study Eng. Appl. Sci. Res. 2022: 49; 235-47.

[16] Ganesh AC, Muthukannan M, Aakassh S, Prasad S, Subramanaian B. Energy efficient production of geopolymer bricks using industrial waste IOP Conf. Ser. Mater. Sci. Eng. 872 2020. https://doi.org/10.1088/1757-899X/872/1/012154

[17] Ganesh AC, Vinod Kumar M, Kanniga Devi R, Srikar P, Prasad S, Kumar MM, Sarath RP. Pervious Geopolymer Concrete under Ambient Curing Mater. Today Proc. 2021: 46; 2737-41. https://doi.org/10.1016/j.matpr.2021.02.425

[18] Ganesh AC, Deepak N, Deepak V, Ajay S, Pandian A. KarthiK. Utilization of PET bottles and plastic granules in geopolymer concrete Mater. Today Proc. 2020: 42; 444-9. https://doi.org/10.1016/j.matpr.2020.10.170

[19] Ganesh AC, Muthukannan M. Effect of Elevated Temperature over Geopolymer Concrete Int. J. Eng. Adv. Technol. 2019: 9; 450-3. https://doi.org/10.35940/ijeat.A1025.1291S419

[20] Ganesh AC, Muthukannan M. A review of recent developments in geopolymer concrete Int. J. Eng. Technol. 2018: 7; 696. https://doi.org/10.14419/ijet.v7i4.5.25061

[21] Ganesh AC, Muthukannan M, Dhivya M, Sangeetha CB, Daffodile SP. Structural performance of hybrid fiber geopolymer concrete beams IOP Conf. Ser. Mater. Sci. Eng. 872 2020. https://doi.org/10.1088/1757-899X/872/1/012154

[22] Ganesh AC, Muthukannan M, Kumar AS, Arunkumar K. Influence of Bacterial Strain Combination in Hybrid Fiber Reinforced Geopolymer Concrete subjected to Heavy and Very Heavy Traffic Condition J. Adv. Concr. Technol. 2021: 19; 359-69. https://doi.org/10.3151/jact.19.359

[23] Ganesh AC, Muthukannan M. Development of high performance sustainable optimized fiber reinforced geopolymer concrete and prediction of compressive strength J. Clean. Prod. 282124543 (12 pages)-124543 (12 pages) 2021. https://doi.org/10.1016/j.jclepro.2020.124543

[24] Sarker PK, Haque R, Ramgolam KV. Fracture behaviour of heat cured fly ash based geopolymer concrete Mater. Des. 2013: 44; 580-6. https://doi.org/10.1016/j.matdes.2012.08.005

[25] Kumar S, Mishra J, Kumar S, Mohammed S, Patel A, Kumar S, Behera U. Materials Today : Proceedings Characterization and utilization of rice husk ash (RHA) in fly ash - Blast furnace slag based geopolymer concrete for sustainable future Mater. Today Proc. 2020.

[26] Paul A, Hussain M. Sustainable Use of GGBS and RHA as a Partial Replacement of Cement in the Stabilization of Indian Peat Sustainable Use of GGBS and RHA as a Partial Replacement of Cement in the Stabilization of Indian Peat Int. J. Geosynth. Gr. Eng. 2020. https://doi.org/10.1007/s40891-020-0185-7

[27] Nuaklong P, Jongvivatsakul P, Pothisiri T, Sata V, Chindaprasirt P. Influence of rice husk ash on mechanical properties and fire resistance of recycled aggregate high-calcium fly ash geopolymer concrete J. Clean. Prod. 2020: 252; 119797. https://doi.org/10.1016/j.jclepro.2019.119797

[28] Komnitsas K, Zaharaki D. Geopolymerisation: A review and prospects for the minerals industry Miner. Eng. 2007: 20; 1261-77. https://doi.org/10.1016/j.mineng.2007.07.011
[29] Songpiriyakij S, Kubprasit T, Jaturapitakkul C, Chindaprasirt P. Compressive strength and degree of reaction of biomass- and fly ash-based geopolymer Constr. Build. Mater. 2010: 24; 236-40. https://doi.org/10.1016/j.conbuildmat.2009.09.002
[30] Fletcher RA, MacKenzie KJD, Nicholson CL, Shimada S. The composition range of aluminosilicate geopolymers J. Eur. Ceram. Soc. 2005: 25; 1471-7. https://doi.org/10.1016/j.jeurceramsoc.2004.06.001
[31] Kusbiantoro A, Nuruddin MF, Shafiq N, Qazi SA. The effect of microwave incinerated rice husk ash on the compressive and bond strength of fly ash based geopolymer concrete Constr. Build. Mater. 2012: 36; 695-703. https://doi.org/10.1016/j.conbuildmat.2012.06.064
[32] Kumar AS, Muthukannan M, Irene ADKB, Arunkumar K, Ganesh AC. Flexural Behaviour of Reinforced Geopolymer Concrete incorporated with Hazardous Heavy Metal Waste Ash and Glass Powder Mater. Sci. Forum 1048 MSF 2022: 345-58. https://doi.org/10.4028/www.scientific.net/MSF.1048.345
[33] Mehta A, Siddique R. Sustainable geopolymer concrete using ground granulated blast furnace slag and rice husk ash: Strength and permeability properties J. Clean. Prod. 2018: 205; 49-57. https://doi.org/10.1016/j.jclepro.2018.08.313
[34] Davidovits J. Application of Ca-based geopolymer with blast furnace slag , a review Proceeding Second Int. Slag Valoris. Symp. 2011: 33-49.
[35] Das SK, Mishra J, Mustakim SM, Adesina A, Kaze CR, Das D. Sustainable utilization of ultrafine rice husk ash in alkali activated concrete: Characterization and performance evaluation J. Sustain. Cem. Mater. 2022: 11; 142-60. https://doi.org/10.1080/21650373.2021.1894265
[36] Moulick KK. Prospective Use of Rice Husk Ash to Produce Concrete in India Int. J. Civ. Environ. Eng. 2015: 9; 324-9.
[37] Habert G, D'Espinose De Lacaillerie JB, Roussel N. An environmental evaluation of geopolymer based concrete production: Reviewing current research trends J. Clean. Prod. 2011: 19; 1229-38. https://doi.org/10.1016/j.jclepro.2011.03.012
[38] Anuradha R, Sreevidyaa R, Rangan, B V VV. Modified Guidelines for Geopolymer Concrete Mix Design using Indian Standard Asian J. Civ. Eng. (Building Housing) 2011: 13; 357-68.
[39] Methods of sampling and analysis of concrete 2018 I 1199 2018 IS 1199-2018.
[40] IS 516 (Part 6) : 2020 2020 Determination of Drying Shrinkage and Moisture Movement of Concrete Samples Burau Indian Stand. 516.
[41] Bureau of Indian Standards 2021 IS 516 : 2021 - Hardened concrete - Methods of test Bur. Indian Stand. 516 1-20.
[42] Chindaprasirt P, Jaturapitakkul C, Chalee W, Rattanasak U. Comparative study on the characteristics of fly ash and bottom ash geopolymers Waste Manag. 2009: 29; 539-43. https://doi.org/10.1016/j.wasman.2008.06.023
[43] Das SK, Mustakim SM, Adesina A, Mishra J, Alomayri TS, Assaedi HS, Kaze CR. Fresh, strength and microstructure properties of geopolymer concrete incorporating lime and silica fume as replacement of fly ash J. Build. Eng. 2020: 32; 101780. https://doi.org/10.1016/j.jobe.2020.101780
[44] Sukontasukkul P, Chindaprasirt P, Pongsopha P, Phoo-Ngernkham T, Tangchirapat W, Banthia N. Effect of fly ash/silica fume ratio and curing condition on mechanical properties of fiber-reinforced geopolymer J. Sustain. Cem. Mater. 2020: 9; 218-3. https://doi.org/10.1080/21650373.2019.1709999
[45] Le VH, Nhan C, Thuc H, Thuc HH. Synthesis of silica nanoparticles from Vietnamese rice husk by sol - gel method Nanoscale Res. Lett. 2013: 8; 1-10. https://doi.org/10.1186/1556-276X-8-58

[46] Alsalman A, Assi LN, Kareem RS, Carter K, Ziehl P. Energy and CO 2 emission assessments of alkali-activated concrete and Ordinary Portland Cement concrete : A comparative analysis of different grades of concrete Clean. Environ. Syst. 2021; 3 100047. https://doi.org/10.1016/j.cesys.2021.100047

[47] Fawer M, Concannon M, Rieber W. Life cycle inventories for the production of sodium silicates Int. J. Life Cycle Assess. 199: 4; 207-12. https://doi.org/10.1007/BF02979498

[48] Tempest B, Sanusi O, Gergely J, Ogunro V, Weggel D. Compressive strength and embodied energy optimization of fly ash based geopolymer concrete 3rd World Coal Ash, WOCA Conf. - Proc. 2009.

[49] Assi LN, Carter K, Deaver E, Ziehl P. Review of availability of source materials for geopolymer/sustainable concrete J. Clean. Prod. 2020: 263; 121477. https://doi.org/10.1016/j.jclepro.2020.121477

[50] Turner LK, Collins FG. Carbon dioxide equivalent (CO2-e) emissions: A comparison between geopolymer and OPC cement concrete Constr. Build. Mater. 2013: 43; 125-30. https://doi.org/10.1016/j.conbuildmat.2013.01.023

Research on Engineering Structures & Materials
journal homepage: http://www.jresm.org
Research Group

Research Article

Process parameter improvement for NITi's electrical discharge machining (EDM) process utilizing the TOPSIS approach

Atish Mane*[a], Pradeep V. Jadhav[b]

Mechanical Eng. Bharati Vidyapeeth Deemed University, College of Engineering, Pune, Maharashtra, India

Article Info

Article history:

Received 26 Aug 2022
Revised 30 Oct 2022
Accepted 6 Dec 2022

Keywords:

Electro discharge Machine (EDM)*;* Shape memory alloy*;* Surface roughness (R_a); Material removal rate (MRR)*;* TOPSIS

Abstract

The current work focuses on finding the ideal set of Electro Discharge Machine (EDM) process variables for machining Shape memory alloy (NiTi). NiTi alloy is a significant class of smart material with several unique properties. There are numerous uses for NiTi in the security, marine, biomedical, and aerospace industries. NiTi is particularly difficult to cut using conventional machining methods due to its hardness; nevertheless, the material can be removed using an electric discharge machining technique. The experiments were carried out using Taguchi's L27 orthogonal array. A Multi-criteria decision-making (MCDM) technique known as TOPSIS is used to optimize the response performance variables of material removal rate (MRR) and surface roughness (SR). TOPSIS combines multiple objectives into a single objective and provides the optimum set of parameters, From the optimization results, the optimal combination of process parameters is obtained at Voltage=30V, Discharge Current= 20A, Ton=35µs, Toff=8µs. Confirmatory experiments show a satisfactory improvement of preference values utilizing TOPSIS in the EDM experimental and initial settings of 1.82.

1. Introduction

According to the state of research, shape memory alloy (SMA) development is proceeding successfully. SMA demand is on the rise for a wide range of engineering components. When used as a binary alloy, nickel and titanium have different element weight percentages in the SMA [1]. Smart materials in the NiTi class have special qualities like super elasticity, high strength, biocompatibility, etc. In the fields of defense, aerospace, and medicine, NiTi alloy is widely applied. This alloy is difficult to machine using traditional machining techniques because it has unique qualities and applications. Instead, this alloy is machined using non-conventional techniques such as electric discharge machining (EDM) [2]. By generating controlled sparks between an electrode with a specific form and an electrically conductive workpiece, electrical discharge machining (EDM), a popular technique for shaping conductive materials, can be utilized to remove material [3]. Sushil Kumar Choudhary et al. examine the research that was done on die-sinking EDM, water-in EDM, dry EDM, and powdered mixed electric discharge machining from inspection through development. He noted that the main advancement in research had improved tool wear and metal removal rate [4]. Azizul Bin Mohamad et al., optimization of EDM parameters process and response parameters using Taguchi method. They observed that pulse on time and discharge current were most effective on the Surface and also duty factor as least influencing the machining process quality [5]. K.M Patel et al. investigated the effect of process parameters on surface quality. They investigated that the most significant factor is discharge current which affects surface quality. Surface roughness increases with an

*Corresponding author: mane.atish@bharatividyapeeth.edu
[a] orcid.org/0000-0002-4549-8004; [b] orcid.org/0000-0002-7167-2387
DOI: http://dx.doi.org/10.17515/resm2022.510ma0826

increase in discharge current and also affects the metal removal rate [6]. Singh Balbir et al. investigate the process of alloying AA 6061/ SiCp using Cu-W powder metallurgy electrodes in EDM. They investigated the effects of peak current, gap voltage, pulse off time, and pulse on time on response parameters metal removal rate, electrode wear, and surface roughness. They analyze that using powder metallurgy improves the surface quality [7].E. Aliakbari et al. found the ideal rotary process parameter setting and deduced from this experiment that the most influential input parameters on MRR, EWR, and SR are current, pulse on time, electrode rotational speed, and electrode shapes [8].Bala Murugan Gopalsamy et al, noticed that the parameters that have the most influence on rough machining are the cut width and depth. The most important factor in finish machining is cutting speed [9]. Ho and Newman presented a review of the electrical discharge machining process and discussed the parameters that are contributing to machining efficiency. EDM process involves many process parameters which can be broadly classified into two categories such as electrical and non-electrical process parameters. They stated that empirical modeling can be better described in the EDM process as it is stochastic in nature [10]. Mr. L.G. Machado et al. give a review on the medical applications of shape memory alloys. The aim of this review paper is to explain the most exciting uses of SMA in the biomedical field and to provide a brief overview of its thermomechanical behavior. These include surgical tools and uses for the heart and joints [11]. Multiple performance characteristic issues require the modeling and optimization of the EDM process. Kasdekar, D. K. et. al. suggested a TOPSIS, Simple Additive Weighting (SAW) method based on entropy to address the multi-performance parameter optimization issue in EDM [12]. Tripathy, S. et. al. assessed the efficiency of improving several performance variables for powder-mixed EDM of H-11 die steel using the copper electrode by combining the Taguchi technique with TOPSIS and grey relational analysis [13]. Vaddi, V. R. et. al. worked on using TOPSIS and the Taguchi technique to optimize EDM machining parameters for titanium alloys (Ti-6Al-4V), taking into account various performance concerns. All of the results demonstrated TOPSIS's ability to address a variety of concrete EDM-related challenges using the Taguchi approach. This technique reduced a multi-performance problem to a single equivalent objective problem [14]. Phan Huu Nguyen et. al. adjusts the process parameters for milling titanium alloy specimens with tungsten carbide. To determine improved process variables including voltage, capacitance, and electrode rotating speed, the Taguchi-TOPSIS approach was applied. To assess the depth of machining, overcut, and tool wear rate, voltage, capacitance, and electrode rotational speed were taken into account. The investigation revealed that the best settings can result in better surface polish and greater machining precision [15].M Somasundaram et. al. carries out studies to mill AZ31 alloy using EDM to optimize process parameters by combining multi-attribute optimization and Taguchi methodologies. In this work, multiple-response optimization was accomplished using Multi-Criteria Decision Making (MCDM) approaches such as the TOPSIS methodology and Grey Relational Analysis (GRA). Due of TOPSIS' flexibility in determining how much weight to give the response based on the need, researchers came to the conclusion that it is the best method for solving real-time multi-criteria problems. With GRA, which has a constant value for all response variables, it is not conceivable. [16].

The current study's objective is to maximize the material removal rate and minimize surface roughness during the machining of NiTi alloy by optimizing the electric discharge machining process parameter. Surface roughness (SR) and material removal rate (MRR) were the output parameters, and pulse current, voltage, gap, and pulse on-off time were the input parameters.

2. Design of Experiment

2.1 Experimental Setup

An EDM machine (Valpak) was used in this study to conduct experiments shown in Fig. 1. An electrode was a rectangular, pure copper plate that measured 40 mm by 40 mm by 20 mm. A moving dielectric fluid, kerosene, kept the workpiece and electrode apart. Shape memory alloy (NiTi) was used as the workpiece's material. For experimentation, shape memory alloy pates with dimensions of 25 mm by 40 mm by 15 mm were used. As a workpiece, NiTi shape memory alloy has been utilized in orthopedics to fix fractured bones.

Fig. 1 EDM setup and Machined plates (Ni-Ti Alloy)

Placing the electrode in the ram hold and fixing it in place. To maintain a very small gap of 50 µm between the electrode tip and the surface of the workpiece, its height was automatically adjusted by the machine with respect to the workpiece. keeping the workpiece in place on the machine's work table's magnetic chuck. Flushing the dielectric fluid up to the height where the electrode sparking region is totally submerged, flooding the volume (work tank) around the workpiece. Perform the machining operation for the specified amount of time. It is possible to see intermittent sparking through the dielectric fluid. Small craters are generated as a result of a high number of current discharges that all contribute to the removal of material from the workpiece. The workpiece is removed from the device and its surface roughness (SR) is checked with Taylor-Hobson Surf Com equipment. The readings are noted down.

2.2. Selection of an orthogonal array

Machining experiments for determining the optimal machining parameters were carried out by setting: For each experiment the combinations of the 4 input parameters viz. Gap Voltage(V) in the range of 25V to 100V, Discharge Current (A) in the range of 10A to 20A, Pulse on-time (Ton) in the range of 35 µs to 100 µs, pulse off-time (Toff) in the range of 5 µs to 39 µs, all having 3 levels (Table 1)

The total degree of freedom when there are three independent variables, each with three levels, is nine. As a result, the chosen orthogonal array must include at least 9 experiments. This condition is satisfied by an L_9 orthogonal. Three levels and four factors were chosen for this investigation. An orthogonal array L_{27} was chosen for this experiment [18].

Table 1. Initial EDM Parameter

EDM Parameters	Unit	Level-1	Level-2	Level-3
Gap Voltage	V	25	30	100
Discharge current	A	10	15	20
Pulse On Time	µs	35	50	100
Pulse Off Time	µs	5	8	9

2.3. Conducting the Experiment

After choosing the orthogonal array, the experiments are carried out using the level combinations. The execution of all the experiments is required. L_{27} orthogonal array was used since there were four components and three levels in this investigation [23].

Table 2. Orthogonal Array of Experimental Combination

Test	Gap Voltage	Discharge current	Pulse On Time	Pulse Off Time
1	25	10	35	5
2	25	10	35	8
3	25	10	35	9
4	30	15	50	5
5	30	15	50	8
6	30	15	50	9
7	100	20	100	5
8	100	20	100	8
9	100	20	100	9
10	25	15	100	5
11	25	15	100	8
12	25	15	100	9
13	30	20	35	5
14	30	20	35	8
15	30	20	35	9
16	100	10	50	5
17	100	10	50	8
18	100	10	50	9
19	25	20	50	5
20	25	20	50	8
21	25	20	50	9
22	30	10	100	5
23	30	10	100	8
24	30	10	100	9
25	100	15	35	5
26	100	15	35	8
27	100	15	35	9

2.4. Machining Performance Measure

Surface Roughness Measurement-

The parameter Ra, which is the most frequently used, was chosen for this study from a variety of surface finish characteristics, including roughness average (R_a), root-mean-square (rms) roughness (R_q), and maximum peak-to-valley roughness (R_y or R_{max}). The experiments were carried out with various Gap voltage, Discharge current, Pulse on-time, and Pulse on-time settings (Table 2). The Taylor-Hobson Surf Com equipment was used to measure the specimens' surface roughness.

Material Removal Measurement-

Machining was executed using a fixed time and the MRR was measured by determining the weight difference of the workpiece before and after machining. The MRR measured in cubic millimeters per minute, was obtained using Eq. (1).

$$MRR = \frac{(W_1 - W_2)}{\rho_w \, t} * 10^3 \quad (1)$$

Where W_1 and W_2 are the work piece weight before and after machining, respectively, ρ_w is the density of the NiTi, SMA, and t is the machining time (min).

3. Result in Analysis

Minitab TM 18 tool is employed for data analysis. Two response parameters from the result in table 3 are selected for study in order to determine the best combination that can produce a high-quality machined surface finish. 27 experiments were carried out in accordance with the L_{27} orthogonal array, with the findings for surface roughness and metal removal rate displayed in table 3.

Table 3. Result Table

Test	Gap Voltage	Discharge current	Pulse On Time	Pulse Off Time	Surface roughness	MRR (mm^3/min)
1	25	10	35	5	5.31	7.375
2	25	10	35	8	5.35	6.146
3	25	10	35	9	5.55	6.914
4	30	15	50	5	6.25	6.062
5	30	15	50	8	6.15	6.056
6	30	15	50	9	6.44	6.062
7	100	20	100	5	6.01	6.062
8	100	20	100	8	5.9	7.375
9	100	20	100	9	6.26	7.375
10	25	15	100	5	6.52	6.291
11	25	15	100	8	6.32	5.531
12	25	15	100	9	6.82	4.425
13	30	20	35	5	4.62	7.375
14	30	20	35	8	4.52	8.749
15	30	20	35	9	5.12	7.375
16	100	10	50	5	5.01	7.375
17	100	10	50	8	5.24	7.375
18	100	10	50	9	5.44	6.914
19	25	20	50	5	6.11	6.062
20	25	20	50	8	5.96	7.375

21	25	20	50	9	5.34	6.146
22	30	10	100	5	5.12	6.062
23	30	10	100	8	5.05	7.375
24	30	10	100	9	5.37	5.531
25	100	15	35	5	5.2	7.375
26	100	15	35	8	5.18	7.375
27	100	15	35	9	5.34	7.375

4. Optimization Using Technique for Order of Preference (TOPSIS) & Results

A technique for multi-criteria decision analysis is called TOPSIS (Technique for Order of Preference by Similarity to Ideal Solution). By determining weights for each criterion, normalizing scores for each criterion, and calculating the geometric distance between each alternative and the ideal alternative, which is the alternative with the best score for each criterion, this compensatory aggregation method compares a set of alternatives. The criteria are assumed to be monotonically growing or decreasing by TOPSIS [14,15].

The steps involved in multi-objective optimization are [16]:

Step 1. Determine the objective and identify the pertinent evaluation criteria.

Step 2. Construct a decision matrix based on all the information available for the criteria. Each row of the decision matrix is allocated to one alternative and each column to one criterion. Therefore, an element, x_{ij} of the decision matrix shows the performance of i^{th} alternative with respect to j^{th} criterion.

Step 3. Obtain the normalized decision matrix, r_{ij} using the following equation:

$$r_{i_j} = \frac{x_{i_j}}{\sqrt{\sum_{i=1}^{m} x_{i_j}^2}} \tag{2}$$

Step 4. Construct the weighted normalized decision matrix.

$$v_{i_j} = r_{i_j} \times w_j \tag{3}$$

Step 5. Determine the Positive ideal Row (IDR) that one with the largest observed value for each column.

$$\text{IDR} = (\max v_{i1}, \max v_{i2}, \ldots\ldots, \max v_{in}) = (v_1^+, v_2^+, \ldots\ldots, v_n^+) \tag{4}$$

Similarly, the Negative-ideal Row (NDR) that one with the smallest value for each column.

$$\text{NDR} = (\min v_{i1}, \min v_{i2}, \ldots\ldots, \min v_{in}) = (v_1^-, v_2^-, \ldots\ldots, v_n^-) \tag{5}$$

Step 6. Measure the distance, d_i^+ for i= 1,2, 3,……,m, of each alternative from the positive ideal one.

$$S_i+ = [\sum_{j=1}^{n} \left(v_{i_j} - v_j^+ \right)^2]^2 \qquad \text{for i= 1,2, 3,……,m.} \tag{6}$$

Similarly, Measure the distance, d_i^- for i= 1,2, 3,……,m, of each alternative from the negative ideal one.

$$S_i- = [\sum_{j=1}^{n} \left(v_{i_j} - v_j^- \right)^2]^2 \qquad \text{for i= 1,2, 3,……,m.} \tag{7}$$

Step 7. Calculate the relative closeness of alternatives to ideal solution by computing what is known as Composite Index (CI).

$$P_i = \frac{d_i^-}{d_i^+ + d_i^-} \tag{8}$$

Step 8. A set of alternatives is arranged in descending order, according to P_i value, indicating the most preferred and the least preferred solutions.

The normalized decision matrix for the provided data is shown in Table 4. Table 6 illustrates the Weighted Decision matrix, respective Euclidian distances, degree of closeness, and ranks for a set of input parameters whereas Table 5 displays the weighting applied to each output response variable. These are all taken from an excel spreadsheet that was created.

Table 4. Normalized Decision Matrix

Experimental Result		Normalized Output	
Surface roughness	MRR (mm^3/min)	Surface roughness	MRR (mm^3/min)
5.31	7.375	0.1811	0.1376
5.35	6.146	0.1825	0.1147
5.55	6.914	0.1893	0.129
6.25	6.062	0.2132	0.1131
6.15	6.056	0.2098	0.113
6.44	6.062	0.2197	0.1131
6.01	6.062	0.205	0.1131
5.9	7.375	0.2012	0.1376
6.26	7.375	0.2135	0.1376
6.52	6.291	0.2224	0.1174
6.32	5.531	0.2156	0.1032
6.82	4.425	0.2326	0.0826
4.62	7.375	0.1576	0.1376
4.52	8.749	0.1542	0.1632
5.12	7.375	0.1746	0.1376
5.01	7.375	0.1709	0.1376
5.24	7.375	0.1832	0.1376
5.44	6.914	0.1856	0.129
6.11	6.062	0.2084	0.1131
5.96	7.375	0.2033	0.1376
5.34	6.146	0.1821	0.1147
5.12	6.062	0.1746	0.1131
5.05	7.375	0.1723	0.1376
5.37	5.531	0.1787	0.1032
5.2	7.375	0.1774	0.1376
5.18	7.375	0.1767	0.1376
5.34	7.375	0.1821	0.1376

The normalized decision matrix has been formed as shown in Table 4.

Table 5. Considered weightage of output response

Output Response	R_a	MRR
Weightage	0.5	0.5

Table 6. Weighted normalized decision matrix, Euclidian Distance & Relative Closeness

Weighted Normalized Output					
Surface roughness	MRR (mm^3/min)	S_i+	S_i-	P_i	Rank
0.0906	0.0688	0.0186	0.0376	0.6691	8
0.0913	0.0574	0.0281	0.0297	0.5145	17
0.0947	0.0645	0.0245	0.0317	0.5636	12
0.1066	0.0566	0.0387	0.0181	0.319	23
0.1049	0.0565	0.0375	0.019	0.3366	22
0.1099	0.0566	0.0413	0.0166	0.2868	25
0.1025	0.0566	0.0356	0.0206	0.3663	20
0.1006	0.0688	0.0268	0.0317	0.5419	14
0.1068	0.0688	0.0324	0.0291	0.4735	18
0.1112	0.0587	0.0411	0.0181	0.3062	24
0.1078	0.0516	0.0429	0.0134	0.2373	26
0.1163	0.0413	0.0562	0	0.0002	27
0.0788	0.0688	0.0129	0.0465	0.7827	2
0.0771	0.0816	0	0.0562	0.9997	1
0.0873	0.0688	0.0164	0.04	0.7094	5
0.0855	0.0688	0.0153	0.0413	0.7294	3
0.0916	0.0688	0.0194	0.037	0.6564	10
0.0928	0.0645	0.0232	0.033	0.5872	11
0.1042	0.0566	0.0369	0.0195	0.346	21
0.1017	0.0688	0.0277	0.0311	0.5288	15
0.0911	0.0574	0.028	0.0299	0.5168	16
0.0873	0.0566	0.027	0.0328	0.5484	13
0.0862	0.0688	0.0157	0.0408	0.7218	4
0.0894	0.0516	0.0324	0.0288	0.4705	19
0.0887	0.0688	0.0173	0.039	0.6927	7
0.0884	0.0688	0.0171	0.0392	0.6964	6
0.0911	0.0688	0.019	0.0373	0.6628	9

The closest and farthest points from the ideal solutions, or the Euclidian distance (S+&S-), are determined. The P_i value, or degree of proximity to the best solution, is calculated from these Euclidean distances, and the highest P_i value is indicated as the first ranking, while the lowest P_i value is marked as the final rank or the 27th rank. Table 7 lists the P_i values,

Euclidian distances, Weighted Normalized Decision Matrix, and the corresponding rank assigned to each set of input parameters based on the P_i values.

Table 7. Summarized TOPSIS table ranking the set of input parameters

Test	Gap Voltage	Discharge current	Pulse On Time	Pulse Off Time	SR	MRR	S_i+	S_i-	P_i	Rank
1	25	10	35	5	5.31	7.3746	0.0186	0.0376	0.6691	8
2	25	10	35	8	5.35	6.1455	0.0281	0.0297	0.5145	17
3	25	10	35	9	5.55	6.9137	0.0245	0.0317	0.5636	12
4	30	15	50	5	6.25	11.0619	0.0387	0.0181	0.319	23
5	30	15	50	8	6.15	10.0563	0.0375	0.019	0.3366	22
6	30	15	50	9	6.44	11.0619	0.0413	0.0166	0.2868	25
7	100	20	100	5	6.01	11.0619	0.0356	0.0206	0.3663	20
8	100	20	100	8	5.9	7.3746	0.0268	0.0317	0.5419	14
9	100	20	100	9	6.26	7.3746	0.0324	0.0291	0.4735	18
10	25	15	100	5	6.52	12.2911	0.0411	0.0181	0.3062	24
11	25	15	100	8	6.32	5.531	0.0429	0.0134	0.2373	26
12	25	15	100	9	6.82	4.4248	0.0562	0	0.0002	27
13	30	20	35	5	4.62	7.3746	0.0129	0.0465	0.7827	2
14	30	20	35	8	4.52	14.7493	0	0.0562	0.9997	1
15	30	20	35	9	5.12	7.3746	0.0164	0.04	0.7094	5
16	100	10	50	5	5.01	7.3746	0.0153	0.0413	0.7294	3
17	100	10	50	8	5.24	7.3746	0.0194	0.037	0.6564	10
18	100	10	50	9	5.44	6.9137	0.0232	0.033	0.5872	11
19	25	20	50	5	6.11	11.0619	0.0369	0.0195	0.346	21
20	25	20	50	8	5.96	7.3746	0.0277	0.0311	0.5288	15
21	25	20	50	9	5.34	6.1455	0.028	0.0299	0.5168	16
22	30	10	100	5	5.12	11.0619	0.027	0.0328	0.5484	13
23	30	10	100	8	5.05	7.3746	0.0157	0.0408	0.7218	4
24	30	10	100	9	5.37	5.531	0.0324	0.0288	0.4705	19
25	100	15	35	5	5.2	7.3746	0.0173	0.039	0.6927	7
26	100	15	35	8	5.18	7.3746	0.0171	0.0392	0.6964	6
27	100	15	35	9	5.34	7.3746	0.019	0.0373	0.6628	9

From Table 7, Based on the relative closeness, we understand that Exp. 14 shows the best set of input parameters while Exp. 12 shows the worst results. The optimal input parameters for the combined EDM machining are shown in Table 8.

Table 8. The optimized set of input parameters (Weightage 0.5-0.5)

Gap Voltage	Discharge current	Pulse on Time	Pulse off Time
30	20	35	8

Confirmation Test:

The confirmation experiment is the last stage in the design of the experiment process's initial iteration. The verification experiment's purpose is to confirm the findings of the TOPSIS analysis phase. It is carried out by adjusting the process parameters to Voltage=30V, Discharge Current= 20A, Ton=35µs, Toff=8µs, as the optimum level and the actual surface roughness obtained is 6.34 µm to 4.52 µm and metal removal rate as 12.75 mm^3/min to 14.75 mm^3/min. Surface roughness and metal removal rate improvement shows that the accuracy of outcomes is increased by the TOPSIS multi-decision-making optimal design.

5. Conclusion

This study helped determine the ideal Shape Memory Alloy Electro Discharge Machine (EDM) parameters to optimize for low surface roughness (SR) and maximize metal removal rate (MRR). In these investigations, 27 sets of tests were carried out utilizing a copper electrode and an L_{27} Taguchi orthogonal array on shape memory alloy. Voltage, Discharge current, Pulse on time, and Pulse off time are some of the input parameters used. From the experiment and design of the experiment, the following conclusions were made; The many objectives are combined by Optimization using the Technique for order of preference (TOPSIS) into a single objective, and the optimum set of parameters, i.e., R_a & MRR, is provided. Table 6 lists the outcomes of the best solutions for both positive and negative ideal solutions. In Table 7, the output performances are sorted according to their proximity coefficient values. The largest MRR and the least amount of surface roughness are closer with the highest proximity coefficient value. By averaging the experiment data, the average proximity coefficient value for MRR and R_a is determined for levels 1-3. The shape memory alloy's MRR and Ra are determined in large part by the EDM machining parameters; among the parameters chosen, a larger current could produce enough discharge energy to melt and evaporate the reinforcement and matrix material. For the ideal good outcome, higher MRR and lower R_a are preferable. The results of the experiment show that voltage and discharge current have more effects. From the experiment, we get poor outcomes while keeping parameters set as Voltage=25V, Discharge Current= 15A, Ton=100µs, Toff=9 µs and best outcomes keeping parameters set as Voltage=30V, Discharge Current= 20A, Ton=35µs, Toff=8µs. Each performance is given a weight factor of 0.5. The optimum results obtained by the TOPSIS method for 0.5-0.5 weightage are as optimum surface roughness is 4.52 µm and metal removal rate as 14.75 mm^3/min by a combination of input parameters as Voltage=30V, Discharge Current= 20A, Ton=35µs, Toff=8µs. Confirmatory experiments show a satisfactory improvement of preference values utilizing TOPSIS in the EDM experimental and initial settings of 1.82.

References

[1]. Adam KM, Winowlin JJT, Samuel RKPS, Mashinini P. Machinability of Shape Memory Alloy Using Electro Spark Erosion Process. Research square. 2021: 1-13,

[2] Sabouni HR, Daneshmand S. Investigation of the parameter of EDM process performed on smart NiTi alloy using graphite tool. Life Sci. J. 2012, 9 (4), 504-510.

[3] Saeed D. Optimization of Electrical Discharge Machining Parameters for Niti Shape Memory Alloy by Using the Taguchi Method. Journal of Marine Science and Technology,2014, 22(4):506-512.

[4] Sushil K C, Jadoun RS , Current Advanced Research Development of Electric Discharge Machining (EDM): A Review, International Journal of Research in Advent Technology, 2014: 273-297.

[5] Azizul BM, Arshad NS, Gulam AQ, Zahid AK, Saini VK. Optimization of EDM process parameters using Taguchi method. International Conference on Applications and Design in Mechanical Engineering,2012.
[6] Patel KM, Pandey PM, Rao PV. Optimisation of process parameters for multi-performance characteristics in EDM of Al2O3 ceramic composite. Int J Adv Manuf Technol. 2010 Apr;47(9-12):1137-47. https://doi.org/10.1007/s00170-009-2249-7
[7] Singh B, Kumar J, Kumar S. Optimization and surface modification in electrical discharge machining of AA 6061/SiCp composite using Cu–W electrode. Proceedings of the Institution of Mechanical Engineers, Part L: Journal of Materials: Design and Applications. 2017 Apr;231(3):332-48. https://doi.org/10.1177/1464420715596544
[8] Aliakbari E, Baseri H. Optimization of machining parameters in rotary EDM process by using the Taguchi method. Int J Adv Manuf Technol. 2012 Oct;62(9-12):1041-53. https://doi.org/10.1007/s00170-011-3862-9
[9] Gopalsamy BM, Mondal B, Ghosh S. Optimisation of machining parameters for hard machining: grey relational theory approach and ANOVA. Int J Adv Manuf Technol. 2009 Dec;45(11-12):1068-86. https://doi.org/10.1007/s00170-009-2054-3
[10] Ho K, Newman S. State of the art electrical discharge machining (EDM). International Journal of Machine Tools and Manufacture. 2003 Oct;43(13):1287-300. https://doi.org/10.1016/S0890-6955(03)00162-7
[11] Machado L, Savi M. Medical applications of shape memory alloys. Braz J Med Biol Res. 2003 Jun;36(6):683-91. https://doi.org/10.1590/S0100-879X2003000600001
[12] Kasdekar DK. MADM Approach for Optimization of Multiple Responses in EDM of En-353 Steel. IJAST. 2015 Aug 31;83:59-70. https://doi.org/10.14257/ijast.2015.83.06
[13] Tripathy S, Tripathy D. Multi-attribute optimization of machining process parameters in powder mixed electro-discharge machining using TOPSIS and grey relational analysis. Engineering Science and Technology, an International Journal. 2016 Mar;19(1):62-70. https://doi.org/10.1016/j.jestch.2015.07.01
[14] Vaddi VR, Ch SR, Bushaboina SK, Banka H. Application of TOPSIS with Taguchi Method for Multi-Attribute Optimization of Machining Parameters in EDM. SAE Tech. Pap. Ser. 2018. https://doi.org/10.4271/2018-28-0033
[15] NGUYEN PH, T M, Pham DV, Shirguppikar S, Nguyen TN, Nguyen TC, et al. Multi-objective optimization of micro EDM using TOPSIS method with Tungsten carbide electrode. Sādhanā. 2022 Sep;47(3):1-12 https://doi.org/10.1007/s12046-022-01900-8
[16] Somasundaram M, Kumar JP. Multi response optimization of EDM process parameters for biodegradable AZ31 magnesium alloy using TOPSIS and grey relational analysis. Sādhanā. 2022 Sep;47(3):1-14 https://doi.org/10.1007/s12046-022-01908-0
[17] Mohd Abbas N, Solomon DG, Fuad Bahari M. A review on current research trends in electrical discharge machining (EDM). International Journal of Machine Tools and Manufacture. 2007 Jun;47(7-8):1214-28. https://doi.org/10.1016/j.ijmachtools.2006.08.026
[18] Mane AB, Jadhav P. Optimization of Response Parameters of Electrical Discharge Machine Using Shape Memory Alloy. International Journal of Mechanical Engineering. 2021; 6(3): 86- 91.
[19] Singh S. Optimization of machining characteristics in electric discharge machining of 6061Al/Al2O3p/20P composites by grey relational analysis. Int J Adv Manuf Technol. 2012 Dec;63(9-12):1191-202. https://doi.org/10.1007/s00170-012-3984-8
[20] Bansiddhi A, Sargeant T, Stupp S, Dunand D. Porous NiTi for bone implants: A review. Acta Biomaterialia. 2008 Jul;4(4):773-82. https://doi.org/10.1016/j.actbio.2008.02.009
[21] Mohd Jani J, Leary M, Subic A, Gibson MA. A review of shape memory alloy research, applications and opportunities. Materials & Design (1980-2015). 2014 Apr;56:1078-113. https://doi.org/10.1016/j.matdes.2013.11.084

[22] Markopoulos AP, Pressas IS, Manolakos DE. A Review On The Machining Of Nickel-Titanium Shape Memory Alloys, Rev.Adv. Mater. Sci. 2015; 42: 28-35.
[23] Mane AB, Jadhav P, Bilgi DS. Enhancement of Surface Finish of Shape Memory Alloy Using Electrical Discharge Machine, Annals of R.S.C.B., ISSN: 1583-6258, 2021; 25(5) 5224- 5232.
[24] Liu X, Shang H, Xu S, Wang Z, Zhang C, Fu Q. Patellar Shape-Memory Fixator for the Treatment of Comminuted Fractures of the Inferior Pole of the Patella. J of Materi Eng and Perform. 2011 Jul;20(4-5):623-8. https://doi.org/10.1007/s11665-011-9862-y
[25] Auricchio F, Boatti E, Conti M, SMA Biomedical Applications, Shape Memory Alloy Engineering,2015, ISBN 978-0-08-099920-3.
[26] Shashikant, Roy A K , Effect of optimization of various machine process parameters on surface roughness in EDM for an EN19 material using Surface Response Methodology, Procedia Materials Science, 2014; 5:1702 - 1709. https://doi.org/10.1016/j.mspro.2014.07.359
[27] Janardhan M. Multi-response optimization of EDM performance characteristics using response surface methodology and desirability function, ARPN Journal of Engineering and Applied Sciences, 2014,2635- 2649.
[28] Balasubramanian P, Senthilvelan T. Optimization of Machining Parameters in EDM Process Using Cast and Sintered Copper Electrodes. Procedia Materials Science. 2014;6:1292-302. https://doi.org/10.1016/j.mspro.2014.07.108
[29] Goyal P. Enhancement of MRR in EDM by Composite Material Electrode on Die Steel, International Journal of Science, Engineering and Technology Research, 2014; 2640-2643.
[30] Saeed D, Ehsan FK, Ali ALN, Vahid M. Optimization of Electrical Discharge Machining parameters for NITI shape memory alloy using Taguchi Method, Journal of Marine Science and Technology, 2014; 22(4):506-512.
[31] Esmail A, Saeed Da, Ali A L N, Vahid M., Analysis and Modeling of Electro Discharge Machining Input Parameters of Nitinol Shape Memory Alloy by De-ionized Water and Copper Tools, Int. J. Electrochem. Sci., 2014; 9: 2934 - 2943.
[32] Alidoosti A, Ghafari-Nazari A, Moztarzadeh F, Jalali N, Moztarzadeh S, Mozafari M. Electrical discharge machining characteristics of nickel–titanium shape memory alloy based on full factorial design. Journal of Intelligent Material Systems and Structures. 2013 Sep;24(13):1546-56. https://doi.org/10.1177/1045389X13476147
[33] Perveen A, Jahan MP. An Experimental Study on the Effect of Operating Parameters during the Micro-Electro-Discharge Machining of Ni-Based Alloy, International Journal of Materials and Metallurgical Engineering. 2016, 10(11): 1381-1387

Research on Engineering Structures & Materials
journal homepage: http://www.jresm.org
Research Group

Research Article

Empirical equations for prediction of split tensile and flexural strength of high strength concrete including effect of steel fiber

P.N. Ojha[a], Brijesh Singh*[b], Pranay Singh

Centre for Construction Development and Research, National Council for Cement and Building Materials, India

Article Info

Article history:

Received 15 Jul 2022
Revised 30 Aug 2022
Accepted 05 Sep 2022

Keywords:

High Strength Concrete;
Flexural Strength;
Split Tensile Strength;
International Code;
Empirical Equation

Abstract

The current Indian Standard IS: 456-2000 has the equation for prediction of flexural strength which is valid only up to concrete strength of 55 MPa and with introduction of High Strength Concrete (HSC) in the standard, there is need to develop equation and relationship which can predict flexural and split tensile strength of HSC including the effect of steel fibres. This study is aimed to develop relationship between the ratios of split tensile to flexural strength which is applicable to concrete having strength range from 15 MPa to 150 MPa. The study is done by analyzing experimentally obtained test results of a total 120 specimens for flexural strength and 120 specimens for split tensile strength. Further study is also conducted on steel fibre reinforced concrete samples by analyzing experimentally obtained test results of a total 24 specimens for flexural strength and 30 specimens for split tensile strength. The results obtained from the test are compared with empirical equations given by International standards and literatures. On the basis of analysis of results, ratio of split tensile strength to flexural strength is recommended for concrete with and without steel fibre having wide strength range from 100 to 120 MPa. Empirical equations for prediction of spilt tensile and flexure strength of normal to high strength concrete is proposed and applicability of proposed equation for evaluation for normal to high strength steel fiber reinforced concrete is also discussed.

1. Introduction

Concrete is generally not designed to sustain tensile forces, understanding and prediction of tensile behavior becomes crucial as it is applicable for estimating stress level under which initiation of cracking may take place. From the structural design point of view of unreinforced concrete for application in structures such as dams or pavements, the role of tensile properties are more important than compressive properties [1-3]. The accurate and realistic value of in situ tensile and compressive strengths of concrete distressed during service period provide an important base for the structural assessment and better decision on repair or rehabilitation. In addition to high degree of variability in results, complexity, cost etc. involved in correlation of concrete tensile strength, it is important to develop realistic constitutive relationship between concrete tensile and compressive strength [4–16]. The concrete as a construction material has a very low tensile strength as compared to its compressive strength which leads to its low resistance to tensile crack which in turn affects safety and durability performance thereby reducing service life of reinforce concrete structures [17-21]. Tensile strength is measured in terms of direct or splitting tension or flexural tensile strength wherein split tensile strength test gives a lower coefficient of variation [22]. The tensile properties of concrete is mainly influenced by

*Corresponding author: brijeshsehwagiitr96@gmail.com
[a]orcid.org/0000-0003-1754-4488; [b]orcid.org/0000-0002-6512-1968; [c]orcid.org/0000-0001-6169-9482
DOI: http://dx.doi.org/10.17515/resm2022.475ma0715

water to binder ratio, characteristics and quantum of fine and coarse aggregates, concrete age, loading rate, addition of fibers etc. [21-27]. High strength concrete (HSC) is generally defined as concrete with a specified characteristic cube strength between 60 and 100 MPa, Major applications for HSC are in offshore structures, columns for tall buildings, long-span bridges and highway structures. Advantage of HSC is the reduction in size of compression elements and amount of longitudinal reinforcement required. Apart from conventional hydraulic cement and supplementary cementitious materials, Silica fume (microsilica) or metakaoline can be used to enhance the strength at high levels (75 MPa and above). In concrete mix proportioning, the role of impact, crushing or abrasion value of aggregate is generally not a significant parameter for normal concrete strength except in case of lightweight aggregate as aggregate is stronger and failure occurs in paste and not from aggregate [25]. However, it is well established that aggregate properties apart from strength, such as size, shape, surface texture, grading, and mineralogy affects concrete strength in different degrees [26-27]. Further, since the interfacial transition zone properties has key role on concrete tensile properties compared to compressive strength, aggregates characteristics has impact on the constitutive relationship between tensile to compressive strength [27-30].

Many international standards and researchers have proposed empirical equations earlier based on experimentation and therefore applicability of these equations may not be suitable for different conditions and concrete ingredients particularly with addition of fibers [4–16]. This study is aimed to develop relationship between the ratios of split tensile to flexural strength which is applicable to concrete having strength range from 20 MPa to 120 MPa. The study is done by analyzing experimentally obtained test results of a total 120 specimens for flexural strength and 120 specimens for split tensile strength. Further study is also conducted on steel fibre reinforced concrete samples by analyzing experimentally obtained test results of a total 30 specimens for flexural strength and 24 specimens for split tensile strength. The results obtained from the test are compared with empirical equations given by international standards and literatures. On the basis of analysis of results, ratio of split tensile strength to flexural strength is recommended for concrete with and without steel fibre having wide strength range from 100 to 120 MPa. Apart from this empirical equation developed are for certain strength range and in this study an attempt has been made to develop empirical equation for strength range of 15 to 150 MPa. Study also includes the comparison of flexural and split tensile strength of fibre reinforced concrete with proposed equations.

2. Materials

Details of Ordinary Portland Cement (OPC) cement, Coarse and Fine aggregate, Fly ash, ultrafine GGBS, Silica Fumes, Superplasticizer, water and steel fiber used for producing concrete mixes are given hereunder.

2.1. Cementitious Materials

OPC 53 grade as per IS 269-2015 [31] is used along with fly ash, ultrafine GGBS and silica fume in mixes based on strength requirement of concrete mix. Detailed physical and chemical characteristics of cement, fly ash, ultrafine GGBS and silica fume are given in Table-1 & 2. The 3-, 7- & 28-days compressive strength of OPC 53 Grade cement are 36.50 MPa, 45.00 MPa and 56.50 MPa respectively. The 28 days compressive strength of controlled concrete (OPC based concrete without fly ash) and concrete sample with fly ash are 38.83 MPa and 31.94 MPa respectively. The 7 days compressive strength of controlled concrete (OPC based concrete without silica fume) and concrete sample with silica fume are 12.66 MPa and 14.56 MPa respectively, when tested as per IS: 1727.

Table 1. Physical properties of materials [31]

S. No.	Properties	Cement	G.G.B.S	Fly ash	UFGGBS	Silica Fume
1.	Fineness(m^2/kg)	323	400	310	2026	16701
2.	Specific Gravity	3.15	2.93	2.28	2.88	2.28

Table 2. Chemical properties of materials

Sl. No.	Properties	Cement	G.G.B.S	Fly ash	UFGGBS	Silica Fume
1	Loss of Ignition (LOI)	2.3	0.33	0.4	0.17	2.73
2	Silica (SiO_2)	20.71	34.41	60.95	33.05	85.03
3	Iron oxide (Fe_2O_3)	4.08	1.18	5.7	0.58	-
4	Aluminium oxide (Al_2O_3)	5.15	18.45	26.67	20.40	-
5	Calcium oxide (CaO)	59.96	36.46	2.08	33.14	-
6	Magnesium oxide (MgO)	4.57	7.00	0.69	7.62	-
7	Sulphate (SO_3)	1.84	0.097	0.29	0.19	-
8	Na_2O	0.42	0.30	0.06	0.19	0.73
9	K_2O	0.56	0.37	1.46	0.58	2.96
10	Chlorides	0.012	0.022	0.009	0.016	-
11	Insoluble Residue	1.25	0.40	-	0.86	-

2.2. Aggregates

Granite type coarse aggregate having maximum size of 20 mm is utilized and crushed fine aggregate (Zone II) as per IS: 383-2016 [32] is used in study for strength level up to 90 MPa. Physical properties of both aggregate is presented in Table-3. To obtain enhancement in packing density of concrete making materials, three different types of aggregates were used namely Fine Quartz Sand (FQS), Ground Quartz (GQ) and River sand for concrete strength level between 90 MPa to 120 MPa. No coarse aggregate was used in concrete mix produced to achieve strength level of 90 MPa to 120 MPa as coarse aggregate was failing before the cement paste and hence strength could not be achieved. Ground Quartz having finer size particles was used as micro filler to increase the packing density of cement aggregate matrix. Its particle size ranges from 0.5 to 63 microns. Particle size distribution are shown in Figure 1. Majority of quartz grains are having size range of 20-30µm. High strength concrete mixes were produced using fine quartz sand having particle size ranging from 150 to 996 microns. Majority of quartz grains are having size range of 300-600µm. Quartz sand used in this study have particle size ranging from 1mm to 3 mm.

2.3. Superplasticizer and Water

A polycarboxylate-based superplasticizer complying with IS: 9103 [34] is used in concrete mixes having w/c ratios as 0.16, 0.18, 0.20, 0.27, 0.30 and 0.36. A naphthalene-type superplasticizer complying with IS: 9103 [34] is used in concrete mixes having w/c ratios as 0.47, 0.50, 0.57 & 0.60. Water meeting IS: 456-2000 limits for construction was utilized in concrete mixing.

2.4. Steel Fiber

The trough and hooked end shaped steel fibers are used for the study. Past studies suggest that these fibers are more efficient with improved pull out resistance and toughness as compared to straight end fibers [4]. The fibers used are 0.55 mm (diameter) and 35 mm (length) having aspect ratio of 63 which meets requirement of ASTM A-820. The photograph of trough and hooked end shaped steel fibers and length of fibres measured

using scale are shown in Figure-2. Tensile strength of the fibers as per the manufacturer's test certificate is 1486.99 MPa.

Table 3. Properties of aggregates

Property		Granite		Fine Aggregate
		20 mm	10 mm	
Specific gravity		2.83	2.83	2.65
Water absorption (%)		0.3	0.3	0.59
Sieve Analysis Cumulative Percentage Passing (%)	20mm	98	100	100
	10 mm	1	68	100
	4.75 mm	0	2	99
	2.36 mm	0	0	89
	1.18 mm	0	0	64
	600 µ	0	0	43
	300 µ	0	0	26
	150 µ	0	0	14
	Pan	0	0	0
Abrasion, Crushing & Impact Value		19,19,13	-	-
Flakiness % & Elongation %		29, 25	-	-

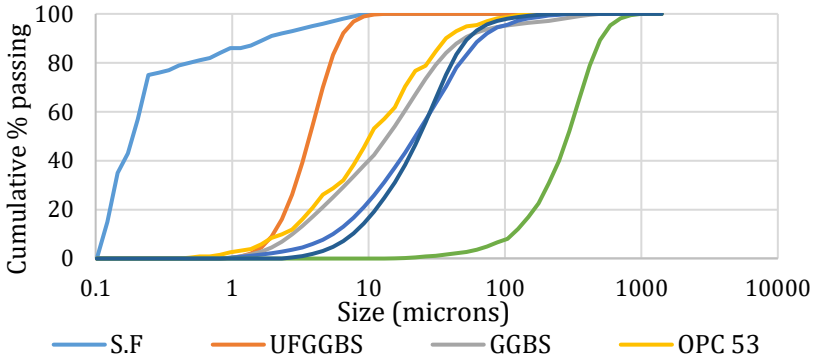

Fig. 1 Materials particle size distribution

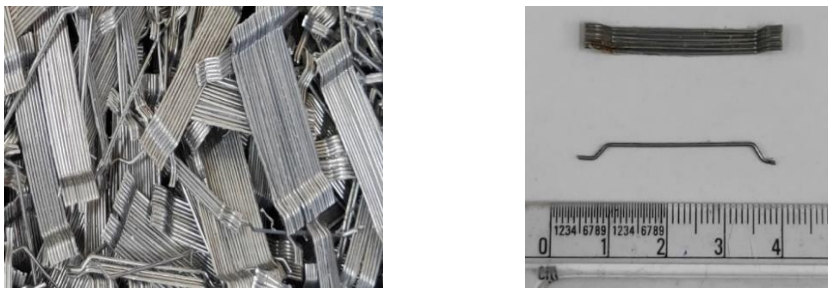

Fig. 2 Trough and hooked end shaped steel fibers

3. Mix Proportion and Compressive Strength of Concrete

The mixes from w/b ratio of 0.60 to 0.16 were adopted to achieve the compressive strength range of 20 to 120 MPa for determining flexural and split tensile strength of concrete. The mix details and 28 days compressive strength are presented in Table-4. The slump of concrete was kept between 80-100 mm. Amount of steel fiber added to the concrete is 1 % of steel fibers by volume of the concrete and it is adopted based on past studies suggesting it as an economical and optimum dose for maximum improvement in overall mechanical performance of concrete [35], [36].

To propose an equation for prediction of the flexural tensile strength; for one mixture, twelve specimens were cast and for total ten mixture without steel fibre referred in the Table-4A, total 120 specimens were tested. To propose an equation for prediction of the split tensile strength; for one mixture, twelve cylindrical specimens were cast and for total ten mixture without steel fibre referred in the Table-4A, total 120 specimens were tested. The experimental results of split tensile and flexural tensile of concrete for strength range between 20 to 110 MPa obtained from testing samples of 3 concrete mixes (Table-4B (Mix:M11-M13)) with steel fibre addition of 1 percent by volume on 30 specimens and 24 specimens respectively are given in section 8. 10 specimens for each of three mixtures were cast for split tensile strength and 8 specimens for each of three mixture were cast for flexural tensile strength. This was done to compare the variation in experimental results with the model developed based on experimental data on flexural tensile and split tensile strength of concrete without steel fibre. For conducting experimental studies, mixes were made in pan type mixer for strength level 20 to 90 MPa and in plenatry mixer for strength level above 90 MPa. The moulds were adequately coated with oil before usage, and casting was done in layers, each of which was vibrated on a vibration table to compact. Specimens were removed from moulds after 24 hours. The laboratory conditions of temperature and relative humidity were monitored during the ambient curing i.e. 27±2^{o}C and relative humidity 65±5 as per IS: 516. The specimens were allowed to become surface dry before being testing in a saturated surface dried state. The compressive strength of hardened concrete were determined using 150 mm size cube as per the procedure given in IS 516. The 28 days average compressive strength of concrete determined from three cube specimens are tabulated in Table-4. Three cylindrical specimens of diameter 150 mm and length 300 mm were also cast for 10 concrete mixtures given in Table-4A (M1-M10) to generate experimental data on compressive strength of cylinder and cubes for comparing empirical equations of different international standards and experimental results.

4. Experimental Study for Determining Split Tensile Strength and Flexural Strength

The split tensile strength was carried out as per IS: 5816 and set up is shown in Figure 3. For split Tensile Strength as per IS: 5816, the cores of 150 mm diameter and 300 mm long complying with the requirements given in IS 516 were used. The 28 days flexural strength of the concrete mixes was determined through beam specimens of size 150 x 150 x 700 mm as per IS: 516 wherein beam was kept on two rollers and load was applied in center and test set up is shown in Figure 4. The clear span of beam used for test were kept as 600 mm. For one mixture, twelve specimens (4 samples with each sample consisting of three specimens) were cast and for total ten mixture without steel fibre referred in the Table-4A, total 120 specimens (40 samples with 4 samples for each mixture) were tested. The findings of the results of split tensile strength and flexural strength of concrete including comparison of proposed models with empirical models given in international standards and literature are given in subsequent sections.

Table 4. Mix design details of concrete mix without steel fibre

Mixture Details	Mix ID						
	M1	M2	M3	M4	M5	M6	M7
w/b	0.60	0.57	0.50	0.47	0.36	0.30	0.27
Cement, kg/m³	200	250	290	290	334	400	400
Fly Ash, kg/m³	50	65	60	72	83	75	75
Silica fume, kg/m³	--	--	--	--	--	25	50
Ultrafine GGBS, kg/m³	--	--	--	--	--	--	--
Total cementitious materials, kg/m³	250	315	350	362	417	500	525
Coarse aggregate 10 mm, kg/m³	795	780	775	777	730	729	754
Coarse aggregate 20 mm, kg/m³	520	525	520	518	487	486	406
Fine aggregate (River Sand), kg/m³	690	685	660	650	726	725	692
Fine aggregate (Quartz Sand), kg/m³	--	--	--	--	--	--	--
Fine aggregate (Ground Quartz Sand), kg/m³	--	--	--	--	--	--	--
Fine aggregate (Coarse Quartz Sand), kg/m³	--	--	--	--	--	--	--
Water, kg/m³	150	180	175	170	150	150	140
Water-reducing admixture, kg/m³	0.60	0.50	0.35	0.40	0.35	0.60	1.00
28 Days average Compressive Strength of Concrete, MPa	24.85	27.85	40.35	45.72	65.14	78.93	89.60

Table 4 (Con). Mix design details of concrete mix without steel fibre

Mixture Details	Mix ID					
	M8	M9	M10	M11	M12	M13
w/b	0.20	0.18	0.16	0.47	0.36	0.20
Cement Quantity, kg/m³	563	480	635	290	334	563
Fly Ash, kg/m³	112	--	95	72	83	112
Silica fume, kg/m³	75	165	139	--	--	75
Ultrafine GGBS, kg/m³	--	165	109	--	--	--
Total cementitious materials, kg/m³	750	810	978	362	417	750
Coarse aggregate 10 mm, kg/m³	640	1033	--	777	730	640
Coarse aggregate 20 mm, kg/m³	427	--	--	518	487	427
Fine aggregate (River Sand), kg/m³	536	640	--	650	726	536
Fine aggregate (Quartz Sand), kg/m³	--	--	516	-	-	-
Fine aggregate (Ground Quartz Sand), kg/m³	--	--	290	-	-	-
Fine aggregate (Coarse Quartz Sand), kg/m³	--	--	371	-	-	-
Steel Fibre % by volume of concrete	150	135	156	1.00	1.00	1.00
Water, kg/m³	1.16	1.20	1.8	170	150	150
Water-reducing admixture, kg/m³	103.55	107.5	127.50	0.40	0.35	1.16
28 Days average Compressive Strength of Concrete, MPa				48.72	68.14	111.55

5. Comparison of Experimental Values of Compressive Strength of Cylinder and Cubes with Different International Standards

The conversion factor for cube to cylindrical compressive strength for the ten concrete mixes without steel fibre (M1-M10) have been worked out (Figure-5). The results indicate

that as compressive strength of concrete increases the ratio of cube to cylindrical strength decreases. IS: 456-2000 recommends fix value of 1.25 up to concrete grade M55 and considering the significant decrease in ratio for grade above M55, values needs to be modified for high grades of concrete. This is also important in assessment of structure where concrete core test is recommended for in-situ verification of strength and cylindrical strength is needed to be converted to concrete equivalent cube compressive strength. The values obtained are used for validating models developed in past which uses either cylindrical or cubical compressive strength in empirical equations. In the present study the cube to cylindrical strength ratio is adopted to be 1.20 upto cube compressive strength of 90 MPa and 1.10 for cube compressive strength above 90 MPa. The assumed ratio is based on the experimental findings and the comparison between the experimental and assumed values are given in Figure 5.

Fig. 3 Test set-up for split tensile strength

Fig. 4 Test set up for flexural strength

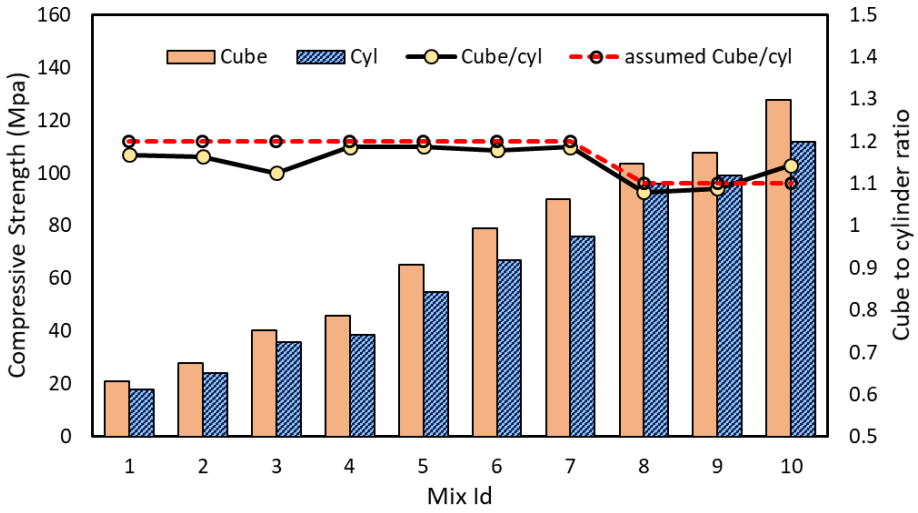

Fig. 5 Comparison of cube to cylinder compressive strength of 20-120 MPa strength

6. Comparison of Proposed Model for Split Strength of Concrete with International Codes and Literature

The experimental results of split tensile of concrete for strength range between 15 to 150 MPa obtained from testing samples of 10 concrete mixes without steel fibre are shown in Figure 6 and 7. In case of experimental results of split tensile strength, for HSC both matrix aggregate separation and transgranular failure was observed. The studies done in past [5 & 19] has shown that ratios of flexural strength to compressive strength increases with increase in the compressive strength of concrete. The ratio of split tensile strength to compressive strength of concrete is about 10 % of compressive strength for normal strength concrete. However, for the high strength concrete it goes down to about 5 % of compressive strength. To propose an equation for prediction of the split tensile strength; for one mixture, twelve cylindrical specimens were cast and for total ten mixture without steel fibre referred in the Table-4A, total 120 specimens were tested. The cylindrical specimen cast from 10 mixes (referred in Table-4A) has compressive strength ranging from 15 to 150 MPa which has been plotted and shown in Figures 6 and 7.

The correlation between the split tensile strength and compressive strength is plotted and proposed equations are having high coefficient of correlation (R^2 = 0.90) using regression analysis. Using regression analysis, it is noted that for both one parameter analysis and two parameter analysis similar level of coefficient of correlation is achieved as shown in Figures 6 and 7. In Figure-6, based on two parameter analysis, the proposed equation for estimating split tensile strength of concrete for compressive strength ranging from 15 to 150 MPa can be 0.42 $fck^{0.6}$ where Fck is the cube compressive strength of concrete. In two parameter analysis, both functions i.e. multiplying factor with Fck and power factor to Fck has been varied. Whereas in single parameter analysis, power function to Fck has been kept constant and only multiplying factor analysis has been carried out to develop a simplified equation for incorporation in Indian Standard which is similar to equations given in other international codes for normal strength concrete. Keeping this in view for simplicity, the proposed equation for estimating split tensile strength of concrete considering single parameter analysis (Figure-7) for compressive strength ranging from 15 to 150 MPa can be 0.63 $fck^{0.5}$ where Fck is the cube compressive strength of concrete.

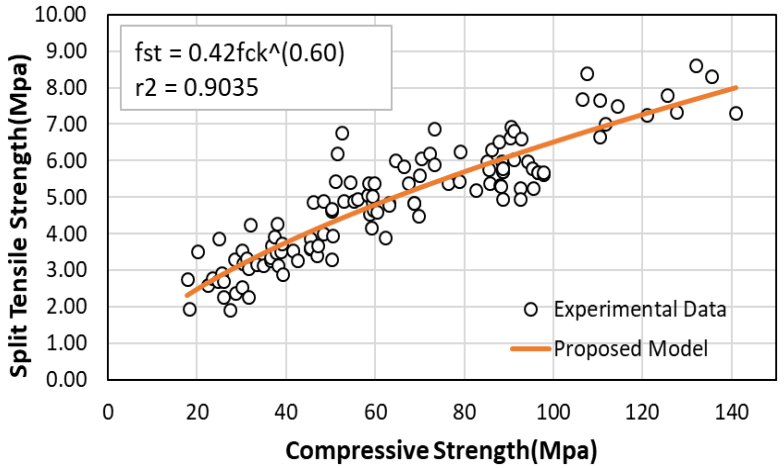

Fig. 6 (a) Derived model for split tensile strength vs compressive strength of concrete considering two parameters

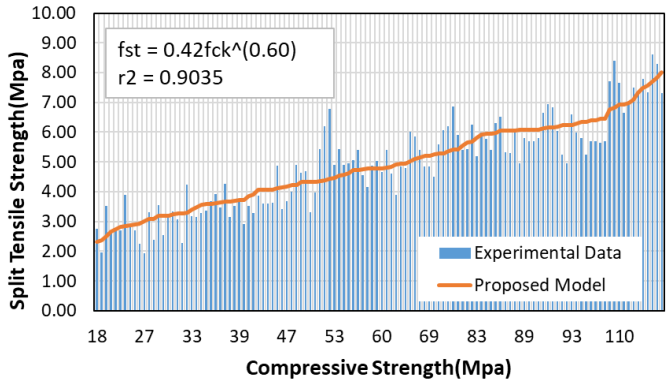

Fig. 6 (b) Comparison of proposed model for split tensile strength vs compressive strength of concrete considering two parameters

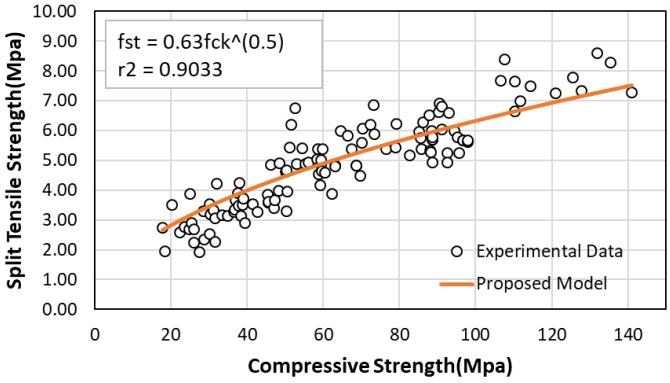

Fig. 7 (a) Proposed model for split tensile strength vs compressive strength of concrete considering one parameter

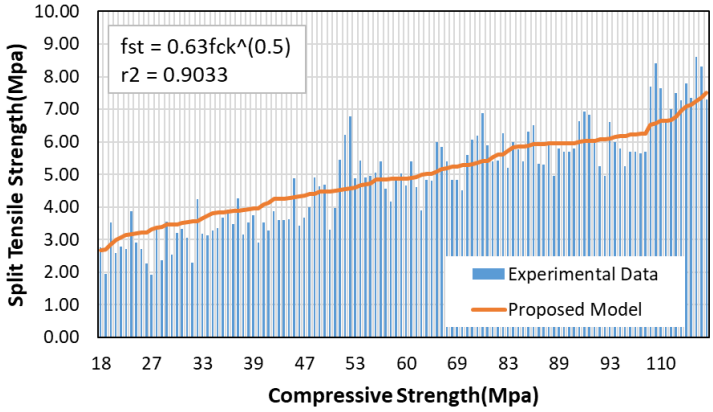

Fig. 7 (b) Comparison of proposed model for split tensile strength vs compressive strength of concrete considering one parameter

Table 5. Previous equation for estimation of split tensile strength of concrete at ambient temperature

Sl. No.	Reference	Previous Equations for estimation of split tensile strength of concrete [MPa]
1	CEB_FIP (1990)	$f_t = 0.3 f_c^{0.67}$
2	ACI 363R-92 (1984)	$f_t = 0.59 f_c^{0.5}$
3	ACI318-99 (2005)	$f_t = 0.56 f_c^{0.5}$
4	Perumal (2014)	$f_t = 0.188 f_c^{0.84}$
5	Rashid et al. (2002)	$f_t = 0.47 f_c^{0.56}$
6	Hueste et al. (2004)	$f_t = 0.55 f_c^{0.5}$
7	Ramadoss (2014)	$f_t = 0.12 f_c^{0.95}$
8	Xu and Shi (2009)	$f_t = 0.21 f_c^{0.83}$
9	Thomas and Ramasamy (2007)	$f_t = 0.57 f_c^{0.5}$
10	Singh et.al. (2021)	$f_t = 0.5 f_c^{0.5}$

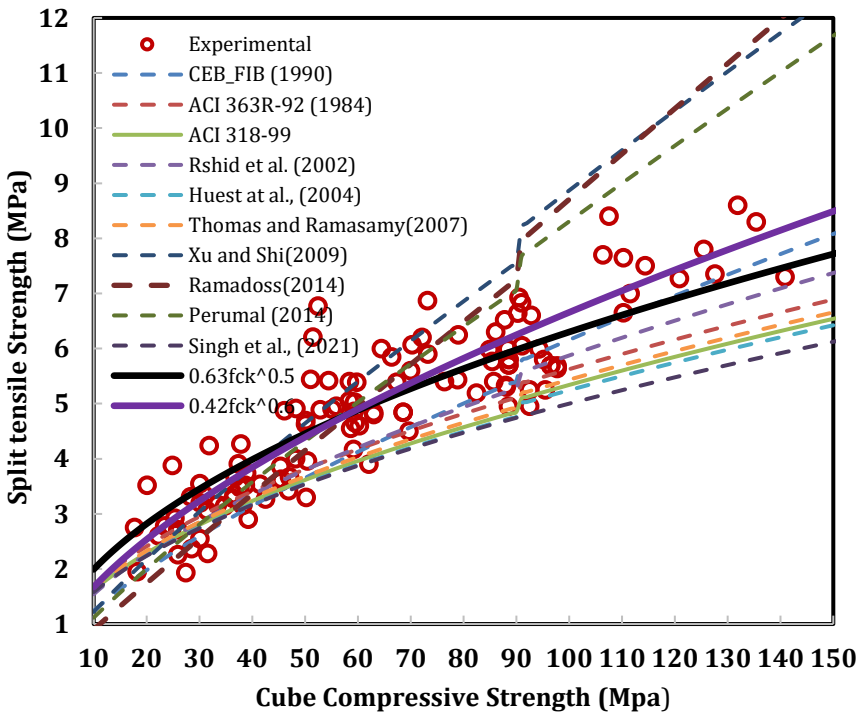

Fig. 8 Comparison of proposed model based on experimental results for spilt tensile strength of concrete in comparison with models proposed in international standards and literature

7. Comparison of Proposed Model for Flexural Strength of Concrete with International Codes and Literature

The experimental results of flexural tensile of concrete for strength range between 15 to 150 MPa obtained from testing samples of 10 concrete mixes without steel fibre are shown in Figures 9 and 10. To propose an equation for prediction of the flexural tensile strength; for one mixture, twelve cylindrical specimens were cast and for total ten mixture without steel fibre referred in the Table-4A, total 120 specimens were tested. The cylindrical specimen cast from 10 mixes (referred in Table-4A) has compressive strength ranging from 15 to 150 MPa which has been plotted and shown in Figures 9 and 10 The correlation between the flexure tensile strength and compressive strength is plotted and an equation is proposed with a high coefficient of correlation (R^2 = 0.94) using regression analysis. Using regression analysis, it is noted that for both one parameter analysis and two parameter analysis similar level of coefficient of correlation is achieved as shown in Figures 9 and 10. In Figure-9, based on two parameter analysis, the proposed equation for estimating flexural tensile strength of concrete for compressive strength ranging from 15 to 150 MPa can be 0.31 $fck^{0.7}$ where Fck is the cube compressive strength of concrete. In two parameter analysis, both functions i.e. multiplying factor with Fck and power factor to Fck has been varied. Whereas in single parameter analysis, power function to Fck has been kept constant and only multiplying factor analysis has been carried out to develop a simplified equation for incorporation in Indian Standard which is similar to equations given in other international codes for normal strength concrete. Keeping this in view for simplicity, the proposed equation for estimating flexural tensile strength of concrete considering single parameter analysis (Figure-10) for compressive strength ranging from 15 to 150 MPa can be 0.83 $fck^{0.5}$ where Fck is the cube compressive strength of concrete.

Comparison of proposed model with previous equations (Table-6) for estimation of flexure tensile strength of concrete at ambient temperature is given in Figure-11. The cubic compressive strength were converted to cylindrical compressive strength for the comparison with previous models wherever applicable based on cube to cylinder ratio determined in section 4.

From Figure 11, it can be seen that ACI: 318, New Zealand code (NZS: 3101), Canadian code CSA: A23.3-14 (2014) and IS-456-2000 estimates flexural strength value on lower side than the actual experimental values for normal and high strength concrete. The difference between the estimated and experimental value increases significantly with increase in concrete strength. The values of flexural tensile strength of concrete estimated through equation proposed by Singh et.al holds good for even higher grades but the study conducted by them was upto 90 MPa only. In the current study the equation has been proposed upto 120 MPa compressive strength of concrete which estimates flexural strength with a reasonable level of consistency.

Table 6. Previous equation for estimation of tensile strength of concrete at ambient temperature

Sl. No.	Reference	Previous Equations for estimation of flexural tensile strength of concrete [MPa]
1	ACI: 318 (2014)	$f_t = 0.62 f_c^{0.5}$
2	NZS: 3101 (2006)	$f_t = 0.6 f_c^{0.5}$
3	CSA: A23.3-14 (2014)	$f_t = 0.6 f_c^{0.5}$
4	IS 456 (2000)	$f_t = 0.7 f_c^{0.5}$
5	Singh et. al. (2021)	$f_t = 0.8 f_c^{0.5}$

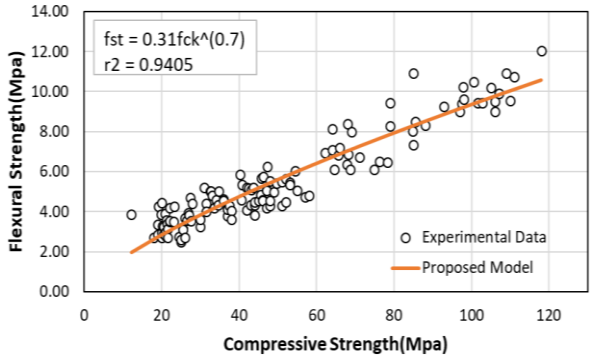

Fig. 9 (a) Proposed model for flexural tensile strength vs compressive strength of concrete considering two parameters

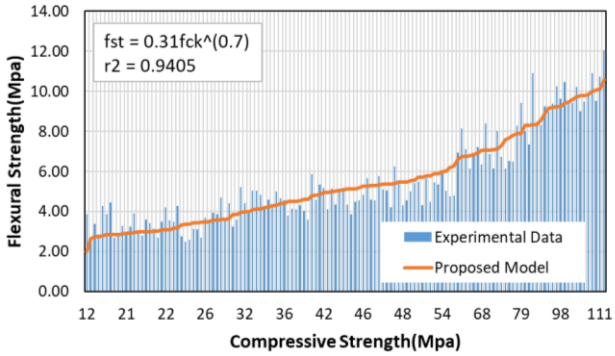

Fig. 9 (b) Comparison of proposed model for flexural tensile strength vs compressive strength of concrete considering two parameters

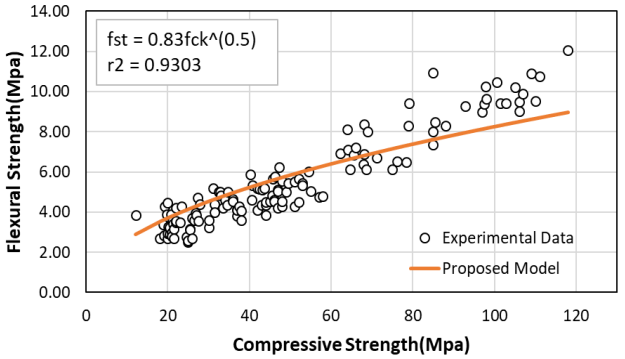

Fig. 10 (a) Proposed model for flexural tensile strength vs compressive strength of concrete considering two parameters

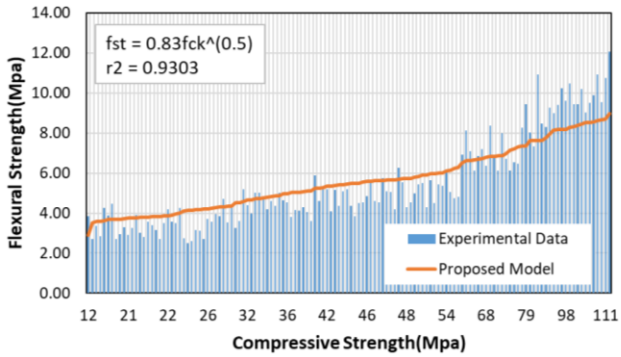

Fig. 10 (b) Comparison of proposed model for flexural tensile strength vs compressive strength of concrete considering one parameter

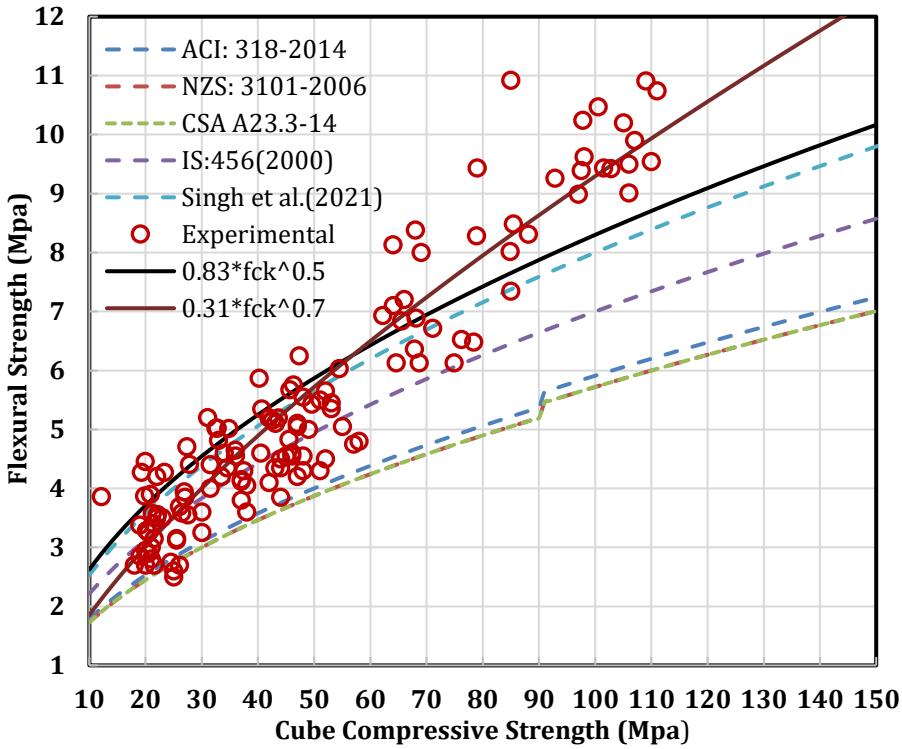

Fig. 11 Comparison of proposed model based on experimental results for spilt tensile strength of concrete in comparison with models proposed in international standards and literature

8. Comparison of Experimental Results of Flexural and Spilt Tensile Strength of Steel Fibre Reinforced Concrete with Proposed Models

The experimental results of split tensile of concrete for strength range between 20 to 110 MPa obtained from testing samples of 3 concrete mixes with steel fibre addition of 1

percent by volume on 30 specimens are shown in Figure 12. Total 10 specimens for each of three mixture were cast and results are analyzed.

In case of experimental results of split tensile strength of steel fibre reinforced concrete, for normal and high-strength concretes matrix aggregate separation was similar to that of concrete without fibre but there is improvement in spilt tensile strength of steel fibre reinforced concrete by 23% on average. The correlation between the split tensile strength of steel fibre reinforced concrete and compressive strength is plotted and when validated with proposed equation high coefficient of correlation (R^2=0.90) using regression analysis has been found. However, the proposed model is underestimating the spilt tensile strength of steel fibre reinforced concrete and it is suggested to use same equation as variation in spilt tensile strength of concrete is on average 23 percent. The experimental results of flexural tensile of concrete for strength range between 20 to 110 MPa obtained from testing samples of 3 concrete mixes with steel fibre addition of 1 percent by volume on 24 specimens are shown in Figure 13. Total 08 specimens for each of three mixture were cast and results are analyzed. Contrary to split tensile strength of fiber reinforced concrete, the experimental values for the flexural strength of steel fiber reinforced concrete shows high deviation from the behavior of plane concrete. The average variation in flexural strength values for steel fibre reinforced concrete with respect to plain concrete was found to be about 107 percent.

As presented in Figure 13, the proposed model for plain concrete depicts a very weak coefficient of correlation between the experimental and modelled values of the flexural strength. The findings indicates a significant improvement in the flexural strength of the concrete with addition of steel fiber. The fiber action also depends on the packing density of concrete used. It was also observed that the mix with intermediate strength shows a higher flexural strength after the addition of steel fiber than the mix of higher strength with significantly improved packing density and wider inter transition zone. The reason for the observed trend can be attributed to higher number of voids for the steel fiber in the intermediate strength mix as compared to highly optimized mix.

9. Evaluation of Ratio of Flexural Strength to Spilt Tensile Strength of Concrete for Strength Range 20 to 120 MPa

Based on the experimental results of 120 specimens tested for flexural tensile strength and 120 specimens tested for split tensile strength of concrete on the concrete prepared with 10 concrete mixes (Table-4), a relationship between flexural and split tensile strength of concrete has been proposed. The correlation between the flexural tensile strength and split tensile strength when plotted (Figure-14) has coefficient of correlation (R^2 = 0.775) using regression analysis has been found. The obtained equation is Fft=1.27 Fspt and the proposed equation can be Fft=1.25 Fspt where Fft is flexural tensile strength of concrete and Fspt is split tensile strength of concrete for the strength range of 20 to 120 MPa. Figure 14 shows the comparison between the experimental values and the derived relation between the split and flexural tensile strength.

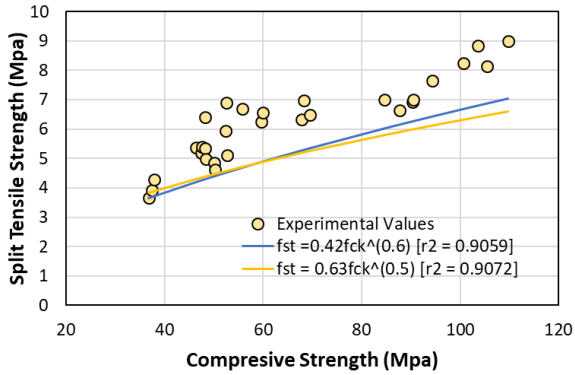

Fig. 12 Comparison of proposed model for split tensile strength vs compressive strength of plain concrete and experimental results of steel fibre reinforced concrete considering both models

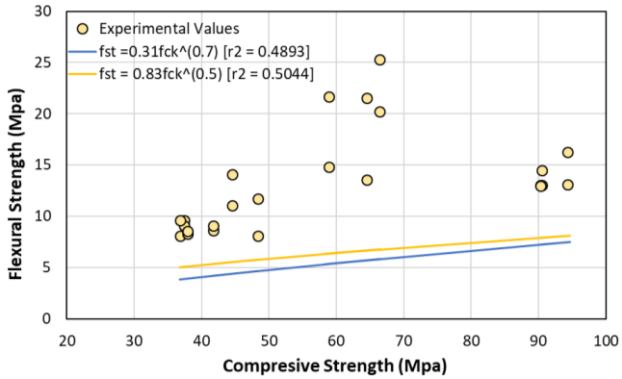

Fig. 13 Comparison of proposed model for flexural tensile strength vs compressive strength of plain concrete and experimental results of steel fibre reinforced concrete considering both models

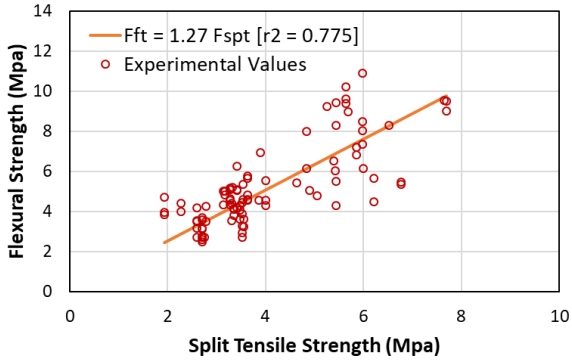

Fig.14 Comparison of proposed model for estimating flexural strength from split tensile strength of concrete

10. Conclusions

The equation for prediction of flexural and split tensile strength from the cube compressive strength in the current Indian Standard IS: 456-2000 is only valid up to concrete strength of 55 MPa. With the inclusion of high strength concrete to the standard, it is necessary to develop a relationship that can predict the approximated flexural and split tensile strength of high strength concrete. Along with this the impact of steel fibers on these two properties needs consideration to check the suitability of empirical equations developed for estimation of flexural and split tensile strength of concrete. The present study attempted to establish a correlation among the splitting tensile strength and flexural strength with compressive strength that is suitable to concrete with strengths between 20 MPa and 120 MPa. A total of 120 test results for split tensile strength and 120 test results for flexural strength were used in the investigation with a total of approximately 24 test results for split tensile strength and about 30 test results for flexural strength of concrete with steel fibers. Findings can be concluded as follow:

- The ratio of cube to cylindrical compressive strength varies with increase in concrete compressive strength. From the experimental investigation, the cube to cylindrical compressive strength is found to be approximately 1.20 upto 90 MPa and 1.10 for 90 MPa to 120 MPa cube compressive strength.
- The relation between the cube compressive strength and the split tensile strength was established as fspt=0.42*fck^(0.60) for two parameter optimisation and fspt=0.63*fck^(0.5) for single parameter optimisation wherein both equations depicts high coefficient of correlation. For simplicity the obtained equation fspt=0.63*fck^(0.5) is recommended for inclusion in codal provisions.
- Similarly the Correlation equation obtained for the estimation of flexural strength from the cube compressive strength is Fft=0.31*fck^(0.7). For simplicity keeping the power 0.5, the equation becomes Fft=0.83*fck^(0.5). Both the equations show a high coefficient of correlation in regression analysis. For simplicity the obtained equation Fft=0.83*fck^(0.5) is recommended for inclusion in codal provisions.
- Addition of steel fibers in concrete mix have different effects on the split and flexural tensile strength of the concrete. With the addition of steel fibers the split tensile strength increases marginally and the equation for the plain concrete can be used for predicting the approximate split tensile strength of fiber reinforced concrete also.
- The fiber action of steel fibers in steel fiber reinforced concrete affects the flexural behaviour significantly. The increase in the flexural strength observed is as high as 107% on average. The proposed equation in this study for plain concrete will underestimate the flexural strength for fiber reinforced concrete and further study is needed to establish the effect of steel fibre strength, shape, percentage, aspect ratio and composition of concrete mix on flexural tensile strength of concrete.
- The ratio between the flexural and split tensile strengths of plain concrete is estimated to be 1.27. The obtained coefficient of correlation is 0.78. Although, the experimental and predicted values does not show a very high coefficient of correlation, flexural strength still can be approximately estimated from the split tensile strength using the equation, Fft = 1.27Fspt.

Acknowledgements

Authors acknowledge the funding received from Ministry of Commerce & Industry, Govt. of India

References

[1] Architectural Institute of Japan, Standard for Structural Calculation of Reinforced Concrete Structures, Chapter 2, AIJ, 1985, pp. 8-11

[2] Bazant ZP, Kazemi MT, Hasegawa T, Mazars J. Size effect in Brazilian split-cylinder tests. Measurements and fracture analysis. ACI Materials Journal, 1991; 88:3 325-332. https://doi.org/10.14359/1987

[3] Patel V, Singh B, Arora VV. Study on fracture behaviour of high strength concrete including effect of steel fiber. Indian Concrete Journal, 2020; 94:4, 1-9.

[4] Rocco C, Guinea GV, Planas J, Elices M. Size effect and boundary conditions in the Brazilian test: experimental verification. Materials and Structures, 1991; 32:217 210-217. https://doi.org/10.1007/BF02481517

[5] Zain MFM, Mahmud HB, Ilham A, Faizal M, Prediction of splitting tensile strength of high-performance concrete, Cem. Concr. Res. 32, 2002; 1201-1208. https://doi.org/10.1016/S0008-8846(02)00768-8

[6] ACI-Committe-363. State of the Art Report on High-Strength Concrete (ACI 363R-92). Farmington Hills, Mich., 1992.

[7] ACI-Committee-318. Building Code Requirements for Structural Concrete (ACI 318-99) and Commentary (318R-99). Farmington Hills, Mich., 1999.

[8] Gaedicke C, Torres A, Huynh KCT, Marines A. A method to correlate splitting tensile strength and compressive strength of pervious concrete cylinders and cores. Construction and Building Materials, 2016; 120: 271-278. https://doi.org/10.1016/j.conbuildmat.2016.08.031

[9] Yan K, Xu H, Shen G, Liu P. Prediction of splitting tensile strength from cylinder compressive strength of concrete by support vector machine. Advances in Materials Science and Engineering, 2013; 2013: Article ID 597257. https://doi.org/10.1155/2013/597257

[10] Arora VV, Singh B, Patel V, Trivedi A. Evaluation of modulus of elasticity for normal and high strength concrete with granite and calc-granulite aggregate. Structural Concrete, 2021; 22:S1. https://doi.org/10.1002/suco.202000023

[11] Saridemir M. Empirical modeling of splitting tensile strength from cylinder compressive strength of concrete by genetic programming. Expert Systems with Applications, 2011; 38:11 14257-14268. https://doi.org/10.1016/j.eswa.2011.04.239

[12] Oluokun FA. Prediction of concrete tensile strength from its compressive strength. Evaluation of existing relations for normal weight concrete. ACI Materials Journal, 1991; 88:3 302-309 https://doi.org/10.14359/1942

[13] Weber M, Thiele C. Correlation between the compressive and tensile strength of old concretes: applicability of the relationship described by DIN EN 1992-1-1. Beton- Und Stahlbetonbau, 2016; 111:10 635-644. https://doi.org/10.1002/best.201600038

[14] Arora VV, Singh B, Jain S. Effect of indigenous aggregate type on mechanical properties of high strength concrete. Indian Concrete Journal, 2017; 91:1 34-44

[15] Arora VV, Singh B, Jain S. Experimental studies on short term mechanical properties of high strength concrete. Indian Concrete Journal, 2016; 90:10 65-75.

[16] Arora VV, Singh B, Patel V. Study on stress strain characteristics of high strength concrete. Indian Concrete Journal, 2018; 92:

[17] Ojha PN, Ojha P.N., Trivedi A., Singh B., Kumar N. S. A., Patel V., Gupta R. K. High performance fiber reinforced concrete - for repair in spillways of concrete dams. Res. Eng. Struct. Mater., 2021; 7(4): 505-522. https://doi.org/10.17515/resm2021.252ma0128

[18] Ojha PN, Singh P, Singh B, Singh A, Mittal P. Fracture behavior of plain and fiber-reinforced high strength concrete containing high strength steel fiber. Research on Engineering Structures and Materials, 2022. https://doi.org/10.17515/resm2022.377ma1228

[19] P. N. Ojha, B. Singh, P. Kaura, and A. Singh, "Lightweight geopolymer fly ash sand: an alternative to fine aggregate for concrete production," Research on Engineering Structures and Materials, 2021, doi: 10.17515/resm2021.257ma0205.
[20] Singh B, Arora VV, Patel V. Experimental study on stress strain behaviour of normal and high strength unconfined concrete. Indian Concrete Journal, 2020; 94:4 10-19.
[21] Carrasquillo RL, Nilson AH, Slate FO. Properties of High-Strength Concrete Subjected to Short-Term Loads. ACI Journal Proceedings, 1981; 78:3 171-178. https://doi.org/10.14359/6914
[22] Rashid MA, Mansur MA, Paramasivam P. Correlations between Mechanical Properties of High-Strength Concrete. Journal of Materials in Civil Engineering, 2002; 230-238. https://doi.org/10.1061/(ASCE)0899-1561(2002)14:3(230)
[23] Paultre P, Mitchell D. Code Provision for High-Strength Concrete- An International Perspective. Concrete International, 2003; 76-90.
[24] Arora VV, Singh B, Patel V, Daniel Y, Mohapatra BN. Stress-Strain Behaviour and Performance Evaluation of High Strength Steel Fibre Reinforced Concrete. Indian Concrete Journal, 2019; 93:12 54-61.
[25] Singh B, Ojha PN, Trivedi A, Patel V, Arora VV. Development Of Empirical Equations For Prediction Of Flexural And Split Tensile Strength For Normal And High Strength Concrete With Granite And Calc-Granulite Aggregate, Indian Concrete Journal, 2021; 95:11 36-46.
[26] Ojha PN, Singh B, Singh A, Patel V, Arora VV. Experimental study on creep and shrinkage behaviour of high strength concrete for application in high rise buildings. Indian Concrete Journal, 2021; 95:2 30-42.
[27] ACI Committee 363, State -of-the Art Report on High -Strength Concrete, ACI Journal, Proceedings Vol.81, No.4, July-Aug.1984, pp. 364-411. https://doi.org/10.14359/10692
[28] Committee Euro-International du Beton, High Performance Concrete, Recommended Extensions to the Model Code 90-Research Needs, CEB Bulletin ' Information, No.228, 1995, 46pp.
[29] Eurocode 2. Design of Concrete Structures-Part 1: General Rules and Rules for Buildings, 2004, 225.
[30] Concrete Society (2004), Design Guide for High Strength Concrete, Technical Report 49, Slough, The Concrete Society.

Research on Engineering Structures & Materials
journal homepage: http://www.jresm.org
Research Group

Research Article

Optimization of hybrid fibre reinforced geopolymer concrete using hardened and durability properties

Kadarkarai Arunkumar*[1,a], Arunachalam Sureshkumar[2,b], Arunasankar Chithambar Ganesh[2,c], Loganathan Parthiban[2,d], Premkumar V [2,e]

[1]*Department of Civil Engineering, Mangalam College of Engineering, Ettumanoor, Kerala, India.*
[2]*Department of Civil Engineering, Sree Vidyanikethan Engineering College, Tirupati, India.*

Article Info

Article history:
Received 20 Jun 2022
Revised 09 Aug 2022
Accepted 11 Aug 2022

Keywords:

Rubber fibre;
Geopolymer concrete;
Durability;
Optimization;
Hybrid fibres

Abstract

Geopolymer concrete is the finest replacement to ordinary portland cement concrete, reducing greenhouse gas emissions in cement production. Most of the binders used in geopolymer concrete require high alkaline solution, high-temperature curing, and a prolonged time for setting. In this study, wood ash, which has an alkaline compound in its composition, is used to replace fly ash. The binder ratio is fixed as 70 percent of fly ash and 30 percent of wood ash. Meanwhile, geopolymer concrete lacks brittleness, energy absorption, and impact strength. The addition of fibres is helped in improving the above-mentioned properties. This study has made an effort to incorporate waste rubber as fibre combined with polypropylene fibre. The various dosage of polypropylene and rubber fibre hybridization such as 0/1, 0.75/0.25, 0.5/0.5, 0.25/0.75, 1/0, and 1/1 is optimized. The impact of various fibre dosages on fresh and hardened characteristics of geopolymer concrete is assessed. Further, the impact of various hybrid fibre dosages on durability was also investigated in this study. As a result, the hybrid fibre dosage of 0.5 percent of PP and 0.5 percent of rubber attained significant performance in all hardened properties. The optimum mix also showed better resistance against all durability properties. The mix with 0.5PP/0.5R gained the maximum compressive strength of 47.30Mpa, which is sufficient to design the paver block for medium traffic conditions as per IS15658-2006.

1. Introduction

Climate change [1,2] due to cement production and energy utilization for production has increased every day. Geopolymer concrete is the growing trend in the construction field, which could help for sustainable development by eliminating cement utilization in concrete and mitigating climate change [3–7]. Geopolymer concrete is made by the chemical reaction of precursors from the aluminosilicate binder with the aid of alkalines and the formation of monomers to develop polymerization, which could create polymerized gel structure for binding [8]. Various industries are producing different waste by-products such as metakaolin, silica fume, granulated blast furnace slag, fly ash, pulverized fuel ash, etc., [9], which can be used in the geopolymer concrete as an aluminosilicate binder [10–15]. The GGBS is a very good precursor. In the alkaline environment, pozzolanic powders (GGBS, metakaolin, silica fume, fly ash, etc.) enter into a chemical reaction [16]. Alkaline activators played a vital role in the chemical reaction of the precursors from the by-products and developing monomers [17,18]. Both hydroxide-based activators and silicate-based activators are needed to promote polymerization. The formation of gel structures has based on the compositions of the aluminosilicate binders and the type of the activator used, such

*Corresponding author: arunapcivil@gmail.com
[a] orcid.org/0000-0002-5745-6864; [b] orcid.org/0000-0001-9406-2576; [c] orcid.org/0000-0001-5004-4587;
[d] orcid.org/ 0000-0001-8106-4556; [e] orcid.org/0000-0002-3641-2520;
DOI: http://dx.doi.org/10.17515/resm2022.450ma0620

as sodium-based activators and potassium-based activators. The waste byproduct which contains less calcium has developed Na-S-H (Sodium Silicate Hydrate) gel, and the high calcium source material produces both the Na-S-H gel and C-A-S-H (Calcium Alumino Silicate Hydrate) gel [19–21]. At the same time, the utilization of potassium-based activators leads to the formation of Potassium Silicate Hydrate (K-S-H) gel [22,23]. The various modes of gel formation are the reasons for achieving strength in geopolymer concrete. However, the geopolymer concrete made with any source material lacked brittleness, impact strength, and energy absorption capacity. Hence, the inclusion of fiber is required to expand the brittle, energy absorption, and impact behavior of geopolymer.

The various studies [24–28] on geopolymer concrete by incorporating different types of fibres and their impact on the strength properties are considered in this study. The utilization of coir fiber in geopolymer concrete enhanced the compressive strength and reduced the flexural strength. The incorporation of raffia fibers in geopolymer concrete decreased both the compressive and flexural strength. The addition of cotton and sisal fibers in geopolymer concrete increased the compressive strength to 28.42 MPa and 25.56 MPa from 24.78 MPa of the control specimen. The bond between fibers (cotton, coir, raffia) and the matrix is weak without any cohesiveness, causing negative impacts over the mechanical properties and inducing the failure pattern [29]. The utilization of steel fibre in geopolymer concrete reduces the workability and provides less crack propagation resistance [26]. Steel fibre addition leads to corrosion failure. Glass fibre decreases workability and provides less crack propagation resistance. Polypropylene fibre increases the first crack load and gives more bonding effect in the concrete structure due to its high aspect ratio and the surface texture [30]. The addition of polypropylene fibre does not influence in increasing the compressive strength. However, polypropylene increases the flexural strength (13 to 36.1 percent) and toughness, and it helps in limiting shrinkage deformation. Capillary pores are reduced by increasing the polypropylene content in geopolymer concrete [31]. Polypropylene fibre increases the ductility of geopolymer concrete and reduces the degree of compressibility and shrinkage ratio. Crack width expansion and propagation resistance is increased with the addition of polypropylene fibres [32,33]. PP fibre addition reduced the ITZ width. However, the improvement in energy absorption and impact energy due to the polypropylene fibre incorporation is insufficient to design the structural member as impact resistance and heavy load members.

Various studies [34–37] were done on the various properties of rubberized geopolymer concrete. The addition of rubber fibre decreased the compressive strength due to lesser bonding between rubber particles and increased the flexural strength and splitting tensile strength. In contrast, an increase in rubber fibre increases the ductility of concrete and reduces the brittleness of concrete [38]. The rubber fibre increases the impact strength and energy absorption capacity of concrete due to its retaining effect on the plastic state [39]. The rubber fibres are incorporated as a replacement for fine aggregate only. A smaller volume fraction of rubber fibre helps limit the decrease in compressive strength [40]. The addition of rubber as a fibre with a smaller volume fraction in GPC has not been carried out. Incorporation of individual fibre led to enlarge the convenient characterstics of concrete to certain limit. Hybridization of two or more fibres exhibits improvements in all properties of concrete due to the fact that each fibre has its own properties [32]. The novelty of the study is to utilize the waste rubber as a fibre in smaller volume fractions and hybridization of both the fibres. Hence, an effort has been made by hybridizing polypropylene and rubber fibres to the effects of hybrid fibre on the properties of geopolymer concrete is studied.

In this study, the optimization of hybrid fibre dosage of polypropylene fibre and rubber fibre is done by mechanical and durability properties. Further, the effect of various hybrid fibre dosages on the mechanical and durability properties of geopolymer concrete is investigated.

2. Materials and Methodology

This study uses the smooth, ultra-fine and spherical shape Fly Ash (FA) as a primary binder [41]. The fly ash is obtained from the Tuticorin thermal power station. The FA used in this study has a specific gravity of 2.82, a loss of ignition (LOI) of 1.79 percent, and a surface area of 325 m^2/kg. Wood Ash is a secondary binder, a waste by-product collected from small-scale industries and hotels [42]. The wood ash is sieved through 90µm to remove large agglomerate fragments and carbonaceous components. The surface area and specific gravity of wood ash are determined as 567 m^2/kg and 2.43. The sodium-based activators such as sodium hydroxide and sodium silicate are used in this study as alkaline activators. Natural river sand having a specific gravity of 2.62, and the particles passing on a 4.75mm sieve are used in this study. Local quarry coarse aggregate having a specific gravity of 2.89 and the size of 10mm is used. The fineness modulus of fine and coarse aggregates are 2.91 and 7.6. The short and discontinuous polypropylene fibre having a length of 24 mm and diameter of 0.3 mm is used in this study. The waste rubber tire is collected from the mechanical workshops and cut into pieces of size 20 mm in length and 0.3 mm in diameter. Table 1 represents the chemical compounds present in the fly ash and wood ash which is found using SEM-EDX analyzer.

Table 1. Chemical compositions of binders

Constituents	SiO_2	Al_2O_3	Fe_2O_3	CaO	MgO	K_2O	TiO_2	C	Others
Fly Ash	45.2	31.8	12.4	2.84	0.83	0.45	-	-	1.01
Wood Ash	47.56	20.32	2.22	3.61	3.02	14.49	1.01	10.22	3.98

Table 2. Mix proportions for various hybrid dosages

MIX ID	FA (kg/ m^3)	WA (kg/ m^3)	NaOH (kg/m^3)	Na_2SiO_3 (kg/m^3)	Sand (kg/m^3)	CA (kg/m^3)	PPF (kg/ m^3)	RF (kg/m^3)
GW30M10C	385	96.3	61.9	154.7	666.5	993.7	0	0
GW30M10CP2	385	96.3	61.9	154.7	666.5	993.7	4.82	0
GW30M10CHy1	385	96.3	61.9	154.7	666.5	993.7	3.61	1.21
GW30M10CHy2	385	96.3	61.9	154.7	666.5	993.7	2.41	2.41
GW30M10CHy3	385	96.3	61.9	154.7	666.5	993.7	1.21	3.61
GW30M10CHy4	385	96.3	61.9	154.7	666.5	993.7	4.82	4.82
GW30M10CR2	385	96.3	61.9	154.7	666.5	993.7	0	4.82

*FA-Fly Ash, WA-Wood Ash, CA-Coarse Aggregate, PPF-Polypropylene Fibre, RF-Rubber Fibre

The mix design is done using the modified guidelines for geopolymer concrete mix design as per IS 10262-2009 [43]. From the mix design, the material quantities are calculated and listed in Table 2. The optimization of binder ratio was already done in the author's previous study [44], hence the optimum binder ratio was taken as 70 percent of fly ash and 30 percent of wood ash. The molarity of the sodium hydroxide, NaOH to Na_2SiO_3 ratio, and the Alkaline solution to Binder ratio are taken from the author's previous study [10] as 10M, 1:2.5, and 0.45. For the hybridization of fibres, both the fibres are varied by 0, 0.75,0.5, 0.75, and 1 of volume fractions. The polypropylene fibers and rubber fibers are added in various proportions, such as 0/1, 0.25/0.75, 0.5/0.5, 0.75/0.25, and 1/0. The mix ID and the quantity of materials are tabulated in Table 2.

3. Experimental Testing Methods

All the specimens are cured at room temperature in this study, not exceeding 28oC. The mechanical properties are measured at the ages of 3, 7, 28, 56, and 90 days of curing. The mechanical properties such as compressive strength, splitting tensile strength, flexural strength, and hardened properties such as ductility factor and impact strength tests are performed in this study. The compressive strength is determined as per IS: 516-1959 [45]

by testing 150mm size cube specimens. The splitting tensile strength test is executed at the age of 3, 7, 28, 56, and 90 days on the cylindrical specimen of size 150 mm x 300 mm, as per the standard procedure given in IS: 5816- 1999. A flexural strength test is performed as per the IS: 516-1959 [45] procedures over the prism specimen of size 500 mm x 100 mm x 100 mm at 3, 7, 28, 56, and 90 days. The measurement of ultimate and yield deflections is done by fixing the dial gauges at the center point while applying flexural load on the prism specimen to find the ductility factor as per IS: 516- 1959. In accordance with ACI committee 544 [46], the impact test is performed with the specimen in a cylindrical shape of size 150 mm x 60 mm. The impact strength is calculated based on the number of blows required to initiate the first crack, the mass of the hammer, and the height of the fall. The durability properties like water absorption, sorptivity, chloride penetration, acid attack, sulphate attack, and marine water-resistance are investigated in this study. The water absorption and sorptivity tests are accomplished as per the procedure given in ASTM C642- 2005 and ASTM-C1585-04. As per the ASTM C1202-2012, the rapid chloride penetration test is performed to find the chloride penetration. In accordance with ASTM C267-1998 [47], the concrete resistance when exposed to 0.8 N for HCl and 1.2 N for H2SO4 solutions is performed. The cube specimens are soaked in acid solutions (HCL-5 percent and H2SO4-5 percent) for 28 days and 56 days. In accordance with ASTM C1012-2015 [48], the concrete resistance when exposed to Na2SO4 (Sodium Sulphate) solutions is tested with a cube specimen. As per ASTM C1012-2015 [48] standards, the concentration of Na2SO4 was maintained at 50g/L, and the samples were soaked in Na2SO4 solutions for 28 days and 56 days, respectively. The concrete resistance when exposed to marine water is tested cube specimen, as per ASTM D1141-1998 [49]. As per ASTM D1141-1998 [49] standards, the marine water was prepared in laboratory and the salinity of marine water was maintained at 37g/L , and the samples were soaked in the marine water container for 28 days and 56 days, respectively.

4. Results and Discussion

4.1. Compressive Strength

This impact of various hybrid dosages on the compressive strength of geopolymer concrete at the ages of 3, 7, 28, 56 and 90 days is assessed. The test results showed that the specimens GW30M10CHy1, GW30M10CHy2, and GW30M10CHy3 exhibited a 20.4, 22.0, and 16.1 percent enhancement in 90 days compressive strength than the control specimen GW30M10C. Meanwhile, the specimens GW30M10CR2 and GW30M10CHy4 exhibit a 10 percent and 0.7 percent enhancement in 28 days compressive strength compared to the control mix GW30M10C. However, the specimens GW30M10CR2 and GW30M10CHy4 show a 20.1 and 32.4 percent decrease in 28 days compressive strength compared to the specimen GW30M10CP2. The enhancement in compressive strength at all ages of concrete is gradual for all the specimens. Figure 1 exhibits that the slight enhancement of compressive strength is noted with various hybrid fibre dosages. The specimen with 0.5 percent PP fibre and 0.5 percent rubber fibre (GW30M10CHy2) has shown maximum performance in all ages of compressive strength. Figure 1 shows that the specimen GW30M10CHy2 exhibits a 43.2, 24.4, 26.8, 26.5, and 22.0 percent enhancement in compressive strength at 3, 7, 28, 56, and 90 days of concrete ages compared to the specimen without fibre (GW30M10C). The specimen GW30M10CHy2 enhanced the 28 days and 90 days compressive strength by 2.4 and 2.3 percent compared to the specimen with 1 percent of PP fibre (GW30M10CP2).

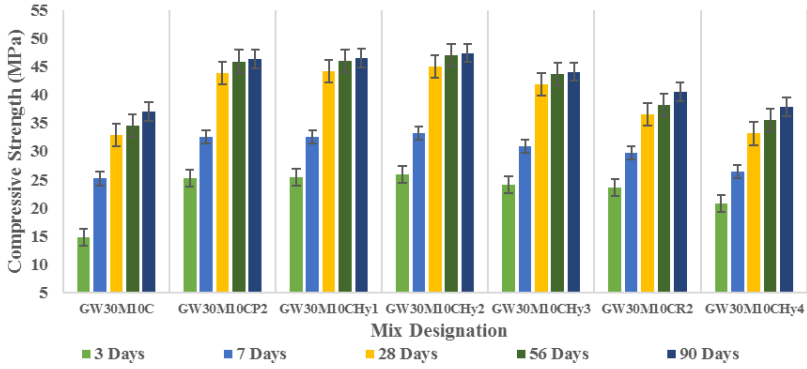

Fig. 1 Compressive strength test results of various hybrid proportions

Meanwhile, the compressive strength of the Hybrid Fibre Reinforced Geopolymer Concrete (HFRGPC) specimen decreases with increasing the rubber fibre content up to 0.5 percent. At the same time, the rubber fibre content exceeding 0.5 percent in fibre hybridization results in a major reduction in the compressive strength. The specimens GW30M10CHy3, GW30M10CR2, and GW30M10CHy4, show a 5.1, 14.2, and 22.4 percent decrease in 90 days compressive strength than the mix with 1 percent PP (GW30M10CP2). The lower degree of compressibility of polypropylene fibre also helped to enhance the strength [50]. The excess quantity of rubber fibre beyond 0.5 percent reduces the strength, due to which develops an unstiffened fibre matrix in the concrete medium. Exceeding the addition of both fibre beyond 1 percent results in a reduction of compressive strength and does not induce any effect than the control mix. In addition, the perfect proportion of low modulus and high modulus fibres showed strength increment [32,51,52]. There has been a considerable increase in the compressive strength with the utilization of both low modulus and high modulus fibers in the matrix.

4.2. Splitting Tensile Strength

The test results show that the specimens GW30M10CHy1, GW30M10CHy2, and GW30M10CHy3 exhibit 26.4, 30.8, and 26.1 percent increase in 28 days splitting tensile strength and 22.0, 26.7, and 21.6 percent increase in 90 days splitting tensile strength than the mix without fibres (GW30M10C). Meanwhile, the mix GW30M10CR2 and GW30M10CHy4 exhibit a 21.4 percent and 14.2 percent increase in splitting tensile strength compared to the control mix GW30M10C. However, the specimens GW30M10CR2 and GW30M10CHy4 show a 1.4 and 10.7 percent decrease in 28 days splitting tensile strength than the specimen GW30M10CP2.

From Figure 2, it can be observed that the hybrid percentage of rubber plays a important role in the enhancement of splitting tensile strength. The specimen with 0.5 percent PP fibre and 0.5 percent rubber fibre (GW30M10CHy2) has shown maximum performance in all ages of splitting tensile strength. Figure 2 shows that the specimen GW30M10CHy2 exhibits a 12.2, 9.7, 10.8, 9.2, and 10.3 percent increase in splitting tensile strength after 3, 7, 28, 56, and 90 days of curing compared to the specimen with 1 percent PP fibre (GW30M10CP2). The specimen GW30M10CHy2 has enhanced the 28 days and 90 days splitting tensile strength by 30.8 and 26.7 percent compared to the specimen without fibre (GW30M10C). Hence, the optimum specimen GW30M10CHy2 has achieved maximum splitting tensile strength compared to all other proportions of hybridization.

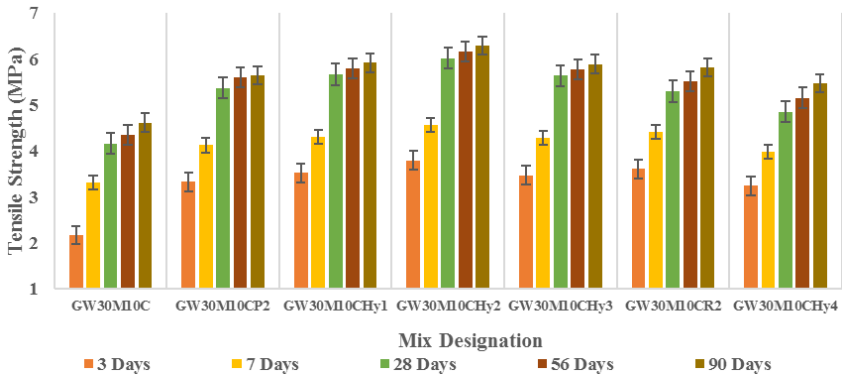

Fig. 2 Splitting tensile strength test results for various hybrid fibre proportions

Meanwhile, the splitting tensile strength of the HFRGPC specimen increases with increasing the rubber fibre content up to 0.5 percent. At the same time, the rubber fibre content exceeds 0.5 percent in fibre hybridization, resulting in reducing the splitting tensile strength. The specimen GW30M10CHy3 showed a decrease in splitting tensile strength compared to specimen GW30M10CHy2. The increase in splitting tensile strength was due to the perfect dispersion of fibres and created a stiffened fibre matrix [32]. The decrease in splitting tensile strength was due to the augmentation of fibres. When the percentage of rubber exceeds 0.5 percent, it develops an unstiffened fibre matrix in the concrete medium. Exceeding the addition of both fibre beyond 1 percent results in reducing splitting tensile strength and does not induce any effect than the control mix. In addition, the perfect proportion of low modulus and high modulus fibres showed strength increment [51,53,54]. It is also observed that there is a considerable increase in the splitting tensile strength with the utilization of both low modulus and high modulus fibers in the matrix.

4.3. Flexural Strength

The test results show that the specimens GW30M10CHy1, GW30M10CHy2, and GW30M10CHy3 exhibit 27.3, 31.7, and 26.9 percent increase in 28 days flexural strength and 22.6, 27.4, and 22.3 percent increase in 90 days flexural strength than the mix without fibre (GW30M10C). Meanwhile, the specimens GW30M10CR2 and GW30M10CHy4 exhibit a 17.5 percent and 0.7 percent increase in flexural strength compared to the control mix GW30M10C. However, the specimens GW30M10CR2 and GW30M10CHy4 showed a 7.4 and 29.4 percent decrease in 28 days flexural strength compared to the specimen GW30M10CP2.

From Figure 3, it is observed that the hybrid percentage of rubber plays a important part in the enhancement of flexural strength. The specimen with 0.5 percent PP and 0.5 percent rubber (GW30M10CHy2) exhibits maximum strength in all age of concrete. Figure 3 shows that the specimen GW30M10CHy2 exhibits a 12.8, 10.0, 11.1, 9.5, and 10.6 percent increase in flexural strength after the respective days of curing, compared to the specimen with 1 percent PP fibre (GW30M10CP2). The specimen GW30M10CHy2 enhanced the 28 days and 90 days flexural strength by 31.7 and 27.4 percent compared to the specimen without fibre (GW30M10C). Hence, the optimum specimen GW30M10CHy2 achieved maximum flexural strength compared to all other proportions of hybridization. The increase in flexural strength was due to the perfect dispersion of fibres and created a stiffened fibre matrix [55]. The strength reduction was by the augmentation of fibres. An unstiffened fibre matrix in the concrete medium is developed when the percentage of rubber exceeds 0.5 percent. Exceeding the addition of both fibre beyond 1 percent results in a reduction of flexural

strength and does not induce any effect than the control mix. In addition, the perfect proportion of low modulus and high modulus fibres showed strength increment [32,52,56]. It is also observed that there is a considerable increase in the flexural strength with the utilization of both low modulus and high modulus fibers in the matrix.

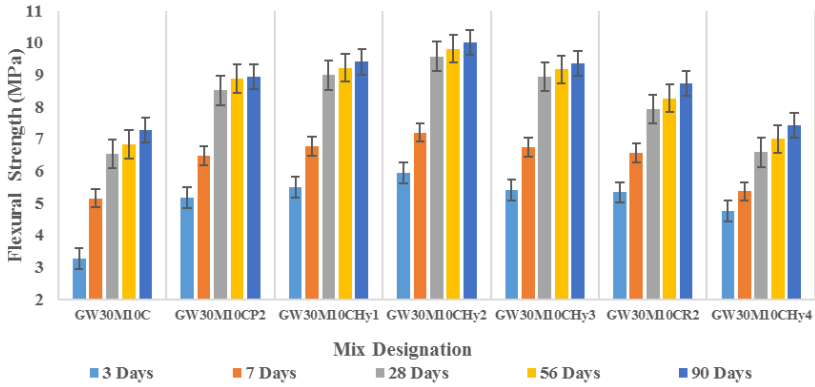

Fig. 3 Flexural strength test results for various hybrid fibre proportions

4.4. Ductility Factor

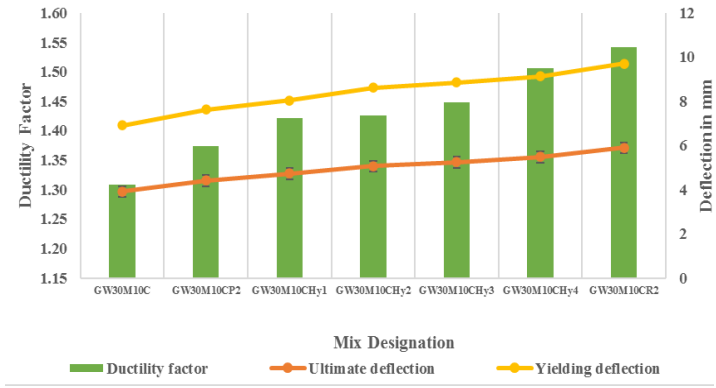

Fig. 4 Ductility factor for various hybrid fibre proportions

The results showed that the specimens GW30M10CP2, GW30M10CHy1, GW30M10CHy2, GW30M10CHy3, GW30M10CHy4, and GW30M10CR2 obtained the ductility factor values of 1.37, 1.42, 1.43, 1.45, 1.51 and 1.54. The specimen with 1 percent rubber fibre (GW30M10CR2) showed a maximum ductility factor value compared to other specimens.

From Figure 4, it can be observed that the utilization of rubber fiber increases the ultimate deflection and yield deflection. The specimen GW30M10CR2 exhibits a maximum increase in ductility due to the rubber fibers, which helps in improving the strength properties [35]. The specimens GW30M10CP2 and GW30M10CHy1 suffer from the least ductility with the higher percentage polypropylene fiber affecting the stability of the mix. The specimen GW30M10CHy2 and GW30M10CHy3 obtained a significant ductility factor than the control specimen GW30M10C. Hence, the ductility is improved with perfect proportion of both the fibers.

4.5. Impact Strength

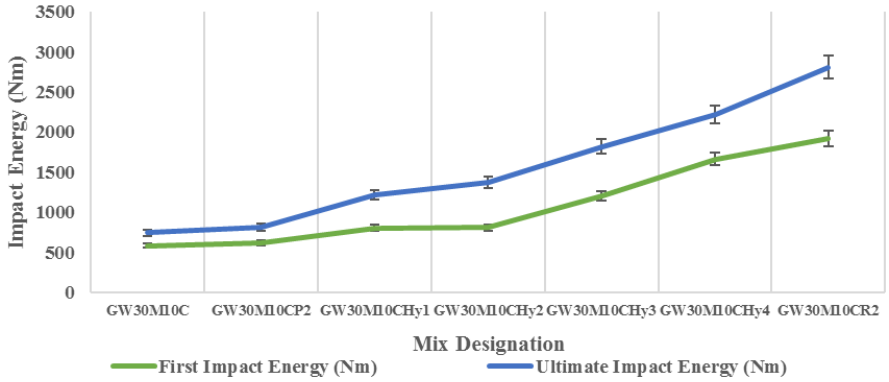

Fig. 5 Impact strength for various hybrid fibre proportions

The result shows that the specimens GW30M10CHy1, GW30M10CHy2, GW30M10CHy3, GW30M10CHy4, and GW30M10CR2 observe the ultimate impact energy of 1212.8, 1370.12, 1815.23, 2223.56 and 2809.12 Nm, respectively. Meanwhile, the number of blows required to obtain ultimate failure was observed by the specimens GW30M10CHy2, GW30M10CHy3, GW30M10CHy4, and GW30M10CR2 as 60, 75, 82, and 128. The specimen with 1 percent rubber fibre (GW30M10CR2) obtained maximum values in ultimate impact energy of 2809.12 Nm. The specimens GW30M10CHy1 and GW30M10CHy2, GW30M10CHy3, GW30M10CHy4, and GW30M10CR2 exhibit 49.30, 68.67, 123.47, 173.73, and 245.82 percent increase in energy absorption compared to the specimen GW30M10CP2.

From Figure 5, it is inferred that the number of blows required to initiate the first crack and ultimate failure increases with the increase in the rubber fiber content and decrease in polypropylene fiber content. Specimen GW30M10CR2 yields maximum impact energy because the rubber fiber increases the energy absorption capacity. The energy-absorbing property of the rubber fibers is higher than the polypropylene fibers [38]. The test results evident that the number of blows for the ultimate crack is enhanced by the higher amount rubber fiber [57]. The maximum enhancement in impact strength is related to the presence of high modulus fibers in a hybrid fiber medium [58]. The specimen GW30M10CP2 yields the least impact energy owing to the poor structural integrity caused by the polypropylene fibers that affect the adhesion between the fiber and the matrix.

4.6. Water Absorption Test

The test results show that the specimens GW30M10CP2, GW30M10CHy1, GW30M10CHy2, GW30M10CHy3, GW30M10CHy4, and GW30M10CR2 have obtained a water absorption percentage of 3.21, 3.11, 3.02, 3.05, 3.30 and 3.32 at 90 days. While increasing the concrete age, the water absorption percentage will increase gradually. However, the increase in water absorption of all the HFRGPC specimens after 90 days is lower than the increase in water absorption at 28 and 56 days. The weight of specimen GW30M10CHy2 at 28 days of water immersion increases by 29.7 g from the initial weight. At the same time, the weight of the specimen GW30M10CHy2 after 56 days of water immersion is increased by 23 g from the weight of the specimen at 28 days. The weight of the specimen GW30M10CHy2 after 90 days of water immersion is increased by 21.6 g from the weight of the specimen at 56 days. Hence, the increase in specimen weight was decreased by increasing the immersion period.

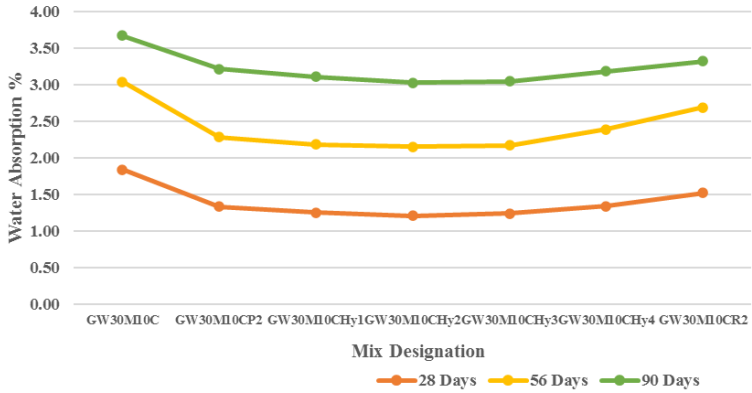

Fig. 6 Water absorption of various HFRGPC specimens

The test results showed that all the HFRGPC specimens exhibit excellent durability in terms of water absorption. The specimen GW30M10CHy2 grasps the minimum water absorption capacity. The specimen GW30M10CHy2 has obtained water absorption percentages of 1.21, 2.17, and 3.05 after 28, 56, and 90 days of water immersion. The porosity of the concrete is significantly reduced, resulting in enhanced resistance to water absorption and minimum water absorption capacity due to the blending effect of both the fibers [59,60].

From Figure 6, it is observed that the water absorption value is maximum in the specimens GW30M10CHy4 and GW30M10CR2. The specimen with higher polypropylene fibres results in lower water absorption than specimens with a high percentage of rubber fibre. However, all HFRGPC specimens observed less water absorption capacity than the specimen without fibres (GW30M10C). The test results show that polypropylene fibre does not influence the geopolymer concrete to absorb more water. Due to its hydrophobic nature [61], polypropylene fibre helped limit the water absorption capacity of HFRGPC specimens.

4.7. Sorptivity

From the results, it can be observed that all the HFRGPC specimens obtained the minimum sorptivity values than the specimen without fibres. Figure 7 represents the sorptivity values of each HFRGPC specimen. From Figure 7, it is inferred that the specimen with a higher percentage of polypropylene fibre obtained the higher sorptivity values. The sorptivity values decrease with increasing the rubber fibre percentage [62]. The observed readings are in agreement with the water absorption test values.

The specimen GW30M10CHy2 has the lowest sorptivity values because polypropylene fibers are hydrophobic and absorb the least water. The specimen GW30M10CP2 exhibits comparatively more sorptivity value due to porosity. However, all HFRGPC specimens observed less sorptivity than those without fibres (GW30M10C). The test results show that rubber fibre does not influence the geopolymer concrete to absorb more water. Due to its elasto-plastic nature, rubber fibre helped limit the sorptivity of HFRGPC specimens.

4.8. Rapid Chloride Penetration Test

RCPT (Rapid Chloride Penetration Test) test results exhibit that the specimens GW30M10CHy2, GW30M10CHy3, GW30M10CHy4, and GW30M10CR2 obtained the minimum values of charges passed through concrete compared to other specimens. When the age of concrete increases, the charge passed increases gradually. The specimen GW30M10CR2 obtained the charge passed are 1980, 2163, 2002, and 2283 after 28, 56, and 90 days of testing, which is the least value compared to other specimens. The charge passed

through the specimen GW30M10CR2 at 56 days of testing increases by 183 coulombs from the charge passed at 28 days. The charge passed through the specimen GW30M10CR2 after 90 days of testing is increased by 120 coulombs from the charge passed through the specimen at 56 days. The porosity of the concrete is greatly reduced, resulting in enhanced resistance to electrical conductivity due to the blending effect of both fibers.

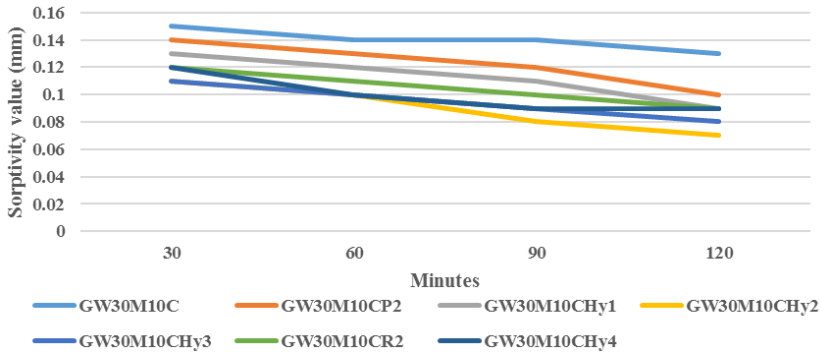

Fig. 7 Sorptivity value of various HFRGPC specimens

The mix with 1 percent PP (GW30M10CP2) displays the minimum resistance for chloride penetration, and the specimen GW30M10CR2 possesses the maximum resistance for chloride penetration. The results showed that the presence of rubber fibers increases the resistance to the flow of chloride ions into the concrete. Due to the high modulus of elasticity, the rubber fibre possesses resistance against the penetration of chloride ions [38]. Ranjith et al. [63] claimed an increase in chloride penetration with increased polypropylene fiber content. Chithambar [55] reported that the penetration of chloride ions in oven-cured samples is slightly more than the charges passed on the ambient cured samples. Hence, the ambient curing of all the specimens gives an excess advantage in resisting the chloride penetration. All the hybrid specimens were in the moderate range as per ASTM standards.

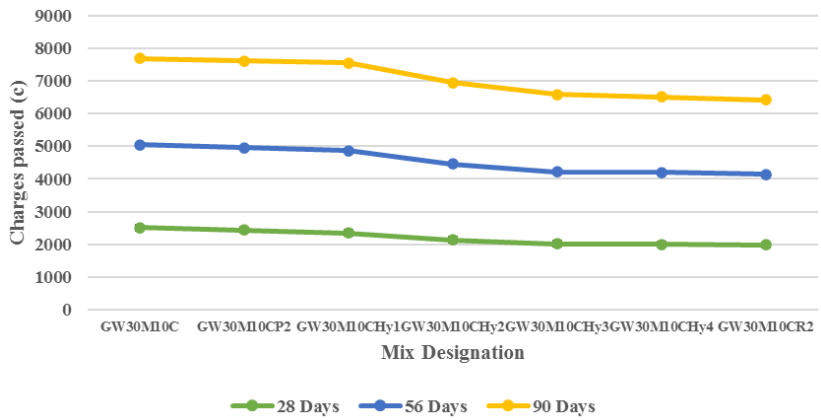

Fig. 8 Electrical resistivity value of various HFRGPC specimens

4.9. Acid Resistance Test

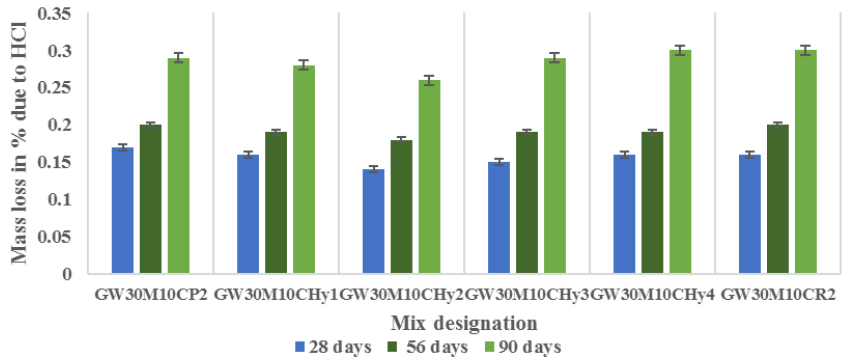

Fig. 9 Mass loss percentage of various HFRGPC specimens under HCL

The test results showed that the specimens GW30M10CHy2, GW30M10CHy3, GW30M10CHy4, and GW30M10CR2 obtained the minimum percentages of mass loss compared to other specimens. The percentages of mass loss increase gradually with the increase in concrete age. From Figure 9 and Figure 10, it is clear that the specimens with various hybrid fibre dosages possesses similar and improved resistance to both the acidic solutions. There is no considerable change in the performance of different fibers in resisting the acid attack. However, it is found that specimen GW30M10CHy2 reported the highest acid resistance due to the blended effect of hybrid fibers matrix in contributing to the less porous structure than other specimens.

From Figure 9 and Figure 10, it is observed that all the specimens have exhibited good acid resistance due to the perfect microstructure of optimized geopolymer concrete. The test results show that all the samples resist the acid attack better than the specimen without fibres (GW30M10C). However, the influence of various proportions of hybrid fibres on the sulphate resistance of the hybrid fibre reinforced geopolymer concrete has to be investigated.

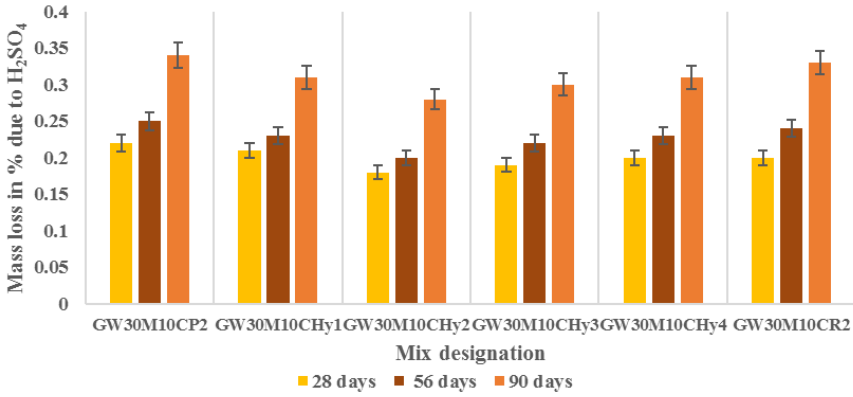

Fig. 10 Mass loss percentage of various HFRGPC specimens under H_2SO_4

4.10. Sulphate Resistance Test

Figure 11 clearly shows the variation in the mass of various HFRGPC specimens under the Na_2SO_4 acid exposures. The results show that the specimens GW30M10CHy2,

GW30M10CHy3, GW30M10CHy4, and GW30M10CR2 have obtained the minimum percentages of mass loss compared to other specimens. The percentages of mass loss increase gradually with the age of concrete increases [64].

All the mix with various hybrid fibre dosages possesses similar and improved resistance against sodium silicate solution. The specimen GW30M10CHy2 reported the highest sulphate resistance due to the blended effect of hybrid fibers matrix in contributing to the less porous structure than other specimens. The test results showed that all the specimens exhibited good sulphate resistance due to the perfect microstructure of optimized geopolymer concrete. The specimen GW30M10CP2 exhibits lower sulfate attack resistance than other HFRGPC specimens. The test results evident that resistance against the sulphate attack is enhanced with the higher percentage of rubber fiber content and reduced with the hugher percentage of the polypropylene fiber content. The presence of polypropylene fibers reduces the resistance to sulphate attack [39,65,66]. The test results show that all the samples resist the sulphate attack better than the specimen without fibres (GW30M10C).

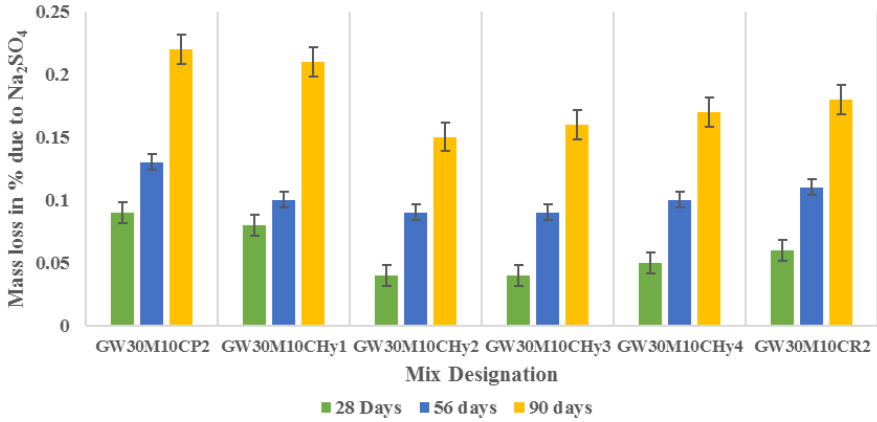

Fig. 11 Mass loss percentage of various HFRGPC specimens under Na_2SO_4

4.11. Marine Water Resistance Test

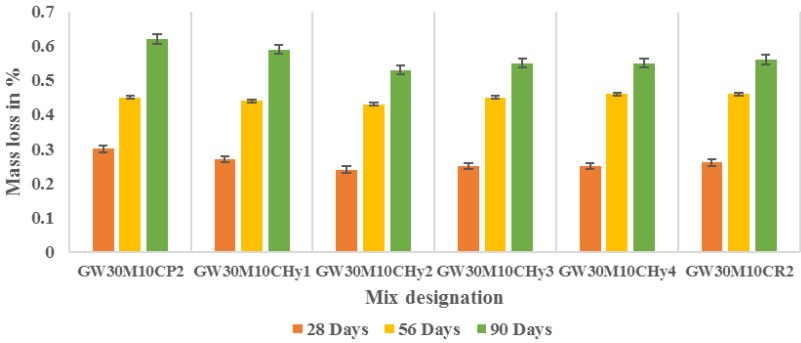

Fig. 12 Mass loss percentage of various HFRGPC specimens under Na_2SO_4

From Figure 12, it is evident that the specimens GW30M10CHy2, GW30M10CHy3, GW30M10CHy4, and GW30M10CR2 have obtained the minimum mass loss percentages compared to other specimens. The percentages of mass loss increase gradually with the age of concrete increases. The entire hybrid fiber specimen possesses similar and better

resistance to marine water. The specimen GW30M10CHy2 reported the highest marine water resistance due to the blended effect of hybrid fibers in a perfect matrix contributing to the less porous structure than other specimens. The high resistance exhibited by the hybrid fiber reinforced concrete specimens GW30M10CHy2, GW30M10CHy3, GW30M10CHy4, and GW30M10CR2 is attributed to the good microstructure induced by the better adhesion between the fibers and the matrix.

The test results showed that all the specimens exhibited good resistance against marine water attacks due to the perfect microstructure of optimized geopolymer concrete. The specimen GW30M10CP2 exhibits lower marine water attack resistance than all other HFRGPC specimens. The test results exhibit that the resistance offered to the marine water attack increases with the rubber fiber content and decreases with the increase in the polypropylene fiber content. The presence of polypropylene fibers reduces the resistance to a marine water attack. The test results show that all the samples resist the attack against marine water better than the specimen without fibres (GW30M10C).

5. Conclusion

This study examines the impact of various hybrid fibre dosages on the hardened and durability characteristics of geopolymer concrete. The specimen with 0.5 percent PP fibre and 0.5 percent rubber fibre exhibits a 26.9 percent, 30.8 percent, and 31.7 percent enhancement in compressive, splitting tensile and flexural strength compared to the specimen without fibre. The utilization of 0.5 percent of polypropylene fibre and 0.5 percent of rubber fibre (GW30M10CHy2) exhibits maximum performance in compressive, splitting tensile and flexural strength. The specimen with 1 percent rubber fibre (GW30M10CR2) observed maximum performance in impact strength and ductility due to the fact of high modulus of rubber fibre; however, the specimen doesn't show a significant effect in hardened properties. The hybrid fibre dosage of 0.5 percent of PP and 0.5 percent of rubber attained significant performance in all hardened properties. The specimen with 0.5 percent polypropylene and 0.5 percent rubber showed less water absorption and sorptivity values. Hybrid fiber reinforced geopolymer concrete with 0.5/0.5- rubber fiber/polypropylene fiber resisted the acid attack, sulphate attack, and marine water attack better than the other hybrid reinforced geopolymer concrete specimens due to the excellent microstructure contributed by the blended action of both the fibers inside the matrix. Hence, it has been chosen as an optimum mix for developing the hybrid fibre reinforced geopolymer concrete. The study developed a hybrid fibre reinforced geopolymer concrete combined with polypropylene fibre and rubber fibre. Moreover, the geopolymer concrete made up of waste materials such as fly ash and wood ash could be sustainable concrete used in cast-in-situ applications. Meanwhile, the maximum compressive strength of the optimum hybrid fibre reinforced geopolymer concrete specimen is about 47.39Mpa. It is sufficient to design the paver block for medium traffic conditions as per IS 15658-2006.

Acknowledgement

The authors acknowledge that this study does not have any funding informations.

References

[1] Loganathan P., and A.B. Mahindrakar. 2020. "Evaluation of surface temperatureand prediction of changes in future projections using quantile to quantile change factor methodologyover cauvery river basin-peninsular India." Indian Journal of Ecology. 47 (2): 312–5.

[2] Loganathan P., and A.B. Mahindrakar. 2020. "Assessment of changes in observed rainfall and prediction of future conditions using quantile delta mapping bias correction technique over cauvery River Basin, India." Indian Journal of Ecology. 47 (3): 708–11.

[3] Mikulčić H., J.J. Klemeš, M. Vujanović, K. Urbaniec, and N. Duić. 2016. "Reducing greenhouse gasses emissions by fostering the deployment of alternative raw materials and energy sources in the cleaner cement manufacturing process." Journal of Cleaner Production. 136 119–32. https://doi.org/10.1016/j.jclepro.2016.04.145
[4] Loganathan P., and A.B. Mahindrakar. 2021. "Statistical downscaling using principal component regression for climate change impact assessment at the Cauvery river basin." Journal of Water and Climate Change. 12 (6): 2314–24. https://doi.org/10.2166/wcc.2021.223
[5] Turner L.K., and F.G. Collins. 2013. "Carbon dioxide equivalent (CO2-e) emissions: A comparison between geopolymer and OPC cement concrete." Construction and Building Materials. 43 125–30. https://doi.org/10.1016/j.conbuildmat.2013.01.023
[6] Loganathan P., and A.B. Mahindrakar. 2021. "Intercomparing the robustness of machine learning models in simulation and forecasting of streamflow." Journal of Water and Climate Change. 12 (5): 1824–37. https://doi.org/10.2166/wcc.2020.365
[7] Loganathan P., and A.B. Mahindrakar. 2020. "Assessment and ranking of CMIP5 GCMs performance based on observed statistics over Cauvery river basin – Peninsular India." Arabian Journal of Geosciences. 13 (22): 1200. https://doi.org/10.1007/s12517-020-06217-6
[8] Davidovits J. 1991. "Geopolymers: inorganic polymeric new materials." Journal of Thermal Analysis. 37 (8): 1633–56. https://doi.org/10.1007/BF01912193
[9] Gundupalli Bhanu Prakash, and V Prem Kumar. 2017. "Carbonation Resistance of SCC." International Journal of Engineering Research and. V6 (10): 140–4. https://doi.org/10.17577/ijertv6is100087
[10] Arunkumar K., M. Muthukannan, A.S. Kumar, A.C. Ganesh, and R.K. Devi. 2022. "Cleaner Environment Approach by the Utilization of Low Calcium Wood Ash in Geopolymer Concrete." Applied Science and Engineering Progress. 15 (1): 1–13. https://doi.org/10.14416/j.asep.2021.06.005
[11] Zhang P., Z. Gao, J. Wang, J. Guo, S. Hu, and Y. Ling. 2020. "Properties of fresh and hardened fly ash/slag based geopolymer concrete: A review." Journal of Cleaner Production. 270 122389. https://doi.org/10.1016/j.jclepro.2020.122389
[12] Suresh Kumar A., M. Muthukannan, and I. Sri Krishna. 2020. "Optimisation of bio medical waste ash in GGBS based of geopolymer concrete." IOP Conference Series: Materials Science and Engineering. 872 12163. https://doi.org/10.1088/1757-899X/872/1/012163
[13] Okoye F.N., S. Prakash, and N.B. Singh. 2017. "Durability of fly ash based geopolymer concrete in the presence of silica fume." Journal of Cleaner Production. 149 1062–7. https://doi.org/10.1016/J.JCLEPRO.2017.02.176
[14] Kabir S.M.A., U.J. Alengaram, M.Z. Jumaat, S. Yusoff, A. Sharmin, and I.I. Bashar. 2017. "Performance evaluation and some durability characteristics of environmental friendly palm oil clinker based geopolymer concrete." Journal of Cleaner Production. 161 477–92. https://doi.org/10.1016/j.jclepro.2017.05.002
[15] Arunachalam S.K., M. Muthiah, K.D. Rangaswamy, A. Kadarkarai, and C.G. Arunasankar. 2021. "Improving the structural performance of reinforced geopolymer concrete incorporated with hazardous heavy metal waste ash." World Journal of Engineering. ahead-of-p (ahead-of-print): https://doi.org/10.1108/WJE-01-2021-0055
[16] Corbu O., A.M. Ioani, A.M.M. Al Bakri, V. Meiţă, H. Szilagyi, and A.V. Sandu. 2015. "The Pozzolanic Activity Level of Powder Waste Glass in Comparisons with other Powders." Key Engineering Materials. 660 237–43. https://doi.org/10.4028/www.scientific.net/KEM.660.237
[17] Malkawi A.B., M.F. Nuruddin, A. Fauzi, H. Almattarneh, and B.S. Mohammed. 2016. "Effects of Alkaline Solution on Properties of the HCFA Geopolymer Mortars." Procedia Engineering. 148 710–7. https://doi.org/10.1016/j.proeng.2016.06.581

[18] Suresh kumar A., M. Muthukannan, R. Kanniga Devi, K. Arunkumar, and A. Chithambar Ganesh. 2022. "Improving the Performance of Structural Members by Incorporating Incinerated Bio-Medical Waste Ash in Reinforced Geopolymer Concrete." Materials Science Forum. 1048 321–32. https://doi.org/10.4028/www.scientific.net/MSF.1048.321

[19] Yip C.K., G.C. Lukey, and J.S.J. Van Deventer. 2005. "The coexistence of geopolymeric gel and calcium silicate hydrate at the early stage of alkaline activation." Cement and Concrete Research. 35 (9): 1688–97. https://doi.org/10.1016/j.cemconres.2004.10.042

[20] Suresh Kumar A., M. Muthukannan, A.D.K.B. Irene, K. Arunkumar, and A. Chithambar Ganesh. 2022. "Flexural Behaviour of Reinforced Geopolymer Concrete Incorporated with Hazardous Heavy Metal Waste Ash and Glass Powder." Materials Science Forum. 1048 345–58. https://doi.org/10.4028/www.scientific.net/MSF.1048.345

[21] Kadarkarai Arunkumar, Muthiah Muthukannan, Arunachalam Sureh Kumar A.C.G. n.d. "Mechanical characterisation of waste wood ash-based green geopolymer concrete incorporated with waste rubber and polypropylene fibre." Int J Environment and Waste Management. XX (XX): (Accepted).

[22] Arunkumar K., M. Muthukannan, A.S. Kumar, A.C. Ganesh, and R.K. Devi. 2021. "Invention of sustainable geopolymer concrete made with low calcium waste wood ash." World Journal of Engineering. https://doi.org/10.1108/WJE-03-2021-0162

[23] Kadarkarai Arunkumar, Muthiah Muthukannan, Arunachalam Sureh Kumar A.C.G., and R.K. Devi. 2022. "Influence of Hybrid Fibres on the Mechanical Characterization of Low Calcium Geopolymer Concrete." Journal of Technology. 37 (4): (Accepted).

[24] Li W., E.D. Shumuye, T. Shiying, Z. Wang, and K. Zerfu. 2022. "Eco-friendly fibre reinforced geopolymer concrete: A critical review on the microstructure and long-term durability properties." Case Studies in Construction Materials. 16 e00894 (10 pages). https://doi.org/10.1016/j.cscm.2022.e00894

[25] Arunkumar K., M. Muthukannan, A. Suresh Kumar, A.C. Ganesh, and R.K. Devi. 2022. "Hybrid fibre reinforced eco-friendly geopolymer concrete made with waste wood ash: A mechanical characterization study." Engineering and Applied Science Research. 49 (2): 235–47. https://doi.org/10.14456/easr.2022.26

[26] Koenig A., A. Wuestemann, F. Gatti, L. Rossi, F. Fuchs, D. Fessel, et al. 2019. "Flexural behaviour of steel and macro-PP fibre reinforced concretes based on alkali-activated binders." Construction and Building Materials. 211 583–93. https://doi.org/10.1016/j.conbuildmat.2019.03.227

[27] Chithambar Ganesh A., M. Muthukannan, R. Malathy, and C. Ramesh Babu. 2019. "An Experimental Study on Effects of Bacterial Strain Combination in Fibre Concrete and Self-Healing Efficiency." KSCE Journal of Civil Engineering. 23 (10): 4368–77. https://doi.org/10.1007/s12205-019-1661-2

[28] Güneyisi E., Y.R. Atewi, and M.F. Hasan. 2019. "Fresh and rheological properties of glass fiber reinforced self-compacting concrete with nanosilica and fly ash blended." Construction and Building Materials. 211 349–62. https://doi.org/10.1016/J.CONBUILDMAT.2019.03.087

[29] Korniejenko K., E. Frączek, E. Pytlak, and M. Adamski. 2016. "Mechanical Properties of Geopolymer Composites Reinforced with Natural Fibers." Procedia Engineering. 151 388–93. https://doi.org/10.1016/j.proeng.2016.07.395

[30] Zhang Z., X. Yao, H. Zhu, S. Hua, and Y. Chen. 2009. "Preparation and mechanical properties of polypropylene fiber reinforced calcined kaolin-fly ash based geopolymer." Journal of Central South University of Technology. 16 (1): 49–52. https://doi.org/10.1007/s11771-009-0008-4

[31] Arunkumar K., M. Muthukannan, A. Dinesh Babu, A.L. Hariharan, and T. Muthuramalingam. 2020. "Effect on addition of Polypropylene fibers in wood ash-fly ash based geopolymer concrete." IOP Conference Series: Materials Science and Engineering. 872 12162. https://doi.org/10.1088/1757-899X/872/1/012162

[32] Sukontasukkul P., P. Pongsopha, P. Chindaprasirt, and S. Songpiriyakij. 2018. "Flexural performance and toughness of hybrid steel and polypropylene fibre reinforced geopolymer." Construction and Building Materials. 161 37–44. https://doi.org/10.1016/j.conbuildmat.2017.11.122
[33] Arunkumar K., A. Suresh kumar, A. Chithambar Ganesh, L. Parthiban, and V. Premkumar. 2022. "Incorporation of Waste Wood Ash and Polypropylene Fibre on the Production of Sustainable GPC." Lecture Notes in Civil Engineering. (Accepted). https://doi.org/10.1007/978-981-19-4040-8
[34] Park Y., A. Abolmaali, Y.H. Kim, and M. Ghahremannejad. 2016. "Compressive strength of fly ash-based geopolymer concrete with crumb rubber partially replacing sand." Construction and Building Materials. 118 43–51. https://doi.org/10.1016/j.conbuildmat.2016.05.001
[35] Luhar S., S. Chaudhary, and I. Luhar. 2019. "Development of rubberized geopolymer concrete : Strength and durability studies." Construction and Building Materials. 204 740–53. https://doi.org/10.1016/j.conbuildmat.2019.01.185
[36] Sreesha S., P. Esakkiraj, V. Sreevidya, and P. Ash. 2020. "Development of Self Curing Geopolymer Concrete Incorporating Expanded Polystyrene, Recycled Coarse Aggregate and Rubber Crumbs." International Journal of Recent Technology and Engineering. 9 (2): 292–6. https://doi.org/10.35940/ijrte.b3489.079220
[37] Charkhtab Moghaddam S., R. Madandoust, M. Jamshidi, and I.M. Nikbin. 2021. "Mechanical properties of fly ash-based geopolymer concrete with crumb rubber and steel fiber under ambient and sulfuric acid conditions." Construction and Building Materials. 281 122571 (11 pages). https://doi.org/10.1016/j.conbuildmat.2021.122571
[38] Gupta T., S. Chaudhary, and R.K. Sharma. 2016. "Mechanical and durability properties of waste rubber fi ber concrete with and without silica fume." Journal of Cleaner Production. 112 702–11. https://doi.org/10.1016/j.jclepro.2015.07.081
[39] Mhaya A.M., M.H. Baghban, I. Faridmehr, G.F. Huseien, A.R.Z. Abidin, and M. Ismail. 2021. "Performance evaluation of modified rubberized concrete exposed to aggressive environments." Materials. 14 (8): 1–25. https://doi.org/10.3390/ma14081900
[40] Arunkumar., M. Muthukannan, A. Suresh kumar, and A. Chithambar Ganesh. 2021. "Mitigation of waste rubber tire and waste wood ash by the production of rubberized low calcium waste wood ash based geopolymer concrete and influence of waste rubber fibre in setting properties and mechanical behavior." Environmental Research. 194 110661. https://doi.org/10.1016/J.ENVRES.2020.110661
[41] Arunkumar K., M. Muthukannan, K. Sureshkumar, A. Chithambar Ganesh, and R. Kanniga Devi. 2021. "Mathematical Formulation for Prediction of Structural Performance of Green Geopolymer Concrete Beams and Columns." Turkish Journal of Computer and Mathematics Education. 12 (10): 3806–15.
[42] ArunKumar K., M. Muthukannan, R. Raja Abinaya, and A. Suresh Kumar. 2022. "Structural Behaviour of Green Geopolymer Concrete Beams and Columns Made with Waste Wood Ash a Partial Substitution Binder." Materials Science Forum. 1048 333–44. https://doi.org/10.4028/www.scientific.net/MSF.1048.333
[43] Anuradha R., and B.V. Sreevidyaa, V. Venkatasubramania, R. and Rangan. 2011. "Modified Guidelines for Geopolymer Concrete Mix Design using Indian Standard." Asian Journal of Civil Engineering (Building and Housing). 13 (3): 357–68.
[44] Arunkumar K., M. Muthukannan, A. Suresh Kumar, A.C. Ganesh, and R.K. Devi. 2021. "Production of Eco-Friendly Geopolymer Concrete by using Waste Wood Ash for a Sustainable Environment." Pollution. 7 (4): 993–1006. https://doi.org/10.22059/POLL.2021.320857.1039
[45] IS 516-1959. 1959. "Method of Tests for Strength of Concrete." Bureau of Indian Standards. 1–30.

[46] ACI Commitee 544-1988. 1988. "Measurement of Properties of Fiber Reinforced Concrete." ACI Materials Journal. 85 583–93.
[47] ASTM-C267-98. 1998. "Standard Test Methods for Chemical Resistance of Mortars, Grouts and Monolithic Surfacings and Polymer Concretes." ASTM International. 4 1–6.
[48] ASTM C1012/C1012M-15. 2015. "Standard Test Method for Length Change of Hydraulic-Cement Mortars Exposed to a Sulfate Solution." ASTM International. (C): 1–5.
[49] ASTM D1141-99. 1999. "Standard for the Preparation of Substitute Ocean Water." ASTM International. 98 98–100.
[50] Al-mashhadani M.M., O. Canpolat, Y. Aygörmez, M. Uysal, and S. Erdem. 2018. "Mechanical and microstructural characterization of fiber reinforced fly ash based geopolymer composites." Construction and Building Materials. 167 505–13. https://doi.org/10.1016/j.conbuildmat.2018.02.061
[51] Sivakumar A., and M. Santhanam. 2007. "A quantitative study on the plastic shrinkage cracking in high strength hybrid fibre reinforced concrete." Cement and Concrete Composites. 29 (7): 575–81. https://doi.org/10.1016/j.cemconcomp.2007.03.005
[52] Ganesh C., J. Sivasubramanaian, M.S. Seshamahalingam, J. Millar, and V.J. Kumar. 2021. "Investigation on the Performance of Hybrid Fiber Reinforced Geopolymer Concrete Made of M-Sand under Heat Curing." Materials Science Forum. 1019 73–81. https://doi.org/10.4028/www.scientific.net/MSF.1019.73
[53] Chithambar Ganesh A., and M. Muthukannan. 2019. "Experimental Study on the Behaviour of Hybrid Fiber Reinforced Geopolymer Concrete under Ambient Curing Condition." IOP Conference Series: Materials Science and Engineering. 561 012014 (9 pages). https://doi.org/10.1088/1757-899X/561/1/012014
[54] Alrefaei Y., and J.G. Dai. 2018. "Tensile behavior and microstructure of hybrid fiber ambient cured one-part engineered geopolymer composites." Construction and Building Materials. 184 419–31. https://doi.org/10.1016/J.CONBUILDMAT.2018.07.012
[55] Chithambar Ganesh A. 2020. Experimental Study on the Behaviour of Hybrid Fiber Reinforced Geopolymer Concrete Made of M Sand. Kalasaliingam Academy of Research and Education, 2020.
[56] de Alencar Monteiro V.M., L.R. Lima, and F. de Andrade Silva. 2018. "On the mechanical behavior of polypropylene, steel and hybrid fiber reinforced self-consolidating concrete." Construction and Building Materials. 188 280–91. https://doi.org/10.1016/J.CONBUILDMAT.2018.08.103
[57] Gupta T., R.K. Sharma, and S. Chaudhary. 2015. "Impact resistance of concrete containing waste rubber fiber and silica fume Trilok." International Journal of Impact Engineering. 83 76–87. https://doi.org/10.1016/j.ijimpeng.2015.05.002
[58] Murugan R.B., C. Natarajan, and S.E. Chen. 2016. "Material development for a sustainable precast concrete block pavement." Journal of Traffic and Transportation Engineering (English Edition). 3 (5): 483–91. https://doi.org/10.1016/j.jtte.2016.09.001
[59] Alomayri T., H. Assaedi, F.U.A. Shaikh, and I.M. Low. 2014. "Effect of water absorption on the mechanical properties of cotton fabric-reinforced geopolymer composites." Journal of Asian Ceramic Societies. 2 (3): 223–30. https://doi.org/10.1016/j.jascer.2014.05.005
[60] Karahan O., and C.D. Atiş. 2011. "The durability properties of polypropylene fiber reinforced fly ash concrete." Materials & Design. 32 (2): 1044–9.
[61] Saloni, Parveen, T.M. Pham, Y.Y. Lim, and M. Malekzadeh. 2021. "Effect of pre-treatment methods of crumb rubber on strength, permeability and acid attack resistance of rubberised geopolymer concrete." Journal of Building Engineering. 41 102448 (10 pages). https://doi.org/10.1016/j.jobe.2021.102448
[62] Luhar S., and U. Khandelwal. 2015. "A Study on Water Absorption and Sorptivity of Geopolymer Concrete." International Journal of Civil Engineering. 2 (8): 1–9. https://doi.org/10.14445/23488352/ijce-v2i8p101

[63] Ranjith S., R. Venkatasubramani, and V. Sreevidya. 2017. "Comparative Study on Durability Properties of Engineered Cementitious Composites with Polypropylene Fiber and Glass Fiber." Archives of Civil Engineering. 63 (4): 83–101. https://doi.org/10.1515/ace-2017-0042

[64] Arunkumar K., M. Muthukannan, A. Sureshkumar, A. Chithambarganesh, and R.K.D. R. 2021. "Mechanical and durability characterization of hybrid fibre reinforced green geopolymer concrete." Research on Engineering Structures and Materials. https://doi.org/10.17515/resm2021.280ma1604

[65] Veronie J., and V. Sreevidya. 2020. "Experimental investigation and comparison on structural behaviour of Ferro-Geopolymer concrete and mortar cubes with conventional cubes." Materials Today: Proceedings. 21 (1): 531–6. https://doi.org/10.1016/j.matpr.2019.06.693

[66] Wasim M., T.D. Ngo, and D. Law. 2021. "A state-of-the-art review on the durability of geopolymer concrete for sustainable structures and infrastructure." Construction and Building Materials. 291 123381 (12 pages). https://doi.org/10.1016/j.conbuildmat.2021.123381.

Research on Engineering Structures & Materials
journal homepage: http://www.jresm.org
MIM Research Group

Review Article

Optimistic and pessimistic impacts of COVID-19 scenario on waste management in developing nations: A review

Ismail Luhar[1]*, Salmabanu Luhar[2]

[1]*Shri Jagdishprasad Jhabarmal Tibrewala University, Rajasthan 333001, India*
[2]*Centre of Excellence Geopolymer & Green Technology (CEGeoGTech), Universiti Malaysia Perlis (UniMAP), Perlis 01000, Malaysia*

Article Info

Article history:

Received 15 Apr 2022
Revised 21 Jun 2022
Accepted 05 Aug 2022

Keywords:

Waste;
Novel Coronavirus;
COVID-19 pandemic;
Personal Protective Equipments (PPEs);
Medical wastes;
Waste management;
Greenhouse Gases (GHGs);
Environmental impact

Abstract

During the lockdown period due to the Covid-19 pandemic, the heaps of unusual wastes of packaging from panic buying, medical wastes from Covid-19 centres and isolation places, as well as discarded single-use safety gears like personal protective equipments are posing challenges not only for health hazards but also escalating the probability of the spread of diverse variants of Novel Corona Virus SARS-COV-2. Unfortunately, the containment of the spreading of the COVID-19 pandemic and subsequent lockdown measures are impacting waste management adversely like anything in almost all corners of the world, especially, in developing nations where there exists lesser awareness with regard to this deadly disease and orderly disposal of these pandemic wastes. Also, the waste hierarchy of the "4R concept", i.e., Reduce, Reuse, Recycle and recovery is negatively influencing during the prevailing epidemic circumstances which hinder the methodical waste disposal useful to save the environments and human health. The scenario of haphazard dumping of this waste is found worst in developing nations which are not fully prepared to face such thorny and all of a sudden difficulty of disposal of piles of these new risky wastes with their limited facilities and staff. However, the developing nations have instituted policies to ensure sustainable management of waste but it proved inadequate against the giant pandemic situations. Surprisingly, both - optimistic and pessimistic, types of impacts are being monitored on environments during the Covid-19 lockdown. Particularly, in the context of developing nations, the present review manuscript assesses both the optimistic and pessimistic impacts of the COVID-19 epidemic on the waste management sector and environment comprehensively along with the ways to address this gigantic Covid-19 waste crisis systematically.

1. Introduction

Generally, global waste management deals with many types of wastes such as municipal solid wastes, hazardous industrial wastes, bio-medical wastes, electrical and electronic wastes (E-wastes), radioactive wastes, and so on. Normally, these kinds of wastes are being disposed of in harmony with the "waste hierarchy" through the "4R concept", which includes reduce, reuse, recycle and recovery. That means it gives top priority for an awareness to reduce the use of non-biodegradable and harmful compounds in the first place which is highly essential. Similarly, the reuse of items instead of dumping them is also an effective measure to mitigate the piles of waste. However, recycling is the most modern and fully efficient route to convert the "waste to wealth" notion scientifically. Recovery refers to extracting commercially valuable materials and energy from wastes by following scientific processes. Thus, the "waste hierarchy" ranks waste management alternatives according to what is the best and most excellent for the environment.

*Corresponding author: jprraj2017@gmail.com
[a] orcid.org/0000-0002-9032-0483; [b] orcid.org/0000-0002-1129-2825
DOI: http://dx.doi.org/10.17515/resm2022.428ma0415

However, in the present Covid-19 pandemic scenario, the emergence of novel kinds of wastes, i.e., pandemic wastes, of discarded safety gears like Personal Protective Equipments (PPEs), facemasks, gloves, goggles, face shields, etc. is most challenging since it may be infectious and hence, can be considered as "hazardous". These novel gigantic healthcare wastes are generated from the medical laboratories, biomedical research facilities, Covid -19 treatment and isolation centres, hospitals, home-isolation sites, etc. Incorrect treatments of the said wastes pose grave risks of transmission of the virus to the waste workers, staff, and the community due to exposure to infectious agents. Also, in developing countries of the world, pitiable waste management emits destructive and deleterious pollutants into the atmosphere. The massive volume of the referred waste generation and its transmittable nature escorts to fear of more spreading of COVID-19 virus creating huge insecurity in the handling and succeeding recycling of the said risky wastes. The unsystematic disposal of the referred wastes may invite the further spreading of Novel Corona Virus in diverse forms having variants, namely, alpha, beta, gamma, lambda, delta plus, epsilon, eta, lota, theta, zeta, and kappa so far detected. Therefore, methodical disposal of them is highly essential in order to keep society more safe and healthy. Normally, waste management includes the collection, transport, valorization and finally the disposal of the waste. More broadly speaking, it includes any action engaged in the waste management system right from waste generation to the ultimate treatment. Sorry to say, in developing or undeveloped nations the brand-new type of hazardous wastes generated during the special circumstances of the pandemic of Covid-19, is being dumped either on open land spaces creating landfills, or in water-bodies, etc. but not going for incineration or biological reprocessing or recycling or energy recovery which are the methodical routes of its safe disposal. For this reason, the negative impact of this incorrect dumping on the environment and the possibility of the spread of deadly diseases has increased in such countries with restricted facilities for disposal of the unexpected heavy load of novel infectious wastes. This is a threat not only to the environment but also to the lives breathing on mother earth. Regrettably, at this time, there are millions of people being crushed by the giant of Covid-19 with lacs of deaths across the globe. Although the COVID-19 pandemic has contributed incredibly to mitigated air, noise and water pollution with enhanced bio-diversity as well as at sites for tourist attraction but the impact of staying-at-home and preventative measures have resulted in an alarm for a correct management of the infectious wastes. The piles of "use and throw" gloves, gowns, masks and other PPEs, etc. produced on a huge scale and converted in form of perilous waste from households and health care and quarantine facilities like hospitals and Covid-19 centres pointing towards the waste emergency escalating the possibility of spreading of COVID-19 through secondary transmission [1]. Not only have those, the uncontrolled dumping, burning in open and incineration may impact air and water quality along with health issues owing to release of toxins [2]. This situation is more perilous in developing nations having limited standard technologies and strategies to deal with a waste emergency through systematic sustainable waste management since it obviously calls for the high cost to implement it fully. Quite a lot of developing nations have adopted safety measures to battle with the referred pollution and to manage the mentioned wastes; however, the present measures taken are inadequate and differ relying upon the context of the nation. What is more to add, the WHO has publicized the guidelines for the management of medical wastes which lend a hand to managing the extremely infectious waste generated during the existing Covid-19 pandemic. The appropriate waste management may slim down the spreading of the COVID-19 virus and accelerate the recycling instead of dumping it in the landfills. Sustainable management is being encouraged by disinfection and sorting these wastes which permits their consumption for precious objectives. As we know, waste management, similar to every environmental attempt, entails stressors and receptors. The earlier are the agents which should be removed, reduced, or managed, such as the waste itself or definite components carried along viz., microbes, organic compounds, heavy metals or energy, etc.

Whereas the later one, by definition, receives the damage caused by the stressors. More often than not, the environmental receptors are classified as human or ecological. Therefore, if a waste carries hazardous infectious viruses that may come in contact with other general healthy public or waste management workers then it is injurious to their health. Additionally, these kinds of wastes can make threats to ecosystems and atmosphere. Debatably, the methodical disposal of waste management offers pre-eminence to human receptors and the safeguarding to public health.

Exhaustively, the current paper reviews the positive and negative impacts of the COVID-19 pandemic on the waste management sector and environment especially keeping an eye on developing countries where there are a lower rate of education, lesser awareness of the deadly disease, and very narrow treatment facilities available for organized waste management to cope up with such a novel, unpredicted, infectious, hazardous and monumental wastes generation along with the ways to get rid of this gigantic Covid-19 waste crisis systematically.

2. Environmental Corollaries During Prevailing COVID-19 Epidemic

Unbelievably, the ongoing COVID-19 pandemic is found impacting in both ways, i.e., optimistic and pessimistic, on the natural environment. The former includes a drop in the pollution of air, water and noise, sparkling of beaches, low GHG footprints, lower down traffic, etc. While on the other hand, the later one is very dangerous because it causes due to the boosted, novel, infectious medical and plastic wastes of safety gears, medical, disinfectants and packaging, etc.; hindrance in the recycling of wastes, redundancy, monetary crises, no functioning of educational and coaching institutes, no exercises in gyms, no entertainment in theatres and cinemas, no ritual or religious functions, limited gathering for marriage and funerals, restricted domestic and international travelling, etc. Also, in the pre-Coid-19 period, the world was facing challenges for environments, contamination generated from industrialization, pollutions of noise, water, air, soil, etc.; extreme use of chemicals for agriculture; etc.; depletion of ozone (O3) layer owing to emissions of GHGs from industries and vehicles leading to a gigantic dilemma of earth-heating, i.e., global warming [3]. Among these titanic prevalent issues, one more deadly disease appeared out of the blue before the lives of the world by which the whole universe feels down in the dumps.

The worldwide disruption resulting due to the pandemic situation prevalent owing to COVID-19 is answerable to a number of impacts on the environment and climate. On account of the complete lockdown in almost all corners of the world, the movement has restricted and a momentous hold up of socio-economic activities found. Besides the air-quality enhancement at so many places, there found a reduction in water contamination in different nations of the world. More to the point, the greater than before use of PPEs viz., facemasks, hand gloves, goggles, face shield, etc. and disinfectants like sanitizers, etc. generated massive quantity of sudden infectious wastes. After their use, they are being dumped haphazardly in nearby open spaces causing negative impacts on the environment and a probability of spread of viruses.

2.1. Optimistic Environmental Impacts

2.1.1 Mitigation of Air Pollution and GHGs Emissions

Optimistically, the COVID-19 lockdown scenario has lead to surprising extensive upbeat impacts on the atmosphere and climates on account of the reduced footprints of air pollution as well as GHGs emissions [4]. Among the developing nations, Indian air pollution is excessively influencing human health adversely and hence, causes roughly over 3.50 lacs new cases of childhood asthma along with about sixteen thousand premature deaths

annually. This huge air pollution is assigned to the presence of fossil fuel burning in open and largely from the exhaust of vehicles in India discharging nitrogen dioxide (NO2) and particulate matter ranging from 2.5-10 μm diameters [5]. There exist plenty of air-pollutants in nature, however, the major among are nitrogen dioxide (NO2), carbon monoxide (CO), Sulphur dioxide (SO2), Ozone (O3), fine (PM 2.5), and coarse particulate matters (PM10), etc. The chief sources of the referred kinds of contaminants are predominantly from diverse industries and the exhaust from automobiles. The poisonous Carbon monoxide (CO) gas emissions are found mainly released from the burning up of fossil fuels and from the operations of heavy machinery. On the other hand, Sulphur dioxide gas (SO2) comes primarily from motor vehicles, power generation plants, domestic heating, etc. These emissions of the said air-pollutant gases into the atmosphere impact harmfully on the human respiratory system, lungs, mucus secretions, etc. The elevated levels of NO2 can influence negatively by causing damage to the respiratory tract of people and augment the susceptibility of a particular individual to and the harshness of respiratory infections and asthma too. Additionally, the long-standing exposure to higher levels of NO2 emissions can pilot to chronic lung diseases. Not only have that, when NO2 reacts with atmospheric air it liberates ozone (O3), which is a key component of smog and can be responsible for worsening bronchitis and emphysema, asthma, permanent injury to lung tissues, etc. Exposure to O3 of the troposphere is considered answerable for an estimated about 10, 00,000 premature death annually. On the other hand, particulate matter (PM) is the main product of acid rain, which can cause deadly diseases of cancer since it can pierce inside the cells of the lungs with ease. There exists two types of PM, i.e., PM10 and PM2.5, relying on the size of the matter. Precisely speaking, the type PM10 possesses a size smaller than 10 mm e.g., the pollens, moulds and dust, etc. While the PM 2.5 is even much smaller than the PM10 creating pessimistic impacts on health such as chronic obstructive pulmonary disease and lower respiratory infection leading to the death of more or less 30, 00,000 persons internationally. Also, Ozone (O3) is one more significantly toxic contaminant generated from destructive gases discharged by vehicles and/or industries, which cause stern breathing predicaments, fall in functions of lungs, triggering asthma and lung-related crises. During the ongoing Covid-19 epidemic, government authorities in almost all parts of the world, especially in developing nations where the spread of the novel Coronavirus is intensive, have compelled the authorities to shut down markets, industries, transportation, etc. during lockdown leading to an abrupt fall in the amount of emissions of greenhouse gases (GHGs). That means, the drastic reduction with regard to air pollution in developing countries is the direct result of the complete shutdown of most of the industries and diminish in automobile traffic reduction during the COVID-19 period [6,7]. So far, the data of levels of air pollution for New York are found in decreasing order when compared to the period prior to lockdown while Covid-19 initiated. Approximately 50% of air pollution is reduced owing to the measures implemented to control the spreading of the Novel Coronavirus. In the same way, an estimation of nearly 50% reduced N2O and Carbon Monoxide (CO) is made for China due to the pack up of heavy industries [8]. Also, the NO_2 emission is one of the significant pointers of international monetary actions indicating mitigation in so many nations, namely, the U.S.A., Canada, China, India, Italy, Brazil etc. owing to the shutdown [3,9]. By and large, NO2 is being released from fossil fuel burning, about 80% of which comes from motor-vehicle exhaust [10]. It is well-known that NO2 is responsible for acid rain through interacting with O2 and H2O, and also for numerous respiratory issues to humans [10]. In accordance with the European Environmental Agency (EEA), the COVID-19 lockdown period is fallen down in the range from 30% to 60% in so many European cities such as Barcelona, Rome, Madrid, Paris and Milan [11]. While in the U.S.A., an emission of NO2 is found declining by 25.5% in the course of the COVID-19 lockdown time in comparison with preceding years. Significantly, the case of Ontario State of Canada displayed the level of NO2 with a decline from 4.5 to 1 ppb [parts per billion (10-9)] [12]. Analogously, the

reduction of up to 54.3% in NO2 emission is recorded in Sao Paulo, Brazil [13]. An assumption is made that vehicles and aviation are the chief contributors for GHG emissions figuring to about 72% and 11% correspondingly. Internationally, the measures taken in the context of the containment of the Coronavirus have exhibited a striking impact on the aviation segment. Several nations imposed restrictions on international travellers to enter, depart or even transit resulting in a drop in movement of air passengers. Therefore, the scheduled flights have been cancelled by commercial aircraft companies worldwide. For illustration, China decreases roughly 50% to 90% capacity for International departure and 70% for domestic flights because of the virulent disease when the comparison is made from January 20, 2020, finally resulting in a cut of almost 17% of the CO2 emissions [14]. What's more, it is found recorded that 96% of air travel has been plunged from a comparable time preceding year worldwide owing to the harsh situation of COVID-19 pandemic, that eventually has influenced the environment. Taken as a whole, the very much lesser use of fossil fuels has slimmed down the GHG emission lending a hand for open battle against universal climate alteration. In harmony with the International Energy Agency (IEA), the exigency for oil has declined by 435,000 barrels internationally in the early 3 months of 2020, when comparison made with the same spell of a period of the preceding year. More to the point, worldwide coal consumption is also trimmed down since lesser demand for energy met within the lockdown period due to the Covid-19 pandemic.

The coal-based Indian power generation plants slimmed down by 26% with a 19% drop of total power generation subsequent to the movement restrictions. While China stood first as the uppermost coal consumer internationally, however, with a decline of 36% when comparing it with the same spell of time of the earlier year from February to the middle of March [5]. In accordance with the climate science and policy website Carbon Brief, U.K.; the ongoing tragedy of COVID-19 has reduced 25% CO2 emission in the Republic of China, and nonetheless below the normal limit more than two months after the country entered lockdown [15]. Also, they estimated that the epidemic period could drop 1,600 metric tons of CO2, equal to beyond 4% of the total global emissions of CO2 in 2019.

2.1.2 Reduced Water Pollution

Sorry to say, water pollution is a most common happening in developing countries, especially in Bangladesh and India. This is mostly because the domestic and industrial wastes are dumped into rivers directly without subjecting them to any methodical treatment [16]. The key sources of emissions of gases and generation of chemical kind of pollutants from industries have been reduced tremendously or fully stopped during the Covid-19 lockdown era lending a hand to minimize the pollution [17,18]. Also, it is reported that the pH-concentration, electric conductivity (EC), Oxygen Demand (DO), Biological Oxygen Demand (BOD) and chemical oxygen demand [COD] have slimmed down greatly in dissimilar monitoring stations during the in-progress Covid-19 lockdown in comparison with the pre-lockdown normal era [17,18]. The chief industrial contaminating sources have either get reduced or entirely shut down during the covid-19 lockdown period helping to mitigate the pollution load as witnessed in the case of the Indian Holy river Ganga, Yamuna, etc. The rivers of the developing nations have touched a noteworthy purity level in the absence of industrial pollution due to the shutdown. In India, in the context of the Holy River Ganga, the observation readings of total of thirty-six real-time monitoring stations were recorded by a government body calthe led Uttarakhand Pollution Control Board of India (UPCB). Incredibly, out of these 36 stations' readings, the river water from twenty-seven stations is found within the acceptable limit [19]. Amazingly, after a gap of 30 years, the dolphins, South Asian River Ganges, are also spotting back in the Holy River Ganga. In Navi Mumbai city, India, tens of thousands of flamingos are reported to gather around. Generally, the birds migrate each year to this area, however,

their presence has boosted extraordinarily during Covid-19 period as observed by local residents. Wonderfully, the UPCB authorities have accounted that water from "Har-ki-Pauri ghat" on the bank of river Ganga – a place near Haridwar is found "potable for drinking" subsequent to chlorination because of the absence of the usual industrial wastes drainage into the river water during Covid-19 shut down period of industries [20]. This sudden and unexpected improvement in the quality of water near the cities of Haridwar and Rishikesh was assigned to the abrupt fall in the number of tourists [19]. In harmony with the real-time monitoring results for water quality, the physic-chemical parameters of the river Ganga are found as, pH from 7.4 to 7.8, biochemical oxygen demand (BOD) from 0.6 to 1.2 mg/L. All of them are falling within the limit of the surface water quality norms set by the Indian government authority. However, in some monitoring stations, with the exception of the total coliform figure, the rest of the other parameters had been found even in agreement with the Indian national drinking water quality standard, which can be utilized devoid of conventional treatment subsequent to disinfection. It is noteworthy that the pH concentration, Oxygen demand, electric conductivity (EC), Bio-chemical Oxygen Demand (BOD) and chemical oxygen demand(COD) have been found to decline significantly in diverse monitoring stations when compared with the figures of the same for Covid-19 lockdown and the pre-lockdown time [21]. Furthermore, the unnecessary gathering of people in public places is prevented by the rules, which has decreased the quantity of tourists and water activities at so many places [22]. There are reports of turning the Canal water clear and reappearances of so many aquatic species during the lockdown. More to add, water pollution is found reduced in the beaches of Malaysia, Indonesia, Thailand, Bangladesh, Maldives, etc. [23]. The food waste quantity is decreased during the COVID-19 lockdown, which in turn, slimmed down the contamination of soil and water. The consumption of water by the industries, particularly by the textile industry, has also been trimmed down due to shutdown during Covid-19 [24]. By and large, the massive quantity of water and soil polluting trashes generated in construction and manufacturing processes are also found to decrease during the lockdown period of a pandemic. What's more, there found a reduction in the emission of polluting gases and marine pollution because of the lesser movement of merchant ships and other vessels in the seas and oceans since the export-import business was affected very badly due to the Covid-19 epidemic.

2.1.3. Reduction in Noise Pollution

Normally, in the pre-Covid-19 era, the key global cities, particularly, of developing nations, are found extremely polluted by elevated noise pollution generated because of the human hustles and bustles viz., automobile traffic on roads, higher volume speakers in markets, and sound of a range of industrial plants and factories, etc. causing loads of uneasiness and health crises to humans and other lives on the earth. Psychologically, noise pollution influences animals and more than ever the birds since they are exceedingly thin-skinned. However, at the present, the chief densely populated cities of the developing nations are experiencing an unexpected and all of a sudden giant fall in noise level pollution as a straight outcome of the imposed COVID-19 lockdown by the government authorities which brought about the incredible decline in all kinds of transport modes and mercantile as well as industrial activities [22]. Generally, noise pollution is the result of the elevated levels of sound, generated from a range of human activities like operating machines, driving vehicles, working for construction, aviation, etc. It may pilot to influence human beings and some other living organisms adversely [22]. In fact, the pollution of noise badly affects bodily processes and injurious to human health creating hypertension, cardiovascular disorders, sleep shortness, etc. which are dangerous if long-standing. It is estimated that approximately 360 million populace is susceptible to hearing loss owing to long-term noise pollution [25]. The World Health Organization (WHO) made an estimate that worldwide over 100 million individuals are facing the challenge of higher noise levels beyond the

recommended border line single-handedly in Europe. Not merely humans, the anthropogenic pollution of noise has impacted pessimistically on even wildlife by altering the balance to detect and avoid the predator and prey. Also, it influences negatively the health of invertebrates that play a significant role to control the environmental course of actions in order to bring about the eco-system balance. During the Covid-19 lockdown period, the patients and their contacts were quarantined and normal people stayed in homes as well as a reduction in communication and economic activities in almost all parts of the world have altogether eventually lowered the noise level to an unbelievable level [22] e.g., the noise level of the capital city of developing country India, i.e., New Delhi, is found with a drastic reduction of about 40% to 50% in the recent Covid-19 lockdown. On the other hand, because of the restrictions on the movement of the vehicles of the general public during the Covid-19 lockdown, the noise levels of Govindpuri metro station, in Delhi is found to represent a reduced noise level of 50 to 60 dB only, otherwise, it was figuring around 100 dB in pre-lockdown time [26]. In harmony with the Central Pollution Control Board of India, the noise level of a residential zone, New Delhi, is incredibly found dropped in the daytime as 40 dB from routine 55 dB while 30 dB in the night from usual 45 dB. Consequently, it has become possible for citizens to enjoy the chirping of birds which they never think about before the Covid-19 lockdown. Moreover, the domestic and international travel restrictions have controlled the transport and aviation industries by reducing the flights and traffic on road drastically in almost all corners of the world piloting to a great reduction in the level of pollution of noise, e.g., Germany has cutback the air-passengers by over 90%; car traffic by more than 50% and trains by >75% than their usual ones [25]. Taken as a whole, the COVID-19 pandemic lockdown together with only lesser financial activities have drastically reduced global noise pollution as a positive impact on the environment and human health. The factors during the Covid-19 pandemic like quarantine, lockdown, work from home, limited global commercial activities, restrictions on domestic and international travels, etc., have altogether trimmed down the noise level in most cities of the world, in particular, in developing countries [22].

2.1.4. Restoration of Ecosystem and Assimilation of Tourist Destinations

Remarkably, the global tourism sector is developing fast in developing countries owing to the progressions in transports and technology contributing notably to the Gross Domestic Product (GDP), i.e., the total market or financial value of all the services and the finished goods produced inside the national border in a definite period of time. However, Lenzen et al [27] has made estimated that the tourism industry is answerable for about 8% of global Green House Gases (GHG) emissions. More often than not, the interesting tourist sites of natural beauty like beaches, national parks, mountains, islands, deserts, mangroves, etc. catch the attention of the tourists. In order to accommodate and facilitate them, there are scores of motels, hotels, restaurants, bars and markets, etc. existing or being developed consuming natural resources and plenty of energy. Puig et al. [28] worked out the carbon footprint in the coastland hotel services, Spain and accounted electricity and other fuels burning up playing a key role for pollution with the highest contribution of the carbon emissions from 2-star hotels. Furthermore, a few tourists make an enormous harsh and dump haphazardly a range of wastes impairing natural beauty and thus, leads to imbalance the eco-system. On account of the local COVID-19 restrictions, the tourists are reduced in quantity all over the world which has impacted negatively on the tourism industry to a great extent [22]. For illustration, Phuket, Thailand, is the most popular destination for international tourists with an average of 5,452 visiting tourists per day witnessing the bad days due to the recent Covid-19 lockdown [29]. Likewise, Cox's Bazar sea beach - the longest unbroken natural sandy sea beach in the world, is also appearing lonesome because of the ban by local administration on public gatherings and tourist travel. Consequently, the colour of seawater is altering from turbid to its original pure appearance

in the absence of any kind of pollution from swimming, playing, riding motorized boats, bathing, etc. On account of the reduction in pollution, surprisingly, a return of dolphins has been encountered along the coast of Bay of Bengal, Bangladesh after so long time [23]. This simply means that nature is getting time to assimilate human annoyance which is resulting in optimistic impacts on ecology.

2.1.5. Sparkling Beaches

Marvellously, the beaches are regarded as an imperative natural resource located in the coastal zones. The beaches are the source of sand, land, fishing grounds, etc. helping the survival of the coastal populace. They contribute to the government with a good source of revenue from tourism. However, normally, the majority of beaches are found densely contaminated on account of anthropogenic actions. In opposition, presently, so many beaches of the world are found sparkling since most of the nations have imposed Covid-19 lockdown to trim down the movement and travel of tourists and public in and in the region of the coastal zones piloting to have cleaner beaches in comparison to the pre-lockdown time and also found spotless and clean waters around the neighbouring regions [22].

2.2. Off-Putting Impacts of COVID-19 Scenario on Environments

2.2.1. Escalation in Wastes

Internationally, the generation of a new-brand type of bio-medical wastes is extensively escalated subsequent to the flare-up of the COVID-19 pandemic which is a prime threat to not merely the general public's health but also to the environment. In spite of the guidelines of authorities concerned and the experts with regard to the correct dumping and segregation of risky medical wastes and plastic-based PPEs as well as organic domestic wastes, the mixing up of all these wastes is knowingly or unknowingly made by some people especially unaware individuals in developing countries with narrow literacy rate are boosting the jeopardy of Covid-19 transmission, and its virus exposure to waste management employees [30]. Furthermore, the colossal quantities of discarded bottles of disinfectants which were utilized to wipe out the novel coronavirus from public places, industries and at residences have not only accumulated in form of piles of wastes with the possibility of being infectious since they may come from isolation and/or treatment centres as well as hospitals for Covid-19. Currently, in this period of deadly virulent disease of Covid-19, a large quantity of used disinfectants are found laying extensively on roads and in markets as well as around residences useful to eradicate novel Coronavirus. This widespread use of disinfectants may be dangerous to the health and lives of some other non-targeted innocent useful species creating an ecological imbalance [31]. These extensive applications of disinfectants may obliterate some other useful organisms which can contribute optimistically to maintaining ecological balances [32]. What is more, the SARS-CoV-2 virus was found present in the faeces of COVID-19 patients and also in municipal wastewater in so many nations like India, etc [33]. For this reason, still further measures for wastewater treatment are the need of the hour, which is a challenging job for developing nations like Bangladesh, etc. where municipal wastewater is directly drained into nearby water-bodies and rivers with no treatment [34]. Particularly, China has already made the procedures stronger for disinfection by using chlorine increasingly to put off the spread of the SARS-CoV-2 virus via the wastewater. However, it is also noteworthy that too much use of chlorine in water may generate destructive by-products at the same time [22]. Likewise, globally, during the present Covid-19 pandemic, the governments have issued guidelines by time to time to wear PPEs as safety gear like a facemask, gowns, hand gloves and other safety equipments in order to protect the general public from the novel coronavirus infection escalating to the healthcare waste quantity at the domestic level [35]. Especially, the generation of this new-fangled waste in form of used plastic-based PPEs has amplified internationally as [32] the case with China where the daily boost in the

production of medical masks as 14.8 million since February 2020, which is much greater than before [36]. The lack of awareness for such a novel infectious waste dumping leads to its randomly throwing away the used face masks, hand gloves, gowns, other PPEs, etc. by most of the people in open spaces or mixing it with other usual household wastes. Thus, the incorrect dumping of these trashes results in blockage in the route of waterways and futhe environmental contamination [22]. The face mask and other plastic-based PPEs are considered as the potential source of micro-plastic fibres in the atmosphere [36]. Generally, Polypropylene is used to manufacture N-95 face masks, and protective Tyvek suits, gloves, as well as face shields, on the surface of which the novel Coronavirus can survive for a long-term period and discharge the dioxin and toxic elements into the atmosphere. Essentially, the guidelines by authorities and health experts suggest that there should be correct disposal and segregation of organic domestic waste as well as of the plastic-based PPEs which are perilous medical wastes. Moreover, the medical waste should not be a mix up with household wastes since it will boost the jeopardy of Covid-19 virus transmission [1]. During the courses of the testing of the suspects of COVID19, diagnosis, treatment of an enormous number of confirmed patients at centres and/or hospitals, as well as disinfection, there found generation of scores of new kinds of infectious and bio-medical wastes [22]. The escalating quantity of the referred wastes is creating a dilemma for its systematic waste management e.g., in Wuhan, China; there is a record generation of over 240 metric tons in a single day for the duration of the outbreak [3], which is approximately 190 m tonnes greater than the pre-Covid-19 period [22]. In developing nations this predicament of methodical waste management is more serious due to limited resources e.g., in Ahmedabad, India, the quantity of generation of medical waste is boosted from 550 to 600kg per day to about 1000 kg per day at the time of the initial phase of Covid-19 lockdown [37]. Therefore, this abrupt and swift ascend of infectious wastes of medical and safety equipment have turned out to be a key quandary for the local waste management authorities of developing nations. In one more capital of developing country Bangladesh, i.e., Dhaka city, these sort of wastes is found generated during COVID-19 as nearly 206 m tonnes of per day [38]. In the same fashion, some other cities, namely, Kuala Lumpur, Manila, Bangkok and Hanoi also experienced an enhancement in generating 154 to 280 m tonnes more medical wastes every day than in the pre-pandemic normal time. Such an unwanted, unpredicted, uninvited, all of a sudden, and infectious hazardous medical wastes generation have alarmed the world, especially developing nations for their correct disposal with restricted facilities. As described earlier, the Covid-19 restrictions on movements and "stay at home" strategies by governmental authorities in almost the whole of the world has piloted to enormous boost in both organic and inorganic kind of wastes. Conveniently, in this present pandemic period, people are buying essential commodities and in some cases foods from online platforms with the home delivery facility, which has accelerated the wastes of packaging mostly in form of plastics and papers leading to the incredible rise in the quantity of household wastes. Not merely have that, the massive medical wastes of used gloves, face masks, disposable aprons and PPEs, syringes, etc., also found generating in treatment centres and hospitals for Covid-19. This unexpected, gigantic and pressing issue created by the present circumstances has put the waste management authorities in the world in a confusing state, especially, in developing countries where the facilities for the same are confined. In the context of developing nations where people are not fully educated, the unawareness of some sections of the society results in random dumping of the said wastes. The haphazard disposal of the referred wastes in landfills or the streets or water bodies, etc., may lead to severe predicaments of human health since these wastes may be infectious and still can carry traces of viral pollutants [35]. Thus, proper waste management has become a momentous challenge for the local waste management authorities, particularly in developing nations. The anxiety fuelled when it has been revealed through the freshly published literature that the novel Coronavirus can exist for a prolonged period on surfaces of diverse objects of day

to day use. Consequently, at this moment, it is a matter of great global concern that the bio-medical wastes generated from the hospitals and/or Covid-19 treatment centres in form of infectious, discarded masks, needles, syringes, bandages, gloves, used tissue, and leftover medicines, etc. should be disposed of appositely with a view to mitigating further spreading of infection of Covid-19 virus and contamination of environments. The enhancement in the quantity of both organic and inorganic kinds of municipal wastes generation is impacting directly or indirectly on the environment through polluting the air, water and soil. In the referred epidemic period, the panic online shopping with home delivery facilities is increased tremendously on account of the quarantine and lockdown policies in many nations piloting to augment the shipped packaging materials waste in form of household wastes [22].

2.2.2. Diminution in Waste Recycling

Due to the curse of the Covid-19 virus spreading in almost all corners of the world, the recycling facilities are affected badly in particular in developing nations. At the present time, this has proved to be a major crisis since waste recycling can not only prevent contamination but also save energy and preserve limited natural resources. As stated earlier, the rising domestic and medical wastes from Covid-19 facility centres and quarantine facilities may bear traces of virus contaminants posing a threat of infection to the workers and staff involved at recycling sites. For this reason, the recycling waste management functions are closed down in so many parts of the world. However, the endeavours are going on to address this challenge by most of the nations for safe and systematic disposal of infectious COVID-19 wastes because waste management of these waste is turning out to be a burning issue and seems to be thorny to practice. Nevertheless, the recycling of waste is an efficient route to put a stop to contamination, save energy, and preserve the restricted natural resources [1]. However, at the moment, a number of nations put off waste recycling to mitigate the transmission of the Covid-19 virus e.g. the U.S.A. narrowed down the recycling programs to nearly 46% at different places since the US government is concerned about the jeopardy of COVID-19 even at recycling units [37]. Worldwide, taken as a whole, there has been noted down an increase in the landfilling and environmental contaminations owing to a disorder of routine municipal waste management, recovery as well as recycling. This situation must bring to an end by opening the recycling plants faster and the recycling must be made at its acme in order to get rid of this hazardous waste keeping the staff and workers safe.

2.2.3. Long Persistence of Novel Corona Virus

Exceptionally, the hottest research in print literature in the context of the behaviour of novel Coronaviruses has revealed that they are capable enough to survive on the cardboard all day while on plastics and stainless steel surfaces for up to 3 days [37]. For this reason, the wastes generated from hospitals, treatment centres, and quarantine facilities should be effectively handled with a view to reducing the spreading of infection and pollution of the environment since it is turning out to be a worldwide concern at this moment.

3. Prospective Measures for Sustainable Environments

To date, nobody can predict the end of the Covid-19 pandemic era and that's why; the prospective measures to keep sustainable environments are the need of the hour in order to maintain the health of lives on the mother planet earth and other natural eco-balances. Therefore, this is a crucial time to make the correct strategies for long-term benefits to manage a sustainable environment scientifically. International response to fight against the COVID-19 pandemic has elicited making mankind united to triumph over the colour changing chameleon type novel coronavirus. Accordingly, with a view to safeguarding the

global environment and human health, joint efforts by all the nations are essential [37], hence, a few potential strategies are being proposed to uphold the sustainability of universal environments.

3.1 Eco-benevolent Industrialization

For any nation, industrialization is the backbone of progress which leads to financial development but at the same time, it should not be perilous to the lives on the earth. Therefore, the pandemic has compelled the world to think about eco-friendly industrial development. Sustainable industrialization necessitates essentially switching over to lesser energy-intensive industrial aspects, employing cleaner fuels and green technologies, and stronger energy competent policies. More to add, the industrialization should be made in some definite zones, keeping a conception in mind that the wastes generated from one industry can be employed as the raw materials for another leading to a lessening of landfills and the green concept of "use of waste for the best" will also be followed to "Go Green" [39]. With the condition not to hinder the national economical growth, industrial zones should be shut down at regular intervals of time as a circular route with the objective of reduction in emission of contaminating gases. As an effective measure towards sustainable industries, the giant industries with lots of workers and staff presence e.g., in the case of readymade garments plants, etc.; essential appropriate distancing and disinfected environment should be maintained in order to trim down the spreading of any contagious hazardous disease like Covid-19.

3.2 Transportation with Abridged Footprints of Pollutions

It is quite noteworthy that the global transportation industry is a great source of polluting the environment through vehicular exhaust mainly. In the interest to cut down these emissions of poisonous gases, etc., it is highly essential to promote the eco-benign transport system like the use of bicycles for shorter distances, public bike and taxi sharing locally as found in China, and people should prefer public transport rather going in their own private individual vehicles for a long journey. More to the point, awareness in people should be brought about to encourage mass usage of transport so that low footprint of contaminating agents will be observed which will be proved not only eco-welcoming but also lend a hand for the sound health of general public of the world especially of developing nations where the pollution on roads has reached its acme.

3.3 Application of Renewable Energy

Indubitably, the application of renewable energy will slim down the exigency of fossil fuels viz., Petroleum oil; coal; natural gas; etc. will play a significant role to trim down the emissions of Green House Gases (GHG) [40]. The worldwide exigency for energy is dropped resulting in the lowered emission and escalated ambient air quality in a number of areas during the COVID-19 pandemic time [22,37]. However, with a view to upholding the everyday requirements and international monetary growth, it is not practical to trim down demand for energy, therefore, the application of sources for renewable energy such as biomass, solar, hydropower, wind, geothermal heat, etc. can meet up the energy demand and mitigates the GHG-emission into the atmosphere.

3.4 Treatment and Reuse of Wastewater

With the purpose to control the water pollution challenges, both municipal and industrial wastewaters should be treated suitably prior to discharge. Moreover, reuse of treated waste water in a non-productive course of actions such as cleaning of roads and flushing of toilets can lighten the burden of surplus water removal.

3.5 Recycling and Reuse of Wastes

As stated above, the circular global economy systems for implementation the production procedures can help to lesser the consumption of raw material and, consequently, waste generation for diminishing the load of wastes and contamination of environments [39]. Both wastes of industrial and municipal origins should be recycled and reused as well as unsafe and communicable medical wastes should be orderly managed as per the guidelines of systematic disposal. In developing nations, many people are with little education and hence, lack an understanding of the Covid-19 virus behaviour and spreading routes, segregation of medical wastes and its final methodical disposal [38]. As a result, the government authorities should bring about full awareness on each and every topic related to the Covid-19 virus and the pandemic period by campaigning through diverse mass media with respect to the fitting waste segregation, its handling and ultimate disposal techniques.

3.6 Restoration of Environments and Eco-tourism

The global tourist sites should be closed at regular intervals of time in order to restore the ecological system. Also, the eco-tourism practices should be made stronger with a view to encouraging sustainable living, cultural safeguarding, and biodiversity protection.

3.7 Behaviour Modifications in Day-to-Day Life

In the interest to trim down the carbon footprint into the atmosphere by means of lesser emissions of GHG globally, some measures have to be taken by bringing behaviour modifications in our day-to-day life viz., optimal consumption of resources, replacing processed food with locally grown food, preparation of compost from the wastes of foods, switching off or unplugging the electronic devices when not in use, as well as ride a bicycle in place of a car locally.

3.8 Global Teamwork

With an objective to meet with the sustainable environmental and conservation of world environmental resources like the universal climate and bio-diversity, joint international endeavours are quite essential. Therefore, at this stage, an effective role of UNEP is much desirable for preparing state-of-the-art policies, making plans for international get-togethers, and harmonization of international leaders for appropriate execution.

As we know, the pandemic is influencing either directly or indirectly the lives on the earth, international economy, the environments, atmosphere, waste management, etc. very adversely. Nowadays, the environmental components are impacted badly resulting in enforced human-influenced modifications in the atmosphere and climate. More to add, it is a pressing need of the hour to work jointly in order to fight against the threat of COVID-19 to mankind. Nobody knows how far the pessimistic impacts of the Covid-19 pandemic will prolong on the environment; hence, the cohesive and time-oriented strategies can make stronger the sustainability for environments by saving the earth from the impacts of worldwide climatic alterations.

4. Conclusion and Discussion

In developing nations of the world, the practices for sustainable waste management were already challenging in the pre-Covid-19 era, which has shockingly turned out to be more exigent and thorny in a prevailing pandemic scenario which is changing not only the national socio-economic conditions but also impacting vigorously on environments, human health, and different essential sectors too. The gigantic escalation of infectious medical, plastic of PPEs and household wastes from Covid-19 quarantine and treatment centres as well as packaging wastes from panic online buying and foods have altogether

compelled us to be cautious of them and find a way to get rid of them methodically. With a view to addressing this fiery dilemma, the developing nations have to look into the matter sincerely and concerned government authorities should take necessary actions for control of generation of such wastes so far it is possible; the systematic collection and segregation of wastes from household organic items, packaging materials, and plastic-based protective equipments and hazardous infectious medical wastes and their orderly disposal; increase in their recycling facilities in order to dispose of finally with no harm to workers and staff of waste management industry. Unknowingly, if there occur mixing up of Covid-19 wastes with the normal day-to-day wastes, it boosts the jeopardy of transmission of this deadly disease and exposes the waste workers and associated staff to the novel Coronavirus which must be avoided. This is a multi-dimensional quandary that necessitates economics, technology, and socio-cultures to go together to get rid of it. This review has found that though the prevalent Covid-19 pandemic circumstances have helped out optimistically through lesser pollutions of noise, water and air where lockdown is imposed or still continue which can be considered as its pros, however, the cons are very horrifying such as a huge increase in plastic pollution through haphazardly dumped single-used plastics in form of wastes of PPEs, medical and packaging, etc., which are more serious and badly impacting on environments and human health as well as waste management staff, especially in the developing nations of the world where the populace is more and literacy rate is less. More to add, the colossal wastes of used disinfectants should also be dumped scientifically and the users must be aware not to destroy non-targeted beneficial organisms helpful to address ecological imbalances in nature. The actions for waste management whereby certain emissions of detrimental gases are found discharging into the atmosphere which is impacting badly on the air-quality resulting into lots of health hazards to the lives on the planet. Analogously, the appropriate measures for wastewater treatment are also turned out to be a need to prevent further spreading of a virus of Covid-19. Not only that, the eco-compassionate industrialization and transport system, as well as stronger eco-tourism practices, can help to a great extent. The utilization of sources for renewable energy can meet up the exigency for energy and thus, reduces the emissions of GHG. There is a pressing need for making aware the general public especially in developing nations fully on every single topic associated with Covid-19 disease through diverse mass media. It is also necessary to know how to deal with the novel wastes during this pandemic. Incredibly, during the Covid-19 lockdown period, the air-contaminants are found reduced dramatically, beaches are sparkling again, restoration of eco-system and assimilation of tourist destination are a few as the positive effect of this pandemic. Significantly, the advanced research works are highly necessitated with the objectives for the development of bio-degradable and eco-benevolent PPEs viz., face masks, gowns, face shields, gloves, etc. to pick up the pace for the agenda en route for attaining the sustainable production of safety gears while mitigating pessimistic impacts on environments. Admirably, the on-hand modern scientific technologies are trying their level best to control the air pollutants, however, still not enough and necessitate more novel effective routes in this direction. More progress of the industries equals more release of air pollutants into the atmosphere, i.e., economic progress is regrettably associated with ostensibly stubborn predicaments, e.g. Global Green House Gases and several toxic compounds are constantly heating the mother earth and consequently, the global temperature is rising day-by-day, which is signalling to a horrible situation and risks to lives living on it in future since the threatening to eco-systems is persistently going-on. The emerging challenges are not readily addressed by the old-fashioned "command and control" approach and therefore, still more improved technologies together with healthier regulations and stringent rules are needed to breathe in fresh and cleaner air. Unquestionably, the improvements for systematic global waste management approaches, especially, in developing nations will certainly translate into enhanced air quality. In the prevailing epidemic circumstances, there is a burning global need for methodical waste management of domestic, quarantine households, medical

treatment centres, hospitals, and other toxic waste generating sources, etc. to be treated as crucial service to the community with a view to mitigating the spread and negative impact of this deadly disease on health, environment and of course, economy. For this reason, the recycling plants must be made fully operative with safety gears to workers and the said wastes must be converted to wealth by accelerating fitting recycling processes. The United Nations Environment Program (UNEP) has also guided the world in ensuring sustainable waste management during this hard period via the treatment of residual wastes like discarded tissues, handkerchiefs and similar organic and packaging wastes, etc. by means of incineration at an elevated temperature of about 1000°C to destroy the novel Coronavirus safely and totally. Thus, a competent role of UNEP is sought-after to a large extent for drafting state-of-the-art policies in this regard. That means, the guidelines are should be followed stringently along with full awareness and joint endeavours by all the nations going hand in hand with a few potential competent strategies to mitigate not only the spread of Covid-19 but also to maintain the environments " Clean and Green".

References

[1] Ma Y, Lin X, Wu A, Huang Q, Li X, Yan J. Suggested guidelines for emergency treatment of medical waste during COVID-19: Chinese experience. Waste Disposal & Sustainable Energy. 2020 Jun;2(2):81-4. https://doi.org/10.1007/s42768-020-00039-8

[2] World Health Organization. Water, sanitation, hygiene, and waste management for SARS-CoV-2, the virus that causes COVID-19: interim guidance, 29 July 2020. World Health Organization; 2020.

[3] Saadat S, Rawtani D, Hussain CM. Environmental perspective of COVID-19. Science of the Total environment. 2020 Aug 1;728:138870. https://doi.org/10.1016/j.scitotenv.2020.138870

[4] Sharma P, Kaur M, Narwal G. Other side of the COVID-19 Pandemic: A review. Pharma Innov. 2020;9:366-9.

[5] CREA (2020)Air quality improvements due to COVID 19 lock-down in India.

[6] ESA, 2020a. https://www.esa.int/Applications/Observing_the_Earth/Copernicus/Sentinel-5P/COVID-19_nitrogen_dioxide_over_China.

[7] ESA, 2020b. https://www.esa.int/Applications/Observing_the_Earth/Copernicus/Sentinel-5P/Coronavirus_lockdown_leading_to_drop_in_pollution_across_.

[8] Caine, P., 2020. Environmental impact of COVID-19 lockdowns seen from space. Sci. Nat.2 April 2020.

[9] Biswal A, Singh T, Singh V, Ravindra K, Mor S. COVID-19 lockdown and its impact on tropospheric NO2 concentrations over India using satellite-based data. Heliyon. 2020 Sep 1;6(9):e04764. https://doi.org/10.1016/j.heliyon.2020.e04764

[10] USEPA, 2016. Nitrogen Dioxide (NO2) Pollution. https://www.epa.gov/no2-pollution/basic-information-about-no2.

[11] EEA, 2020. Air pollution goes down as Europe takes hard measures to combat Coronavirus. European Environmental Agency (EEA), Copenhagen.

[12] Adams MD. Air pollution in Ontario, Canada during the COVID-19 State of Emergency. Science of the Total Environment. 2020 Nov 10;742:140516. https://doi.org/10.1016/j.scitotenv.2020.140516

[13] Nakada LY, Urban RC. COVID-19 pandemic: Impacts on the air quality during the partial lockdown in São Paulo state, Brazil. Science of the Total Environment. 2020 Aug 15;730:139087. https://doi.org/10.1016/j.scitotenv.2020.139087

[14] Zogopoulos E. COVID-19: the curious case of a green virus. Energy industry review. 2020 Mar;11.

[15] Evans, S., 2020. Global emissions analysis: coronavirus set to cause largest ever annual fall in CO2 emissions. Carbon Brief, 4 September 2020.

[16] Bodrud-Doza M, Islam SD, Rume T, Quraishi SB, Rahman MS, Bhuiyan MA. Groundwater quality and human health risk assessment for safe and sustainable water supply of Dhaka City dwellers in Bangladesh. Groundwater for sustainable development. 2020 Apr 1;10:100374. https://doi.org/10.1016/j.gsd.2020.100374
[17] Arif M, Kumar R. Reduction in water pollution in Yamuna river due to lockdown under COVID-19 pandemic.
[18 Yunus AP, Masago Y, Hijioka Y. COVID-19 and surface water quality: Improved lake water quality during the lockdown. Science of the Total Environment. 2020 Aug 20;731:139012. https://doi.org/10.1016/j.scitotenv.2020.139012
[19] Singhal S, Matto M. COVID-19 lockdown: a ventilator for rivers. DownToEarth. Bioresource Technology Reports. 2020;11:100491. https://doi.org/10.1016/j.biteb.2020.100491
[20] Sharma P, Kaur M, Narwal G. Other side of the COVID-19 Pandemic: A review. Pharma Innov. 2020;9:366-9.
[21] Arif, M., Kumar, R., Parveen, S., 2020. Reduction in water pollution in Yamuna river due to lockdown under COVID-19 pandemic. ChemRxiv. https://doi.org/10.26434/chemrxiv.12440525
[22] Zambrano-Monserrate MA, Ruano MA, Sanchez-Alcalde L. Indirect effects of COVID-19 on the environment. Science of the total environment. 2020 Aug 1;728:138813. https://doi.org/10.1016/j.scitotenv.2020.138813
[23] Kundu, C., 2020. Has the Covid-19 lockdown returned dolphins and swans to Italian waterways? The India Today, 22 March 2020.
[24] Cooper, R., Water Security beyond Covid-19. K4D Helpdesk Report 803. Institute of Development Studies, 2020, Brighton, UK.
[25] Sims, J., 2020. Will the world be quieter after the pandemic? https://www.bbc.com /future/article/20200616-will-the-world-be-quieter-after-the-pandemic.
[26] Gandhiok, J., Ibra, M., 2020. Covid-19: Noise Pollution Falls as Lockdown Rings in Sound of Silence. The Times of India. Apr 23, 2020.
[27] Lenzen M, Sun YY, Faturay F, Ting YP, Geschke A, Malik A. The carbon footprint of global tourism. Nature climate change. 2018 Jun;8(6):522-8. https://doi.org/10.1038/s41558-018-0141-x
[28] Puig R, Kiliç E, Navarro A, Albertí J, Chacón L, Fullana-i-Palmer P. Inventory analysis and carbon footprint of coastland-hotel services: A Spanish case study. Science of the total environment. 2017 Oct 1;595:244-54. https://doi.org/10.1016/j.scitotenv.2017.03.245
[29] Cripps, K., 2020. Thailand's most popular island goes into lockdown as Covid-19 cases surge. CNN travel, CNN, 10 April 2020. https://edition.cnn.com/travel/article/phuket-thailand-lockdown/index.html.
[30] Van Doremalen N, Bushmaker T, Morris DH, Holbrook MG, Gamble A, Williamson BN, Tamin A, Harcourt JL, Thornburg NJ, Gerber SI, Lloyd-Smith JO. Aerosol and surface stability of SARS-CoV-2 as compared with SARS-CoV-1. New England journal of medicine. 2020 Apr 16;382(16):1564-7. https://doi.org/10.1056/NEJMc2004973
[31] Didar-Ul Islam SM, Bhuiyan MA. Impact scenarios of shrimp farming in coastal region of Bangladesh: an approach of an ecological model for sustainable management. Aquaculture International. 2016 Aug;24(4):1163-90. https://doi.org/10.1007/s10499-016-9978-z
[32] Singh N, Tang Y, Ogunseitan OA. Environmentally sustainable management of used personal protective equipment. Environmental science & technology. 2020 Jun 29;54(14):8500-2. https://doi.org/10.1021/acs.est.0c03022
[33] Ahmed, W., Angel, N., Edson, J., Bibby, K., Bivins, A., O'Brien, J.W., Choi, P.M., Kitajima, M., Simpson, S.L., Li, J. and Tscharke, B., 2020. First confirmed detection of SARS-CoV-2 in untreated wastewater in Australia: a proof of concept for the wastewater

surveillance of COVID-19 in the community. Science of the Total Environment, 728, p.138764. https://doi.org/10.1016/j.scitotenv.2020.138764
[34] Rahman SH, Islam SM. Degrading riverine ecology of Bangladesh and options for management. SUB J. Sustain. Environ. Develop. 2016;1:11-27.
[35] Calma, J., 2020. The COVID-19 pandemic is generating tons of medical waste. The Verge, Mar 26, 2020. https://www.theverge.com/2020/3/26/21194647/the-covid-19-pandemic-is-generating-tons-of-medical-waste.
[36] Fadare OO, Okoffo ED. Covid-19 face masks: A potential source of microplastic fibers in the environment. The Science of the total environment. 2020 Oct 10;737:140279. https://doi.org/10.1016/j.scitotenv.2020.140279
[37] Somani M, Srivastava AN, Gummadivalli SK, Sharma A. Indirect implications of COVID-19 towards sustainable environment: an investigation in Indian context. Bioresource Technology Reports. 2020 Sep 1;11:100491. https://doi.org/10.1016/j.biteb.2020.100491
[38] Rahman MM, Bodrud-Doza M, Griffiths MD, Mamun MA. Biomedical waste amid COVID-19: perspectives from Bangladesh. The Lancet. Global Health. 2020 Oct;8(10):e1262. https://doi.org/10.1016/S2214-109X(20)30349-1
[39] Hysa E, Kruja A, Rehman NU, Laurenti R. Circular economy innovation and environmental sustainability impact on economic growth: An integrated model for sustainable development. Sustainability. 2020 Jan;12(12):4831. https://doi.org/10.3390/su12124831
[40] Ellabban O, Abu-Rub H, Blaabjerg F. Renewable energy resources: Current status, future prospects and their enabling technology. Renewable and sustainable energy reviews. 2014 Nov 1;39:748-64. https://doi.org/10.1016/j.rser.2014.07.113

Research on Engineering Structures & Materials
journal homepage: http://www.jresm.org
MIM Research Group

Research Article

Performance study of aluminium oxide based nanorefrigerant in an air-conditioning system

Mohammed Dilawar[1a], Adnan Qayoum*[b]

[1]*Department of Mechanical Engineering, National Institute of Technology Srinagar, J&K, India-190006*

Article Info

Article history:

Received 1 July 2022
Revised 14 Sep 2022
Accepted 16 Sep 2022

Keywords:

Nanorefrigerant;
Power Saving;
Heat Transfer Enhancement;
Thermal conductivity;
COP

Abstract

The present issues related to global warming have attracted refrigerants with low Global Warming Potential (GWP). Two of the most promising low-GWP refrigerants, R32 (difluoromethane) and R290 (propane) are flammable. The addition of a flame retardant to R290 or R32 can enhance their flammable characteristics. Trifluoroiodomethane (R13I1) is a flame retardant with an enormously low global warming and can be used as a component of the refrigerant. In addition, dispersing nanoparticles in these refrigerants improves thermal conductivity. Nanorefrigerants are new refrigerants possessing better heat dissipation performance over traditional refrigerants. An ultra-low GWP mixture refrigerant consisting of R32, R161 and trifluoroiodomethane with aluminum oxide (Al_2O_3) nanoparticles is used in the present study. Simulation Model-based theoretical results of R410a and with R410a/Al_2O_3, mixture refrigerant (R32, R161 and trifluoroiodomethane) and nanorefrigerant (R32, R161 and trifluoroiodomethane with aluminum oxide nanoparticles) are carried. The study shows the coefficient of performance (COP) of R410a/Al_2O_3 and M (R32/R161/R13I1)/Al_2O_3 increased by 47.3% and 89.8% respectively. The power-saving up to 31.8% and 47.2% at a volume concentration of 0.09%. The comparison has been made with reference to the R410a/Al_2O_3 system. The thermophysical properties of refrigerants have been calculated using REFPROP (NIST properties of fluid reference). The theoretical model-based calculations are computed in MATLAB software. This study provides an insight in providing appropriate refrigerant substitutes for air conditioning systems.

1. Introduction

In recent decades, R410a has been used broadly as a working refrigerant in air-conditioning systems due to its suitable thermodynamic properties and cycle performance. Global warming has become a critical issue in refrigeration and air-conditioning heat pumps (RACHPs). This can be resolved by selecting very low Global Warming Potential (GWP) refrigerants [1]. In the past few years, manufacturers have also adopted environmentally friendly refrigerants such as R161, R32, R152a, R1270, R1150, R1234yf, etc. R161 (C_2H_5F) has a zero ozone depletion effect and tremendously low GWP_{100} (about 12), and also possesses the most promising thermophysical properties and is considered an alternative to R22 [2]. R13I1 a flame retardant provides outstanding environmental performance with Low Global Warming Potential (LGWP about 1) and zero ozone depletion effect [3].

Another issue is power consumption. Out of the total worldwide electricity consumption, it is estimated that about 17% of electricity is consumed by refrigeration frameworks [4]. From another report, 25 to 30% of electricity is consumed by refrigeration air-conditioning and heat pumps (RACHPs) [5], [6]. In order to acquire the refrigerant with environmental friendly and excellent thermophysical cycle performance, a mixture

*Corresponding author: adnan@nitsri.ac.in
[a] orcid.org/0000-0001-8475-8238; [b] orcid.org/0000-0002-4894-3425
DOI: http://dx.doi.org/10.17515/resm2022.459ma0701

refrigerant composed of R32/R161/R13I1 (i.e., mass fraction 22/48/30) as an alternative for R410a [7]. The new mixture refrigerant is named as M which is shown in Fig. 1. This study examined the viability of using M refrigerant as a substitute for R410a was theoretically investigated from aspects of power-saving, greater cooling effect and environment indicators by dispersing of Al_2O_3 (Alumina) nanoparticles in M refrigerant which is completely ozone-friendly with low GWP (about 149) at volume concentration of 0.09%. And the results are compared with R410a. The mixture consisting of R32, R161 and R13I1 can be estimated by equation 1 [3] and the thermophysical properties of refrigerants are shown in Table 1. The current study of Al_2O_3 has been used as an account of superior thermal conductivity and good stability behavior. In addition, literature has shown that Alumina has the lowest precipitation rate and highest emulsification stability compared to other nanoparticles [8]. The concentration of Al_2O_3 in the current study is limited to 0.09% only. The reason for this is that higher concentrations lead to sedimentation, agglomeration and high pumping power. In addition, higher concentrations result in poor stability [9]–[11]. The benefits of the nanofluids using data from the literature, it has been discovered that, compared to conventional fluids, nanofluids exhibit a significantly greater and substantially temperature-dependent thermal conductivity with enhanced thermophysical and rheological properties, and low sedimentation and agglomeration problems [12].

$$GWP_{mix} = GWP_a \times X_a + GWP_b \times X_b + GWP_c \times X_c \quad (1)$$

where X_a, X_b and X_c denote the mass fraction of components a, b and c respectively.

Table 1. Thermophysical properties of R410a and M refrigerants [7][13].

Refrigerant	R410a	M
Molecular formula (mass %)	R32/R125 (50/50)	R13I1/R32/R161 (30/22/48)
Molecular weight	72.5	93.29
Critical pressure (bar)	49	32.3
Critical Temperature (°C)	72.5	97.7
GWP	2088	149
ODP	0	0
Temperature glide at 25°C	0.1	3.23
Safety classification	A1	~A2L

The use of nano additives in refrigeration and air-conditioning heat pumps (RACHPs) may increase the efficiency of the system [14]. Nanoparticles possess enhanced thermophysical properties and ameliorate the working fluid properties depending upon the particle concentration, operating temperature, and size [15]. The higher the energy efficiency rating, the more efficient the machine. The rating indicators may vary from country to country as shown in Fig. 2 [16].

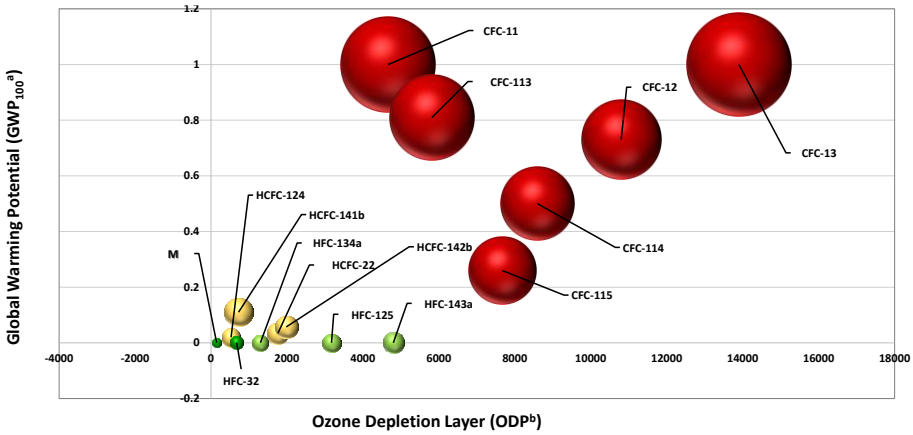

Fig. 1 GWP vs ODP and lifetime of HFCs, HCFCs, CFCs (circles)

Another advantage of nano additives in lubricating oil is to improve the solubility between the compressor lubricant and refrigerant, which offers enhancement in the performance of the system by recirculating more oil back to the compressor. More oil accumulation in the compressor sump which prevents direct contact between the piston and cylinder during motion, improves the mending, rolling, and polishing effects and reduction in the coefficient of friction [17]–[22].

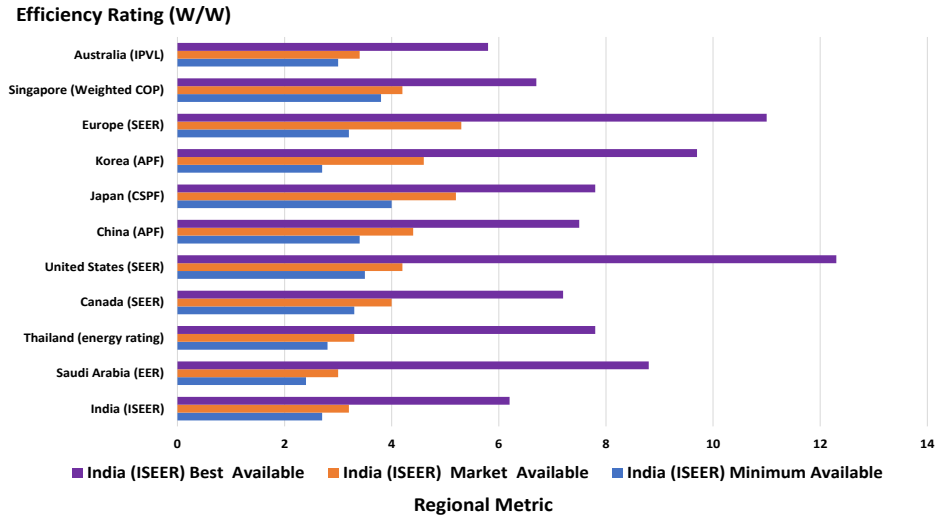

Fig. 2 Efficiency ratings of available AC units by regional metric

Adelekan *et al.* [23] experimental investigation of TiO_2 nano-additives dispersed in R600a refrigerant at 0.1g concentration and observed the highest refrigeration effect, least compressor power and high COP. Marcucci *et al.* [24] explored the use of diamond nanoparticles in polyol ester (POE) refrigerant oil at two mass concentrations, 0.1 and 0.5% in a refrigeration system. The cooling capacity increased by 4%, and 8%. The discharge temperature was decreased by approximately 4 °C. Babarinde *et al.* [25] carried out an experimental investigation of R600a/MWCNT- nanolubricant used in the domestic

refrigerator instead of R134a with a various mass charge of Iso-Butane. The optimum results showed that the lower evaporator temperature was -11 °C, the highest COP and lower power consumption of 0.0639kW. Farid et al. [26] performed an experimental investigation of WO_3 and MWCNT hybrid nanofluids. The thermal conductivity of nanofluid and experimental equation is established to predict the thermal conductivity of nanofluid. According to the obtained results, the role of volume fraction concentration on the thermal conductivity of nanofluids is more effective compared to temperature. Ruhani *et al.* [27] developed a new model for the rheological behavior of Silica-Ethylene glycol/Water (30 vol.%: 70% vol.) hybrid Newtonian nanofluid. The current study investigates the relationship between shear stress and shear rate is linear and the desired fluid is Newtonian. The higher dispersion of the nanoparticles in the base fluid causes the relative viscosity to increase as the volume fraction increases. In another study, the experimental investigation of Multi-walled Carbon Nanotubes (MWCNTs)-titania-Zinc oxide/water-ethylene glycol (80:20) mono and hybrid nanofluid has been studied. The highest thermal conductivity of nanofluid was obtained at a volume fraction of 0.4% at 50°C, which increased by 17.82% and a comparison has been made with base fluid at the same temperature [28], [29]. Yan *et al.* [30] carried out an experimental investigation on the rheological properties of hybrid nanofluid (MWCNTs-ZnO/Water-EG (80:20 volume%)) (non-Newtonian). The viscosity of hybrid nanofluid was evaluated in the temperature range of 25-50°C with various concentrations of 0.075, 0.15, 0.3, 0.6, 0.9 and 1.2% respectively. At the maximum volume fraction concentration at 50, 40 and 30°C, the viscosity is reduced by 21%, 17% and 8% to the reference temperature (25°C).

Tian *et al.* [31] performed Artificial Neural Network (ANN) to investigate the effect of temperature and various volume fractions of Graphene oxide-Alumina hybrid nanoparticles on thermal conductivity. The thermal conductivity of GO-Al_2O_3/Water-EG hybrid nanofluid is significantly affected by the volume percentage of nanoparticles. Hossein and Toghraie [32] explored the use of various nanofluids on the performance of heat pipe. The use of nanofluid instead of water (base fluid) resulted in higher thermal efficiency. As thermal capacity increases, fluid pressure drops and the temperature difference between condenser and evaporator increases. Damola *et al.* [33] performed varied mass charges of LPG (0.2, 0.4 and 70 g) with various concentrations of TiO_2 nanoparticles in mineral oil (MO). The highest COP obtained of 2.8 with a 40 g charge of LPG utilizing a 0.4 g/L concentration of nano oil. Sabareesh *et al.* [22] experimentally evaluated the application of TiO_2 nano-additives in modifying the lubricating Mineral oil (MO) at concentrations of 0.005, 0.01 and 0.015vol% respectively. At 0.01% volume fraction, the maximum COP was enhanced by 17%, and compressor work was reduced by 11%. Ohunakin *et al.* [34] observed energy saving at a low concentration of SiO_2/MO and 50g of charge of LPG refrigerant using 0.4 g/L nanolubricant in a refrigeration system and compared it with pure R134a. The maximum reduction in discharge temperature has been attained with a 50g mass charge of LPG using 0.2g/L. Jiang *et al.* [35] has investigated the performance of a refrigerator (R600a) graphite nanolubricants with mass fraction of 0%, 0.05%, 0.1%, 0.2%, and 0.5% respectively. The power-saving upto 4.55% and certain reductions in condenser temperature, evaporator temperature, discharge pressure and discharge temperature. Kumar *et al.* [36] used the influence of Al_2O_3 nanoparticles in compressor lubricant (MO) at 0.06% mass fraction. It is observed that the power saving upto 11.5% and increment in freezing capacity when POE lubricant is replaced by a blend of MO and Al_2O_3 nano additives. Gill *et al.* [37] studied the performance of Iso-Butane refrigerant selected various mass charges (40g, 60 and 80g) at various concentrations of TiO_2-based nano lubricant of 0, 0.2, 0.4 and 0.6 g/L respectively. The results obtained lower compressor power consumption, reduction in discharge temperature and pull-down time by about 33.3%, 41.92% and 21% as compared with base refrigerant.

Yang *et al.* [38] explored the use of graphene nanosheets in lubricant at various concentrations of 30, 20 and 10 mg/L respectively. The refrigeration effect increased by 5.60% and the cooling capacity of the freezer increased by 4.70% at a concentration of 30 mg/L. The energy saving by utilizing the three concentrations of 20.3%, 19.2% and 15.4% in 24 hours, respectively compared with the base oil. Babarinde *et al.* [39] examined the performance of Iso-Butane environmentally friendly refrigerant in a domestic refrigerator. The graphene nano additives were dispersed in the pure lubricant at different concentrations of 0.6, 0.4 and 0.2 g/L in 50, 60 and 70g with various mass charges of R600a refrigerant. In terms of COP, pull-down time, power consumption and cooling capacity, the results showed that the nanolubricant in R600a outperformed over base lubricant.

Santhana *et al.* [40] investigated the influence of different nanoparticles CNT, ZrO_2, Al_2O_3, and SiO_2 dispersed in Poly-ol Ester (POE) oil at a concentration of 0.1% (w/v). In addition, SiO_2 in POE obtained the maximum increment in COP of 21.8% compared with Al_2O_3, ZrO_2, CNT nanolubricants and pure POE lubricants. Omer *et al.* [41] examined the performance of heat dissipation and thermophysical properties of CuO nano additives in R134a. The results showed that the viscosity and density of the nanorefrigerant significantly increased with the increment of volume concentrations. Nevertheless, these parameters have been reduced accordingly with the increase in temperature. Kosmadakis and Neofytou [42] utilize various nanoparticles in a heat pump working on a vapour compression system to show the enhancement of heat transfer rate during boiling and condensation. This numerical model-based study used suitable refrigerants (R1234yf and R134a) and nanomaterials such as Cu, CuO and Al_2O_3 respectively. The coefficient of performance of the heat pump increased upto 5-6% at 5 wt.% concentration of Al_2O_3 and thereby indicating the superior performance in comparison to CuO or Cu. In addition, there is a total pressure drop upto 3.50%.

From the above literature analysis, it is clear that currently there are no appropriate ultra-low GWP and eco-friendly nanorefrigerants for power saving in the air conditioning system. Furthermore, earlier studies all dealt with the R410a substitute with GWP higher than 150 and there are no nanorefrigerants that can serve as R410a alternatives with GWP less than 150 with suitable thermophysical properties. The ultra-low GWP nano refrigerant-based studies are almost negligibly available in academic libraries. This work considers a Matlab-based simulation study of nanorefrigerants such as R410a/Al_2O_3 and M (R32/R161/R13I1)/Al_2O_3 at 0.09% volume concentration. To add more novelty, a detailed comparison between the refrigerants has been made to arrive at the optimal refrigerant for commercial purposes based on low GWP and other viable parameters. The major benefits of this novel method are low global warming emissions, high coefficient of performance, and power saving.

2. Material and Methods

The properties of the pure refrigerant and nanorefrigerant such as pressure, temperature and enthalpy are calculated through the density of pure and nanorefrigerant at points 1 and 3 as shown in Fig. 8. The density of nanorefrigerant is calculated from the equation 2 [Pak and Cho [43]]. Therefore, (ρ_{NP}), (ρ_{NR}), (ρ_{PR}) and (ϕ) represents the density of nanoparticle, nanorefrigerant, pure refrigerant and volume concentration respectively. The density of Al_2O_3 (alumina) nanoparticles is considered as 3.9 g/cm^3 used in R410a and M (R32/R161/R13I1) refrigerants at a volume concentration of 0.09% by using Eq. 3.

$$\rho_{NR} = m_p \rho_{NP} + (1 - m_p) \rho_{PR} \quad (2)$$

$$\phi = \frac{m_p / \rho_p}{m_p/ \rho_p + m_R/\rho_R} x\ 100 \quad (3)$$

where,
ρ_{NR} = Density of nanorefrigerant in g/m^3,
ρ_{NP} = Density of nanoparticle in g/m^3,
ρ_{PR} = Density of pure refrigerant in g/m^3,
ϕ = volume concentration (%),
m_p = mass of nanoparticle in grams,
ρ_p = Density of particle in g/m^3,
m_R = mass of refrigerant in grams,
ρ_R = Density of refrigerant in g/m^3.

2.1 Theoretical Simulation-Based Model of (R32/R161/R13I1)/Al_2O_3 for Vapour Compression Air Conditioning System

A MATLAB/Simulink model is developed to calculate the performance of the air conditioner in terms of properties of pure and nanorefrigerant through the density of nanorefrigerant by using Eq. 2, to evaluate the net refrigeration effect (NRE), COP and power consumption in Simulink is depicted in Fig. 3. Theoretical comparative numerical analysis and the formulas used as coding (Eqs. 4-8) in MATLAB such as gauges, block parameters of various signals, compressor, condenser, expansion device and evaporator are also shown in Fig. 3.

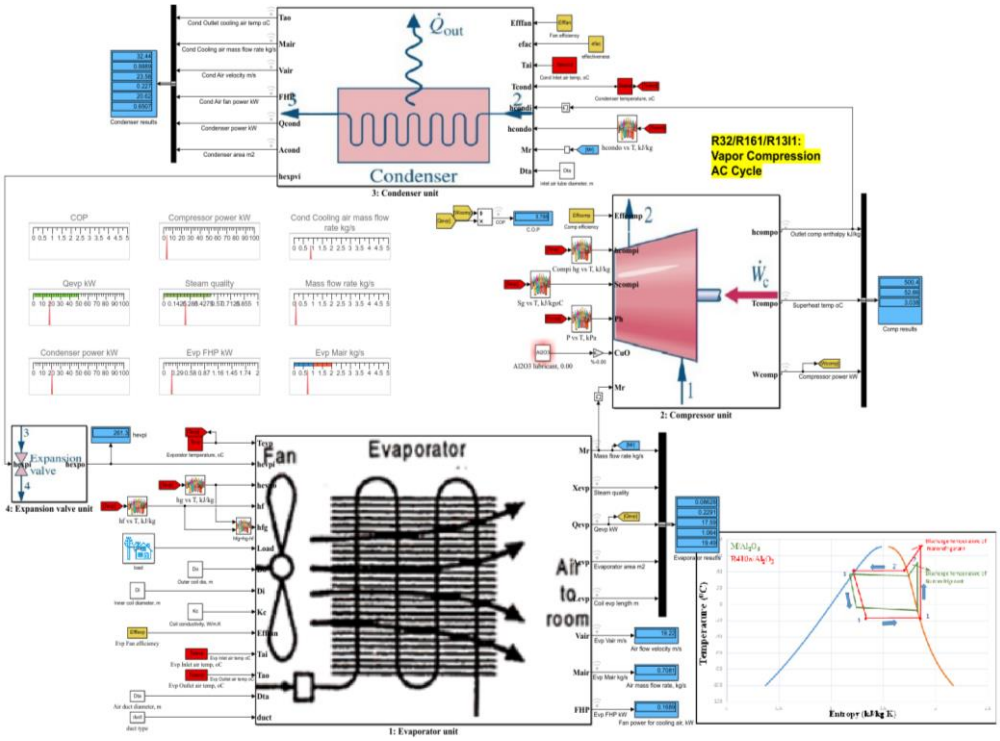

Fig. 3 Air conditioning system using M/Al_2O_3 nanorefrigerant in Simulink

2.2 Theoretical formulation used as coding in MATLAB

The results of M (R32/R161/R13I1)/Al_2O_3 nanorefrigerant have been investigated and compared with the performance of R410a/Al_2O_3 in the system using Eqs. (4)-(8).

Heat extracted (Q_e) is given by

$$Q_e = \dot{m}(h_1 - h_{f3}) \quad \text{(kW)} \tag{4}$$

Compressor work done (kW) or power input is given by

$$W_C = \dot{m}(h_2 - h_1) \quad \text{(kW)} \tag{5}$$

Heat rejected in a condenser (kW) is given by

$$Q_C = \dot{m}(h_2 - h_{f3}) \quad \text{(kW)} \tag{6}$$

Refrigerant mass flow rate is given by

$$\dot{m}_{ref} = \frac{Ref.\ capacity}{h_1 - h_{f3}} \quad \left(\frac{\text{kg}}{\text{s}}\right) \tag{7}$$

Coefficient of performance

$$\text{C O P} = \frac{Q_{evap}}{W_{Comp}} \tag{8}$$

where 'm' is the mass flow rate (kg/s), h_1 is the enthalpy of saturated vapour (kJ/kg), h_2 is the enthalpy of superheated vapour (kJ/kg) and h_{f3} is the enthalpy of saturated liquid (kJ/kg). Fig.4 represents the flowchart of the developed model.

2.3 Assumptions

The important assumptions for leading this kind of theoretical model-based study are.

- Pressure losses at the compressor inlet and outlet ports are neglected.
- Pipelines pressure losses are neglected.
- Heat losses and heat gains from or to the system are ignored.
- Isentropic, mechanical and electric motor compressor efficiencies are considered.
- Degree of undercooling and superheating before compression are neglected.
- No deposition of nanoparticles at the solid wall.

3. Results and Comparison

3.1 Effect of nanoparticle concentration

Fig. 5 shows the graphical representation of variation in COP and power saving with particle concentration for the two refrigerants in the form of bar charts. The charts clearly illustrate that incorporating Al2O3 in M (R32/R161/R13I1) refrigerant improves the COP and power saving compared with pure refrigerants. The coefficient of performance of R410a and M (R32/R161/R13I1) nanorefrigerants at 0.09 vol.%, increased by 47.3% and 89.8% compared to the pure refrigerants. The power consumption of both the nanorefrigerants is reduced by 31.8% and 47.2% respectively.

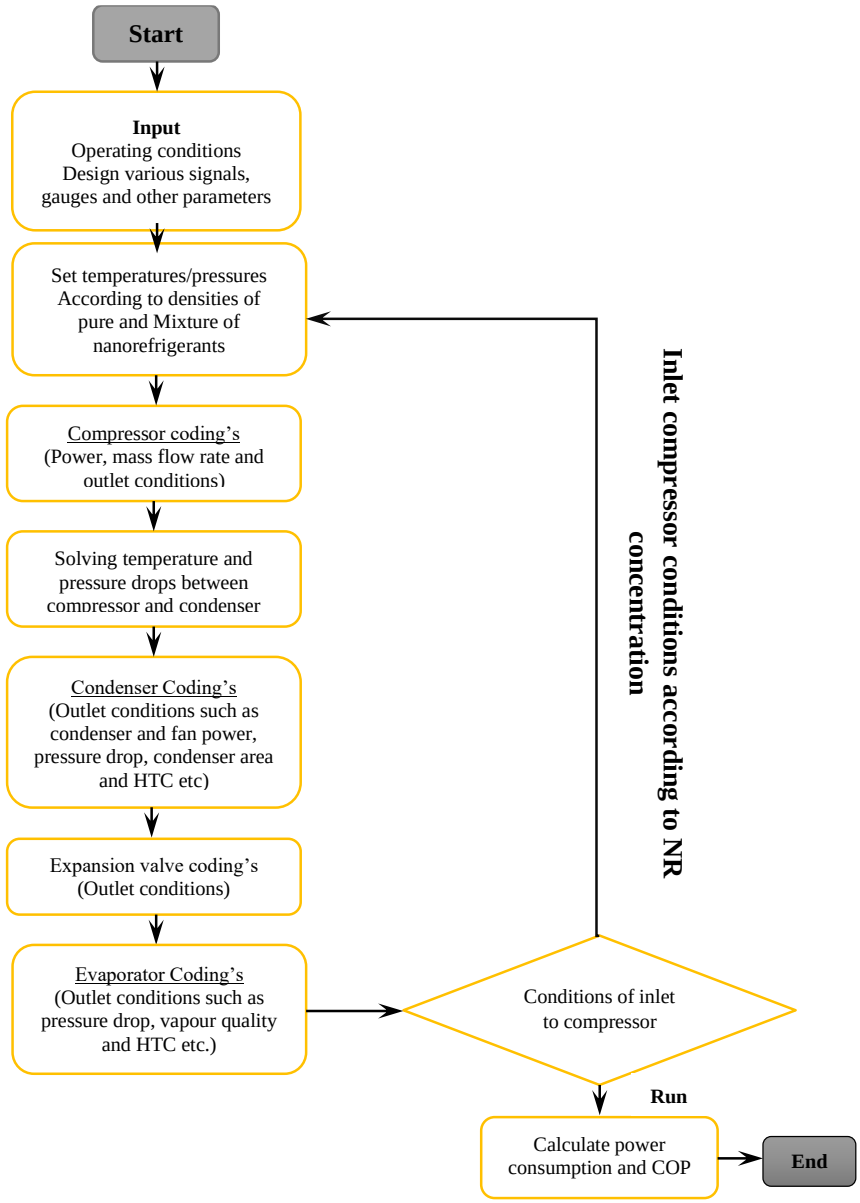

Fig. 4 Developed model flowchart

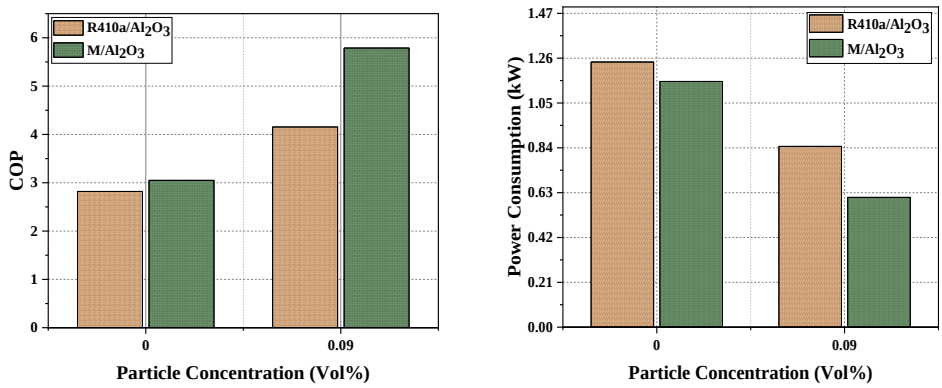

Fig 5. COP and power consumption of the system as the function of particle concentration

Fig. 6 shows the corresponding variation of discharge pressure. The discharge pressure of R410a/Al_2O_3 and M/Al_2O_3 was reduced by 2.6% and 4.51% compared with pure refrigerants of R410a and M.

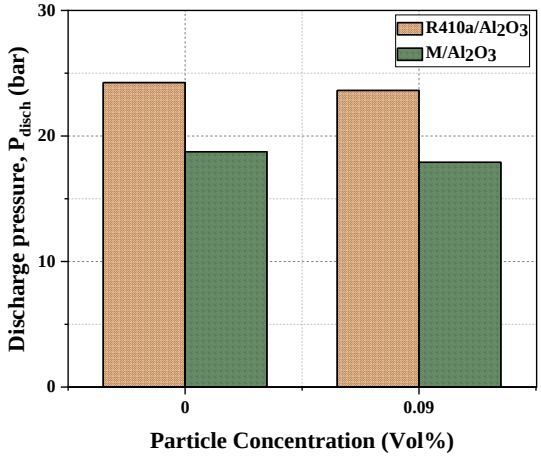

Fig. 6 Discharge pressure versus particle concentration

In addition, Figs. 7 and 8 illustrate the corresponding variation of discharge temperature. As the discharge temperature reduces the heat rejection and absorption increase through the condenser and evaporator. The discharge temperature of R410a/Al_2O_3 and M/Al_2O_3 was reduced by 11.86% and 19.4% compared with pure refrigerants of R410a and M.

3.2 Effect of Particle Concentration on Refrigeration Effect

Fig.9 shows the refrigeration effect versus particle concentration for R410a and M respectively. There is a marked increment in the refrigeration effect at a volume concentration of 0.09% for both refrigerants. The refrigeration effect of R410a/Al_2O_3 and M/Al_2O_3 increased by approximately 4.7% and 7% compared with pure refrigerants.

4. Numerical Method for Characterization of Nanorefrigerant

4.1 Effect of Nanoparticle Concentration on Thermal Conductivity

Fig.10 represents the thermal conductivity of Al_2O_3-R410a and Al_2O_3-R32/R161/R13I1 at a volume concentration of 0.09% and compared with pure refrigerants. The thermal

conductivity of nanoparticles (spherical shape) is measured by using Eq. 9 [44]. The thermal conductivity of Al_2O_3-R410a and Al_2O_3-R32/R161/R13I1 is 0.105 W/mK and 0.124 W/mK respectively. The thermal conductivity of Al_2O_3-R32/R161/R13I1 nanorefrigerant is 18.1% more than that of Al_2O_3-R410a nanorefrigerant. The increase in Brownian motion, as well as the enhanced thermal conductivity of alumina nanoparticles, contributes to the improvement in suspension stability [45].

$$\frac{k_{eff}}{k_f} = \frac{k_p + 2k_f + 2\phi(k_p - k_f)}{k_p + 2k_f - \phi(k_p - k_f)} \quad (9)$$

where ϕ, is the volume concentration of nanoparticles. k_{eff} is the effective thermal conductivity of the nanorefrigerant. k_f and k_p are the thermal conductivities of pure refrigerant and nanoparticles respectively.

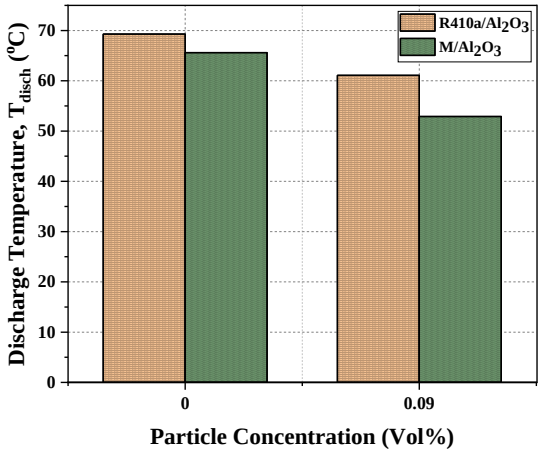

Fig. 7 Discharge temperature versus particle concentration

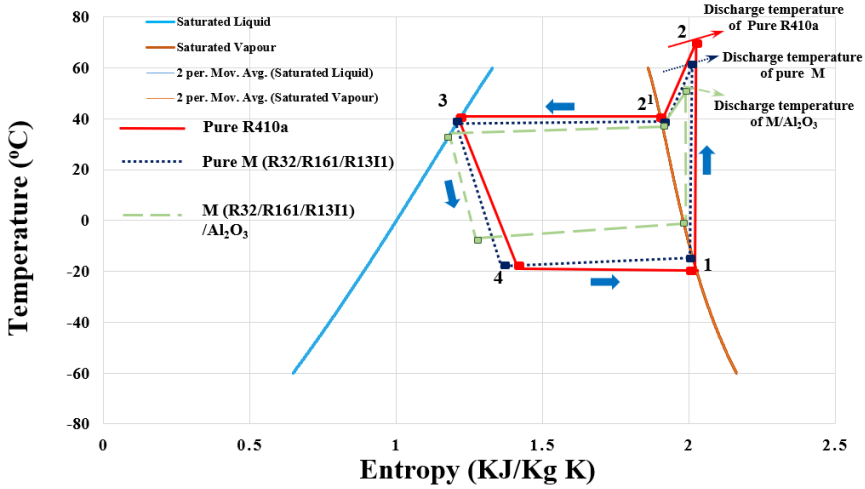

Fig. 8 T-s diagram for pure and nanorefrigerant

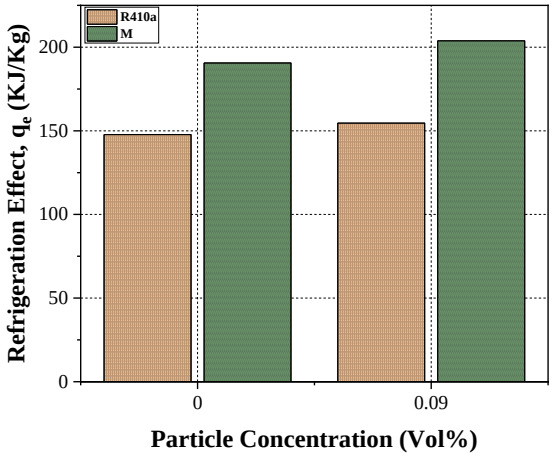

Fig.9 Refrigeration effect versus particle concentration

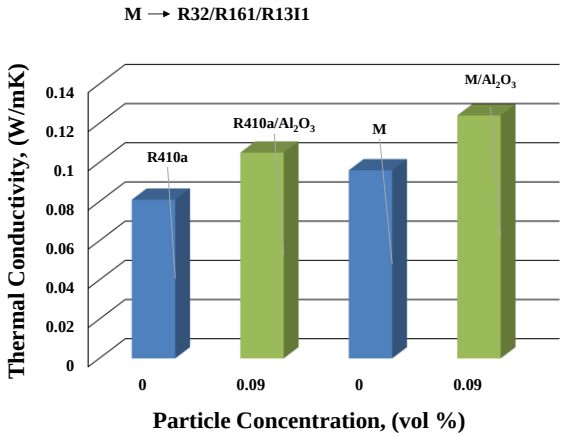

Fig. 10 Influence of nanoparticle (Al_2O_3) concentration on thermal conductivity

4.2 Effect of Nanoparticle Concentration on Viscosity

Fig.11 clearly shows the variation of viscosity of Al_2O_3-R410a and Al_2O_3-R32/R161/R13I1 at a volume concentration of 0.09% and compared with pure refrigerants. The viscosity of Al_2O_3-R410a and Al_2O_3-R32/R161/R13I1 nanorefrigerants was increased by 22.47% and 22.36% compared to the pure refrigerants. The pioneering model for estimating the viscosity of nanofluids was proposed by Einstein in Eq. 10 [46].

$$\mu_{nf} = \mu_{bf}\,(1 + 2.5\phi) \tag{10}$$

where μ_{bf} is the viscosity of the base fluid and μ_{nf} is the viscosity of the nanofluid.

4.3 Effect of Nanoparticle Concentration on Density

The density of R410a/Al_2O_3 and (R32/R161/R13I1)/Al_2O_3 nanorefrigerant was measured by utilizing above mentioned Eq.2. Fig.12 represents the variation of nanorefrigerant densities at a 0.09% volume concentration.

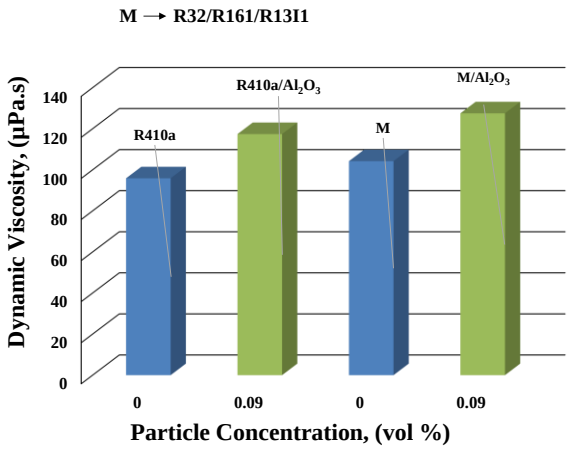

Fig.11. Influence of nanoparticle (Al_2O_3) concentration on dynamic viscosity

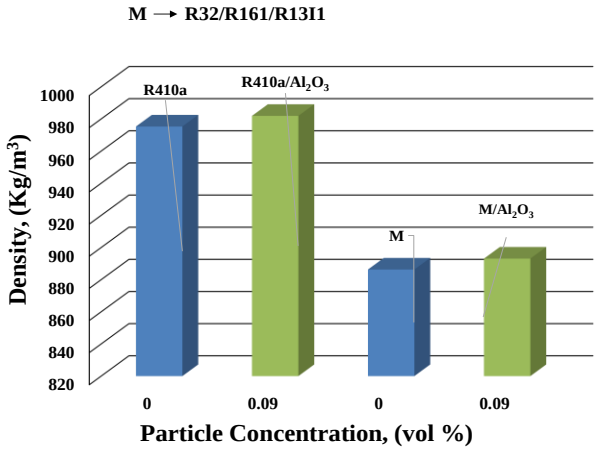

Fig. 12 Variation of the density of R410a/Al_2O_3 and M/Al_2O_3 with particle concentration

5. Conclusions

In the current study, the numerical determination of thermophysical properties, rheological properties, power-saving and long-term ultra-low global warming potential (GWP) mixture of nanorefrigerants (R32/R161/R13I1)/Al_2O_3 were carried out numerically in MATLAB software. The NIST REFPROP software program is used to generate thermophysical properties of the mixture of refrigerants and was developed in MATLAB. The current investigation reinforces the concepts of power saving and environmentally friendly behavior by incorporating an alumina-based nanorefrigerant into the air-conditioning system. The system exhibits improved performance at a volume concentration of 0.09% aluminium oxide. The simulation involving performance has been performed using MATLAB software.

- The COP of R410a and M (R32/R161/R13I1) nanorefrigerants has increased by 47.3% and 89.8%, respectively in comparison to pure refrigerants.

- The discharge temperature of R410a and M nanorefrigerants is reduced by 11.86% and 19.4% respectively and the comparison has been made with pure refrigerants.
- The discharge pressure of R410a and M nanorefrigerants was reduced by 2.6% and 4.51% at a volume concentration of 0.09% compared to pure refrigerants.
- The use of nano additives in R410a and M refrigerants lowers the power consumption of the system by 31.8% and 47.2% respectively.
- In addition, Al_2O_3 nano additives in R410a and M having a volume concentration of 0.09%, increased the net refrigeration effect from 76.7-82% and 79.3-87% respectively.
- Heat extraction is augmented from the evaporator by adding aluminium oxide nanoparticles to the refrigerants.
- The cooling effect or heat extraction of R410a/Al_2O_3 and M/Al_2O_3 nanorefrigerants increased by approximately 4.7% and 7% at a volume concentration of 0.09% compared to pure refrigerants.
- The viscosity and density are increased by adding Al_2O_3 nanoparticles to both refrigerants.
- The viscosity of R410a and M nanorefrigerants was increased by 22.47% and 22.36% at a volume concentration of 0.09% compared to the pure refrigerants.
- The thermal conductivity of R410a/Al_2O_3 and M/Al_2O_3 is 0.105 W/mK and 0.124 W/mK respectively.
- The thermal conductivity of M/Alumina nanorefrigerant is 18.1% more than that of R410a/Alumina.

Nomenclature

Al_2O_3	Aluminium Oxide
COP	Coefficient of Performance
NRE	Net Refrigeration effect, (%)
GWP	Global Warming Potential
$(GWP)_{100}$	Global Warming Potential over 100 years
ODP	Ozone Depletion Potential
M	Mixture (R32/R161/R13I3)
Q	Heat Transfer per Unit Mass, (kW)
Φ	Nanoparticle Volume Concentration, (%)
T	Temperature, (^{o}C)
GHG	Greenhouse Gas
NR	Nanorefrigerant
Vol.	Volume
m_r	Mass of Refrigerant, (kg s^{-1})
ρ	Density, (kg m^{-3})
POE	Poly-Easter Oil
MO	Mineral Oil

Subscripts

Comp	Compressor
Disch	Discharge
Sup	Superheated
c	Condenser
Evap	Evaporator

References

[1] Montzka SA, Dutton GS, Yu P, Ray E, Portmann RW, Daniel JS, et al. An unexpected and persistent increase in global emissions of ozone-depleting CFC-11. Nature. 2018 May;557(7705):413-7. https://doi.org/10.1038/s41586-018-0106-2

[2] Yang Z, Wu X, Wang X, Tian T. Research on the flammable characteristics of fluoroethane (R161) and its binary blends. International Journal of Refrigeration. 2015 Aug;56:235-45. https://doi.org/10.1016/j.ijrefrig.2015.03.020

[3] Zhang N, Dai Y, Feng L, Li B. Study on environmentally friendly refrigerant R13I1/R152a as an alternative for R134a in automotive air conditioning system. Chinese Journal of Chemical Engineering. 2022 Apr;44:292-9. https://doi.org/10.1016/j.cjche.2021.02.028

[4] International Institute of Refrigeration, "29th Informatory Note on refrigeration technologies: The role of refrigeration in the global economy," Nov. 2015, Iir, no. 29, p. 16.

[5] United Nations Environment Programme, The Importance of Energy Efficiency in the Refrigeration and Heat Pump Sectors; 2018; Environment Programme, Briefing Note A, no. May, pp. 1-15.

[6] Gulzar O, Qayoum A, Gupta R. Photo-thermal characteristics of hybrid nanofluids based on Therminol-55 oil for concentrating solar collectors. Appl Nanosci. 2019 Jul;9(5):1133-43. https://doi.org/10.1007/s13204-018-0738-4

[7] Yu B, Ouyang H, Shi J, Guo Z, Chen J. Experimental evaluation of cycle performance for new-developed refrigerants in the electric vehicle heat pump systems. International Journal of Refrigeration. 2021 Sep;129:118-27. https://doi.org/10.1016/j.ijrefrig.2021.04.037

[8] Farhana K, Kadirgama K, Rahman MM, Noor MM, Ramasamy D, Samykano M, et al. Significance of alumina in nanofluid technology. J Therm Anal Calorim. 2019 Oct;138(2):1107-26. https://doi.org/10.1007/s10973-019-08305-6

[9] Jwo C, Jeng L, Teng T, Chang H. Effects of nanolubricant on performance of hydrocarbon refrigerant system. J Vac Sci Technol B. 2009;27(3):1473. https://doi.org/10.1116/1.3089373

[10] Stephen EN, Asirvatham LG, Kandasamy R, Solomon B, Kondru GS. Heat transfer performance of a compact loop heat pipe with alumina and silver nanofluid. J Therm Anal Calorim. 2019 Apr;136(1):211-22. https://doi.org/10.1007/s10973-018-7739-0

[11] Motevasel M, Solaimany Nazar AR, Jamialahmadi M. Experimental study on turbulent convective heat transfer of water-based nanofluids containing alumina, copper oxides and silicon carbide nanoparticles. J Therm Anal Calorim. 2019 Jan;135(1):133-43. https://doi.org/10.1007/s10973-018-7314-8

[12] Kugarajah V, OjhaAK, Hadem H, Dasgupta N, Mishra BN, Ranjand S,Dharmalingam S. Nanoparticles and nanofluids: Characteristics and behavior aspects, Food, Medical, and Environmental Applications of Nanomaterials, 2022; 41-71. https://doi.org/10.1016/B978-0-12-822858-6.00002-9

[13] I.-P. E. supported by A. Research, https://www.ashrae.org/technical-resources/ashrae-handbook. 2017.

[14] Ali B, Qayoum A, Saleem S, Mir FQ. Synthesis and characterization of high-quality multi layered graphene by electrochemical exfoliation of graphite. Res Eng Struct Mater. 2022; 8(3): 447-462. https://doi.org/10.17515/resm2022.384na0121

[15] Bhat AY, Qayoum A. Viscosity of CuO nanofluids: Experimental investigation and modelling with FFBP-ANN. Thermochimica Acta. 2022 Aug;714:179267. https://doi.org/10.1016/j.tca.2022.179267

[16] C. Delmastro, "https://www.iea.org/reports/cooling." 2020, [Online]. Available: https://www.iea.org/reports/cooling.

[17] Ali B, Qayoum A, Saleem S, Mir FQ. "Experimental investigation of Nanofluids for Heat pipes used in solar Photovoltaic Panels (Article in press)," *Journal of thermal engineering*, 2022.
[18] Gulzar O, Qayoum A, Gupta R. Experimental study on stability and rheological behaviour of hybrid Al2O3-TiO2 Therminol-55 nanofluids for concentrating solar collectors. Powder Technology. 2019 Jun;352:436-44. https://doi.org/10.1016/j.powtec.2019.04.060
[19] Gulzar O, Qayoum A, Gupta R. Experimental study on thermal conductivity of mono and hybrid Al 2 O 3 -TiO 2 nanofluids for concentrating solar collectors. Int J Energy Res. 2021 Mar 10;45(3):4370-84. https://doi.org/10.1002/er.6105
[20] Ali MKA, Xianjun H. Improving the tribological behavior of internal combustion engines via the addition of nanoparticles to engine oils. Nanotechnology Reviews. 2015 Jan 1;4(4):< Missing page number>. https://doi.org/10.1515/ntrev-2015-0031
[21] Mohanraj M, Jayaraj S, Muraleedharan C. Environment friendly alternatives to halogenated refrigerants-A review. International Journal of Greenhouse Gas Control. 2009 Jan;3(1):108-19. https://doi.org/10.1016/j.ijggc.2008.07.003
[22] Krishna Sabareesh R, Gobinath N, Sajith V, Das S, Sobhan C. Application of TiO2 nanoparticles as a lubricant-additive for vapor compression refrigeration systems - An experimental investigation. International Journal of Refrigeration. 2012 Nov;35(7):1989-96. https://doi.org/10.1016/j.ijrefrig.2012.07.002
[23] Adelekan D, Ohunakin O, Gill J, Atiba O, Okokpujie I, Atayero A. Experimental Investigation of a Vapour Compression Refrigeration System with 15nm TiO2-R600a Nano-Refrigerant as the Working Fluid. Procedia Manufacturing. 2019;35:1222-7. https://doi.org/10.1016/j.promfg.2019.06.079
[24] Marcucci Pico DF, da Silva LRR, Schneider PS, Bandarra Filho EP. Performance evaluation of diamond nanolubricants applied to a refrigeration system. International Journal of Refrigeration. 2019 Apr;100:104-12. https://doi.org/10.1016/j.ijrefrig.2018.12.009
[25] Babarinde T, Akinlabi S, Madyira D. Energy performance evaluation of R600a/MWCNT-nanolubricant as a drop-in replacement for R134a in household refrigerator system. Energy Reports. 2020 Feb;6:639-47. https://doi.org/10.1016/j.egyr.2019.11.132
[26] Soltani F, Toghraie D, Karimipour A. Experimental measurements of thermal conductivity of engine oil-based hybrid and mono nanofluids with tungsten oxide (WO3) and MWCNTs inclusions. Powder Technology. 2020 Jun;371:37-44. https://doi.org/10.1016/j.powtec.2020.05.059
[27] Ruhani B, Barnoon P, Toghraie D. Statistical investigation for developing a new model for rheological behavior of Silica-ethylene glycol/Water hybrid Newtonian nanofluid using experimental data. Physica A: Statistical Mechanics and its Applications. 2019 Jul;525:616-27. https://doi.org/10.1016/j.physa.2019.03.119
[28] Boroomandpour A, Toghraie D, Hashemian M. A comprehensive experimental investigation of thermal conductivity of a ternary hybrid nanofluid containing MWCNTs- titania-zinc oxide/water-ethylene glycol (80:20) as well as binary and mono nanofluids. Synthetic Metals. 2020 Oct;268:116501. https://doi.org/10.1016/j.synthmet.2020.116501
[29] He W, Ruhani B, Toghraie D, Izadpanahi N, Esfahani NN, Karimipour A, et al. Using of Artificial Neural Networks (ANNs) to predict the thermal conductivity of Zinc Oxide-Silver (50%-50%)/Water hybrid Newtonian nanofluid. International Communications in Heat and Mass Transfer. 2020 Jul;116:104645. https://doi.org/10.1016/j.icheatmasstransfer.2020.104645
[30] Yan S, Toghraie D, Abdulkareem LA, Alizadeh A, Barnoon P, Afrand M. The rheological behavior of MWCNTs-ZnO/Water-Ethylene glycol hybrid non-Newtonian nanofluid by

using of an experimental investigation. Journal of Materials Research and Technology. 2020 Jul;9(4):8401-6. https://doi.org/10.1016/j.jmrt.2020.05.018
[31] Tian S, Arshad NI, Toghraie D, Eftekhari SA, Hekmatifar M. Using perceptron feed-forward Artificial Neural Network (ANN) for predicting the thermal conductivity of graphene oxide-Al2O3/water-ethylene glycol hybrid nanofluid. Case Studies in Thermal Engineering. 2021 Aug;26:101055. https://doi.org/10.1016/j.csite.2021.101055
[32] Kavusi H, Toghraie D. A comprehensive study of the performance of a heat pipe by using of various nanofluids. Advanced Powder Technology. 2017 Nov;28(11):3074-84. https://doi.org/10.1016/j.apt.2017.09.022
[33] Adelekan DS, Ohunakin OS, Babarinde TO, Odunfa MK, Leramo RO, Oyedepo SO, et al. Experimental performance of LPG refrigerant charges with varied concentration of TiO 2 nano-lubricants in a domestic refrigerator. Case Studies in Thermal Engineering. 2017 Mar;9:55-61. https://doi.org/10.1016/j.csite.2016.12.002
[34] Ohunakin OS, Adelekan DS, Gill J, Atayero AA, Atiba OE, Okokpujie IP, et al. Performance of a hydrocarbon driven domestic refrigerator based on varying concentration of SiO2 nano-lubricant. International Journal of Refrigeration. 2018 Oct;94:59-70. https://doi.org/10.1016/j.ijrefrig.2018.07.022
[35] Lou J, Zhang H, Wang R. Experimental investigation of graphite nanolubricant used in a domestic refrigerator. Advances in Mechanical Engineering. 2015 Jan 1;7(2):168781401557101. https://doi.org/10.1177/1687814015571011
[36] Kumar RR, Sridhar K, Narasimha M. Heat transfer enhancement in domestic refrigerator using. International Journal of Computational Engineering Research, 2013; 3: 42-50.
[37] Jatinder G, Ohunakin OS, Adelekan DS, Atiba OE, Daniel AB, Singh J, et al. Performance of a domestic refrigerator using selected hydrocarbon working fluids and TiO2-MO nanolubricant. Applied Thermal Engineering. 2019 Sep;160:114004. https://doi.org/10.1016/j.applthermaleng.2019.114004
[38] Yang S, Cui X, Zhou Y, Chen C. Study on the effect of graphene nanosheets refrigerant oil on domestic refrigerator performance. International Journal of Refrigeration. 2020 Feb;110:187-95. https://doi.org/10.1016/j.ijrefrig.2019.11.008
[39] Babarinde T, Akinlabi S, Madyira D, Ekundayo F. Enhancing the energy efficiency of vapour compression refrigerator system using R600a with graphene nanolubricant. Energy Reports. 2020 Feb;6:1-10. https://doi.org/10.1016/j.egyr.2019.11.031
[40] Santhana Krishnan R, Arulprakasajothi M, Logesh K, Dilip Raja N, Rajendra M. Analysis and Feasibilty of Nano-Lubricant in Vapour Compression Refrigeration System. Materials Today: Proceedings. 2018;5(9):20580-7. https://doi.org/10.1016/j.matpr.2018.06.437
[41] Alawi OA, Sidik NAC. Influence of particle concentration and temperature on the thermophysical properties of CuO/R134a nanorefrigerant. International Communications in Heat and Mass Transfer. 2014 Nov;58:79-84. https://doi.org/10.1016/j.icheatmasstransfer.2014.08.038
[42] Kosmadakis G, Neofytou P. Investigating the effect of nanorefrigerants on a heat pump performance and cost-effectiveness. Thermal Science and Engineering Progress. 2019 Oct;13:100371. https://doi.org/10.1016/j.tsep.2019.100371
[43] Y. I. C. Bock Choon Pak, Hydrodynamic and Heat Transfer Study of Dispersed Fluids With Submicron Metallic Oxide. Experimental Heat Transfer : A Journal of , Thermal Energy Transport , Storage , and Conversion, no. January 2013, pp. 37-41, 2013.
[44] M. J. Clerk, Maxwell. 2010.
[45] Toghraie D, Chaharsoghi VA, Afrand M. Measurement of thermal conductivity of ZnO-TiO2/EG hybrid nanofluid. J Therm Anal Calorim. 2016 Jul;125(1):527-35. https://doi.org/10.1007/s10973-016-5436-4
[46] A. Einstein, Viscosity. 1905.

Research on Engineering Structures & Materials
journal homepage: http://www.jresm.org
Research Group

Research Article

Accuracy evaluation of the output of the spindle assembly of the NT-250I lathe machine

Sherali Yakhshiev*[a], Ilkhom Egamberdiev[b], Akmal Mamadiyarov[c], Khisrav Ashurov[d], Nurbek Khamroev[e]

Department of Mechanical Engineering, Navoi State Mining Institute, Uzbekistan

Article Info

Article history:

Received 14 Sep 2022
Revised 31 Oct 2022
Accepted 01 Nov 2022

Keywords:

Mathematical model; Spindle unit; Shaft; Bearing; Vibration; Lathe

Abstract

The article is devoted to the analysis of the dynamic properties of the spindle assembly. We study elastic properties of supports and mathematical modeling of it. We calculated contact and elastic deformations in roller bearings. We also consider to simulation of contact-elastic displacements of a high-precision roller bearing. Based on a mathematical model, it is shown that the amplitude of oscillations at the spindle speed significantly affects to the quality of work. Due to the non-linearity of the bending coefficients and periodic changes of parameters we show non-linear damping of the rolling bearing.

1. Introduction

The spindle assembly consists of a spindle, supports, and a driving element, that they are usually enclosed in a separate housing. In fact, the spindle unit is a rotary system that has own design features. The design of spindle unit is determined primarily by the scope or manufacturing areas.

The design of the spindle is determined by the following features: a) the size of the spindle, the distance between the supports, and the presence of hole in it for passing materials or other purposes; b) driving parts (gears, pulleys) and their location on the spindle; c) design of supports and type of bearings; d) the method of fixture to the workpiece or tool, that affects the design of the front end of the spindle. Dissipative characteristics of the spindle assembly and frequency response (AFC) of the spindle assembly is determined by following parameters: spindle diameter/length, the distance between the supports, damping parameters and inertial and intrinsic rigidity

Most papers [1,2,3,4,5,6] analyzed influence of the designing parameters of control system for the dynamic quality. The designs of spindle assemblies and their typical calculations are given in these papers [7,8,9,10]. Scientific works on spindle rolling bearings is done by following authors such as: V.S. Balasanyan, V.B. Balmont, V.V. Bushuev. A. Jones, T. Harris, Z.M. Levina, A.M. Figatner, V.E. Pusha A.V. and many other scientists [11, 12, 13,14,15]

A number of works are devoted to the study of the rigidity of bearings: Atstupinas R.V. [16], Baranova I.A. [17], Zhuravleva V.F. [18], Kovaleva M.P. [19] and others. The evaluation of bearing stiffness without technological errors are presented in works [17], in other papers the condition of contact of all balls with rings are carried out [13,15,16], the possibility of incomplete ball contact with rings is taken into account. rings. The elastic properties of ball

*Corresponding author: join_g@mail.ru
[a] orcid.org/0000-0003-3259-9735; [b] orcid.org/0000-0002-7549-2156; [c] orcid.org/0000-0002-8658-6166; [d] orcid.org/0000-0003-0245-3989; [e] orcid.org/0000-0002-0471-5009
DOI: http://dx.doi.org/10.17515/resm2022.523me0914

bearings, as a factor that affects on accuracy of machines, were the subject of research in the works of Novikov L.Z. [18], Kelzon A.S. [19].

According to the majority of researchers, the main sources of noise and vibration of the control system on rolling bearings are the cyclic change in the compliance (stiffness) of the bearing under load and vibration that caused by geometric errors in bearing parts [36]. The elastic properties of bearing assemblies have a significant impact on the spectrum of natural vibration frequencies of mechanical systems.

The accuracy of the spindle assembly is one of the most important indicators of machine accuracy, that has a direct impact on the parameters of the workpiece. Methods for controlling the accuracy of spindle assemblies are in accordance with GOST 22267-76, as well as standards of accuracy and rigidity for individual types of machine tools are provided for a set of checks, the obtained results make it possible to evaluate only the geometric parameters of the machine. Meanwhile, it is known that such checks are insufficient for a reasonable conclusion about the output accuracy of the machine. So, exaggeration of the radial runout of the spindle may not degrade the accuracy of processing.

In this regard, it is advisable to develop such a calculation system that would directly relate the errors of the elements of the spindle assembly with the errors of the machined surfaces. In this case, the spindle assembly should be considered as part of the shaping system of the machine, and all its links and their relative movements (except for the elements of the spindle assembly) should be considered as absolutely accurate.

Here, the problem is solved on the example of analyzing the influence of spindle supports accuracy on a set of machine output parameters such as: geometric accuracy, deviations in the shape, position and dimensions of the machined surface. The purpose of the analysis is to develop requirements for the accuracy of support bearings, as well as to establish the relationship between the input and output errors of the machine for typical turning schemes. A mathematical model of the accuracy of the spindle assembly has been developed, which takes into account the geometric and static errors of the support elements. The model is based on formulas that has input errors, but the spindle assembly errors are taken equal to zero. While constructing a calculation model, the spindle assembly supports are represented by a system of springs. Then six components of the spindle coordinate system position error can be obtained from six static equilibrium conditions, which, in accordance with [20], have a form;

$$C_{\Delta} = P \tag{1}$$

where C is a 6x6 symmetrical stiffness matrix; A is the I vector of the generalized error. $\Delta = (\delta_x, \delta_y, \delta_z, \alpha, \beta, \gamma)^{\tau}$; P - generalized force vector; $P - (P_x, P_y, P_z, M_x, M_y, M_z)^{r}$.

The forces on the rolling elements under the radial load of the bearing are unevenly distributed (Fig. 1). In the perception of the load, only rolling elements located on an arc not exceeding 180^0 (loaded zone). The most loaded is a ball or roller located in the direction of the force on the bearing.

The problem of distribution of forces between rolling bodies is statically indeterminate. Rolling bodies located symmetrically with respect to the plane of action of the force are equally loaded. Let us denote the force on the most loaded rolling body through F_0; on a body located in relation to the load plane at an angle γ (equal to the angular step), - through F_1, at an angle 2γ - through F_2, at an angle $n\gamma$ - through F_n, where n- half of the rolling elements in the loaded area.

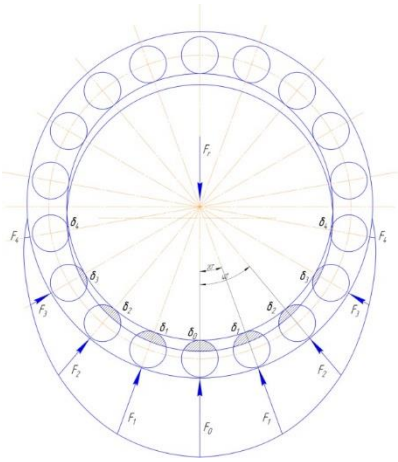

Fig. 1 Scheme of forces distribution on the bearing

2. Calculation and Analysis

We assume for simplicity that the rolling elements are located symmetrically with respect to the load plane.

Equilibrium condition of the inner ring loaded with a radial force is F_r:

$$F_r = F_0 + 2F_1 \cos\gamma + 2\,F_2 \cos 2\gamma \ldots + 2F_n \cos n\gamma \tag{2}$$

In addition to the static equation, we use the displacement equation. Neglecting the bending of the rings and assuming no radial clearance in the bearing, it can be assumed that the convergence of the rolling elements and the rings is equal to the corresponding projections of the total displacement of the ring δ_0,

$$\delta_1 = \delta_0 \cos\gamma, \delta_2 = \delta_0 \cos 2\gamma\,, \delta_i = \delta_0 \cos i\gamma; \tag{3}$$

where *i*- rolling element number.

For ball bearings, the relationship between δ balls and the compressive load F, as follows from the problem of elasticity theory about the compression of elastic bodies,

$$\delta = cF^{\frac{2}{3}} \tag{4}$$

where c – proportionality factor.

The non-linear nature of the dependence is explained by the growth of the contact area with increasing force. Expressing in the equations of displacements the approach in terms of forces, one can write:

$$F_1 = F_0 cos^{3/2}\gamma,\ F_2 = F_0 cos^{3/2} 2\gamma, \ldots, F_i = F_0 cos^{3/2} i\gamma \tag{5}$$

Substituting these dependencies into the equilibrium equation, we obtain

$$F_r = F_0 \left(1 + 2\sum_1^n cos^{5/2} i\gamma\right) \tag{6}$$

From here we determine F_0, and simultaneously multiply the numerator and denominator of the right-hand side by z and introduce the notation

$$k = \frac{z}{1+2\sum_1^n cos^{5/2} i\gamma} \quad (7)$$

Then

$$F_0 = \frac{k \cdot F_r}{z} \quad (8)$$

where z – total number of rolling elements and for bearings with number of balls $z = 10 \ldots 20$ $k = 4.37 \pm 0.01$.

The bearings operated under normal conditions with clearance, balls with an arc is less than 1800, and the most loaded ball is compressed with a force greater than about 10%. The single-row ball bearings is taken $k = 5$ and $F_0 = 5Fr/z$.

In spherical double-row ball bearings, taking into account some uneven distribution of forces between the rows, the force on the most loaded ball is estimated $F_0 = 6Fr/z(cos\alpha)$, where α- angle of inclination of the contact line, z- number of balls in both rows.

The problem is also solved for roller bearings, only the relationship between the convergence of rollers, rings and the compressive load assumed to be linear $\delta = c1F$ (where c1–coefficient).

Similar to ball bearings for roller bearings, the highest force is $F_0 = kFr/z$. For roller bearings with number of rollers $z = 10 \ldots 20, k = 4$. Taking into account the influence of the gap for the calculation, it was taken $k = 4{,}6$, and $k = 5{,}2$ for double row roller bearings. It is considering the uneven distribution of forces between the rows [3, 4].

In angular contact bearings under radial load, the forces on balls and rollers are greater than in radial bearings in relation to $1/cos\alpha$, where α is the contact angle of balls or rollers and rings.

The load distribution between the rolling elements can be somewhat leveled by elastic deformations of the housings. The hole should take the form of an elliptical extended cylinder in the direction of the load. This is possible by designing axle boxes of railway rolling stock.

Axial force with precise manufacturing and the absence of mutual misalignment of the rings is distributed evenly between the rolling elements.

2.1 Calculation Without Taking Into Account the Influence of the Centrifugal Forces of the Rollers

Diameter of outdoor treadmill

$$D_{\text{н}} = D_{\text{в}} + 2d \quad (9)$$

where: $D_{\text{в}}$ - diameter of the inner treadmill

d- roller diameter

Reduced curvature of internal contact

$$\sum \rho_{\text{в}} = \frac{2}{d} + \frac{2}{D_{\text{в}}} \quad (10)$$

Outdoor contact

$$\sum \rho_{\text{н}} = \frac{2}{d} + \frac{2}{D_{\text{н}}} \tag{11}$$

Rolling speed in contacts

$$(U_a + U_b) = \frac{\pi n}{60} \cdot D_{\text{в}} \frac{D_{\text{в}}+2d}{D_{\text{в}}+d} \tag{12}$$

U_α- speed of the outer part

U_b is the speed of the inside

n - speed

Zero approximation for force in contacts per unit of roller contact length

$$\overrightarrow{P_0} = \frac{\delta_\sum \cdot 10^8}{61 \cdot [14{,}832 - lg(\sum \rho_{\text{в}} + \sum \rho_{\text{н}})]} \tag{13}$$

Thicknesses of lubricating layers in contacts

$$h_{\text{в(н)}i} = 0.796 \frac{[\mu_0 \cdot (U_a + U_b)]^{0.75} \cdot \alpha^{0.6}}{[\rho_{\text{в(н)}_i}]^{0.15} \cdot [\sum \rho_{\text{в(н)}}]^{0.4}} = \frac{\text{B}_{\text{в(н)}i}}{[\rho_{\text{в(н)}i}]^{0.15}} \tag{14}$$

where: μ_0- lubrication factor

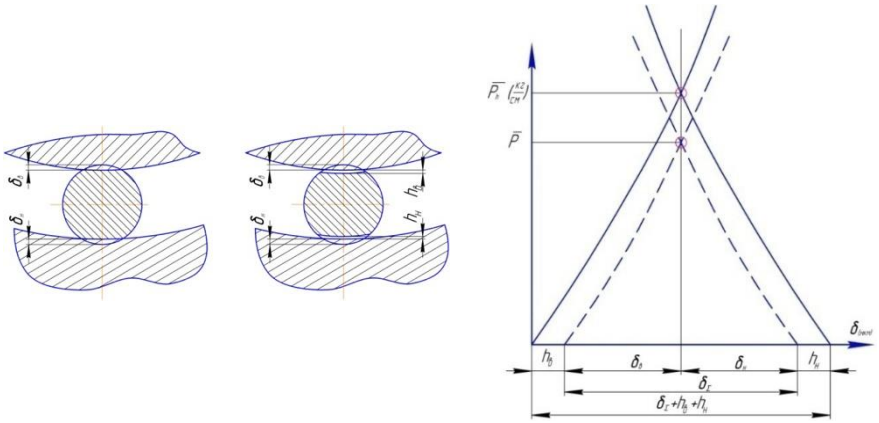

Fig. 1 Forces in contacts without taking into account the centrifugal forces of the rollers

$$\overrightarrow{P_0} = \frac{(\delta_\sum + h_{\text{в}_{i-1}} + h_{\text{н}_{i-1}}) \cdot 10^8}{61 \cdot [15.7 - lg((\overrightarrow{P_{i-1}}) \sum \rho_{\text{в}} + \sum \rho_{\text{н}})]} \tag{15}$$

Here $\delta_\sum + h_{\text{в}_{i-1}} + h_{\text{н}_{i-1}}$ - total tightness on the roller, it is considered that the influence of the wedging action of the lubricating layer in the contacts. The forces are calculated using the inertia method according to (15) with simultaneous refinement of the layer thicknesses (14) $i = 1.2.3.4 \ldots$ to $\frac{P_i - P_{i-1}}{P_i} \leq 0{,}00001$

2.2. Calculation Taking Into Account the Influence of the Centrifugal Forces of the Rollers

Centrifugal force of the roller per unit contact length is

$$\vec{C} = \frac{0{,}855}{10^8} \cdot d^2 \cdot n^2 \frac{l}{l_p}\left(\frac{D_в^2}{D_в + d}\right) \tag{16}$$

where:

l - roller length

l_p - contact length

First, the calculation is carried out assuming that there is no contact with the inner ring.

Force on the outer ring: $\overrightarrow{P_н} = \vec{C}$

Contact deformation with outer ring:

$$\delta_{н_c} = \frac{61}{10^8} \cdot \vec{C} \cdot \left[7{,}85 - \lg\left(\vec{C} \cdot \sum \rho_н\right)\right] \tag{17}$$

Thickness of the lubricating layer in contact with the outer ring:

$$h_{н_c} = 0.796 \frac{[\mu_0 \cdot (U_a + U_b)]^{0.75} \cdot \alpha^{0.6}}{[\vec{C}]^{0.15} \cdot [\sum \rho_н]^{0.4}} = \frac{B_н}{[\vec{C}]^{0.15}} \tag{18}$$

If $(\delta_{н_c} + h_{н_c}) \geq \delta_{\sum}$ then there is really no contact with the inner ring and the durability of the outer ring, and therefore the bearing.

$$H_н = \frac{10^7}{60 \cdot i_н \cdot n} \cdot \left(\frac{\overline{P_{\delta н}}}{\bar{C}}\right)^{\frac{10}{3}} \tag{19}$$

It is clear that the calculation of the bearing life in this case is formal, because in the absence of contact with the inner ring, the normal operation of the bearing is impossible.

If

$$\left(\delta_{н_c} + h_{н_c}\right) \prec \delta_{\sum} \tag{20}$$

Then the roller is in contact with both rings and the calculation is carried out in the following sequence.

We set the force in contact of the roller with the outer ring

$$\bar{P}_н = \bar{P} + 0{,}35 \cdot \bar{C} \tag{21}$$

Then the zero approximation for the force in contact with the inner ring

$$\bar{P}_н = \bar{P} + 0{,}35 \cdot \bar{C} \tag{22}$$

Contact deformation with outer ring:

$$\delta_{н_1} = \frac{61}{10^8} \cdot \overline{P_{н1}} \cdot [7{,}85 - \lg(\overline{P_{н1}} \cdot \sum \rho_н)] \tag{23}$$

Layer thicknesses in contact

$$h_н = \frac{B_н}{[\bar{P}_{н_c}]^{0.15}} \qquad h_{в_{10}} = \frac{B_в}{[\bar{P}_{в_{10}}]^{0.15}} \tag{23}$$

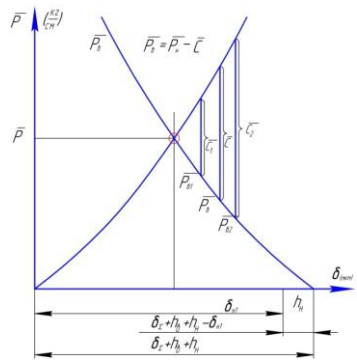

Fig. 3 Force approximation

The next approximation for the force in contact with the inner ring is determined by iteration over

$$\bar{P}_{в1_i}=\frac{\delta_{\sum}+h_{в1_{i-1}}+h_{н1}-\delta_{н1}}{\frac{61}{10^8}\cdot[7{,}85-lg(\overline{P_{в1_{i-1}}}\cdot\sum\rho_в)]}\delta_{н1} \tag{25}$$

Here $i = 1.2.3.4\ldots$ to $\frac{P_i-P_{i-1}}{P_i}\leq 0{,}00001$. The value of the centrifugal force $C1$, corresponded to the accepted force $P_{н1}$, in contact of the roller with the outer ring

$$\bar{C} = \bar{P}_{н1} - \bar{P}_{в1i} \tag{26}$$

We set the following value of the force in contact of the roller with the outer ring

$$\bar{P}_{н2} = \bar{P} + 0{,}45 \cdot \bar{C} \tag{27}$$

We repeat the calculation once again with followings: Рв20, δн2, hн2, hн20, Рв2i, C2. The next value of the force in contact of the roller with the outer ring is determined by the formula

$$\overline{P_{н3}} = \bar{P}_{н1} + (\bar{P}_{н2} - \bar{P}_{н1}) \cdot \frac{\bar{C}-\bar{C}_1}{\bar{C}_2-\bar{C}_1} \tag{28}$$

Further, the calculation is carried out by the iteration method zero approximation for the force in contact with the inner ring

$$\bar{P}_{в_{30}} = \bar{P}_{н3} - \bar{C} \tag{29}$$

Contact deformation with outer ring:

$$\delta_{н_3} = \frac{61}{10^8} \cdot \overline{P_{н3}} \cdot [7{,}85 - \lg(\overline{P_{н3}} \cdot \sum\rho_н)] \tag{30}$$

Layer thicknesses in contact

$$h_{н3} = \frac{B_н}{[\bar{P}_{н_3}]^{0.15}} \qquad h_{в_{30}} = \frac{B_н}{[\bar{P}_{в_{30}}]^{0.15}} \tag{31}$$

The iteration of the force in contact of the roller with the inner ring is determined by the iteration method

$$\bar{P}_{в3i}=\frac{\delta_{\Sigma}+h_{в3_{i-1}}+h_{н3}-\delta_{н3}}{\frac{61}{10^8}[7{,}85-lg(\overline{P_{в3_{i-1}}}\cdot\Sigma\rho_{в})]}\delta_{н1} \quad (32)$$

Here $i = 1.2.3.4 \ldots$ to $\frac{P_i-P_{i-1}}{P_i} \leq 0{,}00001$

The value of the centrifugal force Cv3, corresponding to the accepted force Pnv3, in contact of the roller with the outer ring

$$\overline{C_3} = \bar{P}_{н3} - \bar{P}_{в3i} \quad (33)$$

The iteration of the force in contact of the roller with the outer ring is determined by the formula

$$\overline{P_{нi}} = \overline{P}_{н1} + (\overline{P}_{нi-1} - \overline{P}_{н1}) \cdot \frac{\bar{C}-\bar{C}_1}{\bar{C}_{i-1}-\bar{C}_1} \quad (34)$$

After determining the forces in the contacts, the chipping durability is determined taking into account centrifugal forces.

Contact stresses

$$\sigma_{в(н)} = 610 \cdot \sqrt{\overline{P}_{в(н)} \cdot \Sigma\rho_{в(н)}} \quad (35)$$

Contact area half-width

$$b_{в(н)} = \frac{104}{10^5} \cdot \sqrt{\frac{\overline{P}_{в(н)}}{\Sigma\rho_{в(н)}}} \quad (36)$$

Calculation of contact deformations of the roller.

Fig. 4 shows the diagram of roller bearing position relative to the outer and inner races. On Fig. 4 δн and δв are the total contact deformations of the roller, respectively, between the outer and inner races.

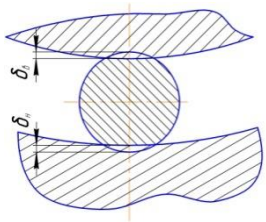

Fig. 2 The total contact strain between the roller and the outer and inner races

Diameter of outdoor treadmill:

$$D_{н} = D_{в}+2d \quad (37)$$

Reduced curvature of internal contact:

$$\Sigma\rho_{в} = \frac{2}{d} + \frac{2}{D_{в}} \quad (38)$$

Outdoor contact:

$$\sum\rho_{н} = \frac{2}{d} + \frac{2}{D_{н}} \quad (39)$$

Total contact strain between roller and outer and inner race.

$$\delta_{\Sigma} = \frac{F_0 \cdot 61[14{,}832 - lg(\sum\rho_{в} + \sum\rho_{н})]}{10^8} \quad (40)$$

3. Results of Calculation

The calculation results of a high-precision roller bearing brand 2-697920L2 installed in the spindle unit of a lathe model NT-250I that is shown in table 1, with the following data d =14 mm, Dв=110 mm, z=20. Since the bearing is double, then z is taken equal to 40.

Table 1. Calculation results

Bearing load P, kg	Force acting on the most loaded roller, F_0 H	Contact deformation δ_{Σ}, mkm
400	1019,2	4,3
300	764,4	3,2
200	509,6	2,1
100	254,8	1

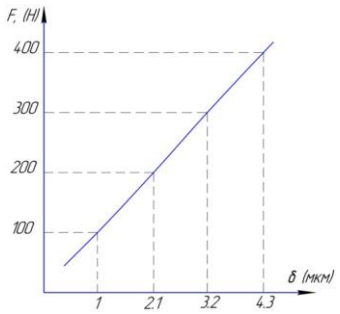

Fig. 3 Graph of the dependence of the contact deformations of the roller depending on its loading

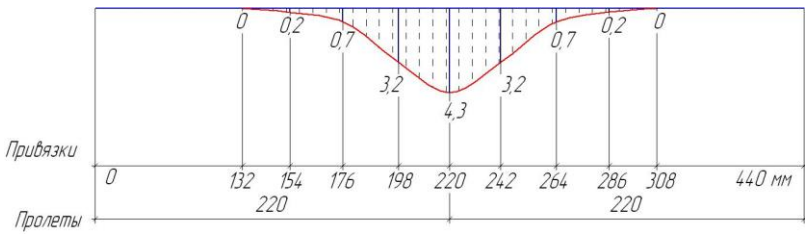

Fig. 4 Graph of the distribution of contact deformations on the outer race of the bearing

We make a static calculation of a beam with one intermediate support under the action of concentrated forces acting on the outer race of the bearing, located in a vertical plane.

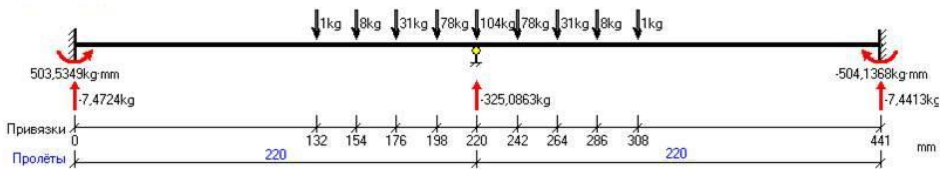

Fig. 5 Geometric diagram of a beam with fixed loads

Border conditions

The boundary conditions at each edge can be:

· hard termination;

· hinge;

· free edge.

Relationships between Deflection, Section Rotation, and M and Q plots. Very interesting relationships are known from the course "Strength of Materials", namely [21,22]:

· the angle of rotation of the section U is the derivative of the vertical displacement w

· the bending moment in section M is the derivative of the angle of rotation U multiplied by EJx;

· shear force in section Q is the derivative of the bending moment M;

· distributed load q is the derivative of the shear force Q

Thus, there are equalities:

$$U(z) = w'(z); \tag{41}$$

$$M(z) = EJx \cdot U'(z); \tag{42}$$

$$Q(z) = M'(z); \tag{43}$$

$$q(z) = Q'(z) \tag{44}$$

When constructing diagrams, we will be guided by formulas (40-43).

The beam is statically indeterminate: the unknown reactions of the intermediate supports and force factors at the ends of the beam cannot be found from the equations of statics. To solve the problem, the method of initial parameters was applied. The differential equation of the bent axis of the beam in this case has the form:

$$EJ_x w(z) = EJ_x w_0 + EJ_x \theta_0 z + M_0 \frac{z^2}{2} + Q_0 \frac{z^3}{6} + \sum_{x_{k<z}} M_k \frac{(z-x_k)^2}{2} + \sum_{x_{k<z}} F_k \frac{(z-x_k)^3}{6} + \sum_{x_k^n<z} q_k \frac{(z-x_k^n)^4}{24} - \sum_{x_k^k<z} q_k \frac{(z-x_k^k)^4}{24} \tag{45}$$

where:

$EJ_x w_0$ - deflection in the left section (up to a factor EJ_x);

$EJ_x Q_0$ - angle of rotation of the left section (also up to a factor EJ_x);

M_0 и Q_0 - bending moment and shear force in the left section.

All these parameters (they are called initial) are unknown. In each of the sums, the summation is carried out over all force factors located to the left of the current section. The second sum (concentrated forces Fk) takes into account the unknown reactions of the supports R1, R2, ... Thus, in equation (45) there are n+4 unknowns, where n is the number of intermediate supports. If all these unknowns are found, then it will be possible to construct a displacement diagram using formula (45) and other diagrams using derivatives of (45), which, by (41-43), given rotation angles:

$$EJ_x\theta(z) = EJ_x\theta_0 + M_0 z + Q_0\frac{z^2}{2} + \sum_{x_k<z} M_k(z-x_k) + \sum_{x_k<z} F_k\frac{(z-x_k)^2}{2} + \sum_{x_k^n<z} q_k\frac{(z-x_k^n)^3}{6} - \sum_{x_k^k<z} q_k\frac{(z-x_k^k)^3}{6} \quad (46)$$

bending moments:

$$M(z) = M_0 + Q_0 z + \sum_{x_k<z} M_k + \sum_{x_k<z} F_k(z-x_k) + \sum_{x_k^n} q_k\frac{(z-x_k^n)^2}{2} - \sum_{x_k^k} q_k\frac{(z-x_k^k)^2}{2} \quad (47)$$

cutting forces:

$$Q(z) = Q_0 + \sum_{x_k<z} F_k + \sum_{x_k^n<z} q_k(z-x_k^n) - \sum_{x_k^k<z} q_k(z-x_k^k) \quad (48)$$

To find these n + 4 unknowns, there are the same number of equations:

- under each support, the displacement is zero - only n equations of the form (45) at those points where the supports are located;
- 2 of any parameters on each edge of the beam are equal to zero - 4 equations in total.
- Depending on the type of boundary conditions will be equal to zero:
- in rigid embedment - movement and angle of rotation;
- when hinged - displacement and bending moment;
- at the free edge - bending moment and shear force.

Here the equation n+4 = 3+4 = 7 are compiled with 7 unknowns. We compiled and solved this system of equations using the Gaussian method with the choice of the leading element for each column.

After compiling and solving the system of equations described in the previous section and calculating all the necessary data for formulas (45-48), we plot displacements, rotation angles, bending moments and shear forces, while the EJx multiplier is calculated depending on the current element assortment. Depend on this multiplier, as can be seen from equations (45-48), only displacements, that is, deflections and angles of rotation.

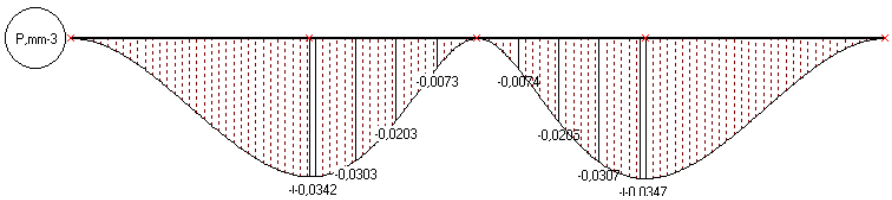

Fig. 8 Diagram of rotation angles [deg-2]

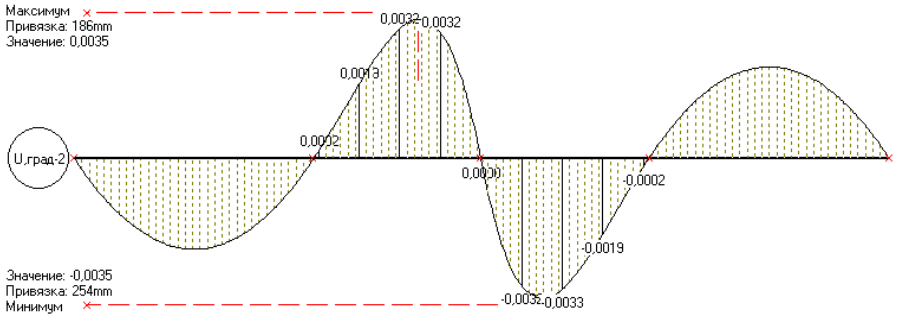

Fig. 9 Plot of bending moments [kgmm]

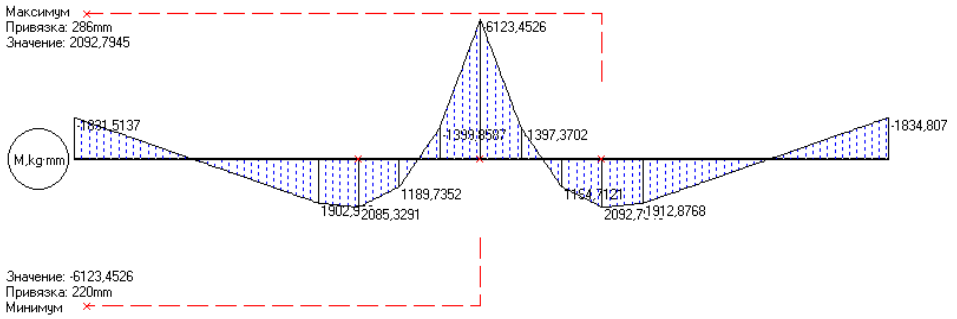

Fig. 10 Diagram of shear forces [kg]

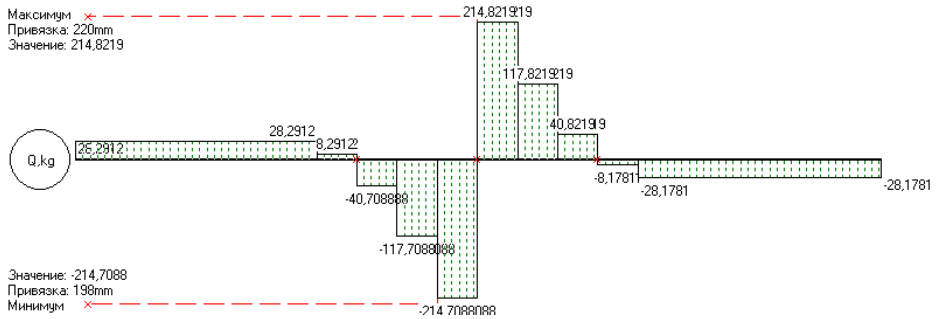

Fig. 11 Obtained results in different values

3.1 Calculation Results

Item characteristics:

Sort: Stripe 7x77

Mass 1 m.p. = 4,21 kg

Moment of inertia, Jx = 712,0000 sm4

Moment of resistance, Wx = 102,0000 sm3

Static half-section moment, Sx = 58,4000 sm3

Steel brand – SHX15 GOST 801-78

Design steel resistance, Ry = 230 MPa

Design shear strength of steel, Rs = 0,58·Ry = 133,40 MPa

Relative deflection - 1/250 span

Elastic modulus, E = 211000 MPa

Verification of strength and stiffness conditions:

Stresses in the beam: normal = Mmax / Wx = 0,5887 < Ry = 230 MPa

tangent = Qmax·Sx / (Jx·tст) = 3,1417 < Rs = 0,58·Ry = 133,4 MPa

Maximum deflection (with safety factor) = 0.0347 mm-3 which is 1/6373316 of the maximum span of 221 mm.

Thus, the total displacement of a roller bearing is the sum of the contact deformations of the rollers and the elastic deformations of the outer race of the bearing. The addition is made graphically, by superimposing on each other diagrams of contact and elastic deformations occurring in the bearing. At the same time, at the point of the smallest elastic deformation of the outer cage, the largest contact deformations of the rollers are observed.

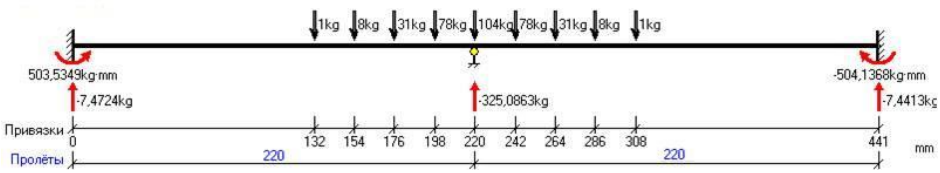

Fig. 12 Reaming the outer race of a bearing with specified loads

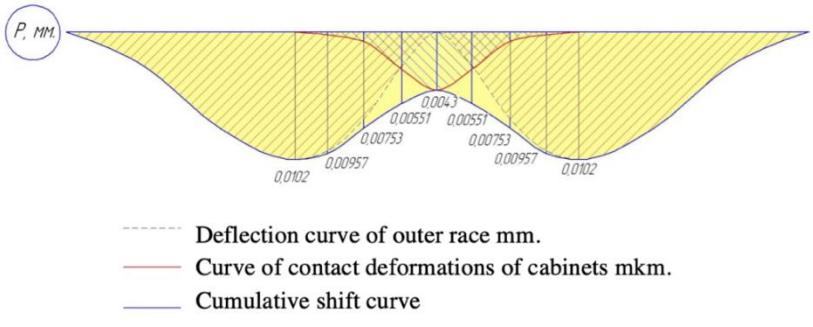

Fig. 13 Diagram of total displacements, mm

4. Numerical Simulation Results and Discussions

The APM FEM system is a tool integrated into KOMPAS-3D for the preparation and subsequent finite element analysis of a three-dimensional solid model (parts or assemblies).

Preparation of a geometric 3D model and setting the material is carried out by means of the KOMPAS-3D system. With APM FEM, you can apply various types of loads, specify boundary conditions, create a finite element mesh, and perform calculations. In this case, the procedure for generating finite elements is carried out automatically.

At the bottom of the dialog is a table of coefficients used in the calculation. Each material can be given a specific set of coefficients. More detailed information about the coefficients can be found in the documentation for the system APM Structure 3D.

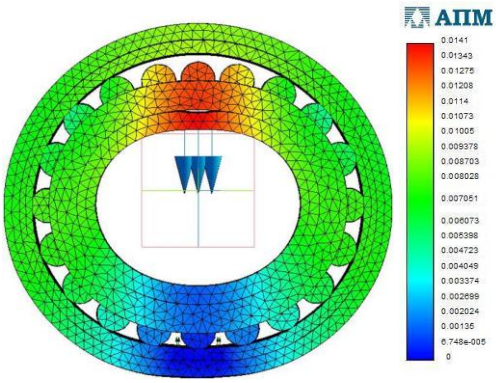

Fig. 14 Static calculation graph

Table 2. Material name: Tube 77x7 Steel SHX15 GOST 800-78

Compressive yield strength [MPa]	1670
Young's modulus [MPa]	211000
Poisson's ratio	0.3
Density [kg/m^3]	7812
Thermal expansion coefficient [1/C]	0.000151
Thermal conductivity coefficient [W/(mK)]	40
Compressive strength [MPa]	410
Fatigue limit (n) [MPa]	209
Fatigue limit (k) [MPa]	139
Name	Meaning
Model weight [kg]	6.645652
Model center of gravity [m]	(-0.002646 ; 0.000105 ; 0)
Moments of inertia of the model relative to the center of mass [kg*m^2]	(0.004798 ; 0.011922 ; 0.011956)
Reaction moment relative to the center of mass [N*m]	(0.268123 ; -0.327184 ; -3.588786)
Total reaction of supports [N]	(-0 ; 3923.000135 ; -0)
Absolute reaction value [N]	3923.000135
Absolute torque value [Nm]	3.61363

Table 3. Static calculation results

Name	Type	Minimum value	Maximum value
Total linear displacement	USUM [mm]	0	0.0141

Reshetov D.N. put forward the hypothesis that the hole should take the form of an elliptical cylinder, elongated in the direction of the load. However, no specific form was proposed. We calculated the shape of the hole. The geometry of which was designed taking into

account the deformation of the bearing. The hole must take the form of an elliptical cylinder, elongated in the direction of the load [7, 8].

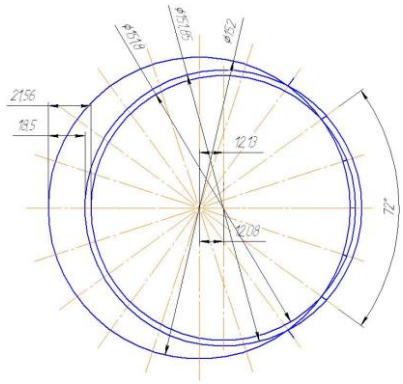

Fig. 15 Suggested hole shape

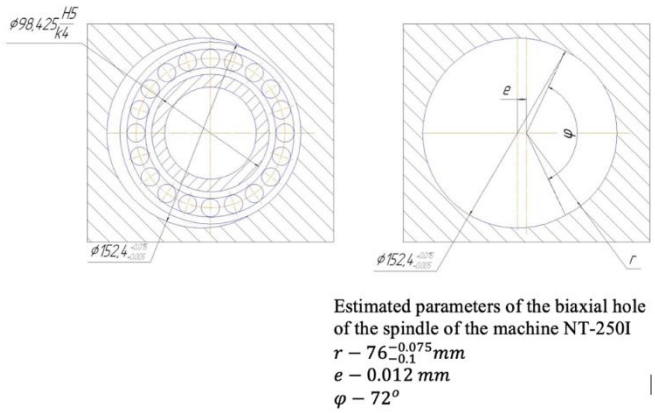

Fig. 16 The main parameters of the spindle unit of the machine NT

5. Conclusions

In the article, on the basis of the performed research, the solution of an urgent scientific problem is given such as the development of requirements for the accuracy of support bearings, as well as the establishment of the relationship between the input and output errors of the machine for typical turning schemes. According to the obtained results the following conclusions are made.

- The elastic system of the spindle group includes a bending system of the workpiece, spindle, spindle supports, devices for fixing the workpiece (chuck, centers, etc.) and a torsional system (more precisely, bending-torsional) of transmission from the engine to the workpiece;
- The degree of load effect from transmission deformation of the spindle assembly depends on the location of the transmission in relation to the supports, rigidity of the supports, their pinching action, the size of the console on which the contact point of the cutter and the workpiece;
- A large share of the influence of shaft bends due to their considerable length is necessary for the location and movement of gears. Significantly specific large

proportion of contact deformations in splined joints is overall balance, which is associated with the use of a large number of movable gears. Thus, the spindle in the process of rotation changes its orientation relative to the cutting tool;

- Analytical functional dependences of the oscillations of the support elements on the force impact from the rotating spindle are obtained, taking into account the preload and the cutting force brought to the support, the own inertial parameters of the SHU support and the stiffness characteristics of the "node-frame" contacts;
- A mathematical model of the accuracy of the spindle assembly has been developed, which takes into account the geometric and static errors of the support elements.
- Calculation of contact and elastic deformations in roller bearings has been developed, as well as contact-elastic displacements of a high-precision roller bearing brand 2-697920L2, installed in the spindle unit of a lathe model NT-250I, have been calculated;
- The shape of the hole is proposed, the geometry of which was designed taking into account the deformation of the bearing. As a result, it was possible to minimize the values of contact and elastic displacements, contact displacements by a factor of two, and elastic displacements by a factor of 3. Thus, for parts with a diameter of up to 50 mm, it becomes possible to achieve 8-9 accuracy grades.

References

[1] Gasparov ES. Ensuring the dynamic quality of high-speed spindle assemblies based on modeling and in-place assessment of the state of supports; Doctoral dissertation, Ulyan State Technical University.
[2] Sayfidinov O. Bognar G. Review on Relationship Between the Universality Class of the Kardar-Parisi-Zhang Equation and the Ballistic Deposition Model. International Journal of Applied Mechanics and Engineering, 2021: 26;4 206-216. https://doi.org/10.2478/ijame-2021-0060
[3] Van V. Study of the influence of milling parameters on the accuracy of machining non-rigid parts.
[4] Sayfidinov O, Bognár G, Kovács E. Solution of the 1D KPZ Equation by Explicit Methods. Symmetry, 2022: 14;4 699. https://doi.org/10.3390/sym14040699
[5] Lizogub VA. Improving the accuracy and productivity of cutting based on the analysis of the design parameters of spindle units on the rolling bearings of machine tools.
[6] Pelevin ON. Modeling of dynamic performance of spindle hydrostatic bearings of processing technological equipment: specialty 05.02. 02 - Mechanical engineering, drive systems and machine parts.
[7] Push AV. Spindle knots. Quality and reliability.
[8] Sayfidinov O, Bognár G. Kardar-Parisi-Zhang interface growing equation with different noise terms. In AIP Conference Proceedings 2022: 2425;1 290006 AIP Publishing LLC. https://doi.org/10.1063/5.0081584
[9] Muminov RO, Kuziev DA, Zotov VV, Sazankova ES. Performability of electro-hydro-mechanical rotary head of drill rig in open pit mining: A case-study https://rudmet.ru/catalog/journal/2129/
[10] Artemenko OR. Promotion of the practicality of milling typography with numerical programming, Master's thesis.
[11] Balmont VB, Gorelik IG, Figatner AM. Calculations of high-speed spindle units. Moscow: VNIITEMR, 1987: 1;52.
[12] Balmont VB, Matveev VA. Instrument rolling supports. M.: Mashinostroenie. 1984.
[13] Muminov RO, Raykhanova GE, Kuziev DA. Improving the reliability and durability of drilling rigs by reducing dynamic loads // Coal. - Moscow, 2021: 5; 32-36. https://doi.org/10.18796/0041-5790-2021-5-32-36

[14] Kulvets AP. Vibrations of rigid shafts rotating in precision bearings / A.P. Kulvets // Proceedings of universities of the Lithuanian SSR. Vibrotechnics, 1973: 3;20 333-339.
[15] Levina ZM. Calculation of stiffness of modern spindle bearings. Machine tools and tools, 1982: 10; 1-3.
[16] Sayfidinov O, Bognár GV. Numerical solutions of the Kardar-Parisi-Zhang interface growing equation with different noise terms. InVehicle and Automotive Engineering, 2020: Nov 25; 302-311. https://doi.org/10.1007/978-981-15-9529-5_27
[17] Figatner AM. Precision rolling bearings of modern machine tools. Moscow: NIIMash. 1981.
[18] Jones AB. A general theory for elastically constrained ball and radial roller bearings under arbitrary load and speed conditions.
[19] Atstupinas RV. Questions of the dynamics of a precision rigid rotor in elastic rolling bearings: Cand. dis. ... Candidate of Technical Sciences: 1970 / Atstupinas R.V. Kaunas, 1970. 24 p.
[20] Atstupinas RV. Investigation of the radial rigidity of rolling bearings, taking into account their manufacture. / R.V. Atstupinas and others // Vibrotechnics, Vilnius, 1970, No. 4.
[21] Yaxshiyev S, Ashurov K, Mamadiyarov AJ. Dynamics of spindle assembly of metal-cutting machine. International Journal of Engineering and Advanced Technology (IJEAT) ISSN: 2249 - 8958, Volume-9 Issue-3, February 2020 https://doi.org/10.35940/ijeat.C6119.029320
[22] Ataullaev AO, Yakhshiev S, Mamadiyarov A. Method for calculating the dynamic characteristics of the spindle assembly Development of science and technology BMTI Uzbekistan. ISSN 2181-8193-2020.

Research on Engineering Structures & Materials
journal homepage: http://www.jresm.org
MIM Research Group

Technical Note

A Review of fatigue behaviour of resistance spot welds

Amruta Pasarkar[a*], Atish Mane[b], Nilesh Singh[c], Avinash Datarkar[d], Nilesh Raut[e]

Bharati Vidyapeeth's College of Engineering, Lavale, Pune

Article Info

Article history:

Received 24 Aug 2022
Revised 13 Nov 2022
Accepted 20 Dec 2022

Keywords:

Resistance spot welding; Sheet thickness; Material properties; Nugget size; Fatigue; Crack propagation

Abstract

Resistance spot welding (RSW) is a solid-state joining process in which sheet metal parts are joined by applying pressure and heat to the faying surfaces. Spot weld failure can cause severe mishap of any mechanical assemblies and can lead to severe damage. Therefore, robust design of spot welds for proper operation is essential. The cyclic stresses occurring on the spot welds in most of the applications result in fatigue failure of welds and decrease their performance efficiency and fatigue strength. This leads to failure of components at very low loads. Thus, it is essential to design the spot welds for fatigue loading conditions for all structures. This study presents the effects of critical factors affecting the fatigue performance of spot welds. The focus is on parameters, namely, sheet thickness, residual stresses, material properties and nugget size of spot welds.

1. Introduction

Resistance spot welding (RSW) is a widely used joining process in automobiles, aerospace, trucks, furniture, nuclear industries etc. to weld sheet metal components [1,2]. Particularly, 90% of the automobile parts are assembled by resistance spot welding process [3]. Spot welding is done in the automotive industry to transfer structural loads during crash. Around 4000 spot welds are performed in a vehicle for higher safety during a crash [4]. The spot-welding process involves thermal, mechanical and electrical interactions along the faying surfaces. Therefore, it is a complicated process and requires many design parameters like weld current, weld time, weld pressure etc. to be considered [5]. This process is also called thermo-mechanical-electrical coupled process. The ease of automation and robotization is the key feature of RSW process.

RSW is a solid-state joining process where the sheet metal parts are joined by heating at the faying surfaces. The resistance to current at the contact surfaces increases the heat and temperature rises. The metal surfaces begin to melt and localized nuggets are formed at the contact between two surfaces. Pressure is also applied on the copper electrodes to ensure proper contact between the surfaces. The current is then stopped and the pressure continues to be acting on the surfaces, which ensures cooling and solidification of the metal s. Spot weld failure can cause severe mishap of any mechanical assembly and can lead to severe damage. Therefore, robust design of spot welds for proper operation is essential.

There is a need to first understand the reasons as to complexity of spot welds and its factors for failure. There are three different zones formed at the weld nuggets, which have different microstructures. The fusion zone (FZ) shows cast structure with columnar grains. It determines the geometry of weld nugget and hence the strength of the spot weld. The heat-affected zone (HAZ), does not melt but undergoes microstructural deviations during

*Corresponding author: amruta.pasarkar@bharatividyapeeth.edu
[a] orcid.org/0000-0002-8530-2280; [b] orcid.org/0000-0002-4549-8004; [c] orcid.org/0000-0002-8700-3735; [d] orcid.org/0000-0001-5298-3684; [e] orcid.org/0000-0002-5873-6526
DOI: http://dx.doi.org/10.17515/resm2022.509me0824tn

heating. This zone can also affect the quality of spot welds. Base metal (BM) does not undergo any microstructural changes [6–8]. It is required to analyze the sensitization and strain hardening characteristics of all three zones for predicting the failure modes of spot welds. The failure analysis thus becomes more complicated. The failure also depends on the weld geometry and stress acting at the weld [9–12]. The difference in the strength of the zones causes strain concentration at the least strength zone and thus, to understand the mechanism of nugget failure, the strain properties of all zones should be studied [13]. The application of pressure on the electrode leads to the formation of an indent on the nuggets, which causes stress concentration at the weld. This causes reduction in the load-bearing capacity of the spot weld. This failure mode should also be considered during the design process [14].

Vehicle parts experience several vibrations due to rough roads, different driving conditions and road accidents. This causes fatigue loading on the spot welded parts and hence can cause fatigue failure of the spot welds [15–18]. The cyclic loading occurring on the vehicle reduces the performance efficiency of the spot welds and the tensile strength decreases considerably with the formation of fatigue crack. This leads to failure of the vehicle part at very low loads. Thus, it is essential to design the spot welds for fatigue loading conditions for all applications [19]. This critical review presents an understanding of the factors that affect the fatigue performance of spot welds. The focus is placed on parameters like sheet thickness, material properties and nugget size of spot welds.

2. Fatigue Failure Modes for Resistance Spot Welds

Resistance spot welds can fail due to many factors such as mechanical properties of the base material, welding time, welding force, sheet thickness, weld diameter. Interfacial (IF) mode, plug failure and pull-out failure (PF) are the three modes of spot welds failure. Crack propagation in IF mode is through FZ and it has a very high effect on the crashworthiness of the vehicle. In the PF mode, the weld nugget delaminates from one or more sheets and crack propagates from the base metal or heat affected zone. This depends on the sheet material and the geometry of the weld nuggets. Both these failure modes largely affect the energy absorption capacity and load-bearing capacity of spot welds. Due to higher energy absorption in the PF mode, spot welds are preferably designed considering the welding parameters for PF mode [20–23]. Fig. 1 shows the three modes of spot weld fatigue fracture. The PF mode in fatigue is divided into three stages: first, the initiation of fatigue crack, second, crack propagation through sheet thickness and third, crack propagation through sheet width [24]. A detail review of the effects of material properties, sheet thickness and nugget size on the fatigue behavior of spot welds is discussed in this paper.

3. Fatigue Performance of Resistance Spot Welds

3.1 Effect of Nugget Size

A study on the effect of different nugget diameters on the fatigue life of spot welds was done by [26]. Spot welding was performed to join two sheets of galvanized steel and austenitic stainless steel. The welding current was varied to get three different nugget diameters of 4 mm, 5 mm and 6 mm. Fatigue tests were performed on the specimens to get the S-N curve. The tests revealed similar fatigue life for all nugget diameters showing a little higher fatigue life for 6-mm nugget diameter.

(a) (b) (c)

Fig. 1 Fatigue failure modes (a) Pull out failure (b) plug failure (c) Interfacial failure [25]

Banerjee et al. [27] considered two specimens P1 and P2 with different RSW current and weld time parameters. Nuggets formed for P1 samples showed diameter of 5.4 mm and P2 samples predicted diameter of 4.42 mm. The samples were tested for fatigue failure at load range of 7.3 to 6.2 kN. The results predicted that even at larger loads, P1 samples exhibit higher fatigue life as compared to P2. Samples of P2 specimen showed interfacial failure mode and P1 samples showed pull-out failure mode.

Kato et al. [28] performed spot welding on three different material steel sheets of varying tensile strength. The welding parameters were controlled to get two different weld diameters of 5 mm and 3.8 mm. Spot welds with lower nugget diameters showed lower fatigue strength. For 5-mm nugget size, the fatigue strength was almost similar for all the three materials. This is due to dominant fatigue crack propagation life. For nugget size of 3.8 mm, the materials with higher tensile strength showed lower fatigue life.

Heewon Cho et al.[25] studied the fatigue and fracture behavior of Transformation Induced Plasticity Steel (TRIP) steels spot welds using two different electrodes of diameters 8mm and 10 mm. The electrodes with larger diameters gave larger nugget size. The fatigue tests showed that the fatigue life is more for larger nugget size. Fatigue fracture showed pull out, HAZ and plug fracture modes. For both the nugget sizes, the crack initiation occurred at the interface of HAZ region. In pull out fracture mode, the crack propagation occurred around the nugget whereas in the HAZ fracture mode, the crack propagated through the thickness of the sheets. However, the plug fracture occurs having characteristics of both HAZ and pull-out fracture. Fig. 2 shows the S-N curve for fatigue fracture of spot welds of TRIP steels for different electrode diameter.

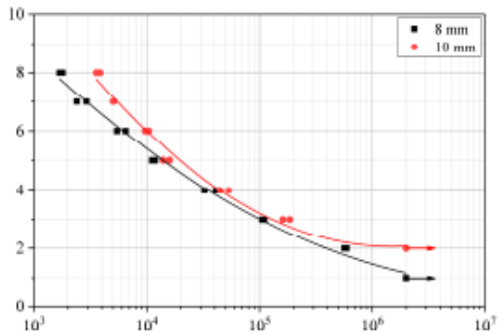

Fig. 2 S-N curve for fatigue fracture of spot welds of TRIP steels for different electrode diameter [25]

A recent study 29] investigated the fatigue life of two sheets of interstitial free steel and high strength niobium micro alloyed steel joined by resistance spot welds. Welding was performed with welding current of 7 kA and 9 kA and an electrode force of 2 kN. The nugget size formed varied due to the different welding currents. Fatigue strength for smaller nugget diameters was found to be high than the larger nugget diameters. This was due to the presence of compressive residual stress in the HAZ and higher micro hardness. The fatigue crack was intergranular, which initiated from interface of HAZ and interstitial free steel side base material.

A study of Akbulut [30] also predicted the influence of nugget size and sheet thickness on the fatigue life of spot welds. Tensile shear specimens of high strength low carbon steel sheets were used for the analysis. Strain-based approach using Coffin Mansion and Morrows mean stress equation was modeled for the specimen analysis. The results show that fatigue life is higher for higher thicknesses because of large elastic and plastic strains. Also, for fatigue life was more for specimens with larger nugget diameter.

Farrahi et al. [31] simulated a finite element model to determine the fatigue damage characteristics of a spotweld on a vehicle body. The results from the FEA model and experimental results were similar. The results showed that the spot welds with small diameters failed in larger number. Approximately 125 spot welds of diameter 2 mm failed due to fatigue. Likewise, spot welds of diameter 4 mm, 6 mm and 8 mm failed in lesser numbers. The comparatively lesser number of spotwelds with 8 mm in diameter failed in fatigue. This can be because the nugget size affects the stiffness of spot welds and thus, the stress concentration at the weld. Thus, the nugget size should be carefully designed to avoid the fatigue failure. Fig. 3 explains the overview of effect of nugget size on fatigue life.

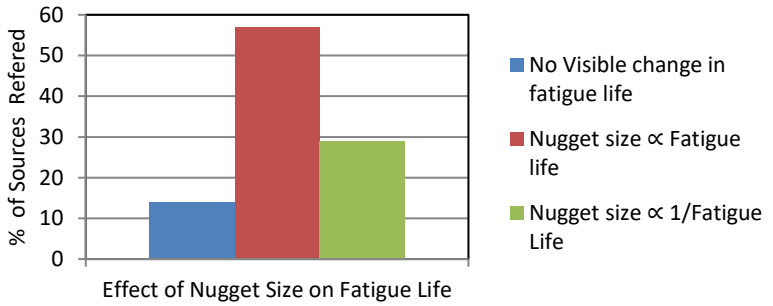

Fig. 3 Overview of effect of nugget size on fatigue life.

3.2 Effects of Sheet Parameters (Geometry/Material)

Bae and Sohn[32] discusses the effect of residual stress, thickness, width and joining the angle of sheet on fatigue life of spot-welds. Fatigue testing was performed for the tensile mode at frequency of 25Hz and stress ratio 0. Variation in fatigue life for different thicknesses is not much significant. However, for smaller loads, the fatigue life increases with an increase in thickness as higher thickness will have higher bending rigidity. Fatigue life decreases as the joint angle increases. However, the effect of sheet width on fatigue life is unpredictable. To consider the effect of residual stress, goodman equation was used to describe a fatigue life equation. It was observed that the there is a significant decrease in fatigue life considering the residual stress at the weld nuggets. Thus, it is essential to consider the residual stress while predicting the fatigue life.

Vural et al. [26] performed fatigue tests on spot welds used to join two similar sheets of austenitic stainless steel and dissimilar sheets of galvanized steel and austenitic stainless steel. Fatigue test results reveal that the spot welds on similar sheets have higher endurance strength than that of dissimilar sheets. This is due to the different expansion properties of different materials. The nugget formed is not symmetrical in the case of dissimilar sheets and thus the fatigue life is lower. Xin Long and Khanna [33] also predicts the fatigue strength of different high strength steel materials. The author mentions that there was no significant change in the fatigue strength of different material spot welds. Fatigue strength depends on loading conditions on spot weld and stress concentration at the weld nugget.

Research shows that with an increase in sheet thickness, the fatigue life decreases. The author modeled the Paris law for determining the effect of sheet thickness on fatigue life of spot weld [34]. In a work of Rahman [35] ,the author considered two specimens of sheet thickness of 1.2 and 0.2 mm for fatigue testing of spot welds. The sheet with 1.2-mm thickness showed larger fatigue life than the other sheet.

Xue, et al. [36] performed fatigue tests to find out the fatigue strength of spot welded dissimilar sheets. AA5754 sheet and high-strength low-alloy (HSLA) steel sheet were welded together with spot welds. The fatigue tests revealed that the fatigue strength of such dissimilar configuration was more than AA5754 welded to itself. Finite element simulation was conducted which enhanced that the larger notch root angle at the weld nugget gives a higher fatigue life as the maximum principal strain is reduced effectively. Fig. 4 explains the overview of effect of sheet material on fatigue life.

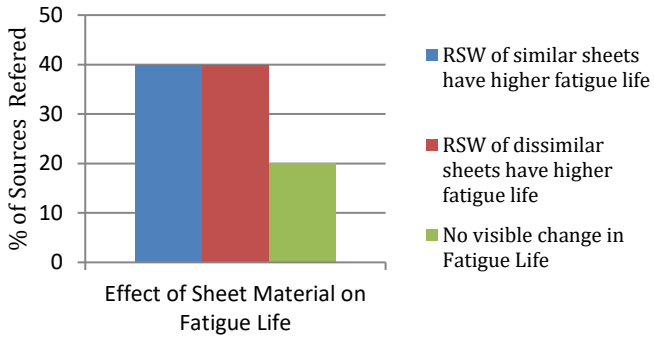

Fig. 4 Overview of effect of sheet material on fatigue life

3.3 Effects of RSW Parameters

Kang et al. [37] studied the fatigue performance of three sheets of dual phase 600 and mild steel welded separately. Two shapes of electrode tip B nose and E-nose were used for welding. Fatigue tests at a frequency of 10 Hz and stress ratio of 0.01 were performed for both the specimens. Tests were also performed for different indentation levels. The results show that the shape of the electrode tip did not affect the fatigue life of DP600 steel spot welds. Also, fatigue life was not significantly affected by the different indentation levels for both the materials. Dual phase 600 material showed larger fatigue life than mild steel. Fig. 5 shows number of cycles to failure for DP600 and mild steel.

Pal [38] predicted the fatigue behavior of spotwelds used to join sheets of martensitic steels. The welding conditions were varied by changing the welding current, weld time and weld force. Thus, for every specimen, the nugget diameters obtained were different. All the

specimens showed similar fatigue characteristics at lower loads, but showed significant variation at higher loads. At the higher loads, interfacial fracture is observed, which propagates through the weld metal. However, the crack fails to propagate through the weld for lower loads. At the lower loads, plug and hole fracture mode is observed. There is transition in fracture mode at 50% loading of the yield stress.

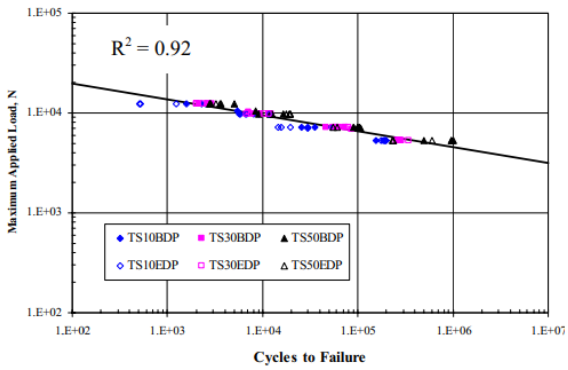

(a)

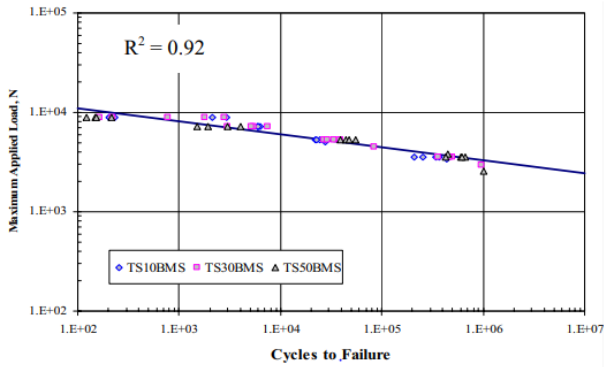

(b)

Fig. 5 (a) No. of cycles to failure for DP600, (b) No. of cycles to failure for mild steel [37]

Duan et al. [39] predicted the fatigue life of spot welds used in tensile shear and cross tension specimens of steel. It was seen that the fatigue limit of the tensile shear specimen was more that than that of the cross-tension specimens. Fatigue cracks for both the specimens were initiated in the HAZ region at the notch tip and also at the interface boundaries of the two sheets. The fatigue crack propagation was through the thickness and then into the width of the sheet before the final fracture for tensile shear specimen. However, the crack propagation for cross tension specimen was completely through the thickness only before the final fracture.

Duan et al. [40] compared the fatigue life of spot weld on two materials high strength steel and mild steel. The high strength steel sheet had a thickness of 1.8 mm and M190 steel had a thickness of 1.2 mm. Fatigue strength was more for high strength steel spot welds due to thicker sheets and proper nugget formed which follows the standard nugget size rule. The

crack initiated at the edges of the sheet or at the interface of two sheets and propagated through the HAZ region.

Rao et al. [41] considered two dissimilar sheet stackups of wrought aluminium and interfacial steels and two similar sheets of wrought aluminium. These materials were spot welded in two configurations first, tensile shear and second coach peel. For the tensile shear configuration, the fatigue life of dissimilar stackup was higher than similar aluminium stackup and for coach peel configuration there was not much difference in the fatigue life of spot welds for both the combinations of materials. The dissimilar materials stackups showed better performance due to larger weld nuggets formed. For both configurations of tensile shear and coach peel, the crack growth was seen from the aluminium sheet.

Ordoñez et al. [42] studied the resistance of spot welds used to join dual phase steels by fatigue tests. It was found that due to the stress concentration at the weld nugget at the fusion zone, the fatigue life of weld decreases. Fatigue failure was initiated at the sheet interface. Compressive residual stresses on spot weld increases its fatigue life. A work of Fujimoto et al. [42] also increased the compressive residual stresses in spot weld lap joints of high strength steel sheets by shot blasting process. The work reported that with the compressive residual stress, the fatigue life of spot weld is improved.

Kang et al. [44] also considered the spot weld joining of aluminium and steel sheets. Three specimens were considered, Al-Al weld, Al-steel weld with positive electrode polarity and Al-steel weld with negative electrode polarity. The fatigue analysis was performed to understand the effect of nugget diameter, notch angle and polarity on the fatigue life of spot welds. The research predicted that the nuggets with negative polarity show the largest fatigue life than the nuggets with positive polarity. Also, the Al-Al sheet nuggets showed the least fatigue life. The results were more significant for tensile shear specimens than for the coach peel specimens. Al-Al sheets, had a lesser nugget size of 6.2 mm whereas the Al-Steel sheets had nugget diameter of 8.5 mm approximately. This also shows that the sheets with larger nugget diameters have larger fatigue life as it would take larger energy to fail. Another consideration showed that, as the notch root angle decreased, the tensile stresses increased. This also affects the fatigue life of spot welds. The spot welds with negative polarity have notch root angle of 33 degrees whereas, the welds with positive polarity had a notch root angle of 11 degrees. Thus, owing to increase in the tensile stresses, spot welds with lesser notch root angle failed at had lesser fatigue life.

4. Fatigue Failure Characteristics

There is a lot of research where results on fatigue life of spot welds is studied. However, study on the fatigue crack initiation and propagation is very difficult as fatigue cracks occur at a very critical area of spot weld at the sheet interface. This area undergoes several microstructural changes and hence it is very difficult to understand the fatigue mechanism from the point of fracture mechanics. Also, fatigue cracks are not easily visible unless the specimen fails through the thickness. As direct observation was not possible, scientist used instruments to study the crack nucleation and propagation after fatigue loading on spot welds [45].

Hassanifard et al. [46] reported that there is higher stress concentration at the circumference of nugget and hence the crack initiation takes place from such areas. Lanciotti and Polese [45] described the fatigue crack initiation and propagation in spot welded stainless steel. The author mentioned that the crack initiation takes place at a distance of 0.93 mm from the spot weld nugget. The crack initiation took place for 10% of fatigue life. Another research [47] considered the use of half cut tensile shear specimens to study the fatigue fracture mechanism in spot weld. Steel sheets of hot rolled high strength

galvanized alloy were spot welded and tested. The spot welds developed crack of depth 0.25mm at 50% of its fatigue life. The crack was measured after the crack initiated and until the early propagation phase. A study was also done to report the effect of fatigue crack on stiffness of spot welds. The experimental results showed that the stiffness is not affected until a large crack is formed [48].

Pouranvari and Marashi [4] reported that there are various different crack propagation modes for spot welds within low cycle and high cycle region. They mentioned that within the low cycle region, the crack propagates through the base material while within the high cycle region; the crack propagates through the HAZ region. (Xu et al.) [16] found that the kinked angle for the fatigue crack was 80 º. (Newman and Dowling) [49] also formulated an equation to calculate J integral and stress intensity factor and reported that the kinked angle for fatigue crack was 75º. The crack propagation can be predicted by calculating the stress concentration at the weld nugget area and the crack growth angle. The tensile shear and cross tension configurations can have plug type and interfacial fracture mode [50]. Fig. 6 (a), (b) shows the plug type fracture mode for tensile shear and cross tension specimen. Fig. 6 (c) shows the interfacial fracture mode for cross tension specimen.

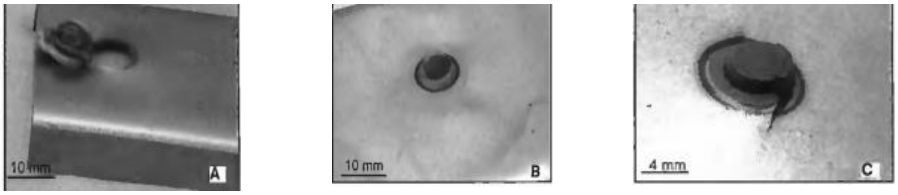

(a) (b) (c)

Fig. 6 (a) Plug type fracture mode for tensile shear (b) For cross tension specimen. (c) Interfacial fracture mode for cross tension specimen [50]

Ma et al. [51] reported that the fatigue fracture initiates in the HAZ region showing plastic deformation at higher load levels. The crack initiates at the nugget area, penetrate through the thickness of sheet and propagate through the base metal along the normal to the load at lower load levels. Also, for intermediate load levels, the fractures initiate at the nugget area and propagate along the circumference, and fractures takes place in the base metal. The natural frequency of spot welds significantly changes after the fatigue life reaches more than 50% of the total fatigue life. At 95% of life, the cracks were visible on the surfaces of the joint [52]. First fatigue crack was seen at approximately 50% of total fatigue life of spot welds.

Cooper and Smith [53] tried observing the fatigue crack length of spot welded mild steel sheets. The authors used tensile shear specimens for the test. The potential drop method was used to estimate the crack length. The principal fatigue mechanism was macro crack propagation in the spot welds and the cracks propagation rate was constant throughout the thickness. A work of Swellam et al. [54] also predicted the fatigue crack mechanism in high strength steel spot welds and galvanized steel spot welds. Nucleation of cracks was the major fatigue mechanism for galvanized steel while crack propagation through thickness was that for high strength steel.

A work of Wang and Barkey [55] reported three different fatigue failure modes. In mode A, the crack initiates away from the spot weld nugget, propagates through the base metal and the crack growth was in a straight line. In the mode B, the crack initiation was at the HAZ region and propagated around the spot weld nugget and finally through the base sheet until fracture to partially break the weld at the nugget edge and partially at the base sheets.

Nugget is rotated before fracture. There is no nugget rotation in mode A. In the mode C, the crack is seen to propagate around the spot weld nugget and fracture is seen when half of the nugget is peeled out of the sheet. The nuggets rotated by about 90 ° before final fracture. Mode A occurs at high cycle tests and mode C occurs at low cycle tests. Mode B occurs between the two. Most cracks propagated in mode C and very few cracks propagated in mode A. For all modes, crack initiated at approximately 50% of the total fatigue life. Fig. 7 shows failure of spot welds due to fatigue in mode A, B, C.

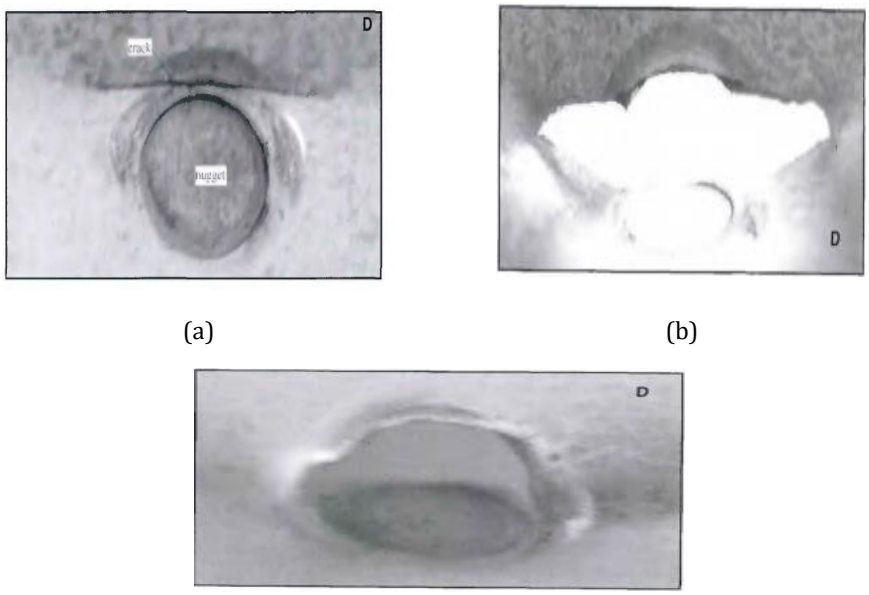

(a) (b)

(c)

Fig. 7 Fatigue failure of spot welds in modes A, B, C [55]

The fatigue fracture mode of spot welds with positive polarity was observed to be interfacial mode. The weld with negative polarity failed with pull-out fracture mode. The specimen with a smaller notch root angle of 11 degrees exhibited a large shear stress at the notch tip and hence the fatigue crack growth was interfacial. Whereas, specimens with a larger notch root angle of 33 degrees, did not show much stress concentration at the notch tip and hence exhibited a pull-out fracture mode at the weld [44].

Mukhopadhyay et al. [56] studied the fatigue failure of DP600 resistance spot welded steels of thickness 1.4 mm .High cycle fatigue tests were conducted for tensile shear configuration at 3.8kN electrode force. The fatigue crack initiated at the HAZ and propagate through the thickness of sheets till complete fracture. The fatigue failure occurred due to stress concentration at the sheets interference and due to strength of DP600 steel.

Table 1. Summary of the effects of different welding factors on fatigue life of spot welds

	Factors	Effect on fatigue life of spot weld
[27], [28], [25], [30]	Nugget size	Larger nugget sizes exhibited a higher fatigue life.
[29]	Nugget size	Fatigue strength for smaller nugget diameters was found to be higher.
[31]	Nugget size	The spot welds with least diameter failed due to fatigue in large numbers
[26]	Sheet material Nugget size	Spot welds used for joining similar sheets have a higher fatigue limit than that of dissimilar sheets. Similar fatigue life for all nugget sizes.
[33]	Sheet material	Different materials do not significantly affect the fatigue strength of spot weld
[34]	Sheet Thickness	With an increase in sheet thickness, the fatigue life decreases
[32]	Sheet thickness Joint angle Residual Stress Sheet width	Fatigue life increases with an increase in thickness. Fatigue life decreases as the joint angle increases. A significant decrease in fatigue life considering the residual stress at the weld nuggets. The effect of sheet width on fatigue life is not predictable.
[35], [40]	Sheet Thickness	The increase in sheet thickness, the fatigue life increases
[36]	Sheet Material Notch root angle	Fatigue strength of such dissimilar configuration of AA5754 sheet and high-strength low-alloy (HSLA) steel was more . Larger notch root angle is beneficial to achieve longer fatigue life .
[37]	Electrode Tip Indentation levels Sheet material	The shape of the electrode tip did not affect the fatigue life of spot weld Not significantly affected by the different indentation levels for both the materials Dual phase 600 material showed larger fatigue life than mild steel.
[38]	Weld Current Weld Time	All the specimens showed similar fatigue characteristics at lower loads but showed a significant variation at higher loads
[39]	Tensile shear configuration Cross Tension configuration	Fatigue limit for tensile shear specimen was more that than the cross-tension specimen.
[42][43]	Compressive residual stress	Fatigue life improves with induced compressive residual stress in spot welds.
[41]	Sheet material	Fatigue life of dissimilar stackup was higher than similar aluminium stackup.
[44]	Nugget diameter Notch angle Polarity	Sheets with larger nugget diameters have larger fatigue life as it would take larger energy to fail As the notch root angle decrease, fatigue life decreases The nuggets with negative polarity showed largest fatigue life than the nuggets with positive polarity

5. Conclusion

Resistance spot welding is a solid-state joining process wherein sheet metal parts are joined by heating at the faying surfaces. It is a complex thermo-mechanical-electrical coupled process. Mechanical structures that undergo extensive vibrations can cause repetitive loading on the resistance spot welds that leads to fatigue failure. Spot welds have different regions of different microstructures and hence, they are very critical to study for its fatigue failure. It is thus important to consider fatigue parameters while designing the resistance spot welding process. This review presents the study of critical factors affecting the fatigue performance of spot welds. The focus is on RSW parameters and sheet parameters. RSW parameters include weld current, weld time, residual stresses polarity while sheet parameters include sheet materials, sheet thickness and nugget size.The findings of the review are as follows:

- It is observed that with an increase in sheet thickness and nugget size, the fatigue life of spot welds increases. This is due to a decrease in the stress concentration at the nugget area.
- Spot welds used for joining sheets of dissimilar material have lesser fatigue life due to the different thermal expansion coefficients of materials.
- Fatigue life improves with increase in compressive residual stresses at the spot nuggets.
- There is no effective change in fatigue strength with change in weld current or weld time.
- Fatigue cracks occur at the sheet interference and hence it is very difficult to study the fatigue crack characteristics.
- Spot Welds with positive polarity failed in an interfacial mode while welds with negative polarity failed with pull-out fracture mode.
- Crack propagation in IF mode is through the FZ. In the pull-out mode, the weld nugget delaminates from one or more sheets and crack propagates from the base metal or heat affected zone.
- Due to higher energy absorption in the pull-out mode, spot welds are preferably designed for this fracture mode.

References

[1] Akkas N. Welding time effect on tensile-shear loading in resistance spot welding of SPA-H weathering steel sheets used in railway vehicles. Acta Phys Pol A. 2017;131(1):52–4. https://doi.org/10.12693/APhysPolA.131.52

[2] Martín Ó, De Tiedra P, San-Juan M. Combined effect of resistance spot welding and precipitation hardening on tensile shear load bearing capacity of A286 superalloy. Mater Sci Eng A. 2017;688(December 2016):309–14.https://doi.org/10.1016/j.msea.2017.02.015

[3] Li YB, Lin ZQ, Shen Q, Lai XM. Numerical analysis of transport phenomena in resistance spot welding process. J Manuf Sci Eng Trans ASME. 2011;133(3):1–8. https://doi.org/10.1115/1.4004319

[4] Pouranvari M, Marashi SPH. Critical review of automotive steels spot welding: Process, structure and properties. Sci Technol Weld Join. 2013;18(5):361–403. https://doi.org/10.1179/1362171813Y.0000000120

[5] Wan Z, Wang HP, Wang M, Carlson BE, Sigler DR. Numerical simulation of resistance spot welding of Al to zinc-coated steel with improved representation of contact interactions. Int J Heat Mass Transf. 2016;101:749–63.https://doi.org/10.1016/j.ijheatmasstransfer.2016.05.023

[6] Sun X, Stephens E V., Khaleel MA. Effects of fusion zone size and failure mode on peak load and energy absorption of advanced high strength steel spot welds under lap shear

loading conditions. Eng Fail Anal. 2008;15(4):356–67. https://doi.org/10.1016/j.engfailanal.2007.01.018
[7] Lin PC, Lin SH, Pan J. Modeling of failure near spot welds in lap-shear specimens based on a plane stress rigid inclusion analysis. Eng Fract Mech. 2006;73(15):2229–49. https://doi.org/10.1016/j.engfracmech.2006.03.017
[8] Pouranvari M, Asgari HR, Mosavizadch SM, Marashi PH, Goodarzi M. Effect of weld nugget size on overload failure mode of resistance spot welds. Sci Technol Weld Join. 2007;12(3):217–25. https://doi.org/10.1179/174329307X164409
[9] Pouranvari M. Failure mode transition in similar and dissimilar resistance spot welds of HSLA and low carbon steels. Can Metall Q. 2012;51(1):67–74. https://doi.org/10.1179/1879139511Y.0000000020
[10] Tumuluru M. Resistance spot weld performance and weld failure modes for dual phase and TRIP steels [Internet]. Failure Mechanisms of Advanced Welding Processes. Woodhead Publishing Limited; 2010. 43–64 p.https://doi.org/10.1533/9781845699765.43
[11] Yang YP, Babu SS, Orth F, Peterson W. Integrated computational model to predict mechanical behaviour of spot weld. Sci Technol Weld Join. 2008;13(3):232–9. https://doi.org/10.1179/174329308X283901
[12] Yang YP, Gould J, Peterson W, Orth F, Zelenak P, Al-Fakir W. Development of spot weld failure parameters for full vehicle crash modelling. Sci Technol Weld Join. 2013;18(3):222–31.https://doi.org/10.1179/1362171812Y.0000000082
[13] Radakovic DJ, Tumuluru M. Predicting resistance spot weld failure modes in shear tension tests of advanced high-strength automotive steels. Weld J (Miami, Fla). 2008;87(4):96–105.
[14] Pouranvari M, Abedi A, Marashi P, Goodarzi M. Effect of expulsion on peak load and energy absorption of low carbon steel resistance spot welds. Sci Technol Weld Join. 2008;13(1):39–43. https://doi.org/10.1179/174329307X249342
[15] Long X, Khanna SK. Fatigue performance of spot welded and weld bonded advanced high strength steel sheets. Sci Technol Weld Join. 2008;13(3):241–7. https://doi.org/10.1179/174329307X249379
[16] Xu J, Zhang YS, Xinmin L, Chen GL. Experimental investigation of fatigue performance of spot welded dual phase sheet steels. Sci Technol Weld Join. 2008;13(8):726–31. https://doi.org/10.1179/174329307X236841
[17] Daneshpour S, Riekehr S, Koçak M, Gerritsen CHJ. Mechanical and fatigue behaviour of laser and resistance spot welds in advanced high strength steels. Sci Technol Weld Join. 2009;14(1):20–5. https://doi.org/10.1179/136217108X336298
[18] Gaul H, Weber G, Rethmeier M. Influence of HAZ cracks on fatigue resistance of resistance spot welded joints made of advanced high strength steels. Sci Technol Weld Join. 2011;16(5):440–5. https://doi.org/10.1179/1362171810Y.0000000031
[19] Miller KW, Chao YJ, Martinez A, Zhu X, Liu S, Wang PC. Quasi-static and impact strength of fatigue damaged spot welds. SAE Tech Pap. 2003;(724):1–8. https://doi.org/10.4271/2003-01-0610
[20] Mahmood TR, Doos QM, Al-Mukhtar AM. Failure Mechanisms and Modeling of Spot Welded Joints in Low Carbon Mild Sheets Steel and High Strength Low Alloy Steel. Procedia Struct Integr . 2018;9:71–85https://doi.org/10.1016/j.prostr.2018.06.013
[21] Sun X. Resistance spot weld failure mode and weld performance for aluminum alloys. Fail Mech Adv Weld Process. 2010;24–42.https://doi.org/10.1533/9781845699765.24
[22] Pouranvari M. Influence of welding parameters on peak load and energy absorption of dissimilar resistance spot welds of DP600 and AISI 1008 steels. Can Metall Q. 2011;50(4):381–8. https://doi.org/10.1179/1879139511Y.0000000008

[23] Sun X, Stephens E V., Khaleel MA. Effects of fusion zone size and failure mode on peak load and energy absorption of advanced high-strength steel spot welds. Weld J (Miami, Fla). 2007;86(1). https://doi.org/10.4271/2006-01-0531
[24] Hilditch TB, Speer JG, Matlock DK. Effect of susceptibility to interfacial fracture on fatigue properties of spot-welded high strength sheet steel. Mater Des. 2007;28(10):2566–76. https://doi.org/10.1016/j.matdes.2006.10.019
[25] Heewon Cho , Sangwoo Nam IH, Oh JH, Kang M, and Young-Min Kim. Fatigue Behaviors of Resistance Spot Welds for 980 MPa Grade TRIP Steel. Metals (Basel). 2019
[26] Vural M, Akkuş A, Eryürek B. Effect of welding nugget diameter on the fatigue strength of the resistance spot welded joints of different steel sheets. J Mater Process Technol. 2006;176(1–3):127–32. https://doi.org/10.1016/j.jmatprotec.2006.02.026
[27] Banerjee P, Sarkar R, Pal TK, Shome M. Journal of Materials Processing Technology Effect of nugget size and notch geometry on the high cycle fatigue performance of resistance spot welded DP590 steel sheets. J Mater Process Tech .2016;238:226–43.https://doi.org/10.1016/j.jmatprotec.2016.07.023
[28] Kato Y, Kakiuchi T, Okita Y, Matsuda H, Ikeda R, Tagawa T. Fatigue behavior of resistance spot welded high strength steel sheets with different nugget sizes. 8th TSME Int Conf Mech Eng. 2017;(December):1219–23.https://doi.org/10.1299/jsmemm.2017.OS0514
[29] Janardhan G, Kishore K, Mukhopadhyay G, Dutta K. Fatigue Properties of Resistance Spot Welded Dissimilar Interstitial-Free and High Strength Micro-Alloyed Steel Sheets. Met Mater Int . 2020;(0123456789)https://doi.org/10.1007/s12540-020-00678-w
[30] Akbulut M. Parametric investigation into fatigue life behaviour of spot welded tensile shear test samples. Proc IMechE Part C J Mech Eng Sci. 2020;1–10. https://doi.org/10.1177/0954406220966352
[31] Farrahi GH, Ahmadi A, Kasyzadeh KR. Simulation Modelling Practice and Theory Simulation of vehicle body spot weld failures due to fatigue by considering road roughness and vehicle velocity. Simul Model Pract Theory 2020;105(August):102168 https://doi.org/10.1016/j.simpat.2020.102168
[32] D. H. BAE, I. S. SOHN AJKH. Assessing the Effects of Residual Stresses on the Fatigue Strength of Spot Welds. Weld J. 2003;(January).
[33] Long X, Khanna SK. Fatigue properties and failure characterization of spot welded high strength steel sheet. Int Journal of Fatigue. 2007;29:879–86. https://doi.org/10.1016/j.ijfatigue.2006.08.003
[34] Zhang Y, Taylor D. Sheet thickness effect of spot welds based on crack propagation. Eng Fract Mech. 2000;67:55–63. https://doi.org/10.1016/S0013-7944(00)00029-1
[35] Rahman. Effects of Spot Diameter and Sheets Thickness on Fatigue Life of Spot Welded Structure based on FEA Approach. Am J Appl Sci. 2009;6(1):137–42. https://doi.org/10.3844/ajassp.2009.137.142
[36] Shi L, Xue J, Kang J, Haselhuhn AS, Carlson BE. Effect of specimen configuration and notch root angle on fatigue behavior of novel dissimilar resistance spot welds of AA5754 to HSLA steel. Procedia Struct Integr. 2021;37(C):351–8. https://doi.org/10.1016/j.prostr.2022.01.095
[37] Kang H, Accorsi I, Patel B, Pakalnins E. Fatigue performance of resistance spot welds in three sheet stack-ups. Procedia Eng .2010;2(1):129–38. https://doi.org/10.1016/j.proeng.2010.03.014
[38] T. K. PAL KC. Resistance spot weldability and high cycle fatigue behaviour of martensitic (M190) steel sheet. Fatigue Fract Eng Mater Struct. 2010;(June):46–52. https://doi.org/10.1111/j.1460-2695.2010.01489.x
[39] Wang B, Duan QQ, Yao G, Pang JC, Li XW, Wang L, et al. Investigation on fatigue fracture behaviors of spot welded Q & P980 steel. Int J Fatigue. 2014. https://doi.org/10.1016/j.ijfatigue.2014.03.004

[40] Wang B, Duan QQ, Yao G, Pang JC, Zhang ZF, Wang L, et al. Fatigue fracture behaviour of spot welded B1500HS steel under tensile- shear load. Fatigue Fract Engng Mater Struct. 2015;(38):914–22. https://doi.org/10.1111/ffe.12289
[41] Rao HM, Kang J, Shi L, Sigler DR, Carlson BE. Effect of specimen configuration on fatigue properties of dissimilar aluminum to steel resistance spot welds. Int J Fatigue. 2018;116:13–21.https://doi.org/10.1016/j.ijfatigue.2018.06.009
[42] Ordoñez JH, Ambriz RR, García C, Plascencia G, Jaramillo D. Overloading effect on the fatigue strength in resistance spot welding joints of a DP980 steel. Int J Fatigue. 2019;121(November 2018):163–71https://doi.org/10.1016/j.ijfatigue.2018.12.026
[43] Fujimoto H, Ueda H, Ueji R, Fujii H. Improvement of fatigue properties of resistance spot welded joints in high strength steel sheets by shot blast processing. ISIJ Int. 2016;56(7):1276–84. https://doi.org/10.2355/isijinternational.ISIJINT-2016-043
[44] Shi L, Kang J, Gesing M, Chen X, Haselhuhn AS, Carlson BE. E ff ect of notch root angle on fatigue behavior of aluminum to steel resistance spot welds. Int J Fatigue. 2020;141(July):105866.https://doi.org/10.1016/j.ijfatigue.2020.105866
[45] Lanciotti A, Polese C. Fatigue crack propagation in tensile shear stainless steel spot welded specimens. Fatigue Fract Eng Mater Struct. 2008;31(1):76–84. https://doi.org/10.1111/j.1460-2695.2007.01202.x
[46] Hassanifard S, Mohtadi-Bonab MAl, Jabbari G. Investigation of fatigue crack propagation in spot-welded joints based on fracture mechanics approach. J Mater Eng Perform. 2013;22(1):245–50. https://doi.org/10.1007/s11665-012-0220-5
[47] McMahon JC, Smith GA, Lawrence F V. Fatigue Crack Initiation and Growth in Tensile-Shear Spot Weldments. In: Potter JM, McHenry HI, editors. Fatigue and Fracture Testing of Weldments . West Conshohocken, PA: ASTM International; 1990. p. 47–77. https://doi.org/10.1520/STP24090S
[48] Davidson JA. A Review of the Fatigue Properties of Spot-Welded Sheet Steels. SAE Trans . 1983 Aug 20;92:35–47.https://doi.org/10.4271/830033
[49] Newman JA, Dowling NE. A crack growth approach to life prediction of spot-welded lap joints. Fatigue Fract Eng Mater Struct. 1998;21(9):1123–32. https://doi.org/10.1046/j.1460-2695.1998.00099.x
[50] Rathbun RW, Matlock DK, Speer JG. Fatigue behavior of spot welded high-strength sheet steels. Weld J (Miami, Fla). 2003;82(8).
[51] Ma C, Chen DL, Bhole SD, Boudreau G, Lee A, Biro E. Microstructure and fracture characteristics of spot-welded DP600 steel. Mater Sci Eng A. 2008;485(1–2):334–46. https://doi.org/10.1016/j.msea.2007.08.010
[52] Shang D-G, Barkey ME, Wang Y, Lim TC. Fatigue Damage and Dynamic Natural Frequency Response of Spot-Welded Joints. SAE Trans. 2003 Aug 23;112:301–8 https://doi.org/10.4271/2003-01-0695
[53] Cooper JF, Smith RA. The measurement of fatigue cracks at spot-welds. Int J Fatigue. 1985;7(3):137–40. https://doi.org/10.1016/0142-1123(85)90023-4
[54] Swellam MH, Kurath P, Lawrence F V, "Electric-Potential-Drop Studies of Fatigue Crack Development in Tensile-Shear Spot Welds," in Advances in Fatigue Lifetime Predictive Techniques, M. R. Mitchell and R. W. Landgraf, Eds. West Conshohocken, PA: ASTM International, 1992, pp. 383-401. https://doi.org/10.1520/STP24170S
[55] Wang G, Barkey ME. Investigating the spot weld fatigue crack growth process using X-ray imaging. Weld J (Miami, Fla). 2006;85(4).
[56] Janardhan G, Mukhopadhyay G, Dutta K. Failure mechanism of resistance spot-welded DP600 steel under high cycle fatigue. Mater Today Proc. 2022;59:1666–71.. https://doi.org/10.1016/j.matpr.2022.03.332

Research on Engineering Structures & Materials
journal homepage: http://www.jresm.org
Research Group

Research Article

Influence of time period and derivation of critical storey limit for RC frame buildings using construction sequence method of analysis

Nehal Mahadevbhai Desai*[a], Sandip Vasanwala[b]

Department of Civil Engineering, Sardar Vallabhbhai National Institute of Technology, Surat, Gujarat, India-395007

Article Info

Article history:

Received 09 Mar 2022
Revised 09 Jun 2022
Accepted 15 Aug 2022

Keywords:

Axial shortening; Construction sequence method of analysis; Critical time period; Critical storey limit; Time-dependent properties of concrete

Abstract

Construction Sequence Analysis (CSA) is a method that follows real-time onsite construction practices like construction sequence, sequential loading, and timing. Properties of concrete, like Creep and shrinkage are time-dependent properties of concrete, so it is crucial to determine the period up to which critical responses are received during a building's life. This study observes the different responses of structural members seeing the long-term effect of concrete properties for up to 50 years, cohesive to the standard lifespan of RC structures in India. The study derives the most critical time during the entire life of the building using the CSA method. According to this study, 98% to 99% of the 50th-year responses are attained within 10950 days after applying live load. The study recommends analysing RC structures for 10950 days using the CSA method instead of ending at the time of live load application or continuing analysis up to 50 years. It is important to know the limit of total storeys above which the behaviour of vertical members becomes vulnerable in RC buildings. The study also determines the critical storey limit of RC moment frame building over which the CSA method must be utilised. Hence, this study uses the CSA and Linear Static Analysis method to analyse 12 RC building models of various beam spans and total storeys. The study concludes that the CSA method should be mandatory for buildings with more than nine stories.

1. Introduction

Structural engineers use the Linear Static method to analyse and design an RC building by simultaneously applying all loads to the building models. An RC structure is gradually loaded as it is built, due to factors including the own weight of structural components, walls, and floor finishing. After construction is finished, occupancy is applied in terms of the live load. All loads are applied in accordance with the order of construction using the Construction Sequence Analysis (CSA) method, and the timing of application matches that of actual construction. Because creep and shrinkage are ongoing processes, the Construction Sequence Analysis (CSAcs) method will yield different results at various points in the analysis. Many researchers have studied CSA method.

Chakrabarti et al. [3] and Chang-Koon Choi et al. [4] argue that the (CSA) method reports responses, which are different from the conventional one-step Linear Static Analysis (LSA) method. Kwak & Kim [10] proposed a construction sequence method that considers deformation in concrete due to its time-dependent properties. A computational method was used by Dinar et al. [6] and Correia & Lobo [5] to investigate the impact of sequencial self-weight on construction. Ha et al. [8] developed an algorithm for the construction stage to assess the outcomes with a laser survey and advised taking into account the time-

*Corresponding author: nehal.desai@scet.ac.in
[a] orcid.org/0000-0001-8767-5649; [b] orcid.org/0000-0003-0083-6257
DOI: http://dx.doi.org/10.17515/resm2022.414st0309

dependent effect of the concrete during the design stage of tall buildings. An improved correction factor approach was proposed by Afshari et al. [1]. Both Secer & Arslan [12] and Zucca et al. [13] found a substantial change in vertical column displacements while using CSA method. One-step analysis yields an unsafe solution in some element zones and an uneconomic solution in others, according to Elansary et al. [7].

Most of these investigators omitted the role of time and primarily assessed responses at the time of live load application. However, Casalegno et al. [2] estimated the difference in vertical displacement for a long time in cable-stayed bridges subjected to creep. They did notice increased deflection due to creep for longer periods.

Additional research is required to fully comprehend the impact of time period on the responses of RC buildings and the consequences of creep and shrinkage. The time period used for structural design and analysis is a crucial concern as most researchers have considered the response at the last stage of construction, i.e. at the application of live load. In order to evaluate that, this study observes two types of responses, the axial shortening and the bending moments for different time periods. The results were compared with the reference results for the 50^{th} year, as RC structures in India are designed for a 50-year life span. The different time periods considered are 365 days, 730 days, 1000 days, 1825 days, 3650 days, 7300 days, 10950 days, 14600 days, and 18250 days from the application of live load, of which the optimal timespan is derived.

Since the CSAcs method is complicated, it is imperative to formulate a critical storey limit, i.e. "a limit for the total numbers of storeys of a building above which the CSA method is recommended". In order to formulate that, this study calculates the percentage difference between the axial strains of vertical members using the CSA method for the critical time period as derived in this study (CSA_{30cs}) and the LSA method at every floor level of selected building models. Based on the percentage difference in axial strain obtained by the CSA_{30CS} method to the LSA method (Δ), columns are divided into different categories, and a critical storey limit for CSA method is recommended for all categories of columns. Twelve RC moment framed building models with RC shear walls of the same plan area but of different spans and total storeys were selected to evaluate the effect of various beam spans and total storey numbers on the critical storey limit. The building models were analysed with the help of Midas Gen 17 [11] software. This study's analysis and design are undertaken as per the Indian standard code of practice.

2. Materials and Methods

2.1. Building Models

A 40-story RC framed building with a 5m X 5m beam grid and plan dimensions of 25m X 25m was chosen to study the combined effect of creep and shrinkage on time span with CSAcs, as illustrated in Fig. 1(a) and Table 1.Twelve building models of symmetrical plan with a central shear wall with a floor height of 3.2m were selected to study the critical storey limit. Hence, three RC moment framed building models of the same plan area of 40m X 40m, but varying plan grids and total numbers of storeys, as shown in Table 1 and Fig. 1(b)-1(d), were selected. Models were initially analysed and designed using the LSA method and the Indian Standard Code of Practice, with live load of 3 kN/m^2, floor finishing load of 1 kN/m^2, and brick wall load of 5 kN/m. The cross-sections of structural members for the A40, B40 and C40 models are shown in Table 3. Similarly, the structural elements are designed for other models through LSA and used for the CSAcs method. Properties of the grade of concrete and steel used for the modelling of buildings are mentioned in Table 2.

Table 1. Description of the selected RC frame building model

Models	Plan size, mxm	Type of plan	Beam grid, m x m	Total storey numbers
A0	25 X 25	Plan A0	5 x 5	40
A40	40 X 40	Plan A	8 X 8	40
A30	40 X 40	Plan A	8 X 8	30
A20	40 X 40	Plan A	8 X 8	20
A10	40 X 40	Plan A	8 X 8	10
B40	40 X 40	Plan B	5.72 X 5.72	40
B30	40 X 40	Plan B	5.72 X 5.72	30
B20	40 X 40	Plan B	5.72 X 5.72	20
B10	40 X 40	Plan B	5.72 X 5.72	10
C40	40 X 40	Plan C	4.44 X 4.44	40
C30	40 X 40	Plan C	4.44 X 4.44	30
C20	40 X 40	Plan C	4.44 X 4.44	20
C10	40 X 40	Plan C	4.44 X 4.44	10

Table 2. Properties of materials used in modelling

Material properties	Reinforcement grade -Fe 415	Concrete grade -M 25
Yield Stress	415 N/mm^2	-
Compressive strength	-	25 N/mm^2
Modulus of Elasticity	2X10^5 N/mm^2	2.5X10^4 N/mm^2
Weight per unit volume	76.973 kN/m^3	23.6 kN/m^3
Poisson's Ratio	-	0.2

Table 3. Cross-sections of members

Floor No.	Column size, m x m			Shear wall size, mm		
	Plan A	Plan B	Plan C	Plan A	Plan B	Plan C
1st to 5th	1.6 x1.6	1.3x1.3	1.1x1.1	550	500	500
6th to 10th	1.4x1.4	1.2x1.2	1.0x1.0	550	500	500
11th to 15th	1.3x1.3	1.1x1.1	0.9x0.9	450	400	400
16th to 20th	1.2x1.2	1.0x1.0	0.8x0.8	450	400	400
26th to 30th	1.0x1.0	0.8x0.8	0.6x0.6	350	300	300
31st to 35th	0.9x0.9	0.7x0.7	0.5x0.5	250	200	200
36th to 40th	0.7x0.7	0.6x0.6	0.4x0.4	250	200	200
Beam Size	0.35x0.75	0.3x0.6	0.3x0.5	-	-	-

2.2. Material Properties Related to Creep & Shrinkage

To calculate the long-term shortening due to creep and shrinkage, IRC: 112-2011 code is used, wherein basic equations for creep co-efficient and the drying shrinkage strain are given. Relative humidity, concrete age at loading, cross-sectional area, concrete strength, notional size of the member in mm, the perimeter of the member in contact with the atmosphere, age of concrete in days at the time considered, cement type, and the temperature adjusted age of concrete at loading in days are all factors taken into account when calculating the co-efficient of creep. While the parameters considered for calculation of the shrinkage strain are mean compressive strength, type of cement, and relative humidity.

2.3. Sequential Loads on Building Models

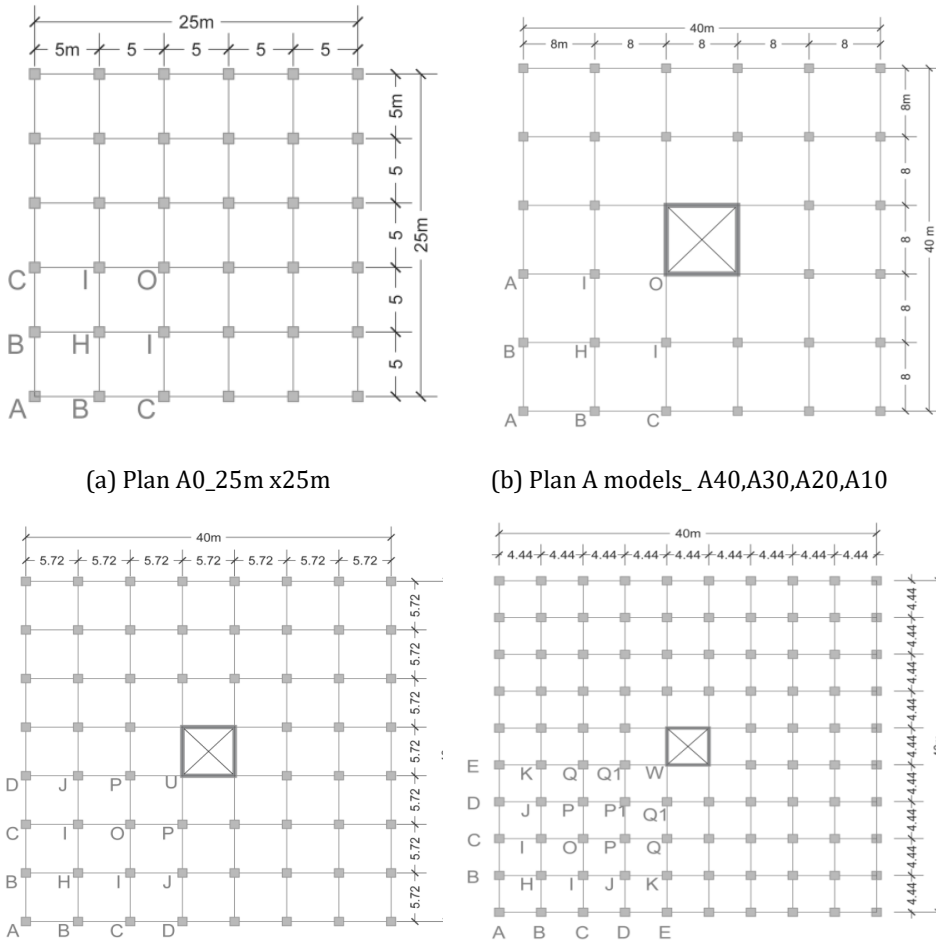

(a) Plan A0_25m x25m

(b) Plan A models_ A40,A30,A20,A10

(c) Plan B models_ B40,B30,B20,B10

(d) Plan C models_ C40,C30,C20,C10

Fig. 1 Plan of different building models

Stage-wise construction loads were applied on all RC building models and analysed by the CSA method for a construction cycle of seven days. For the first slab casting, the formwork was undertaken and concreting of the first slab was done on the third day of construction. As shown in Table 4, different loads were applied at different stages following the actual onsite construction sequence and its timing. These stage-wise loading sequences and timing for all stages were activated considering long-term properties of concrete like creep and shrinkage up to 50 years of a lifetime after occupancy to get a critical time period for A0 building. The analysis was undertaken for 10950 days for twelve models to get critical storey numbers of the RC buildings.

Table 4. Stage-wise sequential loading for the CSA method.

Sr. No.	Type of load	Starting floor	The load cycle begins at/with	Cycle time
1	Self-weight of RC members	the first floor	On the first day of first stage one, i.e., on 22nd day, when the age of first-floor slab is19 days	7 days
2	Load of the brick wall	the first floor	On the first day of fifth stage, i.e., on the 29th day	7 days
3	Load of floor finishing	the first floor	On the first day of sixth stage, i.e., on the 36th day	7 days
4	Live load	on all floors	At the last stage i.e., after allowing 90 days for occupancy after completion of construction work including finishing work.	Single time

3. Results and Discussion

3.1. Critical Time Period

CSAcs is carried out for the 'plan A0' building model. Total axial shortening for all columns were observed. Fig. 2 shows the shortening of column CA at the top floor level at the time of application of live load and for other time periods, which were 365 days, 730 days, 1000 days, 1825 days, 3650 days, 7300 days, 10950 days, 14600 days, and 18250 days from the application of live load by CSA method. The results of axial shortenings for all time periods were compared with the result of the 50th year.

Axial shortening at the top floor of column A was found to be only 14.28mm at the time live load was applied. In contrast, axial shortening was found to be much larger at 57.08mm after 50 years of live load application. After applying the live load at the top floor of CA, the axial shortening was 24.1mm, 41.53mm, 47.1mm, and 54.31mm after 365days, 1000days, 1825days, and 7300days, respectively.

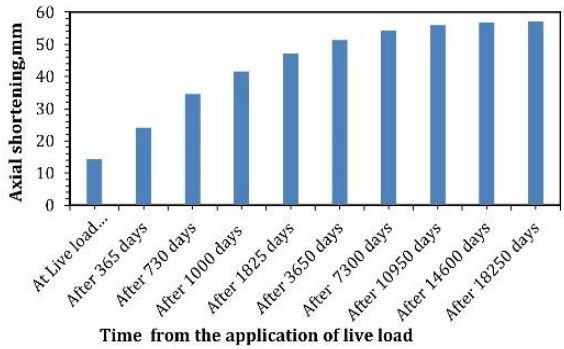

Fig. 2 Axial shortening of column A for the various time period

The findings of the percentage shortening of each column for each time period were compared to the percentage shortening of the 50th year as the base time period to determine the average percentage shortening of all columns, which was then plotted in Fig. 3. (a). Considering the axial shortening as 100 % in all columns after 50 years, the average axial shortening at the moment of live load application was observed to be 51.57%. The average axial shortening was reported to be 61.76%, 82.21 %, 88.55%, and 98.7% for the 50th year, respectively, during periods of 365 days, 1000 days, 1825 days, and 10950 days following the application of live load.

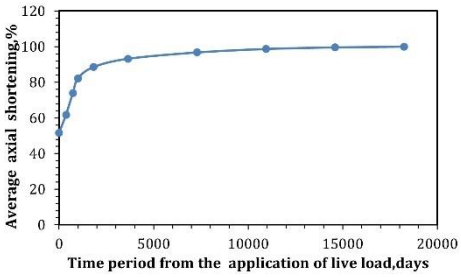

Fig. 3(a) Average axial shortening of columns w.r.t 50 years Shortening

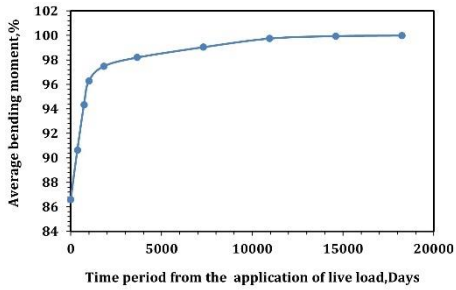

(b) Average bending moment of beam'AB' w.r.t 50 years bending moment

As seen in Fig. 1(a), beam "AB" of "plan A0" is chosen for observation. For every floor level and across all time periods, bending moments were noted at the ends "A," "B," and "AB." The average percentage moment of all floors for each time period, maintaining the 50th year as a base, was calculated at both the supports and mid-span of beam 'AB' and plotted in Fig. 4.

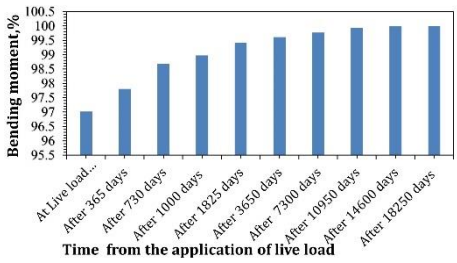

(a) Bending moment at end 'A'

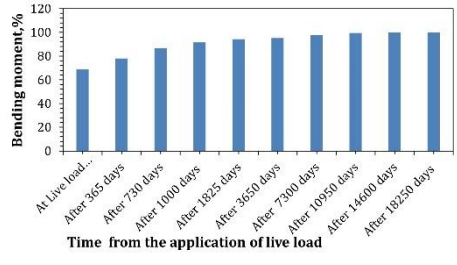

(b) Bending moment at end 'B'

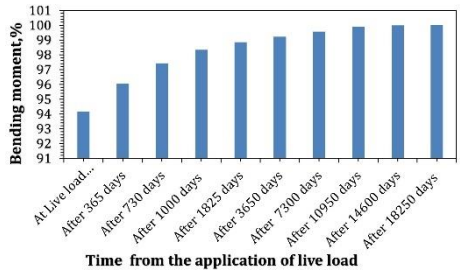

(c) Bending moment at mid-span

Fig. 4 Percentage moment at various locations of beam 'AB' for different time periods

The average moment observed at the time of live load application at end A, end B, and mid-span was 97.02%, 68.63% and 94.15%, respectively, if the bending moment in a beam after 50 years is deemed to be 100%.The average moment at every floor level was observed to be 90.6%, 94.3%, 96.3%, and 99.7% of the axial shortening of the 50thyear; after 365, 730, 1000 and 10950days time period respectively, as in Fig. 3(b).

3.2. Derivation of Critical Storey Limit

As per the time period study, 98.7% of axial shortening and 99.43% of bending moments of the 50th year were observed after 10950 days. Hence, all twelve models were analysed for 10950 days using the CSA method considering the long-term effects of concrete (CSA_{30CS}).

3.2.1 Categorization of Columns

An axial shortening, at every floor level (i), for all twelve building models by CSA_{30CS} method was compared with the LSA method., The 'Δ' parameter was introduced to compare the sensitivity of columns in terms of percentage strain difference induced due to the axial shortening in both methods. The following equation specified the percentage difference (Δ) induced in the axial strain at any floor level-'i'.

'Δ' at any floor level

$$i=\left\lfloor \frac{Strain\ induced\ at\ i^{th}\ floor\ \ by\ CSA30CS - Strain\ induced\ at\ i^{th}\ floor by\ LSA}{Strain\ induced\ at\ i^{th}\ floor\ by\ LSA} \right\rfloor 100 \quad (1)$$

Where strain induces at each floor level, (i^{th} level) =

$$\left\lfloor \frac{[Total\ Axial\ shortening\ induced\ at\ upper\ floor - Total\ Axial\ Shortening\ induced\ at\ lower\ floor\ level]}{Floor\ height\ (Hi)} \right\rfloor \quad (2)$$

A graph representing the 'percentage strain difference (Δ) V/S floor number', for all vertical members of the A30 building model was plotted as shown in Fig. 5. Following observations were made from Fig.5.

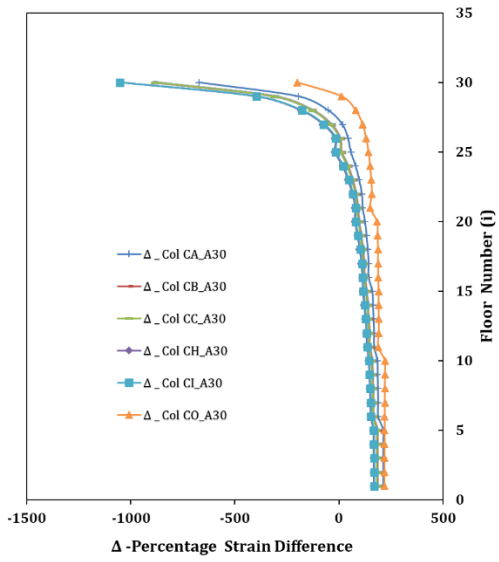

Fig. 5 Δ- percentage strain difference V/S floor number, for model A30

- Percentage strain v/s floor graph of columns CB and CC were similar.
  Percentage strain v/s floor graph of columns CH and CI were similar to Δ.
- Percentage strain v/s floor graph of columns CA and CO were independent of all columns.

Based on these observations, columns of the A30 were divided under four different categories, CAT-I, CAT-II, CAT-III and CAT-IV, as shown in Fig. 6(a).

Similar pattern of graphs was observed with the A40, A20 and A10 models, as shown in

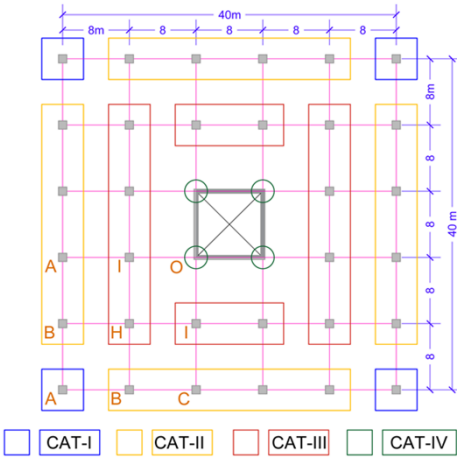

(a) Plan A model

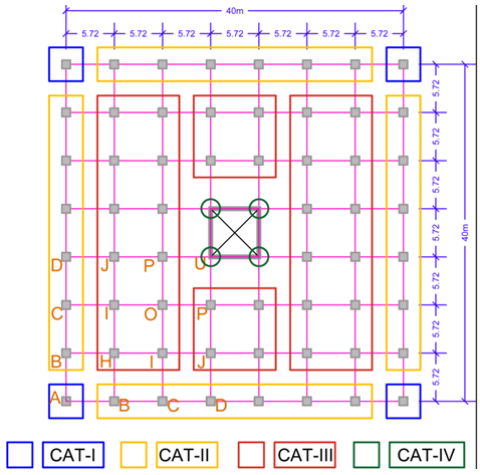

(b) Plan B model

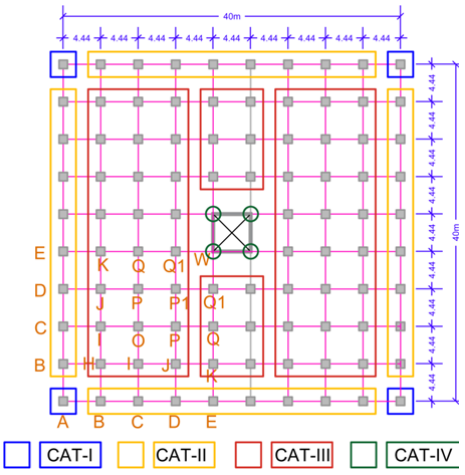

(c) Plan C model

Fig.6 Different categories of columns of plan A ,plan B and plan C models

Fig. 7(a). Hence the columns were divided into four similar categories, as shown in Fig. 6(a)

- It was observed that the sensitivity of the axial strain increases as the building floors increase, as shown in Fig. 7(a) for models A40, A30, A20 and A10.
- Δ for the same column CA was higher in model A40 than in model A10 as shown in Fig. 7(a). As the building's total storey (n) increases, Δ of the column in all categories also increases.
- Maximum variation of Δ was observed within upper 15% to 18% storeys, as shown in Fig. 5 and Fig. 7.

The analysis and observations remain similar for plan B and plan C building models. Hence, all the columns were divided into four similar categories, CAT-I, CAT-II, CAT-III and CAT-IV, as shown in Fig. 6.

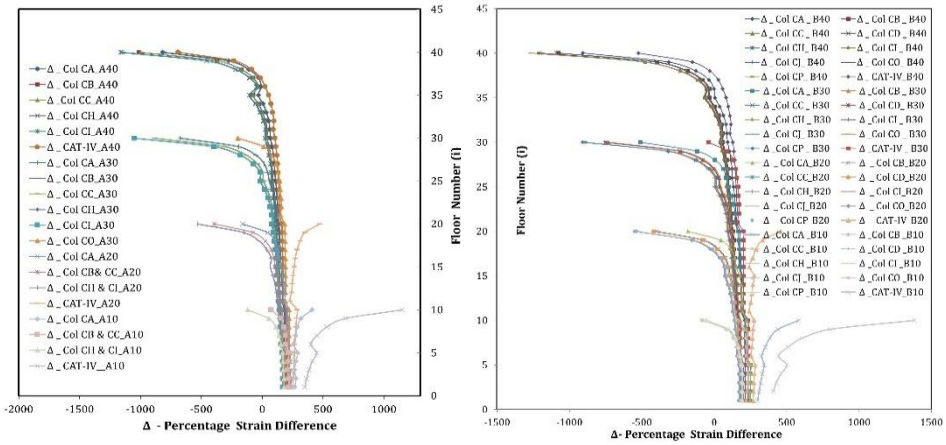

(a) plan A models (b) plan B models

Fig. 7 'Δ -percentage strain difference V/S floor number'_ for plan A and plan B models

3.2.2. Critical Storey Limit of RC Buildings with CSA30CS

It was observed from Fig. 5, Fig. 7, and Table 4 that maximum Δ occurs at the top-most floor level of the building models for all plans and categories of columns. Δ for CAT-I columns for all plan models are as in Table 5.

Table 5. Maximum percentage strain difference (Δ) for CAT-I columns

Building models	Maximum Δ, for columns of CAT-I					
	Plan A		Plan B		Plan C	
	maximum Δ	location	maximum Δ	location	maximum Δ	location
40 storeyed	-818.062	at 40th floor	-906.137	at 40th floor	-806.744	at 40th floor
30 storeyed	-672.761	at 30th floor	-510.508	at 30th floor	-525.674	at 30th floor
20 storeyed	-162.564	at 20th floor	-182.434	at 20th floor	-114.077	at 20th floor
10 storeyed	410.376	at 10th floor	583.192	at 10th floor	574.01	at 10th floor

The CAT-I columns for models C40, C30, C20 and C10 were also studied. The results were plotted in the 'Δ V/S floor number' graph, as shown in Fig. 8. An equation for floor sensitivity limit was extracted by drawing the best-fitted curve using a polynomial model passing through maximum Δ for CAT-I columns of plan C. The extracted equation of storey sensitivity for CAT-I columns of the plan C building model is:

'$n = 1E\text{-}05*\Delta^2 - 0.019*\Delta + 17.421$.'

As seen in the equation and Fig. 8, when the best-fitted curve crosses the vertical axis, the value of Δ becomes zero, and the corresponding total storey number (n) approaches 17.24. Hence this shows that when the CSA30CS method is used, the columns of CAT-I become sensitive when plan C type buildings cross 17 storeys (n). Similarly, plan C's columns of CAT-II, CAT-III & CAT-IV were also analysed. Critical storey limit equations were derived based on the graphical representation of the analysis as plotted in Fig. 9(a)-9(c). The

extracted equations for storey sensitivity of CAT-II, CAT-III, and CAT-IV columns of plan C models are tabulated in Table 6.

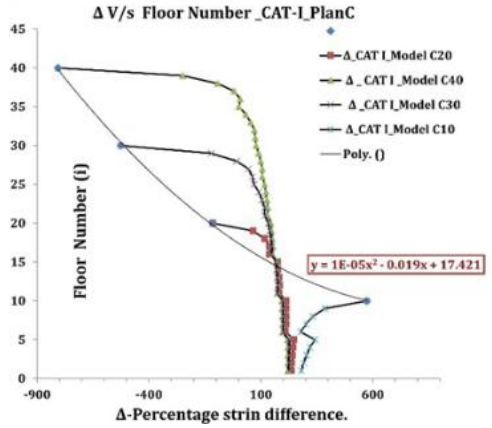

Fig. 8 Critical storey limit for CAT-I columns of plan C

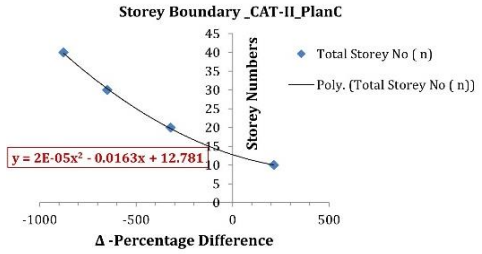

(a) CAT-II of plan C

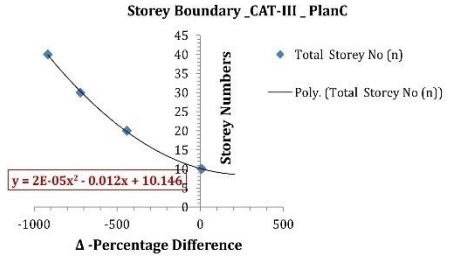

(b) CAT-III of plan C

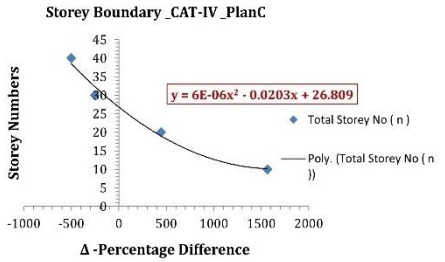

(c) CAT-IV of plan C

Fig. 9 Critical storey limit for columns of plan C.

Similarly, equations for all categories of columns were extracted for plan A and plan B type building models as shown in Fig. 10(a)-10(d), and Fig. 10(e)-10(h),as tabulated in Table 6.

The average critical limit is the storey above which it is advisable to use CSA_{30CS} method for the design of RC buildings. Average critical limits for all categories and models are tabulated in Table 7.

The observation for the above analysis is summarized as follows,

- In a building with storeys more than 16.82, CAT-I columns will be critical.
- In a building with storeys more than 12.13, CAT-II columns will be critical.
- In a building with storeys more than 9.27, CAT-III columns will be critical.
- In a building with storeys more than 27.51, CAT-IV (shear wall) will be critical.

Table 6. Equations of critical storey limit for all categories and columns

Column category	Equation	Sensitivity, in terms of 'n'
	For plan A	
CAT-I	$n = 1E\text{-}05*\Delta^2 - 0.0177*\Delta + 15.595$	15.595
CAT-II	$n = 1E\text{-}05*\Delta^2 - 0.014*\Delta + 11.263$	11.263
CAT-III	$n = 1E\text{-}05*\Delta^2 - 0.0132*\Delta + 8.8111$	8.811
CAT-IV	$n = 2E\text{-}06*\Delta^2 - 0.017*\Delta + 27.108$	27.108
	For plan B	
CAT-I	$n = 8E\text{-}06*\Delta^2 - 0.0179*\Delta + 17.46$	17.46
CAT-II	$n = 9E\text{-}06*\Delta^2 - 0.0164*\Delta + 12.348$	12.348
CAT-III	$n = 7E\text{-}06*\Delta^2 - 0.0178*\Delta + 8.6237$	8.624
CAT-IV	$n = 5E\text{-}06*\Delta^2 - 0.0198*\Delta + 28.612$	28.612
	For Plan C	
CAT-I	$n = 1E\text{-}05*\Delta^2 - 0.019*\Delta + 17.421$	17.421
CAT-II	$n = 2E\text{-}05*\Delta^2 - 0.0163x + 12.781$	12.781
CAT-III	$n = 2E\text{-}05*\Delta^2 - 0.012*\Delta + 10.146$	10.146
CAT-IV	$n = 6E\text{-}06*\Delta^2 - 0.0203*\Delta + 26.809$	26.809

Table 7. Average critical storey limit for columns of all categories and all plans

Column category	Critical storey limit in terms of total storey numbers (n)			
	Plan A	Plan B	Plan C	Average 'n'
CAT-I	15.595	17.46	17.421	16.82
CAT-II	11.263	12.348	12.781	12.13
CAT-III	8.811	8.624	10.146	9.27
CAT-IV	27.108	28.612	26.809	27.51

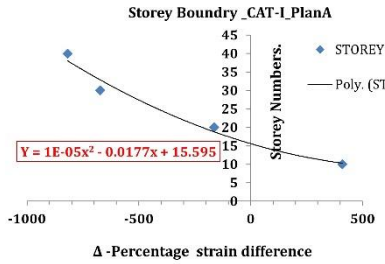

(a) CAT-I of plan A

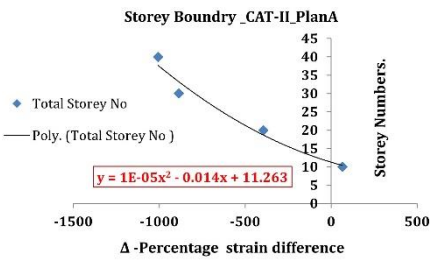

(b) CAT-II of plan A

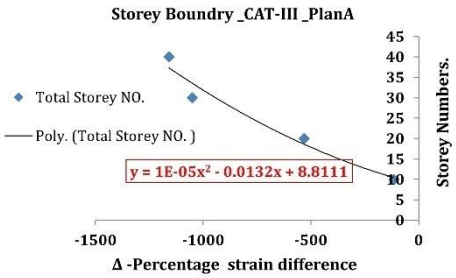

(c) CAT-III of plan A

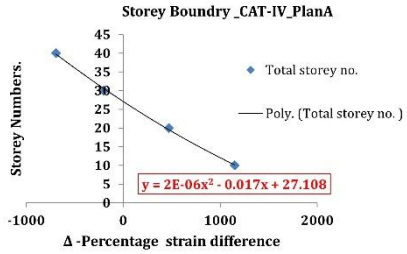

(d) CAT-IV of plan A

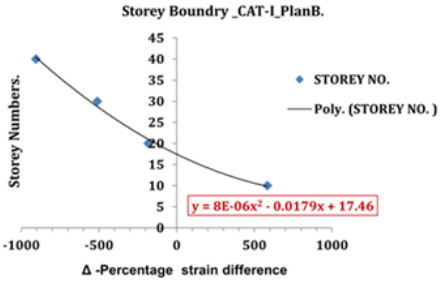

(e) CAT-I of plan B

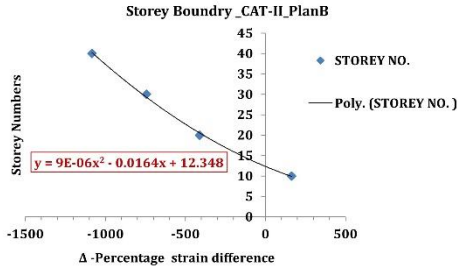

(f) CAT-II of plan B

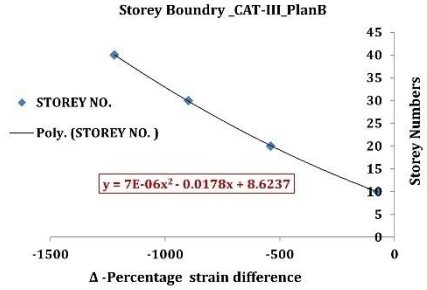

(g) CAT-III of plan B

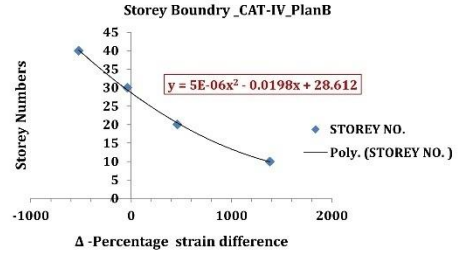

(h) CAT-IV of plan B

Fig. 10 Critical storey limit for columns of plan A and plan B

4. Conclusions

This study determines the critical time period up to which the CSA method should be used to analyse and design the RC framed buildings. Furthermore, it determines the critical storey limit for the RC framed building, over which the CSA method must be used. It is concluded that:

- The rate of axial shortening increase for the first 7300days is significant compared to the days between 7300, i.e., 30 years to 18250 days i.e., 50years, when the analysis is done through the CSA method.
- Only 51.57% of the 50th year axial shortening is achieved at the time of live load application, which is only half of the critical shortening observed at the 50th year.

Whereas 86.6% of the 50th year beam moment is achieved at the time of live load application, which is less than the critical moment observed at the 50th year.

- 98% to 99% of the total 50th year axial shortening and beam moments are observed on completion of 7300days (30 years) from the time of live load application. Therefore, it is advised to analyse using the CSA method up to a minimum time of 30 years after the application of the live load, taking the effects of creep and shrinkage into account, rather than up to 50 years, as the procedure is time-consuming and laborious.
- Behavioural patterns of columns for all building models of various spans and total storeys are divided into four categories. Each category has its own critical storey limit. Hence, if the column crosses this limit, the CSA_{30CS} method must be adopted for the analysis and design of the column instead of the conventional –Linear Static Analysis method for a safe design.
- It is observed that maximum percentage strain difference (Δ) occurs at the top most floor level of a building for all plans and categories of the column. Maximum variation of percentage strain difference (Δ) is observed in the upper 15% to 18% of total storeys.
- As the total storey (n) of a building increase, the percentage difference in strain (Δ) in a column also increases for all categories of columns in building models.
- If the total number of stories is more than or equal to 16, columns of category -I become critical. Similarly, category – II, III & IV columns become critical if the total number of stories is equal to or more than 12, 9, and 27, respectively. Thus, for a building with a total storey number of more than nine storeys, the CSA_{30cs} method should be mandatory to analyse and design RC framed buildings.
- The reduction in the span of beams results in an increase in critical storey limit for all categories of columns.
- The critical storey limit of the shear wall is higher than that of columns.

Acronym

CSA_{CS}	: Construction Sequence Analysis considering creep and shrinkage
CSA_{30CS}	: Construction Sequence Analysis considering creep and shrinkage (CSACS), up to 10950 days (30 years) from the time of live load application
LSA	: Linear Static Analysis Method
Δ	: A percentage difference in axial strain, obtained by the CSA30CS method with respect to LSA method
CA, CB	: Column A, Column B, etc
RC	: Reinforced Concrete
n	: Total storeys in building
i	: ith floor level
wrt	: with respect to
CAT	: Category

References

[1] Afshari MJ, Kheyroddin A, Gholhaki, M. Simplified sequential construction analysis of buildings with the new proposed method. Structural Engineering and Mechanics, 63(1), 77-88; 2017.

[2] Casalegno C, M Sassone, Chiorino MA. Time-Dependent Effects In Cable-stayed Bridges Built by Segmental Construction, Proc. of Third International fib Congress incorporating the PCI Annual Convention and Bridge Conference. Washington DC 2010.

[3] Chakrabarti SC, Nayak GC, Agarwala SK. Effect of sequence of construction in the analysis of multistoreyed building frame. Building and Environment, 13(1), 1-6, 1978. https://doi.org/10.1016/0360-1323(78)90002-1

[4] Choi CK, Chung HK, Lee DG, Wilson EL. Simplified building analysis with sequential dead loads-CFM. Journal of Structural Engineering, 118(4), 944-954, 1992. https://doi.org/10.1061/(ASCE)0733-9445(1992)118:4(944)

[5] Correia R, Lobo PS. Simplified assessment of the effects of columns shortening on the response of tall concrete buildings. Procedia Structural Integrity, 5, 179-186, 2017. https://doi.org/10.1016/j.prostr.2017.07.095

[6] Dinar Y, Rasel MM, Chowdhury MJA, Ashraf MA. Chronological construction sequence effects on reinforced concrete and steel buildings. the International Journal of Engineering and Science (IJES), 3(1), 52-63, 2014.

[7 Elansary AA, Metwally MI, El-Attar, A. Staged Construction Analysis of Reinforced Concrete Buildings with Different Lateral Load Resisting Systems, Engineering Structures, 242, p.112535, 2021 https://doi.org/10.1016/j.engstruct.2021.112535

[8] Ha T, Kim S, Lee S. Prediction of time-dependent lateral movement induced by differential shortening in tall buildings using construction stage analysis. International Journal of High-Rise Buildings, 6(1), 11-19, 2017. https://doi.org/10.21022/IJHRB.2017.6.1.11

[9] IRC:112 (2011), Code of Practice for Concrete Road Bridges, Indian Roads Congress. New Delhi,2011.

[10] Kwak HG, Kim JK. Time-dependent analysis of RC frame structures considering construction sequences. Building and Environment, 41(10), 1423-1434, 2006. https://doi.org/10.1016/j.buildenv.2005.05.013

[11] MIDAS Gen software Engineering Manual: Integrated Solution System for Building and General Structures; available from the URL: http://en.midasuser.com/product/gen_overview.asp

[12] Secer M, Arslan T. Effecs of Construction Sequence on Reinforced Concrete Building Analysis.In International Conference on Numerical Modelling in Engineering (pp. 123-134), 2018. https://doi.org/10.1007/978-981-13-2405-5_10

[13] Zucca M, Longarini N, de Socio F, Migliori I. Construction stage analysis for a new mixed structure building in Milan. International Journal of Structural Glass and Advanced Materials Research,2(1), 66-72, 2018. https://doi.org/10.3844/sgamrsp.2018.66.72

Research on Engineering Structures & Materials
journal homepage: http://www.jresm.org
MIM Research Group

Research Article

Strength and durability assessment of laterized concrete made with recycled aggregates: A performance index approach

Chinwuba Arum[1,a], Stephen Adeyemi Alabi[*1,2,b], Roland Chinwuba Arum[1,c]

[1]*Department of Civil and Environmental Engineering, The Federal University of Technology, Akure, Nigeria*
[2]*Department of Civil Engineering, University of Botswana, Gaborone, Botswana*

Article Info

Article history:

Received 16 Jul 2022
Revised 03 Dec 2022
Accepted 13 Dec 2022

Keywords:

Lateritic soil;
Recycled fine aggregate;
Recycled coarse aggregate;
Strength;
Durability;
Performance index

Abstract

The use of recycled aggregates (RAs) for concrete promotes circular construction while the introduction of lateritic soil (LS) seeks cost reduction in concrete production. This study reports the results of experiments on partial replacement of (i) Akure-pit sand (APS) with recycled fine aggregate (RFA); (ii) RFA with LS; (iii) APS with LS; and (iv) crushed granite (CG) with recycled coarse aggregate (RCA). Replacement levels were from 0% to 70% in steps of 10%. Major tests were compressive strength and sorptivity. The performance index approach was employed to obtain the best performance indices for various material combinations. The results revealed that at 28 days of curing, concretes attained optimum compressive strengths of 15 N/mm^2, 15.1 N/mm^2, 13.1 N/mm^2, and 16.8 N/mm^2, respectively for mixtures produced by partially substituting APS with 70%RFA; RFA with 40%LS; APS with 50%LS; and CG with 50%RCA. The sorptivity was optimal at 2.69x10^{-4} mm/min$^{0.5}$; 3.58x10^{-4} mm/min$^{0.5}$; 3.16x10^{-4} mm/min$^{0.5}$; and 2.86x10^{-4} mm/min$^{0.5}$, respectively for mixtures with partial replacement of APS with 30%RFA; RFA with 40%LS; APS with 40%LS; and CG with 10%RCA. This research will find practical application in construction works utilizing LS and RAs when optimal replacement levels of the conventional aggregates are required, in order to achieve predetermined performance criteria.

1. Introduction

The environmental impact of mining fine and coarse aggregates used in making concrete and the sustainability of the same for concrete production have been called into question in recent times [1]. Therefore, many researchers have begun to investigate the use of construction and industrial waste and by-product materials for concrete production [2-6]. Studies by Ke *et al.* [7] have shown that certain high-quality wastes reduce the cost of producing concrete, improve its durability, as well as mitigate alkali-silica interaction, cracking in mass concrete, and shrinkage-induced cracking. Some of these wastes may chemically react with calcium hydroxide when finely ground and in the presence of water to create compounds that have cementing capabilities comparable to those created during the cement hydration process. Some others are used as alternatives (in full or partial substitution) to the conventional aggregates used in concrete [8]. Some of the wastes used as alternative aggregates include recycled concrete aggregate (RCA) and lateritic soil (LS) [9-12].

Laterite has been identified as a viable supplementary material or alternative to conventional sand [13-14]. This material is readily available in sub-Saharan Africa as a product of weathering. The most popular and widely accepted application of laterite is as bedding material in road pavement construction and brick production. These days,

*Corresponding author: saalabi@futa.edu.ng
[a] orcid.org/0000-0001-7176-7602; [b] orcid.org/0000-0001-8731-6961; [c] orcid.org/0000-0002-8623-2587;
DOI: http://dx.doi.org/10.17515/resm2022.477st0716

researchers are beginning to investigate more productive and effective ways of making durable concrete with laterite. According to Gowda *et al.* [15], a concrete mix where laterite has been used to partially or fully replace river sand is known as laterized concrete. Udoeyo *et al.* [16] assert that substituting sand with laterite can increase the concrete's workability. However, the workability of concrete made from unprocessed laterite is considerably lower than that made from processed laterite [15]. Ettu*et al.* [17], after conducting compressive strength tests on a total of 120 standard 150 mm concrete cubes, concluded that laterite could be used as the sole fine aggregate in structural concrete, entirely replacing sand in each concrete mix. This conflicts with the results of many other researchers who, after their independent experimental-based research, concluded that laterite only has a positive influence on concrete compressive strength up to a certain level [16, 18]. According to Mathew *et al.* [18], laterite can replace 20-40% of sand without affecting the concrete's strength. Balogun and Adepegba [19] as cited by Awoyera *et al.* [20] postulated that the ideal mix (batching by weight) for laterized concrete was 1:1.5:3, provided that the laterite is kept below 50% of the total aggregate content. Laterite is composed mostly of sand, clay, and silt, and its redness in colour is caused by the presence of iron oxide [21-22]. The presence of clay and silt in the laterite particles may make it fall short in the production of high-quality concrete requirements as laid out in BS 882 (1992). Consequently, the clay and silt particles are usually washed off during processing [17]. Onakunle *et al.* [23] corroborated this inference by stating that the strength and stability of lateritic soil cannot be guaranteed under high load and moisture when it has a lot of clay constituents. The suitability or otherwise of laterite as the sole fine aggregate in concrete would depend on the amount of fine particles present in the laterite [17]. According to Osunade [13], as cited by Joshua *et al.* [24], the fineness of the grain size positively correlates with the compressive strength of concrete samples made from laterite. They also opined that the compressive strength of lateritic soil might be hugely related to where the material was collected from. This is based on the premise that different formation processes must have occurred at various source sites [24]. Osadebe & Nwakonobi [25], as cited by Tijani and Mustapha [26], stated that the consistency achieved during mixing might also have a huge influence on the laterite's compressive strength. Batha *et al*. [26] studied the influence of replacing natural sand with polyethylene terephthalate waste up to 50%. It was observed that replacing natural sand generally reduces the strength properties of the concrete beam.

Furthermore, according to Silva *et al.* [27], construction and demolition waste (C&DW) are viable alternative aggregates to conventional materials for low-cost green concrete production. One such C&DW is the recycled concrete aggregate (RCA) being explored for concrete production [28-33]. RCA collected from construction and demolition sites is a viable solution to depleting natural aggregates in various parts of the world [34]. Only aggregates collected from demolition sites and processed into coarse (>5mm) aggregates are known as recycled coarse aggregate (RCA) [35-36]. If processed into fine (<5mm) material, it is known as recycled fine aggregate (RFA) [37]. Dhir OBE *et al.* [38] provide a detailed overview of the properties and composition of recycled aggregates. The demolition quality, and how the aggregate was sorted may determine RCA properties [29, 39]. The properties of the RCA would also depend on that of the parent concrete. Proper design parameters must be adopted to make the properties of RCA comparable with what is obtainable using natural aggregates. Still, the replacement percentage should not be more than 30% to avoid adverse effects on the concrete properties [40].

Many studies have explored using different techniques to obtain RCA properties equivalent to their natural aggregate counterparts [41-43]. It has been reported that concrete containing 30% RCA could perform as well as concrete made from natural aggregates and even better [44-45].

Some researchers Mirjana *et al.* [46] as cited by Khalid *et al.* [47] obtained their recycled concrete aggregates from crushed precast concrete columns and laboratory test cubes. According to Mirjana *et al.* [46], high-quality aggregate does not affect the strength properties of concrete regardless of the replacement levels adopted. In the same vein, the curing condition does not have a considerable effect on the compressive strength of concrete (Fonseca *et al.* [48] as cited by Abdel-Hay [49]). For RCA to be considered acceptable, it must meet a list of criteria. These include an optimum water absorption not greater than 3%, an aggregate relative density of 2.3% or more, and optimum mortar content of not greater than 50% (Butler *et al.* [50] as cited by Zheng *et al*. [51]). On recycled aggregate concrete (RAC), numerous investigations have been conducted [9, 52-61]. Batha *et al*. [62] performed a thorough analysis of the physical and mechanical characteristics of concrete using a 0.1% constant dose of glass fiber and partial replacements of the cement with fly ash up to 40% and sand with pond ash up to 20%. It was determined that the addition of fly ash and pond ash to concrete could generate strong concrete that was also reusable and durable while using less sand, cement, and energy. In another study, Batha *et al*. [63] proposed a mix design method that uses the dense particle packing arrangement principle to create sustainable concrete by partially substituting fly ash and pond ash for cement and sand. It was concluded that using a method of packing density to replace natural sand with pond ash lowers material consumption and building costs while maintaining a clean, green environment without sacrificing strength and durability.

Although studies have been conducted on the utilization of laterite, RFA, RCA, and APS separately as sand and coarse substitutes in concrete, there had yet to be any published research on the combined influence of these constituents on either freshly poured or hardened concrete. On the use of materials as a partial sand replacement in concrete mixtures, there were no specifications. These replacement levels have usually been chosen to enhance concrete performance based majorly on personnel knowledge and experience with the material. It is therefore imperative to design a technique that could enable professionals to make an informed decision on the appropriate levels of replacement for desired performance. Additionally, the study sought to determine the quality of conventional concrete using a performance index (PI) approach to choose the appropriate substitution rate and maximize each mixture's unique properties. Therefore, the overall aim of this research is to obtain the optimal combinations of LS, RFA and RCA that could substitute appropriate fractions of Akure pit sand (APS) and coarse granite (CG) to obtain low-cost and durable green concrete while offering essentially the same strength as when only conventional aggregates are used. Utilizing LS, RFA, and RCA wastes would not only encourage the sustainability of building materials but also contribute to the reduction of landfill sites and environmental degradation.

2.Experimental Strategy

2.1. Materials Adopted

The coarse granite (CG), recycled coarse aggregate (RCA), recycled fine aggregate (RFA), lateritic soil (LS), Akure pit sand (APS), cement and water were the materials used. In order to produce concrete, locally purchased grade CEM 1 42.5R ordinary Portland cement (OPC) conforming to BS 12 [64] was utilized. The oxide content of the cement is displayed in Table 1. In order to assess the actual level of fineness, OPC was allowed to pass through a filter with a 90 μm opening. The CG and APS were obtained in the Akure metropolis and processed in accordance with BS EN 933-11 [65]. In order to comply with BS 882 criteria, the APS underwent a comprehensive sieving process to reduce its impurity and organic material levels [66]. The aggregates were guaranteed to meet the requirements for the medium grading zone [67]. The maximum size of the fine aggregate

was 4.75 mm, while the maximum size of the coarse aggregate was 12.5 mm. The laterite was obtained from a borrow pit in Akure, Southwest Nigeria. The RCA and RFA were obtained from the demolitions of an existing building at Jibowu Crescent, Iyaganku GRA, Ibadan also in the Southwest region of Nigeria. The RCA was manually crushed to the desired particle size of the maximum aggregate size of 12.5 mm with the aid of a rubber hammer. The RFA was also carefully processed to conform with the recommendations of BS EN 933-11 [64]. The impact value and particle size distribution of laterite, RFA, and RCA are all in agreement with BS EN 933-11 [65] and BS EN 933-1 [67]. The various aggregates as well as the OPC used in the investigation are shown in Fig. 1.

Table 1. Chemical composition of the cement

Oxide composition	CaO	SiO_2	Fe_2O_3	Al_2O_3	SO_3	Na_2O	MgO
Cement (%)	61.52	21.02	3.28	5.78	2.04	0.78	2.08

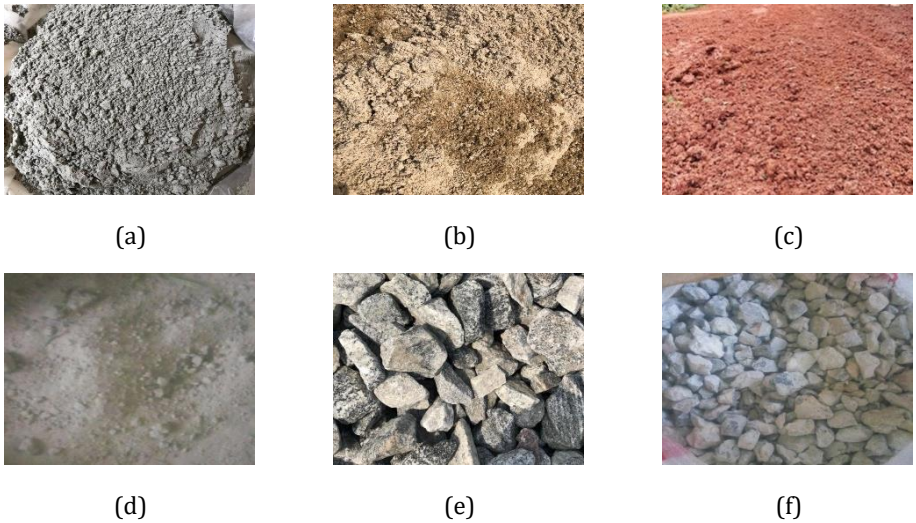

(a) (b) (c)

(d) (e) (f)

Fig. 1. (a) Cement (b) APS (c) LS (d) RFA (e) CG) (f) RCA

Aggregates' specific gravity should be between 2.30 and 2.90, according to ACI [68]. Therefore, laterite, RCA, and RFA all have specific gravity values that are within the acceptable range, making them acceptable for use in concrete. Table 2 presents some calculated properties of aggregates used while the gradation of the aggregates curves and BS EN 933-1 [67] classification are shown in Fig. 2. The aggregates used were found to satisfy the BS requirements. Furthermore, RCA and CG showed similar particle grading in much the same way as the particle gradings of RFA, LS and APS were similar. Both mixing and curing water adhere to BS 3148 [69]. It was determined that there were no sulfate, ferric, alkaline soils, vegetation, or salt present that would have an impact on the qualities of fresh or solidified concrete.

2.2. Proportioning of Concrete Mixtures

The performance of concrete was investigated using four distinct mixtures. The first mix was created by partially replacing APS with RFA at proportion rates of 0% to 70% in steps of 10%; the second combination was made by completely replacing APS with RFA and then partially replacing RFA with LS from 0% to 70% in steps of 10%; the third concrete specimens were formed by partially replacing APS from 0% to 70% in steps of

10%, with lateritic soil; and the final concrete mixture was created by partially replacing coarse granite with RCA at proportion levels of 0% to 70% in steps of 10%. Table 3 lists the precise material proportioning for the concrete mixture utilized in this study. Thirty (30) mixtures in total were prepared, as depicted in Table 3, and their workability, compressive strength and sorptivity were evaluated.

Table 2. Physical properties of aggregates and binders

Physical properties	Binder	Fine aggregate			Coarse aggregate	
	OPC	APS	RFA	LS	CG	RCA
C_u	-	2.18	2.45	2.95	2.50	4.36
C_c	-	1.88	1.67	2.25	1.60	1.91
Specific gravity	3.09	2.70	2.62	2.65	2.70	2.63
Shape	-	-	-	-	Angular	Angular
ACV (%)	-	-	-	-	21.02	20.3
AIV (%)	-	-	-	-	19.85	19.85
Moisture content (%)	-	7.20	5.16	12.5	2.12	3.16
Maximum aggregate size(mm)	-	4.75	4.75	4.75	12.75	19.00
Bulk density (kg/m^3)	-	2682	2138	1630	-	-
Liquid limit (%)	-	-	-	28.20	-	-
Plastic limit (%)	-	-	-	12.10	-	-
Shrinkage limit (mm)	-	-	-	3.00	-	-

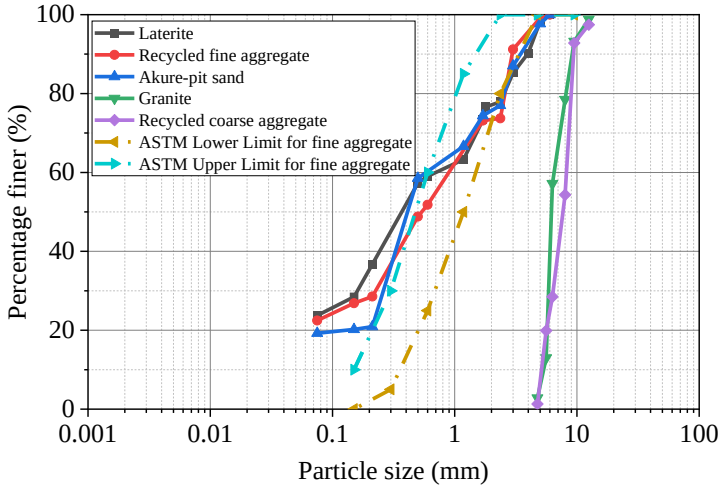

Fig. 2. The grain size distribution of aggregates

2.3. Testing of Concrete Samples

With a water-to-cement ratio (w/c) of 0.53, cement, fine aggregate, and coarse aggregate were all mixed by weight. In order to achieve the desired strength class C15/20, concrete with cement grade 42.5 was employed. The fine and coarse aggregates were first mixed for about five minutes. For roughly 3 to 6 minutes, the cement was vigorously dry-mixed after being added gradually. For about 8 minutes, the mixture was slowly stirred after the addition of the mixing water, until a homogeneous composition became apparent. Before being placed in the necessary moulds in accordance with BS EN, 12350-2 [70], the fresh

property of the concrete, such as slump, was tested in accordance with 1881: Part 102 [71]. The fresh concrete was poured into the 150 mm standard concrete cubic moulds, which had been lubricated with used engine oil to ensure easy demoulding and smooth surface before pouring. The compaction was done manually in about three equal layers for the cube specimens at an average depth of 50 mm and at each layer 25 blows was given using standard rod. The casting was carried out as per the requirements of BS EN, 12390-2 [70]. After 24 hours, the concrete was removed from the moulds and cured in the curing tank, following BS 12390 [72]. At each hydration time at 7 days, 14 days, 28 days, and 56 days, three specimens of concrete cubes produced from each of the concrete mixes were removed from the curing tank, weighed, tested, and recorded for compressive strength. The ELE 2000 compressive strength machine with a loading rate of 6800 N/s was employed. To measure concrete resistance to exposure to aggressive environments, the sorptivity test is adopted. The recommendation of ASTM C1585-13 [73] standard was followed to conduct the sorptivity test. After 7, 14, 28, and 56 days of curing, standard test samples of 100 mm diameter disc with a height of 50 mm were prepared. The samples were immersed in water with a water level not more than 3 mm above the base of the specimen. By appropriately sealing the peripheral surface with a non-absorbent coating, the flow from the peripheral surface is stopped. The amount of water absorbed over 30 minutes was determined by weighing the specimen on a top pan balance. Each weighted operation was finished in 30 seconds after surface water on the specimen was wiped away using a dampened cloth.

2.4. Performance Assessment of Concrete Mix Properties

It is frequently important to show data from different experimental schedules at the same time, as well as a statistical assessment of how concrete performance evolves. That is exactly what the performance index strategy accomplishes. It is a management tool that enables the compilation of multiple pieces of data into a single overall metric. This section explains how to use this technique to create a concrete mixture performance index. The performance indexes work on a simple principle: it condenses a large amount of data into a single number. When working with a small number of indicators, it is known that performance indicator (*PI*) relates data in an easy-to-comprehend format [74-75].

Therefore, the performance index technique is adopted as the improved model for the current study to assess the behaviour of concrete with a portion of Akure-pit sand (APS) and crushed granite (CG) replaced with lateritic soil (LS) and recycled aggregates (RAs) respectively. The details of concrete mixture proportions are given in section 2.2. Moreover, the suitable replacement level is selected using the performance index method. In this study, three performance indicators were selected which are compressive strength and sorptivity. The first step of this approach is to determine the weight rating for each performance indicator (θ_i) using Eq. (1). The highest individual performance indicator (e.g., compressive strength) has a 1.00 weight rating and other compressive strengths are rated relative to the highest compressive strength [74].

$$\theta_i = \frac{p_o}{p_h} \tag{1}$$

where p_o and p_h are respectively, the observed performance (i.e., performance indicator such as compressive strength, and sorptivity) for each concrete mixture and the highest observed performance.

The numeric index (ψ_i) is then determined using Eq. (2), such that the highest numeric index is set to be 5. Therefore, each weight rating of the individual performance indicator

is multiplied by the highest numeric rating [75].

$$\psi_i = 5\theta_i \tag{2}$$

Table 3. Concrete mixture proportions per cubic metre (kg/m^3)

Percentage replacement			Fine aggregate			Coarse aggregate		Cement	Water
RFA (%)	LS (%)	RCA (%)	APS	RFA	LS	CG	RCA		
0	-	-	498.80	-	-	1220	-	425	225
10	-	-	448.92	49.88	-	1220	-	425	225
20	-	-	399.04	99.76	-	1220	-	425	225
30	-	-	349.16	149.64	-	1220	-	425	225
40	-	-	299.28	199.52	-	1220	-	425	225
50	-	-	249.40	249.40	-	1220	-	425	225
60		-	199.52	299.28		1220	-	425	225
70		-	149.64	349.16		1220	-	425	225
	0	-	-	498.80	-	1220	-	425	225
-	10	-	-	448.92	49.88	1220	-	425	225
-	20	-	-	399.04	99.76	1220	-	425	225
-	30	-	-	349.16	149.64	1220	-	425	225
-	40	-	-	299.28	199.52	1220	-	425	225
-	50	-	-	249.40	249.40	1220	-	425	225
-	60	-	-	199.52	299.28	1220	-	425	225
	70	-	-	149.64	349.16	1220	-	425	225
-	10	-	448.92	-	49.88	1220	-	425	225
-	20	-	399.04	-	99.76	1220	-	425	225
-	30	-	349.16	-	149.64	1220	-	425	225
-	40	-	299.28	-	199.52	1220	-	425	225
-	50	-	249.40	-	249.40	1220	-	425	225
-	60	-	199.52	-	299.28	1220	-	425	225
-	70	-	149.64	-	349.16	1220	-	425	225
-	-	10	-	-	-	1098	122	425	225
-	-	20	-	-	-	976	244	425	225
-	-	30	-	-	-	854	366	425	225
-	-	40	-	-	-	732	488	425	225
-	-	50	-	-	-	610	610	425	225
-	-	60	-	-	-	488	732	425	225
-	-	70	-	-	-	366	854	425	225

Based on the essential performance indicators (j indicators), the associated ψ_i are multiplied to obtain a mixture score, (PI)ij as specified in Eq. (3).

$$\left(PI\right)_{ij} = \psi_{i1} \times \psi_{i2} \times \ldots \psi_{ij} \tag{3}$$

The inference from Eq. (3) is that the strength of weighted combinations can help in deciding how to distribute scarce resources. In terms of the relevant necessary numerous indicators, the combination receiving the highest score is the best acceptable mixture. The technique for selecting the right replacement amount to optimize the mixture's unique features to obtain the target performance indicator is briefly represented in the flowchart in Figure 3.

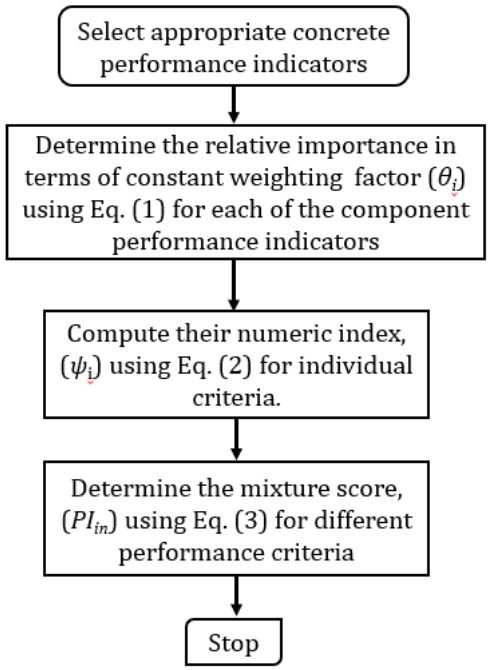

Fig. 3 Optimum concrete mixture based on specific performance criteria

3. Results and Discussion

3.1. Workability of the Concrete

In order to assess how easily and uniformly newly prepared concrete can be poured, compacted, and finished, the concrete's workability was determined. The slump test was used to evaluate flowability. The slump results for each blend are shown in Fig. 4. It was noted that for all the mixtures, the relative value of the slump often increases as the proportion of replacement increases. The moisture content in the aggregate may be the reason for this. Additionally, it was shown that concrete samples made when APS was partially replaced with LS had slump values that were higher than the control mix. This suggests that adding LS alters the cohesiveness of the mixtures, which in turn influences how well they flow. This finding agrees with research findings by Gowda *et al*. [15] and Udoeyo *et al.* [16].

From Fig. 4, the slump values for concrete with LS replacing APS and RFA are generally lower compared to other mixtures. This could be due to the dry surface of RFA and the fact that the presence of kaolinites and illites in LS requires more water to increase the plasticity [22] and workability. The slump value of the concrete mixture when APS is partially substituted with RFA, ranges from 75 mm to 75.5 mm. The slump value of the concrete mixture when APS is partially replaced with LS ranges from 75 mm to 90 mm. The slump value of the concrete mixture when RFA is partially replaced with LS ranges from 74 mm to 75 mm. A relatively lower value was observed in this particular concrete mixture due to the potential of RFA to soak up more water. The slump value of the concrete mixture when CG is partially replaced with RCA ranges from 75 mm to 76 mm. This suggests that all of the mixtures have a medium slump, which was designated by British standards as the most practical and often prescribed consistency. The findings of

this research indicate that the optimum percentage replacement of APS with RFA; APS with LS; RFA with LS; and CG with RCA were 20%, 40%, 40%, and 50% respectively.

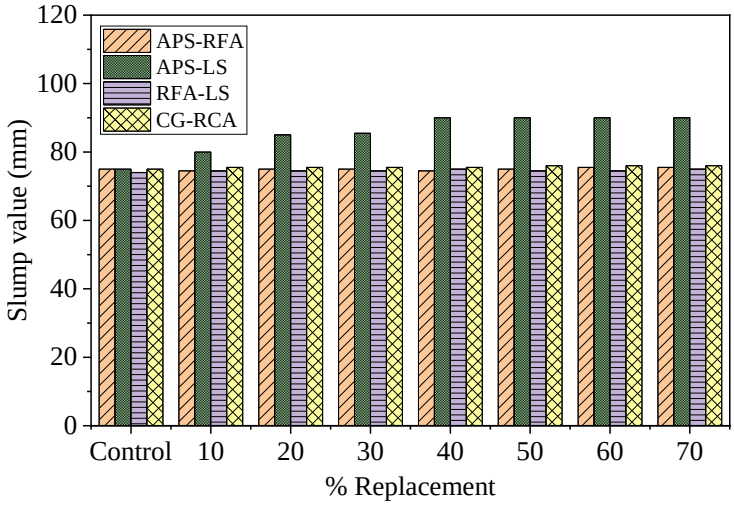

Fig. 4. Slump values of different fresh concrete mixes with varying replacement levels.

3.2. Compressive Strength

Figs. 5 to 8 for the various concrete mixtures illustrate the impact of LS, RFA, and RCA as partial substitutes of APS and CG, on the progression of compressive strength at 7, 14, 28, and 56 curing days. The impact of curing period on concrete compressive strength is typically shown by a steady rise in compressive strength as the curing period increases. From Fig. 5, at maturity ages of 7, 14, 28, and 56 days, the compressive strength of concrete mixtures with RFA replacing APS up to 70% was lower than the control. The reduction ranged from 5.05% with 70%RFA at 14 days to 40.43% with 10%RFA at 7 days when compared with the control mixture (i.e., without RFA). The optimum mix proportion of 70%RFA, which is greater than control mixture by 7.12% at 28 days, can be recommended. According to Fig. 6, the compressive strength of concrete mixtures with LS replacing RFA up to 70% was lower than the control (i.e., the reduction ranges from 3.94% with 40%LS at 14 days to 46.20% with 50%LS at 28 days) at 7, 14, 28, 56 days. When contrasted to the control mixture, at 28 days maturity, the optimum mix proportion of 40%LS is greater by 4.43% and therefore, can be recommended. According to Fig. 7, the compressive strength of concrete mixtures with LS substituting APS up to 70% was lower than that of the control mixture (i.e., without LS) at 7, 14, 28, 56 days (i.e., the loss ranged from 3.45% with 10% LS at 56 days to 39.72% with 70% LS at 7 days). With a difference of 18.89% as contrasted to the control mixture, the optimum mixture percentage of 50%LS can be proposed at 28 days. The high silt/clay proportion observed in Laterite and APS (Fanijo *et al*. [22] and Olanitori and Afolayan [76]), as seen in Fig. 7, may be the cause of the weakening of all concrete compositions. The maximum silt/clay content recommended by ASTM C33 is given to be 10%; meanwhile, for the fine aggregates used, the silt/clay content ranges between 20.20% to 28.48%. This type of fine aggregate is commonly used in most building constructions within the metropolis. This could result in poor adhesion between the concrete composites. However, in a concrete mixture where LS partially replaced RFA; a reduction in compressive strength was observed as laterite content increases up to 10% in the composite matrix, and thereafter a sudden increase in strength was observed, followed by a gradual reduction. A

similar trend was noticed in the concrete mixture in which LS partially replaced APS; the reduction in compressive strength was observed as laterite content increased up to 40% in the composite matrix, after which a sudden rise in strength was observed, before a gradual reduction in strength. This behaviour could be attributed to the poor workability of concrete produced with laterite and RFA. Poor workability makes compaction more difficult, which could have resulted in larger voids and a drop in compressive strength. This result is also consistent with the studies by Ettu *et al.* [17] and Muthusamy and Kamaruzaman [77]. Furthermore, the larger replacement levels of sand with laterite result in lower density than natural sand, resulting in reduced strength. Also, from Fig. 8, at 7, 14, 28, and 56 days of age, the compressive strength of concrete mixtures with RCA replacing CG up to 70% was significantly high only at the replacement level of 50%RCA for all curing ages. However, a relative reduction in strength (i.e., a reduction ranging from 6.96% to 34.03%) when compared with the control mixture (i.e., without RCA) was noticeable in other concrete mixtures. The variation in the water absorption capacity of the aggregates used could potentially be a factor in the loss of compressive strength. A drop in strength could be because of the amount of the adhered mortar on the RCA and poor compaction. The optimum mix proportion of 50%RCA can be recommended at 28 days with an increase in strength of 6.39% when contrasted with the control mixture.

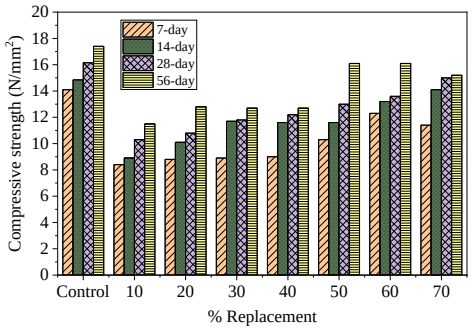

Fig. 5. Compressive strength development of concrete for partial substitution of APS with RFA.

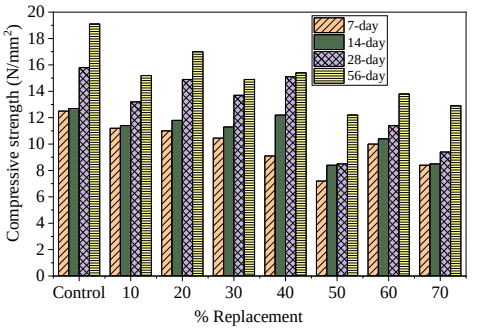

Fig. 6. Compressive strength development of concrete for partial substitution of RFA with LS.

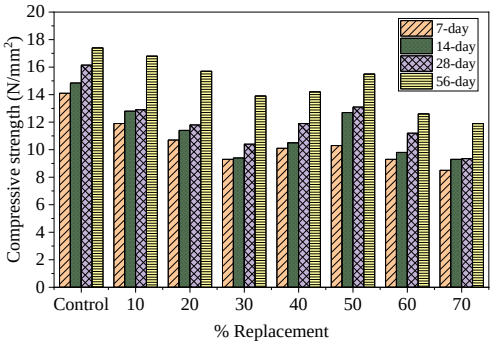

Fig. 7. Compressive strength development of concrete for partial substitution of APS with LS.

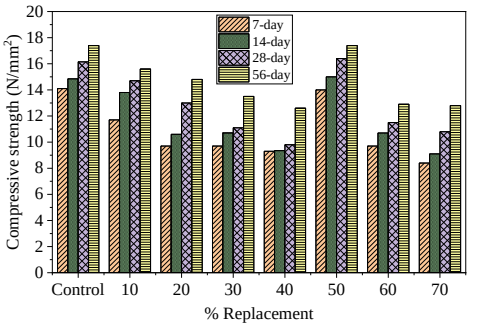

Fig. 8. Compressive strength development of concrete for partial substitution of CG with RCA.

3.4. Outcome of Sorptivity Test

Workability, compressive strengths, durability, and other qualities of fresh and hardened concrete are all influenced by the water content in the matrix and cracking propensity. In other words, to a considerable degree, the penetrability of the pore system determines the performance of concrete in a variety of harsh situations. Figs. 9 to 12 show the variation in the sorptivity with curing age and different concrete mixture proportions. Generally, all the concrete mixtures performed well at prolonged curing age. From Fig. 9, the sorptivity was found to be decreasing at early curing ages for up to 30%RFA replacement. This could be a result of the unsaturated poor formation of the concrete pattern. However, an increase was observed at a substitution level of 30%RFA, after which, the trend continued up to 70%RFA replacement. Considering the long-term application of this type of concrete mixture, a 40%RFA was found to be capable of performing well in an aggressive environment. As seen in Fig. 10, the rate of absorption increases as the curing age increases. This could imply that the pore structure has achieved a fully saturated state. The optimum mix proportion of 30%LS for partial replacement of RFA can be recommended to withstand harsh conditions. From Fig 11, it can be seen that the lower sorptivity ability of these concrete samples may be due to the high silt/clay content preventing the absorption of the water as the laterite requires high water content to be worked upon. This is also evident in the sorptivity value of the mixture in the early curing days. The optimum mix proportion of 70%LS for partial replacement of APS can be recommended to withstand harsh conditions. From Fig. 12, it was observed that the sorptivity increases in the concrete samples as both curing age and percentage replacement increase. This implies that the dry saturation condition of the RCA may be responsible for the high sorptivity behavior when CG was replaced beyond 10%RCA. The optimum mix proportion of 10%RCA for partial replacement of CG can be recommended to withstand harsh conditions.

3.5. Performance Evaluation of Concrete Mixture

The outcomes of the application of the performance index technique are presented in Tables 4 to 11. This method was used to further assist in the selection or identification of optimum concrete mixtures with different performance indicators in the hardened state. The selected properties of the concrete used in this section are critical for particular application to meet construction and design criteria, hence the different best combination with compressive strength, and sorptivity could be chosen. For applications that require compressive strength and sorptivity, PI(1), (see Table 12), the use of 60%RFA to replace APS in the concrete mixture will best meet this performance condition. From Table 7, it can be seen that, for the best performance criteria, in the case where the application requires compressive strength and sorptivity, PI(1), the incorporation of 20%LS replacing RFA in the concrete will be suitable. In a case where the LS is replaced with APS and the compressive strength and sorptivity are required as the performance criteria as presented in Table 9, the use of 50%LS can be recommended. From Table 11, it can be seen that the use of 50%RCA to replace CG in the concrete mixture will meet performance condition PI(1) when compressive strength and sorptivity are required. According to the performance index technique, LS and RAs (i.e., RFA and RCA) can be used as a partial substitution for fine and coarse aggregates in concrete mixtures that satisfy prescribed performance requirements. The amount of the LS and RAs will vary depending on the needed performance characteristics of the blend, which will be application specific. From the foregoing discussion, the performance index approach has been suitably used as a powerful tool to combine multiple data values into a single measure while simplifying the selection procedure.

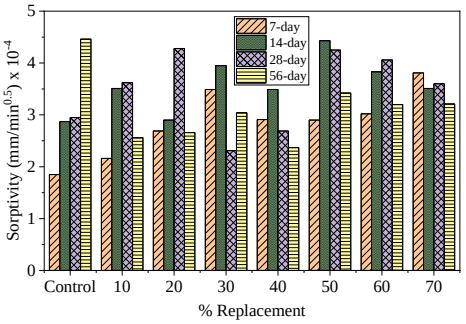

Fig. 9. Sorptivity value of concrete for partial replacement of APS with RFA

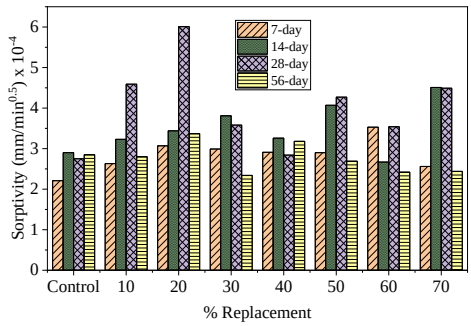

Fig. 10. Sorptivity value of concrete for partial replacement of RFA with LS

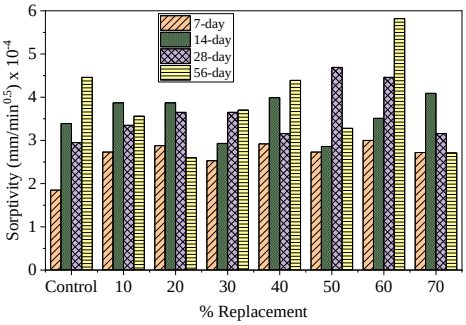

Fig. 11. Sorptivity value of concrete for partial replacement of APS with LS

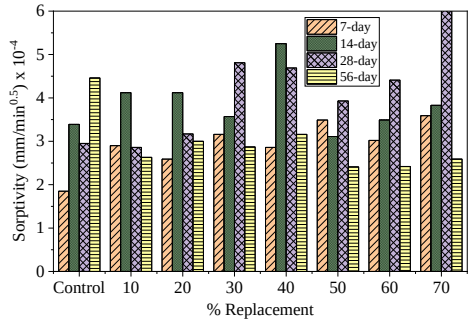

Fig. 12. Sorptivity value of concrete for partial replacement of CG with RCA

4. Concluding Remarks

This study reports the strength and durability behaviours of laterized concrete produced with recycled aggregates, RAs as a substitution for Akure-pit sand, and crushed granite using the performance index strategy. A comprehensive series of experimental tests were executed to assess its mechanical and durability performance. The results of this study led to the following conclusions:

- The flowability of the concrete made with the optimum percentage replacement of APS with RFA; APS with LS; RFA with LS; and CG with RCA at 20%, 40%, 40%, and 50% respectively were found to be satisfactory.
- The concretes made using 70%RFA to partially replace APS; 40%LS to partially substitute RFA; 50%LS to partially replace APS and 50%RCA to partially substitute CG have optimum compressive strengths of 15 N/mm^2; 15.1 N/mm^2; 13.1 N/mm^2; and 16.8 N/mm^2 at 28 days curing age, respectively. All the values satisfy the strength requirement for concrete of 15N/mm^2 characteristic strength, except for the concrete in which LS is used to partially replace APS.
- The concretes made by employing 40%RFA to partially replace APS; 30%LS to partially substitute RFA; 70%LS to partially replace APS and 10%RCA to partially substitute CG have optimum sorptivity of 2.69 x 10^{-4} mm/min$^{0.5}$; 3.58 x 10^{-4} mm/min$^{0.5}$; 3.16 x 10^{-4} mm/min$^{0.5}$; and 2.86 x 10^{-4} mm/min$^{0.5}$ at 28 days curing age, respectively.

- The performance index strategy, which was used to evaluate multiple performance requirements for site-specific application of concrete mixtures, is a helpful way to enable the concrete technologist to select the appropriate laterite and recycled aggregate replacement levels that can maximize the required performance. The findings of this investigation reveal that laterite and recycled aggregate contents may vary and that such variations are mostly determined by the performance requirements of the site-specific concrete mixtures.
- The incorporation of construction and demolition wastes with laterite in the concrete mixtures significantly reduces the amounts of fresh aggregates used for concrete and in addition, leads to cost reduction in Nigeria's cost conditions. The laterized concrete with recycled aggregates is also eco-friendly and will contribute positively to the conservation of natural resources and the overall sustainability of construction materials, a central objective of circular construction.

Acknowledgement

This research was sponsored by the Tertiary Education Trust Fund (TETFUND) of Nigeria through its Institution-Based Research (IBR) Intervention, to which the researchers are grateful.

Appendix

Table 4. Performance index for individual indicator

Performance indicator		Concrete mixture							
		APS	RFA10	RFA20	RFA30	RFA40	RFA50	RFA60	RFA70
Compressive strength	θ_i	1.0	0.64	0.67	0.73	0.76	0.80	0.84	0.93
(N/mm^2)	ψ_i	5.00	3.20	3.35	3.65	3.80	4.00	4.20	4.65
Sorptivity	θ_i	0.69	0.85	1.00	0.54	0.63	0.99	0.95	0.84
(mm/min0.5) x 10^{-4}	ψ_i	3.45	4.25	5.00	2.70	3.15	4.95	4.75	4.20

Table 5. Performance index for multiple performance indicators

Multiple performance indicators	Concrete mixture							
	APS	RFA10	RFA20	RFA30	RFA40	RFA50	RFA60	RFA70
PI (1)	17.25	13.60	16.75	9.86	11.97	19.80	19.95	19.53

Table 6. Performance index for individual indicator

Performance indicator		Concrete mixture							
		APS	RFA10	RFA20	RFA30	RFA40	RFA50	RFA60	RFA70
Compressive strength	θ_i	1.00	0.84	0.94	0.87	0.96	0.54	0.72	0.59
(N/mm^2)	ψ_i	5.00	4.20	4.70	4.35	4.80	2.70	3.60	2.95
Sorptivity	θ_i	0.46	0.76	1.00	0.60	0.47	0.71	0.59	0.75
(mm/min0.5) x 10^{-4}	ψ_i	2.30	3.80	5.00	3.00	2.35	3.55	2.95	3.75

Table 7. Performance index for multiple performance indicators

Multiple performance indicators	Concrete mixture							
	APS	RFA10	RFA20	RFA30	RFA40	RFA50	RFA60	RFA70
PI (1)	11.50	15.96	23.50	13.05	11.28	9.59	10.62	11.06

Table 8. Performance index for individual indicator

Performance indicator		Concrete mixture							
		APS	RFA10	RFA20	RFA30	RFA40	RFA50	RFA60	RFA70
Compressive strength	θ_i	1.00	0.80	0.73	0.64	0.74	0.81	0.69	0.58
(N/mm^2)	ψ_i	5.00	4.00	3.65	3.20	3.70	4.05	3.45	2.90
Sorptivity	θ_i	0.63	0.71	0.78	0.78	0.67	1.00	0.95	0.67
(mm/min0.5) x 10^{-4}	ψ_i	3.15	3.55	3.90	3.90	3.35	5.00	4.75	3.35

Table 9. Performance index for multiple performance indicators

Multiple performance indicators	Concrete mixture							
	APS	RFA10	RFA20	RFA30	RFA40	RFA50	RFA60	RFA70
PI (1)	15.75	14.50	14.24	12.48	12.40	20.25	16.39	9.72

Table 10. Performance index for individual indicator

Performance indicator		Concrete mixture							
		APS	RFA10	RFA20	RFA30	RFA40	RFA50	RFA60	RFA70
Compressive strength	θ_i	0.96	0.88	0.77	0.66	0.58	1.00	0.68	0.64
(N/mm^2)	ψ_i	4.80	4.40	3.85	3.30	2.90	5.00	3.40	3.20
Sorptivity	θ_i	0.48	0.47	0.52	0.79	0.77	0.64	0.72	1.00
(mm/min0.5) x 10^{-4}	ψ_i	2.40	2.25	2.60	3.95	3.85	3.20	3.60	5.00

Table 11. Performance index for multiple performance indicators

Multiple performance indicators	Concrete mixture							
	APS	RFA10	RFA20	RFA30	RFA40	RFA50	RFA60	RFA70
PI (1)	11.52	9.90	10.01	13.04	11.17	16.00	12.24	16.00

Note: In the various concrete mixture notations, the figures following the letters denote the percentage content levels of the respective aggregates.

Table 12. Required performance indicators

Performance indicator	
PI (1)	Compressive strength + sorptivity

References

[1] Alabi SA, Arum C. Mechanical performance of recycled aggregate concrete containing lathe waste steel fibre. Nigerian Journal Technology Development, 2020; 17(4): 306-311. https://doi.org/10.4314/njtd.v17i4.9

[2] Arum C, Mark OG. Partial replacement of Portland cement by granulated cupola slag - sustainable option for concrete of low permeability. Civil and Environmental Research,2014; 6(3): 17-26.

[3] Sathanadam T, Awoyera PO, Vijayan V, Sathishkumar K. Low carbon building: Experimental insight on the use of fly ash and glass fibre for making geopolymer concrete. Sustainable Environment Research, 2016; 27(3): 146-153. https://doi.org/10.1016/j.serj.2017.03.005

[4] Rashid K, Razzaq A, Ahmad M, Rashid T, Tariq S. Experimental and analytical selection of sustainable recycled concrete with ceramic waste aggregate. Construction Building Materials, 2017, 154: 829-840. https://doi.org/10.1016/j.conbuildmat.2017.07.219

[5] Okafor FO, Egbe EA. Models for predicting compressive strength and water absorption of laterite-quarry dust cement block using mixture experiment. Nigerian Journalof Technology, 2017; 36(2):366-372. https://doi.org/10.4314/njt.v36i2.7

[6] Mark OG, Ede AN, Arum C, Jolayemi KJ, Ojuawo I, Ajimalofin D, Adediran J, Babatunde I, Olimaro GB. Fresh characteristics of high-performance self-compacting concrete using induction furnace slag as supplementary cementitious materials. IOP Conference Series: Material Science and Engineering, 2021; 1036(1): 012042. https://doi.org/10.1088/1757-899X/1036/1/012042

[7] Ke G, Li W, Li R, Li Y, Wang G. Mitigation effect of waste glass powders on alkali-silica reaction (ASR) expansion in cementitious composite. International Journal of Concrete Structures and Material, 2018; 12(67). https://doi.org/10.1186/s40069-018-0299-7

[8] Liew KM,Sojobi AO, Zhang LW. Green concrete: Prospects and challenges, Constructionand Building Materials, 2017; 156(15): 1063-1095. https://doi.org/10.1016/j.conbuildmat.2017.09.008

[9] Arum C. Recycling of construction and demolition concrete for sustainable buildings. European Journalof Scientific Research,2011; 52(2): 265-270.

[10] Ogundiran MB, Kumar S. Synthesis of fly ash-calcined clay geopolymers: Reactivity, mechanical strength, structural and microstructural characteristics. Construction and Building Materials, 2016; 125: 450-457. https://doi.org/10.1016/j.conbuildmat.2016.08.076

[11] Sojobi AO, Nwobodo S, Aladegboye O. Recycling of polyethylene terephthalate (PET) plastic bottle wastes in bituminous asphaltic concrete. Cogent Engineering,2016; 3(1): 1133480. https://doi.org/10.1080/23311916.2015.1133480

[12] Awolusi TF,Sojobi AO, Afolayan JO. SDA and laterite applications in concrete: Prospects and effects of elevated temperature. Cogent Engineering, 2017; 4(1). https://doi.org/10.1080/23311916.2017.1387954

[13] Osunade JA. Effect of replacement of lateritic soils with granite fines on the compressive and tensile strengths of laterized concrete. Building and Environment, 2002; 37(5): 491-496. https://doi.org/10.1016/S0360-1323(01)00049-X

[14] Olusola KO, Olugbenga AT. Durability of laterized concrete exposed to sulphate attack under drying-wetting cycles. Civil and Environment Research,2014; 6(3): 33-38. https://doi.org/10.1016/j.conbuildmat.2012.05.033

[15] Gowda SN, Rajasekaran C, Yaragal SC. Significance of processing laterite on strength characteristics of laterized concrete.IOP Conference Series: Material Science and Engineering, 2018; 431(8): 082003 https://doi.org/10.1088/1757-899X/431/8/082003

[16] Udoeyo FF, Iron UH, Odim OO, Strength performance of laterized concrete, Construction and BuildingMaterials, 2006; 20(10): 1057-1062. https://doi.org/10.1016/j.conbuildmat.2005.03.002
[17] Ettu LO, Ibearugbulem OM, Ezeh JC, Anya UC. The suitability of using laterite as sole fine aggregate in structural concrete. 2013; 4(5): 502-507.
[18] Mathew B, Christy F, Joseph B. An investigation of laterite as fine aggregate to developeco-friendly mortar, IOP Conference Series: Material Science and Engineering, 2018; 431(8): 082006. https://doi.org/10.1088/1757-899X/431/8/082006
[19] Balogun LA, Adepegba D. Effect of varying sand content in laterized concrete. InternationalJournal ofCement Composites and Lightweight Concrete, 1982; 4(4): 235-241. https://doi.org/10.1016/0262-5075(82)90027-6
[20] Awoyera P, Akinmusuru JO, Ndambuki J. Green concrete production with ceramic wastes and laterite. Construction and Building Material, 2016; 117, 29-36. https://doi.org/10.1016/j.conbuildmat.2016.04.108
[21] Tijani AM, Mustapha Z. Compressive strength of concrete based on laterite and sea sand mixture. International Journal of Architecture, Engineering and Construction, 2017;6(4): 44-49. https://doi.org/10.7492/IJAEC.2017.023
[22] Fanijo F, Babafemi AJ, Arowoloju O. Performance of laterized concrete made with palm kernel shell as replacement for coarse aggregate. Construction and Building Materials, 2020; 250:118829. https://doi.org/10.1016/j.conbuildmat.2020.118829
[23] Onakunle O, Omole DO, Ogbiye AS, Choudhary AK. Stabilization of lateritic soil from Agbara Nigeria with ceramic waste dust. Cogent Engineering, 2019; 6(1):1710087. https://doi.org/10.1080/23311916.2019.1710087
[24] Joshua O, Amusan LM, Fagbenle OI, Kukoyi PO. Effects of partial replacement of sand with lateritic soil in sandcrete blocks. Covenant Journal of Research and Built Environment, 2014; 1(2): 91-102.
[25] Osadebe NN, Nwakonobi TU. Structural characteristics of laterized concrete at optimum mix proportion. Nigerian Journal of Technology; 2007; 26(1): 12-17.
[26] Ratha B, Dereje, B,Garoma S, Kebede K, Misgana D, Gutema EM.A study on structural behaviour of CFRP laminated concrete beamwith partial replacement of fine aggregate by PET granules. Journal of Building Pathology and Rehabilitation, 2022; 7(58): 1-22. https://doi.org/10.1007/s41024-022-00202-0
[27] Silva RV, de-Brito J, Dhir RK. Properties and composition of recycled aggregates from construction and demolition waste suitable for concrete production. Construction and Building Materials; 2014; 65: 201-217. https://doi.org/10.1016/j.conbuildmat.2014.04.117
[28] Barbudo A, de-Brito J, Evangelista L, Bravo M, Agrela F. Influence of water-reducing admixtures on the mechanical performance of recycled concrete. Journal of Clean Production, 2013; 59: 93-98. https://doi.org/10.1016/j.jclepro.2013.06.022
[29] Pellegrino C, Faleschini F. Recycled aggregates for concrete production: State-of-the-art. In: Sustainability Improvements in the Concrete Industry, Green Energy and Technology. Springer, Cham (2016) 5-34. https://doi.org/10.1007/978-3-319-28540-5_2
[30] Meddah M. Recycled aggregates in concrete production: engineering properties and environmental impact.MATEC Web of Conference 101, 2017; 05021. https://doi.org/10.1051/matecconf/201710105021
[31] Falek K, Aoudjane K, Kadri EH,Kaoua F. Influence of recycled aggregates on the mechanical and tribological behavior of concrete. Energy Procedia, 2017; 139: 456-461. https://doi.org/10.1016/j.egypro.2017.11.237
[32] Etxeberria M. The suitability of concrete using recycled aggregates (RAs) for high-performance concrete. Advances in Construction and Demolition Waste Recycling, 2020; 253-284. https://doi.org/10.1016/B978-0-12-819055-5.00013-9

[33] Tam VW,Wattage H, Le KN, Buteraa A, Soomro M. Methods to improve microstructural properties of recycled concrete aggregate: A critical review. Construction and Building Materials, 2020; 270:121490. https://doi.org/10.1016/j.conbuildmat.2020.121490
[34] Padhi RS, Patra RK, Mukharjee BB, Dey T. Influence of incorporation of rice husk ash and coarse recycled concrete aggregates on properties of concrete. Construction and Building Materials, 2018; 173: 289-297. https://doi.org/10.1016/j.conbuildmat.2018.03.270
[35] BSI. (2006). Concrete - Complementary British Standard to BS EN 206-1, Part 2: Specification for Constituent Materials and Concrete. London: BSI.
[36] Marinković S, Carević V. Comparative studies of the life cycle analysis between conventional and recycled aggregate concrete. New Trends in Eco-efficient and Recycled Concrete, 2019; 257-291. https://doi.org/10.1016/B978-0-08-102480-5.00010-5
[37] Wijayasundara M, Mendis P, Crawford RH. Methodology for the integrated assessment of the use of recycled concrete aggregate replacing natural aggregate in structural concrete. Journal of Clean Production, 2018; 166:321-334. https://doi.org/10.1016/j.jclepro.2017.08.001
[38] Dhir RK, de Brito J, Silva RV, Lye CQ, Properties and composition of recycled aggregates. Woodhead Publishing Series in Civil and Structural Engineering, 2019; 89-141. https://doi.org/10.1016/B978-0-08-100985-7.00005-4
[39] Koper A, Koper W, Koper M. Influence of raw concrete material quality on selected properties of recycled concrete aggregates. Procedia Engineering, 2017; 172: 536-543. https://doi.org/10.1016/j.proeng.2017.02.063
[40] Medina C, de Rojas M, Frias M. Freeze-thaw durability of recycled concrete containing ceramic aggregate. Journal of Clean Production, 2013; 40: 151-160. https://doi.org/10.1016/j.jclepro.2012.08.042
[41] ÇakirÖ, Dilbas H. Abrasion resistance, compressive strength, and elasticity modulus of recycled aggregate concrete (RAC) included lower quality recycled aggregate with and without silica Fume. International Journal of Concrete Technology, 2016; 2(1): 1-18.
[42] Güneyisi F, Gesoğlu M, Kareem Q, Ipek S. Effect of different substitution of natural aggregate by recycled aggregate on performance characteristics of pervious concrete.Materials andStructures, 2016; 49: 521-536. https://doi.org/10.1617/s11527-014-0517-y
[43] Güneyisi E, Gesoglu M, Algin Z, Yazici H. Rheological and fresh properties of self-compacting concretes containing coarse and fine recycled concrete aggregates. Construction and Building Materials, 2016; 113: 622-630. https://doi.org/10.1016/j.conbuildmat.2016.03.073
[44] Verian KP, Jain J, Whiting N, Olek J. Mechanical properties of concretes made with different levels of recycled concrete as coarse aggregates.Proceeding of the International Concrete Sustainability,2011.
[45] Verian KP, Whiting NM,Olek J, Jain J, Snyder MB. Using recycled concrete as aggregate in concrete pavements to reduce materials cost. Publication FHWA/IN/JTRP-2013/18. Joint Transportation Research Program, Indiana Department of Transportation and Purdue University, West Lafayette, Indiana, (2013). https://doi.org/10.5703/1288284315220
[46] Mirjana M, Vlastimir R, Snežana M. Recycled concrete as aggregate for structural concrete.Sustainability, 2010;2(5): 1204-1225. https://doi.org/10.3390/su2051204
[47] Khalid FS, Azmi NB, Sumandi KA, Mazenan PN. Mechanical properties of concrete containing recycled concrete aggregate (RCA) and ceramic waste as coarse aggregate replacement.AIP Conference Proceedings, 2017; 1891(1): 020079. https://doi.org/10.1063/1.5005412

[48] Fonseca N, de Brito J, Evangelista L. The influence of curing condition on the mechanical performance of concrete made with recycled concrete waste. Cement and. Concrete Composites, 2011; 33(6): 637-643. https://doi.org/10.1016/j.cemconcomp.2011.04.002
[49] Abdel-Hay AS. Properties of recycled concrete aggregate under different curing conditions. HBNRC Journal, 2017; 13(3): 271-276. https://doi.org/10.1016/j.hbrcj.2015.07.001
[50] Butler L, Susan L, Tighe L, West JS. Guidelines for selection and use of coarse recycled concrete aggregates in structural concrete. Transportation Research Record: Journal of theTransportation Research Board, 2013; 2335(1): 3-12. https://doi.org/10.3141/2335-01
[51] Zheng C, Lou C, Du G, Li X, Liu Z, Li L. Mechanical properties of recycled concrete with demolished waste concrete aggregate and clay brick aggregate. Results in Physics, 2018; 9: 1317-1322. https://doi.org/10.1016/j.rinp.2018.04.061
[52] Limbachiya M, Meddah S, Ouchagour Y. Use of recycled concrete aggregate in fly-ash concrete. Construction and Building Materials, 2012;27(1): 439-449. https://doi.org/10.1016/j.conbuildmat.2011.07.023
[53] Kurda R, Silvestre JD, de Brito J, Ahmed H. Optimizing recycled concrete containing high volume of fly ash in terms of the embodied energy and chloride ion resistance. Journal of Clean Production, 2018; 194: 735-750. https://doi.org/10.1016/j.jclepro.2018.05.177
[54] Lee J, Jang Y, Park W, Yun H, Kim S. The effect of fly ash and recycled aggregate on the strength and carbon emission impact of FRCCs, International Journal of Concrete Structures and Materials, 2020; 14(17). https://doi.org/10.1186/s40069-020-0392-6
[55] Wonga A, Siriwattanakam A,Nuaklong P, Sata V, Sukontasukkul P,Chindaprasirt P. Use of recycled aggregates in pressed fly ash geopolymer concrete. Environmental Progress and Sustainable Energy, 2019; 39(2):e13327. https://doi.org/10.1002/ep.13327
[56] Shaker MR, Bhalala M, Kargar Q, Chang B. Evaluation of alternative home-produced concrete strength with economic analysis. Sustainability, 2020;12(17): 6746. https://doi.org/10.3390/su12176746
[57] Gonzalez-Coromina A, Etxeberria M. Properties of high performance concrete made with recycled fine ceramic and coarse mixed aggregates. Construction and Building Materials, 2014; 68(15): 618-626. https://doi.org/10.1016/j.conbuildmat.2014.07.016
[58] Collivignarelli MC, Cillari G, Ricciardi P, Miino MC, Torretta V, Rada EC, Abba A. The production of sustainable concrete with the use of alternative aggregates: A review. Sustainability,2020;12(19): 7903 1-34. https://doi.org/10.3390/su12197903
[59] Bheel ND, Meghwar SL, Sohu S, Khoso AR. Experimental study on recycled concrete aggregates with rice husk ash as partial cement replacement. Civil Engineering Journal, 2018;4(10):2305-2314. https://doi.org/10.28991/cej-03091160
[60] Rattanachu P, Toolkasikorn P, Tangchirapat W, Chindaprasirt P, Jaturapitakkul C. Performance of recycled aggregate concrete with rice husk ash as cement binder.Cements and Concrete Composites, 2020;108: 103533. https://doi.org/10.1016/j.cemconcomp.2020.103533
[61] Chindaprasirt P, Cao T. Reuse of recycled aggregate in the production of alkali-activated concrete. Handbook of Alkali-Activated Cement Mortar and Concrete, 2015; 519-538. https://doi.org/10.1533/9781782422884.4.519
[62] Ratha B, Deo S, Ramtekkar G. An experimental study on strength and durability of glass fiber reinforced cement concrete with partial replacement of cement and sand with coal ashes available in Central Chhattisgarh Region. Current Applied Science and Technology, 2022; 22(1): 1-28. https://doi.org/10.55003/cast.2022.01.22.010

[63] Ratha B, Deo S,Ramtekkar G. A proposed mix design of concrete with supplementary cementitious materials by packing density method. Iranian Journal of Science and Technology, Transactions of Civil Engineering, 2020; 44: 615-629. https://doi.org/10.1007/s40996-020-00362-4
[64] BS 12, Specification for Portland Cement, British Standard Institution, London, United Kingdom, 1995.
[65] BS EN 933-11, Tests for geometrical properties of aggregates - Part 11: Classification test for the constituents of coarse recycled aggregate: British Standard Institution London, 2009.
[66] BS 882, Specification for aggregates from natural sources for concrete. British Standards Institution, London, 1992.
[67] BS EN 933-1, Tests for geometrical properties of aggregates - Part 1: Determination of particle size distribution-sieving method: British Standard Institution London, 1997.
[68] American Concrete Institute, ACI Education Bulletin E1-07: Aggregates for Concrete, Developed by Committee E-701: Materials for Concrete Construction, 2007.
[69] BS 3148, Methods of test for water for making concrete, British Standard Institution, London, 1980.
[70] BS EN, 12350-2, Testing of fresh concrete, slump test, British Standards Institution, London, UK. 2019.
[71] British Standard Institution 1881, Testing concrete, Part 102, Published under the authority of the Board of BSI, The Direction of the Cement, Gypsum, Aggregates and Quarry Products Standards Committee, London, United Kingdom, 1983.
[72] BS EN, 12390. Testing of hardened concrete, making and curing specimen for strength Tests, BSI, London, UK, 2019.
[73] ASTM C1585-13, Standard test method for measurement of rate of absorption of water by hydraulic-cement concretes, ASTM International, West Conshohocken, Pa, USA, 2011.
[74] Jordan GS, Prevette S,Woodward S. The performance-based management handbook Volume 5, Analyzing, reviewing, and reporting performance data (2017).
[75] El-Dieb AS, Kanaan DM. Ceramic waste powder an alternative cement replacement - Characterization and evaluation. Sustainable Materials and Technologies, 2018; 17: e00063. https://doi.org/10.1016/j.susmat.2018.e00063
[76] Olanitori LM, Afolayan JO. Effects of pit-sand on resistance on capacities of reinforced concrete. Open Journal of Civil Engineering,2014; 4(4): 328-337. https://doi.org/10.4236/ojce.2014.44028
[77] Muthusamy K, Kamaruzaman NW. Assessment of Malaysian laterite aggregate in concrete, International Journal of Civil and Environmental Engineering, 2012; 12(4): 83-86.

Research on Engineering Structures & Materials
journal homepage: http://www.jresm.org
MIM Research Group

Research Article

Mix ratio design assessment of interlocking paving stone using both destructive and non-destructive methods

Atoyebi O. D.[1,2,a*], Odeyemi S. O.[3,b], Chiadighikaobi P. C.[4,c], Gana A. J.[1,2,d], Onyia S. C.[2,e]

[1]*Landmark University SDG 11 (Sustainable Cities and Communities Research Group)*
[2]*Department of Civil Engineering, Landmark University, Omuaran, Kwara State*
[3]*Department of Civil Engineering, Kwara State University, Malete, Kwara State*
[4]*Department of Civil Engineering, Afe Babalola University, Ado-Ekiti, Ekiti State, Nigeria*

Article Info

Article history:

Received 20 Apr 2022
Revised 01 Aug 2022
Accepted 22 Aug 2022

Keywords:

Interlocking Paving Stone;
Mix Ratio;
Strength;
Rebound Hammer

Abstract

Interlocking paving stones have been produced in most developing countries with no specific method for testing the strength before use. This study presented the mix ratio design assessment of interlocking paving stone strength properties using both destructive and non-destructive methods. Six mix ratios were used to produce the interlocks and tests such as skid resistance, flexural strength, compressive strength and rebound hammer were conducted on 7, 14, 28, 56 and 90 days. All the skid resistance tests had British Pendulum Number (BPN) values greater than 75 specified in Table NA.2 of BS 1338:2003, the interlocking paving stone potential for skid is extremely low. The flexural strength was conducted following IS 15658:2006 and the result ranges from 1.34 – 5.38 N/mm2. The compressive strength result for the mix ratios ranges from 6.20 – 21.78 N/mm2 and mix ratio 1:3 had the highest compressive strength of 19.34, 21.78 N/mm2 at 56 and 90 days respectively. Table 1 of IS 15658:2006 is used to classify the paving stone for use in non-traffic areas based on the compressive strength results. A correlation model was developed combining all the mix ratio average rebound values and compressive strength, the regression equation was produced and an accuracy test was performed to check the regression formula estimates. This study validates the use of a rebound hammer as a non-destructive method on interlocks to predict the compressive strength with 79 % accuracy. Mix ratio 1:3, 1:2 is recommended for use in producing interlocks based on higher compressive and flexural strength.

1. Introduction

Cutting edge interlocking paving stones (IPS) are assuming an imperative role in our transportation industry and construction world as a whole. Paving stones are answers for outdoor application considering their quality, aesthetics and toughness, it is generally favoured in any environmental condition and areas like pedestrian walkways, road surfaces, yards and intersections among other types of pavement design (1–4). IPS requires high compressive strength and efforts have been taken to increase the compressive strength of the paving blocks. The IPS compressive strength can be investigated either by destructive means using the compression testing machine or the non-destructive test means using several methods like the rebound hammer, ultrasonic pulse velocity etc. (3). Paving stones have numerous advantages over asphaltic and concrete pavement such as the engineering durability properties, aesthetically pleasing surfaces, cost-effective maintenance and economical characteristics (5). Like other types of pavements, the design of the IPS will depend on the ecological, traffic movement, subgrade support and the IPS materials (6,7).

*Corresponding author: atoyebi.olumoyewa@lmu.edu.ng
[a] orcid.org/0000-0001-9669-3179; [b] orcid.org/0000-0001-5217-3403; [c] orcid.org/0000-0002-4699-8166;
[d] orcid.org/0000-0001-9122-2490; [e] orcid.org/0000-0001-5119-4704
DOI: http://dx.doi.org/10.17515/resm2022.430st0420

Despite the good engineering properties that IPS possess, it can still fail in cracking, deflection etc. when not properly produced following standard requirements and specification which would need a lot of financial resources from the maintenance budget to replace the failed interlocks. In Nigeria, IPS are used a great deal most especially in areas with high water tables such as the Island areas of Lagos state. IPS are observed to be in their worst conditions after a short period of usage due to factors like the poor condition of the manufacturing process, inadequate sub-base, use of substandard materials, the wide profit margin on the part of the manufacturers causing low quality, low water-cement ratio etc (3). Most of these factors exist because there is no specific standard for the mix designs for IPS and also no specific method to check the strength of IPS produced. Manufacturers in Nigeria resolve to batch by a range to be produced from a bag of Cement. Quality/strength check of concrete is done with the use of destructive tests and the advancement of non-destructive tests. The latter are the tests which are carried out without impairing the present state of the structural element while the formal causes total damage to the tested element. Some examples of non-destructive tests equipment are the rebound hammer (8), Ultrasonic Pulse Velocity (9,10), Infrared thermography (11) etc

Being quick, cheap and non-destructive, the Schmidt rebound hammer test is a method used for the assessment of concrete compressive strength in terms of surface rebound hardness in buildings, rocks etc (12,13). The relationship between the rebound index and the compressive strength of structural elements has relied in the past on empirical relationships using regression analysis (14–19). Past researchers had reason to evaluate the concrete itself to understand the uncertainties surrounding the rebound hammer testing method (15,18–20). The standard process for testing and the association between concrete cube crushing and strength rebound number was established by Indian standards (21). Several factors influence the rebound values, such as the type of cement and aggregate used, the surface condition and moisture content of the concrete, the age of the concrete, and the level of carbonation. The compressive strength of 150mm standard cubes and the rebound number were developed into a correlation, which was included with the device. However, as additional researchers began to explore connections between strength and rebound number, it became clear that strength and rebound number did not have a unique relationship (22). The current recommended approach [18] depicts the strength connection using the same concrete and shaping materials that will be utilized in the construction process. The rebound hammer is only useful for identifying large changes in concrete quality throughout a structure if there is no such association. Numerous researchers have worked on the comparison of compressive strength and rebound hammer values for concrete (14,16-19,23-29). Only a few past works on the comparison of compressive strength and rebound values have been done on IPS (30), which only considered one mix ratio. This research work looked at the relationship between the strengths and rebound values with different mix ratios in the production of IPS, creating a strength template for the quality assessment of IPS with the use of a rebound hammer.

2. Materials and Methods

2.1. Materials

The materials for concrete mix used in the production of IPS for this research work are Dangote 3X Grade 42.5R Portland cement, Quarry dust, Granite chippings, Potable water and engine oil. In the manufacture of the IPS, cement is utilized as a binder. The Dangote 3X cement was gotten in Omu-Aran, Kwara state Nigeria and manufactured by the Dangote group of companies, Nigeria. The 3X depicts extra strength, extra life and extra yield. Dangote cement contains a wide range of qualities that are equivalent to all varieties of cement. It had the lowest proportion of CaO in its composition and the highest amount of Fe2O3 in its composition. The SiO2 percentage value corresponded to the Ordinary Cement of (31). The Al2O3 composition of around 1% corresponded to type IV (32). The MgO and SiO2 values are of type I and its CaO and SO3 percentage composition are of type IV of (32). It has the highest

proportion of uncombined lime, resulting in a low CaO. Its C3S and C3A belonged to type I of (32) while its C2S and C4AF were type IV and type V, respectively, based on their mineralogical composition (Table 1). C4AF was found to be low as a result of the substitution of ferric oxide for alumina, resulting in a rise in C3A and a decrease in C4AF (33).

Table 1. Mineral percentage composition of dangote 3X portland cement

C_3S (%)	C_2S (%)	C_3A (%)	C_4AF (%)	Total Sum (Σ) (%)
33.33	26.47	14.33	4.77	78.9

Quarry dust with fractions of 90 microns as fine aggregate in different mix ratios. The quarry dust was gotten in Omu-Aran Kwara State, Nigeria. The chemical compositions of quarry dust for this research are illustrated in table 2.

Table 2. Chemical composition of quarry dust

SiO_2 (%)	Al_2O_3 (%)	Fe_2O_3 (%)	CaO (%)	MgO (%)	Na_2O (%)	K_2O (%)	TiO_2 (%)	LOI (%)
86.03	17.81	6.44	4.71	2.65	1.47	3.15	0.27	1.09

Granite chippings: Granite chippings with fractions 4-6mm, served as the coarse aggregate in different mix ratios. Portable water for concrete mixing. Engine oil was used as a lubricant on the internal surfaces of the interlock moulds for easy de-moulding of the stones. The interlock moulds (double Tee design interlocking moulds) (figure 1). The depth of the double Tee design interlocking moulds is 60mm which produces a paving stone of 221mm×137mm×60mm

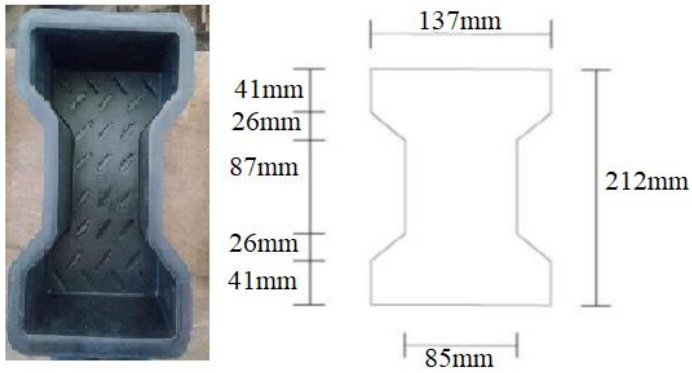

Fig. 1 Double Tee design interlocking moulds

2.2. Experimental Design

Six (6) different mix proportions were considered based on the different sampling of construction sites across the country, IPS manufacturers use different mix designs based on personal gains and material availability. The mix proportions used in this research are borne out of the objective to develop a defined mix proportion for IPS (Table 3). Quarry dust and Granite chippings were varied and used as aggregates, the water-cement ratio of 0.8 was used for the production. The material quantities measured by weight are presented in Table 3.

After mould lubrication, a mixture of cement, quarry dust, granite chippings and water were placed in the moulds following the mix proportions. The cast interlocks were covered with polythene and left for 24 hours at room temperature 20±5°C before being demoulded. The interlocks were cured in water for 7, 14, 28, 56, and 90 days at a temperature of 20±5°C and relative air humidity of (95 ± 5) % to achieve acceptable strength before the physical and

mechanical tests were performed on the interlocks. A total number of 180 interlocking blocks were produced and cured.

Table 3. Mix ratios and material proportions

Mix Ratios	Cement (kg)	Quarry dust (kg)	Granite chippings (kg)	Water (kg)
1:4	13.91	64.93	-	11.13
1:3	17.39	60.87	-	13.91
1:2	23.19	54.11	-	18.55
1:1:2	17.39	40.58	32.61	13.91
1:2:4	9.94	46.38	37.27	7.95
1:1.5:3	12.65	44.27	35.58	10.12

2.3. Experimental Test Procedures

The specimens at the specific curing days were subjected to different tests namely compressive strength test, flexural strength test, skid resistance and Schmidt rebound hammer test. Experimental investigations of IPS on compression and flexure were conducted on an ELE Compression machine with model no 36-3090/01 machine.

2.3.1. Compressive Strength Test

This is the ability of a material to withstand stress without failing determines its strength (34). Failure due to cracking and disintegration is common to interlocks during compression (3). The area (24400mm2) and rate (25Kpa/sec) are set (Figure 2) when the machine is turned on, and the machine's condition is examined. The paving stones are fed into the machine, which subsequently crushes them.

Fig. 2 Compressive strength setup

2.3.2. Flexural Strength Test

The behaviour of materials subjected to basic bending loads is measured using this mechanical testing method. To assess the link between bending stress and deflection, flexural testing involves bending a material rather than pushing or pulling it (35,36). The paving stones and steel rods representing the point loads are inserted into the machine using a predefined value and condition for the machine.

2.3.3. Schmidt Rebound Hammer

The Schmidt rebound hammer test was carried out on the IPS to determine the rebound hammer values used to develop a correlation with the compressive strength to predict the compressive strength of the interlocks. IPS were held in position by the compressive testing machine under a fixed load of 7N/mm2 and measurements of the rebound hammer values were done following BS 1881 (37). The hammer was held horizontally to test opposite sides of the cube after which the values were recorded. An average of 10 readings was taken on each test sample on points 25mm apart.

2.3.4. Skid Resistance Test

The skid-resistance test is used to verify the properties of concrete paving blocks and whether a specific surface finish is suitable for use in anti-skid applications. Skid resistance can be measured in two ways: static and dynamic. The British Pendulum Skid Resistance Tester is a standard device for static measurements. Paving blocks of size 221mm×137mm×60mm were tested (Figure 3). To perform the test, both dry and wet surface measurement is taken, The shoe is rubbed against the surface as the pendulum is drawn back. The British Pendulum Number (BPN) is a read scale reading on the machine depicting friction resistance.

Fig. 3 Skid resistance test setup

3. Result and Discussion

For the destructive tests, the Strength values of the IPS samples were recorded at the failure point. The failure pattern for all samples is almost the same (Figure 4).

3.1. Skid Resistance Test

The skid Resistance test was carried out on the IPS following (38) to determine the British Pendulum numbers. The results obtained on days 7, 14, 28, 56 and 90 are presented in table 4.

Table 4 shows the summary of the average British Pendulum numbers recorded after carrying the skid resistance test in the laboratory on each curing day. Referring to the standard value given in BS 1338, 2006 (38), the specimen potential for slip is extremely low with all the BPN values greater than 75 specified in the code. On average, IPS samples with no granite chippings gave better skid resistance results compared to the samples with granite chippings. Comparing the skid resistance values in Table NA.2 of (39) with the results in Table 4, it can be concluded that the interlock potential for slip is extremely low.

Fig. 4 Strength tests failure mode

Table 4. Average British pendulum numbers

Mix Ratios	7 days		14 days		28 days		56 days		90 days	
	Dry	Wet	Dry	Wet	Dry	Wet	Dry	Wet	Dry	Wet
1:4	122.2	114	100	95.83	119.8	110.8	118.7	110.2	105	99.8
1:3	134.5 120.2		122.7	111.2	135.5	126.8	120.3	108.3	122.7	111.2
1:2	127.5 121.7		116.7	108.8	130.5	122.7	122.7	114.6	116.7	108.8
1:1:2	129.5 125.3		112.2	106.3	129	123.7	133.5	126.7	112.2	106.3
1:2:4	124.3	117	111.2	106	128.5	118.3	122.7	117	111.2	106
1:1.5:3	104.7	101	113.8	109.3	119.7	112.8	115	107.7	113.8	109.3

3.2. Rebound Hammer Test

A rebound hammer test was carried out on the IPS to determine the rebound hammer values. The result obtained from the test at 7, 14, 28, 56 and 90 days are presented in table 5.

Table 5. Average rebound hammer values

Mix ratios	7 days	14 days	28 days	56 days	90 days
1:4	-	10.56	13.08	13.92	14.4
1:3	-	17.45	20.2	22.23	22.57
1:2	-	16.27	17.27	18.77	19.55
1:1:2	-	13.68	14.87	16.05	16.67
1:2:4	-	13.8	13.52	13.02	13.25
1:1.5:3	-	13.75	15.65	14.95	15.55

No rebound hammer value was recorded on the 7th day for all the samples because the rebound hammer values could not be read from the equipment as the values were below the scale reading of 10 on the equipment, this is due to the low strength which is attained after 7 days of curing. The control mix ratio 1:4 and 1:2:4 have the least rebound hammer values on each curing day compared to other mix ratios. Mix ratios 1:3 and 1:2 have the highest average

rebound values. The average rebound hammer values for the mix ratios with granite chippings used as coarse aggregate is greater than the control mix on each curing day except for ratio 1:2:4 rebound hammer values that are lesser on the 56th and 90th day. The average rebound hammer values increased on each curing day.

3.3. Flexural Strength Test

To determine the flexural strength of the IPS, a flexural strength test was performed. The outcome at 7, 14, 28, 56 and 90 days are shown in table 6 and figure 5.

Table 6. Average flexural strength

Mix ratios	7 days (N/mm^2)	14 days (N/mm^2)	28 days (N/mm^2)	56 days (N/mm^2)	90 days (N/mm^2)
1:4	1.79	2.02	2.02	2.69	2.69
1:3	3.58	4.03	4.71	5.38	5.38
1:2	2.24	3.14	3.36	4.03	4.49
1:1:2	2.02	2.69	2.91	3.36	3.36
1:2:4	1.34	2.02	2.02	2.47	2.69
1:1.5:3	2.47	2.69	2.69	2.91	3.63

The flexural strength test was performed according to (40) and the average flexural strength values are shown in Table 6, ranging from 1.34 – 5.38 N/mm2. All of the interlocks' flexural strength increased with age, and the maximum flexural strengths were reached after 90 days. In comparison to the control mix ratio and others, the mix ratios 1:3 and 1:2 had the maximum flexural strength, indicating that they would be ideal for the construction of interlocks.

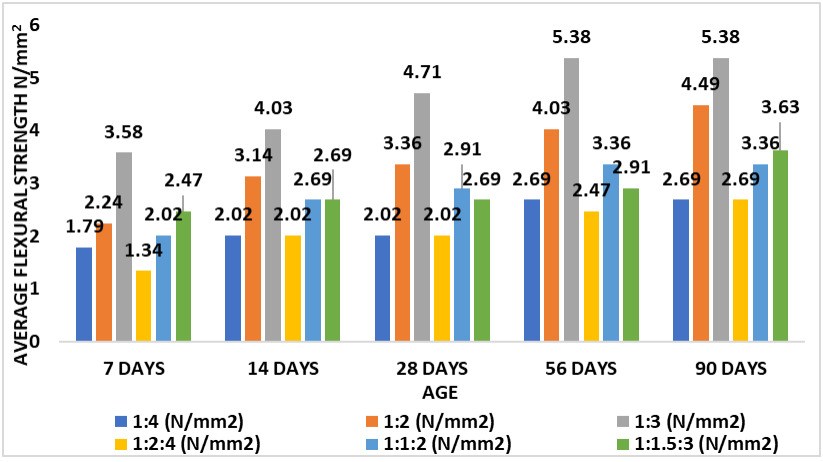

Fig. 5 Average flexural strength with age

The mix ratio with quarry dust had a flexural strength of 5.38 $N/(mm)^2$ (1:3), 4.49 $N/(mm)^2$ (1:2) greater than the control mix flexural strength of 1:4 (2.69 $N/(mm)^2$) on the 90th day (Figure 6). All the mix ratios with granite chippings had a flexural strength of 3.36 $N/(mm)^2$ (1:1:2), 3.63 $N/(mm)^2$ (1:1.5:3) greater than the flexural strength of the control mix 1:4 (2.69 $N/(mm)^2$) except mix ratio 1:2:4 (2.69 $N/(mm)^2$) that had the same value on the 90th day.

3.4. Compressive Strength Test

The compressive strength result obtained at 7 days, 14 days, 28 days, 56 days and 90 days are shown below in table 7 and figure 7.

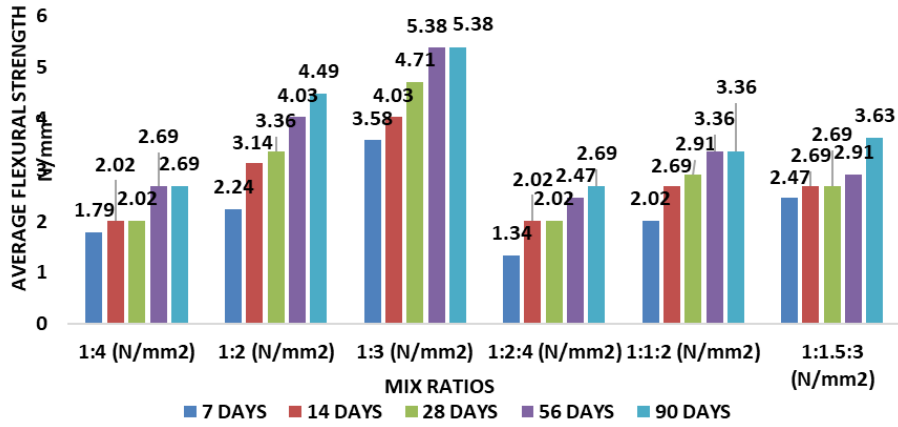

Fig. 6 Average flexural strength with mix ratio

Table 7. Compressive strength result for the different mix ratios

Mix Ratios	7 days (N/mm^2)	14 days (N/mm^2)	28 days (N/mm^2)	56 days (N/mm^2)	90 days (N/mm^2)
1:4	6.20	8.29	9.02	11.23	11.38
1:3	10.37	17.7	16.59	19.34	21.78
1:2	10.92	12.72	15.63	17.71	18.25
1:1:2	10.44	13.75	16.2	16.44	17.40
1:2:4	7.85	11.67	11.55	12.57	13.02
1:1.5:3	12.25	12.77	15.62	17.02	17.30

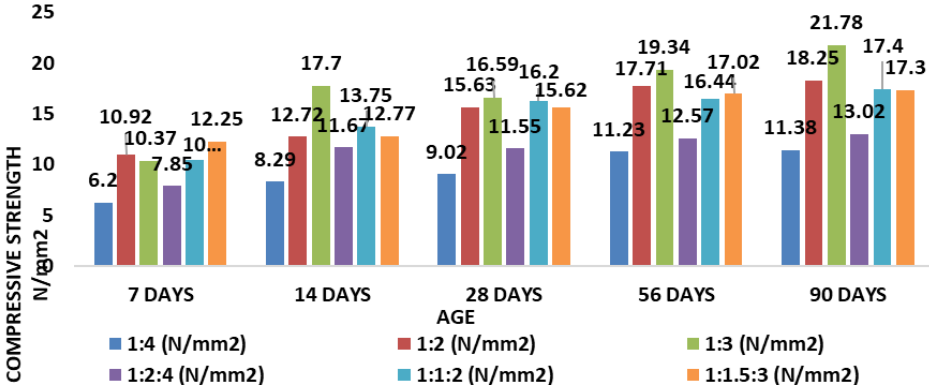

Fig. 7 Average compressive strength with age

The compressive strength test was carried out according to (38), and the average compressive strength values are shown in Table 7, ranging from 6.20 to 21.78 $N//(mm)^2$. As seen in figure 8, the compressive strength of all interlocks increased with age, with maximum compressive strengths reached on the 90th day. They are would be suitable for the construction of interlocks for use in non-traffic areas based on the classification in Table 1 of (40). Mix ratio 1:3 had the highest compressive strength of 21.78 $N//(mm)^2$ and followed closely by (1:2) with a compressive strength of 18.25 $N//(mm)^2$ compared to the control mix (1:4) with a

compressive strength of 11.38 N//(mm)^2 on the 90th day. All the mix ratios with granite chippings had compressive strength of 17.4 N//(mm)^2 (1:1:2), 13.02 N//(mm)^2 (1:2:4) and 17.3 N//(mm)^2 (1:1.5:3) greater than the control mix strength of 11.38 N//(mm)^2 (1:4) on the 90th day,

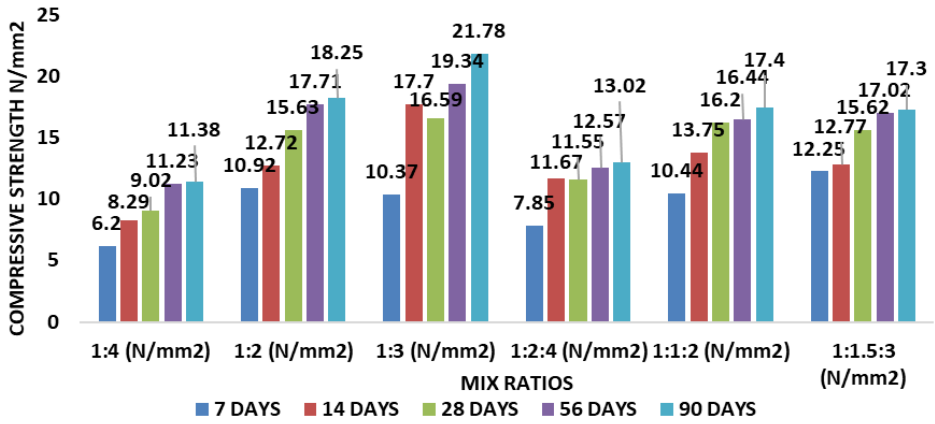

Fig. 8 Average compressive strength with mix ratio

3.5. Correlation Between Compressive Strength and Rebound Hammer Values

One of the objectives of this research work is to develop a correlation model to be used in the fabrication yard and by Engineers on-site to predict the compressive strength of the interlocks using the rebound hammer values gotten after carrying out a non-destructive test using the Schmidt rebound hammer. The average rebound hammer values and the compressive strength values recorded on the 14th, 28th, 56th and 90th day respectively shown in Table 8 were used to develop the correlation in Figure 9.

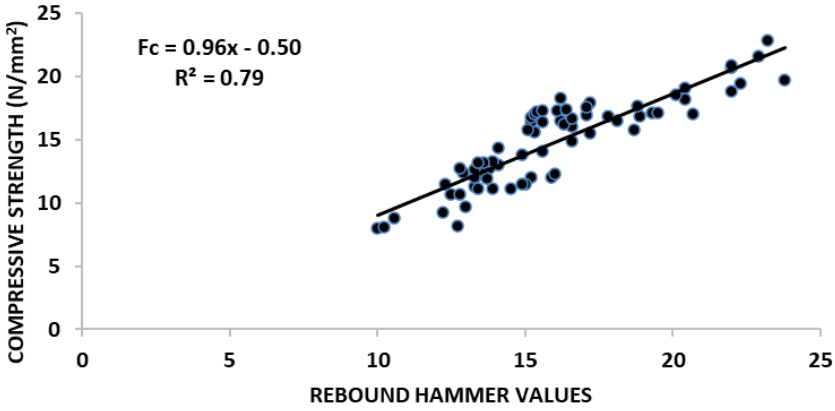

Fig. 9 Correlation graph between compressive strength and average rebound hammer values

Table 8. Compressive strength and average rebound hammer values

S/N	Average Rebound Hammer Values	Average Compressive Strength	Regression Formula Estimates
1	10.56	8.77	9.58
2	10.00	8.03	9.06
3	10.23	8.07	9.28
4	17.80	16.84	16.27
5	15.30	15.57	13.96
6	22.00	20.70	20.14
7	14.90	13.81	13.59
8	15.90	12.05	14.51
9	16.00	12.30	14.60
10	14.10	14.39	12.85
11	15.60	14.10	14.23
12	13.70	12.75	12.48
13	14.10	12.99	12.85
14	12.50	10.70	11.37
15	13.30	11.31	12.11
16	13.40	12.25	12.20
17	13.80	12.79	12.57
18	13.90	13.28	12.66
19	12.20	9.22	11.09
20	12.70	8.16	11.56
21	13.00	9.67	11.83
22	20.70	17.05	18.94
23	18.70	15.82	17.10
24	18.90	16.89	17.28
25	16.60	14.88	15.16
26	17.20	15.53	15.71
27	18.10	16.48	16.54
28	15.60	16.39	14.23
29	15.20	16.39	13.86
30	15.10	15.82	13.77
31	12.30	11.48	11.19
32	13.30	12.01	12.11
33	13.40	11.15	12.20
34	16.20	18.32	14.79
35	15.20	12.01	13.86
36	16.20	16.52	14.79
37	12.80	10.66	11.65
38	13.70	11.93	12.48
39	13.90	11.11	12.66
40	22.00	18.81	20.14
41	23.80	19.75	21.81
42	22.30	19.47	20.42
43	18.80	17.71	17.19
44	20.40	18.24	18.67
45	19.30	17.17	17.65
46	16.60	16.08	15.16
47	17.10	16.97	15.62
48	16.30	16.27	14.88
49	13.60	12.71	12.39

Table 8 (Con). Compressive strength and average rebound hammer values

50	13.30	12.62	12.11
51	12.90	12.38	11.74
52	15.20	16.76	13.86
53	15.30	17.00	13.96
54	16.10	17.30	14.70
55	14.50	11.15	13.22
56	15.00	11.52	13.68
57	14.90	11.48	13.59
58	23.20	22.83	21.25
59	22.90	21.60	20.98
60	22.00	20.90	20.14
61	20.40	19.06	18.67
62	20.10	18.53	18.39
63	19.50	17.17	17.84
64	17.20	17.95	15.71
65	17.10	17.54	15.62
66	16.60	16.72	15.16
67	13.60	13.20	12.39
68	13.40	13.15	12.20
69	12.80	12.71	11.65
70	15.40	17.20	14.05
71	16.40	17.40	14.97
72	15.60	17.30	14.23

4. Conclusion

The study aims at evaluating the mix ratio design assessment of IPS using both destructive and non-destructive methods. The following conclusions are based on the analyses and discussions.

- For improved compressive and flexural strength, less material usage and reduced cost of production, the use of mix ratios 1:3 and 1:2 are recommended for use in the production of IPS with ratio 1:3 giving the best strength. However, in places where granite chippings are readily available and the cost of production would not affect profit, mix ratios 1:1:2 and 1:1.5:3 can be utilized for interlock production.
- The correlation model developed from this research should be utilized both on-site and in the production yard for quality control of the interlocks after the production stage to investigate the compressive strength by the quality control unit before supply and usage of the interlocks.
- The following design strength for IPS is recommended;

Table 9. Recommended design strength for interlocks

Mix ratios	Design strength (N/mm^2)
1:4	10
1:2	17.5
1:3	20
1:1:2	16
1:2:4	12.5
1:1.5:3	17

Acknowledgement

The authors acknowledge that the opportunity given by the Concrete Laboratory of Landmark University to carry out this research work.

References

[1] Djamaluddin AR, Caronge MA, Tjaronge MW, Lando AT, Irmawaty R. Evaluation of sustainable concrete paving blocks incorporating processed waste tea ash. Case Stud Constr Mater [Internet]. 2020;12:e00325. https://doi.org/10.1016/j.cscm.2019.e00325
[2] Gencel O, Ozel C, Koksal F, Erdogmus E, Martínez-Barrera G, Brostow W. Properties of concrete paving blocks made with waste marble. J Clean Prod [Internet]. 2012;21(1):62-70. https://doi.org/10.1016/j.jclepro.2011.08.023
[3] Atoyebi OD, Ikubanni PP, Adesina A, Araoye O V, Davies IEE. Effect of curing methods on the strength of interlocking paving blocks. Cacciola P, editor. Cogent Eng [Internet]. 2020 Jan 1;7(1):1770914. https://doi.org/10.1080/23311916.2020.1770914
[4] Rath B. Effect of asphalt pavement construction on the environment of Ethiopia. Res Eng Struct Mater. 2022;x(xxxx):1-18. https://doi.org/10.17515/resm2022.352ma1010
[5] Ojuri OO. Interlocking Paving Stones Pavement as a Solution to Marshy Roads. Mod Appl Sci. 2012;6(5):91-9. https://doi.org/10.5539/mas.v6n5p91
[6] Jamshidi A, Kurumisawa K, White G, Nishizawa T, Igarashi T, Nawa T, et al. State-of-the-art of interlocking concrete block pavement technology in Japan as a post-modern pavement. Constr Build Mater [Internet]. 2019;200:713-55. https://doi.org/10.1016/j.conbuildmat.2018.11.286
[7] Uygunoğlu T, Topcu IB, Gencel O, Brostow W. The effect of fly ash content and types of aggregates on the properties of pre-fabricated concrete interlocking blocks (PCIBs). Constr Build Mater [Internet]. 2012;30:180-7. https://doi.org/10.1016/j.conbuildmat.2011.12.020
[8] Saha AS, Amanat KM. Rebound hammer test to predict in-situ strength of concrete using recycled concrete aggregates, brick chips and stone chips. Constr Build Mater [Internet]. 2021;268:121088. https://doi.org/10.1016/j.conbuildmat.2020.121088
[9] Parihar HS, Shanker R, Singh V. Effect of variation of steel reinforcement on ultrasonic pulse velocity prediction in concrete beam. Mater Today Proc [Internet]. 2022. https://doi.org/10.1016/j.matpr.2022.04.468
[10] Almasaeid HH, Suleiman A, Alawneh R. Assessment of high-temperature damaged concrete using non-destructive tests and artificial neural network modelling. Case Stud Constr Mater [Internet]. 2022;16:e01080. https://doi.org/10.1016/j.cscm.2022.e01080
[11] Wang S, Sui X, Leng Z, Jiang J, Lu G. Asphalt pavement density measurement using non-destructive testing methods: current practices, challenges, and future vision. Constr Build Mater [Internet]. 2022;344:128154. https://doi.org/10.1016/j.conbuildmat.2022.128154
[12] Basu A, Aydin A. A method for normalization of Schmidt hammer rebound values. Int J Rock Mech Min Sci. 2004;41(7):1211-4. https://doi.org/10.1016/j.ijrmms.2004.05.001
[13] Atoyebi OD, Afolayan JO, Arum C. Analyses and Interpretations of Structural Health Monitoring Data on Reinforced Concrete Buildings: A Critical Review. J Eng Appl Sci. 2019;14(24):9657-66. https://doi.org/10.36478/jeasci.2019.9657.9666
[14] Szilágyi K, Borosnyói A, Zsigovics I. Rebound surface hardness of concrete: Introduction of an empirical constitutive model. Constr Build Mater [Internet]. 2011;25(5):2480-7. https://doi.org/10.1016/j.conbuildmat.2010.11.070
[15] Alwash M, Breysse D, Sbartaï ZM. Non-destructive strength evaluation of concrete: Analysis of some key factors using synthetic simulations. Constr Build Mater [Internet]. 2015;99:235-45. https://doi.org/10.1016/j.conbuildmat.2015.09.023
[16] Tsioulou O, Lampropoulos A, Paschalis S. Combined Non-Destructive Testing (NDT) method for the evaluation of the mechanical characteristics of Ultra High Performance

Fibre Reinforced Concrete (UHPFRC). Constr Build Mater [Internet]. 2017;131:66-77. https://doi.org/10.1016/j.conbuildmat.2016.11.068
[17] Atoyebi OD, Ayanrinde OP, Oluwafemi J. Reliability Comparison of Schmidt Rebound Hammer as a Non-Destructive Test with Compressive Strength Tests for different Concrete Mix. J Phys Conf Ser. 2019;1378(3):1-9. https://doi.org/10.1088/1742-6596/1378/3/032096
[18] Alwash M, Breysse D, Sbartaï ZM, Szilágyi K, Borosnyói A. Factors affecting the reliability of assessing the concrete strength by rebound hammer and cores. Constr Build Mater [Internet]. 2017;140:354-63. https://doi.org/10.1016/j.conbuildmat.2017.02.129
[19] El Mir A, Nehme SG. Repeatability of the rebound surface hardness of concrete with alteration of concrete parameters. Constr Build Mater [Internet]. 2017;131:317-26. https://doi.org/10.1016/j.conbuildmat.2016.11.085
[20] Breysse D. Nondestructive evaluation of concrete strength: An historical review and a new perspective by combining NDT methods. Constr Build Mater [Internet]. 2012;33:139-63. https://doi.org/10.1016/j.conbuildmat.2011.12.103
[21] IS 13311-1 : 1992. Non-Destructive Testing of Concrete - Part 1: Ultrasonic Pulse Velocity. New Delhi; 2004.
[22] Nawy EG. Concrete Construction Engineering Handbook. Second. CRC Press; 2008. https://doi.org/10.1201/9781420007657.ch17
[23] Malhotra VM, Carino NJ. Handbook on Nondestructive Testing of Concrete [Internet]. CRC Press; 2004. (Civil engineering). https://doi.org/10.1201/9781420040050
[24] Carette GG, Malhotra VM. In Situ Tests: Variability and Strength Prediction of Concrete at Early Ages. ACI Symp Publ. 2014;82:114-42.
[25] Ali-Benyahia K, Sbartaï ZM, Breysse D, Kenai S, Ghrici M. Analysis of the single and combined non-destructive test approaches for on-site concrete strength assessment: General statements based on a real case-study. Case Stud Constr Mater [Internet]. 2017;6:109-19. https://doi.org/10.1016/j.cscm.2017.01.004
[26] Jain A, Kathuria A, Kumar A, Verma Y, Murari K. Combined use of non-destructive tests for assessment of strength of concrete in structure. Procedia Eng [Internet]. 2013;54:241-51. https://doi.org/10.1016/j.proeng.2013.03.022
[27] Bilgin N, Copur H, Balci C. Use of Schmidt Hammer with special reference to strength reduction factor related to cleat presence in a coal mine. Int J Rock Mech Min Sci. 2016;84:25-33. https://doi.org/10.1016/j.ijrmms.2016.01.016
[28] Demirdag S, Yavuz H, Altindag R. The effect of sample size on Schmidt rebound hardness value of rocks. Int J Rock Mech Min Sci. 2009;46(4):725-30. https://doi.org/10.1016/j.ijrmms.2008.09.004
[29] Kim J-K, Kim C-Y, Yi S-T, Lee Y. Effect of carbonation on the rebound number and compressive strength of concrete. Cem Concr Compos [Internet]. 2009;31(2):139-44. https://doi.org/10.1016/j.cemconcomp.2008.10.001
[30] Brožovský J, Matejka O, Martinec P. Concrete Interlocking Paving Blocks Compressive Strength Determination Using Non-destructive Methods. In: The 8th International Conference of the Slovenian Society for Non-Destructive Testing. Portoroz, Slovenia; 2005. p. 91-7.
[31] BS 4550-3.1. British Standard Methods of testing cement - Part 3: Physical Tests. Vol. 3. London; 1978.
[32] ASTM C150/C150M-18. Standard Specification for Portland Cement [Internet]. West Conshohocken, PA; 2018. Available from: www.astm.org
[33] Volzenski AV. Mineral binding materials. 4th ed. Stroyizdat, Moscow, Russia; 1986.
[34] Odeyemi SO, Adisa MO, Atoyebi OD, Wilson UN, Odeyemi OT. Optimal water-cement ratio and volume of superplasticizers for blended cement-bamboo leaf ash high-performance concrete. Res Eng Struct Mater. 2022;x(xxxx):1-13. https://doi.org/10.17515/resm2022.382ma0108

[35] Sadiq OM, Atoyebi OD. Flexural Strength Determination of Reinforced Concrete Elements with Waste Glass as Partial Replacement for Fine Aggregate. NSE Tech Trans J Niger Soc Eng. 2015;49(2):74-81.
[36] Atoyebi OD, Sadiq OM. Experimental data on flexural strength of reinforced concrete elements with waste glass particles as partial replacement for fine aggregate. Data Br [Internet]. 2018;18:846-59. https://doi.org/10.1016/j.dib.2018.03.104
[37] BS1881-116. BS 1881 Part 116-1983. Testing Concrete: Method for determination of compressive strength of cubes. UK; 1983.
[38] BS EN 1338. British Standard Testing Concrete paving blocks. Requirements and test methods. West Conshohocken, PA, USA:; 2006.
[39] BS 7941-2:2000. Methods for measuring the skid resistance of pavement surfaces. UK; 2000.
[40] IS 15658:2006. Precast Concrete blocks for paving - Specification. New Delhi; 2006.]

Research on Engineering Structures & Materials
journal homepage: http://www.jresm.org
Research Group

Research Article

Fracture behavior of hybrid fiber reinforced normal strength and high strength concrete: comparison with plain and steel fiber reinforced concrete

P.N. Ojha[a], Pranay Singh[b], Brijesh Singh*[c], Abhishek Singh[d]

Centre for Construction Development and Research, National Council for Cement and Building Materials, India

Article Info

Article history:

Received 15 May 2022
Revised 6 Aug 2022
Accepted 19 Sep 2022

Keywords:

HFRHSC;
Fracture;
Load-CMOD;
Three-point bend test

Abstract

The paper presents an experimental investigation on the fracture behavior of hybrid-fiber reinforced normal strength concrete (HFRC) and hybrid-fiber reinforced high strength concrete (HFRHSC). The hybrid fiber used in the study constitutes of 0.75% steel fiber and 0.25% polypropylene fiber, by volume of the concrete. A three-point bend test on a notched beam has been performed based on the recommendations of RILEM as well as literature. Fracture parameters like the fracture energy, stress intensity factor, energy release rate and characteristic length has been evaluated from the load-deflection and load-CMOD curves. These were compared with values for the plain and steel fiber reinforced concrete reported in literature for similar type of mixes. Result suggests that hybrid fiber improved the fracture performance in comparison to the steel fiber reinforcement in case of normal strength concrete. For higher strength concrete, replacing steel fiber by hybrid fibers caused marginal reduction in the fracture parameters. Compared to plain unreinforced concrete, the fracture behaviour irrespective of the strength improved by addition of the hybrid fibers.

1. Introduction

Innovations in the concrete mix design process and a better understanding of the materials have made it possible to design high strength concrete mixes with improved mechanical properties [1], [2]. However, one of the biggest limitations of high strength concrete is its post-peak brittleness. With increase in strength, concrete tends to suddenly fail without warning. The addition of steel fibres in high strength concrete leads to increase in the ultimate strain value and strain value at peak stress to sustain more deformation during loading, thereby avoiding sudden and brittle failure [3]. For enhancing the post-peak behavior [4], [5] and enabling the ductile failure of concrete, researchers have used different kinds of fiber reinforcement like Kevlar [6] and glass chopped fibers [7] but steel fibers are the most popular and are widely used [8]–[11]. The steel fiber used in the concrete helps in arresting the cracks [12]. It also solves the issue of the explosion of concrete at failure. A significant improvement in fracture parameters has been observed in past [12], [13] after the addition of a certain amount of steel fiber in the concrete mix. Some researchers tried to optimize the amount of steel fiber to be added to the concrete mix and reported it to be approximately 1% of the volume of concrete mix [14].

Apart from the post-peak brittleness, poor fire performance is also a serious concern for higher-strength concrete [15]. For improving the fire performance of the concrete, some special kind of fiber can be introduced in the concrete. Researchers [3], [16] have

*Corresponding author: brijeshsehwagiitr96@gmail.com
[a] orcid.org/0000-0003-1754-4488; [b] orcid.org/0000-0001-6169-9482; [c] orcid.org/0000-0002-6512-1968; [d] orcid.org/0000-0002-2343-5934
DOI: http://dx.doi.org/10.17515/resm2022.433me0515

suggested hybrid fibers [17]–[19] for improved safety in fire and an enhanced ductile failure simultaneously. At elevated temperatures, as encountered during a fire accident, high-strength concrete tends to explode. The reason for the explosion has been credited to the reduction in permeability [20] of the concrete due to denser packing. Due to dense packing of high-strength concrete blocks, the exit of pressurized water vapor gets created due to the rise in the temperature. To counter this phenomena, literature suggests [20] addition of materials in concrete that stay rigid at a lower temperature, but melt with the temperature rise, in an event of a fire accident. It is suggested that the melting point of the material should be much higher than the normal temperature of the environment, but should be sufficiently low to melt before the creation of pressurized steam at extreme temperatures. When the temperature of the concrete increases, the fiber is expected to melt, improving the permeability of the concrete and allowing steam to eject. Polypropylene is a suitable material for this purpose. It is a thermoplastic polymer which is a polymer of propylene. Its melting point varies between 130 degrees to 170 degrees Celsius. The solutions proposed above to tackle the issues give rise to two special classes of concrete – (i) Steel fiber reinforced concrete (SFRC) and (ii) Hybrid fiber reinforced concrete (HFRC). Similarly, two classes can be defined for high strength concrete (compressive strength more than 50 MPa) i.e., (i) Steel fiber reinforced high strength concrete and (SFRHSC) (ii) Hybrid fiber reinforced high strength concrete (HFRHSC).

The addition of steel fiber and polypropylene fiber alters the mechanical and fracture properties of the concrete. Mechanical properties like compressive strength and split tensile strength are evaluated using Indian Standard codes. RILEM recommendation (50-FMC [21]) specifies a method for determining the fracture energy (GF) of mortar and concrete by using stable three-point bend tests on notched beams. As per RILEM, the fracture energy is defined as the amount of energy required to create one-unit area of a crack. The area of a crack is defined as the projected area on a plane parallel to the main crack direction [21]. The fracture energy defined by RILEM is shape dependent, as it significantly increases with increase in the notch depth ratio of the specimen. It can be noted that the size dependence of the fracture energy estimated by RILEM is quite strong.

Past studies on hybrid fiber reinforced concrete have compared the fracture parameters of varying proportion of fibers in concrete mix. Xiangjun et al.,[22] have found maximum fracture performance with approximately 0.9% steel fiber and 0.1% Polypropylene fiber. Alwesabi et al. [14], also reported similar proportion of the fibers for the maximum fracture energy. Smarzewski, and Barnat-Hunek [23] in their investigation reported maximum compressive and split tensile strength for the mix with 0.75% of steel fiber and 0.25% of polypropylene fiber. Based on the findings an optimum choice of 0.25% PPF and 0.75% SF has been adopted in present study to compare it with 1% of steel fiber and the plane concrete mix without fiber. Some of the recent studies on the fracture behavior and crack propagation utilizes techniques like acoustic emission and digital image correlation. The fracture behavior of synthetic fiber reinforced concrete, steel fiber reinforced concrete and hybrid fiber reinforced concrete under flexural loading using Acoustic Emission (AE) technique was conducted by Bhosale, Rasheed, Prakash and Raju [24]. Study by Bhosale et al. highlights that steel fibers gave superior performance followed by hybrid and macro-synthetic fibers. Steel fibers also gives higher toughness than hybrid and macro-synthetic fibers for the fixed fiber dosage. Study also revealed that length of fracture process zone in longitudinal direction is longest in steel fibre reinforced concrete followed by hybrid and macro-synthetic fibers, where fracture process zone is less distributed in case of concrete with macro-synthetic fibers as compared to the concrete with steel or hybrid fibre. Bhosale and Prakash in another study analyzed the crack propagation in synthetic, steel and hybrid fiber reinforced concrete using digital image correlation techniques. The study concluded

that hybrid fiber reinforced concrete had longer cracks than steel fiber reinforced concrete at particular load [25].

The present study attempts to evaluate the effect of adding 1% hybrid fiber [i.e. 0.25% Poly Propylene Fibre (PPF) + 0.75% Steel Fibre (SF)] by volume in the concrete mixes of three different strength ranges. The obtained results have been compared with the findings of Ojha et al. [12]. Ojha et al. [12] studied fracture behaviour of plain and fiber reinforced concrete with a strength range between 30 MPa and 90 MPa. The study presented an elaborate comparison between fracture behavior of concrete with and without fiber. However, the effect of using hybrid fiber in place of steel fiber was not discussed. The concrete mixes reported by Ojha et al. [12], were used for preparation of concrete specimens with hybrid fiber for evaluating the fracture energy. Study was conducted on twelve notched beams to determine fracture parameters such as fracture energy, stress intensity factor, energy release rate, and characteristic length. The three concrete mixes adopted in the study has a compressive strength of 40 MPa, 60 MPa and 90 MPa. The results from the current study has been clubbed with the data presented by Ojha et al. [12], and a comparative analysis has been performed to evaluate the effect of hybrid fiber on the fracture parameters.

1.1 Research Significance

There has been extensive study on the fracture behaviour of hybrid fiber reinforced concrete [14,22,23,26-28], but the novelty of the present study is the use of high strength steel fiber along with polypropylene fibers and consideration of mix in three strength range. The strength of the fibers governs the fracture mechanism in the concrete. For lower strength fibers, the failure may take place by yielding and rupture of the steel fibers in tension, however for higher strength steel fibers the failure takes place through pull up mechanism. Using hooked-end fibers further improves the pull up resistance. The present study considered a hooked-end high strength steel fiber with polypropylene fiber. The literature on fracture performance of high strength hooked-end steel fiber reinforced concrete with polypropylene fiber is sparingly available. Also most of the available studies has been based on single strength range concrete mix. The shape dependent fracture parameters depend on the notch depth ratio and size of the specimen. Different authors have separately studied different strength concrete mix but comparing the fracture parameters becomes difficult due to variations in specimen size, notch depth ratio, aggregate type and loading rate. The present study gives a better comparison of fracture parameters at different strength range of the mix, and different fiber composition in the mix (without fiber, with steel fiber, and with hybrid fiber) through experimental investigation considering consistent notch depth ratio, specimen size and aggregate type. The comparison of present study with existing literature has been shown in table 1.

2. Concrete Ingredients

In present study, granite type coarse aggregate having 20 mm nominal size has been used. Fine aggregate (crushed sand) mostly quartz conforming to specifications of zone II sand as per IS: 383-2016 have been used. Figure 1(a) and 1(b) shows the coarse and fine aggregates used in study. A series of physical and chemical tests were performed on the aggregates and results have been presented in table 2. Ordinary Portland Cement (OPC)-53 grade along with fly ash and silica fume have been used as cementitious binders for preparation of concrete mixes. The physical and chemical properties of cementitious materials have been given in table 3. Polycarboxylic group-based superplasticizer conforming to requirements of IS 9103, has been used in present study to develop mixes of adequate workability.

Table 1. The novelty of present study

Literature	Fiber reinforcement details	Base Concrete mix
Present Study	Hooked-end Steel fiber having 1467 MPa tensile strength and polypropylene fiber.	Three base concrete mix with different strength range. Alteration in mix as per fiber content.
Bencardino et al.,	Hooked-end, 1050 MPa tensile strength steel fiber with polypropylene fiber.	One base concrete mix. Alteration in mix as per fiber content.
Xiangjun et al.,	Hooked-end, 1200 MPa tensile strength steel fiber with polypropylene fiber.	One base concrete mix. Alteration in mix as per fiber content.
Smarzewski, and Barnat-Hunek	Hooked-end, 1100 Mpa tensile strength steel fiber with polypropylene fiber	One base concrete mix. Alteration in mix as per fiber content.
Kazemi et al.,	Hooked-end, 2100 Mpa tensile strength steel fiber, study does not include hybrid fiber effect	One base concrete mix. Alteration in mix as per fiber content.
Ghasemi et al.,	Hooked-end, 1200 MPa tensile strength steel fiber	Discuss self-compacting concrete, One base concrete mix. Alteration in mix as per fiber content.
Alwesabi et al.,	Non-hooked end steel fiber, 2800 Mpa tensile strength	One base concrete mix. Alteration in mix as per fiber content.

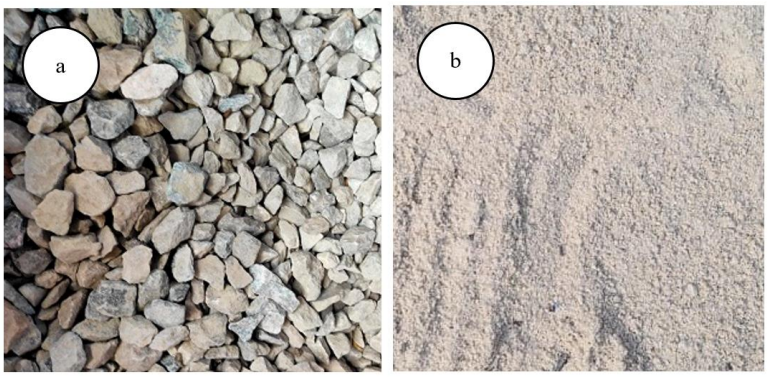

Fig. 1 (a) Coarse aggregate and (b) crushed Fine aggregate

Table 2. Properties of aggregates

Property		Granite		Fine Aggregate
		20 mm	10 mm	
Specific gravity		2.83	2.83	2.65
Water absorption (%)		0.3	0.3	0.59
Sieve Analysis Cumulative Percentage Passing (%)	20mm	98	100	100
	10 mm	1	68	100
	4.75	0	2	99
	2.36	0	0	89
	1.18	0	0	64
	600 µ	0	0	43
	300 µ	0	0	26
	150 µ	0	0	14
	Pan	0	0	0
Abrasion, Crushing & Impact Value		19,19,13	-	-
Flakiness % & Elongation %		29, 25	-	-

Table 3. Physical and chemical properties of cementitious materials

Characteristics	OPC -53 Grade	Silica Fume	Fly Ash
Physical Tests:			
Fineness Blaine's (m^2/kg)	320.00	22000	403
Soundness Autoclave (%)	00.05	-	-
Soundness Le Chatelier (mm)	1.00	-	-
Setting Time Initial (min.) & (max.)	170.00 & 220.00	-	-
Specific gravity	3.16	2.24	2.2
Chemical Tests:			
Loss of Ignition (LOI) (%)	1.50	1.16	0.4
Silica (SiO_2) (%)	20.38	95.02	60.95
Iron Oxide (Fe_2O_3) (%)	3.96	0.80	5.70
Aluminum Oxide ($A_{l2}O_3$)	4.95	-	26.67
Calcium Oxide (CaO) (%)	60.73	-	2.08
Magnesium Oxide (MgO) (%)	4.78	-	0.69
Sulphate (SO_3) (%)	2.07	-	0.29
Chloride (Cl) (%)	0.04	-	0.009
IR (%)	1.20	-	-
Moisture (%)	-	0.43	-

Ojha et Al. [12] incorporated 1% of steel fibers by volume of concrete. Trough and hooked-shaped steel fiber were used in the study. In the present study, 0.75% of steel fiber (SF) and 0.25% of polypropylene fiber (PPF) have been added. The amount of polypropylene fiber has been added to keep a note on the fiber requirement to impart the fire resistance to the concrete as per literature [20], [29]. Also, studies [14] have reported an increase in fracture performance of the concrete by the inclusion of certain amount of polypropylene fiber in the concrete mix along with steel fiber. The steel fiber used in the study has a diameter of 0.55 mm and a length of 35 mm. According to the manufacturer, the tensile

strength of steel fiber is 1468.99 N/mm^2. For PPF, a Polypropylene triangular fiber of 6mm length has been used. The density of SF is 7860 kg/m^3 and the density of PPF is 910 kg/m^3. Detailed properties of the used polypropylene fiber have been given in table 4 and Fig 2 shows the steel and Polypropylene fiber used in the study.

Table 4. Properties of polypropylene fiber

S. no.	Properties	Value
1	Shape	Triangular
2	Cut length (mm)	6
3	Effective Diameter (microns)	20-40
4	Specific Gravity	0.90-0.91
5	Melting Point(degree C)	160-165
6	breaking tenacity (Gpd)	4-6
7	Tensile Strength (estimated in Mpa)	320-490
8	Elongation (%)	60-90
9	Young's Modulus (Mpa)	>4000

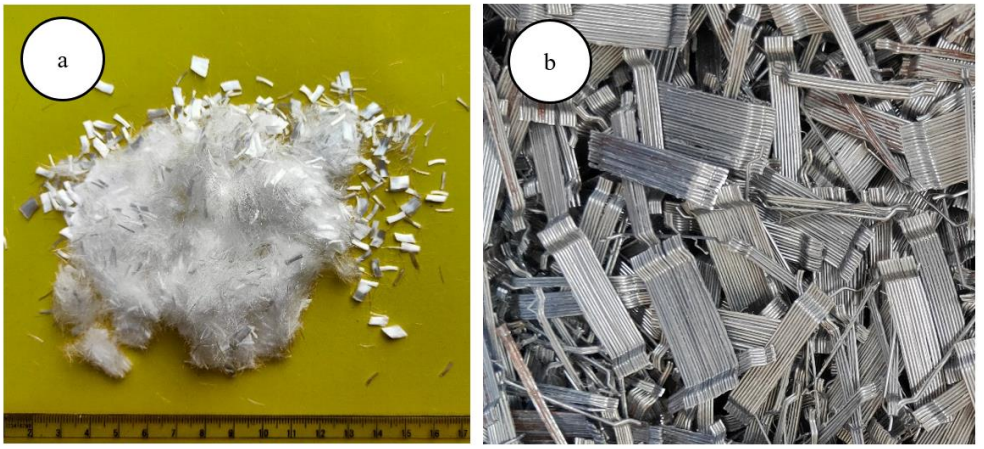

Fig. 2 (a) Polypropylene fiber and (b) steel fiber used in the study

3. Mix Design Details

In present study, concrete mixes (with and without fibers) of different strength ranges were developed and mix design details of concrete mixes have been adopted from previous studies conducted by Ojha et al., [12]. The w/c (water/cementitious content) ratios for the concrete mixes adopted in the study were 0.47, 0.36 and 0.20. For obtaining an optimized mix of 90 MPa, silica fume has been added in the mix. Mix design detail used in the study by the Ojha et al., [12] and the present study has been given in table 5. As given in the table, the concrete mixes studied previously by Ojha et al.,[12] consist of plain concrete and concrete with 1% of steel fiber. In mixes of present study, a combination of 0.75% SF and 0.25% PPF has been used. Such mixes has been referred as Hybrid Fiber-reinforced (1% HF) concrete in the subsequent sections. The mixes were prepared in small batches in a pan type mixer. The terminologies, HF and SF used in for mixes identification represent Steel Fiber and Hybrid Fiber.

The coarse and fine aggregates were first mixed together and combined with half the amount of water in the pan mixture for the preparation of the mix. Thereafter, polypropylene fiber was mixed with the remaining half of the water to be added in the mix in a separate container. The cement, flyash, silica fume, and the water with the polypropylene fiber was then added to the homogenized aggregate mix. After that the superplasticizer was added. Once the constituents were thoroughly mixed, steel fiber was sprinkled uniformly in the pan mixture. The concrete batch was then poured into moulds covered with an anti-adhesive material and then compacted on a vibrating table. To reduce moisture loss after compacting, the samples were covered with foil. All of the samples were kept in a controlled environment at a constant temperature of 27 °C until they were taken out of the moulds after 24 hours and allowed to cure for 28 days in a water tank at 27 °C.

Table 5. Mix Design Details

Mix Id	Fiber (% by volume of concrete)	Total Cementitious kg/m^3	Cement kg/m^3	Fly Ash kg/m^3	Silica Fume kg/m^3	Water kg/m^3	Water/ Total cementitious
A	-	362	290	72	0	170	0.47
A-SF	1% SF	362	290	72	0	170	0.47
A-HF	0.75% SF +0.25PPF	362	290	72	0	170	0.47
B	-	417	334	83	0	150	0.36
B-SF	1% SF	417	334	83	0	150	0.36
B-HF	0.75% SF +0.25PPF	417	334	83	0	150	0.36
C	-	750	548	112	90	150	0.20
C-SF	1% SF	750	548	112	90	150	0.20
C-HF	0.75% SF +0.25PPF	750	548	112	90	150	0.20

4. Experimental Plan

The present section discusses the test procedures adopted for the studies conducted on the concrete specimens of different mixes.

4.1. Compressive strength test

Compressive strength of concrete has been performed on cubical specimen of size 150 mm x 150 mm x 150 mm. The test is performed according to the specification given in IS 516. For the test, 3 sets of cubical specimens were cast using the mix design presented in the table above. The test is performed in a compression testing machine of capacity 3000 KN.

4.2. Split Tensile Strength Test

The split tensile strength of concrete has been estimated using Indian standard IS 516: Part I section I. A specimen with sizes of 300 mm height and 150mm diameter was used for determining split tensile test. The test has been performed on three samples and the average value has been reported.

4.3. Three-point bend test on notched beams

A 3-point bending test based on the method described by RILEM [21], [30] was used to calculate the fracture characteristics. The experiments yielded several fracture parameters, which has been addressed in the following sections. Figures 3(a) and 3(b) illustrate a schematic diagram for the three-point bend test and the laboratory setup for

the actual test. A beam with dimensions of 100mm × 100mm × 500mm and a notch of 35 mm at the mid-span was used as test specimen. Displacement control machine of 300 KN capacity was used for flexural testing of beam specimen. Deflection at mid-span of the beam was recorded using Linear Variable Displacement Transducer (LVDT) and Crack Mouth Opening Displacement (CMOD) at the bottom of the beam was recorded using clip gauge placed between steel knife edges. A total of twelve beams were examined in this investigation as per mix design details listed in Table 5.

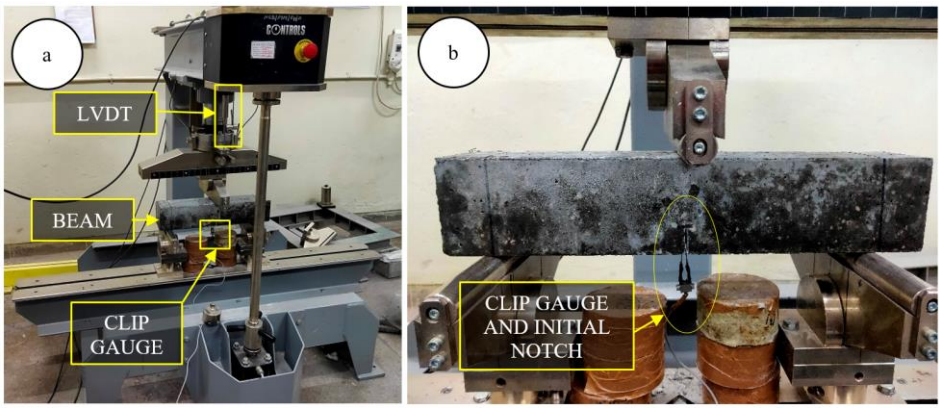

Fig. 3 (a) Experimental setup for three-point bend test (b) Clip gauge and initial notch on the Beam

5. Results and discussions

5.1. Compressive strength and Split tensile strength

Compressive strength and split tensile strength of the hybrid fiber reinforced concrete have been evaluated and compared with the values for the plain and steel fiber reinforced concrete presented by Ojha et al.,[12] for the similar mix. The results have been tabulated in table 6. The change in the compressive strength of normal strength concrete mix with w/c ratio of 0.47 is not significant after the addition of steel or hybrid fiber. This has been established in past study [12] also. But for the concrete mix with w/c ratio of 0.36 and 0.20 about 10% decrease has been observed in the compressive strength after addition of hybrid fibers. However, the compressive strength of the steel fiber reinforced concrete with similar w/c ratio has not changed significantly. The findings suggest that the polypropylene fiber present in the hybrid mix affects the microstructure and interfacial transition zone (ITZ) in optimized and dense mix of higher strength concrete due to its diameter being comparable to the pore size present in the concrete. These fibers has been flexible and can properly fill the voids and improves the compressive strength of the mix when added in extremely small quantity (less than 0.1%) [14]. Also, high-strength concrete consists of silica fume whose functionality in the matrix is most likely to get affected by these hybrid fibers leading to reduction in the compressive strength.

The values of the split tensile strength show a direct correlation with the compressive strength as established in the literature [1]. Similar to compressive strength, addition of steel or hybrid fiber does not affect the split tensile strength of normal strength concrete mix with w/c ration of 0.47. For the concrete mix with w/c ratio of 0.20, addition of steel fiber shows enhancement in the split tensile strength of the mix. For same mix, the addition of the hybrid fiber also shows enhancement in the split tensile strength, but the enhancement is lower than the addition of steel fiber alone. In the concrete mix with w/c ratio of 0.20, the compressive strength reduced significantly after addition of hybrid fiber.

Such significant reduction in the split tensile strength has been not observed in the mix with hybrid fiber and it can be concluded that the fiber action helped in compensating for the matrix strength reduction in higher strength concrete.

Table 6. Compressive strength and split tensile strength

Water/Cementitious (W/C)	Mix Id	Compressive Strength (MPa)	Split Tensile Strength (MPa)
0.47	A	36.90	3.37
	A-SF	37.40	3.95
	A-HF	34.90	3.34
0.36	B	51.60	4.04
	B-SF	53.20	4.73
	B-HF	45.40	3.82
0.20	C	92.20	5.35
	C-SF	91.70	7.19
	C-HF	79.00	6.28

5.2. Load-Deflection and Load-CMOD behavior

The three-point bend test conducted on the notched beams yielded load versus CMOD and load versus midpoint beam deflection curves, which have been presented in figure 4. Each plot in figure 4 consists of three sets of values, the line in green color (Plain) shows the curves for the control beams, i.e. beams without any fiber reinforcement. The curves in the brown (1% SF) represent the curves for beams with 1% of steel fiber reinforcement. These two curves have been incorporated from the study conducted by Ojha et al.,[12]. The lines in purple shows the curves obtained for 1% of hybrid fiber (1% HF) which consists of 0.75% of steel fiber and 0.25 percent of Polypropylene fiber by volume of the concrete. Ojha et al.,[12] gave three sets of curves for each mix design of plain and steel fiber reinforced concrete. In this study, four curves were obtained and reported for the respective four beams tested having 1% of hybrid fiber.

Figure 4(a) and Figure 4(b) shows the load-CMOD and load-deflection curves respectively, for the mix made at w/c ratio of 0.47. It can be observed that curves for 1% of hybrid fiber reinforcement show similar curves as obtained in 1% of steel fiber reinforcement. Peak values of these curves exceed the peak values for steel fiber reinforced beams in some cases. Figure 4(c) and 4(d) show load-CMOD and load-deflection curves for mixes made at w/c ratio of 0.36. Similar to the w/c ratio of 0.47, curves resemble the behaviour of concrete having 1% steel fiber. Also, the peak load in some of the cases exceeded the peaks of the curves for mixes prepared at w/c ratio of 0.36. Figures 4(e) and 4(f) represent the curves corresponding to the mixes prepared at w/c ratio of 0.20. Contrary to the behaviour of mixes prepared at 0.47 and 0.36 w/c ratios, here the curves for hybrid fibers lie in between the curves for the plain concrete and curves for the steel fiber reinforced concrete. These curves have direct implications on fracture parameters as discussed in further sections of this manuscript. Comparing the curves of mixes prepared at different w/c ratios, a gradual increase in the peak load from the mixes made at w/c ratio of 0.47 to 0.36 has been observed. This gradual increase remained approximately unchanged for mixes at w/c of 0.20, which is contrary to the behavior of concrete without fiber and with steel fiber only. Ojha et al., [12] suggested that with an increase in the compressive strength of the concrete, the peak load in the three-point bend test increases for plain and steel fiber reinforced concrete (1% SF). This generalization doesn't hold good for hybrid fiber reinforced concrete tested in the present study. The steel and hybrid fibers used have different tensile strength, therefore have different failure mechanism. Most of the high

strength steel fiber fail by pull out mechanism and not by rupture of the fibers. Higher strength concrete enhances the pull out resistance of the steel fiber thereby improving the peak load taken by the beam in three-point bend test. On contrary the polypropylene fiber may fail by rupture due to its relatively lower tensile strength. Therefore, the strength of concrete and fiber-concrete bond are not only the factors affecting the peak load of a hybrid fiber reinforced concrete beams. The tensile strength of fibers also becomes a crucial factor in case of hybrid fiber reinforced concrete.

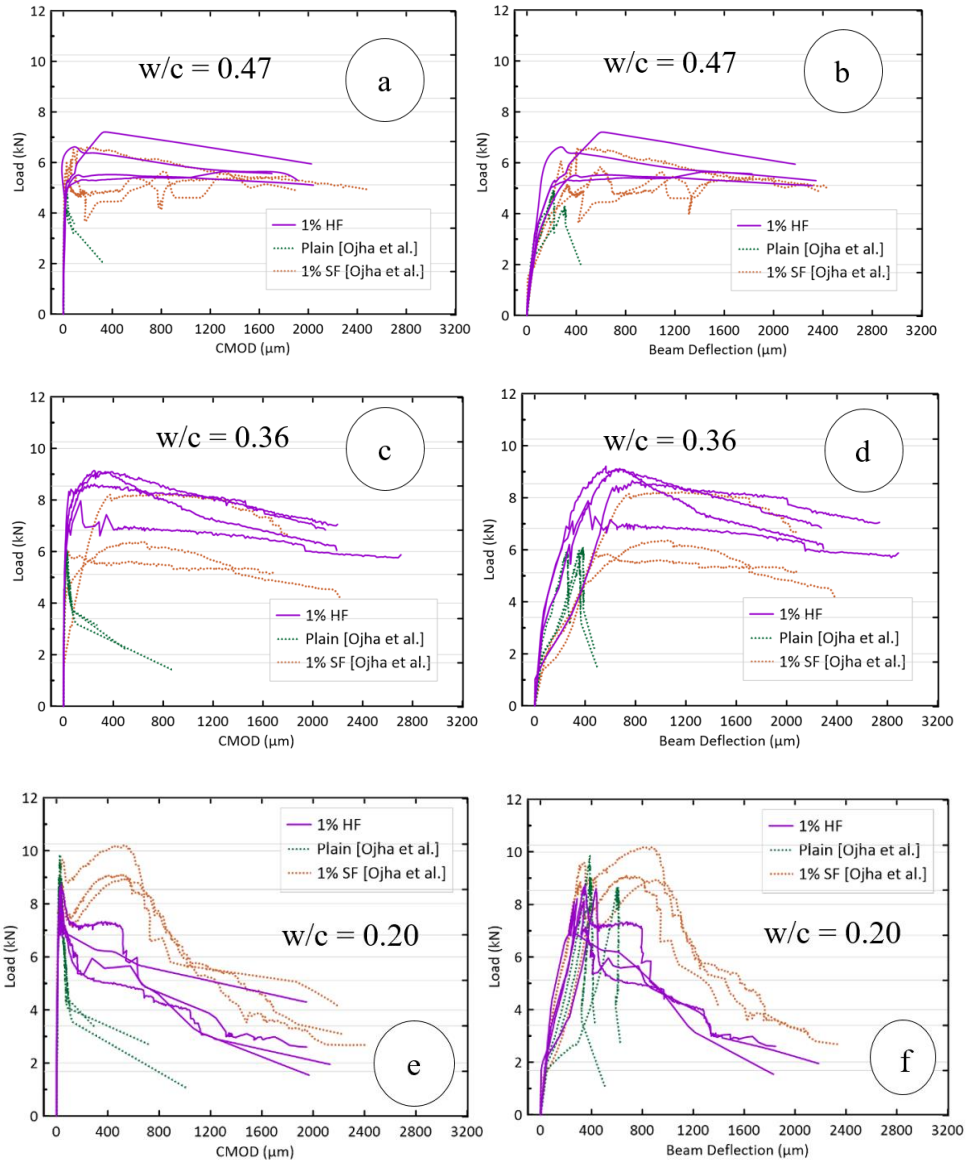

Fig. 4 (a-f) Load-deflection and Load-CMOD behavior of notched beams

5.3. Calculation of initial compliance and modulus of elasticity

The initial part of the load-CMOD curve has a li on where elastic deformation in the beam takes place. Initial compliance is the inverse of the slope of this initial straight

part. Based on the value of initial compliance, the modulus of elasticity of the beam can be calculated. RILEM [30] presented equation (1) to derive the value of modulus of elasticity of the material from the value of initial compliance obtained from the load-CMOD curve.

$$E\ (MPa) = 6S\ \frac{\alpha V_1(\alpha)}{C_i d b^2} \tag{1}$$

Here Ci is the initial compliance and $V_1(\alpha)$ can be calculated using the equation by Tada et al. [31] as follow:

$$V_1(\alpha) = 0.76 - 2.28a + 3.87a^2 - 2.04a^3 + \frac{0.66}{(1-a)^2} \tag{2}$$

Table 7. Initial Compliance (C_i) and Modulus of Elasticity (M.O.E.)

Water/ Cementitious (w/c)	Mix Id	Initial Compliance (10-9 m/N)	M.O.E. (GPa) Calculated from load-CMOD	M.O.E. (GPa) [Arora et al.][27]
0.47	A	5.26	31.08	29.52
	A-SF	4.54	35.17	29.64
	A-HF	5.35	29.96	29.03
0.36	B	5.00	32.27	32.64
	B-SF	4.00	40.55	32.94
	B-HF	3.67	43.71	31.41
0.20	C	2.63	60.61	38.85
	C-SF	2.22	72.63	38.79
	C-HF	2.02	79.53	37.09

Table 7 presents the values of the calculated initial compliance and modulus of elasticity of the mix in table 5. Modulus of elasticity has been calculated using two methods. The first method involves calculation from the initial compliance of load-CMOD curve using equation (1). The second method is based on the method given by Arora et al. [32] , which relates compressive strength with modulus of elasticity. Comparing values of modulus of elasticity of different mixes, it can be observed that the value of initial compliance decreases drastically for higher strength concrete which gives an unrealistic value of modulus of elasticity. Similar findings have been reported in past [12], and therefore for the subsequent sections, values of M.O.E. obtained using method of Arora et al. has been used.

5.4. Fracture Energy

Fracture energy is one of the attributes which can quantify and indicate the material's toughness and resistance against cracks. It is defined as the average energy required to create a unit crack in the material. It is directly related to the area under the load-deflection curve obtained in the three-point bend test of notched beams. Higher fracture energy represents that the material is having a higher resistance to the cracks. In the present study, the fracture is determined using equation (3) as given by RILEM [21].

$$G_f(N/m) = (W_o + mg\delta_o)/A_{lig} \tag{3}$$

G_f denotes the fracture energy, W_o denotes the area under the load-deformation curve for the beam, and m denotes the total weight of the beam including the support and the weight of the part of the loading arrangement that is not attached to the machine but follows the beam until failure. The acceleration due to gravity is g, which equals 9.81 m/s^2. Alig. is the

area of the ligament, which is the area of the projection of the fracture zone on the plane perpendicular to the beam axis. δ_o is the deformation of the beam, at the stage where entire beam height is cracked.

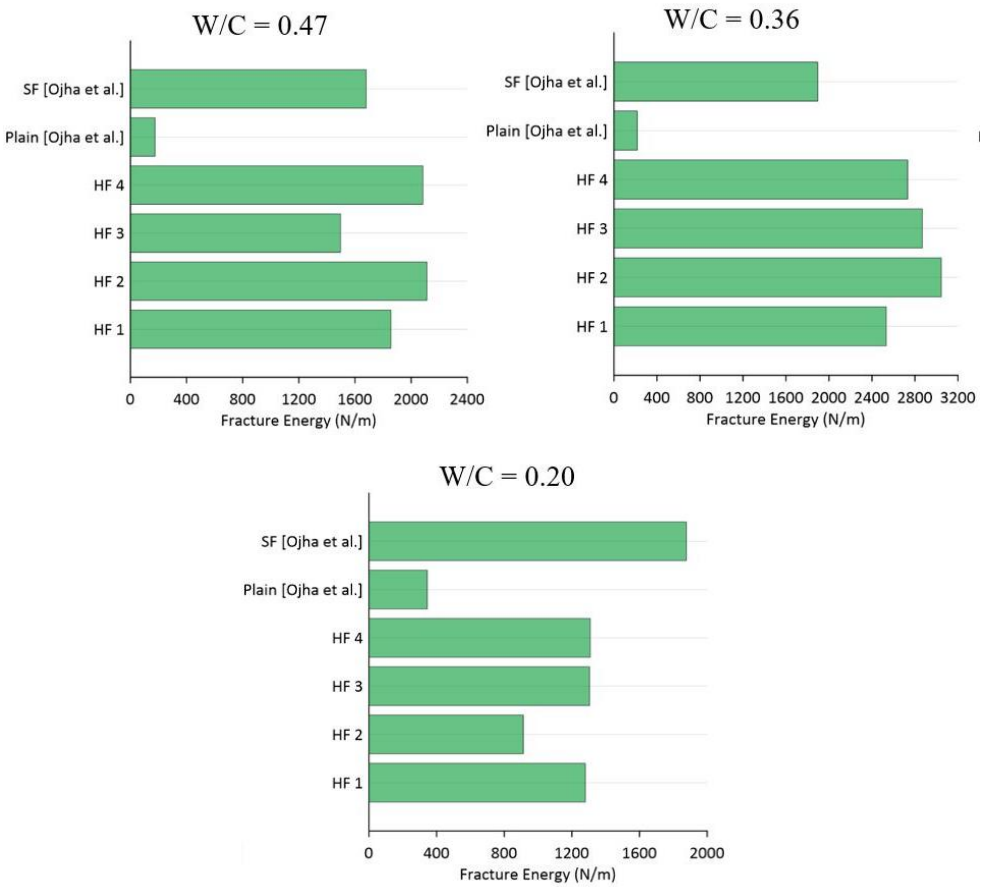

Fig. 5 Calculated fracture energy of beams and comparison with literature

Figure 5 shows the comparison of the calculated fracture energy for the three categories of the concrete mixes studied. In the figure, Plain and SF denotes the average fracture energy obtained by Ojha et al.[12] for the plain and steel fiber reinforced concrete. HF 1 to HF 4 represents the values of the obtained fracture energy for the four beams studied which contains 1% of hybrid fiber (0.25% PPF + 0.75% SF). On comparing the results, it can be seen that there is an increase in the fracture energy of the hybrid fiber reinforced concrete for w/c ratio of 0.47 and w/c ratio of 0.36. These two w/c ratios represent normal to high strength concrete limited up to strength of 50MPa. However, for high strength concrete, hybrid fiber reinforcement gave a lower improvement in fracture performance than the steel fiber reinforcement. The literature [14] also suggested a similar trend for Polypropylene fiber added concrete. The possible explanation to this can be attributed to (a) lower tensile strength of the polypropylene fibers than the steel fibers (b) less available voids and higher packing density in the high strength mix and (c) smaller diameter of the hybrid fibers. With increase in the strength of concrete, the concrete-fiber bond strength increased. This changes the mode of failure of the fibers. In normal strength concrete the failure is mostly from the slippage and pulling out of fibers whereas in higher strength

concrete, the low strength fibers may rupture before pulling out. Since the polypropylene fiber have lower tensile strength than the steel fibers, in higher strength concrete the polypropylene fibers gets ruptured giving a lower fracture energy. Most probably the addition of fibers affects the packing density of the mix reducing its strength and ultimately other mechanical properties. Due to smaller diameter of the hybrid fibers, it may also be interfering with the ITZ of the mix reducing its fracture performance. Additionally, the mix with w/c ratio 0.20 consists of silica fume whose action may be affected by these polypropylene fibers leading to a lower fracture energy.

5.5. Crack Propagation and Crack Pattern

The crack patterns were captured while testing the beams. Figure 6 shows major events during the testing of the beams.

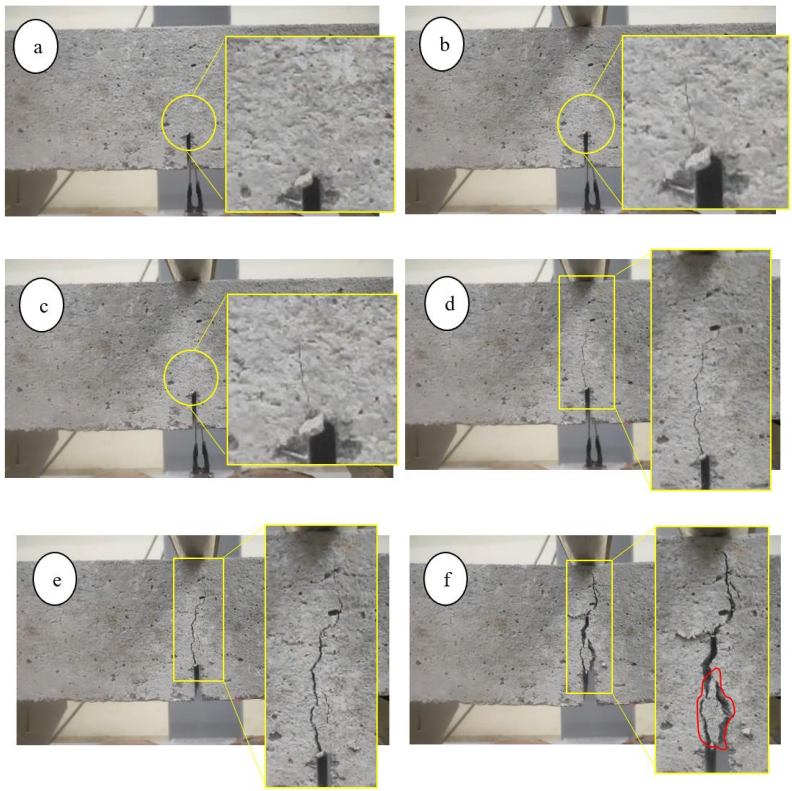

Fig. 6 Crack propagation and crack pattern in hybrid fiber reinforced concrete

In figure 6 (a), no crack on the beam was observed. This picture represents beam before loading. After loading, the visible cracks first initiated near the notch as shown in figure 6 (b) and figure 6(c) after initiation of the first crack it spread rapidly and covers the approximately entire height of the beam. The attached clip gauge has capacity to capture mouth opening up to 2 to 3 mm only and once the CMOD value reaches this value, the clip gauges gets detached. Although it can be seen that in figure 6(e), at the moment of the detachment of the clip gauge, the crack has reached the top portion of the beam, and the beam can be considered to be cracked at the full height. If the loading was continued, a fully damaged beam as shown in figure 6(f) has been obtained. In Figures 6(a) to 6(e), a single hairline crack in the beam which originated from the notch and spread in a single straight line was noticed. But in figure 6 (f), two crack paths originating from the notch and merging

at some beam height was seen. It creates a portion of hanging concrete in the beam, which again affirmed the idea, that although fiber reinforced concrete may get cracked but it will give sufficient time for evacuation as well as it prevents sudden falling off of the cracked concrete to some extent.

5.6. Stress Intensity Factor

The stress intensity factor (KIC) can be used to compare the capacity of material to sustain the stress caused by the residual stresses near the notch's or crack's tip. It can be defined as a measurement for stresses in the crack's immediate vicinity. A material with higher K_{IC} has been considered to have a better fracture and crack initiation and propagation resistance. The stress intensity factor is determined as follows using RILEM [30] as given in equation (4):

$$K_{IC}\,(MPa\sqrt{m}) = 3(P_{Nmax} + 0.5mg)\frac{S\sqrt{\pi a}}{2d^2\,b}f(\alpha) \tag{4}$$

In equation (4) S, a, d and m are Span, height, notch depth, and mass of the beam respectively. P_{Nmax} is the peak load on the beam in the three-point bend test. Alpha is the ratio of a and d i.e., α = a/d = 0.35 for the present study. F(α) is the geometry correction given by equation (5).

$$f(\alpha) = \frac{1.99 - \alpha(1-\alpha)(2.15 - 3.9\alpha + 2.7\alpha^2)}{\sqrt{\pi}(1+2\alpha)(1-\alpha)^{3/2}} \tag{5}$$

Figure 7 shows the values of the calculated characteristic strength as well as the values from the literature. The symbols has their usual meanings as explained for the figure 6. Similar to the fracture energy, the hybrid fiber improved the values of stress intensity factor for normal strength concrete. However, the stress intensity factor gets reduced in case of high strength hybrid fibre reinforced concrete in comparison to the high strength mix with steel fiber alone. The reasoning for this behavior were similar as in case of fracture energy. As explained earlier, in case of high strength concrete, when the dosage of PP fibre exceeds a certain amount (compared to the available voids in high strength concrete), instead of improving, it further deteriorates the fracture properties.

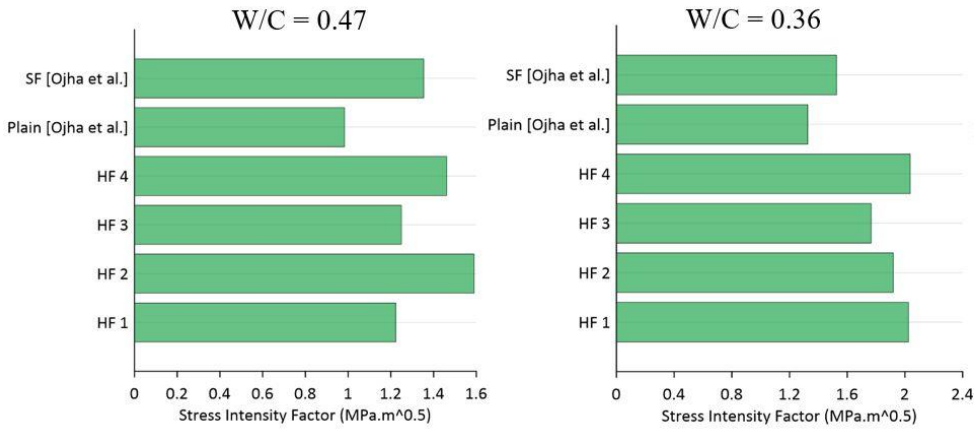

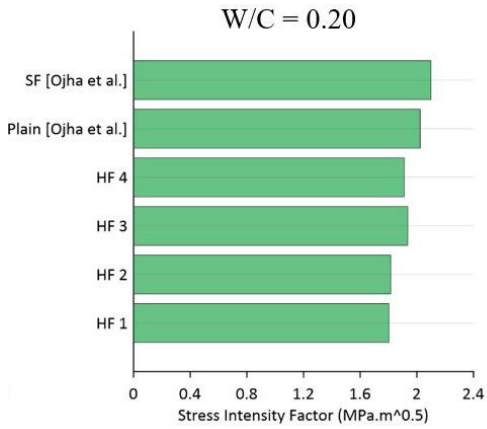

Fig. 7 Calculated Stress Intensity Factor of beams and comparison with literature

5.7. Critical Energy Release Rate

The cracking of the material releases a certain amount of energy and thereby reduces the overall stored potential energy. The decrease in total potential energy with respect to increase in fracture surface area may be calculated quantitatively. The critical energy release rate, or G_{IC}, is the rate at which energy changes, when a material fractures and a new surface is created. The energy release rate is a critical component in evaluating material properties related to fracture and fatigue. G_{IC} is calculated using the equation presented by Taha et al. [33], which is stated in equation (6) as follows:

$$G_{IC}(N/m) = \frac{{K_{IC}}^2}{E} \tag{6}$$

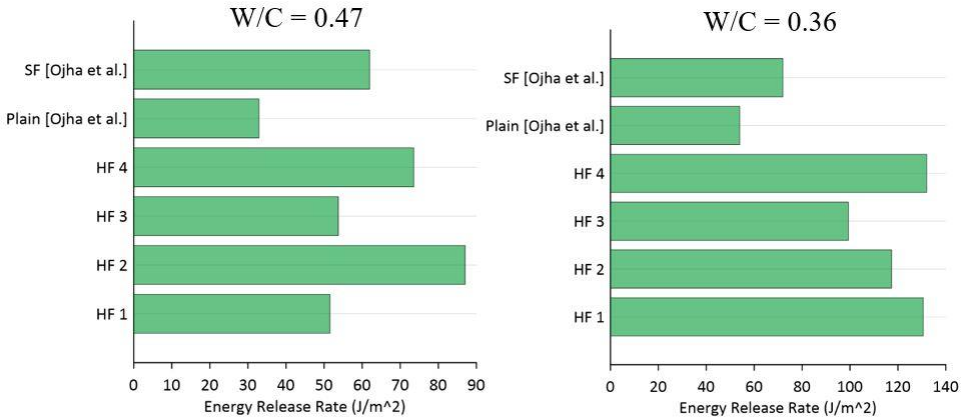

Fig. 8A Calculated energy release rate of beams and comparison with literature

Experimentally obtained values of the energy release rate for the beams and its comparison with plain and steel fiber reinforced concrete is given in figure 8. As the previous trends for the fracture energy, energy release rate also shows a marginal improvement in two beams of w/c ratio 0.47 and all the beams of w/c ratio 0.36.

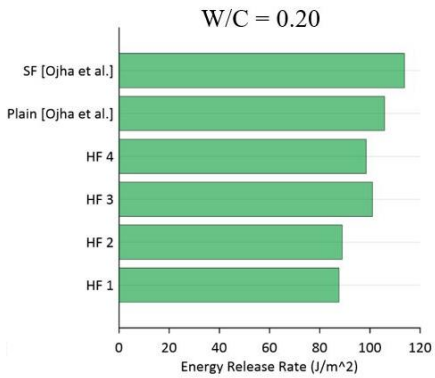

Fig. 8B Calculated energy release rate of beams and comparison with literature

These two w/c ratios represent concrete with available voids for the PPF present in the hybrid fiber. Whereas the dense mix of high strength concrete with w/c ratio of 0.20 got a marginal reduction in the values of energy release rate by addition of hybrid fiber when compared to the steel fiber reinforced concrete. The fiber in the concrete with dense packing disturbed the optimized particle matrix and reduced the amount of potential energy release when new cracked surface gets created.

5.8. Characteristic Length

In non-local continuum formulations, characteristic length is a material parameter that indicates the smallest possible breadth of a zone of strain-softening damage. In discrete fracture models, it may be thought of as the smallest feasible fracture spacing. Finding the characteristic length can help in judging the comparative brittleness of two materials following the beginning of early fractures. Smaller characteristic length materials are more brittle; therefore, fracture propagation is easier in these materials. The equation (7) presented by [34] gives a method to estimate the characteristic length based on Modulus of elasticity (E), Fracture energy (G_f) and split tensile strength (fst).

$$L_{ch}(mm) = \frac{EG_f}{{f_{st}}^2} \tag{7}$$

Calculated values of the characteristic length and the values from the literature has been shown in figure 9.

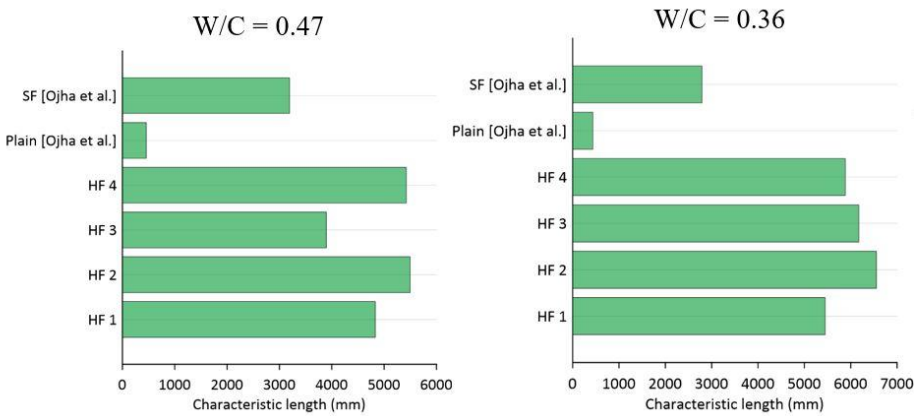

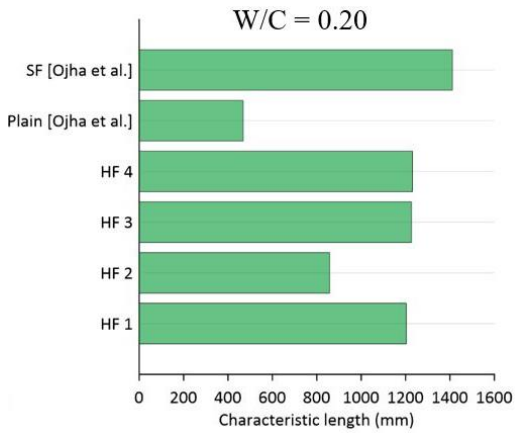

Fig. 9 Calculated characteristic length of beams and comparison with literature

The trend for the characteristic length upon addition of hybrid fiber is similar to other fracture parameters discussed above. The values for the characteristic length after addition of hybrid fiber improved for w/c ratios of 0.47 and 0.36 and it reduced for optimized mix with w/c ratio of 0.20 when compared with steel fiber reinforced concrete. This suggests that crack propagation got easier in the mix with w/c ratio of 0.20 when hybrid fibers were added. The PPF in the hybrid fiber when doesn't find enough voids helps in crack propagation in the concrete. Compared to plain un-reinforced beam, the characteristic length was significantly higher for all the mixes with hybrid reinforcement. This can be credited to the interlocking provided by SF in the hybrid fiber for all the mixes and interlocking provided by PPF in the hybrid fiber for mixes with w/c of 0.47 and 0.36.

Table 8 gives the mean and the standard deviation of the evaluated fracture parameters for the hybrid fiber reinforced concrete beams considered in the study. The standard deviation of concrete with w/c ratio 0.47 has been the highest for the studied fracture parameters suggesting the highest variation in the normal strength concrete. It appears that due to lower strength among all the mixes, the concrete with w/c ratio 0.47 is not able to provide enough and uniform grip to the fibers resulting in more variation among different mix. On contrary the higher strength mix is providing strong and uniform bonding to the fibers giving a lower standard deviation at higher strength.

Table 8. Mean and Standard deviation of the evaluated fracture parameters for hybrid fiber reinforced concrete beams

		Fracture Energy (N/m)	Stress Intensity Factor (MPa.m^0.5)	Energy Release Rate (J/m^2)	Characteristic length (mm)
0.47	Mean	1887.64	1.38	66.47	4912.16
	Standard Deviation	246.44	0.18	16.92	740.53
0.36	Mean	2794.97	1.94	119.81	6016.15
	Standard Deviation	188.00	0.13	15.17	467.28
0.2	Mean	1201.54	1.87	94.03	1130.00
	Standard Deviation	167.16	0.07	6.72	181.53

6. Conclusions

In this paper, the fracture performance of hybrid fiber reinforced concrete with strength in three different ranges – Normal, Normal to High and High strength is studied. The obtained fracture parameters has been compared with the findings for a similar mix of plain and steel fiber reinforced concrete. In total 12 beams were tested, which includes 4 beams from each strength category. Based on the experimental finding and comparative analysis with the literature following can be concluded as given below:

- Addition of hybrid fibers (0.25% Polypropylene + 0.75% steel by volume of concrete) in the concrete does not have a significant impact on the compressive and tensile strength of the normal strength mix with w/c ratio of 0.47. But at higher strength, the hybrid fiber reinforced concrete shows a 10% lower compressive strength than the plain or steel fiber reinforced concrete.
- For normal strength and normal to high strength concrete, the load-deflection and load CMOD curves for the hybrid fiber reinforced concrete shows a better fracture performance as compared to steel fiber reinforced concrete with a significant improvement in the peak load and maximum deflection compared to the plain concrete. Whereas for the high strength concrete, the steel fiber reinforcement shows a better fracture performance than the hybrid fiber reinforcement.
- The fracture parameters – Fracture energy, Stress intensity factor, Energy release rate, and Characteristic length shows similar trends. For high and normal to high strength concrete, addition of hybrid fibers gave slightly better results than steel fiber reinforced concrete but for high strength concrete the steel fiber reinforcement resulted better fracture behaviour than hybrid fiber.
- The issue of brittle failure has been mostly discussed for high strength concrete due to smaller post peak stain capacity in the high strength concrete. Based on the study it was found that, addition of hybrid fibers improved the fracture performance of normal strength concrete and prevented the sudden failure of concrete. But such risk can be mitigated for normal strength concrete by already existing methodologies like by designing under reinforced beam and providing proper detailing of the reinforcement. The normal strength concrete structures are more economically sensitive and therefore it is not necessary to use hybrid fibers in normal strength concrete mixes unless fracture is a critical issue. But in certain special cases where the fracture performance and crack prevention are critical parameters, the proposed hybrid fiber reinforcement can be suitably employed in the normal strength concrete also.

The study concludes that the choice of fiber reinforcement for improving the fracture behaviour of concrete depends upon the strength of the concrete as well as the properties of fibers. For normal and normal to high strength concrete, hybrid fiber reinforcement is more suitable choice than the steel fiber alone. Whereas for higher strength concrete, the high strength steel fiber reinforcement alone performed better than the hybrid fiber reinforcement considered in the study.

Acknowledgements

Authors acknowledge the funding received from Ministry of Commerce & Industry, Govt. of India

References

[1] Arora V V, Singh B, Jain S. Experimental studies on short term mechanical properties of high strength concrete. Indian Concrete Journal, 2016; 90(10): 65-75.

[2] Ojha P N, Singh B, Singh A, Patel V, Arora V V. Experimental study on creep and shrinkage behaviour of high strength concrete. Indian Concrete Journal, 2021; 95 (2): 30-42.
[3] Arora V V, Singh B, Patel V, Daniel Y N, Mohapatra B N. Stress-Strain Behaviour and Performance Evaluation of High Strength Steel Fibre Reinforced Concrete. Indian Concrete Journal. 2019; 93 (12): 54-61.
[4] Singh B, Arora V V, Patel V. Experimental study on stress strain behaviour of normal and high strength unconfined concrete. Indian Concrete Journal. 2020, 94(4), 10-19.
[5] Singh B, Arora V V, Patel V. Study on stress strain characteristics of high strength concrete. Indian Concrete Journal. 2018; 92(6):37-43.
[6] Wang Y, Hu X. Benefits of Short Kevlar Fiber Reinforcement at the Interface for Repair of Concrete-Like Materials. Journal of Materials in Civil Engineering. 2016; 28 (9). https://doi.org/10.1061/(ASCE)MT.1943-5533.0001611
[7] Arslan M E. Effects of basalt and glass chopped fibers addition on fracture energy and mechanical properties of ordinary concrete: CMOD measurement. 2016. Constr. and Building Materials. 2016; 114:383-391. https://doi.org/10.1016/j.conbuildmat.2016.03.176
[8] Sandhya K S, Rajamurugadoss J, Ganesh Prabhu G. Structural and other applications of steel fiber reinforced concrete-a review. International Journal of Scientific and Technology Research. 2019; 8 (10):2317-2322
[9] Liew K M, Akbar A. The recent progress of recycled steel fiber reinforced concrete. Constr. and Building Materials. 2020; 232. https://doi.org/10.1016/j.conbuildmat.2019.117232
[10] Yang D, Zhang B, Liu G. Experimental Study on Spall Resistance of Steel-Fiber Reinforced Concrete Slab Subjected to Explosion. International Journal of Concrete Structures and Materials; 15(1), 2021. https://doi.org/10.1186/s40069-021-00459-8
[11] Ojha P N, Trivedi A, Singh B, Adarsh KNS, Patel V, R. K. Gupta. High performance fiber reinforced concrete - for repair in spillways of concrete dams. Research on Engineering Structures and Materials. 2021. https://doi.org/10.17515/resm2021.252ma0128
[12] Ojha PN, Singh P, Singh B, Singh A, Mittal P. Fracture behavior of plain and fiber-reinforced high strength concrete containing high strength steel fiber. Research on Engineering Structures and Materials. 2022. https://doi.org/10.17515/resm2022.377ma1228
[13] Patel V, Singh V, Arora V V. Study on fracture behaviour of high strength concrete including effect of steel fiber. Indian Concrete Journal. 2020; 94 (4):1-9.
[14] Alwesabi EAH, Bakar BHA, Alshaikh IMH, Zeyad AM, Altheeb A, Alghamdi H. Experimental investigation on fracture characteristics of plain and rubberized concrete containing hybrid steel-polypropylene fiber.Structures.2021; 33:4421-4432, Oct. 2021. https://doi.org/10.1016/j.istruc.2021.07.011
[15] Patel V, Singh B, Ojha P N, Adhikari S. Mechanical Properties of Polypropylene Fiber Reinforced Concrete under Elevated Temperature. Journal of Architectural Environment & Structural Engineering Research. 2021; 4 (2). https://doi.org/10.30564/jaeser.v4i2.3296
[16] Ojha PN, Singh B, Kaura P, Singh A. Lightweight geopolymer fly ash sand: an alternative to fine aggregate for concrete production. Research on Engineering Structures and Materials. 2021. https://doi.org/10.17515/resm2021.257ma0205
[17] Narayanan S, Muniasamy G, Selvaganesh M, Sriram R, Sathish R S, Muthu PP. Critical Review on Flexural and Shear Behaviour of Hybrid Fiber Reinforced Concrete. International Journal of Civil Engineering and Technology. 2019:10 (3).
[18] Pakravan HR, Latifi M, Jamshidi M. Hybrid short fiber reinforcement system in concrete: A review. Construction and Building Materials. 2017: 142.. https://doi.org/10.1016/j.conbuildmat.2017.03.059

[19] Wu H, Lin X, Zhou A. A review of mechanical properties of fibre reinforced concrete at elevated temperatures. Cement and Concrete Research. 2020: 135. https://doi.org/10.1016/j.cemconres.2020.106117
[20] Khoury GA. Effect of fire on concrete and concrete structures. Progress in Structural Engineering and Materials. 2000: 24:429-447. https://doi.org/10.1002/pse.51
[21] R. T.-50 F. M. C. (Draft Recommendation), "Determination of the fracture energy of mortar and concrete by means of three-point bend tests on notched beams," Mater. Struct., vol. 18, no. 106, pp. 285-290, 1985. https://doi.org/10.1007/BF02472918
[22] Dong X, Ding Y, Wang T. Spalling and mechanical properties of fiber reinforced high-performance concrete subjected to fire. J. Wuhan Univ. Technol. (Mater. Sci. Ed.). 2008; 23 (5):743-749. https://doi.org/10.1007/s11595-007-5743-5
[23] Smarzewski P, Barnat-Hunek D. Fracture properties of plain and steel-polypropylene-fiber-reinforced high-performance concrete. Mater. Technol. 2015: 49 (4), 563-571. https://doi.org/10.17222/mit.2014.180
[24] Bhosale A, Rasheed MA, Prakash SS, Raju G. A study on the efficiency of steel vs. synthetic vs. hybrid fibers on fracture behavior of concrete in flexure using acoustic emission. Construction and Building Materials.2018; 199. https://doi.org/10.1016/j.conbuildmat.2018.12.011
[25] Bhosale A B, Prakash SS, Crack Propagation Analysis of Synthetic vs. Steel vs. Hybrid Fibre-Reinforced Concrete Beams Using Digital Image Correlation Technique. International Journal of Concrete Structures and Materials. 2020; 14 (1). https://doi.org/10.1186/s40069-020-00427-8
[26] Bencardino F, Rizzuti L, Spadea G, Swamy RN. Experimental evaluation of fiber reinforced concrete fracture properties. Compos. B Eng. 2010: 41(1)17-24. https://doi.org/10.1016/j.compositesb.2009.09.002
[27] Kazemi MT, Golsorkhtabar H, Beygi MHA, M. Gholamitabar. Fracture properties of steel fiber reinforced high strength concrete using work of fracture and size effect methods. Constr. Build. Mater. 2017; 142:482-489. https://doi.org/10.1016/j.conbuildmat.2017.03.089
[28] Ghasemi M, Ghasemi MR, Mousavi SR. Studying the fracture parameters and size effect of steel fiber-reinforced self-compacting concrete. Constr. Build. Mater. 2019; 201:447-460. https://doi.org/10.1016/j.conbuildmat.2018.12.172
[29] Lee J H, Sohn YS, Lee SH. Fire resistance of hybrid fibre-reinforced, ultra-high-strength concrete columns with compressive strength from 120 to 200MPa. Magazine of Concrete Research. 2012; 64 (6). https://doi.org/10.1680/macr.11.00034
[30] Shah SP. Determination of fracture parameters (KIcs and CTODc) of plain concrete using three-point bend tests. Materials and Structures. 1990; 23 (6,) 457-460. https://doi.org/10.1007/BF02472029
[31] Hiroshi P, Paris C, Irwin GRT. The stress analysis of cracks. Handbook, Del Research Corporation. 1973; (34).
[32] Arora V V, Singh B, Patel V, Trivedi A. Evaluation of modulus of elasticity for normal and high strength concrete with granite and calc-granulite aggregate. Structural Concrete. 2021; 22 (S1). https://doi.org/10.1002/suco.202000023
[33] Taha MMR, El-Dieb AS, El-Wahab MAA, Abdel-Hameed ME. Mechanical, Fracture, and Microstructural Investigations of Rubber Concrete. Journal of Materials in Civil Engineering. 2008; 20 (10). https://doi.org/10.1061/(ASCE)0899-1561(2008)20:10(640)
[34] Sahin Y, Koksal F. The influences of matrix and steel fibre tensile strengths on the fracture energy of high-strength concrete. Construction and Building Materials. 2011; 25 (4). https://doi.org/10.1016/j.conbuildmat.2010.11.084

Research on Engineering Structures & Materials
journal homepage: http://www.jresm.org
Research Group

Research Article

Performance analysis of lead rubber bearing isolation system for low, medium and high- rise RC buildings

Mrudula Madhukumar[a], Helen Santhi M*[b], Vasugi V[c]

School of Civil Engineering, Vellore Institute of Technology, Chennai, India.

Article Info

Article history:

Received 26 May 2022
Revised 03 Oct 2022
Accepted 26 Oct 2022

Keywords:

RC frame;
Base isolation;
Hinge formation;
Lateral displacement;
Performance level;
Ductility

Abstract

Earthquakes are the most vulnerable natural hazard which causes damage to both structure and human life. Even though advanced technologies have invented some degree of predictability in terms of probabilistic measures the main challenge for the structural engineers is to design earthquake-resistant structures. The use of base isolation solutions allows a building to withstand potentially devastating seismic impacts by allowing for flexibility in between building and the foundation. The concept of base isolation system had been suggested in last few decades and getting well established in countries like US, Japan and Turkey. Properly designed and detailed building with base isolation has shown very good performance in past earthquakes and the demand of base isolation has increased. The main focus of this study is to understand the performance and efficacy of base isolation in regular multi-storey RC framed structures with varying heights using lead rubber bearing by response spectrum analysis and pushover analysis. The software used was ETABS 2018 followed by IS 1893(Part 1):2016 and ASCE 7-16 under most credible earthquake. Performance of lead rubber bearing in G+5, G+15 and G+25 storey building models was examined and compared with the fixed base buildings. All the models showed better performance with isolators than the fixed base models. However, the effectiveness of base isolators is more prominent in medium and high-rise buildings.

1. Introduction

The major challenge faced by all Structural Engineers is to provide sufficient strength and stiffness to buildings for resisting lateral loads such as seismic loads and wind loads. Looking at the Indian code particularly, design philosophy evolves around earthquake intensity, with design- based earthquakes having a 10% chance in a 250-year return time and most credible earthquakes having a 2% chance in a 250-year return period. The seismic philosophy in the Indian code requires that the structure have a minimum strength to withstand structural and non-structural contents during earthquakes with intensities less than design- based earthquakes. It is always preferred to design under most credible earthquake if the location is highly prone to earthquake. To make the structure safe base isolation systems are used which reflects the energy from the earthquake before it is transferred to the structure. There are different types of base isolators used in the past few decades. Base isolators are generally categorized into two groups, namely, Sliding system and Elastomeric bearing system. Sliding system uses sliding elements between base and foundation of the building. It is again subdivided into Resilient friction system and Friction pendulum system (Jiying et al. 2021; Yongbo et al. 2021). Whereas Elastomeric bearing system is formed of thin layers of synthetic rubber sandwiched together between steel plates. It is classified into natural rubber bearing, low damping rubber bearing, lead plug bearing and high damping rubber bearing.

*Corresponding author: helensanthi.m@vit.ac.in
[a] orcid.org/0000-0003-1047-4368; [b] orcid.org/0000-0002-8274-7989; [c] orcid.org/0000-0002-0757-6593;
DOI: http://dx.doi.org/10.17515/resm2022.437ie0526

The analysis and design of various base isolation systems were performed to investigate the dynamic characteristics of buildings under ground motions in terms of long period ground motions, epicentral distance effect, beyond design base earthquakes, etc (Sunita et al. 2016; Shoma et al. 2018; Ahmad et al. 2019; Antonello et al. 2019; Mahdi et al. 2020; Feiyan et al. 2021; Jara et al 2021). Some of the studies on natural rubber bearing and lead rubber bearing (Keri et al. 2005; Gordon et al. 2007; Sharbatdar et al. 2011; Young et al. 2016; Parham et al. 2018; Seunghyun et al. 2018) revealed that the inter-storey drift, base shear and top acceleration of base isolated structures are reduced satisfactorily. A few studies were carried out on base isolated irregular buildings and observed effective in resisting the effects of earthquakes (Donato et al. 2016; Fayaz et al. 2018). Base isolation technique could be implemented for retrofitting soft-storey buildings (Fabio et al. 2018). New base isolation systems were developed for low and high-rise buildings and investigated for their seismic performance under different earthquake loadings. From various studies on base isolation systems for buildings' safety against ground movement, in this study, lead rubber bearing is used which is cost effective and commonly used compared to other type of isolators. This study mainly focuses on the behaviour of lead rubber bearing as base isolation system in low, medium and high- rise RC building which is located in high seismic zone V.

2. Methodology

For finding the performance and efficacy analysis of base isolation technology in RC buildings, G+5, G+15 and G+25 storey buildings are analyzed and compared the performance of buildings with increase in stories. The flowchart below shows the different stages of the work. Figure 1 below shows the flow chart representing the methodology of this entire study.

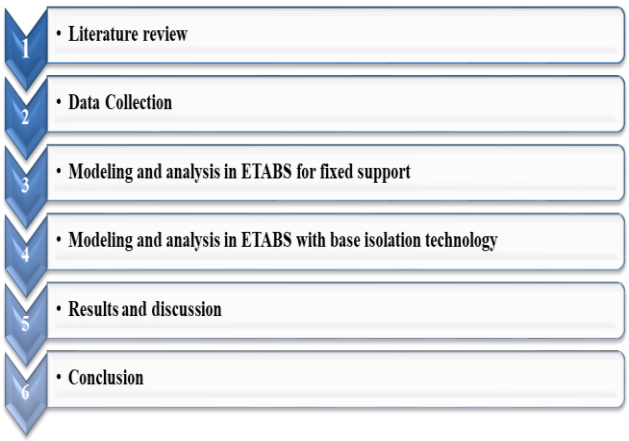

Fig.1 Methodology

3. Specifications

Table 1 shows the specifications of the building models considered in the study. The materials and member sizes were taken to suit the requirements of a G+5, G+15 and G+25 storey RC buildings. The parameters for the seismic analysis were obtained from IS 1893 (2016).

Table 1. Specifications

Sl.No.	Description	Values
1	Materials	M30, Fe500
2	No. of storeys	G+5, G+15, G+25
3	Plan size	81m x 28.5 m
4	Size of beam	Primary beam: 450 mm x 650 mm Secondary beam: 250 mm x 450 mm
5	Size of column	750 mm x 750 mm
6	Floor height	3.5 m
7	Slab thickness	150 mm
8	Seismic zone	V
9	Types of analysis	Response spectrum analysis, Pushover analysis
10	Zone factor(Z)	0.36
11	Reduction factor (R)	Fixed =3, base isolator =1
12	Importance factor (I)	Fixed =1.5, base isolator =1
13	Type of Soil	Type II- Medium Soil

Table 2. shows the live load specification of the building obtained from IS 875:2015 (Part 2) which is applied to the building model.

Table 2. Live load specifications

Sl. No.	Live load	Values
1	LL1(> 3 kN/m^2)	Corridor =4 kN/m^2 Staircase =4 kN/m^2 Office Room=3 kN/m^2
2	LL2(≤ 3 kN/m^2)	Laboratories =3 kN/m^2 Bathroom/Toilet =2 kN/ m^2 X-Ray room/Operating room =3 kN/ m^2 Wards/bedrooms =2 kN/ m^2
3	LL3(Terrace floor)	1.5 kN/ m^2

4. Modeling and Analysis

Modeling and analysis were done in ETABS 2018 as per IS 1893(Part 1):2016 and ASCE 7-16 under most credible earthquake. The analysis used were Response spectrum analysis and push over analysis.

Response spectrum analysis is widely recommended for the analysis and design of buildings against lateral loads due to earthquakes. This method of analysis gives the quantity of lateral loads acting at each floor level of the buildings when they are subjected to earthquakes. This method includes higher modes of vibrations in the analysis and therefore powerful method to understand the seismic behaviour of buildings.

In the present study response spectrum as specified in IS 1893:2016 was used to analyse (Figure 2) the behaviour of three different types of buildings i.e. low-rise, mid-rise and high-rise structures with lead rubber base isolation.

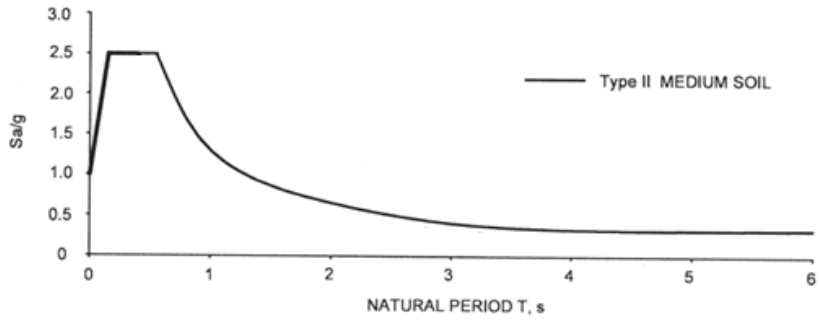

Fig. 2 Response Spectrum (IS 1893:2016)

The parameters considered in this study are displacement, base shear and time period.

- Displacement: It is the distance from which the structural element such as beams, columns and frame moves from its original position. While comparing the displacement with fixed base and base isolator, it gives a clear image how the isolator performs.
- Base Shear: Base shear is the maximum lateral load acting at the base of the building under ground motion due to earthquakes. The percentage reduction in base shear helps to study the performance of base isolation in structure.
- Time Period: When a building is subjected to ground shaking in the case of an earthquake, its time period is its natural period of oscillation.
- Drift: The sideways deflection of the upper floor in relation to the sideways deflection of the lower floor for a particular story is known as building story drift. It's also known as the lateral or sideways displacement of two neighboring stories.

Push over analysis is a simple technique for estimating the strength capacity and global and local damage level of a building in the post-elastic range of behaviour. The procedure to carry out the pushover analysis is explained in the seismic guidelines ATC-40, 1996, FEMA-356, 2000, etc. Modal pattern was used for pushover analysis which combines response from pushover analysis in multiple modes. It can estimate the magnitude and distribution of force demands in the first and higher modes including inelastic response. Automatic hinges were used in this study for assigning hinges to structural elements. P-M2-M3 hinges were assigned to columns and flexural M3 hinges to beams.

From the pushover analysis the different performance levels of buildings can be obtained. Buildings performance levels that are commonly used is shown below,

- Operational: This performance level gives an idea that the building can be used after the earthquake event since the deformations in the buildings are minor.
- Immediate Occupancy: There occurs very limited structural damage and damage to life is negligible. The components retain almost all pre-earthquake characteristics.
- Life Safety: This level ensures the life safety of the occupants from structural or non-structural building components damages.
- Structural Stability: This stage shows the partial or total collapse of the building which reveals the inability of the lateral load resisting elements.

4.1 Fixed Base Building

Modeling and analysis were done in ETABS 2018 followed by IS 1893(Part 1):2016 and ASCE 7-16 under most credible earthquake. The regular plan considered was with 81 x

28.5m plan with floor height of 3.5m. The analysis used were Response spectrum analysis and push over analysis. Building structures are classified into three types namely low-rise (<20 m), mid-rise (20 m to 50 m) and high-rise (>50 m) with respect to the height of the structures (IS 875 (Part 3), 2015). In this study, buildings are designed for all the categories mentioned under the seismic and non-seismic loading conditions. The height of low-rise structure is 19.5m and the height of mid-rise structure is 48.5m and the number of stories in low and mid-rise structure is five and fifteen. High-rise structure consists of 25 stories with a total height of 81.5m. The materials and member sizes were taken to suit the requirements of a G+5, G+15 and G+25 storey RC buildings. Figure 3 represents the plan of RC building for G+5, G+15 and G+25.

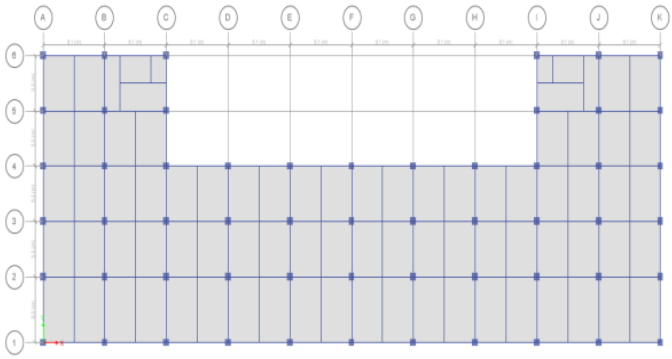

Fig. 3 Plan of RC building

4.2 Lead Rubber Bearing Isolation Device

Figure 4 and 5 show a typical model of lead rubber bearing with different parts mentioned. Rubber and lead layers are arranged in a definite pattern to obtain a lead rubber bearing which will strain first before the building components when it is installed in a building, thereby protection of building is ensured.

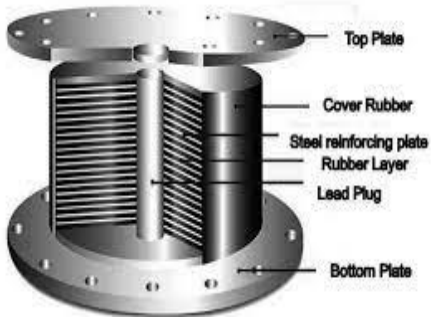

Fig.4 Lead rubber bearing-Typical

4.3 Design of Lead Rubber Bearing

The design of lead rubber bearing is done by using the following steps.

Step 1 (Isolation system force-displacement behavior)

Q_d (System characteristic strength) is found by the available data. (1)

$Q_d = \pi D_L^2 \sigma_{YL}/4$

Where D_L =Lead core diameter (Assumed as 4.5inch)

σ_{YL}= Effective yield stress of lead

lower bound= 1.45-1.75

upper bound = 1.35x(1.45-1.75)

D_B= Bonded rubber diameter (3-6times D_L)

K_d (System post-elastic stiffness)

$K_d = G f_L \pi (D_B^2 - D_L^2)/4T_r$ (2)

G= lower bound= 60-75

upper bound = 75x1.1x1.1

f_L= effect of lead core (ranges from 1.1-1.2)

T_r= less than or equal to D_L

Y=Yield displacement (0.25-1)

Step 2 Equivalent lateral force procedures (MCE)

In this method maximum displacement (D_M) is assumed and then found by iteration method

$D_M = g\, S_{M1} T_M/4\pi^2 B_M$ (3)

Where,

S_{M1} = 0.36 x 1 x 1.36/1 = 0.49

S_{MS} = 0.36 x 1 x 2.5 = 0.9

The effective stiffness and damping in bilinear model is shown in Figure 6.

Effective stiffness k_M

$k_M = K_{d,total} + Q_{d,total} / D_M$ (4)

Effective period T_M

$T_M = 2\pi\sqrt{W/ k_M g}$ (5)

Effective damping β_M. The yield displacement Y is assumed to be 0.6inch

$B_M = 4Q_{d,total}(D_M - Y)/2\pi k_M D_M^2$ (6)

Damping coefficient B_M can be interpolated from Table 17.5-1(ASCE 7-16).

Table 3 and 4 gives the design details and dimensions of the lead rubber bearing under study and are used as input for the modelling and analysis using ETABS.

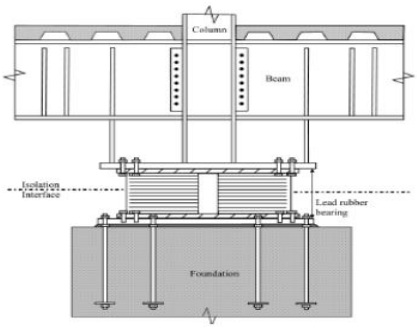

Fig. 5 Detailing of isolation system at column

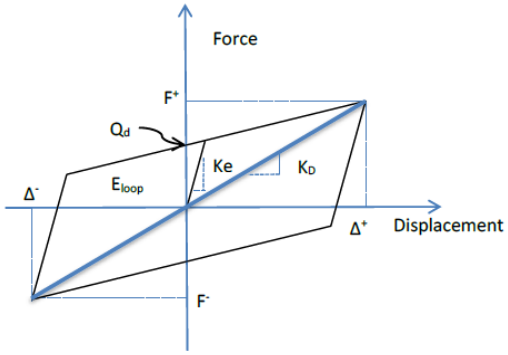

Fig. 6 Effective stiffness and damping in bilinear model

Table 3. Lead rubber bearing dimensions

	G+5	G+15	G+25	Units
N	56	56	56	-
W	77692	220520	363349	kN
D_L	115	130	140	mm
D_B	575	650	700	mm
T_r	115	130	140	mm
Y	15	15	15	mm
σ_{YL}	9.9	12	13.7	N/mm^2
G	413.7	517.1	551.6	kN/m^2

Table 4. ETABS input

ETABS input	G+5	G+15	G+25
Effective Stiffness (U1), kN/m	943060	719860	520335
Effective Stiffness (U2&U3), kN/m	943.06	719.86	520.33
Effective damping (U2&U3), kN-s/m	350	350	350
Post elastic stiffness (U2&U3), kN/m	49912	38993	27112
Yield strength (U2&U3), kN	5744.5	6933.0	11836.3

4.4 Building with Base Isolator

To make the structure safe, base isolation techniques are used which prevents the deformation to the buildings during earthquakes. The main aim of isolators is to reduce

the vibration to the super structure. The present study deals with the performance and efficacy of base isolation in low rise, mid-rise and high- rise building. For that G+5, G+15 and G+25 storey buildings were considered with lead rubber bearing device. Figure 7 represents the closer view of base isolator attached between base and the ground.

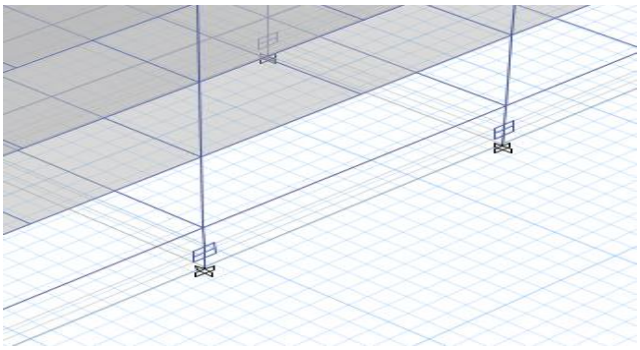

Fig. 7 Closer view of base isolator

5. Results and Discussion

Analysis was done using response spectrum method and the pushover analysis on G+5, G+15 and G+ 25 storey buildings with and without base isolators. Base responses for fundamental time period, first-storey displacement, base shear, and maximum inter-storey drift ratio are given in Table 5, 6, 7 and 8, respectively.

Figures 8, 9 and 10 are the graphical representation for displacement and Figures 11, 12 and 13 are the graphical representation for drift for G+5, G+15 and G+25, respectively. The bar chart comparison for Base shear and Time period for G+5, G+15 and G+25 are represented by Figures 14 and 15, respectively. The provision of base isolators in the buildings made them more flexible which is witnessed from increased fundamental time period of the buildings. The maximum inter-storey drift ratio of the base isolated buildings is considerably reduced and it is very effective in G+15 storey building.

Table 5. Fundamental time period

Building Type	Time period (sec)		
	Fixed base	Base isolated	Increase
G+5	0.949	2.789	2.94 times
G+15	3.387	6.283	1.86 times
G+25	4.816	9.894	2.05 times

Table 6. First-storey displacement

Storey	Displacement (mm)		
	Fixed base	Base isolated	Increase
G+5	16.95	127.11	7.49 times
G+15	19.64	678.46	34.55 times
G+25	20.35	1248.38	61.36 times

Table 7. Base shear

Building Type	Base Shear (kN)		
	Fixed base	Base isolated	Decrease
G+5	31308.86	6595.42	4.75 times
G+15	45811.47	20972.63	2.18 times
G+25	52660.67	36290.18	1.45 times

Table 8. Maximum Inter-storey drift ratio

Building Type	Maximum Inter-storey Drift Ratio		
	Fixed base	Base isolated	Decrease
G+5	0.0107	0.0047	2.27 times
G+15	0.0171	0.0033	5.18 times
G+25	0.0222	0.0118	1.88 times

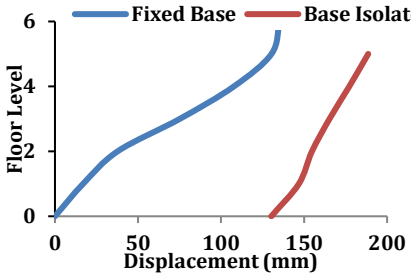

Fig. 8 Displacement for G+5

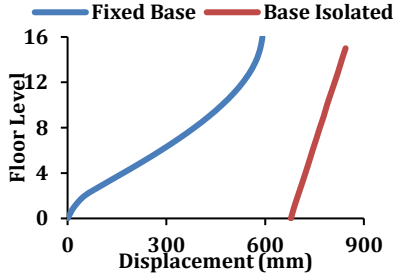

Fig. 9 Displacement for G+15

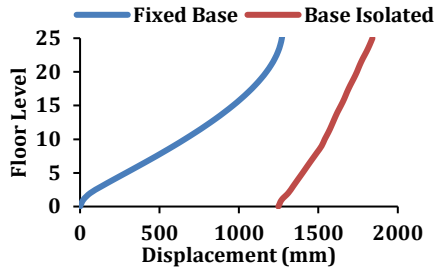

Fig. 10Displacement for G+25

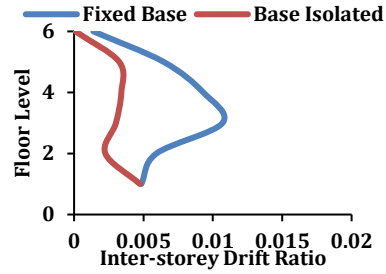

Fig. 11 Inter-storey Drift Ratio for G+5

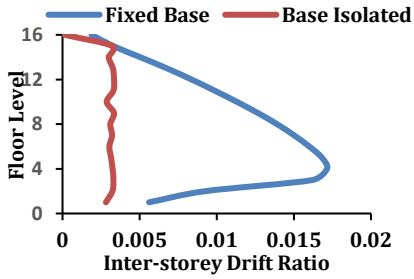

Fig. 12 Inter-storey Drift Ratio for G+15

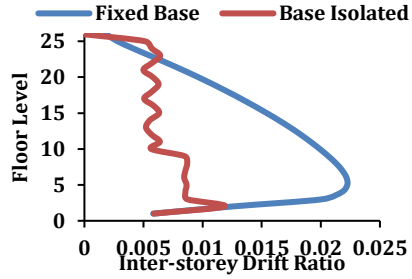

Fig. 13 Inter-storey Drift Ratio for G+25

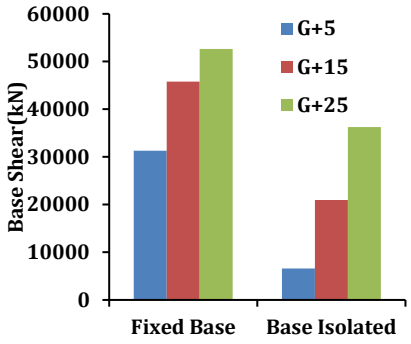

Fig. 14 Base shear

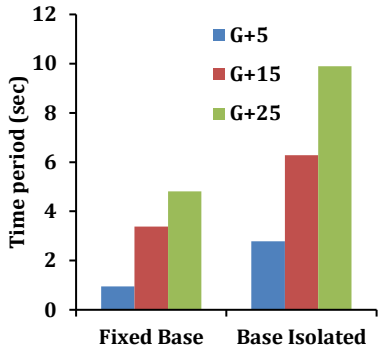

Fig. 15 Time period

Pushover analysis was done to identify the yield capacity and ductility ratio of base isolators compared to fixed structures. Capacity curves were obtained after pushover analysis for both fixed base and base isolator. Figures 16,17 and 18 represent the capacity curve along X direction for G+5, G+15 and G+25 storey buildings, respectively with and without base isolators. It can be seen that the ductility capacity of the base isolated structure has been improved especially in medium and high-rise structures. This behaviour may be due to the flexibility contribution by base isolator.

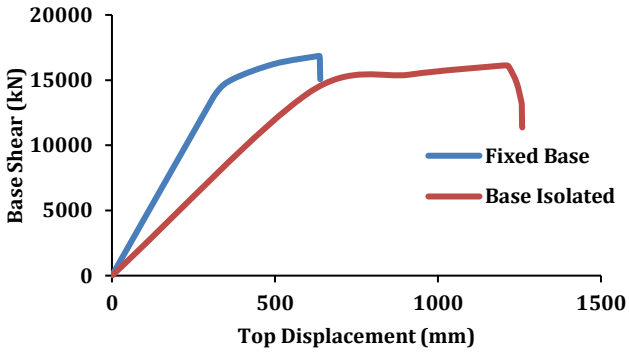

Fig. 18 Capacity Curve for G+5

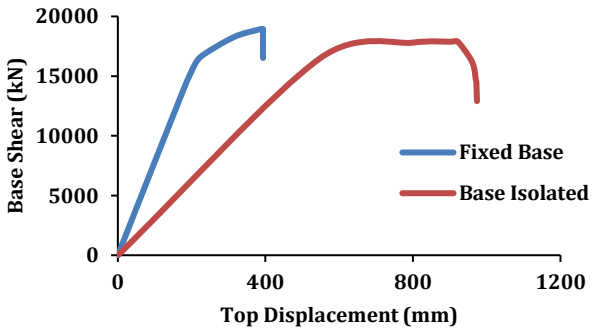

Fig. 17 Capacity Curve for G+15

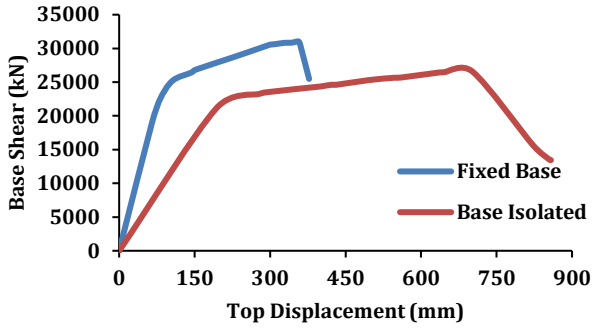

Fig.16 Capacity Curve for G+25

Hinge formation represents the performance level of the structure such as immediate occupancy, life safety and collapse prevention. Details of hinge formation for last step are shown in Table 9. It is observed that no hinges are formed in the buildings with base isolators beyond LS level and this type of behaviour is required and expected for seismic resistant structures. In G+5 storey FB building model, 81% , 16 % and 3 % of total hinges were formed in A-IO, IO-LS and beyond CP damage levels, respectively; whereas in G+5 storey BI building model 85% and 15 % of total hinges were formed in A-IO and IO-LS damage levels, respectively. In G+15 and G+25 storey BI building models, 100 % of total hinges were formed within A-IO level and, in G+15 and G+25 storey FB building models a few hinges were observed in beyond CP level. Hinge formation analysis shows that the base isolation is very effective in G+15-BI and G+25-BI building models when IO level is considered for design. However, when LS is considered for design, base isolation is effective in all the three models under study.

Table 9. Details of hinge formation

	A-IO	IO-LS	LS-CP	>CP	Total
G+5-FB	2984	576	0	112	3672
G+5-BI	3320	576	0	0	3896
G+15-FB	9776	0	0	16	9792
G+15-BI	10016	0	0	0	10016
G+25-FB	15910	0	0	2	15912
G+25-BI	16136	0	0	0	16136

From the above table it is very clear that number of hinges were limited within immediate occupancy for structure with base isolator whereas structure without base isolator exceeds collapse prevention. Typical hinge formation in G+5 is shown in Figure19 and Figure20 for with and without base isolator.

The displacement ductility factor is one of the key outputs of the pushover analysis. Higher the ductility factor higher the capacity of the structure. Table 10 represents the displacement ductility factor for G+5, G+15 and G+25. It can be seen that the ductility factor is very much improved in the G+15 and G+25 buildings with base isolator.

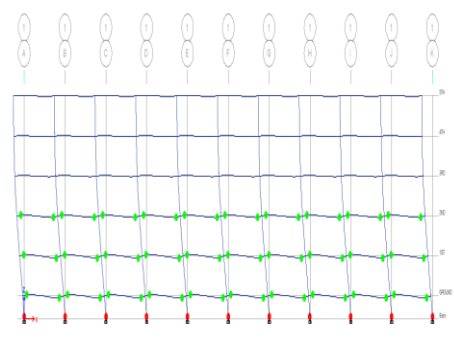

Fig. 19Hinge formation in fixed base

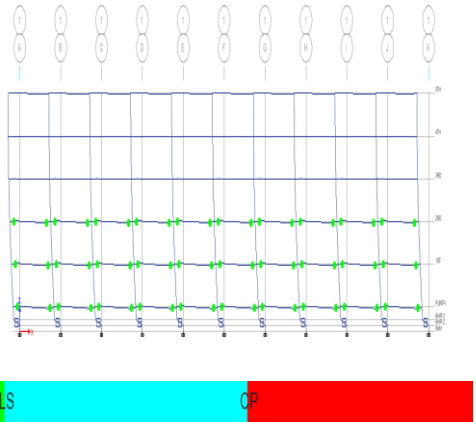

Fig. 20 Hinge formation in base isolator

Table 10. Displacement ductility factor

	G+5		G+15		G+25	
	FB	BI	FB	BI	FB	BI
Ultimate displacement (mm)	377	858	394	12910	639	11384
Yield displacement (mm)	106	193	209	548	320	605
Displacement ductility factor	3.6	4.4	1.9	23.6	1.99	18.8
Ductility improvement	0.8		21.7		18.8	

6. Conclusion

In this paper, performance analysis of lead rubber bearing isolation system for low, medium and high- rise RC buildings using response spectrum analysis and pushover analysis was performed. For understanding the performance of lead rubber bearing, parameters used were, fundamental time period, base shear, first storey displacement and inert-storey drift ratio from response spectrum analysis. Capacity curves and hinge formation were plotted from pushover analysis to study the parameters such as shear capacity and displacement ductility factor. As there is no Indian code describing the design procedures for base isolators, in this project ASCE-7-16 procedure was modified according to Indian standards and done the analysis and following were concluded.

- In base isolation, modal periods are increased more than 40% in G+5, G+15 and G+25 structures, increasing the building's reaction time during earthquake. For G+5 modal period got increased by 65%, G+15 it got increased by 46% and finally G+25 modal period increased by 51%.
- From the response spectrum analysis results, there is a significant reduction in the base shear after incorporating base isolation in the buildings in the order of 1.45 to 4.75 times. Therefore, it is very clear that use of base isolation has a large influence which is very efficient in earthquake prone areas.
- The inter-storey drift ratio of the buildings is significantly reduced, nearly 2 to 5 times after the installation of base isolation device.

- Pushover analysis was done to understand the efficacy of all the three models and concluded that model with base isolation showed a large percentage increase in yield displacement and ductility ratio compared to model without base isolation. It can be seen that the ductility factor is improved significantly in the medium and high-rise buildings with base isolator (nearly 19 to 22 times).
- It is observed that no hinges are formed in the buildings with base isolators beyond life safety level and this type of behavior is required and expected for seismic resistant structures. Hinge formation analysis shows that the base isolation is very effective in G+15-BI and G+25-BI building models when immediate occupancy level is considered for design. However, when life safety is considered for design, base isolation is effective in all the three models under study.
- Performance of lead rubber bearing of G+5, G+15 and G+25 was also understood after the analysis. All three models showed same level of performance with isolators. But still for more safety it is suggested that if storey height is more than G+15 and the location is very prone to earthquake other technologies such as shear wall and dampers can also be added.
- It is concluded that using lead rubber bearing as a base isolation system improves structural stability and protects the building from adverse effects of lateral loads due to earthquakes.

References

[1] Ryan KL, Kelly JM, Chopra AK. "Nonlinear model for lead rubber bearings including axial load effects. Journal of Engineering mechanics, 2005; 131: 1270-1278. https://doi.org/10.1061/(ASCE)0733-9399(2005)131:12(1270)

[2] Warn GP, Whittaker AS, Constantinou MC. Vertical Stiffness of Elastomeric and Lead-Rubber Seismic Isolation Bearings. Journal of Engineering mechanics, 2007; 133: 1227-1236. https://doi.org/10.1061/(ASCE)0733-9445(2007)133:9(1227)

[3] Sharbatdar MK, Hoseini Vaez SR, Amiri GG, Naderpour H. Seismic Response of Base-Isolated Structures with LRB and FPS under near Fault Ground Motions. Procedia Engineering, 2011; 14: 3245-3251. https://doi.org/10.1016/j.proeng.2011.07.410

[4] ASCE/SEI 7-16, Chapter 17, pp167-180.

[5] Choun YS, Park J, Choi IK. Effects of mechanical property variability in lead rubber bearings on the response of seismic isolation system for different ground motions. Nuclear Engineering and Technology, 2014; 46: 605-618. https://doi.org/10.5516/NET.09.2014.718

[6] Cancellara D, De Angelis F. Assessment and dynamic nonlinear analysis of different base isolation systems for a multi-storey RC building irregular in plan. Computers and Structures, 2016: 180; 74-88. https://doi.org/10.1016/j.compstruc.2016.02.012

[7] Tolani S, Sharma A. Effectiveness of Base Isolation Technique and Influence of Isolator Characteristics on Response of a Base Isolated Building. American Journal of Engineering Research, 2016: 5; 198-206.

[8] Mazza F, Mazza M, Vulcano A. Base-isolation systems for the seismic retrofitting of r.c. framed buildings with soft-storey subjected to near-fault earthquakes. Soil Dynamics and Earthquake Engineering, 2018: 109; pp209-221. https://doi.org/10.1016/j.soildyn.2018.02.025

[9] Rofooeia FR, Mirjalilib MR. Dynamic-based pushover analysis for one-way plan asymmetric buildings. Engineering Structures, 2018: 163; pp332-346. https://doi.org/10.1016/j.engstruct.2018.02.052

[10] Shoaei P, Orimi HT, Zahraic, SM Seismic reliability-based design of inelastic base-isolated structures with lead-rubber bearing systems. Soil Dynamics and Earthquake Engineering, 2018: 115; pp589-605. https://doi.org/10.1016/j.soildyn.2018.09.033

[11] Eem SS, Hahm D. Large strain nonlinear model of lead rubber bearings for beyond design basis earthquakes. Nuclear Engineering and Technology, 2018: 51; 600-606. https://doi.org/10.1016/j.net.2018.11.001
[12] Kitayama S, Constantinou MC. Collapse performance of seismically isolated buildings designed by the procedures of ASCE/SEI 7. Engineering Structures, 2018: 164; 243-258. https://doi.org/10.1016/j.engstruct.2018.03.008
[13] Habieb AB, Valente M, Milani G. Effectiveness of different base isolation systems for seismic protection: Numerical insights into an existing masonry bell tower. Soil Dynamics and Earthquake Engineering, 2019: 125;. https://doi.org/10.1016/j.soildyn.2019.105752
[14] De Luca A, Guidi LG. State of art in the worldwide evolution of base isolation design. Soil Dynamics and Earthquake Engineering, 2019: 125;. https://doi.org/10.1016/j.soildyn.2019.105722
[15] Ghasemi M, Talaeitaba SB. On the effect of seismic base isolation on seismic design requirements of RC structures. Structures, 2020: 28; 2244-2259. https://doi.org/10.1016/j.istruc.2020.09.063
[16] Li F, Wang L, Wu Y. Seismic response reduction analysis of large chassis base-isolated structure under long-period ground motions. Earthquake Research Advances, 2021: 1;. https://doi.org/10.1016/j.eqrea.2021.100026
[17] Jara JM, Hernandez EJ, Olmos BA. Effect of epicentral distance on the applicability of base isolation and energy dissipation systems to improve seismic behavior of RC buildings. Engineering Structures, 2021: 230; https://doi.org/10.1016/j.engstruct.2020.111727
[18] Shang J, Tan P, Zhang Y, Han J, Mi P. Seismic isolation design of structure using variable friction pendulum bearings. Soil Dynamics and Earthquake Engineering, 2021: 148;. https://doi.org/10.1016/j.soildyn.2021.106855
[19] Talaeitaba SB, Safaie M, Zamani R. Development and application of a new base isolation system in low-rise buildings. Structures, 2021: 34; 1684-1709. https://doi.org/10.1016/j.istruc.2021.07.077
[20] Liu Y, Kuang JS, Huang Q. Extended spectrum-based pushover analysis for predicting earthquake induced forces in tall buildings. Engineering Structures, 2018: 167; pp351-362. https://doi.org/10.1016/j.engstruct.2018.04.045
[21] Peng Y, Ma Y, Huang T, De Domenico D. Reliability-based design optimization of adaptive sliding base isolation system for improving seismic performance of structures. Reliability Engineering and System Safety, 2021: 205;. https://doi.org/10.1016/j.ress.2020.107167

Research on Engineering Structures & Materials
journal homepage: http://www.jresm.org
MIM Research Group

Research Article

An experimental study on composite steel encased portal frame under cyclic loading

Sheeba Ebenezer J[1,a], Tensing D[2,b], Vincent Sam Jebadurai S[2,c]

[1]*Department of Civil Engineering Salalah College of Technology, UTAS, Salalah, Sultanate of Oman.*
[2]*Department of Civil Engineering, Karunya Institute of Technology and Sciences, Coimbatore, India.*

Article Info

Article history:

Received 08 Apr 2022
Revised 27 Jun 2022
Accepted 01 Jul 2022

Keywords:

Steel encased portal frame; Shear connectors; Yield strength; Ductility; Ultimate load

Abstract

This research paper discusses the study on steel encased portal frame, which utilizes the shear connectors within the specimen to enhance ductility and ultimate load carrying capacity. Shear connectors can significantly boost the specimen's overall strength and load bearing capability. To investigate this behaviour, cyclic static load test on one bare frame and three portal frames were conducted. The specimens have shear connector of spacing variation as 75mm, 100mm and 125mm which were tested at the rate of ±0.1 tonne per cycle. It has been noticed that when shear connector spacing reduces, the ultimate load bearing capacity improves. These tests enabled a detailed analysis through experimental process of failure, hysteresis curve plot, for all the three portal frames. In hysteresis curve, no pinching effect was found whereas yield strength was found to be increased.

1. Introduction

Compressive strength and stiffness of concrete members are greater, and tensile strength and ductility of steel members are greater. When steel and concrete components are combined as composite members, the favourable qualities of both materials are realized. Concrete filled tubular (CFT) members offer advantages such as enhanced axial load capacity, increased ductility efficiency, increased energy absorption capacity, and less strength degradation.

The hollow steel section and the core concrete work together to make the CFT members stronger. The steel tube supports the load, acts as reinforcement and keeps the concrete core inside. The concrete core adds strength to steel tube and stops the steel tube from buckling inward. Typically, vertical loads are transmitted from the steel tube to the core concrete by means of a bond between the steel tube and the concrete. In the last few decades, numerous studies have been undertaken to study the bond strength between the steel tube and concrete in CFST (Concrete Filled Steel Tube) columns. Roeder et al. [1] conducted push-out tests on circular CFST columns, where the in-filled concrete was of moderate shrinkage or little shrinkage. The test findings demonstrated that the shrinkage of the concrete had a negative impact on the bonding in the CFST columns. Chang et al. [2] tested the bond behaviour in CFST columns with expansive concrete. The results demonstrated that expansive concrete enhanced the short-term bond strength of CFST columns.

To provide the dependable transmission of the vertical load at beam-column joints, shear connectors are often placed to the inner wall of the steel tube to ensure the performance of the steel tube and concrete. Among the various forms of shear connectors, the shear

*Corresponding author: vincent@karunya.edu
[a] orcid.org/0000-0001-8908-3671; [b] orcid.org/0000-0001-7806-001X; [c] orcid.org/0000-0002-9820-8103
DOI: http://dx.doi.org/10.17515/resm2022.426ie0408

studs are widely used as the shear connectors. Shakir-Khalil [3] carried out a series of push-out tests with different types of shear connector, and the results suggested that the ultimate push-out load was a function of the interface type, cross-section shape and size, which led to a better understanding of the load transfer mechanism in beam-column connections in composite construction. Li An et al. [4] presented push-out tests of studs in normal and high strength concretes. The results demonstrated that the compressive strength of the concrete had a substantial impact on the strength of the stud connections. Pil-Goo Lee and Chang-Su Shim [5,6] investigated the static and fatigue behaviours of large shear studs up to 30 mm diameter, which were beyond the limits of the current design codes. Weichen Xue [7] conducted push-out tests on the shear studs in order to investigate the factors that affect stud behaviour. The mechanism of shear studs was investigated, a new description of the stud load-slip relationship was presented, and a model for determining the shear stud bearing capacity was established.

Because CFT is so important, it has been the subject of a lot of research for a while now.

Beam column junction is the most important part of a reinforced concrete frame. It is subjected to extreme of stress when the ground shakes a lot. This has a direct effect on the structure. Shear connectors must be added to the CFT in order for the structure to perform well. The spacing of shear connectors was adjusted during this study, and the differences in the findings for the same load increments were observed and compared experimentally for each specimen.

2. Research Background

Various ways for resisting seismic load have been investigated throughout the years in terms of materials, geometry, and design. In recent years, a new branch has been noted to have piqued the interest of numerous researchers, which is "Concrete filled steel tubes." Within this category, testing with shear studs has showed a lot of promise in terms of load carrying capacity and ductility.

Study was carried out by Yang Wen [8], Lai-Yun [9], Matsui C [10], Ben Mou [11], Shuaike Feng[12] regarding analysis of Seismic Behaviour of CFRST (Concrete Filled Rectangular Steel Tube) Beam and Column Joints. According to the research, CFRST beam and column joints exposed to minor cycle reversal loads have plump hysteretic loops, increasing strength and stiffness degeneration, and high stiffness. After the joints achieved the ultimate load, significant ductility and subsequent deformation capability were detected, indicating that the joints met the seismic design criteria.

Jingbo Liu [13], Liu Y B [14], Seyed Rasoul [15] presented the theoretical effect of the column-to-beam strength ratio and axial compression ratio on the failure mechanism of concrete-filled square steel tube frame structures. The researchers looked at multi-storey composite bay frames with varied column-to-beam strength ratios and axial compression ratios. For the strong column-weak beam failure, solutions for acceptable column-to-beam strength ratio values with varying column axial compression ratios were established.

Faxing Ding [16], Aslani, F [17], Ellobody, E [18] , Jingfeng Wang [19], Qi-shiZhou[20] investigated about CFST (Concrete Filled Steel Tube) column to steel-concrete composite beam under lateral cyclic loading. In Single storey one-bay in-plane frames the seismic performance was investigated using some parameters like the slenderness ratio. These composite frames were found to perform well during earthquake.

Kun Wang [21], L. Fang, B. Zhang [22], K. Wang [23], K. Wang [24] analysed the Theoretical study of the hysteretic actions of prestressed composite joints with CFST. Lateral cyclic loading was applied to pre-stressed and unstressed composite specimens. Shear failure within the panel zone and flexural failure at the beam ends were seen in pre-stressed joint

specimens; only flexural failure at the beam ends was observed in non-stressed joint specimens. Specimens exhibited typical hysteretic behaviour after testing.

Studies were carried out by Toshiaki Fujimoto[25], Gia Toai Truong[26], Jiansheng Fan [27], A.Niroomandi [28] on seismic behaviour of SRC columns and beam-column junctions in Composite Structural Systems. It was discovered that CES columns and beam-column junctions perform better seismically than SRC columns.

Nader Fanaie [29], Bin Wang [30], Xian Li [31] conducted experiments to learn more about the behaviour of a rigid connection between a steel beam and a CFT column with external T stiffeners. Concentrated stress at the place where the stiffener groove welds to the beam flange and column web leads in an unexpected brittle failure, hence reducing the connection's ductility.

Vijayalakshmi, D.D [32], Hallam [33], Fanaie, N [34], Yong Fang[35], Yansheng Du[36], Xianggang Liu[37], Jiepeng Liu[38], Faesal Alatshan[39], Xuetao Lyu[40], Fang Yuan[41] conducted experimental study on confined column behaviour under axial load. It was done to learn about the distribution of shear connectors in thin-walled short Concrete Filled Steel Tube (CFST) columns and found that smaller the gap between shear connectors, the greater the CFST efficiency.

Studies were carried out by John Francis. K [42], Ahmed Elremaily [43], Dalin Liu a [44], Georgios Giakoumelis [45], Sherif M [46] on Confined column behaviour under axial load. The link between shear connector distribution and the action of thin-walled, short Concrete Filled Steel Tube (CFST) columns was researched, and it was revealed that the closer the shear connectors are, the more efficient the CFST.

Hsuan-Teh Hu [47], Zhi-Liang Zuo [48], Qiyun Qiao[49], Yanlei Wang[50], Morteza Naghipour[51], Yanlei Wang[52], S.Seangatith[53], Bin Wang[54], BaochunChen[55] conducted experimental study on the columns of CFT exposed to an axial compressive force and bending moment. Using the nonlinear finite element program ABAQUS, researchers compared CFT columns with varying cross sections to experimental data. The square CFST column has less confining effect than circular CFST columns, however square CFST columns stiffened with reinforcing ties give the same confining effect as circular CFST columns.

Young-chan Kim[56] , Hollow Steel Section (HSS) and Concrete-Filled Steel Tube (CFST) sections were utilised in the simulation process, and it was discovered that the HSS system is vulnerable to damage even when seismic protection measures are taken into account.

Qian Wang[57] demonstrated that the shear resistance and shear stiffness of large-diameter, high-strength studs are greater than those of conventional stud connectors. Nadiah Loqman[58], The purpose of this paper is to examine the applicability and efficiency of composite beams with precast concrete slabs and bolted shear connectors by analysing the structural behaviour of composite beam systems, such as their strength, stiffness, slip behaviour, failure mode, and sustainability, as determined by experiment and numerical studies. K.Sathish Kumar[59], the general behaviour of composite beams with shear connectors under bending, the influence of a variety of significant characteristics was investigated. Rahul Tarachand Pardeshi[60], review of several types of shear connectors, their uniqueness and characteristics, testing techniques, and conclusions from the last decade were studied. The literature, effectiveness, and applicability of the various types of shear connectors, such as headed studs, perfobond ribs, fibre-reinforced polymer perfobonds, channels, pipes, Hilti X-HVB, composite dowels, demountable bolted shear connectors, and shear connectors in composite columns, are investigated in depth. Raj[61], the efficient and economical use of shear connectors in Steel-Concrete composite sections is examined.

Despite the fact that this research involves a progressive trend, it has mostly concentrated on steel encased columns and steel encased beams. Many researchers proved that the members with steel enclosed columns and steel encased beams successfully enhance the ultimate load bearing capacity and ductility when compared to typical RCC. There has been very little experimental work on steel enclosed column and beam frames, and little theoretical research has been done. Because it is well known that the 'Beam Column junction' is the most essential component of the structure and is very certain to break during seismic loading, this research study was experimentally focused on the combined effect of steel encased column and beam.

3. Materials and Methods

3.1. Material Properties

The concrete with load carrying capacity of 25MPa was made in accordance to IS456:2000 and IS10262:2009 where the slump of concrete was kept to be 200mm for the ease of flow in the mould. The mild steel rods as shear connectors were of 6mm diameter and 150mm length, having 7850kg/m3 density and yield strength of 250N/mm2 were used. These rods increased the shearing capacity of the frame by connecting the concrete and the steel tube. The Galvanised Iron steel plate of 1.2mm thickness with various lengths was used. This plate provided the confinement to the concrete infill, which resulted in increase in load carrying capacity.

The shear connectors shall be spaced so as to transmit shear and to prevent separation between the concrete and the steel, considering an appropriate distribution of design shear force. The advantages of shear studs over other forms of connectors are that the welding process is quick and simple permit more satisfactory compaction of the concrete around the connectors, and provide equal shear strength in all directions. Shear connectors must be designed to provide static strength, and for fatigue loading.

Grade designation	M25 concrete
Type of cement	OPC 53 grade
Maximum Nominal size of aggregate	20mm
Minimum cement content	300kg/m^3 (As per IS456 Table 5 page 20)
Maximum water cement ratio	0.50
Workability	75- 100mm
Specific gravity of cement	3.15
Specific gravity of Coarse aggregate	2.74
Specific gravity of Fine aggregate	2.68 (M sand)
Mild steel rods as shear connectors	6mm diameter and 150mm length
Density	7850kg/m^3
Yield strength	250N/mm^2
Galvanized Iron steel plate	1.2mm thickness
Density	7800kg/m^3
Yield strength	250N/mm^2

3.2. Test Specimen

A series of 3 portal frames sections were filled with concrete and were given static cyclic loading to observe the behaviour of frames. All the 3 frames had the height of 1.1m and width of 1.15m with the sectional area of 150mm x 150mm (Fig 1). Concrete of the grade M25 was filled within the hollow frame and the open faces were cured for 28 days.

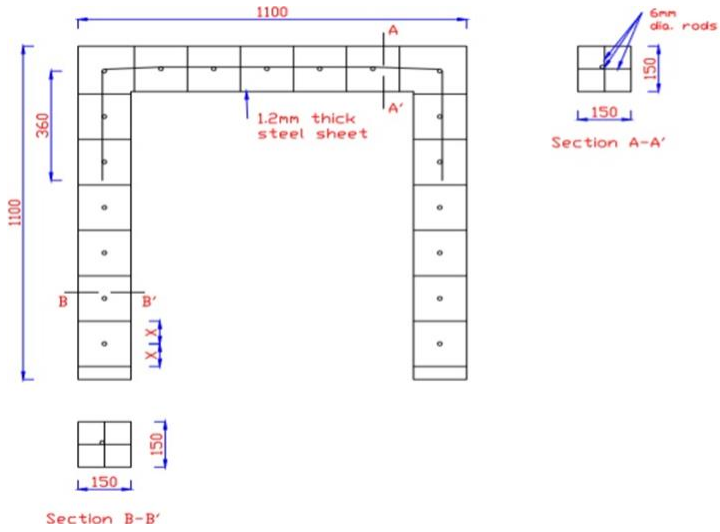

Fig 1. General Schematic Diagram of portal frame (all units in mm)

All the steel used for this research was GI sheet. The steel plate was 1.2mm thick; this as done to reduce the percentage of steel used and makes the specimen as "Thin walled structure". Fig 1 shows the general geometry of all the three specimens.

The parameters selected to research were the spacing and number of shear connectors in the portal frame and the others such as size of beam, beam width, height of column, column size, shell thickness; steel rod section and qualities of concrete were kept unchanged throughout the research. The portal frames were named as SP-75, SP-100 & SP-125. SP-75 had the shear connector spacing of 75mm, SP-100 had the shear connector spacing of 100mm & SP-125 had the shear connector spacing of 125mm. These shear connectors were welded inside the frame section such that they connected two opposite faces of the square section.

The steel casing was made into a C-shape first such that one faces of the specimen is open; this was done for the ease to weld the internal shear rods, once the shear rods were welded in place, a rod was placed in the beam with development length of it going into the columns. Then the open face was closed by welding a steel plate. This steel plate was also connected with inner shear rods via welding as well. The steel plate was welded fully along the edges to ensure maximum strength as well as to avoid concrete slurry spillage while filling. Once the steel mould was ready, a high workability M25 concrete was poured from the column openings into the steel encasement. The maximum aggregate size was 12mm; this size was used to avoid blocking of the concrete due to aggregates getting stuck in spaces.

The specimen was kept upside down and the concrete was poured and the casing was tilted and manually shaken to help the concrete to compact properly along with regular tamping with a 16mm rod.

Fig 2 and Fig 3 shows the reinforcement details of raft footing which is connected to the concrete filled steel tube (CFST) frame.

3.3. Experimental Test Setup

The necessary specimens were named and arranged with a spacing of 5 cm prior to testing. All specimens were tested with the help of removable base under fixed support conditions on both sides, i.e. front and back.

Fig 2. Welded shear connectors

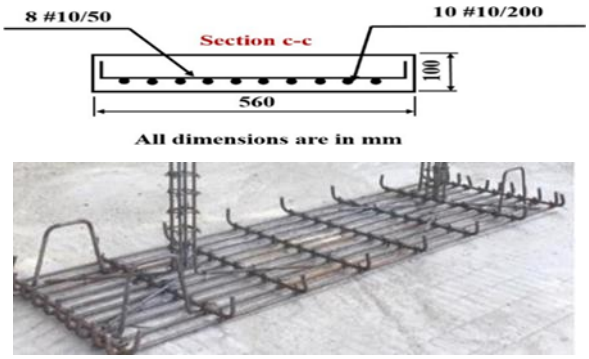

Fig. 3 Reinforcement details of raft footing

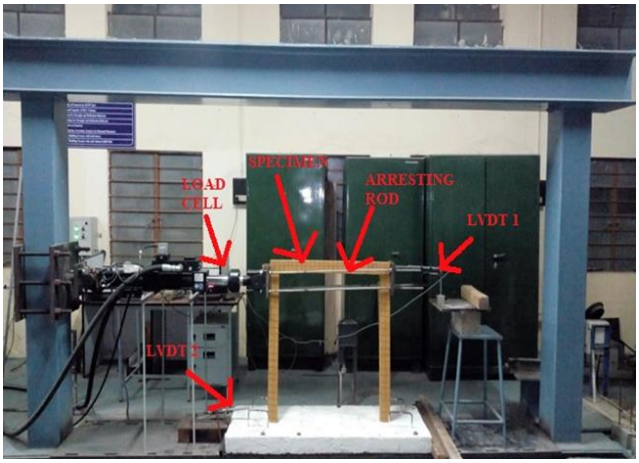

Fig. 4 General Test Setup

All the specimens were tested under a cyclic loading frame of 50T capacity (Fig. 4) to observe their behaviour under static cyclic loading. The load was applied at the beam column joint via a hydraulic jack coupled with a load cell to observe the deflection. The load was applied at the rate of ±0.1 tonne per cycle. With loading gap of 1kN, 3 cycles of loading were applied for each loading resulting in 10 cycles of loading per specimen. Simultaneously, two LVDTs were fixed on the specimen, of which one was fixed at the middle of the top edge (LVDT 1) and one was fixed at the centre of the column (LVDT 2).

These were used to note the corresponding deflections for each load. Out of these two LVDTs, only the readings from LVDT-1 were taken and LVDT-2 was used only as a control. 3.3.2. Specimen Specification. A total of 3 specimens and bare frame specimen were cast and subsequently tested.

Table 1. Specimen Specification

Spacing of studs	Specimen ID	No. of Specimens
	Bare frame	1
75mm	SP-75	1
100mm	SP-100	1
25mm	SP-125	1

4. Results and Discussions

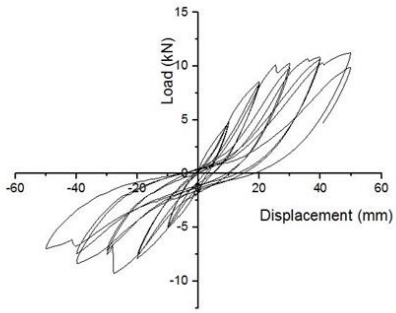

(a) Bare frame hysteresis curve

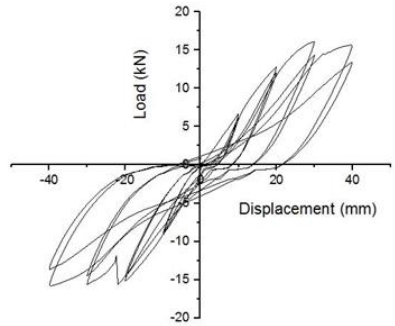

(b) SP-75 hysteresis curve

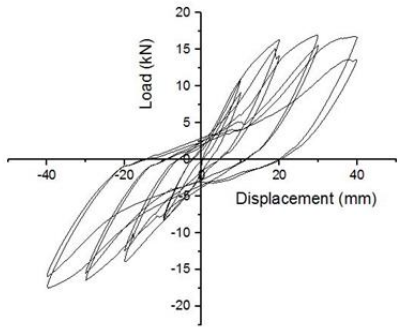

(c) SP-100 hysteresis curve

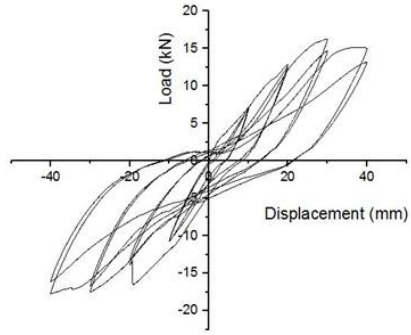

(d) SP-125 hysteresis curve

Fig. 5 Hysteresis Curves

Figure 5 depicts the lateral load-displacement hysteretic curves for all specimens. Throughout the early period, the hysteretic curves followed a straight line, indicating the specimens were in a state of elastic deformation. After yielding, the regions of the hysteretic loops started rising gradually, likely to result in plump forms, and a few residual deformations were noticed after unloading; after the peak value was achieved, the lateral loads decreased dramatically as the lateral displacements increased, demonstrating high ductility. Overall, all specimens performed well since the hysteretic curves were plump and there was no substantial pinching.

Table 2. Load – Deflection observed values

Spacing of studs	Assigned Name	Maximum observed Load (kN)	Load increase in % compared to bare frame	Maximum observed Deflection (mm)	Deflection decreases in % compared to bare frame
	Bare frame	11	-	46.67	-
75mm	SP-75	15	36.36	35.02	24.96
100mm	SP-100	14	27.27	28	40
125mm	SP-125	13	18.18	38.99	16.45

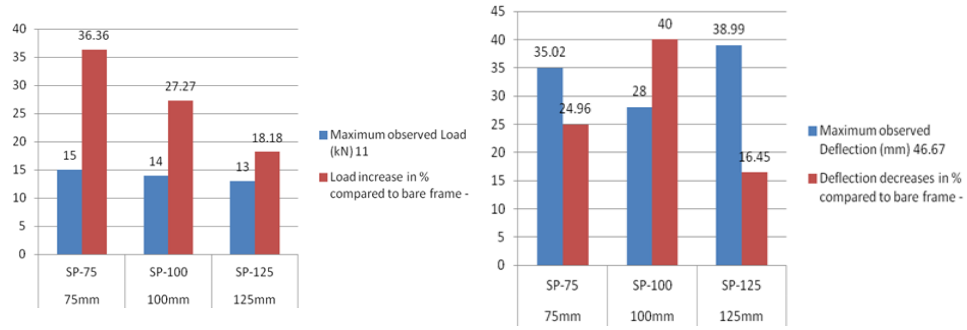

(a) (b)

Fig. 6 (a) Maximum Load and percentage increment (b) Maximum Deflection and percentage decrement

From Table 2, the load-carrying capacities of the three specimens' viz., SP-75, SP-100 and SP-125 were comparatively more than the bare frame compared with displacement. The maximum load-carrying capacity observed in SP-75 was 15 kN. SP-75 outperformed the bare frame by 36.36 percent in load-carrying capacity. Similarly, when compared to the bare frame, the SP-100 and SP-125 improved by 27.27 percent and 18.18 percent, respectively. Fig 6 (a) shows the maximum observed load and load increase in % compared to bare frame and Fig 6 (b) shows the maximum observed deflection and deflection decreases in % compared to bare frame. According to BS 8110 total deflection is Span/250 with limiting span/depth ratio. Further, the deflection occurs after constructing the finishes and partitions is Span/500 or 20mm, whichever is lesser.

Eurocode 2 also limits the deflection to Span/250 and span over effective depth ratio is used to check the limits. The method of calculation is little different from the BS 8110 Part 1. Further, it also limits the deflection that occurs due to the construction of finishes and partitions to Span/500. Eurocode 2 does not provide a table as BS 8110 Part 1, but it provides equations and charts to check the deflections.

Table 3. Area under the curve

Spacing of studs	Assigned Name	Area Under the Curve (mm^2)
-	Bare frame	428.47
75mm	SP-75	532.14
100mm	SP-100	775.91
125mm	SP-125	727.88

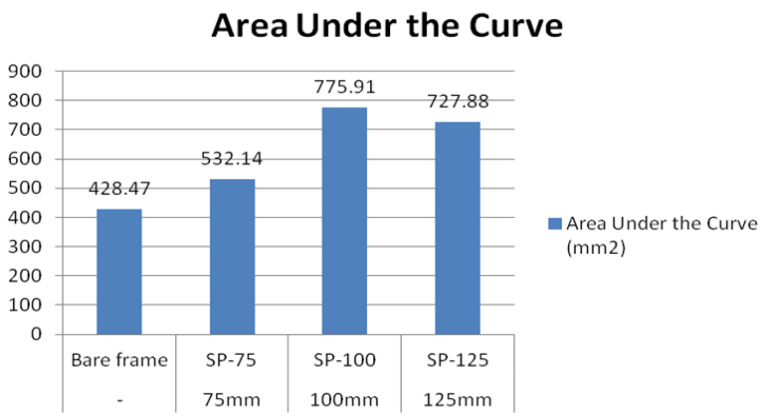

Fig. 7 Area under the curve

One of the most essential criteria for estimating the seismic behavior of specimens is their energy dissipation capability. Because of the development of the plastic hinges, the energy dissipation capacity of specimens SP-100 and SP-125 was clearly greater than the others after yielding. However, according to table 3 and figure 6, the energy dissipation capacity for bare frame and SP-75 was lower.7

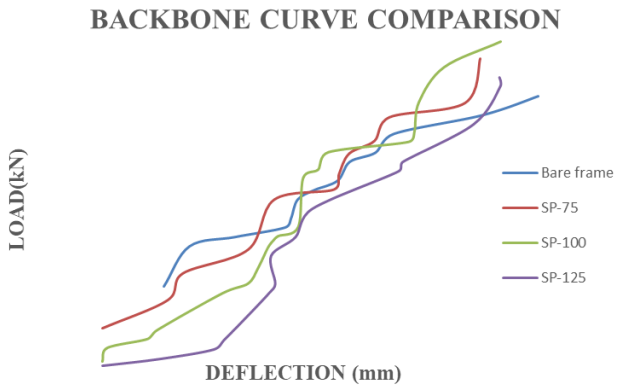

Fig. 8 Comparison of backbone curves of bare frame, SP-75, SP-100 & SP-125

Backbone curves are used to reflect the significance of lateral load and ductility properties. It demonstrates that lateral loads have improved and ductility has improved. In the above Fig 8 with regard to the negative loads we are able to observe that, the area under each curve is in ascending order, which confirms the actual fact that lesser shear connector spacing increases the ductility of the specimen. Thus it can even be said that with increase in shear connector spacing the specimen gets more brittle. It can be concluded the shear connector spacing of 75mm takes more load with considerably more deflection. As a result, it's clear that as the gap between shear connectors shrinks, the ultimate load bearing capacity increases.

4.1 Failure Mode

Specimen bare frame has crushing of concrete on the surface as shown in Figure 9 (a). As shown in Figure 9 (a), the crushing of concrete is mainly concentrated in the corner of the specimen. In Figure 9 (b), for specimen SP-75 cracks are observed at the beam and column

joint, which are highlighted in the red circle. In Figure 9 (c), for specimen SP-100 the area inside the red circle is the slippage occurred in beam-column joint after the test. In Figure 9 (d), for specimen SP-125, crack occurred below beam-column joint. After the completion of all the tests, the steel tube has been cut open so as to observe the side of the core concrete. From the observation, there is significant shear failure in the concrete, while there are no significant damages to the rest of the concrete. Usually, for the shear connectors inside a CFST tube, there is shear failure of the concrete or the shear failure of the shear connector.

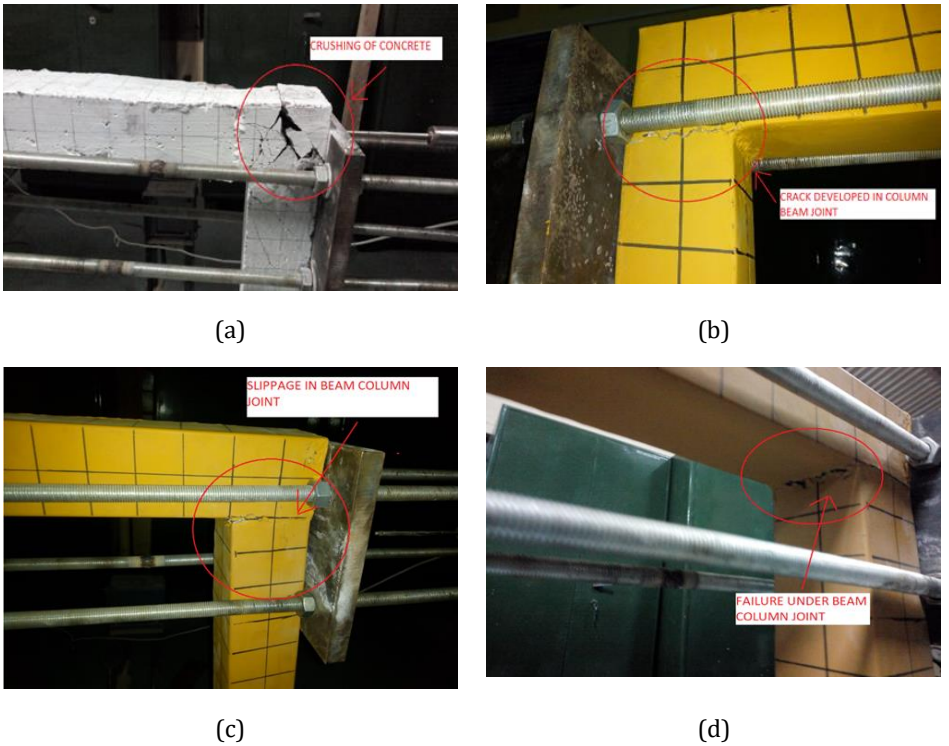

(a) (b)

(c) (d)

Fig. 9 (a) Failure of bare frame, (b) Failure of SP-75 (c) Failure of SP-100 (d) Failure of SP-125

5. Conclusions

Composite frames made of steel tubular reinforced concrete columns and beams showed high ductility. As the spacing between shear connectors reduces, the ultimate load bearing capacity improves owing to the increased confinement effect and the improvement in ductility is evidenced by the presence of a broad plateau in the load deflection curves obtained for specimens with varying spacing's of shear studs. No pinching effect is observed in any of the hysteresis loop, which is attributed to the effective confinement attained due to steel encasement. The member takes load even after the concrete inside is crushed which could be observed from the load cells and LVDTs. The encasement avoids the spalling of the concrete, which can increase the safety for the people who are evacuating. It is speculated that the ultimate load carrying capacity increases due to the confinement effect of the steel.

In the Figure 8, with regard to the negative loads it can be clearly observed that, the area under each curve is in ascending order, which confirms the actual fact that lesser shear connector spacing increases the ductility of the specimen. Thus it can even be said that with increase in shear connector spacing the specimen gets more brittle. It can be concluded the shear connector spacing of 75mm takes more load with considerably more deflection. As the spacing of shear connectors decreases, the ultimate load carrying capacity increases due to the enhancement in confinement effect. As the spacing of shear connectors decreases, the ductility increases which is evident from the large plateau in the load deflection curves obtained for the specimens with different spacing of shear studs. Steel welds should be avoided near the beam column joints.

Later this study will be done analytically using software and also experimentally with other specimen sample and the comparative study will be done.

From previous literature work it is observed that, behaviour of CFST (Concrete Filled Steel Tube) frame structure is needed to be considered for study. Therefore, in this research, to attain strength against seismic load and economy in construction, uses of CFST (Concrete Filled Steel Tube) frames were studied.

References

[1] Roeder CW, Cameron B, Brown CB. 1999. Composite action in concrete filled tubes. Journal of structural engineering, 125(5), pp.477-484. https://doi.org/10.1061/(ASCE)0733-9445(1999)125:5(477)

[2] Xu C, Chengkui H, Decheng J, Yuancheng S. Push-out test of pre-stressing concrete filled circular steel tube columns by means of expansive cement. Construction and building materials, 23(1), pp.491-497, 2009. https://doi.org/10.1016/j.conbuildmat.2007.10.021

[3] Shakir-Khalil H. Pushout strength of concrete-filled steel hollow section tubes. Structural Engineer. 1993 Jul 6;71(13).

[4] An L, Cederwall K. Push-out tests on studs in high strength and normal strength concrete. Journal of constructional steel research, 36(1), pp.15-29, 1996. https://doi.org/10.1016/0143-974X(94)00036-H

[5] Shim CS, Lee PG, Yoon TY. Static behavior of large stud shear connectors. Engineering structures. 2004 Oct 1;26(12):1853-60. https://doi.org/10.1016/j.engstruct.2004.07.011

[6] Pil-Goo L, Chang-Su S, Sung-Pil C. Static and fatigue behavior of large stud shear connectors for steel-concrete composite bridge. J. Constr. Steel Res. 2005;61:1270-85. https://doi.org/10.1016/j.jcsr.2005.01.007

[7] Xue W, Ding M, Wang H, Luo Z. Static behavior and theoretical model of stud shear connectors. Journal of bridge engineering. 2008 Nov;13(6):623-34. https://doi.org/10.1061/(ASCE)1084-0702(2008)13:6(623)

[8] Wen Y. Analysis of seismic behaviour of concrete-filled rectangular steel tubular beam and column joints based on performance. In2011 International Conference on Electric Technology and Civil Engineering (ICETCE) 2011 Apr 22 (pp. 1954-1957). IEEE.

[9] Wu LY, Chung LL, Tsai SF, Shen TJ, Huang GL. Seismic behavior of bolted beam-to-column connections for concrete filled steel tube. Journal of constructional steel research. 2005 Oct 1;61(10):1387-410. https://doi.org/10.1016/j.jcsr.2005.03.007

[10] Matsui C. Strength and behavior of frames with concrete filled square steel tubular columns under earthquake loading. InProceedings of the international specialty conference on concrete filled tubular structures 1985 Aug (pp. 104-111).

[11] Mou B, Liu X, Sun Z. Seismic behavior of a novel beam to reinforced concrete-filled steel tube column joint. Journal of Constructional Steel Research. 2021 Dec 1;187:106931. https://doi.org/10.1016/j.jcsr.2021.106931
[12] Feng S, Guan D, Guo Z, Liu Z, Li G, Gong C. Seismic performance of assembly joints between HSPC beams and concrete-encased CFST columns. Journal of Constructional Steel Research. 2021 May 1;180:106572. https://doi.org/10.1016/j.jcsr.2021.106572
[13] Liu JB, Li X. Realization of strong column-weak beam failure mode for concrete-filled square steel tubular frame structure. InAdvanced Materials Research 2012 (Vol. 446, pp. 424-428). Trans Tech Publications Ltd. https://doi.org/10.4028/scientific5/AMR.446-449.424
[14] Liu YB. Research on Seismic Performance and Fragility Analysis for Steel-Concrete Composite Structural Systems (Doctoral dissertation, PhD Dissertation, Tsinghua University, Beijing, 21-38.
[15] Mirghaderi SR, Mahmoudi B, Gharavi A, Dolatshahi KM, Epackachi S. Experimental investigation of moment resisting frames with perforated shear link. InStructures 2021 Aug 1 (Vol. 32, pp. 516-531). Elsevier. https://doi.org/10.1016/j.istruc.2021.03.060
[16] Ding FX, Yin GA, Jiang LZ, Bai Y. Composite frame of circular CFST column to steel-concrete composite beam under lateral cyclic loading. Thin-Walled Structures, 122, pp.137-146, 2018. https://doi.org/10.1016/j.tws.2017.10.022
[17] Aslani F, Uy B, Tao Z, Mashiri F. Behaviour and design of composite columns incorporating compact high-strength steel plates. Journal of Constructional Steel Research. 2015 Apr 1;107:94-110. https://doi.org/10.1016/j.jcsr.2015.01.005
[18] Ellobody E, Young B, Lam D. Behaviour of normal and high strength concrete-filled compact steel tube circular stub columns. Journal of Constructional Steel Research. 2006 Jul 1;62(7):706-15. https://doi.org/10.1016/j.jcsr.2005.11.002
[19] Wang J, Wang H. Cyclic experimental behavior of CFST column to steel beam frames with blind bolted connections. International Journal of Steel Structures. 2018 Sep;18(3):773-92. https://doi.org/10.1007/s13296-018-0089-8
[20] Zhou QS, Fu HW, Ding FX, Liu XM, Yu YJ, Wang LP, Yu ZW, Luo L. Seismic behavior of a new through-core connection between concrete-filled steel tubular column and composite beam. Journal of Constructional Steel Research. 2019 Apr 1;155:107-20. https://doi.org/10.1016/j.jcsr.2018.12.002
[21] Wang K, Luo H. Test on hysteretic behaviour of prestressed composite joints with concrete-encased CFST columns. Advances in Civil Engineering. 2019 Aug 14;2019. https://doi.org/10.1155/2019/4523045
[22] Fang L, Zhang B, Jin GF, Li KW, Wang ZL. Seismic behavior of concrete-encased steel cross-shaped columns. Journal of Constructional Steel Research. 2015 Jun 1;109:24-33. https://doi.org/10.1016/j.jcsr.2015.03.001
[23] Wang K, Lu XF, Yuan SF, Cao DF, Chen ZX. Analysis on hysteretic behavior of composite frames with concrete-encased CFST columns. Journal of Constructional Steel Research. 2017 Aug 1;135:176-86. https://doi.org/10.1016/j.jcsr.2017.03.011
[24] Wang K, Yuan SF, Chen ZX, Zhi HX, Shi GL, Cao DF. Experimental study on hysteretic behavior of composite frames with concrete-encased CFST columns. Journal of Constructional Steel Research. 2016 Aug 1;123:110-20. https://doi.org/10.1016/j.jcsr.2016.04.024
[25] Fujimoto T, Kuramoto H, Matsui T. Seismic performance of columns and beam-column joints in composite CES structural system. InProceeding of the 14th World Conference on Earthquake Engineering 2008.
[26] Truong GT, Dinh NH, Kim JC, Choi KK. Seismic performance of exterior RC beam-column joints retrofitted using various retrofit solutions. International Journal of Concrete Structures and Materials. 2017 Sep;11(3):415-33. https://doi.org/10.1007/s40069-017-0203-x

[27] Fan J, Li Q, Nie J, Zhou H. Experimental study on the seismic performance of 3D joints between concrete-filled square steel tubular columns and composite beams. Journal of Structural Engineering. 2014 Dec 1;140(12):04014094. https://doi.org/10.1061/(ASCE)ST.1943-541X.0001013
[28] Niroomandi A, Maheri A, Maheri MR, Mahini SS. Seismic performance of ordinary RC frames retrofitted at joints by FRP sheets. Engineering Structures. 2010 Aug 1;32(8):2326-36. https://doi.org/10.1016/j.engstruct.2010.04.008
[29] Fanaie N, Moghadam HS. Experimental study of rigid connection of drilled beam to CFT column with external stiffeners. Journal of Constructional Steel Research. 2019 Feb 1;153:209-21. https://doi.org/10.1016/j.jcsr.2018.10.016
[30] Wang B, Liang J, Lu Z. Experimental investigation on seismic behavior of square CFT columns with different shear stud layout. Journal of Constructional Steel Research. 2019 Feb 1;153:130-8. https://doi.org/10.1016/j.jcsr.2018.10.004
[31] Li X, Zhou T, Li J, Kuang XB, Zhao YW. Seismic behavior of encased CFT column base connections. Engineering Structures. 2019 Mar 1;182:363-78. https://doi.org/10.1016/j.engstruct.2018.12.076
[32] Vijayalekshmi DD, Tensing DD. An experimental study on steel concrete composite beams with shear connectors under pure torsion. International Journal of Emerging Technology and Advanced Engineering, ISO. 2014;9001(2008):202-9.
[33] Hallam MW. The behaviour of stud shear connectors under repeated loading. 1976 Aug.
[34] Fanaie N, Esfahani FG, Soroushnia S. Analytical study of composite beams with different arrangements of channel shear connectors. Steel Compos. Struct., Int. J. 2015 Aug 1;19(2):485-501. https://doi.org/10.12989/scs.2015.19.2.485
[35] Fang Y, Wang Y, Zhang B, Dong J. Behaviour of concrete-filled thin-walled corrugated steel tubes under cyclic axial compression. Thin-Walled Structures. 2021 May 1;162:107630. https://doi.org/10.1016/j.tws.2021.107630
[36] Du Y, Gao D, Chen Z, Zheng Z, Wang X. Behaviors of FRP confined rectangular concrete-filled thin-walled steel tubular stub columns using high-strength materials under axial load. Composite Structures. 2022 Jan 15;280:114915. https://doi.org/10.1016/j.compstruct.2021.114915
[37] Liu J, Yang Y, Liu J, Zhou X. Experimental investigation of special-shaped concrete-filled steel tubular column to steel beam connections under cyclic loading. Engineering Structures. 2017 Nov 15;151:68-84. https://doi.org/10.1016/j.engstruct.2017.07.021
[38] Liu X, Xu C, Liu J, Yang Y. Research on special-shaped concrete-filled steel tubular columns under axial compression. Journal of Constructional Steel Research. 2018 Aug 1;147:203-23. https://doi.org/10.1016/j.jcsr.2018.04.014
[39] Alatshan F, Osman SA, Hamid R, Mashiri F. Stiffened concrete-filled steel tubes: A systematic review. Thin-Walled Structures. 2020 Mar 1;148:106590. https://doi.org/10.1016/j.tws.2019.106590
[40] Lyu X, Xu Y, Xu Q, Yu Y. Axial compression performance of square thin walled concrete-Filled steel tube stub columns with reinforcement stiffener under constant high-Temperature. Materials. 2019 Apr 2;12(7):1098. https://doi.org/10.3390/ma12071098
[41] Yuan F, Huang H, Chen M. Effect of stiffeners on the eccentric compression behaviour of square concrete-filled steel tubular columns. Thin-Walled Structures. 2019 Feb 1;135:196-209. https://doi.org/10.1016/j.tws.2018.11.015
[42] John Francis. K, Tensing. D.Studies on behaviour of confined column under axial load. International Journal of Engineering Science Invention Research & Development; Vol. II Issue VI II 2016 February.
[43] Elremaily A, Azizinamini A. Behavior and strength of circular concrete-filled tube columns. Journal of Constructional Steel Research. 2002 Dec 1;58(12):1567-91. https://doi.org/10.1016/S0143-974X(02)00005-6

[44] Liu D, Gho WM, Yuan J. Ultimate capacity of high-strength rectangular concrete-filled steel hollow section stub columns. Journal of Constructional Steel Research. 2003 Dec 1;59(12):1499-515. https://doi.org/10.1016/S0143-974X(03)00106-8
[45] Giakoumelis G, Lam D. Axial capacity of circular concrete-filled tube columns. Journal of Constructional Steel Research. 2004 Jul 1;60(7):1049-68. https://doi.org/10.1016/j.jcsr.2003.10.001
[46] Younes SM, Ramadan HM, Mourad SA. Stiffening of short small-size circular composite steel-concrete columns with shear connectors. Journal of advanced research. 2016 May 1;7(3):525-38. https://doi.org/10.1016/j.jare.2015.08.001
[47] Hu HT, Huang CS, Chen ZL. Finite element analysis of CFT columns subjected to an axial compressive force and bending moment in combination. Journal of Constructional Steel Research. 2005 Dec 1;61(12):1692-712. https://doi.org/10.1016/j.jcsr.2005.05.002
[48] Zuo ZL, Cai J, Yang C, Chen QJ, Sun G. Axial load behavior of L-shaped CFT stub columns with binding bars. Engineering Structures. 2012 Apr 1;37:88-98. https://doi.org/10.1016/j.engstruct.2011.12.042
[49] Qiao Q, Li J, Mou B, Cao W. Axial compressive behavior of reinforced concrete-filled stainless steel tube (RCFSST) stub columns: Experimental research. Journal of Building Engineering. 2021 Dec 1;44:103431. https://doi.org/10.1016/j.jobe.2021.103431
[50] Wang Y, Chen G, Wan B, Han B, Ran J. Axial compressive behavior and confinement mechanism of circular FRP-steel tubed concrete stub columns. Composite Structures. 2021 Jan 15;256:113082. https://doi.org/10.1016/j.compstruct.2020.113082
[51] Naghipour M, Yousofizinsaz G, Shariati M. Experimental study on axial compressive behavior of welded built-up CFT stub columns made by cold-formed sections with different welding lines. Steel Compos. Struct. 2020 Jan 1;34(3):347.
[52] Wang Y, Cai G, Larbi AS, Waldmann D, Tsavdaridis KD, Ran J. Monotonic axial compressive behaviour and confinement mechanism of square CFRP-steel tube confined concrete. Engineering Structures. 2020 Aug 15;217:110802. https://doi.org/10.1016/j.engstruct.2020.110802
[53] Seangatith S, Thumrongvut J. Behaviors of square thin-walled steel tubed RC columns under direct axial compression on RC core. Procedia Engineering. 2011 Jan 1;14:513-20. https://doi.org/10.1016/j.proeng.2011.07.064
[54] Wang B, Liang J, Lu Z. Experimental investigation on seismic behavior of square CFT columns with different shear stud layout. Journal of Constructional Steel Research. 2019 Feb 1;153:130-8. https://doi.org/10.1016/j.jcsr.2018.10.004
[55] Chen B, Lai Z, Yan Q, Varma AH, Yu X. Experimental behavior and design of CFT-RC short columns subjected to concentric axial loading. Journal of Structural Engineering. 2017 Nov 1;143(11):04017148. https://doi.org/10.1061/(ASCE)ST.1943-541X.0001879
[56] Kim YC, Shahriyer H, Hu JW. Seismic Performance Evaluation According to HSS and CFST Columns of 3D Frame Buildings with Rubber Friction Bearing (RFB). Materials. 2022 Feb 9;15(4):1281. https://doi.org/10.3390/ma15041281
[57] Wang Q, Liu Y, Luo J, Lebet JP. Experimental study on stud shear connectors with large diameter and high strength. In2011 International Conference on Electric Technology and Civil Engineering (ICETCE) 2011 Apr 22 (pp. 340-343). IEEE. https://doi.org/10.1109/ICETCE.2011.5776113
[58] Loqman N, Safiee NA, Bakar NA, Nasir NA. Structural behavior of steel-concrete composite beam using bolted shear connectors: A review. InMATEC Web of Conferences 2018 (Vol. 203, p. 06010). EDP Sciences. https://doi.org/10.1051/matecconf/201820306010
[59] Kumar KS, Tamizhazhagan T. Design and Analysis of Steel Concrete Composite Beams by using Shear Connectors.

[60] Pardeshi RT, Patil YD. Review of various shear connectors in composite structures. Advanced Steel Construction. 2021 Dec 1;17(4):394-402.
[61] Raj PV. An analytical and experimental investigation of shear connectors in composite sections. International Research Journal of Engineering and Technology. 2017 June.

Research on Engineering Structures & Materials
journal homepage: http://www.jresm.org
Research Group

Research Article

Seismic performance analysis of RCC benchmark problem with magnetorheological damper

Benita Merlin Isabella Kennedy[1,2a], Joel Shelton Joseph[3,b], Arunraj Ebanesar[1,c], Daniel Cruze*[1,4,d]

[1]*Department of Civil Engineering, Karunya Institute of Technology and Sciences, Coimbatore, India*
[2]*Department of Civil Engineering, Nadar Saraswathi College of Engineering and Technology, Theni, India*
[3]*Department of Civil Engineering, RGM College of Engineering and Technology, Kurnool, India*
[4]*Department of Civil Engineering, Hindustan Institute of Technology and Science, India*

Article Info

Article history:

Received 21 May 2022
Revised 29 Aug 2022
Accepted 15 Oct 2022

Keywords:

Vibration control; Benchmark Buildings; MR Damper; Numerical Model; Damping

Abstract

Incorporation of the seismic response control system plays a vital role in structural engineering. Conventional method of structural design involves the higher flexibility and lower damping characteristics during the application of seismic loads which leads to inelastic deformation to an acceptable limit. Modern technique of seismic energy dissipation aims towards achieving stringent performance requirement. This paper aims towards analysis of structural response of the benchmark building with semi active damper namely magnetorheological damper. The magnetorheological damper work depends on the Structural Control Algorithm and Current input. G+5 Reinforced Concrete Building response is studied with a connection of large scale 200KN MR Damper (MRD) for three proposed numerical models, namely Kelvin Voight Model, Hyperbolic Tangent model and Maxwell Non-linear Slider model. The predictive ability of numerical models is analyzed for varying current. For simulating seismic application three earthquake data were considered, El Centro, Imperial Valley and Northridge. Numerical models of MR Damper are studied under varying current and exponential value. The comparison of displacement and base Shear of the structure response gives satisfactory response in the analysis.

1. Introduction

During Structural Control can be achieved through both internal damping and external damping. Vibration of the Structure occurs due to structural resonance, specific frequency at which the dynamic motion will get amplified. Amplification of dynamic motion can be reduced by adding effective energy dissipation device. Internal damping involves the joint damping, where external damping involves the active damping, passive damping. The phase between both passive damping and active damping is semi active damping. Semi active device plays a successful role during dynamic loading condition because of its dynamically varying property with a minimal amount of power [1]. Effective performance is expected to be offered by a semi active device over a variety of amplitude and frequency range. This paper presents the study of performance of the magnetorheological damper for various proposed numerical models under varying current and exponential value. Low voltage power will be required for the working of MR damper [2-3]. Optimum current shows better structural response reduction. By the application of MR damper to the structure, during the application of dynamic load, structural response such as displacement, acceleration and base shear can be reduced. The Hysteretic behaviour of MR

*Corresponding author: danielckarunya@gmail.com
[a] orcid.org/0000-0001-6404-7076; [b] orcid.org/0000-0002-1687-8059; [c] orcid.org/0000-0002-2455-2139; [d] orcid.org/0000-0002-4024-4742;
DOI: http://dx.doi.org/10.17515/resm2022.435ie0521

damper is a function of amplitude excitation and also depends on the current. Magnetorheological fluid is a non-Newtonian fluid with shear yield strength and the reaction of the fluid can be controlled by varying the Magnetic field condition and current [4]. Magnetorheological fluid shows significant changes in rheological property such as transition to semi solid state from free-flowing state. In case of pre-yield stage MR fluid shows viscoelastic behaviour and in case of post yield stage, it shows viscous Newtonian fluid [5]. To predict the performance of MR damper when connect to the structure under different magnetic field for the varying excitation appropriate method should be used. This involves the appropriate selection of numerical models for the modelling of MR damper [6]. The focus of the research to study the performance analysis of 200KN magnetorheological MR damper for seismic application under different numerical model condition. Even though passive devices, including base isolation, metallic friction damper, viscoelastic dampers are commercially successful in energy dissipation, control force in MR damper can be varied by appropriate adjustment in stiffness and damping characteristics [7]. Stiffness and other damping properties of MR damper will vary based on the numerical models proposed for MR damper. Three proposed numerical models used for modelling of large-scale MR dampers used in this study are Kelvin Voight model, Hyperbolic Tangent model, Maxwell Non-Linear slider model [8]. RD-8041-1 MR Damper has the stroke length of 55 mm and has the extended length till 208 mm. The body of the MR Damper is 42.1 mm and the shaft diameter is 10 mm. The maximum damping force is 2.45 kN at 1 Ampere current. The structure is analysed for a variable stiffness of MR damper. Variable stiffness and damping properties depend upon the numerical model in which one of the parameters current (I) plays a major role [9]. In the present research work, the analysis of the G+5 benchmark building with 200 kN capacity MR Damper for three proposed numerical model is investigated.

2. Structural Model

The structural model considered for study is a 6 storey RCC building. Damping ratio of the structure is considered as 5% for all modes and mode shape of the structure is shown in Fig. 4 and Fig. 5 [10]. Detail of the structure is shown in Table1. RCC Benchmark building is designed in accordance with Argentina code IC103. The total mass per floor is 1x106 kg. Youngs modulus of the concrete E=24,800Mpa, fundamental period T1 =0.374s. The seismic acceleration for Northridge has 1.82 g, El Centro has 0.15 g and Imperial Valley has 0.21 g. RCC Benchmark Building with MR Damper is shown in Fig. 1.

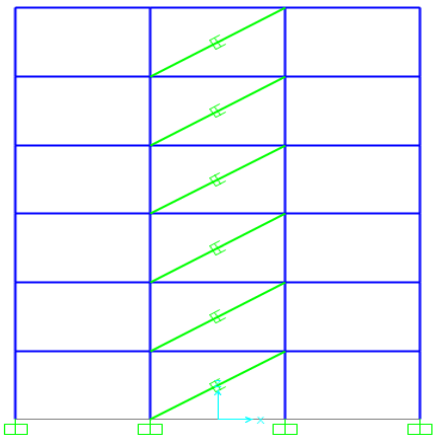

Fig. 1 RCC benchmark building with MR damper

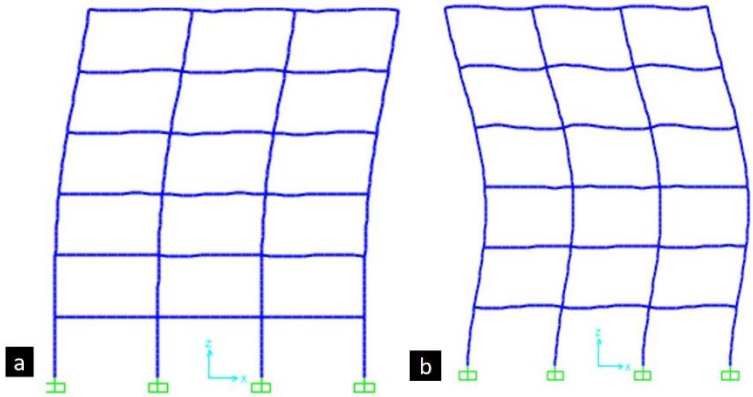

Fig. 2 Mode shapes of RC benchmark building (a) First mode shape (2.67Hz), (b) Second mode shape (7.69Hz)

Table 1 Structure details

SI.No	Design Data of 6 Storey Building	
1.	Structure type	RC
2.	Number of storey	G+5
3.	Storey height	3m
4.	Grade of concrete	M30
5.	Beam size (all stories)	0.25m x 0.45m
6.	Column 1 size (Exterior)	0.60m x 0.60m
7.	Column 2 size (Exterior)	0.55m x 0.55m
8.	Column 3 Size (Exterior)	0.50m x 0.50m
9.	Column 4 Size (Interior)	0.65m x 0.65m

3. Numerical Model of MR Damper

In order to define the significant properties of the MR damper in structural control problems, some numerical models have been proposed to describe the damping properties. High appropriate models selected for modelling of damper show higher accuracy in capturing Hysteretic response. Among all models, parametric models are found to be efficient in modelling of MR Damper [11]. Structure has been studied for three parametric models, namely Kelvin Voight model, Hyperbolic Tangent model, Maxwell Non-Linear Slider model.

3.1. Kelvin Voight Model

Kelvin – Voight model consist of spring and dash pot in parallel. It assumes strain in the spring and strain in dashpot to be same. Kelvin – Voight model is assumed to have no bending due to the parallel arrangement. The schematic diagram of the model is shown in Fig. 3

$$\sigma = E\varepsilon + \eta\dot{\varepsilon} \quad (1)$$

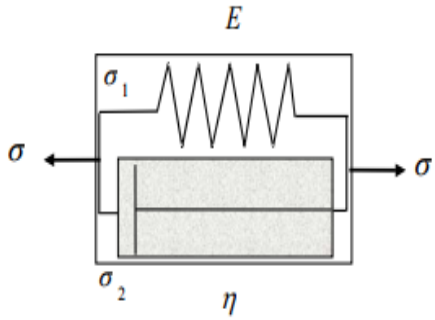

Fig. 3 Kelvin Voight Model

The stress and strain in mentioned in the equation as σ and ε. H is the viscosity of the material. In Magnetorheological damper modelled with Kelvin Voight model, there is a change in damping coefficient for different value of current input. Damping exponent changes show the higher potential of response reduction. When there is no change in damping exponent α, the response of the bare structure and the structure with MRD Kelvin Voight model are same. [12] On decreasing the exponent value to 0.1 MRD shows the seismic response reduction. Building shows 35% seismic response reduction when the magnetorheological damper is modelled with kelvin Voight model with lower exponential value is shown in Fig. 4.

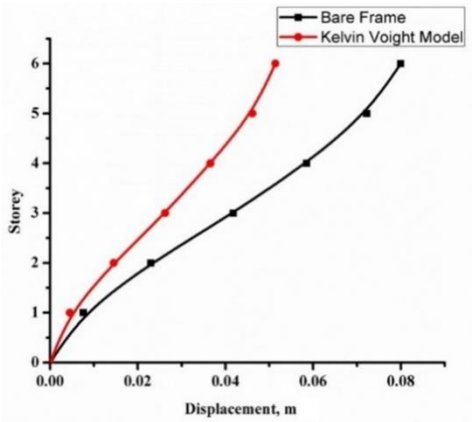

Fig. 4 Displacement distribution of Kelvin Voight and Bare frame model for El Centro 1940 earthquake

Damping Exponent is the parameter of the damper that decides the Force- Displacement graph of the damper. MRD KV model is analyzed for varying current and exponent. Potential of reponse reduction in displacement are found to be occurring in I=2A and α=0.1. Percentage of response reduction is found to be 35% in this condition is shown in Table 2.

Table 2. Comparison of maximum displacement of bare frame and Kelvin Voight model

Bare Frame (Displacement, mm)	Kelvin Voight Model MR Damper (Displacement, mm)
79.6mm	51.1mm

3.2. Hyperbolic Tangent Model

Hyperbolic Tangent model was a numerical model developed for ER Damper [13]. Damping behaviour includes both pre-yield and post yield behaviour shows in Fig. 5.

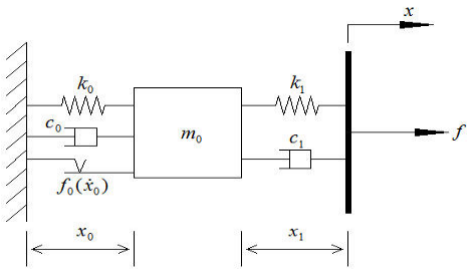

Fig. 5 Hyperbolic Tangent Model

The damping force of HPT (MRD) is given in equation (2) and (3)

$$f = C1(x - x0) + k1(x - x0) \quad (2)$$

$$m_0x_0 + (c_0 + c_1)\, x_0 + f_0 \tan h\,(x_0\, V_{ref}) = c_1x + k_1x \quad (3)$$

Where f = damping force; C0 and K0 are damping coefficient and stiffness at low velocity, C1 and K1 for higher velocity. f0 is the coefficient associated with the nonlinear friction element. Parameters of Hyperbolic Tangent Model is shown in Table 3.

Stiffness provided by the damper should be equal to the force required to resist the external excitation. When the damper possesses higher stiffness in the structure, during energy dissipation some energy will be stored in damper and it returns to the structure and cause structural oscillation. In case of higher stiffness, energy absorbed by the damper in return results in higher flexibility [14]. In Hyperbolic Tangent model when there is an increase in current, stiffness of the structure will decrease because in hyperbolic tangential model MR damper stiffness achieved in the low Ampere will be equal to the stiffness required for the damping force. MR Damper behaviour is studied under varying current from 0A to 2A. The response reduction of the structure is found to be occur in 0.5A. Analytical study shows that when the exponent value is gradually decreased to 0.1, results in a maximum displacement reduction at 0.5A. Story height divided by interstory displacement gives the interstory drift index.

Hyperbolic Tangent models shows 64% reduction in displacement at 0.5A for the exponential value of 0.5 and 76% reduction in displacement for the exponential value of 0.1 at 0.5A shows in Fig. 8 and Fig. 7. The comparison of displacement is shown in table 4, table 5 for α=0.5 and α=0.1.

Analytical results show that the drift reduction is found to be occurring at 1A and 0.5A in hyperbolic Tangent model shown in Fig. 8 and Fig. 11. [15] Drift is higher in the structure when the MRD is supplied with electrical source of higher ampere. Hence 0.5A current is taken as the optimum value for HPT MRD and is numerically compared with other models.

Table 3. Parameters of Hyperbolic Tangent Model

Parameters	Units
K0=(0.00001i4-0.00010i3+0.00013i2+0.00023i+0.00062)	kN/mm
K1= (-2.43069i4-23.75859i3-80.7025i2 +110.6199i+55.08)	kN/mm
C0= (-0.00979i4+0.09325i3-0.29955i2-0.3580i+0.1264)	kN.s/mm
C1= (0.00618 i4 -0.06726i3+0.2669i2-0.46060i+0.35673)	kN.s/mm
M0 = (0.00016i4- 0.00162i3+ 0.00548i2-0.00705i+ 0.00485)	kg
f 0 =1.51702 I4 -10.26630 i3 +2.79030i2 +94.55682i +6.19194	kN
Vref= 0.11574i4 +1.36241i3 -6.18813i2 +13.11819i +0.75927	mm/s

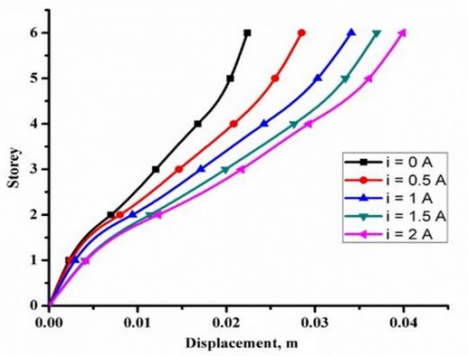

Fig. 6 Displacement distribution of Hyperbolic Tangent Model under varying current from 0A to 2A for the damping exponent (α=0.5)

Table 4. Comparison of maximum displacement of bare frame and Hyperbolic Tangent Model under varying current from 0A to 2A for the damping exponent (α=0.5)

Current	Bare Frame	0A	0.5A	1A	1.5A	2A
Displacement(mm)	79.6	22.3	28.6	34	37	39.5

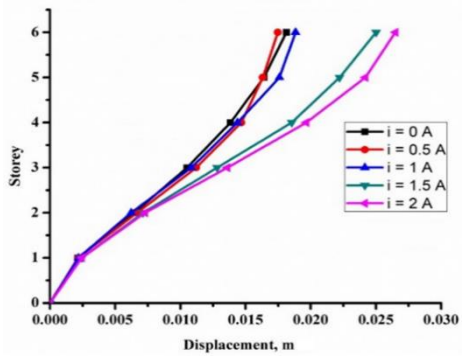

Fig. 7 Displacement distribution of Hyperbolic Tangent Model (HPT MRD) under varying current from 0A to 2A for the damping exponent (α=0.1)

Table 5. Comparison of maximum displacement of bare frame and Hyperbolic Tangent Model under varying current from 0A to 2A for the damping exponent (α=0.1)

Current	Bare Frame	0A	0.5A	1A	1.5A	2A
Displacement(mm)	79.6	18	16.5	18.9	25	26.6

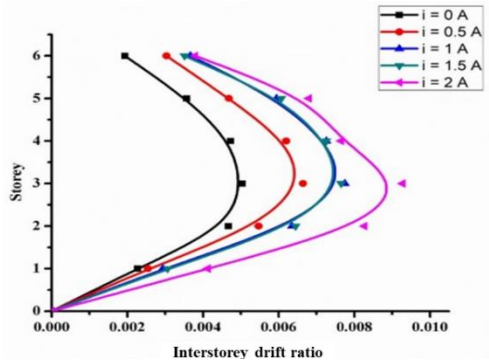

Fig. 8 Interstorey Drift distribution of Hyperbolic Tangent Model under varying current from 0A to 2A for the damping exponent (α=0.5)

3.3. Maxwell Nonlinear Slider Model

Models used for modelling of large scale MR Damper in practice are Bouc Wenn model, Hyperbolic Tangent model. Bouc Wenn model and Hyperbolic Tangent model parameters give a detail account about post yield behaviour of MRD [16]. When a MR Fluid undergoes shear deformation during seismic application, Shear thinning, and shear thickening will occurs [17]. Due to this inaccurate prediction of Damper force at higher velocities may occur. In MNS model parameters are identified for both pre yield and post yield behaviour of MR Damper, So that the response of MNS MRD can be evaluated separately for post yield and pre yield behaviour.

In Pre-Yield mode, Maxwell element with Dashpot and Spring Constant are used to determine the damper force.

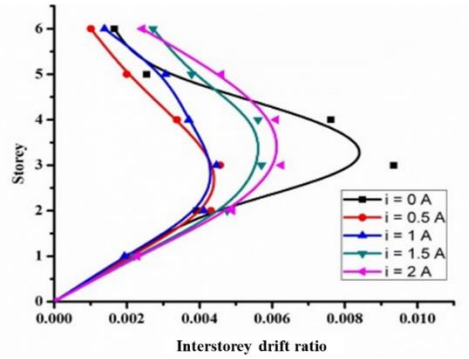

Fig. 9 Interstorey Drift distribution of Hyperbolic Tangent Model (HPT MRD) under varying current from 0A to 2A for the damping exponent (α=0.1)

$$f = k\,(y - z) = cz \tag{4}$$

Parameters of MNS MRD are calculated using the following equation;

$$c = \frac{1}{u_0 m}\frac{f_0^2 + f_m^2}{f_m} \tag{5}$$

$$k = \frac{1}{u_0}\frac{f_0^2 + f_m^2}{f_0} \tag{6}$$

K refers to spring constant and c indicate the dashpot constant. In Post Yield behaviour, shear thinning and shear thickening behaviour of non-Newtonian fluid are described based on Hershel – Bulkley visco plasticity theory [18]. Hershel bulkey model to describe quasi static behaviour and is found to be efficient comparing to other models used to describe the Non-Newtonian behaviour of MR Fluid under different modes shown in Fig. 10.

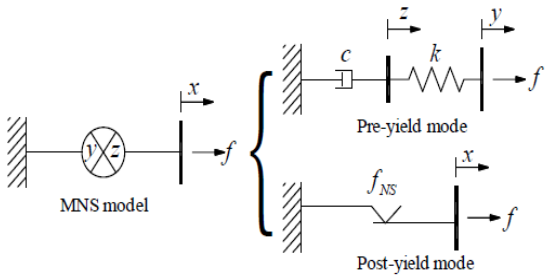

Fig. 10 Maxwell Non-Linear Slider Model

Comparing Displacement of the structure for varying current, it is found that displacement is reduced for 1A. Base shear is constant from 1A to 2A with little variation [19]. Analysis with MNS MR Damper performance shows that response reduction is higher when current varies from 1A to 2A and 1.5A shows more displacement when compared to 1A and 2A. (Fig. 11 and Fig .12).

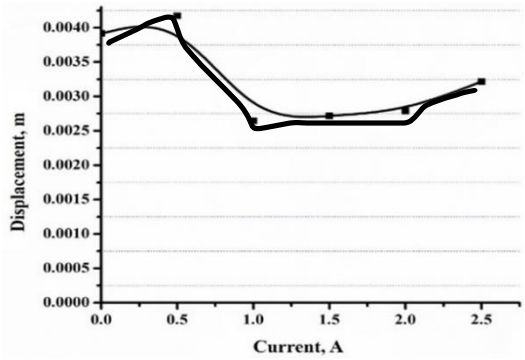

Fig. 11 Displacement distribution of Maxwell Non-Linear Slider Model under varying current from 0A to 2.5A

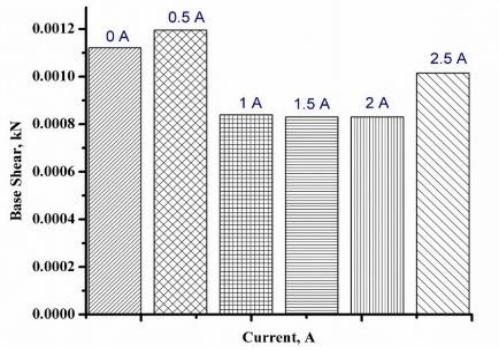

Fig. 12 Comparison of base shear using Maxwell Non-Linear Slider Model under varying current from 0A to 2.5A

4. Results and Discussion

The results are obtained in terms of displacement, Inter storey drift and Base shear for the RCC benchmark building. Time History Analysis using SAP 2000 is done for varying models of MRD for different ground motion data. Analysis results include the performance of MRD under three different numerical models Kelvin Voight model, Hyperbolic Tangent model and Maxwell nonlinear slider model [20]. Each model is analysed for varying current and exponential value. Each model shows good performance when the exponential value is varied according to the performance of MRD. Kelvin Voight model and Hyperbolic Tangent models show good performance when exponential value is reduced and Maxwell Nonlinear Slider model show response reduction in the exponential value of α=0.5.

4.1. Displacement

Table 6. Percentage of Reduction Displacement in Kelvin Voight, Hyperbolic Tangent, Maxwell Non-Linear Slider model compared with bare frame model for El Centro 1940 earthquake

Models	KV Model	HPT Model	MNS Model
% Reduction	35%	71%	79%

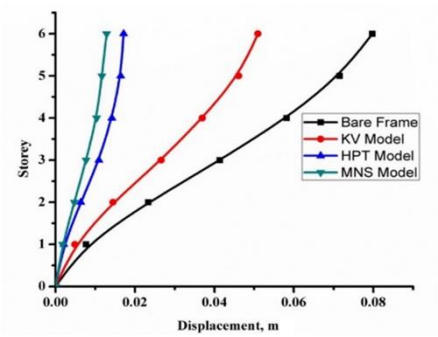

Fig. 13 Displacement distribution of Kelvin Voight, Hyperbolic Tangent, Maxwell Non-Linear Slider and Bare frame model for El Centro 1940 earthquake

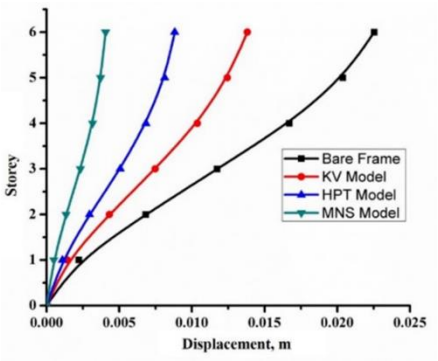

Fig. 14 Displacement distribution of Kelvin Voight, Hyperbolic Tangent, Maxwell Non-Linear Slider and Bare frame model for Northridge earthquake

Table 7. Percentage of Reduction Displacement in Kelvin Voight, Hyperbolic Tangent, Maxwell Non-Linear Slider model compared with bare frame model for Northridge earthquake

Models	KV Model	HPT Model	MNS Model
% Reduction	38%	61%	78%

Lateral Displacement of G+5 RCC Building shows better performance with MRD compared to bare frame for varying ground motion shows in Fig. 15, Fig. 16 and Fig. 17. For Elcentro ground motion, displacement percentage reduction of KV model, HPT model and MNS each model is 35%, 71%, 79% respectively. During Seismic application of Northridge MRD shows 38%, 61% and 79% and Imperial Valley 20.36%, 49% and 69% for KV model, HPT model and MNS model respectively shown in table 6, table 7, table 8.

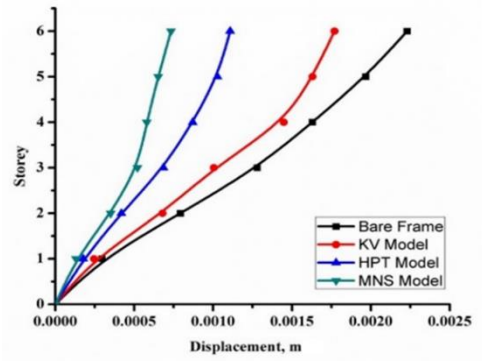

Fig. 15 Displacement distribution of Kelvin Voight, Hyperbolic Tangent, Maxwell Non-Linear Slider and Bare frame model for Imperial Valley earthquake

Table 8. Percentage of Reduction Displacement in Kelvin Voight, Hyperbolic Tangent, Maxwell Non-Linear Slider model compared with bare frame model for Imperial Valley earthquake

Models	KV Model	HPT Model	MNS Model
% Reduction	20.36%	49%	69%

4.2. Inter Storey Drift

This paper presents the study of inter storey drift of G+5 RCC Building with and without MRD. Story Drift of structure with MRD under three models for optimum current is analysed and studied.

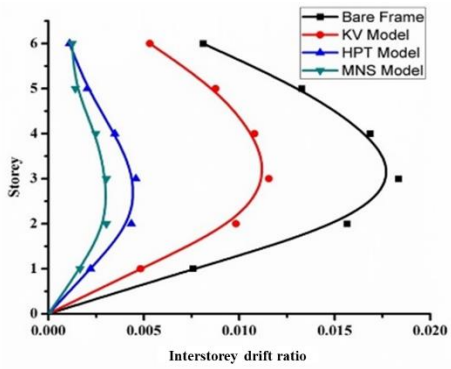

Fig. 16 Distribution of interstorey drift ratio of Kelvin Voight, Hyperbolic Tangent, Maxwell Non-Linear Slider and Bare frame model for El Centro 1940 earthquake

Comparative analysis of the storey drift for models of MRD shows MNS model and HPT model show maximum reduction in drift of the structure. All three model shows the drift within the limit. Kelvin Voight model shows least response reduction compared to other two models shown in Fig. 18, Fig. 19 and Fig. 20.

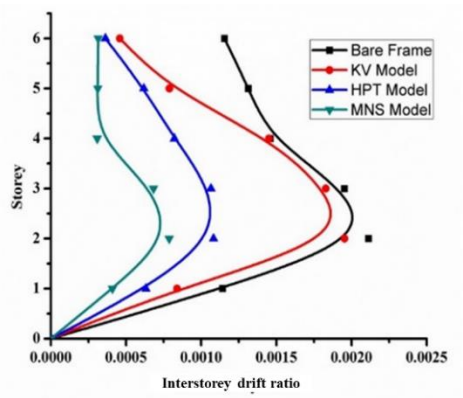

Fig. 17 Distribution of interstorey drift ratio of Kelvin Voight, Hyperbolic Tangent, Maxwell Non-Linear Slider and Bare frame model for Imperial Valley earthquake

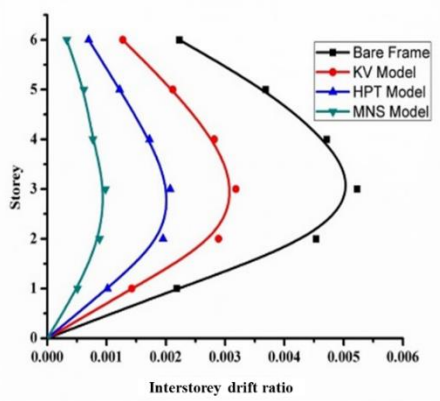

Fig. 18 Distribution of interstorey drift ratio of Kelvin Voight, Hyperbolic Tangent, Maxwell Non-Linear Slider and Bare frame model for Northridge earthquake

4.3. Base Shear

Base shear is the maximum lateral force occurs at the base of the building. Base shear maxima or minima will depend upon the soil condition, fixidity condition, probability of ground motion, ductility, strength and weight of the building and natural period. When the natural period of the structure is higher, flexibility of the structure will be also higher. Flexible structure will experience low acceleration compared to stiffer building [21-22]. When the flexibility of the structure is increased it will show low base shear compared to stiffer building. At the same time flexibility of the structure should be within limit to reduce the lateral displacement of the structure. MRD shows good performance in both displacement reduction and base shear reduction with lower lateral displacement.

For El Centro 1940 all three models shows response reduction in base shear with least lateral displacement. Percentage of Base shear reduction for El Centro 1940 is 28%, 56%, 61% respectively for KV model, HPT model and MNS model respectively. MRD under the application of Imperial valley and Northridge shows 62%, 68%, 81% and 28%, 56% and 81% for KV model, HPT model and MNS model respectively shown in Fig. 22, Fig. 23 and Fig. 24. Among all models MNS show higher potential of response reduction shown in table 9, table 10 and table 11 [23-25].

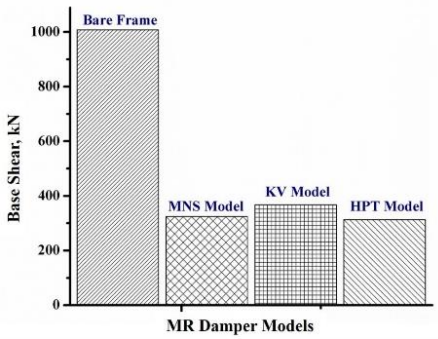

Fig. 19 Base shear comparison of Kelvin Voight, Hyperbolic Tangent, Maxwell Non-Linear Slider and Bare frame model for El Centro 1940 earthquake

Table 9. Percentage reduction of base shear in Kelvin Voight, Hyperbolic Tangent, Maxwell Non-Linear Slider model compared with bare frame model for El Centro 1940 earthquake

Models	KV Model	HPT Model	MNS Model
% Reduction	28%	56%	61%

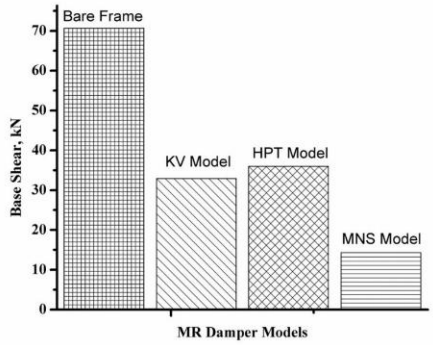

Fig. 20 Base shear comparison of Kelvin Voight, Hyperbolic Tangent, Maxwell Non-Linear Slider and Bare frame model for Imperial Valley earthquake

Table 10. Percentage reduction of base shear in Kelvin Voight, Hyperbolic Tangent, Maxwell Non-Linear Slider model compared with bare frame model for Imperial Valley earthquake

Models	KV Model	PT Model	MNS Model
% Reduction	62%	68%	81%

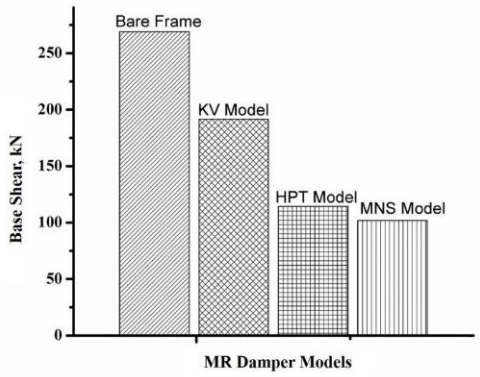

Fig. 21 Base shear comparison of Kelvin Voight, Hyperbolic Tangent, Maxwell Non-Linear Slider and Bare frame model for Northridge earthquake

Table 11. Percentage reduction of base shear in Kelvin Voight, Hyperbolic Tangent, Maxwell Non-Linear Slider model compared with bare frame model for Northridge earthquake

Models	KV Model	PT Model	MNS Model
% Reduction	28%	56%	61%

5. Conclusions

The results show that the response of the structure is reduced in higher percentage when it relates to magnetorheological damper. The Large scale 200KN MR Damper (MRD) for three proposed numerical models were investigated. For various currents and various earthquakes numerical models were analyzed. Numerical models of MR Damper are studied under varying current and exponential value. Parameters were studied using SAP2000 software which involves displacement, base Shear, and interstorey drift.

- In Kelvin Voight model reduction in damping property such as damping exponential shows the response reduction where the higher damping exponential shows no response reduction.
- In Hyperbolic Tangent model even with low exponential value, increase in current shows lower stiffness. Reduction in displacement and other seismic response parameter found to be occur under limit at 0.5A.
- In Maxwell Non-Linear slider model response reduction is found to be higher at the value of 1A to 2A, where 1A shows maximum reduction.
- Each Parametric model shows variation in response reduction based on the variation in excitation.
- G+5 RCC building shows maximum response reduction when connected with MRD modelled with MNS model.
- Base Shear of MNS and HPT are more or less equal for Elcentro earthquake input Data.
- Base Shear of HPT MRD is higher than the other two models for Imperial Valley input data.
- The reduction in base shear El Centro seismic excitation is 28%, 56%, 61% respectively for KV model, HPT model and MNS model respectively.

- For the seismic excitation of Imperial valley and Northridge shows 62%, 68%, 81% and 28%, 56% and 81% for KV model, HPT model and MNS model.
- This result helps the research working on MR Damper to select the model for their analytical investigation
- The future work can be extended for steel buildings subjected to various earthquakes with self-powered MR Damper configuration and optimal positioning of MR Damper

Acknowledgement

The authors thank Karunya Institute of Technology and Sciences, Coimbatore, Tamilnadu, India for their constant support. We also extend our acknowledgement to the Department of Science and Technology (Grant No: DST/TSG/STS/2015/30-G).

References

[1] Dyke SJ, Spencer BF, Sain MK, Carlson JD. Modeling and control of magnetorheological dampers for seismic response reduction. Smart Materials and Structures, 1996; 5:5 565-575. https://doi.org/10.1088/0964-1726/5/5/006

[2] Jiang Z, Christenson R. A comparison of 200 kN magneto-rheological damper models for use in real-time hybrid simulation pretesting. Smart Materials and Structures, 2011; 20:6. https://doi.org/10.1088/0964-1726/20/6/065011

[3] Jiang Z, Christenson RE. A fully dynamic magneto-rheological fluid damper model. Smart Materials and Structures, 2012; 21:6. https://doi.org/10.1088/0964-1726/21/6/065002

[4] Kim J, Lee S, Min KW. Design of MR dampers to prevent progressive collapse of moment frames. Structural Engineering and Mechanics, 2014; 52:2 291-306. https://doi.org/10.12989/sem.2014.52.2.291

[5] Lavan O, Levy R. Optimal design of supplemental viscous dampers for linear framed structures. Earthquake Engineering and Structural Dynamics, 2006; 35:3 337-356. https://doi.org/10.1002/eqe.524

[6] Lee SK, Lee SH, Min KW, Moon BW, Youn K, Hwang J. Performance evaluation of an MR damper in building structures considering soil-structure interaction effects. The Structural Design of Tall and Special Buildings, 2009; 18:1 105-115. https://doi.org/10.1002/tal.430

[7] Rodríguez A, Iwata N, Ikhouane F, Rodellar J. Model identification of a large-scale magnetorheological fluid damper. Smart Materials and Structures, 2009; 18:1. https://doi.org/10.1088/0964-1726/18/1/015010

[8] Sapiński B, Filuś J. Analysis of parametric models of MR linear damper. Journal of Theoretical and Applied Mechanics, 2003; 41:2 215-240.

[9] Soong TT, Spencer BF. Supplemental energy dissipation: state-of-the-art and state-of-the- practice. Engineering Structures, 2002; 24:3 243-259. https://doi.org/10.1016/S0141-0296(01)00092-X

[10] Caterino N. Semi-active control of a wind turbine via magnetorheological dampers. Journal of Sound and Vibration, 2015; 345, 1-17. https://doi.org/10.1016/j.jsv.2015.01.022

[11] Spencer BF, Carlson JD, Sain MK, Yang G. On the current status of magnetorheological dampers: seismic protection of full-scale structures. In Proceedings of the 1997 American Control Conference (Cat. No.97CH36041) (pp. 458-462 vol.1). https://doi.org/10.1109/ACC.1997.611840

[12] Strecker Z, Roupec J, Mazurek I, Machacek O, Kubik M, Klapka M. Design of magnetorheological damper with short time response. Journal of Intelligent Material Systems and Structures, 2015; 26:14 1951-1958. https://doi.org/10.1177/1045389X15591381

[13] Vafaee MH, Saffari H. A modal shear-based pushover procedure for estimating the seismic demands of tall building structures. Soil Dynamics and Earthquake Engineering, 2017; 92: 95-108. https://doi.org/10.1016/j.soildyn.2016.09.033
[14] Wang DH, Liao WH. Magnetorheological fluid dampers: a review of parametric modelling. Smart materials and structures, 2011; 20:2 023001. https://doi.org/10.1088/0964-1726/20/2/023001
[15] Yang G, Spencer BF, Carlson JD, Sain MK. Large-scale MR fluid dampers: Modeling and dynamic performance considerations. Engineering Structures, 2002; 24:3 309-323. https://doi.org/10.1016/S0141-0296(01)00097-9
[16] Yang MG, Chen ZQ, Hua XG. An experimental study on using MR damper to mitigate longitudinal seismic response of a suspension bridge. Soil Dynamics and Earthquake Engineering, 2011; 31:8 1171-1181. https://doi.org/10.1016/j.soildyn.2011.04.006
[17] Junhui L, Duo W, An DJ, Hu H, Yang X, Wenhui Z. Structural design and control of a small-MRF damper under 50 N soft-landing applications. IEEE Trans. Industr. Inf, 2015; 11:3 612-619. https://doi.org/10.1109/TII.2015.2413353
[18] Yi WJ, He QF, Xiao Y, Kunnath SK. Experimental Study on Progressive Collapse-Resistant Behavior of Reinforced Concrete Frame Structures. ACI Structural Journal, 2008; 105:4 433-439. https://doi.org/10.14359/19857
[19] Asghar Maddah A, Hojjat Y, Reza Karafi M, Reza Ashory M. Reduction of magneto rheological dampers stiffness by incorporating of an eddy current damper. Journal of Sound and Vibration, 2017; 396: 51-68. https://doi.org/10.1016/j.jsv.2017.02.011
[20] Choi KM, Cho SW, Jung HJ, Lee IW. Semi-active fuzzy control for seismic response reduction using magnetorheological dampers. Earthquake engineering & structural dynamics, 2004; 33:6 723-736. https://doi.org/10.1002/eqe.372
[21] Ding Y, Zhang L, Zhu HT, Li ZX. A new magnetorheological damper for seismic control. Smart Materials and Structures, 2013; 22:11 115003. https://doi.org/10.1088/0964-1726/22/11/115003
[22] Kciuk S, Turczyn R, Kciuk M. Experimental and numerical studies of MR damper with prototype magnetorheological fluid. Journal of Achievements in Materials and Manufacturing Engineering, 2010; 39:1 52-59.
[23] Wróbel JK, Cortez R, Fauci L. Modeling viscoelastic networks in Stokes flow. Physics of Fluids, 2014; 26:11 388-391. https://doi.org/10.1063/1.4900941
[24] Gonenli C, Das O. Effect of crack location on buckling and dynamic stability in plate frame structures. J Braz. Soc. Mech. Sci. Eng. 2021; 43: 311. https://doi.org/10.1007/s40430-021-03032-2
[25] Das O, Ozturk, H, Gonenli C. Finite element vibration analysis of laminated composite parabolic thick plate frames. Steel and Composite Structures, 2020; 35:1 43-59.

Research on Engineering Structures Materials

Content

Research Group